Series in BioEngineering

Gurbinder Kaur

Bioactive Glasses

Potential Biomaterials for Future Therapy

Springer

Series in BioEngineering

More information about this series at http://www.springer.com/series/10358

Gurbinder Kaur

Bioactive Glasses

Potential Biomaterials for Future Therapy

Springer

Gurbinder Kaur
School of Physics and Materials Science
(SPMS)
Thapar University
Patiala
India

ISSN 2196-8861 ISSN 2196-887X (electronic)
Series in BioEngineering
ISBN 978-3-319-45715-4 ISBN 978-3-319-45716-1 (eBook)
DOI 10.1007/978-3-319-45716-1

Library of Congress Control Number: 2016949628

Printed on acid-free paper

This Springer imprint is published by Springer Nature
The registered company is Springer International Publishing AG
The registered company address is: Gewerbestrasse 11, 6330 Cham, Switzerland

A Dedication to Dr. Larry Hench (The man who revolutionized the medical science)

Acknowledgments

During my journey of book writing, there are many people, who have knowingly and unknowingly helped me in the successful completion of this project. At this overwhelming moment of accomplishment, first of all I am indebted to **Dr. O. P. Pandey, Dr. B. Chudasama, Dr. Gary Pickrell, Dr. Kulvir Singh, and Dr. N. Sriranganathan** whose understanding, encouragement and personal attention have always provided decisive and energetic support. **Dr. Pandey** was the one who stood by me during my struggling days and is among one of the strongest pillars of my career. Without his support, I would have never been able to accomplish most of the milestones of my career. I have never seen a dedicated and hard working supervisor like **Dr. Chudasama** who can come forward for his students all the time and never leave any stone unturned so as to make them reach the zenith. **Dr. Singh** has given rational freedom to his students so that they can add wings to their imagination. **Dr. Gary Pickrell and Dr. N. Sriranganathan**, provided the most conducive and comfortable environment to me during my stay in USA and are superb mentors. I am short of for all of them as they are indispensable part of my journey and cannot be amputated. I feel honored to be able to work as a Post-Doc under such talented supervisors who have big soul to accommodate every aspect of their students. Their diligence, persistence and vitality is highly admirable.

All the faculties and staff of Physics Department (Guru nanak Dev University), SPMS (Thapar University) and MSE (Virginia Tech, USA) are acknowledged who never turned me down whenever I approached for any help. I cannot forget the support provided by **Dr. S.S. Sekhon**, during the toughest phase of my life. His motivation and zeal for hard work has enlightened my path always.

This book gradually emerged amid the friendships that provided their most lasting lessons. It is a pleasure to mention my good friends especially from **Functional materials lab and Ceramic Research lab**, who made my working atmosphere very conducive.

Finally my most personal source of gratitude is my husband, my true soulmate **Dr. Vishal Kumar** who is my enduring strength. Thanks for erasing the word nightmare from the dictionary of my life. During every downhill of my life, he was

the one who lifted up my spirits and helped me in innumerable ways. It is only and only due to him that I could put lot of working hours tirelessly. Honestly, he sheltered me through every thick and thin situation and took the entire burden off my shoulders. He was full of patience and support during the time when my work schedule became too hectic. This book would not have been possible at all without him. He was more concerned about my important schedules and kept on reminding me about it along with my diet chart!

Dear mom and dad, I have let so many years pass without thanking you both. But you haven't let a single second pass without loving me unconditionally. I am highly thankful to my **parents-in-law and parents** for their support, encouragement, care, understanding and creation of a pleasant atmosphere for me. Especially my father-in-law **Sh. Surinder Kumar** and my father **Sh. Harbhajan Singh**, the strong pillars of my career have always motivated me to fly high and change the dreams into realities. I am very lucky to have wonderful in-laws family for whom I am more of a daughter. I doubt that I will ever be able to convey my appreciation fully, but I owe them my eternal gratitude.

Besides this, above all, thanks to the **almighty** beneath the blue sky for bestowing me with his precious blessings! With every passing day, I start believing in you more and more as you have filled my life with wonderful things, which I could never ever think about. Thanks for protecting me, sheltering me and blessing me in the best ways!!

Dr. Gurbinder Kaur

Contents

About the Author and Contributors

About the Author

Dr. Gurbinder Kaur holds her B.Sc (Hons. Physics) and M.Sc. (Hons. Physics) from Guru Nanak Dev University, Amritsar. Dr. Gurbinder began her teaching career at D.A.V. College, Amritsar, where she taught from 2004 to 2005. Her second academic appointment was at RR Bawa DAV college, Batala where she served as Head of the Physics Department from 2005-2009. Then she moved to Thapar University, Patiala to pursue her research work in the field of solid oxide fuel cells (SOFC) and received her doctorate in 2012. Her Ph.D dissertation was based on "Investigations on interfacial interaction of glass sealants with electrolytes and interconnect for solid oxide fuel cells (SOFC)." She published more than 45 research papers in the field of Materials Science. She has two other books on "Solid Oxide Fuel Cell Components: Interfacial compatibility of SOFC glass seals" (Springer, NY) and "Modern Physics" by McGraw Hill Pvt. Ltd. She also carried her research in the field of Biomedical Enginnering and Bioglasses. She is recipient of fellowship under the RFSMS scheme of University Grants Commission (UGC). She also received fellowship under Women-Scientist Scheme, DST, New Delhi from 2010-2012. After completing her Doctorate, she moved to Virginia Tech, USA to work as a Post-Doctoral Fellow with Dr. Gary Pickrell. She is a recipient of Post-doc Scholarship from UGC, New Delhi for pursuing research work in the field of bioglasses. She works on a variety of different materials and applications including high temperature energy materials, bioactive materials and optical materials.

Contributors

Dr. J.C. Mauro Senior Research Manager, Science and Technology Division, Corning Incorporated, Corning, New York, USA

Dr. V. Kumar Assistant Professor, Sri Guru Granth Sahib World University, FatehGarh Sahib, Punjab, India

Dr. G. Pickrell Professor, Materials Science and Engineering, Virginia Tech, Blacksburg, VA-24060, USA

Dr. N. Sriranganathan Professor, Department of Biomedical Sciences and Pathobiology, Virginia Tech, Blacksburg, VA-24060, USA

Dr. S.G. Waldrop Department of Biomedical Sciences and Pathobiology, VirginiaTech, Blacksburg, VA-24060, USA

Abbreviations

ADSCs	Adipose-derived stem cells
ALP	Alkaline phosphate activity
AMS	Absorbable metal stents
APTT	Activated partial thromboplastin time
BAEC	Bovine aortic endothelial cells
BCP	Biphasic calcium phosphate
bFGF	Basic fibroblast growth factor
BGC	Bioactive glass-ceramic
BM	Biodegradable metals
BMG	Bulk metallic glasses
BMPs	Bone morphogenetic proteins
BMUs	Basic multicellular units
BSA	Bovine serum albumin
CAD/CAM	Computer-aided design and manufacturing
CAM	Chorioallantoic membrane
CDHAp	Calcium-deficient hydroxyapatite
CEC	Cyclic extrusion and compression
CFA	Fluoride-containing apatite
CHA	Carbonate hydroxyapatite
CLSM	Confocal laser scanning microscopy
CMHAS	Carboxymethyl high amylose starch
CMS	Carboxymethyl starch
CPCs	Calcium phosphate ceramics
CPPD	Calcium pyrophosphate dihydrate
CPSs	Calcium phosphate cements
CTE	Coefficient of thermal expansion
CVD	Chemical vapor deposition
DCP	Dicalcium phosphate
DCPA	Dicalcium phosphate anhydrous
DCPD	Dicalcium phosphate dehydrate

DNA	Deoxyribonucleic acid
ECAP	Equal channel angular pressing
ECM	Extracellular cellular matrix
ELISA	Enzyme-linked immunosorbent assay
ELPs	Elastin-like polypeptides
ETM	Early transition metal
FAp	Fluorapatite
FGF	Fibroblast growth faction
FGF-2	Fibroblast growth factor-2
FHA	Fluoridated hydroxyapatite
GFA	Glass-forming ability
HA	Hydroxyapatite
HAECs	Human aortic endothelial cells
HAp	Hydroxyapatite
HASMCs	Human aortic smooth muscle cells
HBSS	Hank's balanced salt solution
HCA	Hydroxyl carbonate apatite
hESCs	Human embryonic stem cells
hFOBs	Human fetal osteoblastic cells
hGH	Human growth hormone
HIF-1α	Hypoxia inducible factor-1
HMVEC	Micro-vascular endothelial cells
HPLC	High-performance liquid chromatography
HPT	High-pressure torsion
HUVECs	Human umbilical vein endothelial cells
IBBC	Interface bioactive bone cement
ITT	Inverse temperature transition
LCST	Lower critical solution temperature
LDI	Lysine diisocyanate
L-PGA	Poly (L-glutamic Acid)
LTM	Late transition metal
MAO	Micro-arc oxidation
MAPK	Mitogen-activated protein kinase
MBCP	Macroporous biphasic calcium phosphate
MBG	Mesoporous bioactive glass
MCL	Medium chain length
MCPA	Monocalcium phosphate anyhydrous
MCPM	Monocalcium phosphate monohydrate
MMC	Mitomycin C
MMP	Matrix metallic proteinase
NCA	N-carboxyanhydride
OCP	Octacalcium phosphate
OXA/OAp	Oxyapatite
PAA	Polyaspartic acid
PBLG	Poly (γ-benzyl-L-glutamate)

PBT	Polybutylene terephthalate
PCEP	Poly[bis(carboxyethyl-phenoxy) phosphazene]
PCL	Poly-ε-caprolactone
PCPP	Poly [bis(carboxyphenoxy) phosphazene]
[PCPPSA]	Poly [(Carboxy phenoxy propane-sebacic acid)]
PDGF-BB	Platelet-derived growth factor
PDLA	Poly D,L-lactide
PDLLA	Poly (D,L lactic acid)
PDMS	Polydimethylsiloxane
PDP	Polydepsipeptides
PDS, PDO	Polydioxanone
PE	Polyethylene
PEA	Polyesteramides
PEG	Polyethylene glycol
PEG, PEO	Poly(ethylene oxide)
PGA	Poly(glycolic acid)
PHA	Poly(hydroxyl alkanote)
PHBV	3-hydroxyvalerate
PHBV	Polyhydroxybutyrates
PHEA	Poly(N-2 hydroxy ethyl)-D,L aspartamide
PHEMA	Poly(hydroxyl ethyl methacrylate)
PIIID	Plasma immersion ion implantation and deposition
PLA	Poly(lactic acid)
PLCL	Poly(L-lactide/ε-caprolactone)
PLF	Poly(lactide-co-ethylphosphate)
PLGA	Poly(lactic-co-glycolic acid)
PLLA	Poly(L-lactide)
PMMA	Poly(methylmethacrylate)
PNIPAM	Poly(N-isopropylacrylamide)
POE	Poly(ortho esters)
PP	Polypropylene
PPE	Polyphosphoester
PPF	Poly(propylene fumarate)
PPy	Polypyrrole
PRP	Platelet-rich plasma
PS	Polysulfone
PT	Prothrombin time
PTA	Transluminal angioplasty
PTFE	Polytetrafluoroethylene
PVA	Polyvinyl alcohol
PVDF	Poly(vinylidene fluoride)
rhBMP-2	Recombinant human bone morphogenic protein-2
RNA	Ribonucleic acid
RS	Rapid solidification
SBF	Simulated body fluid

SCL	Short-chain length
SNALPs	Stable nucleic acid lipid particles
SPS	Spark plasma system
STZ	Shear transformation zone
TEOS	Tetraethylorthosilane
TGF-3	Transforming growth factor beta-3
TGF β-1	Transforming growth factor beta-1
TGF-β	Transforming growth factor-β
THA	Total hip arthroplasty
TSS	Two-step sintering
TTCP	Tetracalcium phosphate
UHMWPE	Ultra-high molecular weight polyethylene
VEGF	Vascular endothelial growth factor
VIC	Valvular interstitial cell proliferation
β-TCP	Tricalcium phosphate
γ-PGA	Poly-γ-glutamic acid

Chapter 1
Biomaterials Influencing Human Lives

Gurbinder Kaur

Biomaterial development has influenced human lives to a large extent by its versatile medical applications and very promising future. The field of biomaterials has been experiencing steady and strong growth as large number of pharmaceutical firms and manufacturer companies are investing in the production and development of new commercialized biomaterial products. The biomaterials are designed in a way to prevent biological rejection, least interaction with the biology of host, adequate mechanical strength, and ability to undergo biodegradation over a period of time. There are certain imperative parameters, which every biomaterial needs to fulfill for its implementation as a vital replacement for human organs. This chapter would list the importance, requirements, and applications of the biomaterials.

1.1 Understanding 'Biomaterial'

'Biomaterial' is non-vital material with unique properties such as cytocompatibility, biodegradation, bioactivity, adequate mechanical strength, and osteoinduction/osteogenesis/osteoconduction capability. The biomaterial industry is dominating the market for medical applications as $\sim$42 billion dollars expenditure has been done on the biomaterials with an expected growth rate of $\sim$15–18 % over the next years. The reason behind this large industry is their impact on improving human life quality. The life expectancies of the aged people have increased because biomaterials have opened a range of medical devices for limb replacements, skin, dentures, artificial arteries, mechanical heart valves, nerve guidance tube, stents, and pacemaker. With the aging, a strong need for the repair/replacement of hard and soft tissues along with the uninterrupted function for long term is there. After the revolution of molecular biology in 1970s, combined with the advancing proteomics and genomics, biomaterials design and functioning have opened a new pathway for the medical science. Over the past decades, biomaterials have been the most

G. Kaur, *Bioactive Glasses*, Series in BioEngineering,
DOI 10.1007/978-3-319-45716-1_1

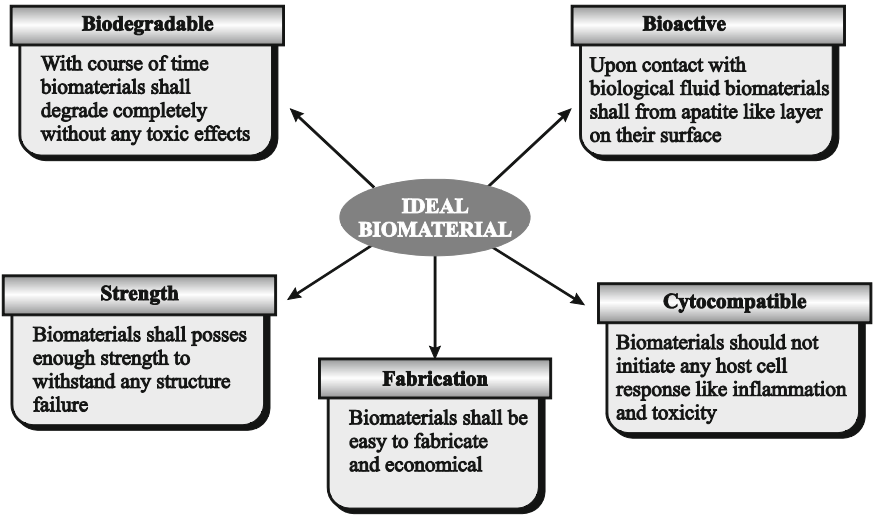

Fig. 1.1 Requirements for the potential biomaterials

sought-after objective for the academician, research and development professionals and industries. Figure 1.1 portrays the requirements for the biomaterials to be used for various medical applications.

Biological system designing has been one of the most challenging fields due to their stringent requirements (as mentioned in Fig. 1.1) to be fulfilled. The biomaterial development also requires the exposure to multidisciplinary sciences such as mechanics, chemistry, materials science, biology, medicine, surface science, and bioengineering. In addition to this, the effort and input of various government agencies and research & development organizations have promoted the biomedical/biomaterial sciences.

1.2 Categories of Biomaterials

The first generation biomaterials were developed in 1960s and 1970s, whose main aim was to accomplish desired amalgam of physical and chemical properties to match as that of the host tissue (with minimum or no cytotoxic response). The main motto for designing this era biomaterials was ‘inertness’ to avoid any biological rejection and foreign body reaction. During 1980–1990, the emphasis of research shifted toward the development of bioactive materials, which could elicit biological response at biomaterial/host interface. Over the course of time, biomaterials have been indispensable part for various applications in dental restorations, cardiovascular stents/valves, and orthopedics. Last 10 years have been a revolutionary period

for the development of biomaterials as the progress of molecular biology laid a strong foundation for understanding the concepts such as biocompatibility, degradation kinetics, and synthesis techniques. Present decade is witnessing the biomimetic/smart biomaterials, which mimic nature's hierarchial structures. The conventional biomaterials can be categorized into four categories, all with their merits and demerits are discussed in the preceding sections.

1.2.1 Polymers

The polymers constitute an important class of biomaterials. The structure property, chemistry composition, porosity, and degradation rate of polymers are the common deciding factors for their respective applications. The polymers find suitability for drug delivery, bone replacement, fracture fixation, extracellular matrix mimickers, and cartilage repair. Polymers can be synthetic or natural, i.e., natural polymers consist of collagen, chitosan, alginates, polysaccharides, albumin, elastin, and polyamino acids, whereas synthetic polymers consist of polymethylmethacrylate (PMMA), polyethylene (PE), polyurethanes, polyanhydrides, poly(orthoesters), poly(esteramide), poly(glycolic acid) (PGA), and poly(lactic-*co*-glycolic acid) (PLGA). For orthopedic and dental surgery, acrylic bone cements, polylactides, PGA, and polyhydroxybutyrates (PHBV) find potential applications. Highly cross-linked polyethylene (HXLPE) and ultra high molecular weight polyethylene (UHMWPE) pass low friction and high impact strength making them apt for the knee inserts and acetabular livers. US food and drugs administration (US-FDA) has approved various polymers such as PGA, poly-ε-caprolactone (PCL), PLGA, PMMA, and UHMWPE for their safe use in the human body. Polymers are rapid-degrading materials; hence their degradation rates need to be adjusted by incorporating filler materials into polymer matrix. There are various steps involved during polymer–tissue interaction and are depicted in Fig. 1.2.

Tissue reaction may be observed when polymers come in contact with the immunoactive sites. The reaction may include osteolysis, steriles drainage, or osteolytic lesions. Non-degradable polymers such as polyethylene, polypropylene, polyvinyl alcohol (PVA), poly(*N*-isopropylacrylamide) (PNIPAM), and polytetrafluoroethylene (PTFE) find their potential role in orthopedic applications. Polypropylene is a methylated version of polyethylene and is used for load-bearing applications, molar/mandibular reconstructions, and repair of ventral incisional hernia. PVA is one of the first polymers to be used as artificial cartilage because it can retain high water content as that of cartilage. PNIPAM has feature to undergo reversible temperature transition and this change in temperature makes it excellent drug delivery vehicle. PTFE possesses hydrophobic and lipophobic character and therefore used in orthopedic devices and dental restoration materials. The biodegradable nature polymers like alginates chitosan have yielded promising results for chondrocyte proliferation. Chitosan minimizes foreign body reactions

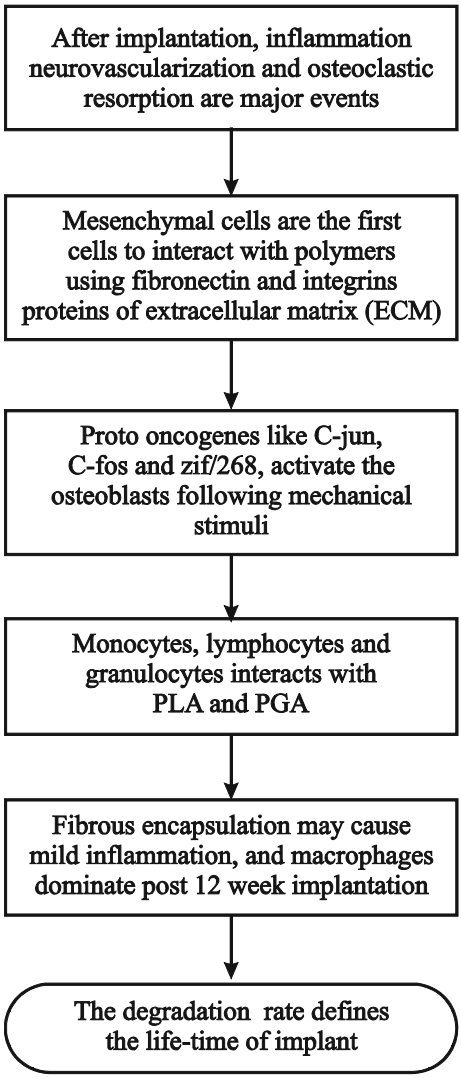

Fig. 1.2 Diagrammatic depiction of polymer–tissue interaction

and exhibits similarity with the cellulose and hyaluronic acid. Brain dura mater replacement, urinary tract infections, cardiovascular applications, and digestive tract problems can be cured with the bacterial cellulose. Hyaluronic acid yields biodegradable scaffold material for tissue regeneration (when ester derivative of hyaluronic acid HYAFF®11 is treated with the benzyl alcohol). Proteins like fibrin play imperative role during the wound-healing process. Fibrin initiates blood coagulation by forming gel-like microfibrillar network, hence acting as tissue adhesives for the wound repair. Collagen is natural polymer and is found in the connective tissues such as cartilage, bone, skin, tendon, and ligaments. Collagen

scaffolds are naturally degraded by serine proteases and matrix metalloproteinases allowing cell-mediated degradation. Chitosan exhibits structural similarity with natural glycosaminoglycans and they modulate various functions such as cell migration, proliferation, and differentiation. Chitosan is generally insoluble in organic solvents and is degraded in vivo by lysozyme enzyme. Chitosan is used for tissue engineering applications due to its non-antigenic property, biocompatibility, and cytocompatibility.

Biodegradable synthetic polymers such as polyurethanes and polyanhydrides are widely investigated for tissue engineering applications. Polyurethane has high endurance, flexural strength, and wear resistance as well as it possesses structure similar to that of human proteins. Polyanhydrides are excellent drug delivery vehicles and a polyanhydride-based device Gliadel® is used for brain tumor treatment. The drug delivery kinetics of polyanhydrides can be increased by incorporating polyethylene glycol (PEG) into the polymer structure. PLA, PGA, and PLGA scaffolds have revealed enhanced osteoblast proliferation and alkaline phosphate activity (ALP). PLGA is a drug delivery vehicle for gonadotrophin-releasing hormone LUPRON DEPOT®, which is used to treat prostate cancer. Poly-ε-caprolactone (PCL) possesses autocatalyzed bulk hydrolysis and slow degradation making it applicable for the long-term applications. Polydioxanone (PDS) sutures are stronger than the microfilament sutures and PDS rings have been used for tricuspid heart valves. To increase the lifetime of polymers and non-toxic reactions, implant processing, polymer synthesis, and sterilization still need to be studied in vast detail.

1.2.2 Metals

Metals possess high tensile strength, wear and fatigue resistance making them suitable for the load-bearing applications. Although metals do not possess bioactive properties, but upon coating with biopolymers and polymers, they become biocompatible. The rigidity and plasticity of metals make them excellent material for stents. From decades, titanium, cobalt–chromium, 316 L steel, and tantalum have been used as implant materials. Titanium and its alloys enhance bone remodeling and inhibit bone resorption. Titanium alloys provide excellent corrosion resistance because of the formation of extremely stable passive TiO_2 layer on their surface. Some of the common Ti alloys are Ti6Al4V, Ti6Al7Nb, and Ti5Al2.5Fe, which find extensive clinical applications. Though the specific strength of Ti is high, but the release of vanadium/aluminum has raised some toxicity issues. When Fe and Nb are used instead of vanadium, the diffusion issues can be avoided for titanium alloys. Due to the carbon content in CoCrMn alloys, the formation of carbide phases such as M_6C, $M_{23}C_6$, and M_7C_3 is promoted (M is usually chromium), leading to high wear resistance of CoCrMn alloys. When the implant is give nitric acid treatment, then the formation of chromium and molybdenum oxides may occur

on the alloy surface leading to corrosion resistance. Magnesium metal implants possess good biocompatibility and mechanical strength though its degradation kinetics are fast. Mg-based systems such as Mg–Si, Mg–Ca, Mg–Zr, Mg–Al, and Mg–rare earth are studied for biomedical applications. No inflammatory reactions and high corrosion resistance could be seen for the Mg–Ca–Zn system, whereas Mg–Sn system exhibits high yield strength, tensile strength, and elongation. It has been observed that the Mg metal-based implant undergoes faster degradation when implanted in regions of higher blood flow than those implanted within the cortical tissue. Iron-based metal implants have similar properties as that of stainless steel and Mn is the most commonly used alloying element for Fe alloys. Fe–Mn alloys yield high tensile strength and lower degradation rates. To enhance the degradation kinetics, variety of secondary phases is added to the Fe-matrix. Zn-based metallic glasses have yielded promising results for bone repair due to their biocompatibility, mechanical strength, and corrosion resistance. Tungsten has been used as an embolic material for tumor-nourishing vessels, whereas tantalum contains interconnected pores as that of the human cancellous bone. Noble metals like platinum/iridium are corrosion resistant and promote neuromuscular response. Mercury, tin, silver, and copper metals are used as dental amalgam materials.

1.2.3 Ceramics and Glasses

Refractory polycrystalline materials such as hydrides, sulfides, selenides, metallic oxides, and carbides constitute the versatile category of ceramics. Ceramics are usually hard and brittle materials and possess elastic moduli comparable to human bone. Ceramics such as Al_2O_3 and ZrO_2 are used as artificial femoral heads/acetabular linens due to their high durability and excellent mechanical strength. The structure and property relations of ceramics are influenced by the electronegativity between positions/negative ion and radius ratio. Glasses are amorphous solids, which lack long-range structural order and exhibit open structure. The bioactive glasses were introduced in 1970s by Larry Hench and the first commercialized glass is named as Bioglass®. The bioactive glasses are excellent materials for clinical applications due to their high bioactivity, biocompatibility, and flexibility of compositions. Bioactive ceramic-like yttrium glass microspheres have been fabricated to deliver therapeutic radiations (β-rays) to liver via arteries. For the bioceramics, the implant tissue response can be shown in Fig. 1.3.

Al_2O_3 has been widely used for the biological fixation and morphology fixation. In biological fixation, the bone ingrowth occurs on porous inert implants, which attaches mechanically the material to the bone whereas for morphology fixation, the nearly inert ceramics attach into surface irregularities by pressing the devices into defect. For the morphological fixation, nearly inert implant is structurally weak due to the localized death of bone. Moreover, the high elastic modulus of implant may cause improper loading of the bone.

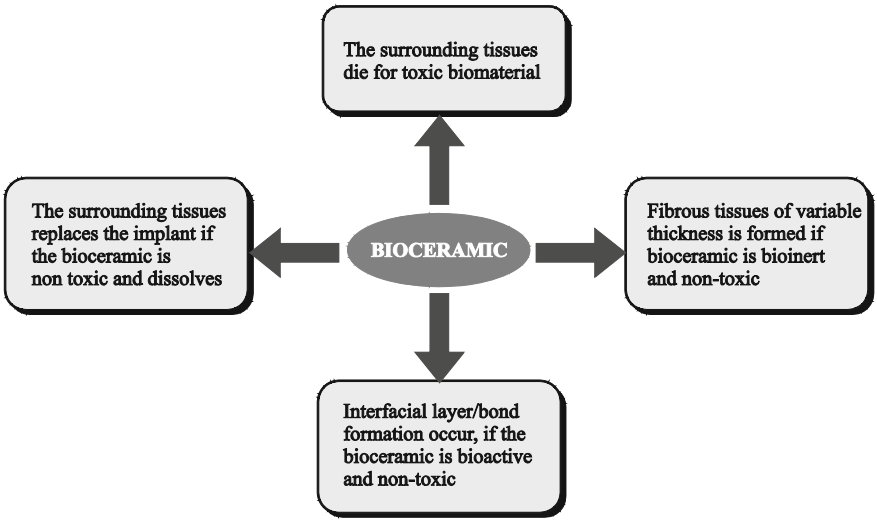

Fig. 1.3 Scheme of interaction between bioceramic implant–host tissues

Table 1.1 Properties of alumina and zirconia

Properties	Zirconia	Alumina
Chemical composition	$ZrO_2 + Y_2O_3 + MgO$	$Al_2O_3 + MgO$
Purity (%)	95–97	99.9
Porosity (%)	<0.1	<0.1
Density (g/cm^3)	5–6	3–4
Young's modulus (GPa)	200–220	350–380
Bending strength (MPa)	500–1000	>500
Compression strength (MPa)	2000–2100	4000–4200
Poisson's ratio	0.3	0.23
Hardness (HV 0.1)	1200–1250	2100–2200
Fractine Toughness (MPa $m^{1/2}$)	Up to 10	4
Coefficient of thermal expansion (CTE) $\times$ 10^{-6}/K	11	8

High purity Al_2O_3 (>99.5 %) was the first bioceramics to be used clinically for load-bearing hip prostheses and dental implants. To aid sintering and limit grain growth process during sintering, small amount of magnesia may be added to the Al_2O_3. Alumina possesses high wear resistance, high strength, and corrosion resistance. Zirconia has replaced Al_2O_3 in many applications, as it possesses high strength than alumina. Zirconia has been used in hemiarthroplasty head implants due to its excellent biocompatibility and low friction with articular cartilage. Table 1.1 gives the comparison of properties of ZrO_2 and Al_2O_3.

Table 1.2 Composition and properties of glass/glass ceramic

Property	A-W (glass ceramic)	Ceravital® (glass ceramic)	Bioglass®
Composition	$34.2SiO_2$–$16.3P_2O_5$–$44.9CaO_2$–$0.5CaF_2$–$4.6MgO$	$46.2SiO_2$–$20.2CaO$–$25.5Ca(PO_3)_2$–$2.9MgO$–$4.8Na_2O$	$45SiO_2$–$6P_2O_5$–$24.5CaO$–$24.5Na_2O$
Vicker hardness	680	295	450–460
Young's modulus (GPa)	118	100–160	32–36
Tensile strength (MPa)	–	400	200
Compressive strength (MPa)	1050–1100	500	40–45
Fracture toughness (MPa $m^{1/2}$)	3.34	4.5–4.8	2

Due to presence of yttria, zirconia can be radioactive but no adverse reports have been presented. Bioactive glass/ceramics are osteoconductive, biocompatible, and bond well to the bone without any fibrous connective tissue interface. Upon implantation of bioactive glasses on to the defect site, the exchange of ions takes place between the glass and surrounding media. Commonly known as simulated body fluid (SBF) leading to formation of bone-like apatite layer on the surface. This biological apatite is partially replaced by bone after long-term implantation because apatite promotes cellular adhesion and proliferation of osteogenic cells. The composition and mechanical properties of most common glass-ceramics used in various biomedical applications are shown in Table 1.2.

Glass ceramics have modulus of elasticity $\sim$100 GPa and possess resistance to the surface damage. For the osteoinduction and bone integration, the bioactive glass shall exhibit macroporous structure. The resorption, bioactivity, vascular ingrowth, and osteoblast differentiation are highly promoted due to the porosity.

Calcium phosphate cements, such as tricalcium phosphate ($Ca_3(PO_4)_2$) (TCP), hydroxyapatite ($Ca_{10}(PO_4)_6$) (HAp), and dicalcium phosphate ($CaHPO_4$) are most commonly used bone-substituting materials. The Ca/P ratio of these ceramics is in close agreement with the mineral phase of bone and hence these are used for facial surgery, dental implants, jawbone reconstruction, and spinal surgery. The degradation of β-TCP is initiated by cellular mechanisms and chemical processes, whereas due to insoluble nature of HAp, the in vivo degradation is mainly influenced by cellular mechanisms. TCP has low mechanical strength; hence the bone augmentation process cannot be supported by them individually. Therefore, the biphasic calcium phosphate (BCP) scaffolds are developed, which consists of variable β-TCP and HA amounts leading to enhanced mechanical properties. Plaster of Paris ($CaSO_4$) has been used as bone void filler and cures with limited exothermic reaction. Ostocalcium phosphates have been promising scaffold

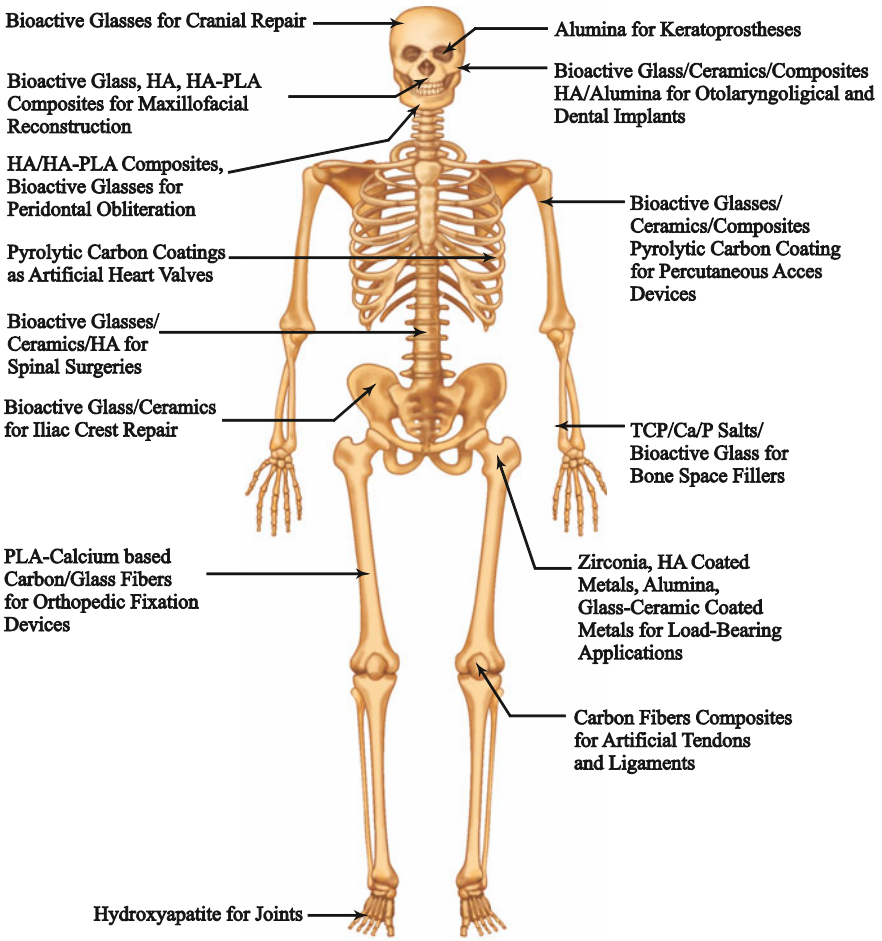

Fig. 1.4 Applications of biomaterials/bioactive glasses inside the human body

materials for bone formation because it is a biological precursor of the bone apatite crystals. The calcium phosphate cements have been used in the vertebral augmentation of mechanically stable factures (in children especially). Figure 1.4 lists the applications of glass/ceramics inside human body indicating their importance.

1.2.4 Composites

Composite materials consist of two or more distinct phases/constituents. Composites offer the advantage of better mechanical and bioactive properties and

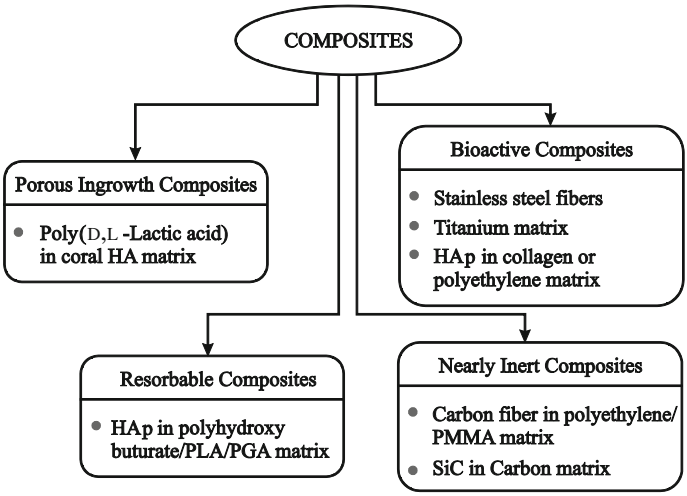

Fig. 1.5 Characteristics of the different composites

hence been an intense topic of research. One of the strongest composites is A-W glass ceramic containing tetragonal ZrO_2 particles, i.e., the fracture toughness of 4 MPa $m^{1/2}$ and bending strength of 700 MPa, could be obtained for A-W/ZrO_2 composite. Composites can be porous ingrowth, bioactive, nearly inert phase, and resorbable as depicted in Fig. 1.5.

Human cortical bone is itself a composite of compliant collagen fibrils and brittle hydroxyl carbonate apatite (HCA) layer. The composite stiffness can be calculated with the help of Voigt and Reuss models. According to Voigt model, Young's modulus (E) of the composite can be given by:

$$E = E_i V_i + E_m V_m \tag{1.1}$$

where E_i and E_m are the Young's modulus of inclusion and matrix, respectively; V_i and V_m are the volume fractions of inclusions and matrix, respectively ($V_m = 1 - V_i$).

According to Reuss model, Young's modulus can be given by:

$$\frac{1}{E} = \frac{V_i}{E_i} + \frac{V_m}{E_m} \tag{1.2}$$

Hence, the upper and lower limits of composite stiffness can be described by Voigt and Reuss relations. Composites used in orthopedics are intended for dual purposes, i.e., to improve the mechanical performance and improvement of biological and non-biological functions. Bone morphogenetic proteins (BMP) and $BaSO_4$ incorporated bone cement improves the biological and non-biological functioning, whereas carbon fiber reinforced materials enhance mechanical

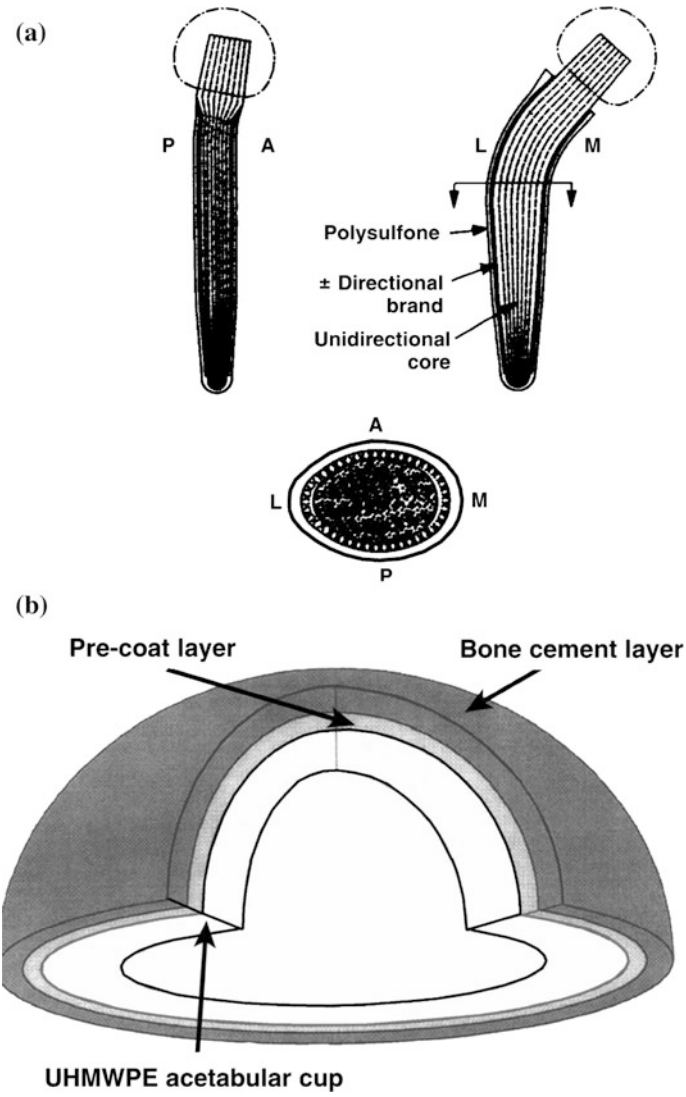

Fig. 1.6 **a** Carbon–polysulfone composite femoral stem construction and **b** precoating of bone cement layer combined with crosslinking of UHMWPE over acetabular cup outer surface (Magee et al. 1988; Park et al. 1999)

properties. Hip replacement prostheses are the components of carbon fibers in polysulfone and polyether ether ketone matrix. Figure 1.6a, b gives the carbon polysulfure femoral stem constructions and acetabular cup for hip joint prostheses carbon reinforced ultra high molecular weight polyethylene body with HAp.

Table 1.3 Ceramic polymer composite scaffolds

Ceramic	Polymer	Porosity (%)	Pore size (μm)
HAp	PLGA-Collagen	87	350–430
Bioglass®	PLA	–	50–200
β-TCP	Poly propylene fumarate (PPF)	65–75	150–300
β-TCP	PLA	80–90	125–150
HAp	Collagen	49–85	30–300
HAp-βTCP	Chitosan	–	300–600
HAp	PCL	85–90	150–200
HAp	Chitosan/gelatin	–	300–500

Dental composite resins are the restorative materials for anterior/posterior teethes. The composite scaffolds are usually made of biodegradable polymers with ceramic-like HAp. Table 1.3 lists ceramic polymer composite for bone scaffolds composite.

Collagen and PLGA exhibit quite high biodegradability and biocompatibility. Every constituent of composite shall be non-toxic to the body environment. Anyhow, PLGA degradation products are acids, which can be a matter of concern if they are produced in large quantities.

1.3 How Does Biomaterials Interact with Host Tissue?

Over the course of years, biomaterials have successfully replaced/segmented host tissue especially those suffering from the bone and cartilage injuries. For the normal healing of injured tissues, a series of events take place starting from the inflammation to the clot formation (Fig. 1.7a). In contrast to this, when biomaterial is implanted inside the body, the foreign body reactions are initiated as shown in Fig. 1.7b.

During natural healing, the blood is pumped onto the injured area and the blood fibrinogen cleaves into fibrin promoting the platelet aggregation. The macrophages get accumulated at the wound site and clean the wound site. Subsequently, the clot is converted to the vascularized granulation tissue, which gets replaced by the extracellular cellular matrix (ECM) deposited by fibroblasts. However, when the biomaterial is implanted inside host tissue, immediate protein adsorption occurs on its surface, which never occurs during normal healing process. This is followed by the adherence of leukocytes, thereby upregulating cytokines. Macrophages may fuse together to yield a multinucleated giant cell and thereby a typical 50–200 μm thick collagenous fibrous tissue surrounding the biomaterial is formed.

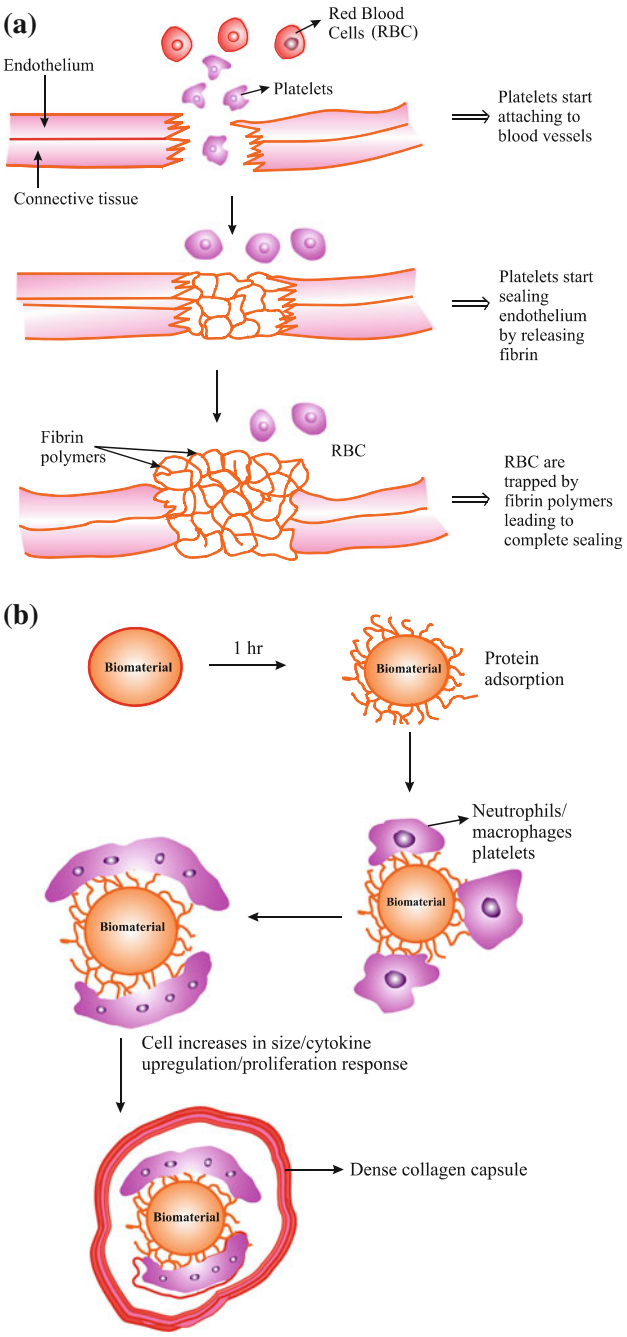

Fig. 1.7 **a** Normal wound healing and **b** series of events after biomaterial implantation inside human body

1.4 Surface Modification of Biomaterials

Within the biomaterial and biological system, the unwanted harsh reactions may occur. The surface topography and chemistry are very important parameters for the protein adsorption, host response, and cell interaction. Hence, the surface chemistry must be modified to control the protein adsorption and interaction with the signaling molecules. For the surface modification, the materials characteristics shall be changed from hydrophobic to hydrophilic along with altering surface characteristics. There are many methods employed for coating bioactive surface to make their characteristics unique. The following methods are commonly used for the optimization of the biological surface.

(a) ***Metal Surface Pretreatment Layer***

Devices such as stents, pacemakers, vena cava filters, and guidewires are prepared partially/fully from the metals like stainless steel. For the uninterrupted functioning of these metal devices, the blood–tissue compatibility, good adhesion of materials coating on the metallic surfaces, and wettability are required. Several polymers incorporated with carboxylic acids have been used as coating for the improvement of interaction with metallic substrates. The carboxyl functional urethane and acrylic/ethylene family polymers are commonly used coating materials. One of the best suitable materials is polyethylene glycol (PEG) due to its high protein and cell resistance. PEG attaches via sticky segment to gold and titanium surfaces, and these surfaces could resist cell adhesion up to 2 weeks in vitro. Hydrosiloxane materials have been used for the treatment of oxidizable metal surfaces and provide attachment of silicone polymers to the metallic surfaces. Polymer blends have been used for preparing the coatings for drug incorporation and providing required drug release characteristics to the coated metal surface. Desired coating modulus and durability could be obtained by choosing material with higher modulus and processing parameters.

(b) ***Photochemical coupling***

Biomaterials usually display inert behavior toward the hydrocarbon-rich groups, whereas form bonds with high-energy short-lived reactive species including free radicals and diradicals. These radicals are rapid, compatible with device manufacturing, and reactive in aqueous solutions. For the surface modification, photochemical covalent coupling is the most widely used approach for polymeric materials. Figure 1.8 gives the generation of photochemical radical from the aromatic ketone group.

Photocoupling mechanism provides hydrolytic stability due to the formation of stable C–C bonds between the hydrocarbon-carbonyl group on the biomaterial surface. Photoactivatable aromatic carbonyl group can be incorporated easily into the coating materials irrespective of their molecular weights or size. Many photoreactive agents are available and they must possess thermochemical reactive group and photoreactive component. The photoreactive coating reagents can be of

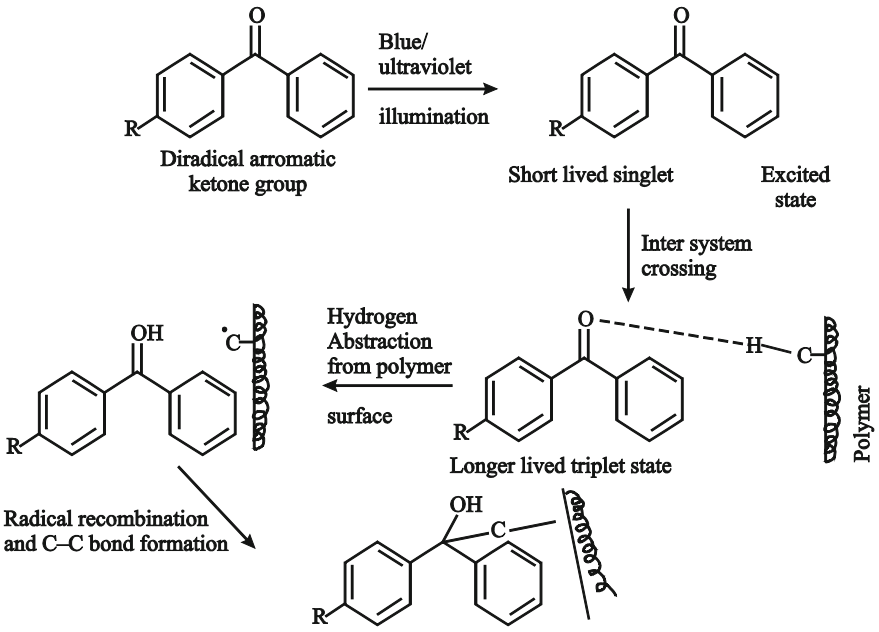

Fig. 1.8 Photochemical coupling mechanism

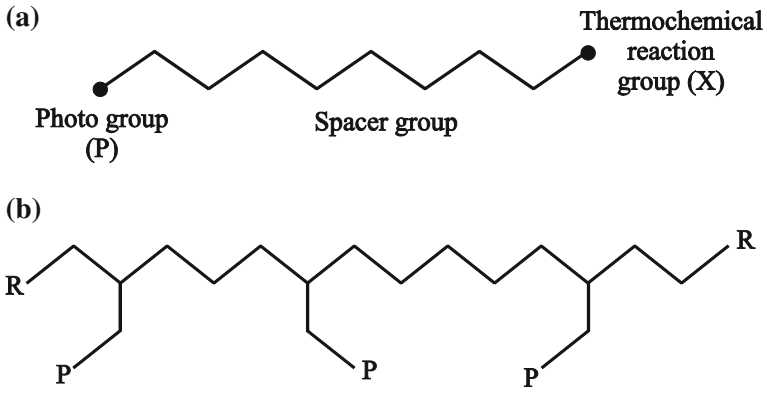

Fig. 1.9 **a** Heterobifunctional and **b** multifunctional reagents

two types: heterobifunctional and multifunctional reagent (Fig. 1.9) Heterobifunctional reagents consist of photoreactive group P, a spacer group, and thermochemically reactive group.

The space group is used to hold the functional group away from hydrophobic environment and can be of varying composition and lengths. Thermochemical reaction group includes tosylate esters, isothiocyanates, aldehydes, epoxides, and

hydrazides, whereas the photogroup is basically an aryl ketone with second group in para position to felicitate the space group attachment.

(c) ***Photoimmobilized surface modifications for increasing blood compatibility***

During any surgical procedures, the medical devices involved must possess improved blood compatibility so as to avoid any medical complications. Heparin coatings have been developed to improve the performance of blood-contacting devices. Heparin is an anticoagulant and given intravenously during any surgical procedure to avoid any kind of coagulation. Heparin coatings provide required local catalytic activity for the enzyme inhibition required for fibrin formation. In addition to this, heparin reduces the adhesion and activation of platelets, along with reducing blood protein adsorption. Heparin coatings have demonstrated good potency and durability when exposed to different physical conditions. Photoheparin reagents are tested in an acute canine fugular vein implant model for dog and then the veins were isolated surgically and opened longitudinally for the surface modified and control rod inspection, which indicated significantly reduced platelets attachment on the phosphoheparin treated rod.

Multifunctional reagents are obtained by the reaction of polymerizable monomers/multifunctional monomeric/preformed polymeric molecules with the heterobifunctional reagents. The polymers possess multiple polymeric sites along their backbone for the attachment of multiple photogroups. The level of biological activity is determined by the photogroup content.

Anyhow, there are some potential regulatory issues with heparin-based coatings due to their medicinal nature. Hence, other novel photoimmobilized alternatives have been researched to create blood compatible surfaces. Surface passivation is one such technique, which prevents adhesion of proteins and thrombogenic cells onto the underlying substrate, hence preventing any blood clotting.

1.5 Clinical Applications of Biomaterials

Biomaterials have been the best substitutes for the damaged tissue, as they maintain/replace the function of wide spectrum of human tissues starting from tissue engineering to various surgeries, and smart biomaterials are required at every level. By adjusting the growth factors, nutrients, proteins, and geometry constructs, the biomaterials can be tailored according to the clinical usage as follows:

(a) ***Tissue engineering***

The scaffolds are the backbone of tissue engineering which are 3-D bone-like constructs and can be combined with the growth factors, living cells as biologically active molecular for tissue repair or segmentation. The processing techniques, nature of biomaterial, and composition deeply affect the scaffold structure. The scaffold shall be porous enough to allow the cell migration, proliferation, and vascularization.

Moreover, the scaffold shall be strong enough to withstand the stress produced in physiological environment and also provide strong mechanical interlocking at the tissue–implant interface. Scaffolds can have macro-, micro-, or nanoporosity, i.e., macroporous scaffolds have pores >50 μm, whereas microporosity is <10 μm. Microporosity favors osteogenesis, whereas microporosity gives higher scaffold area increasing cell differentiation. To maximize the ion exchange rate and felicitate diffusion, pore interconnectivity shall be ~100 % with interconnection size of at least 100 μm. Microporous CaP have been used as drug carrier especially for BMP-2, vancomycin, and heparin loading with the bone growth factors.

(b) ***Bone and Cartilage***

Though bone healing is spontaneous process naturally but during critical traumatic injuries, tumor resections, or bone cancers, the bone reconstruction becomes necessary using osteoconductive, osteoinduction, and osteogenic materials. Composite bone scaffolds comprising of polymer/ceramic fusion have been the potential candidates due to their high compressive strength and biodegradation. Tumor-like lesions have been treated with $TricO_s$ (Biomatlante, Vigneux de Bretagne, France) granules, which are biphasic calcium phosphate with 40 % β-TCP and 60 % HA. Composite scaffolds made from aliphatic polyesters/tricalcium phosphate have been used for the reconstruction of segmental tibial defects in sheep.

Collagen is the major structural components of the extracellular matrix (ECM) of various connective tissues. The collagen regulates cellular events as adhesion, migration, proliferation, and differentiation and hence is primary focus for the cartilage implant. Chondrocyte-laden collagen I membranes and hydrogels have been promising clinical materials for the chondrocyte implantation. Collagen hydrogels can take desirable shapes and cause limited, inflammatory reactions. Figure 1.10 demonstrates the treatment of articular cartilage defect at medial femoral condyle for 31-year-old male using α chondrocyte-laden collagen I hydrogel (CaReS®, Arthro kinetics, krems, Austria). After 30.2 months, a significant relief from pain was observed and 80 % of the patients rating of treatment were good/very good.

(c) ***Plastic Surgery***

Craniofacial and breast surgeries for the enhancement of features have been gearing up over the last decades. The must regulatory used implants are breast from the connective and reconstructive point of view and silicone gel implants have been used extensively for breast augmentation/reconstruction. The silicone elastomer may get ruptured or the elastomer fragmentation may occur causing it to come in contact with the body tissues causing capsular construction, infection, and granulomatous inflammation. Current work is also focused on the surgery free procedures to prevent any scarring, pain, and host tissue response. The recent work has been done to utilize vascular pedicles for forming an effective vascular network coupled with computer-aided design and manufacturing (CAD/CAM) technology.

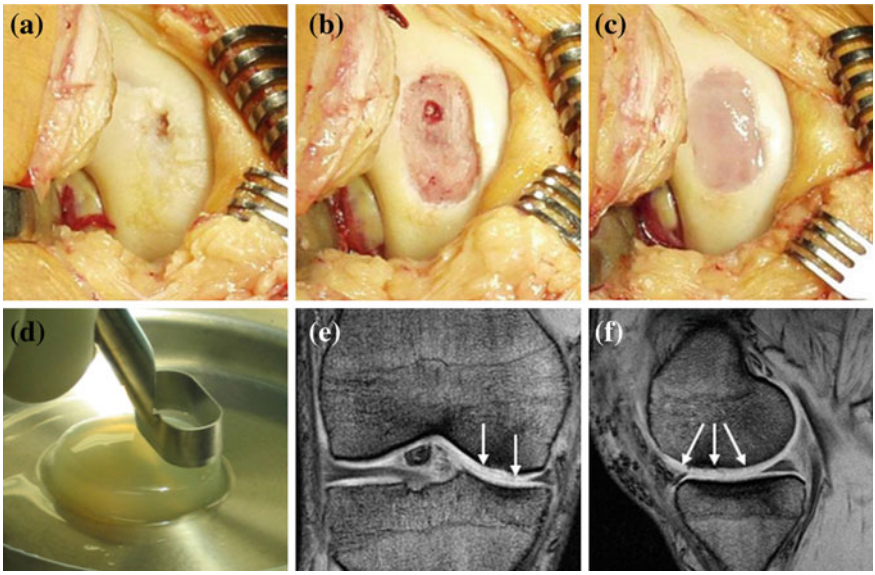

Fig. 1.10 **a** Matrix ACI using Collagen Type I hydrogel, **b** medial femoral condyle in a 31-year-old male with articular cartilage defect, **d** debridement down to the subchondral bone with shape of the chondrocyte-laden collagen I hydrogel (CaReS) customization, **c** implantation of the tailored hydrogel into the cartilage defect, **e** Coronal and **f** sagittal T1-weighted MRI images of the femoral condyle, 12 months postimplantation showing excellent lateral bonding to the adjacent healthy cartilage (Holzapfel et al. 2013)

For any biomaterial, the cost effectiveness, implant survival, mortality, host tissue response, and pain relief are the major considerations. According to the application, the tissue engineer can choose suitable biomaterial from among metals, ceramics, polymers, or composites, such that safe, clinically effective, structurally strong, and reproducible material can be obtained.

Bibliography

Magee FP, Weinstein AM, Longo JA, Koeneman JB, Yarp RA (1988) A canine composite femoral stem: an in vivo study. Clin Orthop Relat Res 235:237–252

Park KD, Kang YH, Park JB (1999) Interfacial strength between molded and UHMWPE-MMA monomer treated UHMWPE powder. J Long-Term Eff Med Implants 9:303–318

Holzapfel BM, Reichert JC, Schantz JT, Gbureck U, Rackwitz L, Nöth U, Jakob F, Rudert M, Groll J, Hutmacher DW (2013) How smart do biomaterials need to be? A translational science and clinical point of view. Adv Drug Deliv Rev 65:581–603

Ratner BD, Bryant SJ (2004) Biomaterials: where we have been and where we are going? Annu Rev Biomed Eng 6:41–75

Kaur G, Pandey OP, Singh K, Homa D, Scott B, Pickrell G (2013) A review of bioactive glasses: their structure, properties, fabrication, and apatite formation. J Biomed Mater Res A 102: 254–274

Ishihara K, Ziats NP, Tierney BP, Nakabayashi N, Anderson JM (1991) Protein adsorption from human plasma is reduced on phospholipid polymers. J Biomed Mater Res 25:1397–407

Rahaman MN, Liang W, Day DE, Marion NW, Reilly GC, Mao JJ (2005) Preparation and bioactive characteristics of porous borate glass substrates. Ceram Eng Sci Proc 26:3–10

Shen MC, Horbett TA (2001) The effects of surface chemistry and adsorbed proteins on monocyte/macrophage adhesion to chemically modified polystyrene surfaces. J Biomed Mater Res 57:336–45

Kaur G, Sharma P, Kumar V, Singh K (2012) Assesment of *in-vitro* bioactivity of SiO_2-BaO-ZnO-B_2O_3-Al_2O_3 glasses: an optico-analytical approach. Mater Sci Eng C 32(7): 1941–1947

Behling CA, Spector M (1986) Quantitative characterization of cells at the interface of long-term implants of selected polymers. J Biomed Mater Res 20:653–666

Salthouse TN (1984) Some aspects of macrophage behavior at the implant interface. J Biomed Mater Res 18:395–401

Kaur G, Pickrell G, Kimsawatde G, Allbee H, Sriranganathan N (2014) Synthesis, cytotoxicity, and hydroxypatite formation in 27-Tris-SBF for sol-gel based CaO-P_2O_5-SiO_2-B_2O_3-ZnO bioactive glasses. Sci Rep. doi:10.1038/srep04392

Williams DF (1987) Definitions in Biomaterials. Program biomedical engineering, 4th edn. Elsevier, Amsterdam

Hoppe A, Guldal NS, Boccaccini AR (2011) A review of the biological response to ionic dissolution products from bioactive glasses and glass-ceramics. Biomaterials 32:2757–2774

Shin H, Jo S, Mikos AG (2003) Biomimetic materials for tissue engineering. Biomaterials 24:4353–4364

Chen QZ, Rezwan K, Armitage D, Nazhat SN, Boccaccini AR (2006) The surface functionalization of 45S5 Bioglass (R)-based glass-ceramic scaffolds and its impact on bioactivity. J Mater Sci-Mater Med 17(11):979–987

Kaur G, Pickrell G, Sriranganathan N, Kumar V, Homa D (2016) Review and the state of the art: sol-gel or melt quenched bioactive glasses for tissue engineering J Biomed Mater Res: B Appl Biomater 104(6):1248–1275. doi:10.1002/jbm.b.33443.

Leach JB, Bivens KA, Patrick CW, Schmidt CE (2003) Photocrosslinked hyaluronic acid hydrogels: natural, biodegradable tissue engineering scaffolds. Biotechnol Bioeng 82:578–589

Hench LL (1991) Bioceramics: from concept to clinic. J Am Ceram Soc 74:1487–1510

Gross U, Kinne R, Schmitz HJ, Strunz V (1988) The response of bone to surface active glass/glass-ceramics. CRC Crit Rev Biocompat 4:2

Kaur G, Pickrell G, Pandey OP, Singh K, Chudasama BN, Kumar V (2016) Combined and individual Doxorubicin/Vancomycin drug loading, release kinetics and apatite formation for the CaO-CuO-P_2O_5-SiO_2-B_2O_3 mesoporous glasses, RSC Adv (2016) 6:51046–51056

Huebsch N, Mooney DJ (2009) Inspiration and application in the evolution of biomaterials. Nature 462(7272):426–432

Anderson JM, Rodriguez A, Chang DT (2008) Foreign body reaction to biomaterials. Semin Immunol 20:86–100

Park JH et al (2009) Systematic surface engineering of magnetic nanoworms for in vivo tumor targeting. Small 5:694–700

Park J (2008) Bioceramics: properties, characterizations, and applications. Springer.

Chan BP, Leong KW (2008) Scaffolding in tissue engineering: general approaches and tissue-specific considerations. Eur Spine J 17(4):467–479

Bellucci D, Sola A, Cannillo V (2013) Bioactive glass-based composites for the production of dense sintered bodies and porous scaffolds. Mater Sci Eng C Mater Biol Appl 33:2138–2151

Arcos D, Regí MV (2010) Sol–gel silica-based biomaterials and bone tissue regeneration. Acta Biomater 6:2874–2888

Bellantone M, Coleman NJ, Hench LL (2000) Bacteriostatic action of a novel four component bioactive glass. J Biomed Mater Res 51:484–490

Rezwan K, Chen QZ, Blaker J, Boccaccini AR (2006) Biodegradable and bioactive porous polymer/inorganic composite scaffolds for bone tissue engineering. Biomaterials 27: 3413–3431

Fu Q, Saiz E, Rahaman MN, Tomsia AP (2011) Bioactive glass scaffolds for bone tissue engineering: state of the art and future perspectives. Mater Sci Eng C 31:1245–1256

Roether A, Boccaccini AR, Hench LL, Maquet V, Gautier S, Jérome R (2002) Development and in vitro characterization of novel bioresorbable and bioactive composite materials based on polylactide foams and bioglassfor tissue engineering applications. Biomaterials 23:3871–3878

Maquet V, Boccaccini AR, Pravata L, Notingher I, Jérome R (2004) Porous poly (α-hydroxyacid)/ bioglass composite scaffolds for bone tissue engineering I: preparation and in vitro characterization. Biomaterials 25:4185–4194

Chen JP, Chang YS (2011) Preparation and characterization of composite nanofibers of polycaprolactone and nanohydroxyapatite for osteogenic differentiationof mesenchymal stem cells. Colloids Surf B 86:169–175

Lee J, Guarino V, Gloria A, Ambrosio L, Tae G, Kim et al YH (2010) Regeneration of Achilles' tendon: the role of dynamic stimulation for enhanced cell proliferation and mechanical properties. J Biomater Sci 21:1173–1190

Jeong SI, Kim SH, Kim YH, Jung Y, Kwon JH, Kim et al BS (2004) Manufacture of elastic biodegradable PLCL scaffolds for mechano-active vascular tissue engineering. J Biomater Sci Polym Ed 15:645–660

Albrektsson T, Johansson C (2001) Osteoinduction, osteoconduction and osseointegration. Eur Spine J 10:96–101

Minardi S, Corradetti B, Taraballi F et al (2015) Evaluation of the osteoinductive potential of a bio-inspired scaffold mimicking the osteogenic niche for bone augmentation. Biomaterials 62:128–137

Wang L, Zhang B, Bao C et al (2014) Ectopic osteoid and bone formation by three calcium-phosphate ceramics in rats, rabbits and dogs. PLoS One 9(9):e107044

Daculsi G, Fellah BH, Miramond T (2014) The essential role of calcium phosphate bioceramics in bone regeneration. In: Bennissan B (ed) Advances in calcium phosphate biomaterials. Springer-Verlag, Berlin, pp 71–96

Saiz E, Gremillard L, Menendez G et al (2007) Preparation of porous hydroxyapatite scaffolds. Mater Sci Eng C-Biomim Supramol Syst 27(3):546–550

Chapter 2
Polymers as Bioactive Materials-I: Natural and Non-degradable Polymers

Gurbinder Kaur

Over the past decade, the use of polymeric materials has increased tremendously. Polymeric materials have found wide applications in bone, vascular, skin, cartilage, and liner regeneration. Apart from this, the polymeric biomaterials find potential applications in cell encapsulation, and cardiac and striated muscle regeneration, along with the drug delivery. Polymers are broad-spectrum materials and can be designed to suit the tissue of interest, i.e., for bone applications; the chosen polymer shall exhibit high hardness and compressive strength to withstand the body weight, whereas for the skin grafts, the designed polymer must possess large shear stress. This chapter deals with the various polymers and their applications as biomaterials. The emphasis has been given on the diversity among the polymers and their impact on the biological applications.

2.1 Requirements for the Biodegradable Biomaterial

A biomaterial is regarded as material intended to undergo a series of chemical surface reactions to replace damaged tissue/organ and hence retaining the normal body functions. For the normal functionality of the biomaterials, a number of factors such as physical/chemical/biological compatibility are required. These prerequisites for any biomaterial dictate the desired shape, size, and configurations of the implant for uninterrupted working. Figure 2.1 lists some of the parameters required for the ideal biomaterials.

The biomaterial must not be immediately encapsulated or attacked by the body. In addition to this, the material properties of the extracellular matrix must be well understood, to resume the normal body functioning as done by native tissue components. Before the implantation of materials, the potential toxicity of materials breakdown products must be well known. Various factors affect the biocompatibility of polymeric materials; e.g., lubricity, surface energy, molecular weight,

G. Kaur, *Bioactive Glasses*, Series in BioEngineering,
DOI 10.1007/978-3-319-45716-1_2

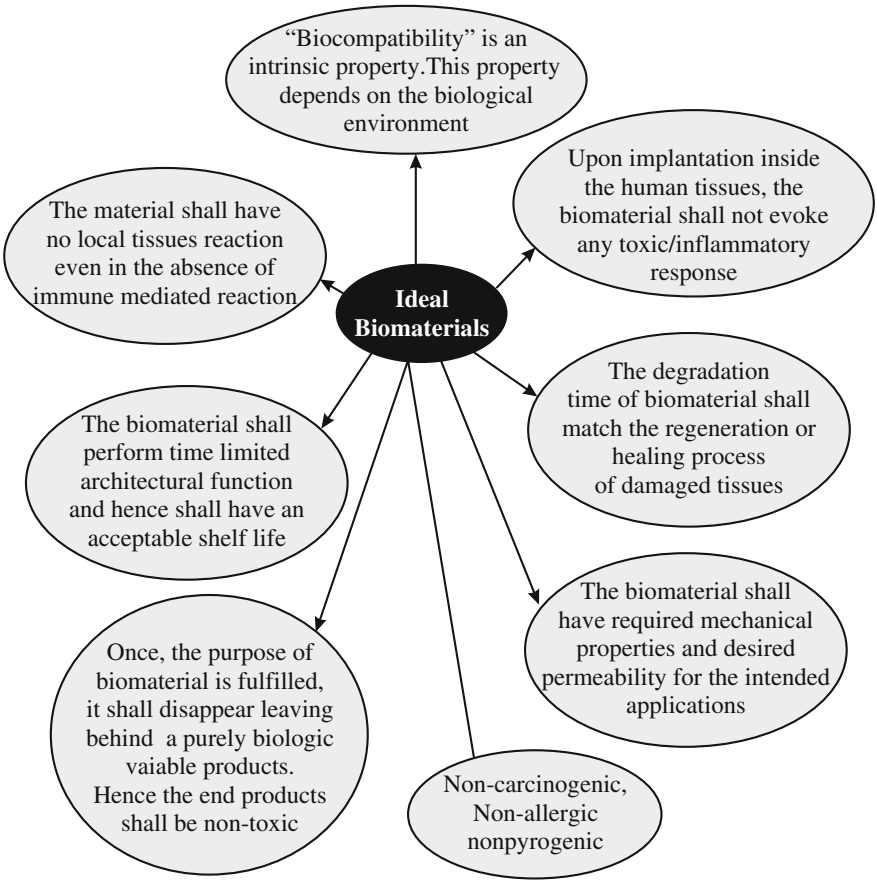

Fig. 2.1 Requirements for the ideal biomaterials

hydrophilicity, hydrophobicity, degradation mechanism, material chemistry, and erosion are the key factors in determining the polymer biocompatibility.

2.2 Polymeric Biomaterials

As compared to metals or ceramics, the polymers offer ease of fabrication, reasonable cost, and easy secondary processability along with tailored mechanical and biological properties. The polymers basically consist of multiple monomers as repeating units. Condensation is the basic process for the polymerization process to take place as shown below:

$$\underset{\text{(Amine)}}{\text{R-NH}_2} + \underset{\text{(Carboxylic acid)}}{\text{R}'\text{-COOH}} \rightarrow \underset{\text{(Amide)}}{\text{R}'\text{CONHR}} + \underset{\text{(Water)}}{\text{H}_2\text{O}} \quad (2.1)$$

Equation (2.1) gives the reaction to yield polyamide such as nylon. Nylon was the first commercial polymer synthesized in 1930. The length of the polymer chain can be controlled by different parameters such as temperature, pressure, the type of catalyst, and the time for which the polymerization process shall take place.

The polymeric biomaterials can be categorized on the basis of different criteria. For example, on the basis of occurrence, the polymers can be classified as synthetic and natural biomaterials. On the basis of degradation ability, polymers can be biodegradable and non-biodegradable. Furthermore, the degradation of polymer materials can be synthetic or natural. In the preceding sections, we will discuss about the various types of polymers. Broadly speaking, the polymers fall into the non-biodegradable and biodegradable categories. We will discuss non-biodegradable polymers first, which find potential application in cartilage repair. Biodegradable polymer can form temporary scaffold for the biochemical as well as mechanical support, which will degrade subsequently leaving behind regenerated tissue.

2.3 Non-biodegradable Polymers

Non-biodegradable polymers materials cannot be decomposed or broken down by the natural agents, hence making them immune to the natural process. The non-biodegradable polymers find extensive applications in the biomedical arena such as vascular grafts, porous scaffolds, implantable drug delivery systems, catheters, dialysis tubing, oxygenation and detoxification membranes, device coatings for improved blood compatibility, and bone pins/screws.

The common non-biodegradable polymers are listed in Table 2.1 along with their structure and application.

2.3.1 Polyethylene (PE)

Polyethylene is a prominent class of non-biodegradable material. It has high ductility as well as low friction, whereas its strength and hardness are low. The high-density polyethylene exhibits high compressive modulus and good flexural strength; hence, they are used extensively in orthopedic devices. But, the debris gets accumulated due to frictional erosion causing long-term health issues. The polyethylene fibers coated with hydroxyapatite (HAp) powder yielded the polymer characteristics as that of natural cartilage. These polymers were then incorporated into the rabbit articular cartilage, and it was observed that hyaline-like cartilage covered the articular surface, whereas the fibrous tissue covered the bone defect without any implant. Almost 70 % of the area was surrounded by the polymer after

Table 2.1 Chemical composition and application of non-biodegradable polymers for biomedical applications

Name	Structure	Application
Polyethylene (PE)	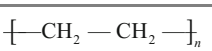	High strength for catheters and orthopedic implants
Poly(vinylidene fluoride) (PVDF)	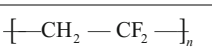	Used in immunoblotting as an artificial membrane
Poly (tetrafluoroethylene) (PTFE)		PTFE grafts are used to bypass stenotic arteries, dental fillings, and guided tissue regeneration
Poly(propylene) (PP)	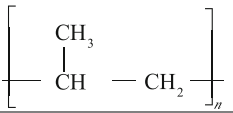	Drug delivery, sutures, and meshes
Poly(vinylalcohol) (PVA)	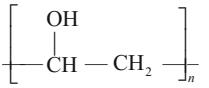	Matrix for sustained drug delivery and emulsifier in drug encapsulation process
Poly (dimethylsiloxane) (PDMS)	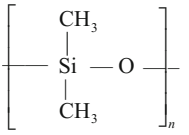	Ocular lens, fillers in silicon, breast implants, drug delivery, and gas exchange membranes
Poly(ethylene terepthalate) (PET)	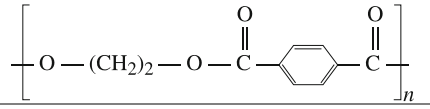	Meshes for abdominal surgery and vascular grafts
Poly(sulfone) (PS)	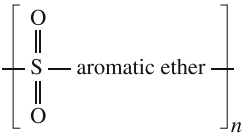	Membranes and hollow fibers for the immobilization of biomolecules especially in extracorporeal devices
Poly(hydroxyl alkanote) (PHA)	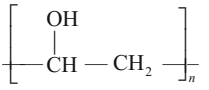	Tendon repair devices, bone marrow scaffold, ligament grafts, and ocular cell implants

(continued)

Table 2.1 (continued)

Name	Structure	Application
Poly(ethylene oxide) (PEG, PEO)	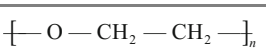	Device passivation toward cell encapsulation, precipitant for plasma DNA isolation, foam and spandex cushions, potentiator to enhance antigen, and antibody detection
Poly(methyl methacrylate) (PMMA)	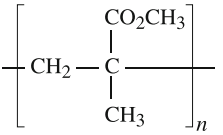	Ocular lens bone cement, dentires, and bioprocess chromatography cosmetic surgery
Poly(butylene terephthalate) (PBT)	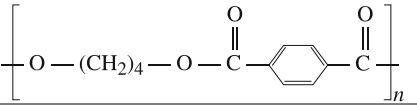	Dentures and fibers for toothbrushes
Poly(hydroxyl ethyl methacrylate) (PHEMA)	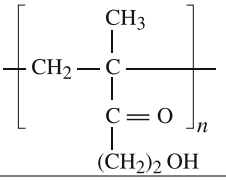	Optical implant and soft contact lens
Polydioxanone (PDS, PDO)	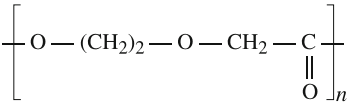	Surgical sutures, plastic surgery, drug delivery, and cardiovascular applications
Polypyrole (PPy)	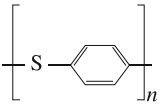	Vehicle for drug delivery and container for proteins
Poly(*N*-isoprpyl acrylamide) (PNIPAM)	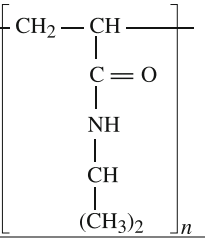	Biosensors, drug delivery (pH sensitive), and gel actuators for converting external stimuli into mechanic motion

24 weeks of the implantation. This indicated that the polyethylene material significantly induced high cartilage formation.

Polypropylene (PP) which is a methylated variant of PE also finds load-bearing applications, due to its excellent fiber-forming capability. For the molar and mandibular reconstruction, PP is used along with the delivery of tetracycline (an antimicrobial agent) to the root canal. Superior clinical results have been obtained, when PP meshes are used as a prosthetic in repairing ventral incisional hernia.

2.3.2 Polyvinyl Alcohol (PVA)

Polyvinyl alcohol (PVA) is a linear synthetic polymer produced by full or partial hydrolysis; i.e., the hydrolysis process removes the acetate group. PVA is used as a biomaterial because of its bioadhesiveness, non-carcinogenic nature, non-toxicity, and biocompatibility. Figure 2.2 shows the common biological applications of PVA.

PVA results in low cell adhesion as compared with other hydrogels. PVA hydrogels possess high tensile strength and elongation endowing it with a property apt for making soft contact lens. PVA cryogels of 2–3 mm thickness have been found suitable to withstand the mechanical stresses during mechanical applications. PVA is among the first synthetic polymers to be used as an artificial cartilage. Cartilage has chondrocytes with low mitotic ability, hence making its regeneration difficult. PVA contains water content almost same as that of cartilage, and even it can swell to accommodate higher water content. The commercialized PVA is Salubria™ (Atlanta, GA), which is synthesized by freeze/thaw cycle of 0.9 %

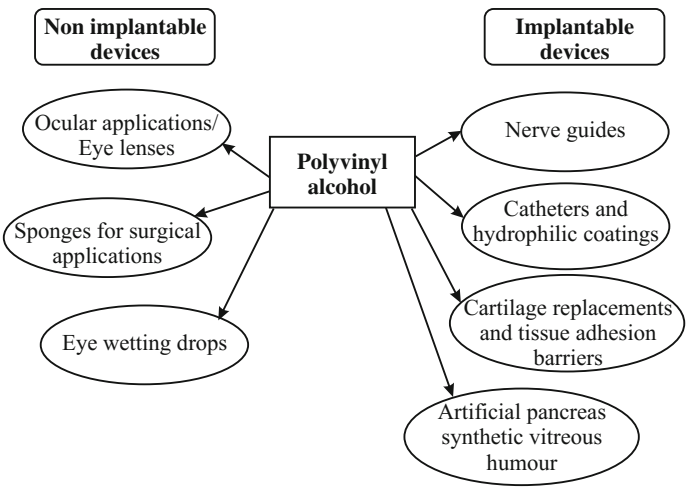

Fig. 2.2 Applications of PVA for the medical devices

saline solution and PVA polymers. The mechanical attributes of material can be tailored by the ratio of PVA and H_2O. Usually, the orthopedic implants fail due to wear causing the loosening of the joints. It has been reported that the thicker the PVA, lower the wear factor. Moreover, the wear factor also gets reduced upon lowering the water content in PVA. PVA with 80–90 % water content showed no adverse or detrimental effects on the surrounding tissues upon subcutaneous and intramuscular implementation into rabbits. PVA mixed with carboxymethylated cellulose forms a PVA gel, which is used as an adhesion barrier. PVA/chitosan cross-linked with genipin is non-toxic and biocompatible during in vivo studies. Furthermore, PVA/carboxymethyle/chitosan combination serves as an excellent drug carrier vehicle. PVA hydrogel Salubria™ was implanted into 12 patients with chondral defects on the femoral condyles. Then, MRI and two level X-ray imaging were performed on them. It was observed that no dislocation, loosening, or synovialytic joint reaction occurred after four months of operation. PVA hydrogel Cartiva® also resulted in positive results except one case, where joint loosening could be observed. Upon implantation, Salubria™ sometimes resulted in joint loosening and dislocation. It was concluded that the multiple devices were implanted at the reaction sites, causing them to be freely floating, which is subjected to the expulsion with time and loading.

2.3.3 Poly(N-Isopropylacrylamide) (PNIPAM)

Poly(*N*-isopropylacrylamide) is best suited for the thermoresponsive systems; i.e., these polymers undergo reversible temperature induced sol-gel transition, when heated or cooled. Poly(*N*-isopropylacrylamide) (PNIPAM) is utilized for the cancer therapeutics via drug delivery mechanism. PNIPAM is a LCST (lower critical solution temperature) polymer, which means that below a particular temperature, the polymer exists in water-soluble form and the polymer chains are swollen. Above this temperature, water is expelled out of polymer chains leading to its shrinkage. Furthermore, the aggregation/precipitation of polymer chains occurs attributed to the hydrophobic interactions among the polymer chains. This particular temperature of phase transition is termed as the cloud point. PNIPAM finds application in the thermoresponsive systems because the change in temperature is a stimulus for drug delivery, and hence, these polymers have special place in the category of smart polymers. The LCST of PNIPAM is 32 °C, and as far as the structure of PNIPAM is concerned, the amide moiety is hydrophilic, whereas the isopropylic is hydrophobic moiety.

Due to the low LCST of PNIPAM, it can be used as an injectable hydrogel for the cartilage applications. PNIPAM is conjugated with particular molecule for targeted drug delivery, hence increasing the therapeutic action of the drugs. At the target area, the PNIPAM-loaded drugs are exposed to temperature above LCST, i.e., >32 °C, which causes PNIPAM to collapse, thereby releasing the drug. PNIPAM is reported to expel almost half of its water content, when the polymer

temperature is increased to 37 °C. Anyhow, too much loss of water is also not desirable as that would lead to structural loss of polymer causing its decreased potential for tissue regeneration.

Due to low LCST, PNIPAM is investigated for the regulation of cell attachment/detachment from the grafted matrices. Below LCST, the PNIPAM is hydrophilic in nature and hence does not interact with the cell components, whereas above LCST, they would behave as nanogels interacting with the cells. PNIPAM hydrogel is used for photothermal-driven drug delivery applications along with photodynamic therapy. Volume transitions are achieved where PNIPAM is attached with photosensitive moieties, and the whole arrangement is subjected to the irradiation at resonance wavelength as that of photosensitive moieties. When light of resonance wavelength falls on the PNIPAM-conjugated photosensitive entities, then the absorbed light energy is converted to heat energy. Consequently, the temperature rises and the polymer expels out water. If drug is loaded inside polymer matrices, then the same shrinking mechanism leads to the drug release at target area. The most commonly used photosensitive moiety is gold nanorods.

2.3.4 Polytetrafluoroethylene (PTFE)

Highly polarized C–F bonds are the backbone of aliphatic polymers such as polytetrafluoroethylene (PTFE). Chemours discovered PTFE in 1938, and its brand name is Teflon. PTFE is synthetic fluoropolymer with high molecular weight and low coefficient of friction. The PTFE displays London dispersion forces, i.e., weak intermolecular forces attributed to quantum-induced instantaneous polarization multipoles in the molecules. These forces endow PTFE with hydrophobic and lipophatic character. PTFE finds applications in ankle foot orthotic devices, where orthotic device is an external device used to modify the neuromuscular/skeletal system characteristics. It prevents calluses, foot ulceration, and blisters caused in foot due to friction. PTFE also finds applications in dental restorative materials. PTFE grafts are used to bypass abnormally narrowed blood vessels commonly known as strictures and stenosis. Another commonly generic trademark of stretched PTFE is Gore-Tex, which is waterproof, but microporous in nature allowing water vapor to pass through them. Under anisotropic loading, Teflon structure consists of axially aligned pores (along the stretching direction) making its microporous. Gor-Tex is inert inside the human body; hence, it can be used for internal medical applications.

The permeability of Gore-Tex allows the oxygen to pass through it and allows the tissue growth through the material. Gore-Tex has also been used in the form of mesh barriers to avoid any lesions or adhesions on the surrounding tissues. The Gore-Tex soft tissue patch is the common material used for soft tissue repairs especially for hernia repair, temporary bridging of facial defects, and inguinal herniorrhaphy. Gore-Tex offers inertness, softness, biocompatibility, and higher strength making it desirable material for the mesh applications. Large aortic and carotid vascular grafts also utilize Gore-Tex. Another form of Teflon is STING

(Subureteric Teflon Injection), which is used to cure Vesicoureteral reflux (VUR) in children. In vesicoureteral reflux, the urine flows back into the ureters from the bladders. VUR causes bacteria, which can cause kidney scarring and infection, thereby damaging it. Gore-Tex patches and STING injections are used together to cure the VUR.

2.3.5 Other Polymers

Polyvinylidene fluoride (PVDF) is purely thermoplastic fluoropolymer and resistant to solvents. It has high crystalline character of ~60 %, and glass transition temperature is −35 °C. The polymers with low glass transition temperature (T_g) are well suited for the vascular applications. PVDF is used as an artificial membrane with almost 0.2–0.4 mm pore size for the immunoblotting applications. In the proteins' immunoblotting, proteins are transferred on to the PVDF membranes using electricity. These proteins are stained with antibodies corresponding to the target proteins. PVDF is also used in designing sterilizing filters for high-performance liquid chromatography (HPLC) applications. Another polymer, polypropylene (PP), behaves like PE in various properties. PP is resistant to organic solvents and fatigue. PP exhibits excellent fiber-forming properties, and its meshes are used as prosthetic for repairing abdominal defects. PP can withstand the heat of autoclave; hence, it can be used in the sterilizing devices for medical applications. PP has been used to cure hernia with positive clinical outcomes, and its meshes are found to erode the tissues and are also prone to cracking; hence, FDA has issued many warnings. Poly(dimethylsiloxane) (PDMS) is commonly referred to as silicones with exceptional flow properties. PDMS has been used in contact lens, hair conditioners, and skin moisturizing lotions. It is also used in the breast implants as filler materials. Silastic® is a variant of PDMS and serves as an excellent drug carrier. In addition to this, the Silastic® has found applications in orbital implant and facial reconstructive surgeries.

Polyethyleneterepthalate (PET) known by the brand name Dacron® is among the common thermoplastic polymer which degrades slowly. Over past 20–30 years, the area of cardiovascular surgery has been revolutionized because Dacron® vascular grafts proved to be excellent alternatives to autologous transplantation. Polyethylene oxide (PFO/PEG) belongs to the class of aliphatic polyethers and is component of stable nucleic acid lipid particles (SNALPs). PEG is used as a dispersant in the toothpaste, for the plasmid DNA isolation as well as protein crystallization. PEG is commonly used precipitant and exhibits protein inhibitory potential due to organization of H_2O around PEG polymer chain.

Polymethylemethacrylate (PMMA) has been used as a bone cement under trade name Palacos®. Other trade names of PMMA are Perspex, Acrylite, Plexiglas, and Lucite. PMMA is used for ocular applications due to its biocompatibility with soft tissues for orthopedic surgeries. PMMA is supplied in the powder form, whereas its counterpart MMA is liquid in nature. MMA is considered to be carcinogenic and

hence affects the tissues upon long-term contact. PMMA is used in dental applications especially dentures. PMMA loaded with bioactive materials are sold under the trade name Palamed®G and Refobacin®. PMMA bone cement Osteopal®V is injected in the vertebral body to cure the compression fracture.

Polyhydroxyethyl methacrylate (PHEMA) is used for the fabrication of articular cartilage. More acrylic acid yields higher negative charge densities causing large osmotic pressures. PHEMA does not induce inflammatory response and remain attached to the cartilage tissue. PHEMA structures are more flexible, hence making them mechanical compatible with the adjacent cartilage

2.4 Biodegradable Polymers

The biodegradation of polymers can be done enzymatically or hydrolytically. Usually, synthetic polymers undergo hydrolytic degradation, whereas natural polymers are subjected to the enzymatically governed degradation. Based on the mode of occurrence, the polymers can be categorized as synthetic and natural polymers. The difference between synthetic and natural polymers is illustrated in Fig. 2.3.

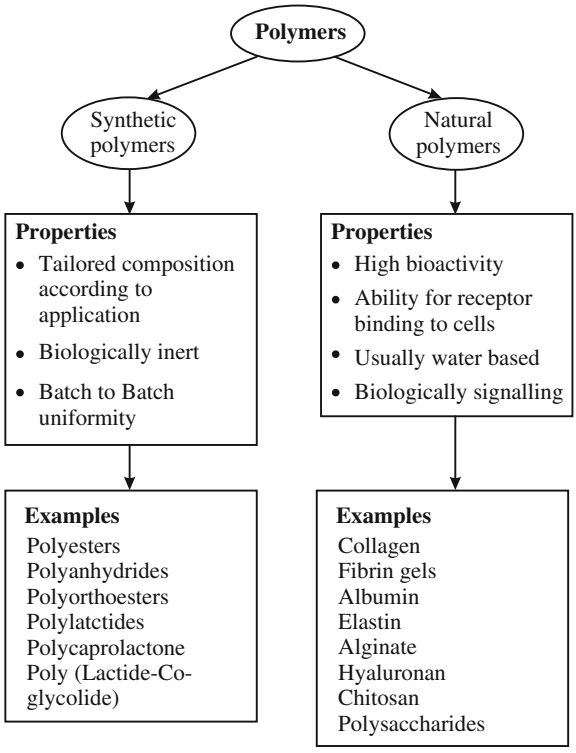

Fig. 2.3 Polymers on the basis of origin

2.5 Enzymatically Degraded Polymers

Most of the enzymatically degraded proteins are natural in origin. These natural polymers are investigated as vehicles to mimic the cartilaginous extracellular environment. Natural polymers or enzymatically degraded polymers attract the interest of research community because of their commercial availability, high biocompatibility, and ability to mimic the cartilage environment. The use of natural polymers is limited as scaffolds because their rapid degradation might lead to loss of properties. In addition to this, the inherent bioactivity of these polymers may cause considerable immunogenic response, making it necessary to purify these polymers before any biological application. Figure 2.4 gives the schematic of different enzymatically degraded polymers. Enzymatically degraded polymers include proteins, polysaccharides, natural amino acids, and polyesters with microbial origin.

2.6 Polysaccharides

Polysaccharide is one of the most commonly used materials in different biomaterial applications. Polysaccharides consist of monosaccharide units linked together via glycosidic linkages. Their structure may be linear or branched, and upon their hydrolysis, oligosaccharides and monosaccharides are obtained as end products. The most common polysaccharides are glycogen, starch, and cellulose.

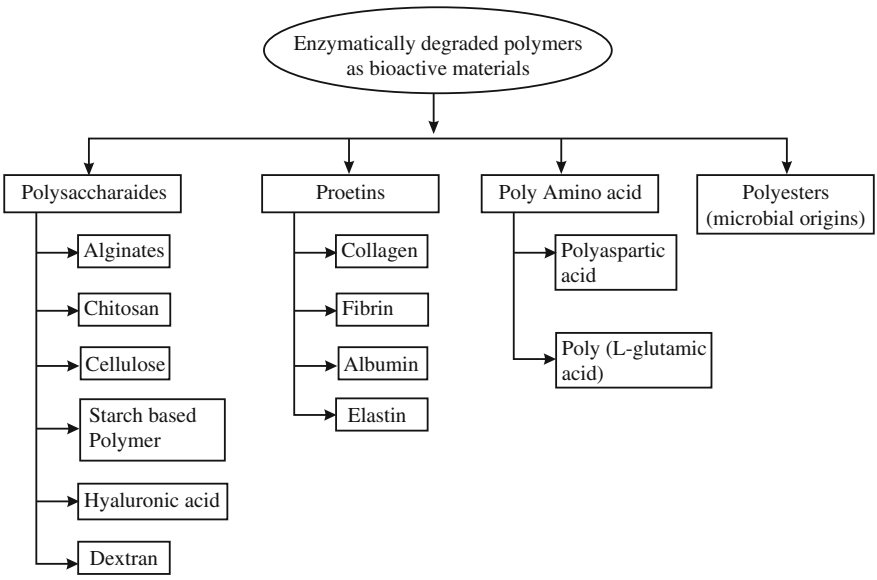

Fig. 2.4 The types of enzymatically degraded polymers as biomaterials

Polysaccharides can be heteropolysaccharides, i.e., consisting of different monosaccharide moieties, or homopolysaccharides, i.e., consisting of single monosaccharide moiety. Polysaccharides may contain polymers, which are synthesized by fungi/bacteria. Prokaryotic cells produce polysaccharides, whereas most of the carbohydrate polymers are derived from eukaryotes such as plants, animals, and algae. Although polysaccharides have low thermal, chemical, and mechanical stability, they offer excellent water solubility, non-toxicity, chemical modification, and ability to withstand pH variations.

2.6.1 Alginate (Alginic Acid)

Alginates comprises of two repeating monosaccharide units, i.e., D-mannuronic acid and L-guluronic acid linked glycosidically. Alginates are water-soluble non-branched polysaccharides. The structure of alginate is shown in Fig. 2.5.

Alginate cannot be regarded as random copolymer; rather, it is a block copolymer consisting of two uronic acids with different sequential arrangements and chain lengths. Depending on the type of source of extraction, the alginate composition varies in terms of uronic acid ratio, i.e., the ratio of mannuronic and guluronic acid plays deciding role in determining the properties of alginate. Alginates are extracted from three different species of brown algae, *Macrocystis pyrifera*, *Ascophyllum nodosum,* and *Laminaria hyperborea*. But before any application, alginates must be purified to avoid any material degradation.

Alginates are non-toxic in nature and hence used in edibles along with tissue regeneration and drug delivery applications. Alginic acids are derived from alginates, when the algae-extracted alginates are reacted with an acid. When alginate acid is exposed to the divalent cations like calcium, a three-dimensional gel is formed quickly attributed to the high acid content of alginic acid. These gel-like structures further encapsulate cells and molecules. The calcium alginate gels are stable in water environment but can be degraded enzymatically, especially in the presence of EDTA chelating agent. The COOH groups are present on alginic acid,

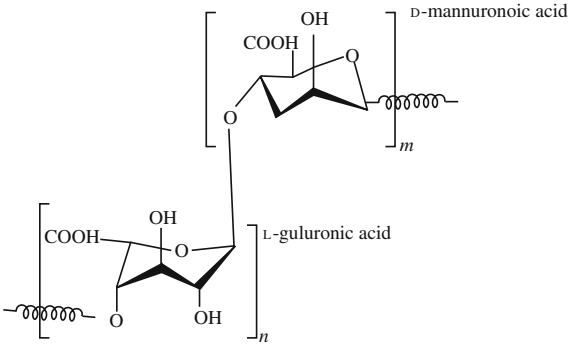

Fig. 2.5 Alginate structure comprising of L-guluronic acid and D-mannuronic acid

which are highly reactive in nature, and these COOH groups can be modified groups to make them suitable for various applications. For example, relatively stable hydrogels can be obtained when chelating cation and COOH group react together via ionotropic gelation in the presence of divalent cations such as Sr^{2+}/Ba^{2+}. Anyhow, for calcium alginate gels, the calcium can diffuse out of the gel over time leading to poor structure and loss of mechanical strength. However, the alginate hydrogels are difficult to sterilize and handle causing poor control over the gelation kinetics.

The alginate-based polymers are modified chemically by periodate causing polymer backbone oxidation. This process enhances the degradation of alginate because urinate residue is changed to open chain. Gamma irradiation-produced alginates are also biodegradable making them more applicable for bone regeneration. Alginate gels have poor cell adhesion, but when modified with cell binding peptides, they can be used as potential scaffold materials. Alginates have been combined with chondrocytes and implanted on the target area. In vivo results indicated that chondrocytes have been viable producing extracellular matrix compatible to as that of cartilage. Chitosan/alginate gel composites have been found to be clinically proven material for new bone generation. Proteins and bioactive factors can be encapsulated within the cross-linked alginate gels, which enhance the efficiency and targetibility for the protein-based alginate gel drug delivery system. Alginate have shown promising results for the chondrocyte proliferation, but some issues regarding the immune response can crop up as alginates are not native to the human body. Neither do alginate exists within ECM nor within cartilage. The lack of complete degradation is the potential cause of the immune response.

Mannuronic acid can induce inflammatory response; hence, alginate with >70 % guluronic acid has also been synthesized. For the production of optimal gels, 1–1.5 % alginate and 30–50 mM $CaCl_2$ solutions can be used. If $CaSO_4$ is used instead of $CaCl_2$, then the polymerization process decreases. Anyhow, the cartilage cultured in alginate gels can resemble the native tissue, but still, the spatial and structural differences exist. Alginate possess polyanionic characteristic, but both mannuromic and guluronic acids contain negatively charged functional groups, which neutralize the electrostatic conditions created by sulfated proteoglycoans in native tissue, thereby creating a conductive environment for chondrocyte proliferation.

2.6.2 Chitosan (Chitin)

Chitin is offer considered to be cellulose derivative as it displays structural similarity to cellulose. Chitin is composed of $\beta(1 \rightarrow 4)$-linked 2-acetamaide-2-deoxy-β-D-glucose (*N*-acetyl glucosamine). It has $NHCOCH_3$ acetamide groups at C-2 position, which separates it from the cellulose. Chitin is fully acetylate polymer forming the arthropod exoskeleton and internal structure of invertebrates. Chitosan is the principle derivative of chitin and linear polymer of $\alpha(1 \rightarrow 4)$-linked

2-amino-2-deoxy-β-D-glucopyranose (Fig. 2.6). More clearly, chitosan can be easily derived by *N*-deacetylation by varying extent making it a copolymer of *N*-acetylglucosamine and glucosamine. Chitin and chitosan are basic polysaccharides unlike alginates and cellulose. They can be dissolved in various media to form oxysalts and films.

Chitin is produced from the crustacean shell, and its processing is feasible from the astaxanthin, which is a carotenoid present in the shell. Figure 2.7 gives the processing of chitosan from the crustacean shell.

Chitin is hydrophobic, whereas chitosan has hydrophilic surface, which promotes cell adhesion proliferation and differentiation, and chitosan has various biological applications as it is endowed with good biocompatibility with the host (Fig. 2.8).

Chitosan does not initiate strong immune response and hence minimizes foreign body reaction. Chitosan forms a wide range of anionic polymers and polyelectrolyte

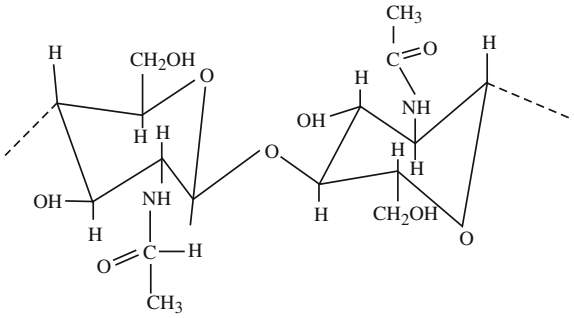

Fig. 2.6 Structure of chitosan

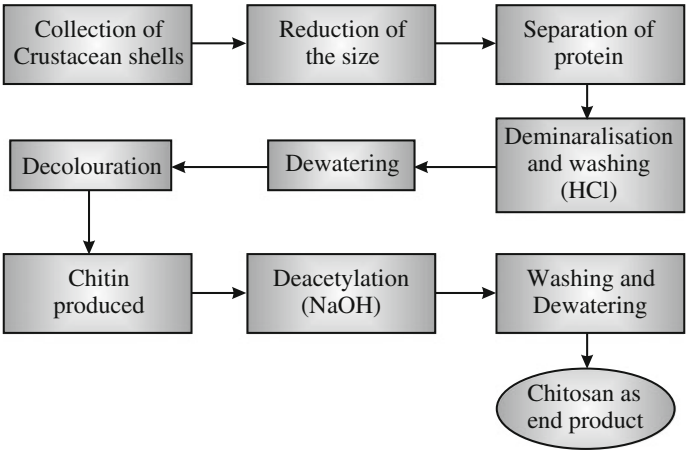

Fig. 2.7 Schematic of chitosan and chitin processing

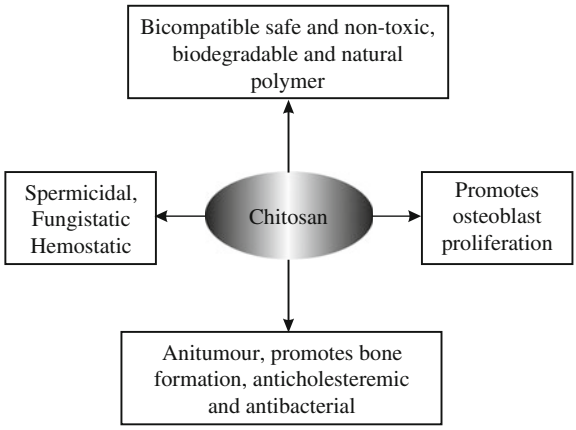

Fig. 2.8 Various properties/applications of chitosan

complexes. Apart from cellulose, it also exhibits similarly with the hyaluronic acid present in human body. Chitosan is degraded by enzymes such as lysozyme, chitosanase, and papain. Lysozyme causes the degradation of chitosan in vivo via the hydrolysis of acetylated residues. If chitosan is highly deacetylated, then its degradation rate lowers down. Similarly, high crystallinity and cross-linking densities of chitosan also lower down its degradation kinetics. Chitosan does not induce inflammatory response inside the host body nor it shows fibrous encapsulation upon implantation.

Chitosan also exhibits stimulatory effect on the macrophages because lysozyme degrades the chitosan in vivo producing oligomer, which causes macrophage activation. Chitosan heals wounds as its degradation produces *N*-acetylglucosamine, a major constituent of dermal tissues. Chitosan enhances chondrogenesis when the chitosan scaffolds are loaded with the growth factor. Chitosan loaded with TGF β-1 (transforming growth factor beta) promoter cartilage regeneration. Chondrocytes cultured on the chitosan substrates preserved morphology along with the cell-specific ECM synthesis. In addition to this, cartilage defects can be treated well when chitosan scaffolds are seeded with the chondrocytes. This indicates that the chitosan is osteoconductive and promotes bone formation both in vivo and in vitro, but the mechanical weakness of chitosan limits its applications especially for the load-bearing fields. Chitosan hydrogel has been found to be potential drug delivery vehicle. Chitosan interacts with the cell membrane, resulting in reorganization of structure causing enhanced permeation. Chitosan is very strong mucoadhesive because the negatively charged mucous membrane interacts strongly with the positive charges of chitosan. Hence, the permeation and mucoadhesive properties make it a very suitable vaccination formulation for the oral and nasal treatments. Chitosan can form microspheres/nanopheres/nanofibers without using organic solvents.

2.6.3 Cellulose

Cellulose is the most abundant polymer in nature. It is a simple polysaccharide without any branching or substituent group. Plants are the common source of cellulose, though it can be obtained from algae and by bacterial biosynthesis. Different derivations of cellulose can be obtained when the hydroxyl groups of cellulose react with various chemical agents. For instance, hydroxyethyl cellulose with functional group $–CH_2CH_2OH$ is used as a pharmaceutical excipient. Another derivative of cellulose, cellulose sulfate (with functional group $–SO_3H$), is an anticoagulant, contraceptive, and used as microbicide for human immunodeficiency virus (HIV). Other derivatives of cellulose are hydroxypropyl cellulose (with group $–CH_2CH(OH)CH_3$), carboxymethyl cellulose (with group $–CH_2COOH$), ethylcellulose (with group $–CH_2CH_3$), and ethylhydroxy ethyl cellulose (with group $–CH_2CH_2OH/–CH_2CH_3$), which are used in pharmaceutical industry.

Cellulose has formula $(C_6H_{10}O_5)_n$ and consists of $\beta(1 \rightarrow 4)$-linked D-glucose monomer units, as depicted in Fig. 2.9.

The glycosidic linkage in cellulose can be broken down by enzymes such as glycoside hydrolases, cellulases, and glucosidases. Mammals have got limited ability to digest cellulose. Anyhow, ruminants have symbiotic anaerobic bacteria such as cellulomonas in rumen that produce cellulase enzymes to breakdown cellulose. Acetobacter xylinum, a bacteria, produces cellulose, which has different properties from the plant cellulose. Bacterial cellulose has high strength, water-holding ability, high crystallinity, nanofibrous structure, and biocompatibility. Bacterial cellulose is used in bone grafts, tissue engineering, blood vessel engineering, and wound healing applications. Bacterial cellulose scaffolds support the growth and proliferation of human chondrocytes. Bacterial cellulose has flexible shape, which can be molded to take the desirable geometry. This property finds application in urinary tract, digestive tract, brain dura mater replacement, and cardiovascular applications. Gengiflex® and Bioprocess® are the trade names of bacterial cellulose. Microbial cellulose can also be obtained from the brown algae species, phaeophyta; golden algae, chrysophyta; and red algae, rhodophyta. Apart from Acetobacter xylinum, cellulose is also produced from Gram-positive bacteria, such as sarcina ventriculi, and Gram-negative bacteria species, such as pseudomonae, salmonella alcaligenes, azotobacter, and rhizobium. Microbial cellulose has also been used for the bladder neck suspensions and wound dressings.

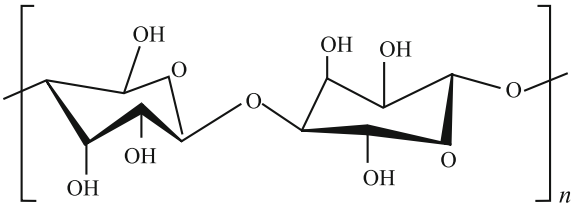

Fig. 2.9 Structure of cellulose

2.6.4 Hyaluronic Acid (Hyaluronan)

Hyaluronic acid/hyaluronan is highly hydrated polyanionic macromoleculte with molecular weight ranging from 10^3 to 10^7. It is linear polysaccharide consisting of alternating repeating units of 3-*N*-acetyl-D-glusamine, β-1 and 4-D-glucoronic acid-β-1, as shown in Fig. 2.10. ECM in various connective tissues consists mainly of hyaluronic acid. Hyaluronan signals the cell activity and morphogenesis and interacts with binding proteins proteoglycans and other bioactive molecules. Hyaluronan has viscoelastic properties, and it is water soluble.

Hyaluronan is extracted mainly from bovine vitreous humor, rooster combs, synovial fluid, and umbilical cord. Matrix metalloproteinases found in the extracellular matrix and free radicals such as nitric oxide degrade the hyaluronan. In addition to this, hyaluronan can form monosaccharides and disaccharides when acted upon lysosomal enzymes. Furthermore, these monosaccharides and polysaccharides are converted to water, carbon dioxide, and ammonia via the Krebs cycle. Hyaluronan is synthesized within the cells under the action of three glycosal transferases: hyaluronan synthase-1, hyaluronan synthase-2, and hyluronan synthase-3 (Has-1, Has-2, and Has-3). Hyaluronan synthase-2 is regarded as principle enzyme involved in hyaluronan synthesis during embryogenesis.

Rapid resorption and high water solubility limit the use of hyaluronan as bioactive material. Hence, photo cross-linking and covalent cross-linking have been implied to improve hyaluronan properties and its molecular structure. The aqueous solubility of hyaluronan can be varied from completely water soluble to insoluble hydrogels by varying the nature and quantity of alcohol used for esterifying the COOH group on glucuronic acid. One of the hyaluronan derived polymers is HYAFF®11, which is an ester derivative. When HYAFF®11 is treated with benzyl alcohol, then biodegradable scaffold biomaterial for tissue regeneration could be obtained. HYAFF®11 has not only provided a biocompatible matrix for cellular proliferation but also supported the chondrocyte phenotype. HYAFF®11 potential is well demonstrated when the mesenchymal progenitor cells from the rabbit bone marrow are seeded onto the HYAFF®11 sponges yielded enhanced cartilage/bone formation. There is another derivative of hyaluronan, which is obtained after treating it with ethyl alcohol, i.e., HYAFF®7. HYAFF®7 also degrades at predictable rates and shows good biocompatibility with the matrix.

Collagen deposition and angiogenesis are enhanced by hyaluronan as the tissue repair is promoted due to epithelial and mesenchymal cell migration. Cross-linking of hyaluronan hydrogels influences the diffusion kinetics and tissue regeneration by

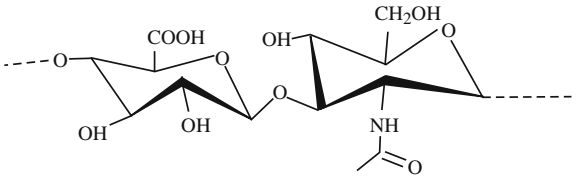

Fig. 2.10 Structure of hyaluronan

encapsulated mesenchymal stromal cells. Hyaluronan hydrogel has been used for cardiac repair. The excellent biocompatibility, tunable degradation, and non-toxicity of hyaluronans endow them with molecule and drug delivery applications. Photo cross-linked hyaluronan are also explored as a biological substitute for heart valves. The degradation products of hyaluronan gels increase valvular interstitial cell proliferation (VIC). Hyaluronan hydrogels are also investigated for developing a system to central human embryonic stem cell (hESC) renewal and differentiation. Photopolymerized hyaluronan has been used as micro-devices such as micro-bioreactor systems, which allow 3-D growth and differentiation of hESCs.

2.6.5 *Dextran*

Dextran is a complex branched homopolysaccharides of α-1, 6-D-glucopyranose units with glucosidic linkage, whereas branching begins from α-1, 2, α-1, 3, or α-1, 4 linkages as shown in Fig. 2.11.

Dextrans are synthesized from sucrose by microbial species such as *Saccharomyces cerevisiae*, *Lactobacillus sanfrancisco*, *Lactobacillus plantarum,* and *Leuconostoc mesenteroides*. Dextrans are hydrophilic and exhibit high molecular weight. The hydroxyl groups present on dextrans can be modified to design scaffold with desirable characteristics. Dextrans are used as heparin substitutions for the anticoagulant therapy and blood plasma extender. Dextrans are also used to decrease vascular thrombosis. Dextrans bind with exrythrocytes, vascular endothelium, and platelets, thereby reducing platelets adhesiveness. Dextrans act as a plasminogen activator by inhibiting α-2 antiplasmin. In addition to this, hypovolemia is also treated using dextrans as potential osmotic agents. In emergency, when blood is not available, dextran is used to replace lost blood because it can supply necessary electrolytes to sustain vital functioning of body. The iron dextran injection is used to cure anemic deficiency. Clinical grade dextrans are used in drug delivery systems and for storing organs for transplantation.

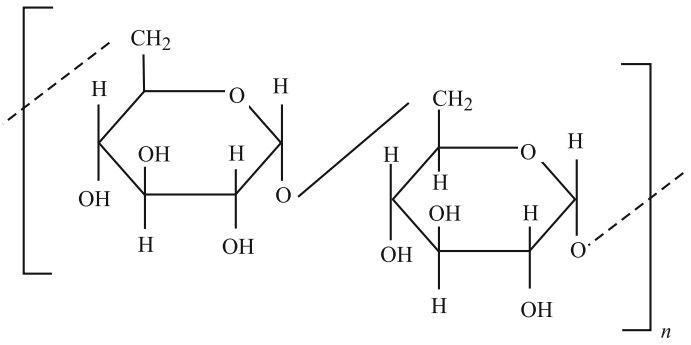

Fig. 2.11 Structure of dextran fragment

The sulfonic esters of dextrans exhibit anticoagulant action provided each glucose unit must have certain minimum numbers of sulfate groups. The cryogels made out of dextran exhibit good biocompatibility and biodegradation when implanted as scaffold materials.

2.6.6 Starch Compounds

Starch is one of the most abundant polysaccharide present in plant especially in the amyloplast of seeds/tubers. Starch is made up of two main structural components (Fig. 2.12):

- Amylose—linear polymer consisting 15–20 % of starch and consisting of glucose molecules linked with α-D-(1–4) linkages (poly(1, 4-α-D-glucopyranose));
- Amylopectin—branched polymer constituting majority of starch and consisting of branched molecule with α-D-(1–6) and α-D-(1–4) linkages (1, 6–α-D-glucopyranose).

Starch is biodegradable and can be designed as bone cements and 3-D scaffold materials. When starch-based polymers are modified, then they can be used in wide range of biomedical applications. Carboxymethyl starch (CMS) is used for the release of 5-aminosalycylic acid to the colon. CMS is also used to deliver stable bioactive proteins into intestine within 6 h of intake. Carboxymethyl high amylose starch (CMHAS) with degree of substitution within 0.9–1.2 for the acetaminophen is regarded as delayed release excipient. The starch acetate fiber supports the fibroblast adhesion and possesses better water stability and mechanical properties. Starch acetate-coated tablets act as a potential drug delivery carrier for colon targeting especially for dyphylline drug. Hydroxy propylation improved the sustained release ability of propranolol hydrochloride under simulated gastrointestinal conditions. Starch phosphate also yielded better release kinetics over native starch tablet for ziprasidone and metroprolol tartrate. Starch acrylics graft copolymers provided pH sensitive matrix for paracetamol drug release. Starch-based polymer

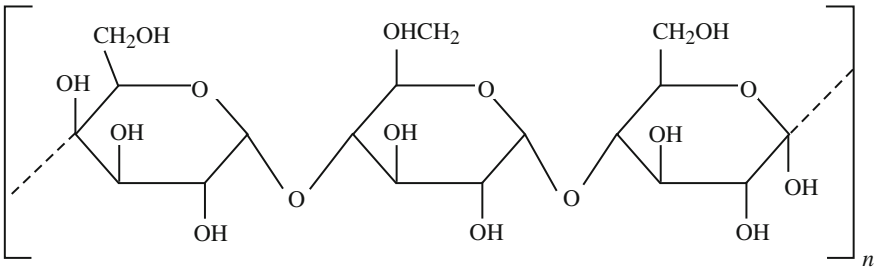

Fig. 2.12 Structure of starch unit

usually degrades by α-amylase followed by phagocytosis by marcophages. Glucose and glucose derivatives are obtained as by-products of starch degradation.

2.7 Proteins

Proteins belong to one of the most prominent fields of biomaterials consisting of long chains of amino acids known as polypeptides. Many enzymes are proteins, which help in catalyzing biochemical reactions. Proteins such as actin and myosin are vital components of muscles. Therefore, proteins are preferred as biomaterials in various applications such as scaffolds for tissue engineering, drug delivery carriers, hemostatic agents, drug delivery carriers, hemostatic agents, and sutures. Human body can synthesize proteins via the following mechanism (Fig. 2.13).

Proteins have been found as component of ECM matrix of native tissues for scaffolds in tissue engineering collagen, albumin, fibrin, and elastin as protein biomaterials.

2.7.1 Collagen

Although there are many types of collagen proteins identified in humans, type I–IV are the most common collagen proteins. Type I collagen is found in abundance inside human body especially for the musculoskeletal tissue and skin. Type-I collagen consists of ∼20 % amino acid, and molecular weights of collagen are 300 nm and 300,000, respectively.

The repeating unit of protein, i.e., glycine, comprises of $(\text{Glycine–x–y})_n$, where x and y are usually proline and hydroxyproline. The repeating sequence of glycine

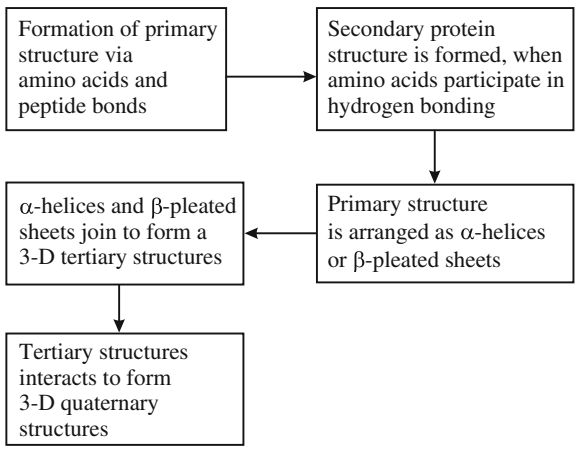

Fig. 2.13 Mechanism of protein synthesis

produces left-handed α-chain helical structure. When 10 polypeptide chains arrange, then right-handed helical secondary structure is produced. Three α-chains wrap around to form a common tripeptide sequence in collagen to form a tightly packed sequence (Fig. 2.14).

Collagen can undergo enzymatic degradation by the action of enzymes such as metalloproteinase and collagenases to yield amino acids. Collagen has excellent biological and degradation properties, which make them suitable for the biomedical application. In addition to this, the degradation rate of collagen can be tailored using various cross-linking agents or enzymatic pretreatment. Collagen exhibits low antigenicity and high cell binding properties making them suitable for tissue engineering applications. Studies have shown that upon seeding MSC, onto collagen gels, followed by its implantation in osteochondral defects in rabbits led to hyaline cartilage and bone formation. Duragen® is a three-dimensional collagen matrix graft developed for spinal dural repair. Diabetic and ulcer wounds have been cured using novel spongy collagen matrix under the brand name Promogran®. Acellular collagen matrices obtained from human cadavers are used as wound dressings under the trade name Alloderm® and Biobrane®. Collagen is used as a hemostatic agent as it initiates the coagulation cascade. Collagen-based sealant comprising of bovine thrombin and bovine collagen under the brand name Sulzer-spine® Tech is used during spinal and cardiovascular surgical procedures.

Collagen has been a promising drug delivery vehicle for antibiotics especially gentamicin under the trade name Collatamp®-G, Septocoll®, and Sulmycin® Implant and many more. Collagen is also investigated for plasmid DNA delivery as it protects gene vector/plasmid DNA from enzymatic reactions or immunological responses. Collagen microspheres can enhance cell density of chondrocytes without loss of viability. Anyhow, the biological activity of seeded cells depends heavily on the composition and structure of collagen. For instance, type I collagen matrix would produce scaffolds with pore size 20–83 μm and porosity is 87 %, whereas type II collagen resulted in pore size of 88 mm and porosity is 85 %, when prepared by freeze-drying process. Reports showed that basic fibroblast growth factor (bFGF) enhanced the cartilage regeneration and chondrocyte activity within collagen scaffolds. Collagen has been used as protein carrier vehicle, and recombinant human bone morphogenic protein (rhBMP-2) is one such protein to be tested for anterior lumbar spinal fusion. Collagen is extracted from the bovine/equine Achille's tendons or porcine skin. Collagen-based biomaterials sometime produce

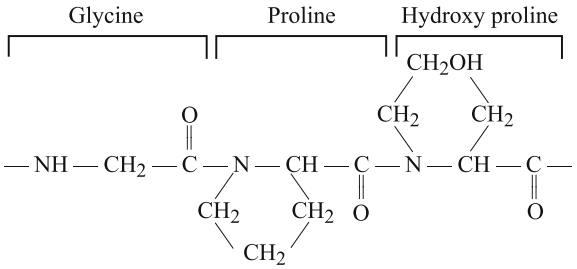

Fig. 2.14 Chemical structure of tripeptide sequence for collagen protein

mild immunogenicity due to the presence of antigenic sites in the central helix. Another disadvantage of collagen is its high degradation leading to loss of mechanical properties. Hence, the high reactivity of collagen proteins is exploited by cross-linking them with various agents such as polyepoxy, polyethylene glycol, and multifunctional aldehydes. Matrix made by cross-linking collagen fibers with modified hyaluronan was implanted in rat cranial defect yielding good biocompatibility and improved osteoconductivity.

2.7.2 Fibrin

Fibrin is a naturally occurring non-globular protein, which plays an indispensible role during wound healing. Fibrin is derived from fibrinogen, a 360 kPa glycoprotein synthesized in liver by hepatocyte. When fibrinogen becomes active, then the polymerization process starts to produce fibrin. Fibrinogen is a hexamer containing two sets of three different chains with α-, β-, and γ-subunits linked by disulfide bonds. The α- and β-chains contains ligands with specific affinity for the respective binding pockets. When fibrinogen is inactive, then each ligand is surrounded by peptide sequence, which acts as a protective covering. When enzyme thrombin is present in its vicinity, then the ligand becomes active due to cleavage of peptide sequence. Furthermore, the hydrogen bonds and electrostatic interaction connects the ligands of one fibrinogen molecule with the binding pockets of other fibrin molecules, resulting in the formation of 3-D network. The three-dimensional network of fibrin gel can be converted to covalent hydrogel by the enzymatic action of factor XIIIa. Factor XIIIa is a transglutaminase enzyme activated by thrombin. Factor XIIIa chemically cross-links lysine and glutamine residue found on with α-, β-, and γ-chains of the fibrin molecules, thereby causing the breakdown of 3-D network. Fibrin is also dissociated by an enzyme plasmin, a serine protein that dissolves the clots. Hence, plasmin introduces the process of fibrinolysis that prevents blood clot from become large and problematic. Figure 2.15 depicts the combined action of fibrinogen structure and its conversion to fibrin.

Fibrinogen exhibits excellent biodegradability and biocompatibility, which enhances cell adhesion and proliferation. Bioseed® is a fibrin-based product used to treat chronic wounds. Fibrin allows the cell to mountain phenotype and is found to be non-toxic for chondrocytes. In vivo observation regarding fibrin as a scaffold material for neocartilage formation is also studied. It has been revealed that fibrin forms cartilaginous extracellular matrix, though the DNA concentration and glycosaminoglycan are slightly lower than the bovine cartilage. Fibrinogen induces minimal response again xenografts in athymic mice; hence, it is investigated as potential drug delivery vehicle. Fibrin undergoes hydrolytic and enzymatic degradation; hence, they are modified in order to stabilize them for longer durations. One such fibrin gel system is available under the brand name Tissucol®, which contains aprotinim, a polypeptide, which inhibits serine proteases. Anyhow, the addition of aprotinin and tranexamic acid to fibrin gels inhibits fibrinolysis, but at the same

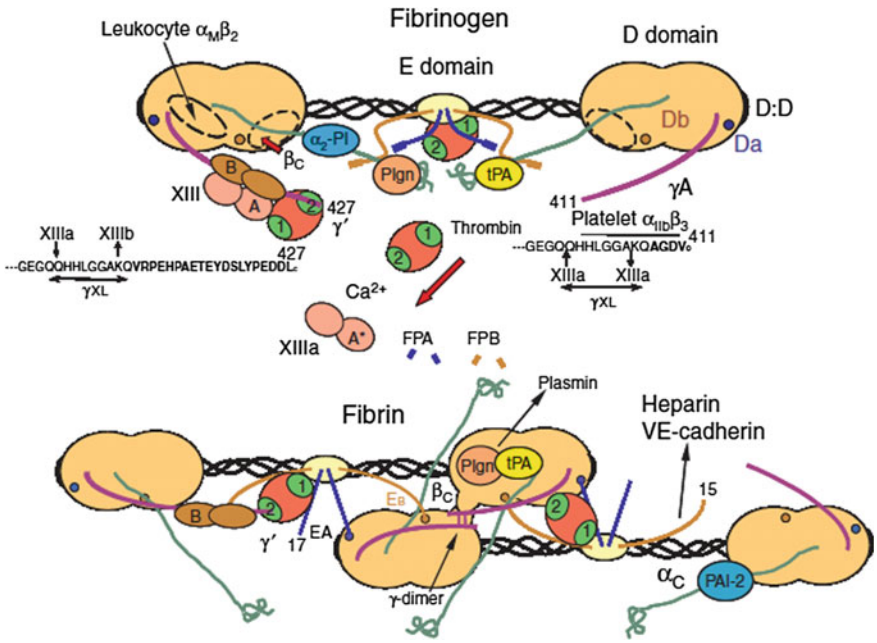

Fig. 2.15 Fibrinogen structure and its conversion to fibrin along with thrombin-mediated conversion factors XIII to XIIIa (Mosesson 2005)

time, chondrocyte phenotype and viability were greatly affected. The tissue segmentation capability of fibrin still needs to be widely addressed because the rapid degradation of fibrin gels raises stability issues causing the chondrocytes to migrate away from the target area.

2.7.3 Elastin

Elastin is a protein in the connective tissue and endows them with the elastic properties so that they regain their shape after deformation. Elastin is highly cross-linked and insoluble polymer comprised of tropoelastin molecules. Humans have only one tropoelastin gene (ELN), and the expression of ELN occurs only before birth and during the first few years of life. ELN expression is decreased during the adult age as the body makes less elastic during that period of time. ELN gene encodes protein rich in glycine and proline. Tropoelastin is composed of pentapeptides, hexapeptides, tetrapeptides, and non-apeptides. The process of elastic fiber formation involves microfibrils with fibrillin-1 as the major component and lysyl oxidases enzymes, which contribute to the cross-linking. Figure 2.16 indicates the formation of elastin fibers via enzymes and microfibrils.

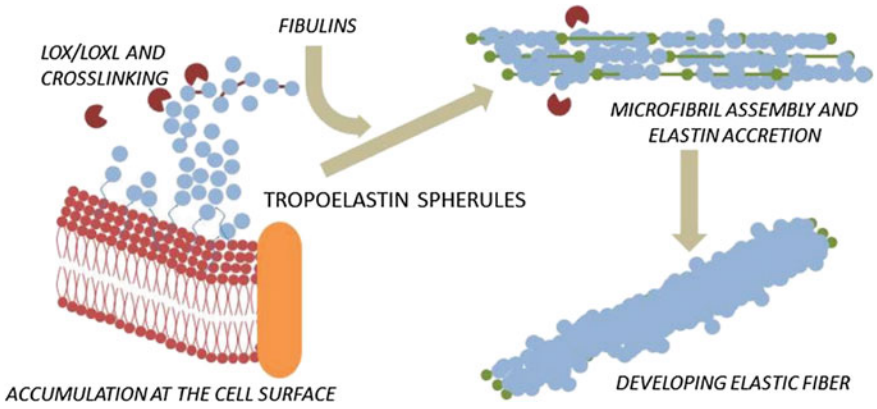

Fig. 2.16 Schematic of elastin fiber formation (Weiss 2011)

The tropoelastin accumulates in the form of spherules on the cell surface. The applications of elastin get limited due to its non-soluble nature along with its immune response. When synthetic elastins are developed from recombinant human tropoelastin, then the issues of non-solubility of elastin is resolved. The synthetic elastins exhibit promising mechanical and biological properties. Elastin-like polypeptides (ELP) are one such artificial polypeptide obtained from human topoelastin. ELP consist of polypeptide Val-Pro-Gly-X-Gly with X as a guest amino acid except proline. ELP are non-immunogenic, non-toxic, biocompatible, and biodegradable. The LCST of ELP is low, and they are pH, temperature, and guest amino acid sensitive. ELP's potential applications are drug release at targets and recombinant protein purification. ELP exhibit almost same shear modulus as that of cartilage. ELP is found to enhance the stem cell differentiation without the addition of any chondrocyte-specific growth factors. ELP also promoted the synthesis and accumulation of articular ECM for adult stem cells and chondrocytes. The load-bearing capabilities of ELP could be increased when it is enzymatically cross-linked via tissue transglutaminase. ELP are also used for vascular graft tissue engineering and ocular tissue engineering. In liver tissue engineering, when ELP coats ≥ 80 % of culture surface, then spheroid formation occurs which increases hepatocyte function.

Elastin materials show an interesting property of inverse temperature transition (ITT), i.e., transition from disordered to ordered state at high temperature when temperature is increased above 25 °C, and then, elastin and tropoelastin undergo folding. The property of ITT endows elastin materials to be used as drug delivery vehicles. ELP are attractive as copolymers and particularly attractive for cell recovery and cell sheets for scaffold free tissue engineering.

2.7.4 Albumin

Almost 50 % of total plasma mass of human body is composed of globular proteins known as albumin. Albumin is water soluble and undergoes heat denaturation. Two commonly used albumins are human serum albumin and bovine serum albumin, which is used for medical applications. Serum albumins bind bilirubin, thyroid hormone, fatty acids, and water. Liver synthesis albumin as proalbumin with *N*-terminal peptide. Before the release of albumin in the rough endoplasmic reticulum, the terminal peptide is removed and the Golgi bodies cleave the proalbumin to albumin.

Albumin contains high content of cystine, aspartic, lysine, and arginine acids with low methionine and tryptophan. Albumin exhibits good biocompatibility and is biodegradable as almost every human tissue can degrade albumin. Albumin is used in drug delivery applications and coatings for cardiovascular devices. Albumins also show degradation in the presence of pepsin. Albumin treats burns and upgrades the low protein levels due to surgery or liver failure conditions. Albumin hemostasis is regulated in all human tissues with almost 60 % being degraded in kidneys, liver, and muscles. The patients with cirrhosis are treated with albumin as it provides anti-oxidation, endothelial protection, and plasma expansion.

2.8 Polyamino Acids

Amino acids comprise a wide range of biodegradable polymers due to their versatile applications. Amino acids have been exploited for prosthetic implants and drug delivery applications. Amino acids can be natural and synthetic; poly-γ-glutamic acid (γ-PGA), poly(ε-L-lysine), and cyanophycin are natural polyamino acids with single type of amino acid (Fig. 2.17).

γ-PGA is highly biodegradable and very promising material for synthesizing the scaffolds. Benzyl ester of γ-PGA degrades slowly in phosphate buffer solution depicting pH-dependent controlled diffusion. γ-PGA is water-soluble anionic homopolyamide composed of D- and L-glutamic acid units. γ-PGA is produced by microbes such as bacillus species, Cnidaria, and hydrozoa. Poly-L-lysine is also of bacterial origin and possesses anti-tumor, anti-viral, and anti-bacterial activities. Anyhow, poly-L-lysine is cytotoxic, which limits its application. Cyanophycin is another polypeptide separated from cyanobacteria containing α-amino-α-carboxy-linked L-aspartic acid residues and L-arginine residues bounded to β-carboxylic group endowing it with polydisperse character. However, there are limited reports for these polyamino acids to be used as biomaterials.

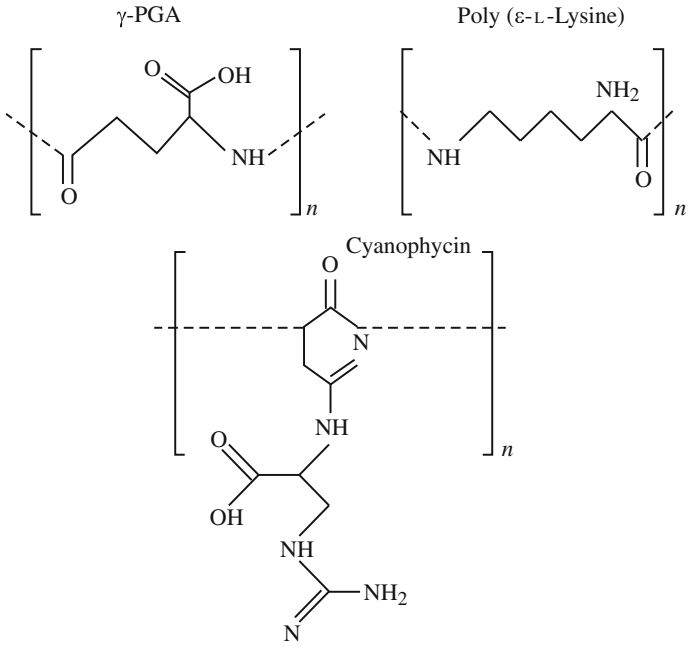

Fig. 2.17 Structure of the natural polyamino acids

2.8.1 Poly(L-Glutamic Acid) (L-PGA)

Poly(L-glutamic acid) differs from naturally occurring glutamic acid and consists of L-glutamic acids primarily linked through amide bonds. Synthetically L-PGA is prepared from poly(γ-benzyl-L-glutamate) by treating with hydrogen bromide and removing benzyl protecting group. Other methods of preparing L-PGA include peptide-coupling reactions and alkaline hydrolysis of poly(L-methyl glutamate). To obtain high molecular weight polymers of poly(γ-benzyl-L-glutamate) (PBLG), the *N*-carboxyanhydride (NCA) of γ-benzyl-L-glutamate is polymerized using triethylamine (Fig. 2.18).

When the pH is increased to 5.5, then PGA shows a structural change from rod-like α-helix form to coil structure. The coil regions are more susceptible to the enzymatic attacks. Furthermore, the sequential distribution of copolymers and the composition affect degradation rates considerably. PGA is susceptible to the lysosomal degradation, and the main degradation products are tripeptides and tetrapeptides. Degradation of PGA also leads to monomeric L-glutamic acid, suggesting that cysteine proteases are involved in the degradation.

PGA has been used as a control for drug delivery studies as it can be tolerated up to accumulated dose of 1.8 g/kg and single dose of 800 mg/kg. Though PGA is non-immunogenic but can show some immunogenic response when conjugated to a

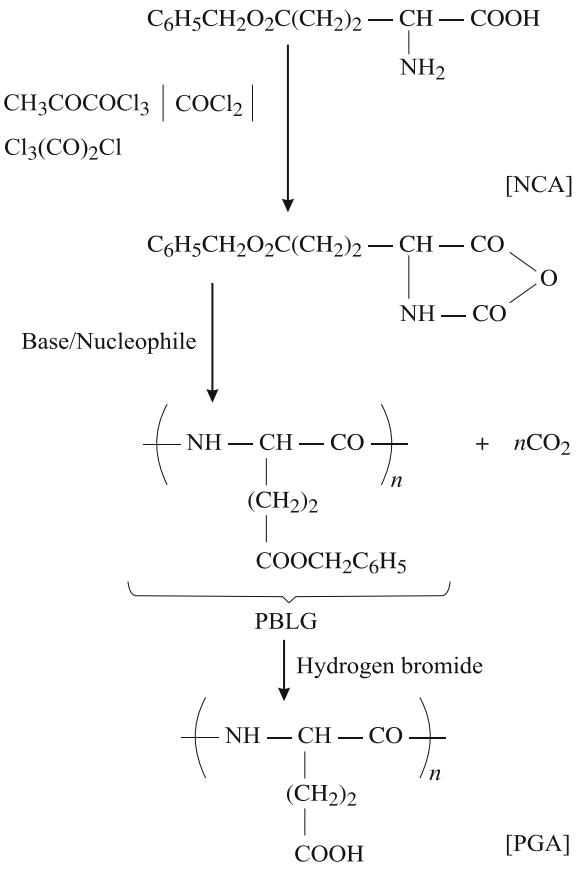

Fig. 2.18 Reaction scheme for PGA synthesis

drug. Anti-tumor drugs such as doxorubicin and danorubicin are attached to PGA via hydrolytically labile ester bonds and hydrazone bonds. Though PGA–oligopeptides–doxorubicin are active, their activity increases with increasing degradability of spacer. The α-carboxylate side chains of the polymers are modified by adding bioactive ligands, which modulate the polymer properties. L-PGA is a biodegradable biological adhesive when cross-linked with gelatin. L-PGA has enabled the development of biodegradable MRI contrast agent. PGA-paclitaxel conjugates are synthesized via ester bonds. Paclitaxel (TXL and Taxel) is an anti-tumor agent, which promotes tubulin polymerization and microtubule assembly. PGA-TXL reduced systems toxicity and caused regression of well-established solid tumors. PGA-TXL is the first PGA conjugate used for clinical trials.

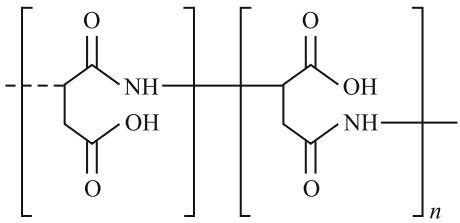

Fig. 2.19 Structure of the polyaspartic acid

2.8.2 Poly(Aspartic Acid)

Polyaspartic acid (PAA) is highly water-soluble ionic polymer (Fig. 2.19). PAA can be used as super absorber, antiscalant, and dispersant. Polyaspartic acid can be synthesized after condensation of aspartic acid via three commonly used techniques, i.e., thermal polymerization of maleic acid and ammonium hydroxide, thermal condensation of aspartic acid, and catalyzed polymerization of aspartic acid.

The biodegradability of PAA is affected by the branching structures and irregular end group in polyaspartic acid. Lysosomal enzymes are also involved in the degradation of PAA. Bacteria such as Sphigomonas and Pedobacters are also studied to induce degradation of PAA. PAA block copolymers along with other biodegradable polymeric moieties form drug delivery vehicles α,β-poly(*N*-2 hydroxy ethyl)-D, L aspartamide (PHEA) are investigated as a plasma expander due to its water-soluble nature along with biocompatibility.

2.9 Microbial Polyesters

Microorganisms such as euckaryotes and prokaryotes are known to synthesize polyester. Polyhydroxyalkanoates (PHA) are one such polyester synthesized from microorganisms, especially Gram-positive/Gram-negative bacteria. Microorganisms accumulate PHA comprising of hydroxycarboxylic acids, with carboxyl group at the end and hydroxyl group at 3-, 4-, 5-, and 6-positions. PHA falls in two categories depending on number of carbon atoms present in the chain, i.e., short chain length (SCL) PHA with 3–5 carbon atoms and medium chain length (MCL) PHA with 6–14 carbon atoms. PHA is attractive biomaterial due to wide range of their mechanical and biodegradable properties. However, PHA is not easy to fabricate and their extraction is quite time-consuming. Due to its low mechanical strength limits, it cannot find much utility in load-bearing applications. The monomer of PHA, Poly(3-hydroxybutyrate), is of interest, as it is used for bone plates, nails, screws, and temporary stents for tissue engineering applications. PHB is biocompatible with many cell lines including epithelial cell, chondrocytes, and osteoblasts. PHB has shown no chronic inflammatory responses even after implantation for 12 months in bone tissue segmentation. PHB has shown proliferation of chondrocytes along with phenotype presentation when seeded onto rabbit articular cartilage.

Bibliography

Mosesson MW (2005) Fibrinogen and fibrin structure and functions. J Thromb Haemost 3: 1894–1904
Weiss AS (2011) The science of elastin. Elastagen Pvt. L Ltd
Chandra R, Rustgi R (1998) Biodegradable polymers. Prog Polym Sci 23:1273–1335
Naira LS, Cato T (2007) Laurencin, biodegradable polymers as biomaterials. Prog Polym Sci 32:762–798
Tian H, Tang Z, Zhuang X, Chen X, Jing X (2012) Biodegradable synthetic polymers: preparation, functionalization and biomedical application. Prog Polym Sci 37:237–280
Zhang Q, Lin D, Yao S (2015) Review on biomedical and bioengineering applications of cellulose sulfate. Carbohydr Polym 132:311–322
Sutherland IW (1996) Extracellular polysaccharides, 2nd edn. Biotechnology
Nettles DL, Chilkoti A, Setton LA (2010) Applications of elastin-like polypeptides in tissue engineering. Adv Drug Deliv Rev 62:1479–1485
Gunatillake PA, Adhikari R (2003) Biodegradable synthetic polymers for tissue engineering. Eur Cells Mater 5:1–16
Burdick JA, Prestwich GD (2011) Hyaluronic acid hydrogels for biomedical applications. Adv Mater 23:41–56
Nagapudi K, Brinkman WT, Thomas BS, Park JO, Srinivasarao M, Wright E, Conticello VP, Chaikof EL (2005) Viscoelastic and mechanical behavior of recombinant protein elastomers. Biomaterials 26:4695–4706
Bronzino JD (2006) Biomedical engineering fundamentals, 3rd edn. CRC press
Gijpferich A (1996) Mechanisms of polymer degradation and erosion. Biomaterials 17:103–104
Lee GN, Na J (2013) Future of microbial polyesters. Microb Cell Fact 12:54
Kohane DS, Langer R (2008) Polymeric biomaterials in tissue engineering. Pediatr Res 63: 487–491
Seal BL, Otero TC, Panitch A (2001) Polymeric biomaterials for tissue and organ regeneration. Mater Sci Eng R 34:147–230
Buckwalter JA (1983) Articular cartilage. Instr Course Lect 32:349–370
Mie M, Mizushima Y, Kobatake E (2008) Novel extracellular matrix for cell sheet recovery using genetically engineered elastin-like protein. J Biomed Mater Res B Appl Biomater 86:283–290
Henschen A, Lottspeich F, Kehl M, Southan C (1983) Covalent structure of fibrinogen. Ann NY Acad Sci 408: 28–43
Ochubiojo1 EM Starch AR From food to medicine, scientific, health and social aspects of the food industry (Intechophen)
Puppi D, Chiellini F, Piras AM, Chiellini E (2010) Polymeric materials for bone and cartilage repair. Prog Polym Sci 35:403–440
Huang S, Cao Z, Davie EW (1993) The role of amino-terminal disulfide bonds in the structure and assembly of human fibrinogen. Biochem Biophys Res Commun 190:488–495
Urry DW (1997) Physical chemistry of biological free energy transduction as demonstrated by elastic protein-based polymers. J Phys Chem B 101:11007–11028
Meh DA, Siebenlist KR, Brennan SO, Holyst T, Mosesson MW (2001) The amino acid sequences in fibrin responsible for high affinity thrombin binding. Thromb Haemost 85:470–474
Lim DW, Nettles DL, Setton LA, Chilkoti A (2007) Rapid crosslinking of elastin-like polypeptides with hydroxymethylphosphines in aqueous solution. Biomacromolecules 8:1463–1470
Srokowski EM, Woodhouse KA (2008) Development and characterisation of novel cross-linked bio-elastomeric materials. J Biomater Sci Polym Ed 19:785–799
Ferry JD (1988) Structure and rheology of fibrin networks. In: Kramer O (ed) Biological and synthetic polymer networks, Elsevier Applied Science, Amsterdam, the Netherlands, pp 41–55
Cappello J, Crissman J, Dorman M, Mikolajczak M, Textor G, Marquet M, Ferrari F (1990) Genetic-engineering of structural protein polymers. Biotechnol Prog 6:198–202

Sahni A, Francis CW (2000) Vascular endothelial growth factor binds to fibrinogen and fibrin and stimulates endothelial cell proliferation. Blood 96:3772–3778

Wang Y, Bian Y-Z, Wu Q, Chen G-Q (2008) Evaluation of three dimensional scaffolds prepared from poly(3-hydroxybutyrate-co- 3-hydroxyhexanoate) for growth of allogeneic chondrocytes for cartilage repair in rabbits. Biomaterials 29:2858–68

Mosesson MW (2003) Fibrinogen gamma chain functions. J Thromb Haemost 1:231–238

Jordan SW, Haller CA, Sallach RE, Apkarian RP, Hanson SR, Chaikof EL (2007) The effect of a recombinant elastin-mimetic coating of an ePTFE prosthesis on acute thrombogenicity in a baboon arteriovenous shunt. Biomaterials 28:1191–1197

Agrawal CM, Athanasiou KA, Heckman JD (1997) Biodegradable PLA/PGA polymers for tissue engineering in orthopaedica. Mater Sci Forum 250:115–128

Sanderson JE (1988) Bone replacement and repair putty material from unsaturated polyester resin and vinyl pyrolidone. United States Patent 4(722948):1–14

Nelson JF, Stanford HG, Cutright DE (1977) Evaluation and comparison of biodegradable substances as osteogenic agents. Oral Surg 43:836–843

Storey RF, Wiggins JS, Mauritz KA, Puckett AD (1993) Bioabsorbable composites. II: Nontoxic, L-lysinebased (polyester-urethane) matrix composites. Polym Compos 14:17

Temenoff JS, Mikos AG (2000) Injectable biodegradable materials for orthopaedic tissue engineering. Biomaterials 21:2405–2412

Alsberg E, Anderson KW, Albeiruti A, Franceschi RT, Mooney DJ (2001) Cell-interactive alginate hydrogels for bone tissue engineering. J Dent Res 80:2025–2029

Atala A, Kim W, Paige KT, Vacanti CA, Retik AB (1994) Endoscopic treatment of vesicoureteral reflux with a chondrocyte-alginate suspension. J Urol 152:641–643

Chen G-Q (2009) A microbial polyhydroxyalkanoates (PHA) based bio- and materials industry. Chem Soc Rev 38:2434–2446

Zhao K, Deng Y, Chen CJ, Chen GQ (2003) Polyhydroxyalkanoate (PHA) scaffolds with good mechanical properties and biocompatibility. Biomaterials 24:1041–1045

Deng Y, Lin X-S, Zheng Z, Deng J-G, Chen J-C, Ma H et al (2003) Poly(hydroxybutyrate-co-hydroxyhexanoate) promoted production of extracellular matrix of articular cartilage chondrocytes in vitro. Biomaterials 24:4273–4281

Lee SY (1996) Bacterial polyhydroxyalkanoates. Biotechnol Bioeng 49:1–14

Park SJ, Kim TW, Kim MK, Lee SY, Lim S-C (2012) Advanced bacterial polyhydroxyalkanoates: towards a versatile and sustainable platform for unnatural tailor-made polyesters. Biotechnol Adv 30:1196–1206

Cui YL, Qi AD, Liu WG, Wang XH, Wang H, Ma DM et al (2003) Biomimetic surface modification of poly(-lactic acid) with chitosan and its effects on articular chondrocytes in vitro. Biomaterials 24:3859–3868

Yamane S, Iwasaki N, Majima T, Funakoshi T, Masuko T, Harada K et al (2005) Feasibility of chitosan-based hyaluronic acid hybrid biomaterial for a novel scaffold in cartilage tissue engineering. Biomaterials 26:611–619

Tripathi L, Wu LP, Meng DC, Chen JC, Chen GQ (2013) Biosynthesis and characterization of diblock copolymer of P(3-hydroxypropionate)-block-P (4-hydroxybutyrate) from recombinant Escherichia coli. Biomacromolecules 14:862–870

Al-Karawi AJM, Al-Daraji AHR (2010) Preparation and using of acrylamide grafted starch as polymer drug carrier. Carbohydr Polym 79(3):769–774

Boesel LF, Mano JF, Reis RL (2004) Optimization of the formulation and mechanical properties of starch based partially degradable bone cements. J Mater Sci Mater Med 15(1):73–83

Jung YK, Kim TY, Park SJ, Lee SY (2010) Metabolic engineering of Escherichia coli for the production of polylactic acid and its copolymers. Biotechnol Bioeng 105:161–171

Lee JW, Na D, Park JM, Lee J, Choi S, Lee SY (2012) Systems metabolic engineering of microorganisms for natural and non-natural chemicals. Nature Chem Biol 8:536–546

Lee SY, Mattanovich D, Villaverde A (2012) Systems metabolic engineering, industrial biotechnology and microbial cell factories. Microb Cell Fact 11:156

Choi SG, Kerr WL (2003) Water mobility and textural properties of native and hydroxypropylated wheat starch gels. Carbohydr Polym 51(1):1–8

Duarte ARC, Mano JF Reis RL (2009) Preparation of starch-based scaffolds for tissue engineering by supercritical immersion precipitation. J Supercrit Fluids 49(2):279–285

Heinze T (2005) Carboxymethyl ethers of cellulose and starch—a review. Chem Plant Raw Mater 3:13–29

Lahiji A, Sohrabi A, Hungerford DS, Frondoza CG (2000) Chitosan supports the expression of extracellular matrix proteins in human osteoblasts and chondrocytes. J Biomed Mater Res 51:586–595

Deng Y, Zhao K, Zhang X-f, Hu P, Chen G-Q (2002) Study on the threedimensional proliferation of rabbit articular cartilage-derived chondrocytes on polyhydroxyalkanoate scaffolds. Biomaterials 23:4049–4056

Eiselt P, Yeh J, Latvala RK, Shea LD, Mooney DJ (2000) Porous carriers for biomedical applications based on alginate hydrogels. Biomaterials 21:1921–1927

Paige KT, Cima LG, Yaremchuk MJ, Vacanti JP, Vacanti CA (1995) Injectable cartilage. Plast Reconst Surg 96:1390–1398

Suh JKF, Matthew HWT (2000) Application of chitosan-based polysaccharide biomaterials in cartilage tissue engineering: a review. Biomaterials 21:2589–2598

Kaur G, Pandey OP, Singh K, Homa D, Scott B, Pickrell G (2013) A review of bioactive glasses: their structure, properties, fabrication, and apatite formation. J Biomed Mater Res A 102: 254–274

Kaur G, Sharma P, Kumar V, Singh K (2012) Assesment of *in-vitro* bioactivity of SiO_2-BaO-ZnO-B_2O_3-Al_2O_3 glasses: an optico-analytical approach. Mater Sci Eng C 32(7): 1941–1947

Kaur G, Pickrell G, Sriranganathan N, Kumar V, Homa D (2016) Review and the state of the art: sol-gel or melt quenched bioactive glasses for tissue engineering. J Biomed Mater Res B Appl Biomater 104(6):1248–1275. doi:10.1002/jbm.b.33443.

Kaur G, Pickrell G, Pandey OP, Singh K, Chudasama BN, Kumar V (2016) Combined and individual Doxorubicin/Vancomycin drug loading, release kinetics and apatite formation for the CaO-CuO-P_2O_5-SiO_2-B_2O_3 mesoporous glasses. RSC Adv 6:51046–51056

Kaur G, Pickrell G, Kimsawatde G, Allbee H, Sriranganathan N (2014) Synthesis, cytotoxicity, and hydroxypatite formation in 27-Tris-SBF for sol-gel based CaO-P_2O_5-SiO_2-B_2O_3-ZnO bioactive glasses. Sci Rep. doi:10.1038/srep04392

Chapter 3
Polymers as Bioactive Materials II: Synthetic/Biodegradable Polymers and Composites

Gurbinder Kaur

In the previous chapter, we have discussed the natural biodegradable polymers, which are usually degraded by enzymes. In this chapter, we will discuss the main synthetic polymers generally degraded hydrolytically. Synthetic polymers can be curved into different sizes and shapes. Furthermore, the physical chemical and degradation properties can be modified in accordance with the application requirement. The polymer components, blends, and copolymers have also proven to be successful bioactive materials due to their enhanced superior properties. But, they lack sometimes in biological responses due to their synthetic origin.

3.1 Hydrolytically Degradable Polymers

For a material to be hydrolytically degradable, it shall have labile chemical bonds. Amides, methanes, orthoesters, anhydrides, esters, and carbonates are among common materials, which are susceptible to the hydrolytic attack. Polyurethane materials are prepared by the polycondensation reaction between alcohol/amines and diisocyanates. Polyurethanes find applications in vascular grafts, medical implants, and cardiac pacemakers, due to their biocompatibility. Degrapol® is the commonly used biodegradable poly(ester urethane) for developing highly porous scaffolds.

3.1.1 Polyurethanes

Polyurethanes are composed of organic units linked together by the urethane links. When an isocyanate containing $R–(N=C=O)_{n\geq 2}$ group reacts with polyol $R'–(OH)_{n\geq 2}$ in the presence of UV light or catalysts, polyurethanes are produced. Aromatic or aliphatic isocyanates can be used for the polyurethane production.

G. Kaur, *Bioactive Glasses*, Series in BioEngineering,
DOI 10.1007/978-3-319-45716-1_3

Aliphatic isocyanates such as hexamethylene diisocyanate ($C_8H_{12}N_2O_2$, HDI) and isophorone diisocyanate ($C_{12}H_{18}N_2O_2$, PDI) are less reactive than aromatic isocyanates such as diphenylmethane diisocyanate ($C_{15}H_{10}N_2O_2$, MDI) and toluene diisocyanate ($C_9H_6N_2O_2$, TDI). Following reaction kinetics are usually followed for the polyurethane formation

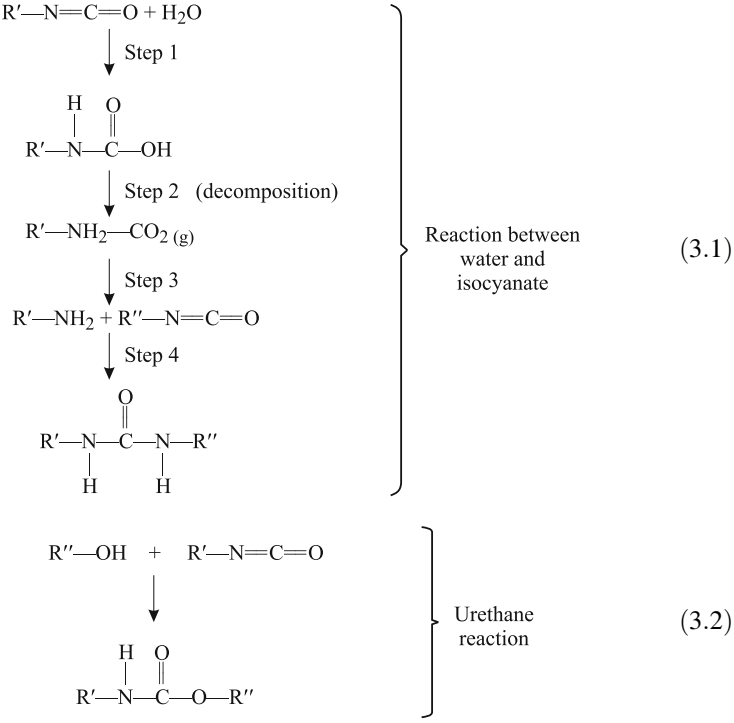

Usually LDI (lysine diisocyanate) and BDI (1,4-diisocyanatobutane) are less toxic isocyanates whereas aromatic MDI and TDI are reported to be toxic. PolyNova® is an LDI-based polyurethane system developed for the orthopedic applications. Porous scaffolds made of HDI and polycaprolactone (PCL) diol with 1,4(3,6-dianhydro)-D-sorbitol (isosorbide diol) are proposed as the cancellous bone graft substitutions. These porous scaffolds lead to regeneration of neocancellous bone after 6 months of implantation inside the sheep's iliac crest defects. Though polyurethanes are actively involved in medical applications such as wound dressings, draper beddings, the most common application is its use in short-term implants. Polyurethanes provide high strength, flexural endurance, and abrasion resistance making it suitable for various medical applications. Polyurethane elastomers possess molecular structure almost similar to that of the human proteins. Polyurethane elastomers are also used in biomimetic and antithrombic properties.

Another scaffold of polyurethane obtained from PCL diol and HDI with different chain extents did not induce any strong inflammatory response after 14 days of

implantation into dorsal skinfolds of mice. Polyurethanes synthesized from HDI, PCL diol, and isosorbide diol prove to be a good bone construct as the osteoblasts support cell growth, differentiation, and neo-vessel formation of the endothelial cells.

Furthermore, the osteoconductivity can be enhanced if hydroxyapatite nanoparticles are seeded onto the polyurethane porous scaffold matrix. Hybrid scaffold system has also been developed in which the chondrocytes are encapsulated in a fibrin hydrogel before seeding onto the polyurethane scaffolds. This improved the cell and extracellular matrix (ECM) retention and also maintained chondrocyte phenotype. The homogeneity of cartilage tissue is enhanced after the subcutaneous implantation of hybrid scaffold with bovine chondrocytes into the mice.

3.1.2 Polyanhydrides

Polyanhydrides are the most commonly used materials for drug delivery applications. The most innovative application of polyanhydrides is a device Gliadel®, which is used to treat brain cancer. Polyanhydrides are excellent bioactive agents for short-term controlled drug delivery as they degrade rapidly and possess limited mechanical properties.

Polyanhydrides have hydrophobic backbone with hydrolytically labile anhydride linkages and the hydrolytic degradation can be controlled by manipulating polymer composition. Figure 3.1 demonstrate the importance and advantages of polyanhydrides to be used as bioactive materials.

In 1980, Langer used the polyanhydrides for the drug delivery applications because of their hydrolytical unstable nature. The glass transition temperature (T_g) of polyanhydrides is also low and lies in the range of 50–100 °C. Polyanhydrides can be

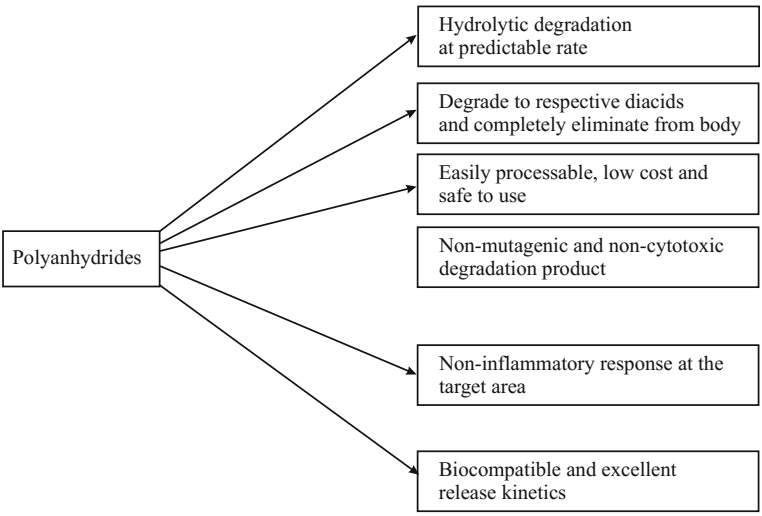

Fig. 3.1 Advantages of polyanhydrides as biomaterials

synthesized by techniques such as interfacial condensation, dehydrochlorination, melt condensation, and ring-opening polymerization. For heat-sensitive monomers, the melt condensation is not the apt method, since it occurs at an elevated temperature. The following reaction scheme yields the polyanhydrides via dehydrating agents.

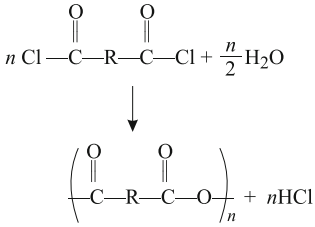

(3.3)

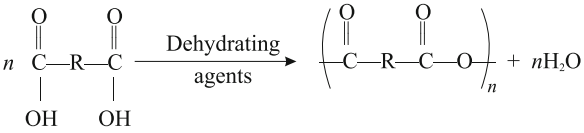

(3.4)

Polyanhydrides may contain anhydride group in the backbone or as side chain and their degradation is shown in the following reaction mechanism

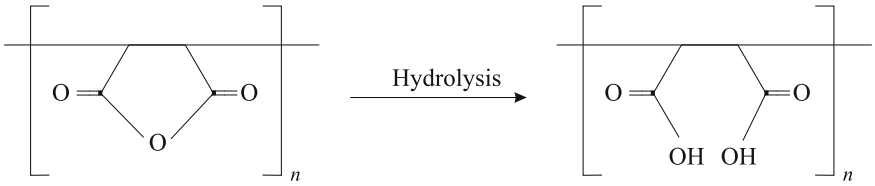

(3.5)

Anhydride group in side chains do not undergo molecule weight change after breakdown of anhydride bond

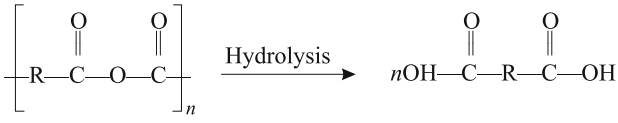

(3.6)

Anhydride group in backbone degrades to shorter chains after breakdown of anhydride bonds

Polyanhydrides have wide potential for the drug delivery applications. If polyethylene glycol (PEG) groups are incorporated on the polyanhydrides, and then the hydrophilicity increases enhancing drug delivery kinetics. In contrast to this, the imide group incorporation in polyanhydrides causes enhanced mechanical properties of the resulting polymer. Drugs are incorporated into the polyanhydride via

compression or melt molding techniques. The most extensively research polyanhydride for drug delivery mechanism is poly[(carboxy phenoxy propane-sebacic acid)] [PCPPSA]. The degradation products of this polymer are biocompatible and non-toxic. Moreover, the copolymers can be varied, which results in zero-order drug release over a range of time. The US FDA has approved it as a drug delivery of chemotherapeutic agent BCNU for treating brain cancer (under trade name Gliadel®). Another drug Septacin® is carried by copolymer of sebacic acid and erucic acid for treating osteomyelitis. Polyanhydrides are devices for anticoagulants, neuroactive agents, local anesthetics, and eye disorders. Polyanhydrides have also been investigated for the oral delivery of insulin and plasmid DNA. Polyanhydrides are also investigated in drug delivery of heparin for treating restenosis. Though polyanhydrides are ideal candidates for the drug delivery systems, their mechanical properties are not competitive especially for the load-bearing applications. But when the imide segments are added to the polymer backbone of polyanhydrides, poly (anhydride-*co*-imides) are formed which are high strength polymers. A wide range of imides such as poly[pyromellitylimidoalanine-*co*-1,6-bis (*p*-corboxyphenoxy) hexane] (PMA ala: CPH)] have been studied for biomedical applications. When these imides are implanted on the rat tibia, cortical bone and endosteal bone could be seen around the defect region. This reveals that the enhanced osteoconduction and osteocompatibility of these polymers. The mechanical strength can also be increased if the acrylic functional groups are incorporated into the polyanhydride matrix. The degradation rate and mechanical strength of the cross-linked polyanhydrides depend on the nature of monomeric units. Furthermore, the degradation rate of polyanhydrides can be balanced by adjusting the hydrophilic and the hydrophobic polymer components. The release rate of drug in polyanhydrides is affected by drug solubility, drug loading, and polyanhydride geometry.

3.1.3 Poly(Ester Amide) (PEA)

Polyesteramides (PEA) are polymers with ester–amide linkages and possess cuspian properties of polyamides and polyesters. Polyesters have better flexibility and solubility, whereas polyamides are mechanically strong. Hence, the combination of both endows polyesteramides with the enhanced properties. The polyesteramides degrade via hydrolytic cleavage of ester bonds. The degradation rate can be further increased by incorporating amino acid into the polymer backbone. Polyesteramides can be synthesized via solution polycondensation, melt polycondensation, and interfacial polycondesation. Melt polycondensation is demonstrated in Fig. 3.2 to yield PEA.

Hydrogels from unsaturated L-phenylalanine-based PEAs and poly(ethylene glycol) diacrylate loaded with paclitaxel have been prepared. The drug release kinetics was faster when placed in enzymatic media rather than the aqueous medium. PEA microspheres have been investigated to be drug carriers for the cancer treatment. The electrospun PEA nanofibers are also found to be potential

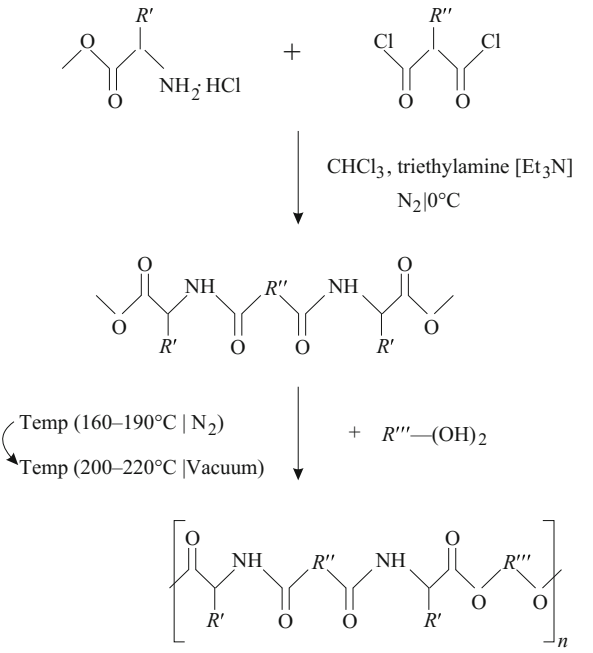

Fig. 3.2 Schematic of PEA synthesis by the melt polycondensation

candidates for the drug delivery of 4-amino-TEMPO nitroxyl radicals. PEA loaded with ibuprofen, demonstrated the growth and proliferation of epithelial cells derived from Madin-Darby canine kidney. The ibuprofen release could be sustained up to almost 83 days. PEA-based coatings are able to support natural healing by promoting growth of appropriate cells for tissue repair along with inhibition of the anti-inflammatory response. PGAs are also applicable in vascular tissue engineering as they were able to support human coronary artery smooth muscle cells via their attachment, growth, and proliferation. PEA enhances integrin signaling, mandatory for cell survival migration, growth, and proliferation. The 3-D scaffolds have been generated from PEAs, which have shown promising results for the tissue segmentation applications. Poly(ester amides) based on α-amino acids and α-hydroxy acids are polydepsipeptides (PDP), which are non-toxic and release α-hydroxy acids/α-amino acids as degradation products. The 3-D scaffolds and porous sponges based on PDP promote cell adhesion and growth. Furthermore, the sponges are biodegradable and the biodegradation rate kinetics are dependent on the depsipeptide amount in copolymers. PEAs have been used to bind plasmid DNA (pDNA), and it demonstrates an ability to transfer rat vascular smooth muscle cells (comparable to Superfect®, commercial transfection reagent). During the gene therapy, functional genes or deoxyribonucleic acid (DNA)/ribonucleic acid (RNA) fragments are transferred onto specific cells to prevent or cure the disease. The gene therapy shall protect the genetic material from undesirable interactions and display highest cell specific action. PDP-based carriers for pDNA display less

toxicity for human embryonic kidney 293. A sustained release over a period of 18 days was observed followed by an initial rapid burst.

3.1.4 Poly Orthoesters (POE)

Polyorthoesters have hydrolytically labile orthoester linkages, but are hydrophobic enough so that their degradation in aqueous environment is not very rapid. By varying the diols and levels of chain flexibility, the glass transition temperature, degradation, and pH can be controlled and tailored. Due to the pH sensitivity of polyorthoesters, they have been extensively used for drug delivery applications. Four different classes of polyorthoesters have been developed as follows:

(a) ***Poly(Orthoester) I (POE I)***

These poly(orthoesters) were developed by the Alza Corporation and named under Chronomer which changed to Alzamer®, The structure of POE I polymer and its preparation scheme is shown in Fig. 3.3.

POE I hydrolyzes in aqueous environment and may undergo autocatalytic hydrolysis reaction. Hydrolysis of POE I produces γ-butyrolactone which quickly opens up to γ-hydroxybutyric acid. The orthoester linkages are highly acid sensitive; hence, the polymer shall be stabilized using a base to avoid any uncontrolled effects. POE I find applications in the delivery of the contraceptive steroid levonorgestrel, narcotic antagonist naltrexone, and treating burns. Anyhow, the lower T_g and hydrolytic nature of this polymer limits its applications.

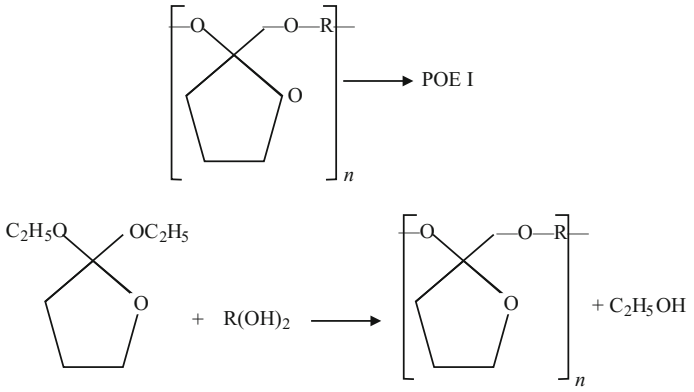

Fig. 3.3 Structure and preparation scheme of POE I polymer

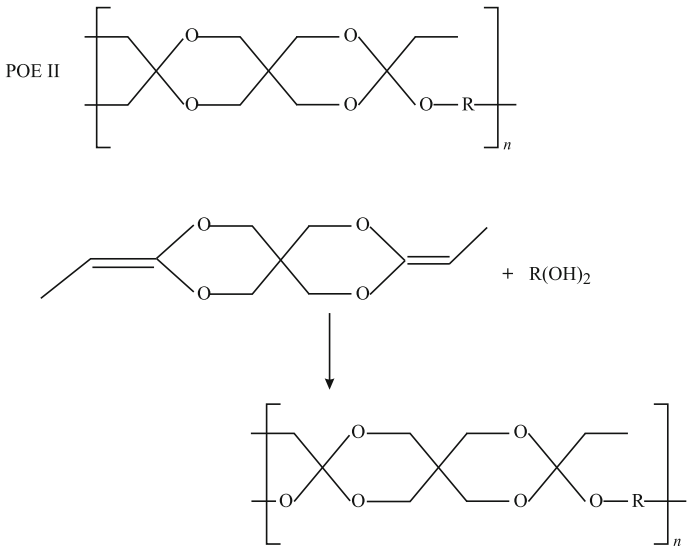

Fig. 3.4 The structure of POE II and its preparation from diol and 3,9-diethyl-idene 2,4,8,10-tetraoxaspiro undecane

(b) *Poly(Orthoester) II (POE II)*

Poly(orthoester) II was found at SRI International (Stanford Research Institute) and its structure as well as preparation route is shown in Fig. 3.4.

POE II is a very stable polymer as it is hydrophobic in nature and limited water availability is there for the hydolytically labile orthoester linkages. The mechanical and thermal properties of the polymer can also be tailored by varying diols so that the obtained POE II can have properties in the range of glassy materials to semiconductors. The polymer erosion rates of POE II can be controlled by lowering pH of polymer–water interface.

(c) *Poly(Orthoester) III (POE III)*

POE III was also developed by SRI International and then extensively studied by University of Geneva. The structure and reaction mechanism of POE III is depicted in Fig. 3.5.

POE III possesses flexible backbone and is semisolid material at room temperature. Hence, the drugs can be loaded easily by mixing them with POE III at room temperature without using any solvents. POE III has been extensively investigated for the ocular applications, especially for the release of fluorouracil, zero-order release kinetics have been demonstrated. POE III does not yield reproducible results and its synthesis is quite difficult.

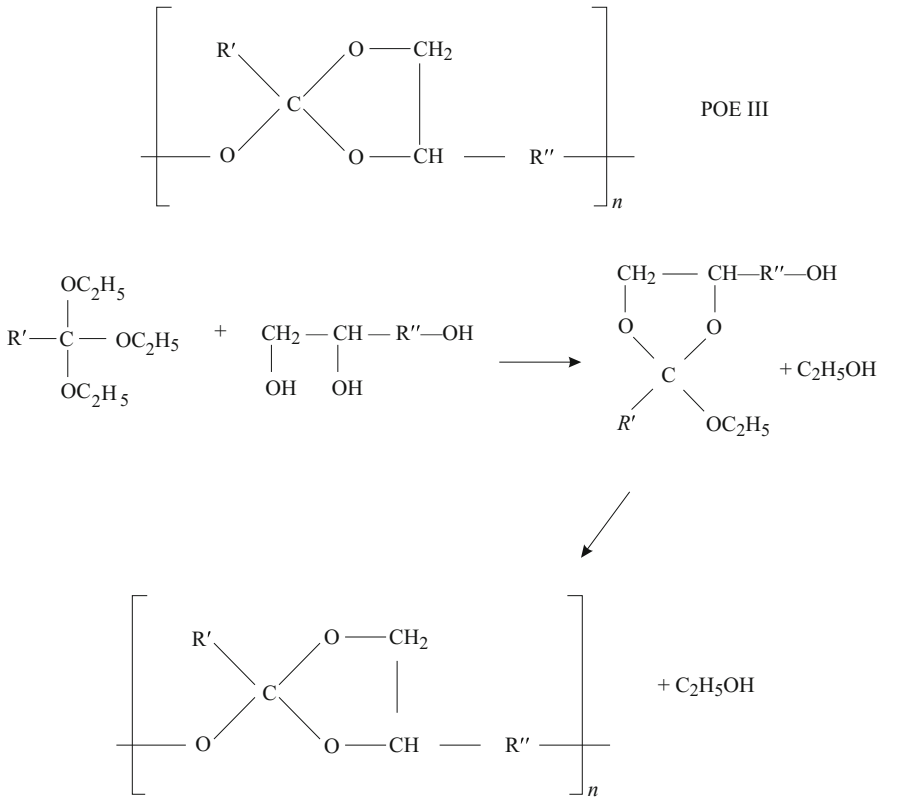

Fig. 3.5 Structure and preparation of POE III

(d) *Poly(Orthoester) IV (POE IV)*

POE IV is synthesized by modifying POE, hence controlling erosion rates due to high stability of POE II. The synthesis of POE IV is shown in Fig. 3.6.

The drug delivery rates are controlled by considering two types of drugs, i.e., macromolecular drugs and low molecular weight water-soluble drugs. For macromolecular drugs, e.g., peptides and proteins, the solvent less incorporation in the form of strands is done at a lower temperature than the protein denaturation temperature. For the water-soluble drugs, the hydrophilicity of the matrix is increased accelerating erosion rates and matrix swelling causing difficulty of drug release. Anyhow, POE IV has shown acceptable release kinetics for 5-fluorouracil and hence depicting its good drug carrier ability. Poly(orthoesters) has also found applications in curing periodontal diseases and estrus synchronization in sheep. Poly(orthoesters)-based semisolid materials have been injected intravitreally, intracamerally subconjuctivally, and suprachoroidally in rabbits. For all of them, the polymer exhibited excellent biocompatibility and surprisingly longer lifetimes than the anticipated lifetime.

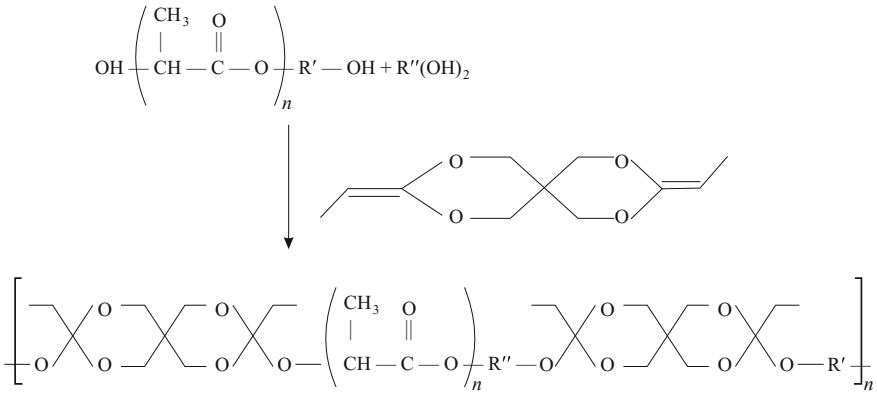

Fig. 3.6 Demonstration of POE IV synthesis

3.1.5 Polyphosphoester (PPE)

Polyphosphoesters have been investigated in drug delivery, tissue engineering, and gene delivery applications. Polyphosphoesters can be hydrophobic or water soluble. The general structure of polyphosphoester is shown in Fig. 3.7.

Water-soluble polyphosphoesters find potential applications for gene delivery. The DNA molecule is negatively charged and it interacts electrostatically with the cationic polymer resulting in complex formation shielding DNA from enzyme degradation as well. Polyphosphates and polyphosphoramides have been studied as potential gene carriers as they successfully bind to DNA-forming complexes. Hydrophobic polyphosphoesters have been drug delivery vehicles for proteins, DNA-forming complexes. Hydrophobic polyphosphoesters degrade under hydrolytic or enzymatic action in physiological conditions leading to the formation of alcohol, diols, and phosphate as the end products.

Polyphosphates and polyphosphoramides have been synthesized from precursor poly(1, 2-propylene H-phosphonate) obtained by the ring-opening polymerization of cyclic monomer 4-methyl-2-oxo-2-hydro-1,3,2-dioxaphospholane. The biomedical potential of new class of PPE, which is a copolymer of PPE and poly D, L-lactide (PDLA) has been evaluated. These PPE are known as poly(lactide-*co*-ethylphosphate) (PLF) and their T_g is inversely proportional to the weight % of phosphoesters segment in the copolymer. PLF has been used as drug carriers especially for local drug delivery of chemotherapeutic agent paclitaxel (trade name PACLIMER®). The formulation PACLIMER® contains 10 % (w/w) paclitaxel in

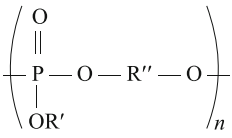

Fig. 3.7 Structures of polyphosphoester

PLF microspheres with median volume diameter ~50 μm. When PACLIMER® microspheres were implanted in the peritoneal cavity of Sprague-Dawley rats, only small fragments of microspheres could be seen 28 days of postimplantation. PACLIMER® microspheres were used for phase I human trial for ovarian cancer and OVCAR-3 murine tumor model. Mice that received 400 mg/kg PACLIMER® microsphere dose lived longer than the ones who were treated with 40 mg/kg Taxol®. PACLIMER® microspheres demonstrated their efficiency for two Xenograft models: A549 and H1299 in treating lung cancer. The tumor growth was largely inhibited when the PACLIMER® microspheres were given an intratumoral injection rather than with the Taxol®. PPEs degrade due to the cleavage of backbone along with side groups producing less positively charged end products, hence contributing to enhanced release of plasmid DNA. The transfection efficiency of PPEs is enhanced if the conjugation of specific ligands, nuclear localization signals, or endothysolytic elements nuclear localization signals or endolysolytic elements can be done.

3.1.6 Polyphosphazenes

Polyphosphazenes are hybrid polymers and their backbone consists of alternating phosphorous and nitrogen atoms, where the organic substituents are linked as side groups with the phosphorous atom as follows (Fig. 3.8).

The precursor of polyphospazenes is polydichlorophosphaze, which is hydrolytically unstable. Hence, the precursor must be readily substituted with the nucleophilic substituents to obtain stable polyphosphazene. Polydichlorophosphaze can be obtained by the ring-opening polymerization of hexachlorophosphazene or by the living cationic chain growth polymerization of chlorophosphoranimine as shown in Fig. 3.9.

The polyphosphazene backbone degrades due to the hydrolytic action to yield low toxicity compounds such as phosphates and ammonia. However, the side groups are hydrophobic in nature, which prevents polymer backbone from hydrolysis. Hence, the properties of polyphosphazenes depend highly on the side groups. If the polyphosphazenes are substituted with hydrophobic alkoxy side group, then extremely hydrolyticlly stable structure is obtained. On the contrast, if polyphosphazenes are substituted with hydrophilic amino groups, then unstable polymer is obtained.

The amino acid ester polyphosphazenes are the most extensively studied polyphosphazene for the biomedical applications. When the amino acid

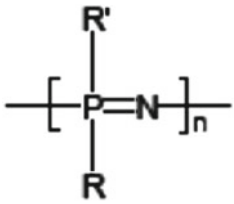

Fig. 3.8 Structure of phosphazene

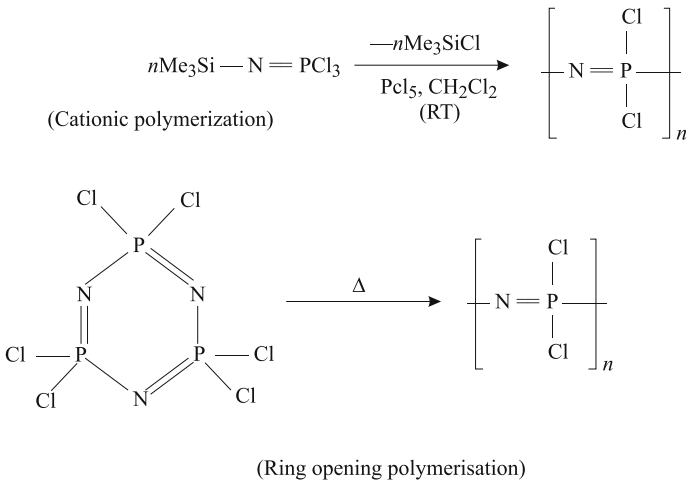

Fig. 3.9 Preparation routes of the polyphosphazene

polyphosphazene is substituted with glycine ethyl ester, fastest degradation is obtained. The ethylglycinate substituted polyphoshphazenes have been used for the skeletal tissue regeneration, and the growth of MC3T3-E1 osteogenic cell line could be observed. Due to the presence of imidazolyl side groups in the polymer, an increased degradation rate and reduced cell attachment/growth on polymer surface could be observed. Alanine-based polyphosphazenes are proposed as self setting cements and also supported the proliferation as well as ALP activity of the primary rat osteoblasts. Blends of poly(lactide-*co*-glycolide) (PLGA) and poly[(ethylalanato), –(*p*-phenyl phenoxy), phosphazene] were fabricated using different weight ratios. Though cell adhesion and proliferation could be seen in the rat osteoblasts, the phenotypic expression was also enhanced. Microcapsules of poly [(alanine ethyl ester)] phosphazene and poly[80 %(phenyl-alanine ethyl ester)/20 % (imidazolyl)] phosphazene are developed for the treatment of periodontal diseases. The polyphosphazene membranes prepared from 20:80 ratio of imidazole and alanine ethyl ester yielded better healing of the rabbit tibia defect. Phenylalanine ethyl ester and imidazole are used in molar ratio of 80:20 to prepare microspheres for the controlled release of insulin. The insulin release depicted bimodel behavior, yielding burst release during first two h and then slow release from 2 to 70 h. Polyphosphazene matrix is biodegradable and permeable; hence, it has been investigated as a vehicle for protein delivery also. Polyphosphazene blends have been prepared using two polyphosphazenes differing in their degradation rate for the drug delivery applications. Ethyl glycinate and phenylalanate polyphosphazenes have been studied for the in vitro release of anti-tumor agent mitomycin C (MMC). The release of MMC was slower from poly[bis(phenyl alanato)] phosphazene as

compared to poly[bis(ethylglycinato)] phosphazene, whereas for the blend, increasing phenylalanato decreased the release profile.

Though the alkoxy substituted polyphosphazenes have not been studied as drug delivery vehicles, the presence of reactive hydroxyl groups can generate water solubility and hence provide cross-linking sites for the bioactive agents. Polycarboxylate polyphosphazenes have proven to be potent immunological adjuvants; poly[bis(carboxyphenoxy) phosphazene] (PCPP) has enhanced immune responses upon coadministration with array of viral and bacterial antigens. Poly[bis (carboxyethyl-phenoxy) phosphazene] (PCEP) has shown potent adjacent activity in mice, sheep, pigs, etc., indicating its safety and effectiveness.

3.1.7 Poly(Propylene Fumarates) (PPFs)

PPF is synthetic linear polyester, which is made of repeating units of unsaturated double bond in transconfiguration. The presence of unsaturated sites in the polymer backbone acts as a cross-linking site. The ester linkages of PPF undergo hydrolysis and fumaric acid are formed, which is naturally occurring substance found in tri-carboxylic acid cycle (Krebs cycle). Another end product is 1, 2-propane diol, which is commonly used diluent for the various drug formulation. Figure 3.10 gives the scheme of preparation of PPF.

Before cross-linking, PPF is a liquid and hence it can be casted into desirable shapes implants by injection molding or compression molding. It can also be injected into cavities that the irregular shape of defects can be filled and then followed by in-site cross-linking. Anyhow, the inside cross-linking yields toxic response because the unreacted macromers act as unreacted agents when exposed to biological environment. Incorporation of fillers help in forming cross-linking net, hence increasing the mechanical strength of the PPFs. Calcium carbonate, calcium sulfate, and tricalcium phosphate enhanced the mechanical strength of PPFs (up to 30 MPa). The cross-linked PPFs obtained by copolymerizing with acrylic

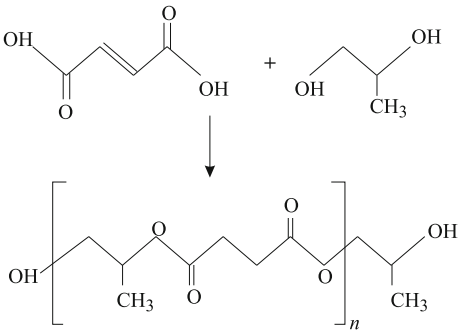

Fig. 3.10 Formation of poly (propylene fumarate)

monomers such as *N*-vinyl pyrolidone and methyl methacrylate demonstrated compressive strength of up to 12 MPa. Cross-linked polymers demonstrate in vivo and in vitro bone formation. The PPF composite exhibits good osteoconductive properties, and the ceramic fillers act as pH buffer by inhibiting PPF autocatalytic degradation. PPF matrix with PLGA microsphere loaded with osteogenic peptide was implanted in rabbit segmental defects. 12 weeks of postimplantation, 80 % of the defect showed bridging and hence displayed good bone growth around the defect region. Even after 18 weeks, the porous PPF exhibited minimal degradation and maintained structural support with minimal prolonged inflammatory response due to the degradation products. PPF/CaSO4/tricalcium sulfate composites demonstrated the mechanical properties close to human cancellous bone.

3.1.8 Polyesters

Poly(α-esters) contain labile aliphatic ester linkages in their backbone. These are biodegradable synthetic polymers, which are widely investigated for preparing 3-D scaffolds polyesters also include the poly(α-hydroxy acids) and these materials allow degradation through de-esterification. Poly(α-esters) is developed via condensation polymerization ring-opening and bacterial bioprocess routes. Anyhow, the synthesis of high molecular weight polymers is difficult via polycondensation route; hence, it is not widely investigated. Poly(α-esters) have nonlinear erosion kinetics such that polymer matrices degrade across their cross section. Following section lists some potential polyesters to be investigated as biomaterials.

3.1.8.1 Poly(Lactic Acid) and Poly(Glycolic Acid)

Poly(glycolic acid) (PGA) is one of the first biodegradable polymer, which is rigid thermoplastic with high crystallinity (45–50 %). Its high crystallinity contributes to its high solubility in organic solvents (except fluorinated organic solvents) and high tensile modulus. The glass transition and melting temperature of PGA are 37 and 225 °C, respectively. PGA is highly sensitive to the hydrolytic degradation; hence, careful control of processing conditions shall be done during extrusion, compression molding, and injection fabrication techniques.

PGA-based implants are also fabricated using particular leaching method and solvent casting. The self-reinforced PGA is mechanically stiffer and may exhibit modulus of ~12.5 GPa; hence, PGA are also used for making bone internal fixation devices (Biofix®). The degradation of PGA yields natural metabolite, which makes it very useful for resorbable sutures. The degradation process occurs via two stages: The first stage involves the diffusion of H_2O within the amorphous regions of the matrix causing hydrolytic chain scission of the ester groups. Second stage involves the degradation of predominantly crystalline regions formed after

amorphous region erosion (during first stage). PGA losses its strength within 1–2 months and mass within 6–12 months, respectively, when hydrolyzed.

Resorbable sutures such as Dexon® (first biodegradable suture approved by US FDA, 1969) exhibit first-stage degradation during the first 21 days and second-stage degradation during the next 28 days. As Dexon® sutures demonstrated bulk weight loss of ~4.2 %, hence sudden loss of mechanical properties occurred. Glycolic acid is the degradation product, which is resorbable, but at higher concentrations, they may be toxic. This glycolic acid is further connected to CO_2 and H_2O, which are ultimately removed from the human body. Figure 3.11 shows the cyclic lactone and corresponding polymer. Polyglycolide materials are also used as dural substitutes because they exhibit good skin-closing ability without needing any suture.

Poly(lactic acid) (PLA) is chiral molecule and exist in three isomeric forms, i.e., D(−), L(+) and racimic (D, L) (Fig. 3.11). Poly(L) lactic acid and poly(D) lactic acid are the optically active forms, which exist as semicrystalline solids. Racemic poly (D,L lactic acid) results in amorphous polymers. PLA is more hydrophobic than the PGA, and it degrades to form lactic acid, which is normally present inside human

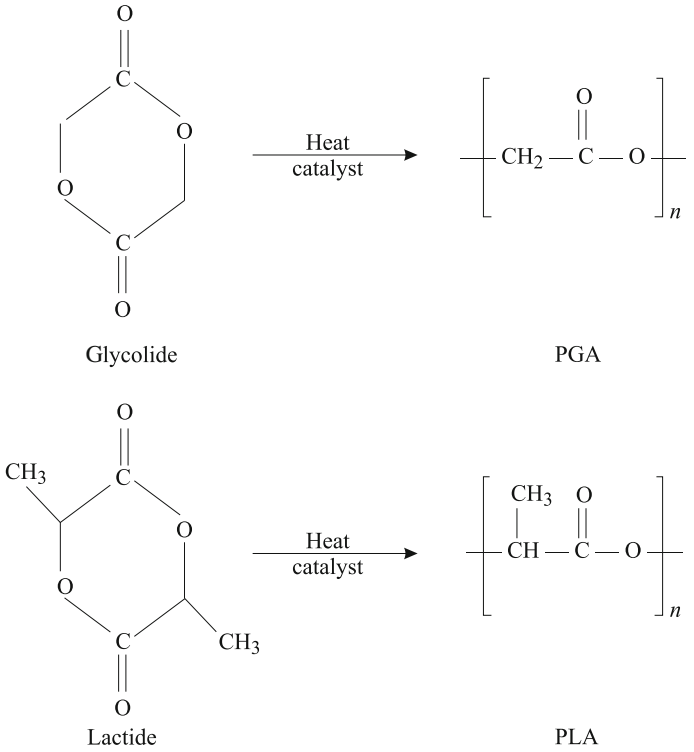

Fig. 3.11 Structure of cyclic lactones and their corresponding polymers

body. Lactic acid further gets incorporated into tricarboxylic acid cycle and gets excreted out as H_2O and CO_2.

Poly(L-lactide) (PLLA) exhibits 37 % crystallinity and the degree of crystallinity depends upon the polymer processing parameters and the molecular weight PLLA is an ideal biomaterial for load-bearing applications as it has high tensile strengths and high modulus ~4.8 GPa. The glass transition temperature and melting temperature of PLLA are 60 and 180 °C, respectively. PLLA fibers exhibit high strength and hence investigated as scaffolding material for ligament replacement. An injectable PLLA (trade name Sculptra®) is approved by the US FDA for treating lipoatrophy (loss of facial fat). When hydroxyapatite (HAp) is incorporated into electrospun PLLA fibers, the proliferation of preosteoblast cell is highly enhanced. PLLA powders incorporating nanosized demineralized bone powder are implanted in skull defects of rats, resulted in the new bone formation. The compatibility of PLLA scaffolds to osteoblast-like cells is highly enhanced by coatings of hydroxyapatite/collagen. PLLA/hydroxyapatite scaffold showed improved osteoblast proliferation, and the presence of collagen enhanced the cell attachment, proliferation, and alkaline phosphatase (ALP) activity. Many commercially available PLLA includes Meniscal Stinger, Bio-Anchor®, BioScrew®, Phantom Suture Anchor®, and Clearfix Meniscal Dart®, etc. High molecular weight PLLA can degrade between 2 and 6 years for complete resorption in vivo.

In poly(D,L lactic acid) (PDLLA), L- and D-units are randomly distributed attributing it with an amorphous character and T_g ~55–60 °C. PDLLA shows less strength (~2 GPa) due to its amorphous nature and losses its mass within 12–16 months upon hydrolysis. Its degradation is fast making it desirable for the drug delivery applications. When PDLLA is blended with polyethylene glycol (PEG), the scaffold hydrophilicity increases causing more rapid release of protein loaded into scaffold matrix.

Bovine chondrocytes were seeded into PGA and PLLA scaffolds and then inserted subcutaneously in the backs of athymic mice. The cellular adhesion reached ~54 % and chondrocyte morphology and phenotype were much better supported by PGA than by PLLA. PGA scaffolds showed the cellular growth rate twice as that of PLLA and hence exhibited promising results for long-term in vivo applications. PDLLA porous matrix was seeded with rabbit costal chondrocytes, and then, the constructs were press fit into drilled articular cartilage defects in rabbits. Six weeks of postimplantation, cartilaginous tissue was observed, and the biochemical analysis obtained that the new cartilage content was 80:20 ratio for type I and type II, respectively. The effectiveness of poly(esters) as cellulose scaffold materials have also been investigated. Adult human chondrocytes were seeded onto 90:10 ratio blend of PGA/PLLA. PGA/PLLA degraded faster and lowered the pH below physiological range after 21 days. At 10 mg/ml monomer concentration, PGA caused complete reduction is chondrocyte activity, but PLA did not inhibit chondrocyte activity. The chondrocyte from sheep articular cartilage were seeded on the PLLA/PDLLLA blend in 80:20 ratio. Nine weeks of postimplantation, the chondrocytes exhibited proliferation and excellent round morphology.

Fig. 3.12 Chemical structure of PLGA

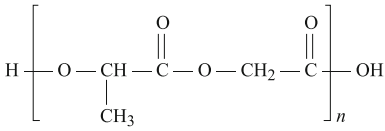

3.1.8.2 Poly(Lactide-*co*-Glycolic Acid) (PLGA)

PLGA is extensively investigated for the biomedical applications due to their wide range of composition flexibility and superior results and other polymers. For the copolymerization of PLGA, both poly(L-lactic acid) and poly(D,L lactic acid) are used. Figure 3.12 gives the PLGA structure.

For the PLGA, two main series are investigated, i.e., (L) lactic acid/glycolic acid and (D,L) Lactic acid/glycolic acid. Compositions for the (D,L) Lactic acid/glycolic acid in the range 0–70 % and (L) lactic acid/glycolic acid in the range of 25–75 % are amorphous in nature. The 70:30 ratio for glycolic acid/lactic acid (GA/LA) has highest water uptake and hence readily degradable. The 85:15 ↔ (LA/GA), 75:25 ↔ (LA/GA), and 50:50 ↔ (LA/GA) degrade in approximately 5–6 months, 4–5 months, and 1–2 months, respectively. Different compositions of PLGA are available under many commercial names such as PANACRYL®, VICRYL®, VICRYL RAPID®, and PURASORB®. PANACRYL® suture contains higher LA/GA ratio, so that the degradation rates can be decreased. VICRYL® suture contains, GA/LA in 90:10 ratio, whereas VICRYL RAPID® is an irradiated version of suture, which has higher degradation rate. LA/GA in ratio 80:20 is used to synthesize Purasorb®, which is a semicrystalline bioresorbable copolymer.

PLGA polymers exhibit excellent cell adhesion and proliferation, and its approval by US FDA has made it very popular for the tissue engineering applications. PLGA degradation rate is affected by the crystallinity, T_g, LA/GA ratio and hydrophilic/hydrophobic ratio. PLGA has different degradation kinetics for surface and bulk, i.e., bulk degradation is enhanced by autocatalysis, and surface degradation occurs via diffusion of soluble oligomers and neutralization of carboxylic end groups using external buffer. Usually the bulk degradation occurs for these polymers because bulk has higher water penetration. PLGA is widely used for drug delivery applications. The drug release occurs through the random scission of the polymer without polymer weight loss. Whereas during the second stage. Weight loss occurs. The equation for drug release is given through following equation:

$$\frac{\partial C(x,\ t)}{\partial t} = \frac{1}{x^2}\frac{\partial}{\partial x}\left(x^2 D \frac{\partial C(x,\ t)}{\partial x}\right) \tag{3.7}$$

where $C \rightarrow$ drug concentration,
$x \rightarrow$ radial position,
$D \rightarrow$ drug diffusivity (dependent of molecular weight of polymers), and
$t \rightarrow$ time.

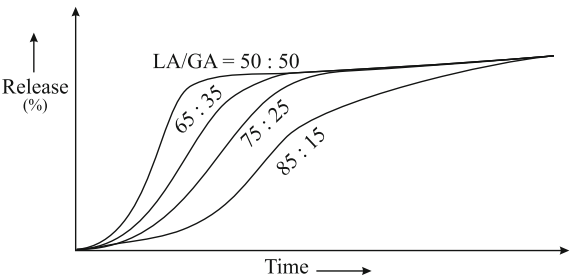

Fig. 3.13 Drug release profile for different LA/GA ratio

The Eq. (3.7) can be solved with the help of following boundary equations:

$$\left.\begin{array}{l} \left.\frac{\partial C(x,t)}{\partial x}\right|_{x=0,t=0} = 0 \\ C(x,t)|_{x=R,t>0} = 0 \\ \text{(if particle is spherical with radius } R) \end{array}\right\} \text{Boundary conditions}$$

After time t, the drug concentration can be related to initial drug distribution, the molecular weight as function of time is given by

$$C(x,t)|_{t=0} = f(x)$$

During hydratic degradation, the molecular weight as function of time is given by

$$M(t) = M(t=0)\exp[-kt] \tag{3.8}$$

$M(t = 0)$ is the molecular weight of polymer at time $t = 0$ and k represents polymer degradation constant. Using the boundary conditions, the degradation rate can be calculated for the polymer. The PLGA degradations follow a biphasic curve as shown in Fig. 3.13. During the first phase, drug on the surface is released as a function of penetration of water into polymer matrix. During the second phase, drug is released progressively through thicker drug-depleted layer.

A very common PLGA-based drug delivery vehicle for gonadotropin releasing hormone is LUPRON DEPOT® and is used to treat the prostate cancer. The controlled release of drugs/proteins via microspheres, microcapsules, and nanofibers has been studied. Anyhow, the protein denaturation may occur within the drug delivery vehicle due to the bulk degradation of the polymer.

3.1.8.3 Poly(ε-Caprolactone) (PCL)

ε-caprolactone is the monomeric unit of poly(ε-caprolactone), which is aliphatic linear polyester and possess auto-catalyzed bulk hydrolysis. PCL is hydrophobic and semicrystalline in nature, and hence its degradation process is low, which makes it very useful for long-term applications. The PCL also degrades via random

Fig. 3.14 General structure of PCL

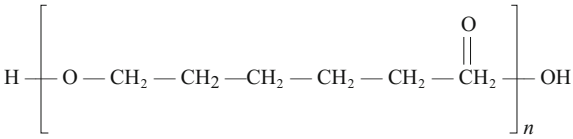

hydrolytic ester cleavage and weightless when oligomers diffuse out of the bulk, PCL has T_g −60 °C and the melting point within 55–60 °C. The general structure of PCL is given in Fig. 3.14.

PCL-based scaffolds when implanted along with bone marrow MSCs into the non-critical size defects in rabbit femurs, promoted new tissue formation along with neo-tissue vascularization. When PCL is blended with other materials, the mechanical properties also get enhanced along with the tailoring of degradation kinetics. When PCL is blended with polyethylenimine to obtain PCL nanofibers, scaffold hydrophilicity, and hence, adhesion and proliferation of the cells seeded onto the surface also increase. Copolymers of ε-caprolactone and D,L-lactide possess high degradation rates. A copolymer suture of glycolide and ε-caprolactone are used commercially under the trade name MONACRYL®. Wollestonite nanoparticles are used as bioactive fillers for PCL scaffolds and the polymer matrix composite exhibited improved Young's modulus and tensile strength upon 0.5–1.0 with the incorporation of wollastonite nanoparticles. PCL/hydroxyapatite composites have also been investigated by many researchers. PCL/hydroxyapatite composites improve osteoconductivity due to good polymer-osteoblast interaction. Increasing hydroxyapatite content in the composite also enhances the elastic modulus and tensile strengths. PCL degrades slowly and degradation products are non-toxic; hence, it is investigated as a drug delivery vehicle. The contraceptive Capronor® is developed for a long-term treatment and releases levonorgestrel.

3.1.8.4 Polydioxanone (PDS)

The first polydioxanone was used in 1981 by ethicon as a microfilament suture. The cyclic lactone of PDS is shown in Fig. 3.15.

PDS has very low T_g in the range of −10 to 0 °C and undergoes degradation by the scission of ester backbone. PDS can be synthesized via oxidative dehydrogenation of diethylene glycol in the presence of the copper oxide catalysts

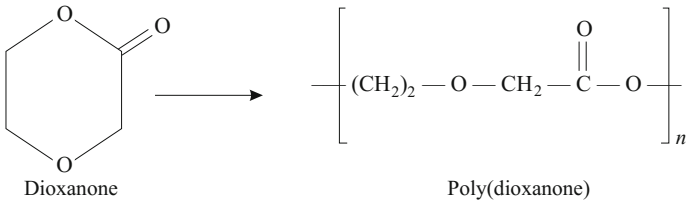

Fig. 3.15 Lactone and structure of PDS

(275 °C/H_2 atmosphere). Other techniques include reaction of sodium glycolate and chloroacetic acid to yield hydroxy acid, which undergoes cyclization (in the presence of $MgCO_3$). PDS® suture is FDA approved and exhibits greater strength than the monofilament sutures. However, the PDS® is not retained as long as the PLA-based sutures, and loosening of fine surgical knots also occurs. PDS® possesses low surface friction, which makes knot retention difficult. PDF-based rings have been approved for tricuspid heart valve repair and pediatric mitral as well. Johnson and Johnson commercialized PDS plates (PDS™ flexible plates), which are histoconductive and promoted bone regeneration in orbital floor reconstruction. PDS exhibits higher flexibility compared to PLA/PGA, hence making it attractive polyester. Electrospun PDS patch was studied in rotator cuff repair. No visible clumps of cells could be seen 21 days of postimplantation, though tendon derived cells exhibited growth, adhesion, and proliferation on the PDS patches. The PDS electrospun valved transannular patch seeded with mesenchymal stem cells was implanted into the lamb. Echography and MRI demonstrated three-layered tissue consisting of endothelium-like structure, collagen-rich central structure, and vascularized loose connecting tissue layer.

PDS elastin scaffold yielded mechanical properties similar to that of human artery and pig. Elastin provides bioactivity and elasticity to the prosthetics, whereas PDS yields mechanical integrity. PDS/elastin (50:50) combination composite closely mimics the native femoral artery compliance. PDS/hydroxyapatite composites exhibit better mineralization capability than the PLGA scaffolds, when in contact with simulated body fluid. PDS/PCL blend scaffold was fabricated using salt leaching and compression molding techniques. Chondrocytes showed adhesion and cells expressed spindle-like appearance onto the scaffold. In addition to this, after 3 weeks of culture, collage type II was expressed.

3.2 Composites: As Bioactive Materials

The composite materials exhibit improved degradation and bioactive properties. Ceramics and polymers are usually combined to fabricate biomedical material ceramics are mechanically stronger than the polymers and the degradation kinetics of polymers make then suitable for drug delivery applications. Table 3.1 lists the ceramic polymer composite designed for the biomedical applications. Hydroxyapatite is widely used as a biocompatible ceramic material for making composites. It has resemblance to the human bone ($Ca_{10}(PO_4)_6(OH)_2$) and its Ca/P ratio promotes the bone regeneration.

Hydroxyapatite (HAp)/collagen I scaffolds resulted in the significant increase of elastic modulus and tensile strength of the composites. When calcium phosphate is incorporated into chitosan, the compressive modulus is highly enhanced and also impacts the adhesion of MSCs. Chitosan/HAp composite also promotes the apatite formation as well as attachment, proliferation, and differentiations of osteoblast-like

Table 3.1 Biocomposites and their properties

Biocomposite		Modulus (MPa)
Polymer	Ceramic	
PLGA	Hydroxyapatite (HAp)	1.1×10^3
PLLA	HAp fiber	$(6.4–12.8) \times 10^3$
PLGA	Amorphous CaP	65
PLGA	Bioglass®	51
PLGA	HAp	2–7.5
PLLA	HAp	10–14
PDLLA	HAp fiber	$(1.75–2.5) \times 10^3$
Collagen	HAp	
Chitosan	HAp	2.15×10^3
PGA	Bioglass®	0.5–2
PLLA	$Ca_3(CO_3)_2$	$(3.5–6) \times 10^3$
PDLLA	Bioglass®	0.65–1.2
PDLLA	A/W glass	0.075–0.12
Chitosan/gelatin	β-TCP	3.94–10.88
Human cortical bone		$(12–18) \times 10^3$
Human cancellous bone		(100–500)

cells. HAp-reinforced PHB composite yielded improved mechanical properties and high in vitro bioactivity. 3-hydroxyvalerate (PHBV)/HAp composite implants have been found morphologically and biologically active for the osteoblast and osteocyte proliferation. PLLA/HAp nanocomposite scaffolds prepared by freeze drying yielded high compressive strength and cytocompatibility. Preosteoblast cell proliferation was enhanced by HAp incorporation into PLLA fibers. Furthermore, the differentiation of preosteoblast cells is enhanced by doing HAp coating on the PLGA porous membrane. PCL/HAp nanocomposite scaffold yielded enhanced tensile strength and elastic modulus, which further increased with the HAp content. In addition to this, if TCP is incorporated into PCL scaffold, then both bioactivity and bioresorbability is increased. PPF/HAp composites yield increased material hydrophilicity and serum protein adsorption on the surface, enhancing cell attachment and proliferation (after 4 days of cell culture).

3-Hydroxyhexanoate/PHB blends containing 40 wt% of PHB have better mechanical properties and the composite-supported growth and proliferation of chondrocytes. Rabbit articular chondrocytes seeded on PHB/3-hydroxyhexanoate blends, depicted higher mRNA level of collagen II of chondrocytes. Natural materials, like *N*-succinyl chitosan, collagen is used to coat PLGA for improving their interaction with chondrocytes. PDLLA/PEG blends result in increased hydrophilicity of scaffold resulting in rapid release of loaded protein.

Bibliography

Langer RS, Vacanti JP (1999) Tissue engineering: the challenges ahead. Sci Am 280:86–89
Chandra R, Rustgi R (1998) Biodegradable polymers. Prog Polym Sci 23:1273–1335
Shalaby SW, Burg KJL (2003) Absorbable and biodegradable polymers (advances in polymeric materials). CRC press, Boca Raton
Domb AJ, Wiseman DM (1998) Handbook of biodegradable polymers. CRC Press, Boca Raton
Lakshmi S, Cato N, Laurencin T (2007) Biodegradable polymers as biomaterials. Prog Polym Sci 32:762–798
Lakshmi S, Katti DS, Laurencin CT (2003) Biodegradable polyphosphazenes for drug delivery applications. Adv Drug Deliv Rev 55:467–482
Piskin E (1995) Biodegradable polymers as biomaterials. J Biomat Sci Polym Ed 6:775–795
Albertsson AC (2002) Degradable aliphatic polyesters, advances in polymer science, vol 157. Springer, Berlin Heidelberg, Germany
Gunatillake P, Mayadunne R, Adhikari R (2006) Recent developments in biodegradable synthetic polymers. Biotechnol Ann Rev 12:301–347
Tian H, Tang Z, Zhuang X, Chen X, Jing X (2012) Biodegradable synthetic polymers: preparation, functionalization and biomedical application. Prog Polym Sci 37:237–280
Gunatillake PA Adhikari R (2003) Biodegradable synthetic polymers for tissue engineering. Eur Cells Mater 5:1–16
Bronzino JD (2006) Biomedical engineering fundamentals, 3rd edn. CRC press
Gijpferich A (1996) Mechanisms of polymer degradation and erosion. Biomaterials 17:103–104
Kohane DS, Langer R (2008) Polymeric biomaterials in tissue engineering. Pediatr Res 63: 487–491
Seal BL Otero TC, Panitch A (2001) Polymeric biomaterials for tissue and organ regeneration. Mater Sci Eng R 34:147–230
Puppi D, Chiellini F, Piras AM, Chiellini E (2010) Polymeric materials for bone and cartilage repair. Prog Polym Sci 35:403–440
Ferry JD (1988) Structure and rheology of fibrin networks. In: Kramer O (ed) Biological and synthetic polymer networks, Elsevier Applied Science, Amsterdam, the Netherlands, pp 41–55
Cappello J, Crissman J, Dorman M, Mikolajczak M, Textor G, Marquet M, Ferrari F (1990) Genetic-engineering of structural protein polymers. Biotechnol Prog 6:198–202
Mercier NR, Costantino HR, Tracy MA, Bonassar LJ (2005) Poly(lactide-coglycolide) microspheres as a moldable scaffold for cartilage tissue engineering. Biomaterials 26:1945–1952
Lietz M, Dreesmann L, Hoss M, Oberhoffner S, Schlosshauer B (2006) Neuro tissue engineering of glial nerve guides and the impact of different cell types. Biomaterials 27:1425–1436
Cortesini R (1995) Stem cells, tissue engineering and organogenesis in transplantation. Transpl Immunol 15:81–89
Williams JM, Adewunmi A, Schek RM, Flanagan CL, Krebsbach PH, Feinberg SE et al (2005) Bone tissue engineering using polycaprolactone scaffolds fabricated via selective laser sintering. Biomaterials 26:4817–4827
Schwartz I, Robinson BP, Hollinger JO, Szachowicz EH, Brekke J (1995) Calvarial bone repair with porous D,L-polylactide. Otolaryngol Head Neck Surg 112:707–713
Ma PX (2004) Tissue engineering. In: Kroschwitz JI (ed) Encyclopedia of polymer science and technology, vol. 12. John Wiley & Sons Inc, New York, pp 261–291
Mikos AG, Sarakinos G, Lyman MD, Ingber DE, Vacanti JP, Langer R (1993) Prevascularization of porous biodegradable polymers. Biotechnol Bioeng 42:716–723
Wang Y, Bian Y-Z, Wu Q, Chen G-Q (2008) Evaluation of three dimensional scaffolds prepared from poly(3-hydroxybutyrate-co- 3-hydroxyhexanoate) for growth of allogeneic chondrocytes for cartilage repair in rabbits. Biomaterials 29:2858–2868
Vacanti JP, Morse MA, Saltzman WM, Domb AJ, Peter-Atayde A, Langer R (1998) Selective cell transplantation using bioabsorbable artificial polymers as matrices. J Pediatr Surg 23:3–9

Agrawal CM, Athanasiou KA, Heckman JD (1997) Biodegradable PLA/PGA polymers for tissue engineering in orthopaedica. Mater Sci Forum 250:115–128
Sanderson JE (1988) Bone replacement and repair putty material from unsaturated polyester resin and vinyl pyrolidone. United States Patent 4(722948)1–14
Nelson JF, Stanford HG, Cutright DE (1977) Evaluation and comparison of biodegradable substances as osteogenic agents. Oral Surg 43:836–843
Storey RF, Wiggins JS, Mauritz KA, Puckett AD (1993) Bioabsorbable composites. II: nontoxic, L-lysinebased (polyester-urethane) matrix composites. Polym Compos 14:17
Temenoff JS, Mikos AG (2000) Injectable biodegradable materials for orthopaedic tissue engineering. Biomaterials 21:2405–2412
Li LC, Deng J, Stephens D (2002) Polyanhydride implant for antibiotic delivery—from the bench to the clinic. Adv Drug Deliv Rev 54:963–986
Kumar N, Langer RS, Domb AJ (2002) Polyanhydrides: an overview. Adv Drug Deliv Rev 54:889–910
Laurencin CT, Norman ME, Elgenxy HM, El-Amin SF, Allcock HR, Pucher SR et al (1993) Use of polyphosphazenes for skeletal tissue regeneration. J Biomed Mater Res 27:963–973
Li C (2002) P oly(L-glutamic acid)–anticancer drug conjugates. Adv Drug Deliv Rev 54:695–713
Gopferich A, Tessmar J (2002) Polyanhydride degradation and erosion. Adv Drug Deliv Rev 54:911–931
Heller J, Barr J, Steven Y, Khadija NG, Abdellauoi S, Gurny R (2002) Poly(ortho esters): synthesis, characterization, properties and uses. Adv Drug Deliv Rev 54:1015–1039
Chen G-Q (2009) A microbial polyhydroxyalkanoates (PHA) based bio- and materials industry. Chem Soc Rev 38:2434–2446
Goonoo N, Jeetah R, Bhaw-Luximon A, Jhurry D (2015) Polydioxanone-based bio-materials for tissue engineering and drug/gene delivery applications. Eur J Pharm Biopharm 97:371–391
Fonseca AC, Gil MH, Simoes PN (2014) Biodegradable poly(ester amide)s—A remarkable opportunity for the biomedical area: review on the synthesis, characterization and applications. Prog Polym Sci 39:1291–1311
Schrier J, Fink B, Rodgers J, Vasconez H, DeLuca P (2001) Effect of a freezedried CMC/PLGA microsphere matrix of rhBMP-2 on bone healing. AAPS Pharm Sci Tech 2:73–80
Wenk E, Meinel AJ, Wildy S, Merkle HP, Meinel L (2009) Microporous silk fibroin scaffolds embedding PLGA microparticles for controlled growth factor delivery in tissue engineering. Biomaterials 30:2571–2581
Zhao K, Deng Y, Chen CJ, Chen GQ (2003) Polyhydroxyalkanoate (PHA) scaffolds with good mechanical properties and biocompatibility. Biomaterials 24:1041–1045
Zhao Z, Wang J, Mao H-Q, Leong KW (2003) Polyphosphoesters in drug and gene delivery. Adv Drug Deliv Rev 55:483–499
Baker MI, Walsh SP, Schwartz Z, Boyan BD (2012) A review of polyvinyl alcohol and its uses in cartilage and orthopedic applications. J Biomed Mater Res Part B 100B(5)1451–1457. doi:10.1002/jbm.b.32694.
Deng Y, Lin X-S, Zheng Z, Deng J-G, Chen J-C, Ma H et al (2003) Poly(hydroxybutyrate-co-hydroxyhexanoate) promoted production of extracellular matrix of articular cartilage chondrocytes in vitro. Biomaterials 24:4273–4281
Lee SY (1996) Bacterial polyhydroxyalkanoates. Biotechnol Bioeng 49:1–14
Park SJ, Kim TW, Kim MK, Lee SY, Lim S-C (2012) Advanced bacterial polyhydroxyalkanoates: towards a versatile and sustainable platform for unnatural tailor-made polyesters. Biotechnol Adv 30:1196–1206
Cui YL, Qi AD, Liu WG, Wang XH, Wang H, Ma DM et al (2003) Biomimetic surface modification of poly(-lactic acid) with chitosan and its effects on articular chondrocytes in vitro. Biomaterials 24:3859–3868
Tripathi L, Wu LP, Meng DC, Chen JC, Chen GQ (2013) Biosynthesis and characterization of diblock copolymer of P(3-hydroxypropionate)-block-P (4-hydroxybutyrate) from recombinant Escherichia coli. Biomacromolecules 14:862–870

Al-Karawi AJM, Al-Daraji AHR (2010) Preparation and using of acrylamide grafted starch as polymer drug carrier. Carbohydr Polym 79(3):769–774

Jung YK, Kim TY, Park SJ, Lee SY (2010) Metabolic engineering of Escherichia coli for the production of polylactic acid and its copolymers. Biotechnol Bioeng 105:161–171

Mano JF, Sousa RA, Boesel LF, Neves NM, Reis RL, Bioinert (2004) Biodegradable and injectable polymeric matrix composites for hard tissue replacement: state of the art and recent developments. Compos Sci Tech 64:789–817

Armentano I, Dottori M, Fortunati E, Mattioli S, Kenny JM (2010) Biodegradable polymer matrix nanocomposites for tissue engineering: a review. Polym Degrad Stab 95:2126–2146

Lee JW, Na D, Park JM, Lee J, Choi S, Lee SY (2012) Systems metabolic engineering of microorganisms for natural and non-natural chemicals. Nature Chem Biol 8:536–546

Lee SY, Mattanovich D, Villaverde A (2012) Systems metabolic engineering, industrial biotechnology and microbial cell factories. Microb Cell Fact 11:156

Choi SG, Kerr WL (2003) Water mobility and textural properties of native and hydroxypropylated wheat starch gels. Carbohydr Polym 51(1):1–8

Deng Y, Zhao K, Zhang X-f, Hu P, Chen G-Q (2002) Study on the threedimensional proliferation of rabbit articular cartilage-derived chondrocytes on polyhydroxyalkanoate scaffolds. Biomaterials 23:4049–4056

Jaklenec A, Hinckfuss A, Bilgen B, Ciombor DM, Aaron R, Mathiowitz E (2008) Sequential release of bioactive IGF-I and TGF-b1 fromPLG microsphere-based scaffolds. Biomaterials 29:1518–1525

Rezwan K, Chen QZ, Blaker JJ, Boccaccini AR (2006) Biodegradable and bioactive porous polymer/inorganic composite scaffolds for bone tissue engineering. Biomaterials 27:3413–3431

Boccaccini AR, Blaker JJ, Maquet V, Day RM, Jérôme R (2005) Preparation and characterisation of poly(lactide-co-glycolide) (PLGA) and PLGA/Bioglass® composite tubular foam scaffolds for tissue engineering applications. Mater Sci Eng C 25:23–31

Kikuchi M, Koyama Y, Yamada T, Imamura Y, Okada T, Shirahama N et al (2004) Development of guided bone regeneration membrane composed of [beta]-tricalcium phosphate and poly(-lactide-coglycolide-co-caprolactone) composites. Biomaterials 25:5979–5986

Kaur G, Pandey OP, Singh K, Homa D, Scott B, Pickrell G (2013) A review of bioactive glasses: their structure, properties, fabrication, and apatite formation. J Biomed Mater Res A 102: 254–274

Kaur G, Sharma P, Kumar V, Singh K (2012) Assesment of *in-vitro* bioactivity of SiO2-BaO-ZnO-B2O3-Al2O3 glasses: an optico-analytical approach. Mater Sci Eng C 32 (7):1941–1947

Kaur G, Pickrell G, Sriranganathan N, Kumar V, Homa D (2016) Review and the state of the art: sol-gel or melt quenched bioactive glasses for tissue engineering, J Biomed Mater Res B Appl Biomater 104(6):1248–1275. doi:10.1002/jbm.b.33443

Kaur G, Pickrell G, Pandey OP, Singh K, Chudasama BN, Kumar V (2016) Combined and individual Doxorubicin/Vancomycin drug loading, release kinetics and apatite formation for the CaO-CuO-P2O5-SiO2-B2O3 mesoporous glasses. RSC Adv 6:51046–51056

Kaur G, Pickrell G, Kimsawatde G, Allbee H, Sriranganathan N (2014) Synthesis, cytotoxicity, and hydroxypatite formation in 27-Tris-SBF for sol-gel based CaO-P2O5-SiO2-B2O3-ZnO bioactive glasses. Sci Rep. doi:10.1038/srep04392

Chapter 4
Biodegradable Metals as Bioactive Materials

Gurbinder Kaur

In 1895, Lane first introduced metal plates for bone implants. Due to the corrosion-related problems of metals, 18–8 stainless steels were introduced in the 1920s, which attracted the attention of many clinical researchers due to its corrosion-resistant properties. Since 2000, the research interest is more inclined toward the synthesis and applications of biodegradable metals. The metallic biomaterials have found variety of applications in treating fractured bones, congenial cardiovascular defects, orthodontic veins filling, narrowed arteries, and many more. Market survey indicates that US$12 bn of microelectronic medical implants are dominating the biomedical materials. In the present chapter, the focus is on the metallic biomaterials, their synthesis routes, and applications in biomedical science.

4.1 Why Metallic Biomaterials?

Metals are being used for fabrication of surgical implants and devices for load-bearing application. The metals do not possess biofunctionalities, but when they are coated with biopolymers or apatites, then they become bioactive and blood compatible. Metals find variety of applications in dentistry and orthopedics. Metals are widely used in fabricating stents and stent grafts, which open stenotic blood vessels. The rigidity of metals maintains dilation, and their plasticity yields expansion of vessels (Fig. 4.1).

Once the stents open a narrow artery, then the vessel remodels and the stents degrade, which gets replaced by the new arterial vessel tissue. Similarly, temporary orthopedic implants such as bone fixation screw/pins join the fractured bone, and once the bone joint is formed, the implants degrade and are replaced by new tissues. The imperative condition for degradation is that the initial degradation for metallic biomaterials must be slow to maintain the mechanical integrity. After the vessel remodeling is complete, the degradation kinetics shall be at a faster pace without any accumulation of toxic end products.

G. Kaur, *Bioactive Glasses*, Series in BioEngineering,
DOI 10.1007/978-3-319-45716-1_4

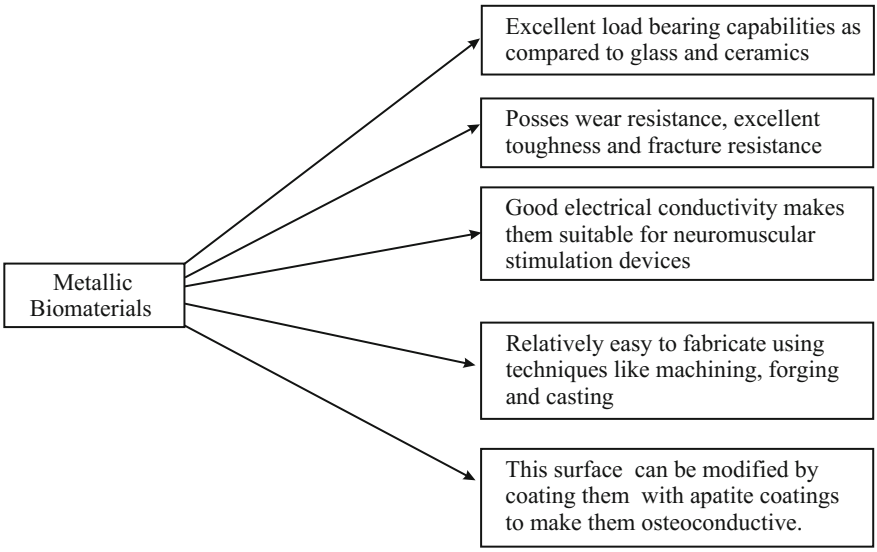

Fig. 4.1 Key characteristics of metallic biomaterials

4.2 Implant Applications of Metals

The metal implants can be used for dental, orthopedic, and cardiovascular applications. Some common applications are listed in Table 4.1.

Ti alloys, stainless steels, and CoCr alloys are the most used metals for implants. 316L stainless steel has molybdenum and carbon content up to 0.03 %, which makes it corrosion resistant. CoCr alloys have excellent wear resistance and are used for heavily load-bearing applications (such as ankle joints). Titanium possesses excellent tensile strength and is a lightweight metal (with density 4.48 g/cm^3). Precisions metals such as silver, platinum, and gold are used in dental restorations due to their good corrosion resistance and ductility. X-ray markers have

Table 4.1 Applications of metal implants

Metal	Applications	
Stainless steel/Co–Ni alloys	Osteosynthesis/joint arthroplasty	Orthopedic implants
Ni–Ti/Ti alloys/316L SS/Ta	Osteosynthesis/bone augmentation	Orthopedic implants
316L SS/Ti6Al4V/CoCrMo/Pure Fe/Mg–Al alloy	Stents/artificial valve	Cardiovascular implants
316L SS/TiNi/Au/Amalgam	Orthodontic wire filling	Dental applications
316L SS/Ti/CoCrMo	Artificial eardrum, screws, and plates	Otorhinology and Craniofacial applications

been made by tantalum because it possesses excellent X-ray visibility. The magnesium-based, iron-based, and zinc-based metal alloys have been used for cardiovascular applications. All these applications will be discussed in the following sections, but first of all, it is important to study the metal structure property relationship, for better understanding of their use in biomedical applications.

4.3 Structure/Property of Metals

The atom of molten metals rearranges into crystal structure upon cooling. Metals are characterized by metallic interatomic bonding, such that the interatomic bonds are non-directional due to close positioning of neighboring atoms attributed to high coordination numbers of 8 or 12 for most of the metals. Metals are endowed to the plastic deformation and high electrical/thermal conductivities. The three common crystal structures for metals are body-centered cubic (bcc), face-centered cubic (fcc), and hexagonal close-packed (hcp). Anyhow, for the real metal crystals, the lattice contains defects such as dislocations vacancies and grain boundaries. The existence of metals in specified cell structure depends largely on lowest free energy and temperature. For instance, cobalt-based alloys exhibit fcc crystalline structures above $\sim$850 °C, whereas titanium and its alloy are hcp below $\sim$900 °C. If the temperature, processing conditions, or other kinetic parameters are altered, then the phase transformation may occur and, sometimes, the phase transformation may result in secondary phase formation in which the phase transformation is undesirable.

4.3.1 Structure-Sensitive and Structure-Insensitive Properties

The dislocations, plastic deformation, yield strength, ductility, fatigue strength, and wear resistance are structure-sensitive properties for metals. Young's modulus/shear modulus and Poisson's ratio which are independent of microstructural effects and processing parameters are structure-insensitive properties of metals.

Every structure of metal has different properties and exhibits peculiar behavior under loading applications. The crystal undergoes elastic deformation when external force is applied. Anyhow, when the force is removed, the crystal returns to its original shape/size. Along the slip planes/crystallographic planes, the line defects provide easy movements. Dislocations can be edge or screw and occur within crystalline solid, and their migration along the crystal lattice yields plastic deformation. The strength of interatomic bonding dictates the required force for dislocation movement/gliding along a crystal plane. Usually, the sharp geometrical discontinuities act as stress concentrators and hence the initiation point of crack-free

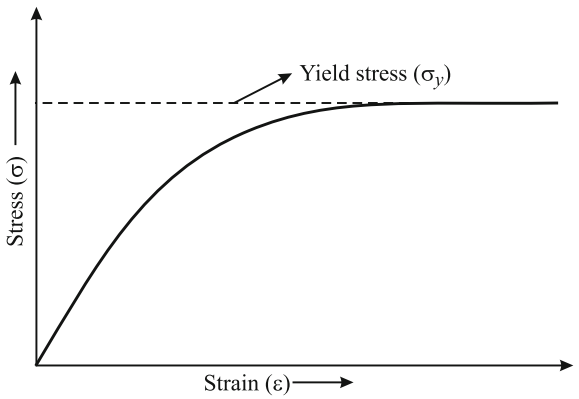

Fig. 4.2 The yield stress behavior for the metal

zones. When the applied stresses are above yield stress (σ_y) of a material, then considerable plastic deformation and dislocation occur in the crystal lattice as depicted in Fig. 4.2.

The yield stress (σ_y) of a material is the stress corresponding to either 0.1 or 0.2 % plastic strain. The metal shall be resistant to the dislocation glide; hence, the yield strength must be increased by methods such as solution strengthening, strain hardening, grain refinement strengthening, or precipitation hardening. The solid solution strengthening increases the dislocation resistance via theaddition of elements to pure metal. During strain hardening, the metal is mechanically worked above the yield stress, which results in dislocation tangling/pileups, thus preventing any further dislocation gliding. When the grain size is finer, then high yield strength can be obtained according to Hall–Petch relation, i.e.,

$$\sigma_y = \sigma_o + \frac{C}{\sqrt{d}} \tag{4.1}$$

where σ_o and C are empirically determined parameters and d is the mean grain size. Hence, for small grains, the number of grain boundaries/surface area would be large, leading to inhibition of the dislocation movements as the glide directions change at every grain boundary function. This mechanism of increasing yield strength via reducing the grain size (up to a limit, where Eq. 4.1 holds good) is known as grain strengthening. When non-metallic dispersoids are incorporated within the metal crystal structure, then dispersion strengthening takes place. Formation of second phase precipitates also interfaces with dislocation glides causing precipitation hardening.

For the metal implants, the fracture toughness (K) shall be high, so that the load-bearing tendency gets boosted up. The plastic deformation can blunt sharp flaws, hence reducing local stress concentrations, thereby increasing fracture resistance, and metallic biomaterials posses this special feature over ceramic biomaterials (Al_2O_3/ZrO_2). Metallic biomaterials shall be resistant to the fatigue failure, which results in the slow propagation of cracks causing lattice failure, thereby

limiting its use as a biomaterial. Fatigue failure is the failure of a material after undergoing a lengthy period of repeated stress/strain cycles. During fatigue failure, the local crack invitation is promoted through the slip bands acting as stress concentrators. It should be noted that increasing yield strength results in high fracture strength/fatigue resistance, but the ductility is compromised. Hence, the parameters shall be optimized by careful selection of material processing procedures.

The structure-insensitive properties, stress and strain, exhibit linear relation except at high temperature (at high temperature, the creep deformation occurs due to rapid atomic diffusion). The Young's modulus (E) is given as follows:

$$\text{Young's modulus} = E = \frac{\sigma}{\varepsilon} = \frac{\text{Stress}}{\text{Strain}} = \left(\frac{1}{r_o}\right)\left(\frac{\mathrm{d}F}{\mathrm{d}r}\right) \tag{4.2}$$

where r and r_o, represent interatomic and equilibrium spacing between atoms, F is interatomic force, and σ and ε are stress and strain, respectively. Hence, Young's modulus is associated with the equilibrium spacing (r_o) and slope of force–distance curve (Fig. 4.3).

$$\left(\begin{array}{l}\text{At maxima; } \dfrac{\mathrm{d}U}{\mathrm{d}r} = 0, \text{ minimum potential energy} \\ \text{and hence, maximum force of attraction}\end{array}\right)$$

In a 3-D structure of metals/materials, the net interatomic forces (F) acting in equilibrium positions are zero ($F = \frac{\mathrm{d}U}{\mathrm{d}r}$, U = potential energy, and r is the interatomic spacing). The potential energy of the system increases, when the atoms are

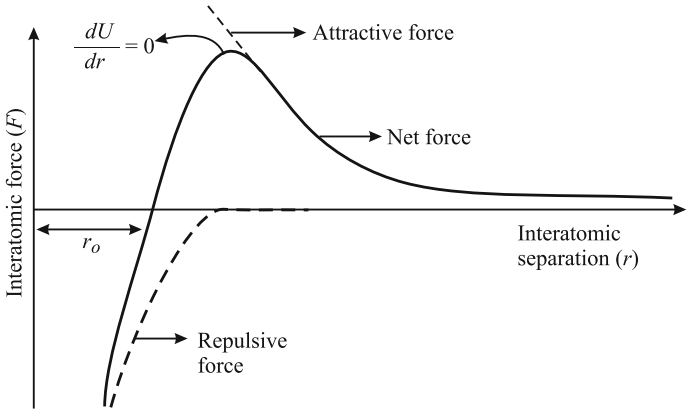

Fig. 4.3 Force–interatomic separation curve

Table 4.2 Mechanical properties of metallic biomaterials

Metal/material	Young's modulus (E) in GPa	% Elongation	Yield strength (σ_{yield}) in MPa
Stainless steel (316L SS)	193–195	40–43	190–195
Pure Iron-/Iron-based	200–210	30–40	150–700
Magnesium alloy (WE 43)	44–45	4–5 %	150–155
Al_2O_3	350–400	–	–
Ni–Ti	25–45	8–9	70–150
Ta	188–190	1–30	150–350
CoCr alloys/cobalt-based	200–240	20–50	240–520
Titanium-/Ti-based alloys	100–120	10–15	480–800

replaced from their equilibrium position under the impact of external forces. The potential energy (U) can be expressed as a sum of attractive and repulsive energies:

$$U = -\frac{A}{r^a} + \frac{B}{r^b}, \quad a < b \tag{4.3}$$

The first term $-\frac{A}{r^a}$ is attributed to the attraction between atoms as they are brought closer approaching the equilibrium spacing r_o. The second term $-\frac{B}{r^b}$ comes into existence due to the repulsion between atoms, when they are too close ($r < r_o$). The Young's modulus is hence affected from both the forces (Eq. 4.2). Table 4.2 lists the mechanical properties of metallic biomaterials.

Usually, titania develops TiO_2 layer on its surface, which acts as a protective film. Similarly, phenomenon happens for chromia-containing alloys as well because chromium forms chromium oxide layer on its surface. When vanadium and aluminum are incorporated into titanium, then the tensile strength is greatly increased.

4.3.2 *Biocompatibility and Corrosion of Metals*

For the metal-based implantable devices inside the human body, the metals must be biologically compatible but least toxic to the tissues in its vicinity. The best metallic implants must exhibit no inflammatory response, immunologic reactions, or allergic stimulations. The metallic artificial implant must be accepted by the body tissues on the whole. The metallic implants must generate cellular/tissue response, without any undesirable effects in the host body.

The biocompatibility of metals is highly influenced by the corrosion of metallic biomaterials. Fretting, pitting, and fatigue are common corrosion problems at the

metal implantation sites. Hence, only few metals qualify all the conditions required by a metallic implant. Fretting corrosion occurs at the area of contact surface after undergoing repeated load, initiating friction among the areas under contact. Fretting corrosion behavior of metallic implant is determined by the chemical composition of alloy, corrosive medium, and stress levels at the contact surface areas. Corrosion resistance can obtained from dense, well-adhered protective oxide surface layers, typically ~5–10 nm thick. Hence, Ti–Ni, Co–Ni, CoCrMo, and Ta are among some metals/metal alloys, which rely on the formation of passive oxide layer for corrosion resistance. Plasma spray method has been implied to coat apatite on the metal substrates such as Ti. Some metals such as Au, Pd, Pt, and Pt-Ir metals display acceptable in vivo properties, though they do not rely on passive film formation. Gold and palladium are used for dental crowns and dental bridge constructions. Pt and Pt-Ir materials are used for fabricating cardiac pacemakers and neuromolecular stimulation electrodes.

Cobalt and titanium alloys have been coated with titanium nitride to improve the corrosion resistance. Other methods to improve corrosion resistance include electropolishing and sand blasting of surfaces, short peening, and chemical composition modification.

4.4 Degradation Behavior of Biodegradable Metals (BM)

The biodegradable metals degrade through the corrosion mechanism leading to hydroxides, oxides, and hydrogen gas as by-products. The sequence of reaction follows the mechanism as shown in Fig. 4.4.

Figure 4.4 demonstratesthe metal oxides into metal ions as soon as it comes in contact with body fluid via an anodic reaction, i.e.,

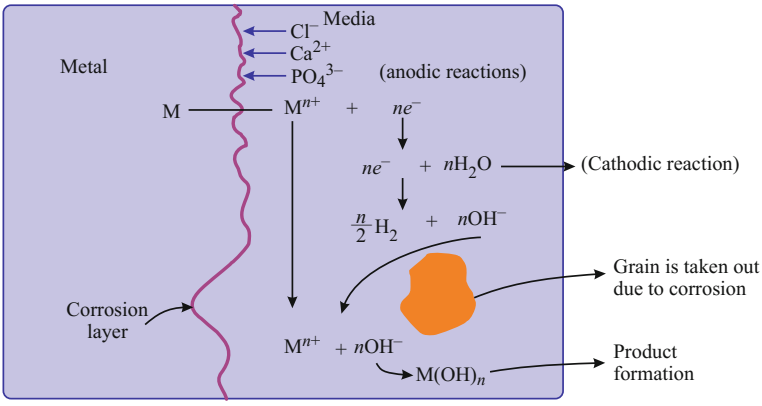

Fig. 4.4 Schematic representation of biodegradable metal degradation

$$M \rightarrow M^{n+} + ne^{-} \tag{4.4}$$

These electrons are consumed by water for reduction. Biodegradable metal dissolution gets speeded up when organic molecules such as lipids, amino acids, and proteins get adsorbed on the BM surface. The water reduction produces hydroxide which interact with oxidized metal ion, leading to the formation of $M(OH)_n$ corrosion layer formation as demonstrated:

$$nH_2O + ne^{-} \rightarrow \frac{n}{2}H_2 + n(OH)^{-} \tag{4.5}$$

$$M^{n+} + n(OH)^{-} \rightarrow M(OH)_n \tag{4.6}$$

The Cl–, PO_4^{3-}, and Ca^{2+} ions migrate onto the BM. The $M(OH)_n$ protective layer breaks down upon the chlorine adsorption, leading to pitting corrosion. The calcium phosphate layer deposits onto the undissolved $M(OH)_n$ layer due to the saturation of Ca^{2+} and PO_4^{3-} in the body fluids. With the time, the cells proliferate and adhere adjacent to the corrosion product layer, whereas the eroded BM gets disintegrated as separate entities and get merged into the surrounding media. This kind of mechanism is observed for the Mg-based metals, but rarely observed for the iron-based metals. Instead of Eq. 4.5, Fe-based metals follow oxygen reduction, i.e.,

$$2H_2O + O_2 + 4e^{-} \rightarrow 4OH^{-} \tag{4.7}$$

Moreover, self-catalysis is the cause of degradation of Fe-based BMs as the Cl^{-} ions accumulate in pits causing pH of the solution to decrease. The erosion or pitting corrosion is rarely observed in Fe-based metals. Anyhow, the Mg- and Fe-based implants get adapted to the human body and eventually get completely dissolved, thereby healing the damaged tissue without undesired reactions. The degradation kinetics of metals are affected by many factors, such as time of implantation, dissolved oxygen, organic/inorganic molecule, stress, and buffer. As the implantation time progresses, a fast reduction in bending strength is observed especially for the magnesium-based biodegradable metals. Iron-based BMs are less susceptible to stress corrosion cracking when in contact with the simulated body fluid. If the electrolyte contains high dissolved oxygen, then Eq. (4.7) gets faster and hence the degradation rates speed up. The organic molecules such as proteins/lipids block the initial degradation by forming a protective layer on the metal surface. Anyhow, the proteins such as globulin, transferrin, serum, and fibrinogen increase dissolution rate of pure iron and alloys such as 316L SS and 304. Bovine serum albumin (BSA) enhanced the anodic dissolution of 316L and 304 but decreased the corrosion potential. The presence of inorganic ions such as Cl^{-} also breaks down the passive film of corrosion products on surface, causing pitting corrosion. When the stress on BMs is increased, then the corrosion rates also increase. The fluid shear stress may also influence the corrosion, and blood flow also brings oxygen onto

metal surface, accelerating the corrosion rates. The buffering agents such as Tris-HCl and Hepes affect the degradation rate. The buffering system HCO_3^-/CO_2 induces the $MgCO_3$ precipitation by consuming OH^- ions.

4.5 Different Metals as Bioactive Materials

The biodegradable metals essentially contain the metallic elements, which can be metabolized by human body. Once the tissue healing is complete, the BMs corrode and degrade in vivo, without any inflammatory response. The following scheme gives the various BMs used in various medical applications.

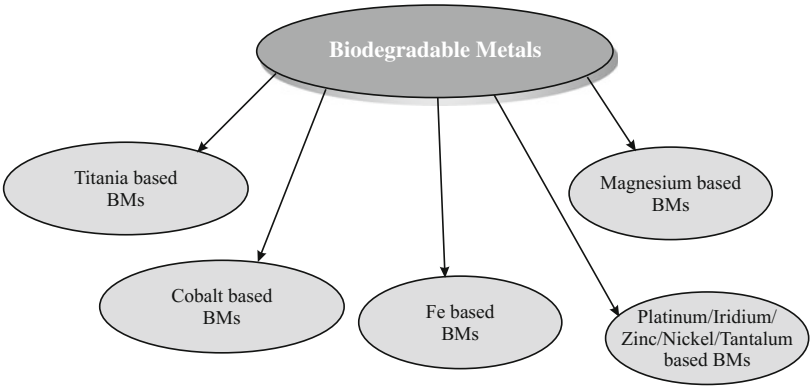

The following sections demonstrate the BMs with their detailed degradation, corrosion mechanism, and applications. Titania- and Cobalt-based metals have revolutionized the field of biomedical engineering, but magnesium iron- and zinc-based BMs are the new categories, which have abundant potential as bioactive material.

4.5.1 Titania-Based BMs

Titania-based alloys have been an imperative part of orthopedic implants since the 1960s. The titania possesses low elastic moduli of 100–110 GPa, excellent in vivo corrosion resistance, and formation of stable TiO_2 passive oxide layer. Titanium exists in two forms: α-phase (hexagonal close-packed at low temperature) and β-phase (body-centered cubic at temperature >883 °C). β-phase further consists of β is amorphous stabilizers such as V, Nb, Ta, and Mo; whereas β-eutectoid stabilizer consists of W, Cr, Co, Mn, Ni, Si, and Fe stabilizers (Fig. 4.5). C, N, Al, and O are commonly α-stabilizers.

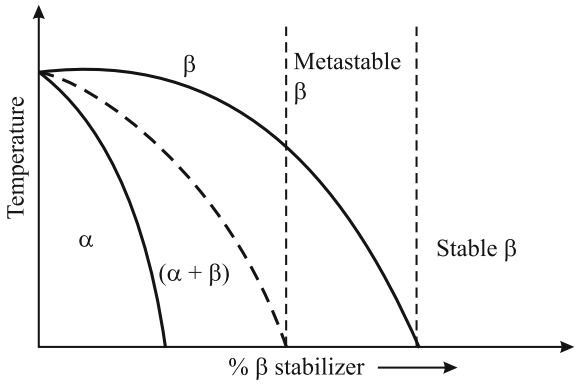

Fig. 4.5 Pseudobinary diagram for Titanium

As clear from phase diagram, the regions for titanium-based alloys decide their applications as potential biomaterials. β–Ti/near β–Ti alloys contain high β-stabilizer elements and are usually characterized with high molybdenum content >10 %. The human cortical bone has modulus of 10–20 GPa, whereas Ti/Ti alloys have Young's modulus ∼110 GPa, whereas the β–Ti alloys retain 100 % β-phase on cooling from the β-transus. β-structures such as Ti–35Nb–5Ta–7Zr (TNZT) have low elastic modulus of 55–75 GPa and relatively low fatigue strength. When β-TNZT is annealed to two phase (α + β), the α-phase precipitation occurs causing elevation in elastic modulus as well as strength of the alloy. Ti–13Nb–13Zr is near β–Ti alloys with Young's modulus of ∼64–70 GPa. Commercially available Ti is known as commercial purity CPTi and is used for endorseous dental implants, fracture repair, and spinal fusion. CPTi contains oxygen, hydrogen, and nitrogen as minor constituents, which enhance the mechanical properties via interstitial solid solution strengthening. The (α + β) Ti alloy has better mechanical properties than the CPTi and hence is used for the load-bearing applications. The best examples of (α + β) Ti alloys are Ti5Al2.5Fe, Ti6A17Nb, and Ti6Al4V, which are used extensively for clinical purpose. The size and distribution of α-/β-phase region strongly determine the mechanical properties of (α + β) Ti alloys. (α + β) Ti-based implants exhibit superior corrosion fatigue properties and excellent corrosion resistance.

Ti/Ti alloy powders are sintered to obtain porous orthopedic implants with high surface area. The sintering process shall be done in non-oxidizing or high vacuum at temperature >1250 °C, followed by cooling of furnace to room temperature. The colonies of lamellar (α + β) structure are obtained throughout the structure, and α and β lamellae are oriented in different directions in these colonies, but α ↔ β crystallographic orientation is common. These colonies contribute to the mechanical strength of the alloy. The mechanical strength of common titania-based alloys is given in Table 4.3.

Table 4.3 Mechanical properties of Ti alloys

Alloy	Young's modulus (E) (GPa)	% elongation	Yield stress (σ_{yield}) (MPa)
Ti13Nb13Zr	75–85	10–15	860–910
Ti12Mo6Zr2Fe	75–85	15–20	1000–1050
Ti35.5Nb7.3Zr5.7Ta	55–65	18–20	793–795
Ti6Al4 V	110	10–15	860
Ti5Al2.5Fe	110	6	820

4.5.2 Cobalt-Based BMs

The implants of cobalt-based BMs can be obtained via number of steps, i.e., obtaining a cast of the implant, and then cutting, grinding, and polishing to obtain a smooth surface of the final implant. The CoCrMn alloys possess excellent wear resistance due to high C content, leading to the formation of carbide phases, such as M_6C, M_7C_3, and $M_{23}C_6$, where M is usually chromium. Co alloy powders are obtained by hot isostatic pressing, and CoCrMo implants mainly consist of (Cr, Mo, Ni) as major elements, (Mn, Fe, Si, N) as minor elements, and $C \approx 0.05$–0.25 wt%. The CrCrMo alloys usually melt between 1350 and 1450 °C and form cored structure on solidification with austenite face-centered cubic (fcc) as major phase enriched in C, Mo, and Cr. At room temperature, usually metastable fcc phase is retained due to the sluggish transformation of fcc to hcp. Faulted fcc zones (known as stacking faults) may be produced after subsequent aging at below 890 °C. $M_{23}C_6$ precipitation is favored for aging between 650 and 850 °C in hcp zones, increasing the yield strength but compromising with material ductility. Intermetallic phases and Cr/Mo/C-rich regions and carbide networks may be formed during the solidification process. The internal porosity within the CoCrMn alloys can be eliminated by not isostatic pressing, which further improves the quality of castings. The corrosion resistance of CoCrMn alloys depends on the formation of chromium-and molybdenum-containing oxides, which usually result when the implant is given a nitric acid solution treatment. High carbon content in these alloys increases the wear resistance, whereas lower carbon content increases the alloy formability. The CoCrMo implant surfaces are modified by either sintering CoCrMo powders to the bone interfacing surface in order to achieve bone–implant fixation without using any acrylic bone cement. Figure 4.6 shows the phase diagram of Co–Cr, and Table 4.4 gives the composition of some commonly used CoCrMo alloys and Co–Ni alloys for medical applications.

The Cr-, Mn-, and C-rich interdendritic zones usually occur at approximately 1235 °C (eutectic temperature). The eutectic structures are formed in the CoMnCr alloys, which are rich in carbides, intermetallic phases along the substrate grain boundary-forming pathways for the easy crack propagation. To decrease this undesirable crack propagation, the CoMnCr alloy shall be slowly cooled from normal sintering temperature to below eutectic melting temperature. Cooling below eutectic melting temperature decreases the amount of carbides, γ-phases, and intermetallics. Table 4.5 gives the properties and applications of CoCrMo-based alloys.

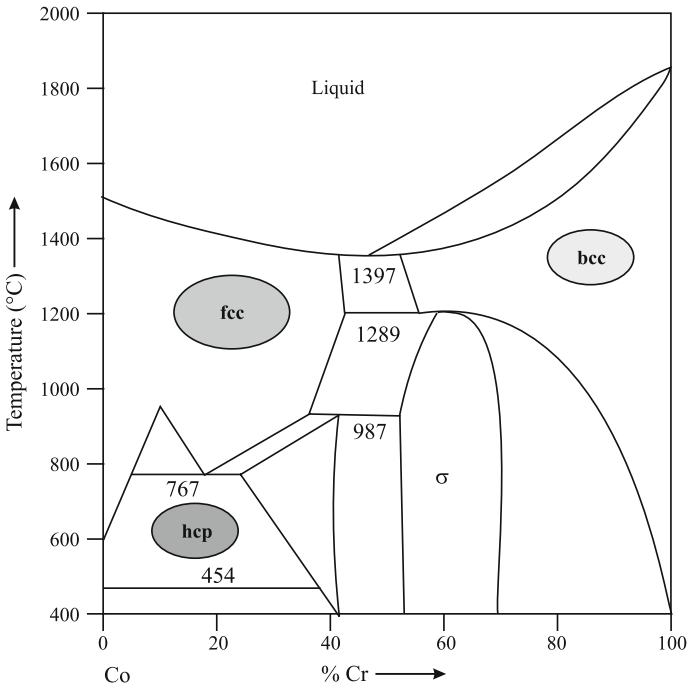

Fig. 4.6 Cobalt chromium phase diagram

Table 4.4 Composition of CoCrMo/Co–Ni alloys

Name	Cr	Mo	Ni	Fe	C	Mn	Si	P	S	W	Other
CoCrMo cast alloy (F75)	27–30	5–7	1	0.75	0.35	1	1	0.02	0.01	0.2	0.3 Al, 0.25 N
HS25	19–21	–	9–11	3	0.05–0.15	1–2	0.4	0.04	0.03	14–16	–
MP35 N	19–21	0.9–10.5	33–37	1	0.025	1–2	0.15	0.015	0.01	–	1Ti
Elgiloy	19–20	6–8	14–16	Balance	0.15	1–2	1.2	0.015	0.015	–	39–41 Co, 0.1 Be
F799 (high C)	26–30	5–7	1	0.75	0.25	1	1	–	–	–	0.25 N
5799 (low C)	26–30	5–7	1	0.75	0.05	1	1	–	–	–	0.25 N
F563	18–22	3–4	15–25	4–6	0.05	1	0.5	–	0.01	3–4	0.5–3.5 Ti

Table 4.5 Applications of CoCrMo alloys

Alloy	Tensile strength (N/mm^2)	Elongation (%)	Application
CoCrMo (cast)	650–1000	8–25	Bone plates/screw, artificial heart valves, hip, knee, and shoulder joint implants
CoCrMo (wrought)	1170–1600	8–25	Finger, knee, shoulder, and hip joint implants
CoCrNiMo	800	40–50	Hip stems
CoCrWNi	900–1200	40–60	Wires, artificial heart valves, surgical instrument, and joint implant

4.5.3 Magnesium-Based BMs

Magnesium-based BMs are widely investigated biodegradable implants due to their good mechanical properties and biocompatibility. The systems such as Mg–Ca, Mg–Sr, Mg–Sn, Mg–Zn, Mg–Si, Mg–Ag, Mg–Zr, Mg–Al, and Mg–RE (rare earth) are among the potential systems for biomedical applications. Though Mg is safe metal, but its corrosion is accelerated due to the presence of impurities such as iron, copper, and nickel. It is observed that upon increasing iron concentration up to 26–48 ppm, the Mg degradation is accelerated 3–60 times.

For the Mg–Si alloy system, Mg_2Si intermetallic compound precipitates out because Si exhibits almost no solid solubility in Mg. Mg–Si alloys are strengthened due to Mg_2Si phase precipitation (Mg_2Si is low density, high hardness, low coefficient of thermal expansion, and high melting temperature phase). For Mg-1 wt% Si alloys, the yield strength and elongation are 80 MPa and 14.83 %, respectively. Anyhow, the Mg–Si alloys exhibit higher degradation rate than the pure Mg metal because Mg_2Si phase exhibits potential difference with α-Mg matrix. It is reported that by introducing Zn and Ca into Mg_2Si, the corrosion resistance and mechanical properties of Mg–Si alloys can be improved. The Mg-based BMs with amorphous structures have higher corrosion resistance and lower elastic modulus due to single defect-free structure. Mg–Zn–Ca BMs exhibit high corrosion resistance, high cell viabilities, and no inflammatory reaction in vivo. Zn and Ca possess solubility of 6.2 wt% and 1.34 wt%, respectively, in Mg. Zn enhances the aging and solid solution strengthening effect of the alloy. If the Zn content is increased up to 4 wt%, then the ultimate tensile strength and elongation of Mg–Zn alloys increase, but above 4 wt% of Zn, the corrosion resistance and mechanical properties of the alloy system get deteriorated. The degradation rate of Mg–Zn alloys can be controlled by the addition of Sr, Ca, and Mn. For instance, 0.2 wt% addition of Ca to Mg–4Zn alloy reduces the degradation rate to almost one-third of its as-cast alloy. When supersaturated Ca and Sr are added to Mg, then Mg_2Ca and $Mg_{17}Sr_2$ phase precipitation occur along the grain boundaries. These intermetallic phases may enhance the creep properties, but can act as potential source for crack initiation, hence accelerating the degradation rate. Mg–0.6Ca exhibits improved bending and comprehensive strength,

whereas above 0.6 wt% Ca addition, these properties are deteriorated. 2.31 % Zn addition to Mg–3Ca yields three eutectic phases: α-Mg, $Ca_2Mg_6Zn_3$, and Mg_2Ca, which improves the ductility and strength of the alloy along with the decreased degradation rate. Mg–3Sr alloys have higher strength, but more than 3 wt% Sr, and the corrosion resistance is deteriorated. Mg–1Ca–0.5Sr alloy exhibits slow degradation rate in Hank's solution and possesses compressive strength of 275 MPa. Upon adding 1 wt% Y in Mg–1Ca alloy, the ductility is improved, whereas corrosion resistance, biocompatibility, and compressive strength get decreased.

Mg–Sn/Mg–Al/Mg–Zr-based alloy systems have also yielded improved corrosion resistance, and Mg–1Sn alloys yield high elongation, tensile strength, and yield strength than the as-cast alloy. Mg–5Sn yields intermetallic phase Mg_2Sn, but adding Ca to this system suppresses the intermetallic formation and refines dendrite microstructure, hence improving the shear strength and creep resistance. Aluminum possesses maximum solubility of 12.7 wt% in Mg, and its addition in Mg improves the corrosion resistance due to the formation of Al_2O_3 film on the alloy surface. Anyhow, Mg–Al system is prone to neurotoxic reactions and hence is not much studied candidates for biomedical applications. The Mg–Zr system exhibits high specific damping capacity, which suppresses the stress generated at bone/implant interface. Mg–1Zr system yields high strength ductility, elongation (27 %), tensile strength (171 MPa), and decreased corrosion rate. Adding Sr, Sn, and Ca to the Mg–Zr decreases the degradation rate. Zr and Ca shall be 1 wt% and Sr < 2 wt%, for their best results in the biomedical applications.

When rare earth (RE) elements are added to the magnesium, then an improvement in strength and creep is resistance to be observed. Y, Gd, Ge, Er, Tm, Yb, Lu, Dy, and Tb exhibit high solid solubility limit, whereas Sm, Pr, Eu, Cs, La, and Nd yield low solubility limit in Mg. Mg–11.4Y–25.3Dy–23.49Gd composition reduced intermetallic formation and galvanic couple formation. For Mg–Y, Mg–Gd, and Mg–Dy system, the optimum addition of Y, Gd, and Dy shall be 2, 15, and 10 wt%, respectively, for biomedical applications. Pure Mg exhibits corrosion current density of 10 $\mu A/cm^2$, whereas Nd addition corresponds to 3.53 wt% Nd ↔ 20 $\mu A/cm^2$, Ce corresponds to 4.76 wt% Ce ↔ 60 $\mu A/cm^2$, and La corresponds to 5.07 wt% La ↔ 30 $\mu A/cm^2$, respectively. Mg–(2–4) Nd–(0.1–0.5)Zn–(0.3–0.6)Zr yield ultimate tensile strength of 300 MPa with 30 % elongation, hence making it applicable for implant fabrication. The surface modification of Mg BMs has been done to slow down the degradation rate. The degradation rate can be reduced up to 90 % after surface modification as shown in Fig. 4.7.

For the lifetime of medical devices, the durability of coating, its topography, and bonding strength to the substrate are very important. Usually, a compact coating is expected to yield best results, but, the hydrogen bubbles are always generated during the coating. Grinding, milling, laser shock peening, machining, and burnishing are the common mechanical methods to improve the surface of Mg-based BMs. When a superficial metal oxide is chemically bonded to the Mg alloy surface, then chemical conversion coatings are produced. For instance, Mg alloy are given a pretreatment in NaOH solution to form $Mg(OH)_2$ layer, which gets converted to MgF_2 upon immersion in HF acid. The fluoride treatment enhances the osteoblasts

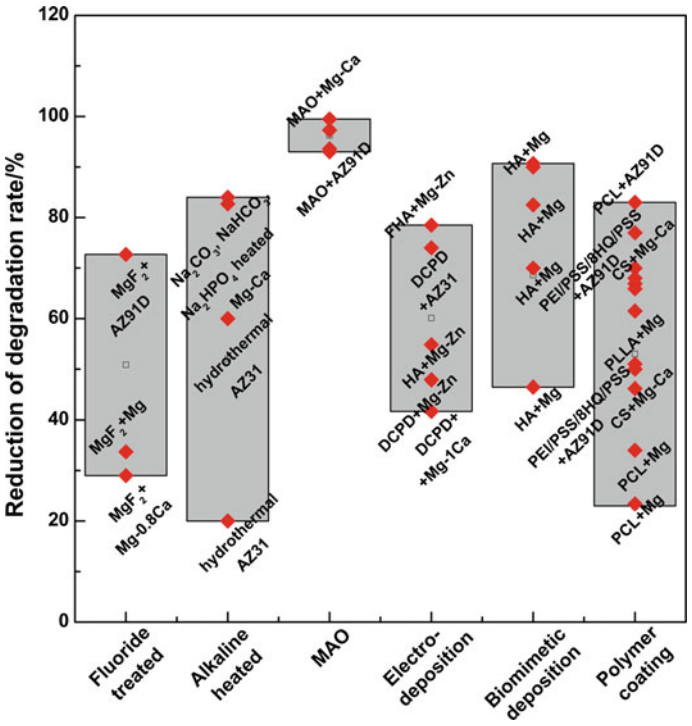

Fig. 4.7 Effect of coating on the corrosion resistance of Mg alloys substrates (Zheng et al. 2014)

stimulation and hence osteosynthesis. For Mg–1Ca alloy, the alkali treatments yielded corrosion rates in the order of $NaHCO_3$ treated < Na_2HPO_4 treated < Na_2CO_3 treated. For the enhanced bioactivity and biocompatibility of the Mg alloy surfaces, the electrodeposition techniques using $NaNO_3$, $NH_4H_2PO_4$, and $Ca(NO_3)_2$ electrolyte systems have used to deposit HA, fluoridated hydroxyapatite (FHA), and brushite layers on Mg surface. Micro-arc oxidation (MAO) can remarkably enhance the corrosion resistance, wear resistance, and adhesion strength of Mg-based BMs. The MG63 cell proliferation was promoted on alloy surface, when Mg–Ca was treated at 360 V via MAO to produce superior corrosion resistance. The coatings with controlled microstructure can be obtained via solgel treatment using colloidal solution as the processor to synthesize an integrated network. Degradable polymer coatings such as polycaprolactone (PCL), poly(D-L-lactide-co-glycolide) (PLGA), and poly(L-lactic acid) (PLLA) are used for Mg alloys. The viscosity, polymer weight and its concentration define the thickness of surface coating on Mg-alloy surface ultrafine grained structure of Mg BMs obtained by rapid solidification (RS), high pressure torsion (HPT), cyclic extrusion and compression (CEC) and equal channel angular pressing (ECAP) increase the corrosion resistance and mechanical properties. The RS yielded grain size of 200–500 nm for Mg–3Ca alloy, and a reduced degradation rate from 21 to (0.36–1.43) mm/year could be seen.

The Mg-based BM degradation rate is strongly related to the local environment. The Mg BMs implant within cortical tissue yield slower degradation than the bone tissue implants with higher blood flow. Only 5 % of Mg–Mn–Zn alloy degraded in the cortical bone 6 weeks postsurgery as compared to the 95 % degradation of implant within the bone marrow. For bare Mg BM implant, subcutaneous gas cavities could be seen for 70 % of the cases, which could be related to the different hydrogen solubility and diffusion coefficients for the tissues. Anyhow, the gas cavities are not seen in the surface-modified BMs due to the restriction of coalescence of hydrogen gas bubbles on the metal surface. AE21 and WE43 bare stunts are studied for animal models, and Mg-based absorbable metal stents (AMS) have been investigated for clinical trials as well and reported in Table 4.6.

Table 4.6 Clinical trials and applications for Mg-based BMs

Material	Finding
Mg–Ca alloy pins (femora bones of rabbits)	Femora bone of rabbits exhibited new bone formation after 3 months postimplantation, and the pins degraded within 90 days
Mg–Zn–Mn alloy rods (rat femora)	Bone marrow implantations yield high degradation rates than cortical bone tissue of rat femora. New bone tissue could be seen around magnesium implant 6 weeks postimplantation
Mg–Al/Y/Li/RE alloy pins (guinea pig femora)	Implanted in guinea pig femora, the subcutaneous gas bubbles could be seen after 1 week but disappeared gradually
Mg–Al alloy stents (coronary artery of swine)	Implanted in coronary artery of domestic swine. Neointimal proliferation and rapid biocorrosion causing loss of integrity within 35–36 days along with inflammatory response
Mg–Y–RE stents (coronary artery of swine)	Intimal hyperplasia could be reduced with vascular brachytherapy for stents implanted inside coronary artery of domestic swines. Anyhow, when Mg–Y–RE stents are implanted inside coronary artery of minipigs, then degradation started 28 days postimplantation and no thrombosis inflammation on the fibrin deposition could be seen
AMS (newborn baby aortic arch)	Restenosis observed 3 weeks postimplantation. $CaPO_4$ and fibriotic structure could be seen
AMS (lower limb vascular stents for 20 patients)	No blood/vessel toxicity and 72.4 % clinical patency after 24 months
WE 43 (Coronary arteries of 63 patients)	Angiography indicated increased diameter stenosis of 17 % after 4 months. Only small amount of original stunts could be seen embedded into intima
DREAMS (Coronary arteries, 46 patients)	Two out of 46 patients had target lesion failure 6 weeks postimplantation. No considerable change in vasoreactivity could be seen between 6 and 12 months. No death or thrombosis could be seen
AMS–INSIGHT (Coronary artery, 117 patients)	No death after 30 days postimplantation. Lower angiographic patency rate of 31.8 % could be seen as compared to those treated with percutaneous transluminal angioplasty (PTA), i.e., PTA yielded 58 % patency rate

4.5.4 Fe-Based BMs

Iron-based systems such as Fe–3C, Fe–3S, Fe–3W, Fe–30Mn–1C, Fe–10Mn–1Pd, Fe–30Mn, and Fe–30Mn–6Si have been studied extensively. Fe-based BMs have similar properties as that of stainless steel. For biodegradable stents, Fe-based BMs are the preferred candidates due to their high ductility (elongation 80 %) and high strength of up to 1450 MPa, but the ferromagnetism of Fe interfaces with certain imaging devices such as magnetic resonance imaging. In order to obtain faster degradation rates along with MRI compatibility, the Fe surface and compositions are modified by electroforming, powder metallurgy, and inkjet 3-D printing. The properties of iron-based alloy are listed in Table 4.7.

Mn is the most suitable alloying element for the iron as it displays excellent microstructural, magnetic, corrosion, and toxicological behavior. Fe–Mn alloys have high strength and lower degradation rate. Powder sintering method followed by series of cold rolling and resintering cycles yielded Fe–Mn binary alloys with higher ultimate strength. Fe–(20–25)Mn alloys yield higher ultimate tensile strength but lower degradation rates and ductility than the Fe–(30–35)Mn alloys (Table 4.7). With the increase in Mn content, the magnetic susceptibility of Fe–Mn alloys decreased. Silica and carbon addition further enhanced the degradation kinetics; i.e., Fe–30Mn–6Si and Fe–30Mn–1C alloys have high degradation kinetics than the Fe–30Mn alloy. A variety of secondary phases has been added to the pure Fe matrix to obtain faster degradation kinetics and Fe–W, Fe–CNT, and Fe–Fe_2O_3 are three main composites prepared via spark plasma sintering technique. The CNT increased

Table 4.7 Properties of iron-based alloys

Alloy	Metallurgical conditional	Yield strength (MPa)	Ultimate tensile strength (MPa)	Elongation
Pure Iron	Annealed plate	150	210	40–42
Fe–10Mn	Forged	650	1300	14
Fe–30Mn	Cast	125	366	55
Fe–35 Mn	Sintering + thermomechanical treatment	235	550	32
Fe–Pd–Mn	Cost + heat treatment	850	1450	11
Fe–20Mn	Powder metallurgy	420	700	8
Fe–30 Mn	Powder metallurgy	240	520	20
Fe–35Mn	Powder metallurgy	230	430	30
Fe–3Co	Rolled	455–460	648	5.5
Fe–3S	Rolled	440	810	8.3
Fe–3 W	Rolled	465	712	6.2

the degradation rate to 4.3 μg/cm^2/h, whereas W/Fe_2O_3 could enhance the degradation rate to 2.8 μg/cm^2/h as compared to the degradation of pure Fe (2.62 μg/cm^2/h). Fe–30 Mn scaffolds obtained from 3-D printing yield mixed phase alloy (martensitic ε + austenitic γ-phases) with open porosity of 36.3 %.

Anyhow, the 3-D printed Fe–Mn scaffold yield higher corrosion and degradation as compared to the pure iron. Good in vitro cytocompatibility of MC3T3-E1 cell seeded on Fe–Mn scaffolds was observed. The biocompatibility and surface modification of iron-based alloys can be done by implanting lanthanum ions into pure Fe plasma nitriding (Fe_4N and $Fe_{2-3}N$ are obtained in nitride layer) and plasma immersion ion implantation and deposition (PIIID). Fe–O layer is formed on the Fe surface which reduces the degradation rates. The WST-8 arrays of extract of pure Fe with human umbilical vein cells yielded cell proliferation. The WST-1 arrays using 3T3 fibroblast cells yielded inhibitory effect for Fe–35 Mn alloy. Fe stents were first implanted into the descending aorta of New Zealand white rabbits and minipigs. No inflammatory response or neointimal proliferation could be seen. During the implantation, stents maintained their mechanical integrity and no adverse effects could be seen 12 months postimplantation. The long-term biocompatibility of pure Fe in the porcine descending aorta was checked for 360 days in comparison with 316L SS stents. The neointimal proliferation from iron stents was comparable to that of 316L SS stents, and no organ toxicity was found. Fe wire implantation into rat artery lumens yielded corrosion of Fe wire with the artery wall, whereas the blood-contacting Fe wires were more or less corrosion free. Iron stents implanted into the coronary artery of eight minipigs showed no necrosis inflammation or thrombosis. These results were similar to as that of vision stents. Table 4.8 gives the iron-based BMs applications

Table 4.8 Fe-based BMs and their applications

Material	Finding
Pure Fe stents (minipigs and descending aorta)	No iron overload or iron-related toxicity, and neointimal proliferation
Pure Fe stents (coronary artery and domestic swine)	Signs of degradation after 28 days. No evidence of inflammation or fibrin deposition
Pure iron stent (coronary artery porcine)	Discoloration of vascular wall adjacent to the stent. Degradation started 28 days postimplantation
Pure iron foils (tails of mice)	Iron implants degraded slowly and lead to local accumulation of Fe. Accompanied by some inflammation without toxicity
Pure iron stent (porcine and descending aorta)	Accumulation of degradation products adjacent to stent and within adventitia accompanied by macrophages, and no iron overloading or toxicity
Nitrided iron stent (porcine and iliac arteries)	Formation of endothelial cell layer on stented vessel wall, 30 % loss of stent luminal diameter, and accumulation of corrosion products

4.5.5 Other Biodegradable Metal

(a) Zn-based BMs

Zn is the abundant transition metal element present in human body. Zinc is an important part of regulatory proteins and cofactor for enzymes. The corrosion rate of Zn is faster than iron but lower than magnesium. Pure Zn has low plasticity (<30 %) and low strength (<20 MPa). Zn–(1–3)Mg alloys were prepared for medical applications, and Zn–1 Mg yielded significant increase in the mechanical properties as compared to the mechanical behavior of pure Zn.

Zinc-based metallic glasses have been developed as an alternatives material for bone repair and fixation materials. The amorphous and nanocrystallinity enhance the corrosion resistance, mechanical behavior, and biocompatibility as compared to its alloy counterpart. The quasicrystallinity and nanocrystallinity introduce homogeneity, higher surface-to-volume ratio, increase in grain boundaries, and reduction in local segregation. Zinc-based $Zn_{38}Ca_{32}Mg_{12}Y_{18}$ metallic glass exhibits higher strength >600 MPa and small magnetic susceptibility of 22.3×10^{-6}. The metals such as Ca/Mg/Ti/Zr and non-metals ZnO/Al_2O_3/apatite incorporation into zinc matrix yield composite material with enhanced corrosion resistance, biocompatibility, and strength. Pure zinc wires placed in rat's arteries degraded at a unique rate of 0–2 mm/year. After removal of zinc wires, the rat arteries were healthy.

(b) Tantalum and tungsten

Tantalum (Ta) has been used as bone augmentation templates. The formation of stable Ta_2O_3 layer on its surface makes it biocompatible with the biological media. Tantalum structures with tensile strength of $\sim$63 MPa, fatigue strength of $\sim$23 MPa, and compressive strength $\sim$60 MPa, respectively, can be obtained by chemical vapor deposition (CVD) process. Tantalum structure contains interconnected pores with mechanical properties similar to as that of human cancellous bones.

Tungsten (W) is an embolic material for the tumor-nourishing vessels. The degradation of W is slow, but upon implantation, its level gets pronounced in the blood and urine of patients. The W coils implanted in clavain arteries of New Zealand rabbits depicted corrosion and increase in serum tungsten levels started at 15 min after implantation. Inside human body, tungsten concentration > 50 μg/l caused cytopathological effects on dermal fibroblasts, smooth muscle cells, and endothelial cells. Below <50 μg/l of tungsten concentration, no such effects could be seen.

(c) Ni–Ti alloys (nitinol)

Ni–Ti (nitinol) finds application in dental, orthopedic, and cardiovascular applications. Nitinol exhibits pseudoelastic properties and exhibits Young's modulus of 28–41 GPa for martensitic phase. The phase diagram for nitinol is shown Fig. 4.8.

Nitinol exhibits good corrosion resistance and shape memory effect. Ni–Ti intermetallic compound exhibits moderate solubility range for Ti/Ni excess. Upon

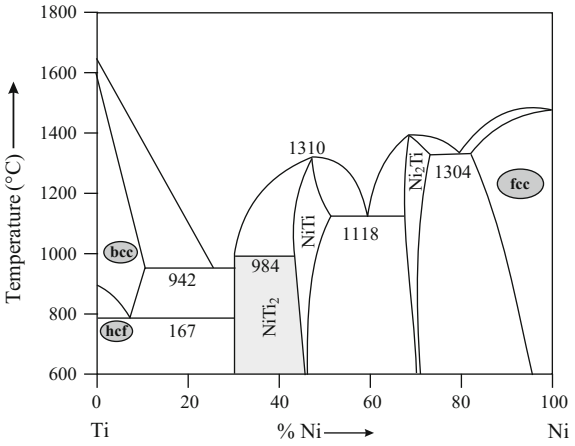

Fig. 4.8 Phase diagram for Ni–Ti alloys

cooling from a high temperature above as that of body temperature to low temperature causes austenite phase transformation (distorted bcc unit cell structure) to martensite. Austenite–martensite transformation can be induced by mechanical deformation. Nitinol is used for fracture fixation devices, cages for use during spinal fusion, and spinal rods for scoliosis. Due to the pseudoelasticity of nitinol, they are used as cardiovascular stents as the stent can expand following implantation into artery. Due to large working range of Ni–Ti alloys, they can be used as orthodontic wires for tooth repositioning.

(d) Platinum/iridium and dental alloys

The noble metals such as platinum/iridium stimulate neuromuscular response and are corrosion resistant. The Pt–Ir alloy exhibits solid strengthening and hence enhanced mechanical properties compared to Pt pure metal. Dental amalgams compare of Hg, Ag, Sr, and Cu. Copper shall be > 6 wt%, as it prevents the formation of Sn–Hg intermetallic phase. When these alloys are mixed with liquid mercury, then intermetallic compounds such as Cu_3Sn, Cu_6Sn_5, Ag_2Hg_3, and Ag_3Sn are formed. The common products of these alloys in oral environment limit the further corrosion by forming amalgam–tooth interface. Au–Ag–Pt/Au–Cu–Ag–Pd/Ag–Pd/Pd–Cu–Ga/Au–Ag–Pd–In are the common compositions used as dental alloys.

Bibliography

Zheng YF, Gu XN, Witte F (2014) Biodegradable metals. Mater Sci Eng R 77:1–34
Pilliar RM (2009) Metallic Biomaterials. In: Narayan R (ed) Biomed Mater 84872:32
Pilliar RM (1983) Powder metal-made orthopaedic implants with porous surfaces for fixation by tissue ingrowth. Clin Orthop Rel Res 176:42–51

Pilliar RM (1987) Porous-surfaced metallic implants for orthpedic applications. J Biomed Mater Res 1:1–33

Ma J, Zhao N, Zhu D (2015) Endothelial cellular responses to biodegradable metal zinc ACS. Biomater Sci Eng 1:1174–1182

Hermawan H, Ramdan D, Joy RP (2011) Djuansjah, metals for biomedical applications, biomedical engineering —from theory to applications edited by Prof. Reza Fazel

Akahori T, Niinomi M (1998) Fracture characteristics of fatigued Ti6Al4 V ELI as an implant material. Mater Sci Eng A 243:237

Amis AA, Bromagen JD, Lazvin M (1987) Fatigue fracture of a femoral sliding compression screw-plate device bone union. Biomaterials 8:153

Azushima A, Kopp R, Korhonen A, Yang DY, Micari F, Lahoti GD, Groche P, Yanagimoto J, Tsuji N, Rosochowski A, Yanagida A (2008) Severe plastic deformation (SPD) processes for metals. CIRP Annal Manuf Technol 57:716

Black J, Hastings G (1998) Handbook of biomaterial properties, Chapman Hall

Browne M, Gregson PJ (2000) Effect of mechanical surface pretreatment on metal ion release. Biomaterials 21:385

Brune D (1986) Metal release from dental biomaterialsm. Biomaterials 7:163

Buford A, Goswami T (2004) Review of wear mechanisms in hip implants: paper I—general. Mater Des 25:385

Chen Q, Liu L Zhang S-M (2010) The potential of Zr-based bulk metallic glasses as biomaterials. Front Mater Sci China. 4:34

Chiba A, Lee S-H, Matsumoto H Nakamura M (2009) Construction of processing map for biomedical Co28Cr6Mo0.16N alloy by studying its hot deformation behavior using compression tests. Mater Sci Eng A 286:513–514

Dearnley PA, Dahma KL, Çimenoglu H (2004) The corrosion–wear behaviour of thermally oxidised CP-Ti and Ti6Al4V. Wear 256:469

Fleck C, Eifler D (2010) Corrosion, fatigue and corrosion fatigue behaviour of metal implant materials, especially Ti alloys. Intl J Fatigue 32:929

Geringera J, Foresta B, Combrade P (2005) Fretting-corrosion of materials used as orthopaedic implants. Wear 259:943

Han YS, Hong SH (1999) Microstructural changes during superplastic deformation of Fe24Cr7Ni3Mo0.14 N duplex stainless steel. Mater Sci Eng A 266:276

Hanawa T (2004) Metal ion release from metal implants. Mater Sci Eng C 24:745

Hermawan H, Mantovani D (2009) Degradable metallic biomaterials: the concept, current developments and future directions. Minerv Biotecnol 21:207

Hermawan H, Alamdari H, Mantovani D, Dubé D (2008) Iron-manganese: new class of degradable metallic biomaterials prepared by powder metallurgy. Powder Metall 51:38

Hermawan H, Dubé D, Mantovani D (2010) Developments in metallic biodegradable stents. Acta Biomater 6:1693

Komotori LJ, Hisamori N, Ohmoric Y (2007) The corrosion/wear mechanisms of Ti6Al4V alloy for different scratching rates. Wear 263:412

Krishna VG, Prasad YVRK, Birla NC, Rao GS (1997) Processing map for the hot working near-alpha Ti alloy 685. J Mater Proc Technol 71:377

Kumar S, Narayanan TSNS, Raman SGS, Seshadri SK (2010) Evaluation of fretting corrosion behaviour of CP-Ti for orthopaedic implant applications. Tribol Intl 43:1245

Kuroda D, Niinomi M, Morinaga M, Kato Y, Yashiro T (1998) Design and mechanical properties of new [beta] type Ti alloys for implant materials. Mater Sci Eng A 243:244

Lee SH, Nomura N, Chiba A (2008) Significant improvement in mechanical properties of biomedical CoCrMo alloys with combination of N addition and Cr-enrichment. Mater Trans 49:260

Li Z, Gu X, Lou S, Zheng Y (2008) The development of binary Mg-Ca alloys for use as biodegradable materials within bones. Biomaterials 29:1329

Morais LS, Serra GG, Muller CA, Andrade LR, Palermo EFA, Elias CN, Meyers M (2007) Titanium alloy mini-implants for orthodontic anchorage: Immediate loading and metal ion release. Acta Biomater 3:331

Nguyen HQ, Deportera DA, Pilliara RM, Valiquettea N, Yakubovich R (2004) The effect of sol–gel-formed calcium phosphate coatings on bone ingrowth and osteoconductivity of porous-surfaced Ti alloy implants. Biomaterials 25:865

Okazaki Y, Gotoh E (2008) Metal release from stainless steel. CoCrMoNiFe and NiTi alloys in vascular implants. Corr Sci 50:3429

Oztürk O, Türkan U, Ahmet EE (2006) Metal ion release from nitrogen ion implanted CoCrMo orthopedic implant material. Surf Coat Technol 200:5687

Reclarua L, Eschlera P, Lerf R, Blatter A (2005) Electrochemical corrosion and metal ion release from CoCrMo prosthesis with Ti plasma spraycoating. Biomaterials 26:4747

Roland T, Retraint D, Lu K, Liu J (2006) Fatigue life improvement through surface nanostructuring of stainless steel by means of surface mechanical attrition treatment. Script Mater 54:1949

Schinhammer M, Hänzi AC, Löffler JF Uggowitzer PJ (2010) Design strategy for biodegradable Fe-based alloys for medical applications. Acta Biomater 6:1705

Schroers J, Kumar G, Hodges T, Chan S, Kyriakides T (2009) Bulk metallic glasses for biomedical applications. J Mater 61:21

Shahryari A, Omanovic S, Szpunar JA (2008) Electrochemical formation of highly pitting-resistant passive films on biomedical grade 316LVM stainless steel surface. Mater Sci Eng C 28:94

Tritschler B, Forest B, Rieu J (1999) Fretting corrosion of materials for orthopaedic implants: a study of a metal/polymer contact in an artificial physiological medium. Tribol Intl 32:587

Wang YB, Zheng YF, Wei SC Li M (2011) In vitro study on Zr-based bulk metallic glasses as potential biomaterials. J Biomed Mater Res 96:34

Weiss I, Semiatin SL (1999) Thermomechanical processing of alpha Ti alloys—An overview. Mater Sci Eng A 263:243

Xin Y, Liu C, Zhang X, Tang G, Tian X, Chu PK (2007) Corrosion behavior of biomedical AZ91 magnesium alloy in simulated body fluids. J Mater Res 22:2004

Yang K, Ren Y (2010) Nickel-free austenitic stainless steels for medical applications. Sci Technol Adv Mater 11:1

Zhang E, Yang L (2008) Microstructure, mechanical properties and biocorrosion properties of MgZnMnCa alloy for biomedical application. Mater Sci Eng A 497:111

Lia H, Zhenga Y, Qin L (2014) Progress of biodegradable metals, progress in natural science. Mater Int 24:414–422

Kaur G, Pandey OP, Singh K, Homa D, Scott B, Pickrell G (2013) A review of bioactive glasses: their structure, properties, fabrication, and apatite formation. J Biomed Mater Res A 102: 254–274

Kaur G, Pickrell G, Sriranganathan N, Kumar V, Homa D (2016) Review and the state of the art: sol–gel or melt quenched bioactive glasses for tissue engineering. J Biomed Mater Res B Appl Biomater 104(6):1248–1275. doi:10.1002/jbm.b.33443

Chapter 5
The Potential of Glasses/Ceramics as Bioactive Materials

Gurbinder Kaur

The composition flexibility for polymers provides them with their unique characteristics, but their low mechanical strength cannot withstand the stresses required in many applications. The use of biodegradable polymer scaffolds for the regeneration of bones is limited and challenging. These polymers lack a mechanically biocompatible hydroxyapatite (HAp) inorganic phase. Metals have high strength, wear resistance, and ductility. However, their high corrosion rate and low biocompatibility are undesirable for living tissues, and the high diffusion of metal ions may lead to allergic reactions. Some composites have cross-linked elastomers, which give them high elastic moduli, which in turn are beneficial for biocompatibility. Ceramics generally possess good biocompatibility along with resistance to corrosion and compression. The scaffolds fabricated from calcium phosphate-based inorganic materials or bioceramics such as bioactive glass are endowed with higher mechanical strength.

Bioactive glass and glass–ceramics are used for bone repair and are being developed for tissue engineering applications. Due to their versatile properties and composition flexibility, bioactive glasses are very attractive materials for producing scaffolds devoted to bone regeneration. The important feature of bioactive glasses, which makes them suitable candidates for bone tissue engineering, is their ability to enhance revascularization, osteoblast adhesion, enzyme activity, and differentiation of mesenchymal stem cells as well as osteoprogenitor cells. The motivation of this chapter is to provide an overview of the general requirements, composition, fabrication technique, structure–property relationship with hydroxyapatite formation, and future perspectives of bioglasses. Along with this, some metallic glasses have also been investigated for biomedical and technological applications in tissue engineering. Many trace elements have also been incorporated in the glass network to obtain the desired properties, which have beneficial effects on bone remodeling and/or associated angiogenesis.

G. Kaur, *Bioactive Glasses*, Series in BioEngineering,
DOI 10.1007/978-3-319-45716-1_5

5.1 Introduction to Bioactive Glasses

Bioceramics/Bioactive glasses belong to special category of materials, which have positively influenced the quality of life. Bioceramics can exist in three forms, i.e., polycrystalline materials (hydroxyapatite), monocrystals (sapphire), and as composites (polyethylene-hydroxyapatite). Broadly a bioactive material epitomizes a material that is designed for inducing target-specific biological activity. To be more precise, a bioactive material represents a material, which follows a two-step process upon its implantation inside the body. The first step involves specific surface reactions especially with simulated body fluid (SBF) and during the second step, the formation of a hydroxyapatite (HAp) like layer occurs, which is responsible for the interactions within hard and soft tissues. Upon implantation inside the host tissue, bioceramics exhibit time-dependent kinetic modification on the surface by forming a biological interface of hydroxyapatite layer. The imperative criterion to decide the biological activity of a biomaterial in vivo is the formation of a HAp-like surface interaction layer when immersed in a simulated body fluid (SBF) in vitro. Anyhow, some materials such as dicalcium phosphate dehydrate do not show direct bone bonding in vivo in spite of the in vitro formation of an HAp-like surface layer when immersed in a SBF. In contrast to this, β-TCP shows extensive bonding to bone but does not always lead to the formation of an HAp-like material in a SBF.

Hench and coworkers developed the first bioactive glass based on SiO_2–Na_2O–CaO–P_2O_5 system (Bioglass VR), 40 years ago. In 1969, Hench and coworkers discovered that certain glass compositions possessed excellent biocompatibility as well as the ability to bond bone. The bioactivity of this glass system can vary from surface to bulk degradable and hence can be resorbed within 10–30 days in tissue. 45S5BioglassW contains 45 % SiO_2, 24.5 % Na_2O, 24.4 % CaO, and 6 % P_2O_5, in weight percent and the phase diagram as proposed by Hench is given in Fig. 5.1.

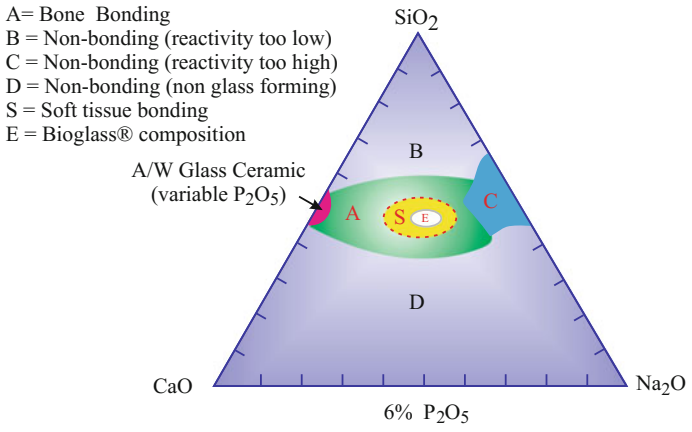

Fig. 5.1 Phase diagram indicating the glass-forming region as proposed by Hench (2006)

This invention brought a revolutionary aspect in the development of biomaterials and doped system of bioactive glasses for the human body. Since 1969, various groups are actively engaged in evolving bioactive glasses as the potential breakthrough in tissue engineering and regenerative medicines. Thereafter, many research groups and scientists engrossed themselves in the study of silicate, phosphate, borate, and other doped system of glasses for biomedical applications. Gradually, this perspective explored inert materials for implantation and to promote natural tissue regeneration. Ancient civilizations such as Egyptians, Chinese, and Indian used biomaterials for reconstructing the defective parts of the body, whereas bioglass has been in clinical use since 1985 in the form of a fine particulate for dental application (Perioglas, NovaBone, USA) to the present.

The word 'bioactive glass,' means the glass which, should be compatible with the surrounding living tissues, non-mutagenic, non-carcinogenic, and non-antigenic, in order to avoid any adverse effect on the cells. One of the imperative requirements for any biomaterial (including bioactive glasses) is their resorbability, i.e., over a period of time after implantation; the biomaterials shall degrade thereby its replacement by the natural host tissue. Resorbable biomaterials require stable interface during the degradation period, and the resorption rates should be matching for the easy repair of tissues. The main reason due to which bioactive glasses attract lots of attention is their capability to offer broad change in properties even after little tailoring of their chemical composition. Moreover, after incorporating metal ions in the compositions, target-specific bioactive glasses can be obtained.

Bioactive glass cells of biomedical interest are sowed into the scaffold, where a scaffold represents a macroporous 3-D structural device endowed with the environmental conditions promoting tissue regeneration along with possessing similar geometry as that of host-replacement tissues such as bone cells. Bone has a unique structure of sheathed cells in composite matrix composed of apatite phase and collagen fibers. It is endowed with excellent mechanical properties such as hardness and flexural strength. However, due to age-related problems, osteoarthritis and osteoporosis, the bond needs regeneration, which is possible via implantation or transplantation. For the implantation process, man-made biocompatible materials especially scaffolds are used for the purpose of regeneration. The dissolution of glass network occurs, which leads to the formation of silica-rich layer followed by the formation of calcium phosphate apatite layer on the glass surface. Apatite layer formation is dependent upon the glass surface, composition, and pore size as well as the preparation conditions. The bioactive glasses belong to class A category of bioactive materials as they exhibit strong tendency to bond with soft tissue and the bone via the formation of HCA layer [20].

A significant amount of research work has been carried out to develop silicate, borate/borosilicate bioactive glasses, and phosphate glasses. Some metallic glasses have also been investigated for biomedical and technological applications in tissue engineering. To this extent, many trace elements have also been incorporated in the glass network to obtain the desired properties, which have beneficial effects on bone

remodeling and/or associated angiogenesis. Over the last four decades, the interest in the field of biomedical application of bioactive glasses has been amplified. This is a field of intense research, which is clearly expressed in the increasing number of publications in the field of bioactive glasses, their properties, and applications.

5.2 Requirements for the Bioactive Glasses/Ceramics

Bioactive glasses should be designed in such a way so that they provide appropriate structural compatibility without any detrimental effects on the host living tissues. Bioactive glasses are significant biomaterials due to their ability to control the rate of bioresorption and a range of chemical/biological properties. By tailoring the processing conditions, i.e., melt-quenching or sol-gel method and initial composition of bioactive glasses, application-specific and design target bioactive glass can be developed. Consequently, bioactive glasses are endowed with superior ability to support osteoblast differentiation from stem and progenitor cells along with bone and vascular tissue regeneration. This capability of bioactive glasses is attributed to their tunable mechanical properties and better biodegradation rates compared to other bioceramics. The bioactive glasses can also act as promising filler materials/coatings for polymer structures. While producing porous scaffolds, dental materials, or filler materials, using bioactive glasses, the properties of bioactive glasses dependent on their powders/particles of various shapes and sizes, and granulates of different sizes should be well-thought-out. While designing the compositions of bioactive biomaterials, the risk of toxicity shall also be taken into consideration so that the release of elements is lower than their biologically safe levels and hence exhibits no or negligible cytotoxicity.

Bioactive glass exhibits an amorphous structure, whereas glass–ceramics are crystallized glasses. Glass ceramics are obtained through a process in, which the glass is heated at a fixed temperature and duration in controlled atmosphere. Upon controlled heat treatment of the glass, a glass–ceramic is formed, which exhibits superior mechanical properties with respect to its parent glass such as viscous behavior, toughness, and hardness. Glass ceramics consist of crystalline phases embedded inside an amorphous glassy matrix. The crystallization of glasses affects the bioactivity of glass as shown by many researchers as well. The results of Filho and coworkers yielded the decreased level of bioactivity upon crystallization of bioactive glass, probably making it an inert material. Kaur and coworkers studied the in vitro bioactive behavior of crystallized glasses and found decreased bioactivity for the crystallized glasses, whereas the mechanical strength was enhanced. Same trend of mechanical strength is observed for the silicate 13-93 glass and borate 13-93B3 bioactive glass scaffolds, which have a higher compressive strength and elastic modulus values after crystallization. In contrast to this, for the 45S5 glass, the crystallization leads to a decrease in the mechanical strength of glass–

ceramic scaffolds with low strength (<1 MPa). It can be concluded that the glass ceramic is mechanically stronger than the amorphous glass, and at the same time, the bioactivity is greatly reduced.

This competition between the bioactive behavior and mechanical strength has been addressed after the discovery of the Na-containing glass, 45S5BioglassW. 45S5BioglassW has been sintered to obtain a mechanically strong crystalline phase inside a residual glassy matrix. In a biological environment, it remains biodegradable as well as bioactive, whereas at body temperature, this crystalline phase transforms into an amorphous calcium phosphate. It has also been observed that the biodegradation profile of the 45S5BioglassW matches well with the healing profile of bone. This desirable property is a unique feature of this 45S5BioglassW and has not previously been reported for any other materials such as hydroxyapatites, alloys, polymers, or calcium phosphates.

Some of desired parameters for bioactive glasses/glass-ceramics to function as a suitable biomaterial are listed as below:

1. When the bioactive glasses are in contact with SBF, there must be a formation of a hydroxyapatite layer on the glass surface.
2. The bioactive glasses must exhibit required mechanical properties to withstand any kind of pressure or strain for preventing any structural failure during the patient's normal routine activities as well as during handling of the material.
3. The scaffolds prepared from bioactive glasses must exhibit mechanical properties that are comparable to those of the host tissue to be replaced for enhanced compatibility.
4. Biocompatibility of bioactive glasses is an indispensable property, which means they should be non-toxic and hence promote cell adhesion and cell proliferation.
5. The architecture of scaffolds prepared from bioactive glasses should have a porous three-dimensional (3-D) structure for cell proliferation, vascularization, and diffusion of nutrients, which provides a regulated microenvironment for new tissue synthesis.
6. Almost every bioactive glass requires a thermal heat treatment for making 3-D scaffolds. The heat treatment process at crystallization temperature leads to nucleation and growth of crystalline phases embedded in an amorphous matrix of glass. These crystallized phases must not hamper any bioactive process inside the cell/tissue by inducing cytotoxic effect on the host tissues.
7. For bone engineering, the 3-D scaffolds prepared from the bioactive glass should possess controllable interconnected porosity to support vascularization in order to direct cells to grow into the required physical structure. A typical porosity of 90 % along with a pore diameter of at least 100 μm is required for proper vascularization of the tissue.
8. Bioactive glasses shall not exhibit any inflammatory response and demonstrate immunogenicity or cytotoxicity.

9. Tissue scaffolds must exhibit neogenesis as they provide a temporary structure for cells to synthesize new tissue. However, they must degrade into nontoxic products, which can be easily resorbed or can be excreted by the body. In addition to this, the surface and the bulk material must be sterile.
10. For commercialization, the bioactive glass should be economical while still maintaining the desired features.

Hence, all these criteria are desirable to obtain suitable bioactive glasses for the biomedical and technological applications.

5.3 Introduction to Glasses and Its Components

Glass is an amorphous material with no long-range order of atoms, lacking periodic atomic structure and exhibiting glass transformation region (Fig. 5.2). Glasses are usually brittle and optically transparent. In glass, the atoms are arranged in random manner like a liquid and behave like a super stiffed liquid. Usually the dimension of glasses may extend on three scales, i.e.,

- 2–10 Å—Local atomic arrangements
- 30 few thousand Å—Sub-microstructure scale
- Microns–millimeters—Microstructure/macrostructure

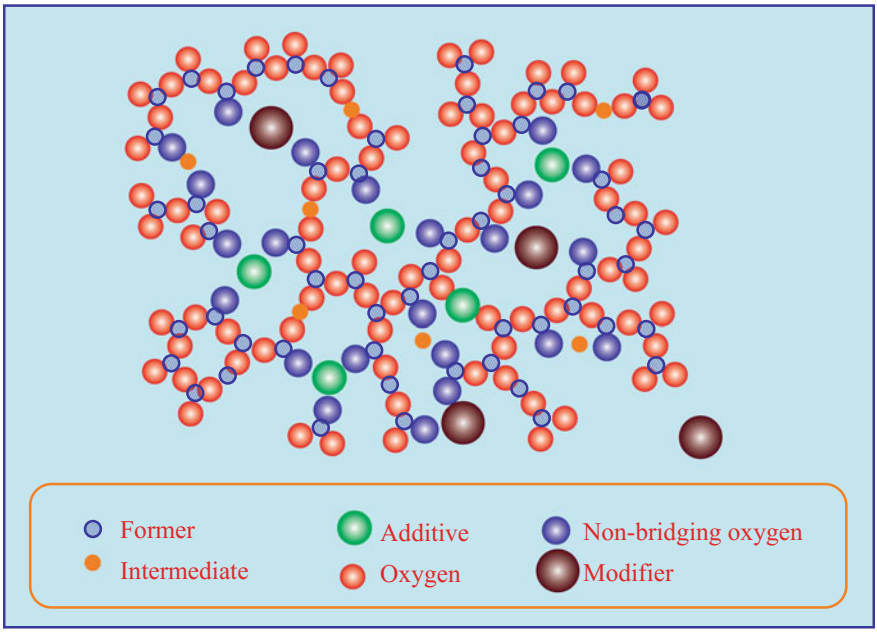

Fig. 5.2 Schematic of glass structure

Glasses and crystals have the same building blocks (cation polyhedra) arranged in a different pattern; e.g., glasses have broader distributions of bond angles. Every glass exhibits time-dependent glass transformation behavior. The glass transformation occurs over a region and hence cannot be characterized by single temperature. If a liquid crystallizes, then a discontinuous change in enthalpy is observed at melting temperature but if no crystallization occurs, then the volume of liquid decreases almost at same rate as that occurring above the melting temperature until a decrease in coefficient of thermal expansion occurs. Any material that may be metallic, organic, or inorganic is considered as a glass if it exhibits a glass transformation.

The raw materials for glass making shall be pure and the classification of raw batch materials can be one in following ways (Table 5.1):

(a) Glass Network Formers: The glass formers form the backbone of glass network. The bond strength for glass formers lie in the range of 60–80 kcal/mol. Glass formers exhibit high field strength (1–2) and low coordination number (CN) between 3 and 4. A glass may contain one ore more glass formers, and commonly used oxide glass formers are SiO_2, B_2O_3, P_2O_5, etc. Sulfur, tellurium, and selenium are the glass formers for chalcogenide glass. Usually, the glass gets their generic names from the formers. For example, if a glass has significant amount of B_2O_3 and SiO_2, then the glass is known as borosilicate glass, whereas if the glass has significant P_2O_5 and SiO_2, then the glass is phosphosilicate glass. Oxides such as Sb_2O_3, Al_2O_3, Ga_2O_3, V_2O_5, and Bi_2O_3 act as glass formers when mixed with other oxides. These oxides do not form glass on their own until and unless they are vapor deposited or rapidly quenched. ZrF_4 and BeF_4 are the common halide glass formers. For making pure silica glasses, high melting temperature is required. Hence, to reduce the melting temperature, fluxes such as Na_2O, PbO, Li_2O, and K_2O are used. However, alkali oxide fluxes may lead to the property degradation.

(b) Glass Modifiers: Glass modifiers occupy random positions in the glass network and modify the network by providing additional oxygen ions. These additional oxygens are known as non-bridging oxygens and they are not a part of polyhedral units (Fig. 5.2). The bond strength for modifiers lies in the range of 30–40 kcal/mol. The field strength of modifiers is low ≈0.35. Modifiers possess high coordination number between 6 and 8. Modifiers usually locate themselves in the glass structure. The glass modifiers such as alkaline earth oxides help in reducing the melting temperature of glass and improve the glass properties. Usually, the concentration of modifiers is less than that of the fluxes (Table 5.1).

(c) Glass Intermediates: Glass intermediate exhibits dual nature as they can either work as network former or a network modifier. These oxides have intermediate coordination and field strength, i.e., CN between 4 and 8, and field strength between 0.84 and 0.04. Their bond strength also lies in the intermediate range of formers and modifiers, i.e., 50–60 kcal/mol. Aluminum, zinc, titanium, and zirconium are among common intermediate oxides.

(d) Fining Agents: Fining agents are present is very small amount such that they do not affect other properties of glass. Fining agents release large bubbles, which carry smaller bubbles to the surface and seed over there. Arsenic and antimony are

Table 5.1 Some glass formers, modifiers, and intermediate oxides with their properties

Role of oxide	M in MO_x	Valence electrons	Coordination number	Dissociation energy E_d per MO_x (kcals)	Single bond strength (kcals)
Glass former	Si	4	4	424	106
	B	3	3	356	119
	Al	3	4	402–317	101–79
	Ge	4	4	431	108
	As	5	4	349	87–70
	V	5	4	449	112–90
	P	5	4	442	111–88
	Zr	4	6	485	81
	Sb	5	4	339	85–68
Modifier	Na	1	6	120	20
	K	1	9	15	13
	Li	1	4	144	36
	Cs	1	12	114	10
	Mg	2	6	222	37
	Ca	2	8	257	32
	Sr	2	8	256	32
	Ba	2	8	260	33
	Pb	4	6	232	39
	Sn	4	6	278	46
	Pb	2	4	145	36
	Zn	2	4	144	36
	Ga	3	6	267	45
	In	3	6	259	43
	Th	4	12	516	43
	Cd	2	4	119	30
	La	3	7	406	58
	Y	3	8	399	50
	Rb	1	10	115	12
	Hg	2	6	68	11
Intermediate	Al	3	6	317–402	53–67
	Zn	2	2	144	72
	Pb	2	2	145	73
	Ti	4	6	435	73
	Cd	2	2	119	60
	Zr	4	8	485	61
	Be	2	4	250	63
	Th	4	8	516	64

very well-known fining agents. NaCl, CaF_2, NaF, and Na_3AlF_6 are other fining agents. Fining agents may also absorb O_2 from the bubbles and reduce the size of seed such that seed shrinks below critical radius and hence, the bubble disappears. Halides are very useful; anyhow they change the viscosity of melt.

(e) Colorants: Colorant oxides usually belong to 4f rare earth or 3d transition metal series. Colorants bestow the glass with different colors, e.g., copper, vanadium, iron, manganese, gold, and silver. Gold and silver produce color in glass by formation of colloids. Sometimes, glass is required to be free of any unintentional colorants (such as iron oxides present in sand), and then other colorants are used to counteract their effect and are known as decolorants.

5.4 Theories of Glass Formation

5.4.1 Structural Theories

Various theories and criteria have been given for the glass formation. According to Goldschmidt criterion, the ratio of cation to anion radii for simple oxides A_mO_n shall be between 0.2 and 0.4 for the glasses to vitrify. This radius ratio corresponds to the tetrahedral coordination; i.e., the cation is surrounded by 4 oxygens. Though Goldschmidt proposed that the melts, which contain tetrahedral coordination of cations, are favorable for making glasses, the technical explanation for this assumption was still lacking. Zachariasen could successfully explain why certain coordination numbers are favoured for the glass formation. Zachariasen random network theory formed the basis of glass formation and this theory is the most commonly followed and hence successful theory. He observed that the silicate crystals have tetrahedral network (symmetrical non-periodic and connected with each other at corners) and readily form glass. Hence, the 3-D network is extended over all the directions with isotropic property attributed to the amorphous nature of glasses. He elucidated following points during his studies and these postulates are to be satisfied by a melt for the glass formation:

- Oxygen atom can be linked to only two network atoms. The oxygen should not have higher coordination number to form a non-periodic network; otherwise, the variations in oxygen–cation–oxide bond angles get diminished.
- The cation coordination number shall also be small and lie within 3–4. For silicate (SiO_2) and phosphate (P_2O_5) network, tetrahedral coordination is observed, whereas for borate (B_2O_3) network, the coordination is 3. Moreover, sufficient network cations shall present to withstand continuous network structure.
- The oxygen polyhedra share the corners and cannot be present at edges. This makes the glass structure more open and the cations are located far apart from each other.
- The network can be 3-D, if at least 3 corner oxygens of a polyhedron are shared. This requires sufficient bonds linking the network polyhedra.

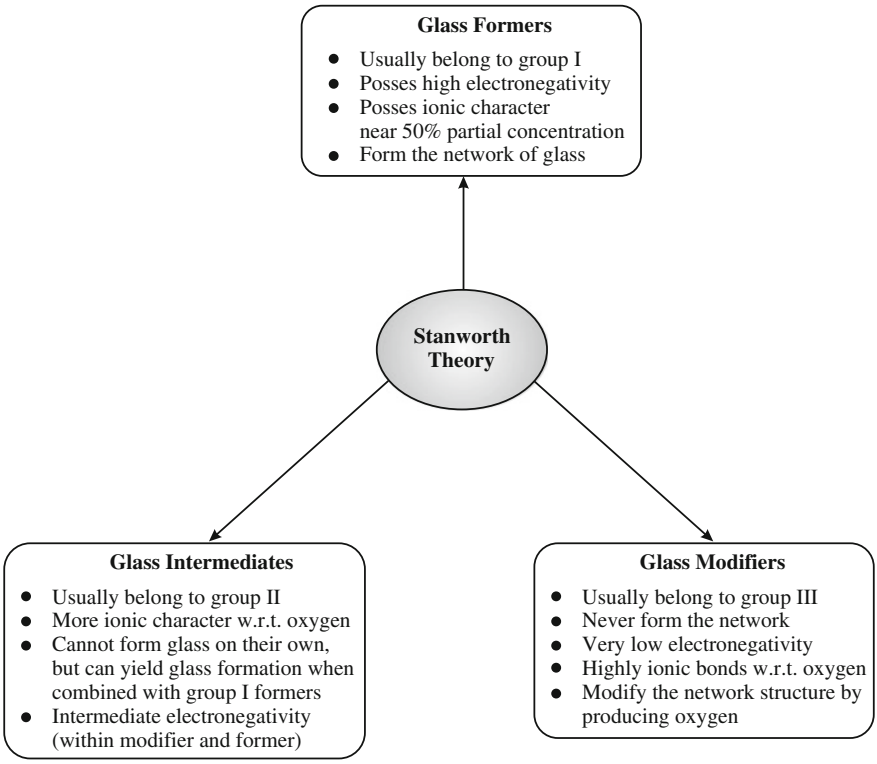

Fig. 5.3 Postulates of Stanworth theory

According to Smekal, glass-forming melts fall into two categories, i.e., inorganic compounds containing partially covalent and partially ionic bonds and organic/inorganic compounds forming chain structures via van der Waals' bonds between the chains and covalent bonds within chains. Smekal theory was based on the bond nature of material. Smekal considered that pure ionic or pure covalent materials cannot form glasses because highly ionic bonds do not form network structures due to lack of directional characteristics. Covalent bonds exhibit sharp defined bond angles, hence limiting the formation of non-periodic network. Dietzel suggested that the cation oxygen bond strength can be regarded as an effective tool to determine the cation behavior. Hence, the cations in oxide glasses have been classified on the basis of field strength. The field strength for a cation with Z valence and 'a' as the distance between the cation and oxygen is given as follows:

$$F_s = \text{Field strength} = \frac{Z}{a^2} \tag{5.1}$$

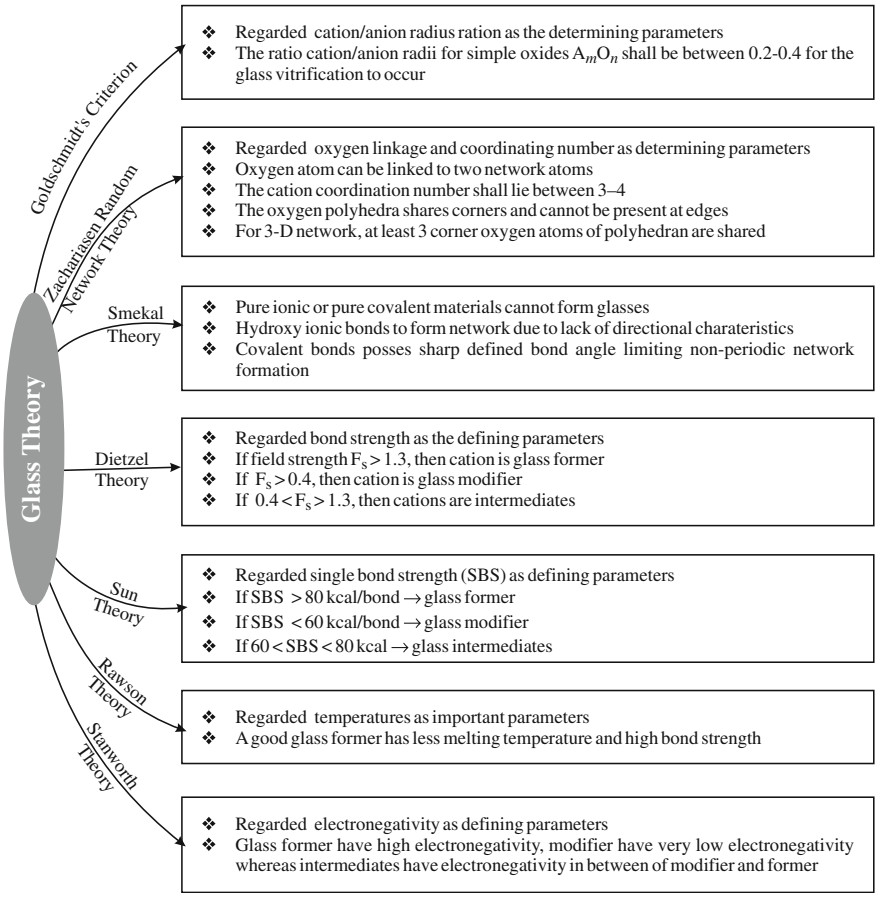

Fig. 5.4 Assumptions of various glass theories

Low field strength implies low cation oxygen bond energy and vice versa. On the basis of field strength, the role of cations can be mentioned as follows:

- $F_s > 1.3 \rightarrow$ Glass former
- $F_s > 0.4 \rightarrow$ Glass modifiers
- $0.4 < F_s > 1.3 \rightarrow$ Intermediates

According to Sun, during cooling process, the strong bonds prevent the structural orientation of melt into crystalline geometry, hence favouring the formation of glass. The bond strength can be defined as the dissociation energy per number of cation–anion bonds in the coordination unit. The dissociation energy (E_d) for a molecule can be defined as the energy required to dissociate an oxide into its individual oxide as follows:

$$A_xO_y \rightarrow xA + yO \tag{5.2}$$

$$\left[\text{Hence, Single bond strength (SBS)} = \frac{E_d}{\text{Coordination no.}} \text{ kcal/bond}\right]$$

On the basis of SBS, the role of cations can be defined as follows:

- SBS > 80 kcal/bond—Glass formers
- SBS < 60 kcal/bond—Glass modifiers
- 60 < SBS < 80 kcal/bond—Intermediates

The oxides with high SBS have high viscosity because they are difficult to be reformed into ordered lattice upon cooling and hence act as good glass formers. Rawson theory considered temperature to be an important parameter in defining the nature of network oxides. He considered a low melting temperature with large bond strength for oxide to be a good glass former. However, the oxide with high melting temperature and similar bond strength is comparatively less competitive network former. Stanworth used the concept of electronegativity of the cation to determine their role in glass network as demonstrated in Fig. 5.3. The glass theories and various assumptions are summarized in Fig. 5.4.

5.4.2 Kinetic Theories

Good glass formers yield glass upon moderate cooling of melt, whereas the poor glass formers require rapid cooling rate. Hence, the material is said to form glass when it is cooled rapidly such that the structural reorientation cannot take place due to insufficient time, and crystallization can be prevented. The crystallization process involves nucleation of crystal sites and then growth of crystal on those sites to a detectable size. The crystallization process can be classified as homogeneous or heterogeneous. When the crystal is formed within the melt, the process is homogeneous, whereas when the crystal is formed due to some impurities, the crystallization process is heterogeneous. The material will form amorphous glass when no nuclei are present, thereby preventing the crystallization of the melt. To determine the concentration of nuclei, the sample can be reheated to a temperature where the nuclei grow to detectable sizes. [For most of instruments such as differential thermal analysis (DTA) and differential scanning calorimetry (DSC), this method is used.] The temperature at which the crystal grows to detectable size is known as peak crystallization temperature (T_c) (Fig. 5.5) and T_x represents onset crystallization temperature.

The nucleation rate (**I**) is obtained, by dividing the concentration of nuclei by total time of isothermal heat treatment at nucleation temperature, i.e., $\mathbf{I} = \frac{dN}{dt}$. Usually two barriers exist for the formation of a nucleus, i.e., thermodynamic barrier and kinetic barrier. The thermodynamic barrier involves free energy change (ΔG),

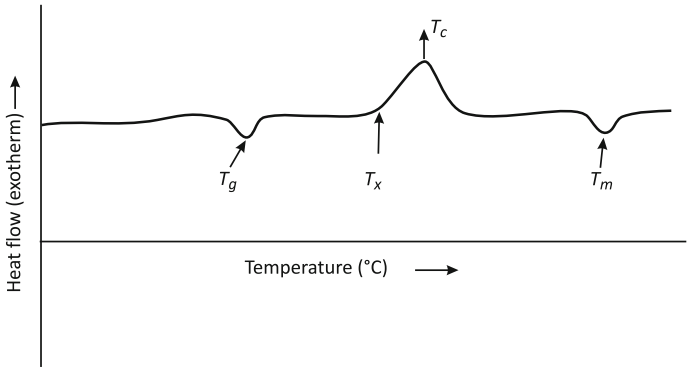

Fig. 5.5 Typical DSC thermogram for the glass (Kaur et al. 2016a)

whereas kinetic barrier involves the growth of an ordered phase from disordered lipid. The expression for nucleation rate is given as:

$$\mathbf{I} = A \exp[-(E^* + \Delta G)/kT] \tag{5.3}$$

where k is the Boltzmann constant, T is the absolute temperature (in K), A is the constant, E^* is the thermodynamic barrier, and ΔG is the kinetic barrier. The constant A is given by

$$A = 2n\mathbf{V}^{1/3}\left[\frac{kT}{n}\right]\left[\frac{\gamma}{kT}\right]^{1/2} \tag{5.4}$$

n = Formula units for crystallizing components
γ = Interfacial free energy/area for crystal melt
$\mathbf{V}$ = Volume/unit

Using the approximations, A can be written as follows:

$$A = n_{\mathrm{V}}\left[\frac{kT}{n}\right] \tag{5.5}$$

The nuclei will grow only if it exhibits certain critical size; otherwise, it will redissolve. When crystals are formed inside the melt, the surface free energy increases due to formation of new interfaces (e.g., melt/crystal interface) within the melt, whereas volume for energy decreases because crystals are ordered than the melt. We can combine both the energies as follows:

$$E = \underbrace{\frac{4}{3}\pi r^3 \Delta G}_{\text{Volume energy}} + \underbrace{4\pi r^2 \gamma}_{\text{Surface energy}} \tag{5.6}$$

When nuclei size increases, the energy E increases and nuclei becomes unstable. ΔG is negative below the melting point; hence, if nucleus grows to a large size, then the first term will dominate and E will decrease (negative ΔG), which stabilizes the nuclei. The expression for the thermodynamic barrier for the nucleation is given by:

$$\Rightarrow E^{\circ} = -\frac{16\pi\gamma^3 \mathbf{V}_{\mathrm{m}}^2}{3\Delta G^{\circ 2}} \tag{5.7}$$

(The free energy change/mole, ΔG, is given by $\Delta G^{\circ} = \mathbf{V}_{\mathrm{m}}\Delta G$, $\mathbf{V}_{\mathrm{m}}$ = molar volume of crystal phase). The heterogeneous nucleation can be written as:

$$\mathbf{I}^* = A^* \exp\left[-\frac{(E^* + \Delta G)}{kT}\right] \tag{5.8}$$

$$\left[A^* = \frac{nkT}{h} \text{ and } E^* \text{ depends on contact angle of nucleus with substrate}\right]$$

If the melt has high viscosity, then there will be high kinetic barrier and nucleation rate subsequently decreases. However, viscosity is temperature dependent; if the temperature increases, then viscosity decreases, which leads to decrease of the kinetic barrier.

5.5 Fabrication Techniques of Bioactive Glasses

Usually, the bioactive glasses are prepared using two techniques: melt-quenching and sol-gel technique. Both the processes result in different porosity, mechanical properties, uniformity, and especially bioactive properties. Sol-gel glasses have inherent mesoporous character, which is attributed to their pore diameter in the range of 2–50 nm. In contrast to this, the melt-quenched glasses have enhanced mechanical properties such as hardness and flexural strength. Glass industry dominates a major portion of economy for USA and European countries and the glass making has evolved through different techniques. The glass is also an indispensable material for sophisticated applications in optoelectronics, biomedical engineering, photonics, and biotechnologies.

5.5.1 Melt-Derived Technique

In the melt-quenching technique, glass is obtained by fusing a mixture of raw materials and subsequent solidification by quenching into glass frits. In melt-quenching technique, glass is prepared by taking required stoichiometric amounts of different constituent oxides or carbonates of high purity (99.9 %). These

constituents are first mixed together by ball mill in an acetone medium. The glass mixture should be calcined at 500 °C for 2 h so that the gaseous substances (moisture + gas) are released out of the composition. The calcined powder obtained after ball milling is melted at high temperatures in a high resistance furnace depending upon the composition chosen. The temperature of the furnace can go up to 1500 °C for certain aluminosilicate compositions, whereas borate and phosphate compositions melt at lower temperatures of 1200–1300 °C. The melt is then poured into molds to produce rods/cylinders or any other desired shape of interest. The melt can also be quenched in air using copper plates to obtain frits. The quenched glass is then annealed at 500 °C to remove the internal stresses from the glasses. Sometimes, the glass-forming batch is heated prior to the melting process in order to release the combined water of hydration or hydroxyl groups. Glasses containing less than 10 % alkali oxide are difficult to melt due to their high viscosities. Generally, the silica content should be less than 60 mol% to allow the glass to bond with bone if it is obtained by melt-quenching. Hench casted 45 % SiO_2–24.5 % Na_2O–24.5 % CaO–6 % P_2O_5 bioactive glass composition, which was easy to melt as it was near to the ternary eutectic. Dr. Ted Greenlee designed a rat femoral implant model and small rectangular implants were made out of the glass, which were inserted into the rats at the Gainesville, Florida Veterans Administration Hospital.

Figure 5.6a, b gives the schematic of the melt-quenching process and sol-gel technique. Sometimes, the glasses are air quenched to avoid any crystallization. When higher cooling rates are required, the glasses can be quenched in liquid such as water, liquid nitrogen, or mercury. By quenching in cold water, granules and pieces of different sizes collectively known as frits can be obtained and they can be easily powdered. The calefaction effect limits the cooling rate to 100 °C/s; i.e., an insulating vapor layer at the glass–liquid interface is formed. For achieving ultrafast cooling rates, the glass should be splat quenched by keeping the glass in contact with some solid material with high thermal conductivity such as copper.

Many types of melting furnaces are used and a specific example of a continuously working furnace is shown in Fig. 5.7. Steel supports hold both tanks of the cross-fired furnace and rods fix the walls. Burners generate flames, which cross the melt level perpendicularly to the melt stream in the melt basin and thereafter leave the room above the glass level through the opposite burner port. After every 30 min, the direction at which the flame heats the batch is switched. The hot exhaust gases pass through the checker chamber before being discharged via the chimney. In the checker chamber, the heat is used for heating the refractory bricks that store the heat. This is followed by cooling the exhaust gases to a temperature around 700 °C, which is still high enough for a following preheating batch before the exhaust gases reach the chimney. Upon switching the flame direction, the cold air used for the combustion reaction passes the heated refractory bricks. The refractory bricks preheat the combustion air via heat transfer and this regenerative system saves energy. Furthermore, the air used in combustion can also be preheated in the recuperator. This heat exchanger fit for high temperatures acts continuously

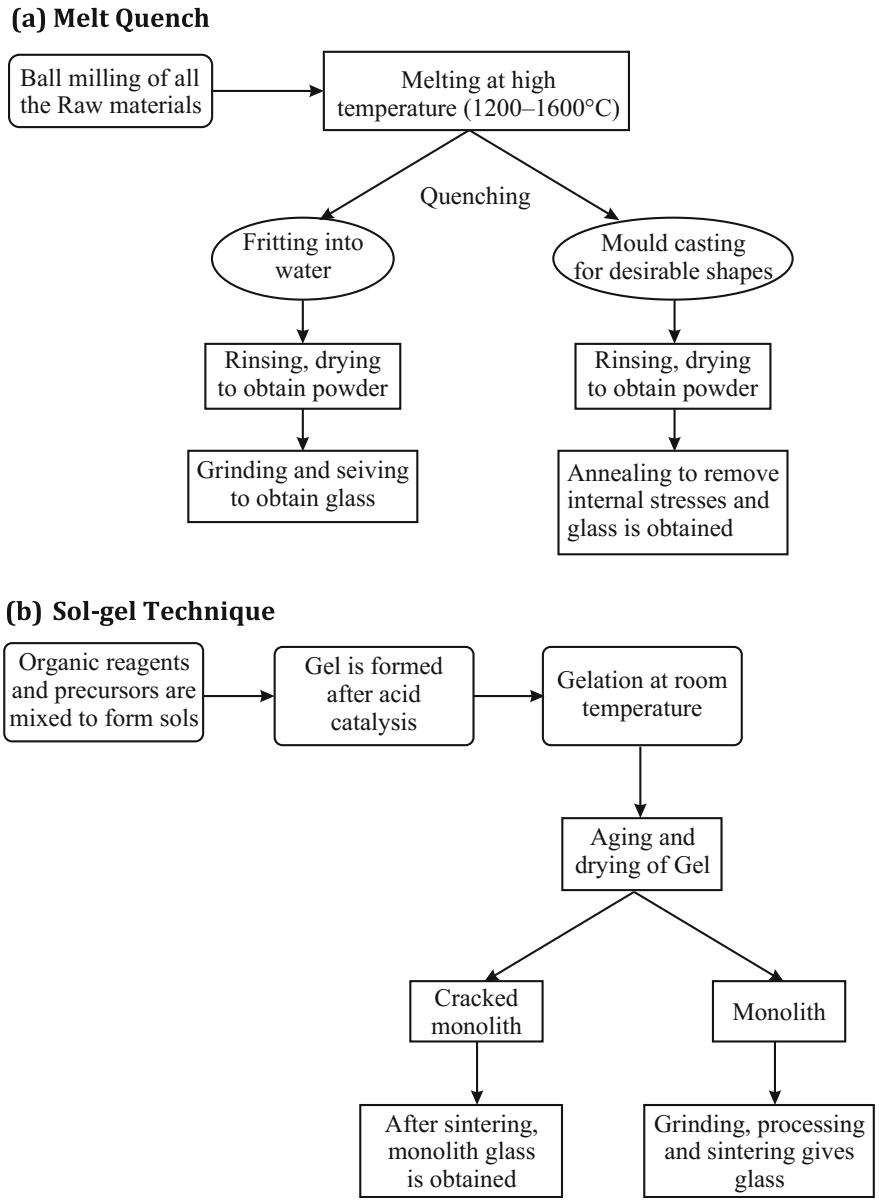

Fig. 5.6 Synthesis route of glasses **a** melt quench technique and **b** sol-gel technique

with separated, crossed streams of heated exhaust gases and cold combustion air and thereby allows recovering waste heat from the hot exhaust gases. On industrial scales, the glasses are produced by the floating technique as depicted in Fig. 5.8.

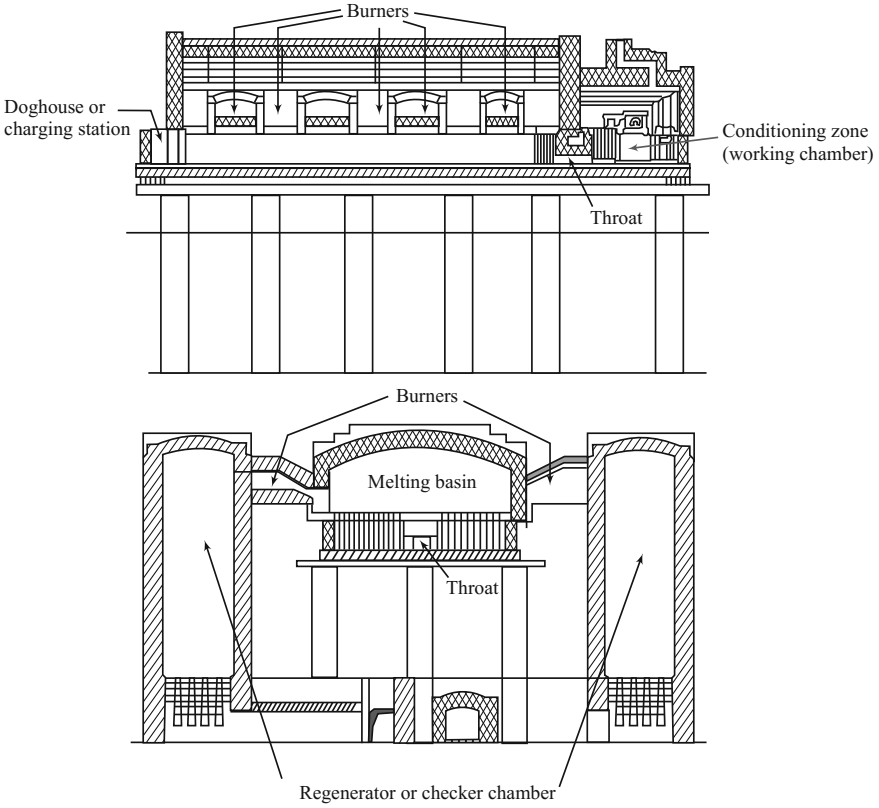

Fig. 5.7 Two-house fuel oil heated cross-fired furnace having two tanks for melting and conditioning or working (Hulsenberg et al. 2008)

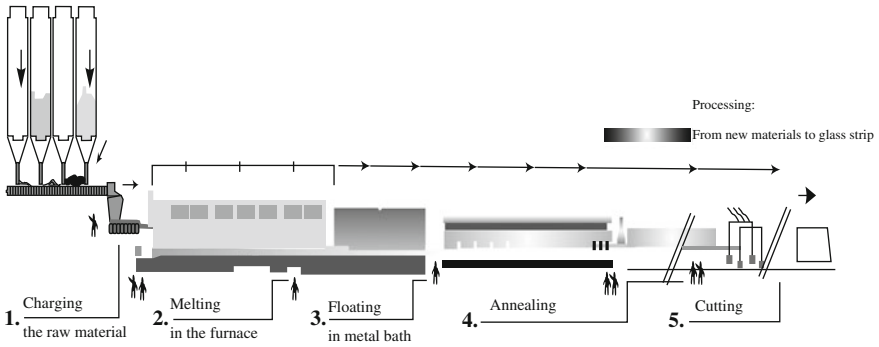

Fig. 5.8 Preparation of float glass

5.5.2 Sol-gel Technique

Using the sol-gel method for glass making, bone bonding and HAp layer formation can be obtained with glasses having up to 90 mol% silica. The sol-gel process involves hydrolysis, polymerization, gelation, drying, and a dehydration process. Sol (or solution) evolves toward the formation of a gel-like diphasic system (with the aid of surfactant) containing both a liquid phase and solid phase. Its morphology can range from discrete particles to continuous polymer networks. For the sol-gel methodology, the organic precursors are used for gelation and drying to prepare the amorphous glass. Sols are the dispersions of colloidal particles (diameter of 1–100 nm) in a liquid, whereas a gel is a rigid network comprised of interconnected pores (in sub-micrometer) and polymeric chains (in micrometers). An interconnected 3-D network is formed via the hydrolysis and polycondensation of an organometallic precursor, subsequently turning it to a gel. Gels are usually classified as aerogels, alcogels, and xerogels. Aerogels are low-density gels (80 kg/m^3) with large pore volumes (up to 98 %), which are produced upon the removal of pore liquid from the rigid network of solid gel such that the network does not collapse. In alcogels, the pore liquid is usually alcohol based, whereas the xerogels are produced by the thermal removal of pore liquid, which usually results in shrinkage of the monolith. The schematic illustration of sol-gel process is shown in Fig. 5.6b. After mixing all the organometallic precursors together, the hydrolysis of liquid alkoxide precursors with the deionised water. The hydrolysis of silicon alkoxide by the water then forms silanol groups ($Si(OH)_4$), which interact with each other forming Si–O–Si bonds. This eventually forms silica network (SiO_2) via polycondensation process during which the water is given out as a by-product. The hydrolysis (Eq. 5.10) and the polycondensation (Eq. 5.10) processes are shown as follows (where R = CH_3, C_2H_5, C_3H_7):

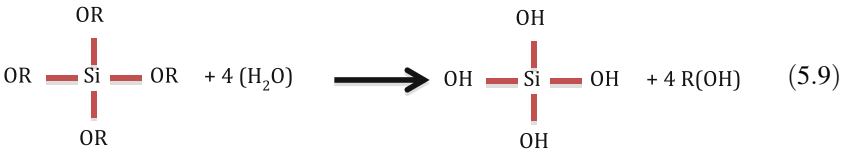

(5.9)

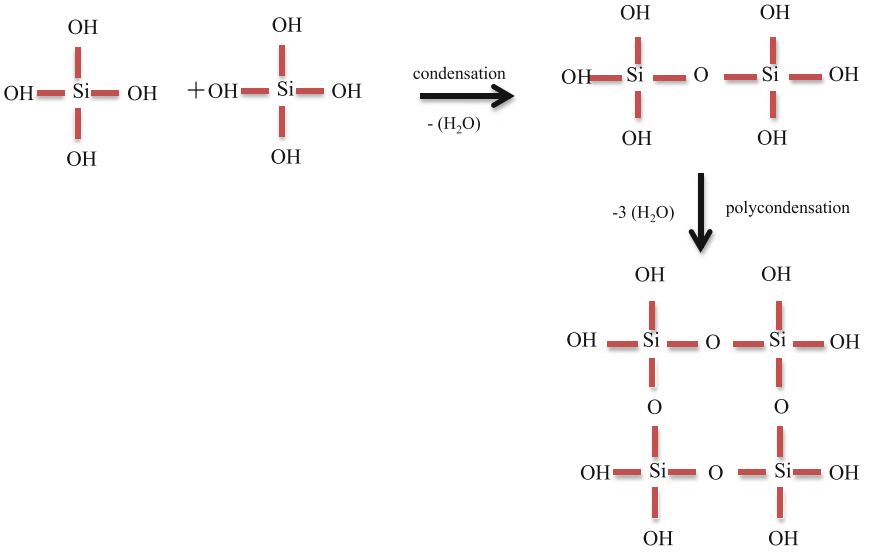

(5.10)

Si^{4+} possesses high field strength and hence, the highly nucleophilic hydroxyl ions (OH^-) tend to attack silicon ion. Both the hydrolysis and the polycondensation are simultaneous processes and their kinetics are affected by several factors such as composition, alkoxide precursor, pH, temperature, pressure, concentration of different ion species, and **R** factor (**R** = [moles of water]/[moles of tetra ethyl orthosilicate (TEOS)]). The hydrolysis and condensation rate constants are small for the bulkier alkoxide groups; i.e., the rate constant of hydrolysis (k_H) for R = $(CH_3)_2CH(CH_2)_3CH(CH_3)CH_2$ is 3×10^{-3} L/mol/s as compared to the k_H of 51×10^{-3} L/mol/s for C_2H_5 group.

Once the sol formation occurs, the gelation process is followed in which 3-D network is formed with time by condensation and cross-linking of silica particles and other colloids. Basically, sol is less viscous liquid, whereas during the process of gelation an abrupt increase in the viscosity is observed. The gelation point (t_g) is the point at which the gel behaves like an elastic solid due to the enhanced interconnectivity of more and more particles. The sharp increase in viscosity during the gelation is also defined as the freezing of a particular polymer structure at the gelation point. The gelation time depends on the nature of alkoxide group, solvent concentration, and the amount of water used for the hydrolysis. Heavy alkoxy groups and increase in the hydrolysis water content increase the gelation time relatively. Gelation is followed by the syneresis/aging of a gel, during which the increase in the strength and decrease in porosity are observed due to the continued process of polycondensation and reprecipitation of the gel network. During the process of the aging, phase transformation also occurs and hydrothermal treatment can accelerate the aging process. The aging process affects physical properties such

as pore volume, surface area and density of the gel, and hence the resulting glass structure. The drying of aged gel must be done properly by removing the pore liquid from the interconnected rigid 3-D network. The gel should be strong enough to resist any catastrophic cracking due to the capillary stresses developed within the aged gel network during the drying process. Furthermore, the highly porous solid is formed upon the silanol (Si–OH) removal/dehydration from within the pore network. When the resulting gel is heated at high temperature, the elimination of pores results in the densification of network.

5.5.3 *Other Fabrication Techniques for Glass Derivatives*

In 1963, Pietrokowsky developed a device in which a molten droplet is expelled from a crucible and then pressed between two metallic plates. The quenching speeds were 10^5 °C/s and uniform plate thickness without any holes could be produced. In 1967, Zarzycki and coworkers produced flakes of B_2O_3–PbO–Al_2O_3 glasses by cooling molten droplet between two rapidly rotating steel rollers. On the contrary, Chen and coworkers in 1976 used metallic Cu–Be wheel spinning at 300–1800 rpm to produce ribbons of metallic glasses. Furthermore, under the action of the centrifugal force, the quenched ribbon slips out of the wheel. Topol and coworkers in 1973 used laser-spin melting in which the rod-shaped target is spun at 8000–30,000 rpm (heated by a CO_2 laser) and small droplets are produced. The phosphate glasses have potential application as guides for muscle or nerve repair. For these soft-engineering purposes, the phosphate glasses are spun to fabricate glass fibers. Metallic glasses are also prepared by melt-spinning, atomic evaporation, and RF sputtering, among other methods, to obtain dimensions up to 100 μm. In order to obtain bulk dimensions, conventional mold casting is used. The setup used by the HUST group is shown in Fig. 5.9.

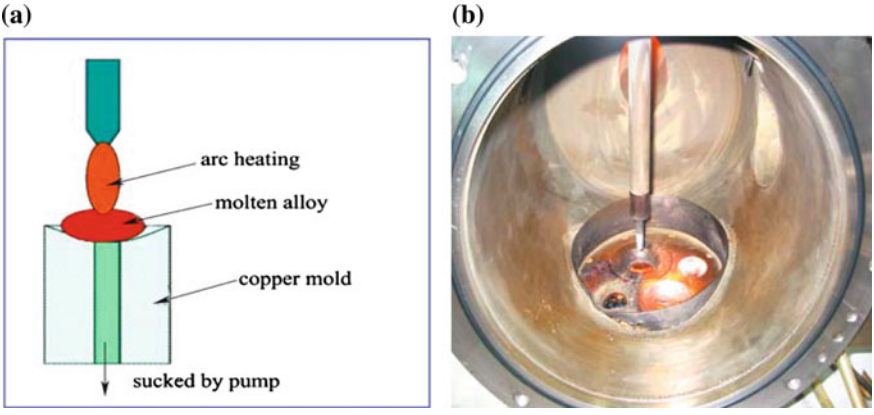

Fig. 5.9 Mold-casting setup used by HUST group for the glass synthesis (Chen et al. 2010)

The fabrication method has a great impact on determining the structural properties of the biomaterial. The mechanical strength, pore size, and pore interconnectivity are critical parameters for bioactive glass scaffolds. A sol-gel process has been used to prepare porous scaffolds of a few bioactive glasses, such as the glass-designated 58S, with the composition (mol%): 60 % SiO_2, 36 % CaO, 4 % P_2O_5. Though the prepared scaffold possessed a similar microstructure as that of dry human trabecular bone, the pore structure consisted of interconnected macropores (>100 μm) resulting from the foaming process and nanopores (less than several tens of nanometers). This may be attributed to the fact that these pores are inherent to the sol-gel process. Nanopores present in the glass prepared from a sol-gel method yield a high surface area, which leads to degradation and a faster conversion of these glasses to HAp than scaffolds of melt-derived glass with the same composition. In addition, the sol-gel method provides high purity glasses with more homogeneity. Moreover, a lower processing temperature is required. However, these sol-gel-derived scaffolds have low strength (2–3 MPa) and consequently they are suitable for substituting defects in low-load sites only.

Interconnected pores with a mean diameter (or width) between neighboring pores of 100 μm or greater and open porosity of >50 % are the criteria for tissue growth. One method for forming a scaffold is to thermally bond a random packing of loose particles in a mold of the desired geometry. However, the scaffolds prepared by this method lacks the desired porosity range and connectivity. Disordered macroporous structures of polymers and bioceramics can be produced by freezing of aqueous solutions and suspensions. Porous scaffolds with an oriented microstructure have been prepared by optimized and controlled freezing technique as it leads to preferred direction of ice-growth. An oriented microstructure is more beneficial than the random microstructure as it can provide higher strength in the direction of orientation. Mixing the bioactive glass particles with some organic material and then removing it before the sintering process is also a useful method, but does not fully resolve the pore size issues. However, silicate, borosilicate, and borate bioactive glass have been prepared with porosities in the range 60–90 % using polymer foam replication method. This method usually produces scaffolds similar to human trabecular bones. Sponge replication is a very advantageous processing technique for making scaffolds, as it is relatively inexpensive and quick. The main drawback of using this technique is the lower mechanical strength of the scaffolds. Scaffolds produced by the polymer burning-out method show higher mechanical strength than that obtained through sponge replication. An electrospinning method is also used to produce nanofibrous bioactive glass scaffolds. These glasses have high surface area, even more than sol-gel-derived glasses (Fig. 5.10). In addition to this, the composition of silica can be varied over a larger composition range. Melt-quenched nanofibers are pliable and have a rapid degradation rate; because of its fine fiber diameter, it has potential applications in the regeneration of non-loaded bone defects and the healing of soft tissue.

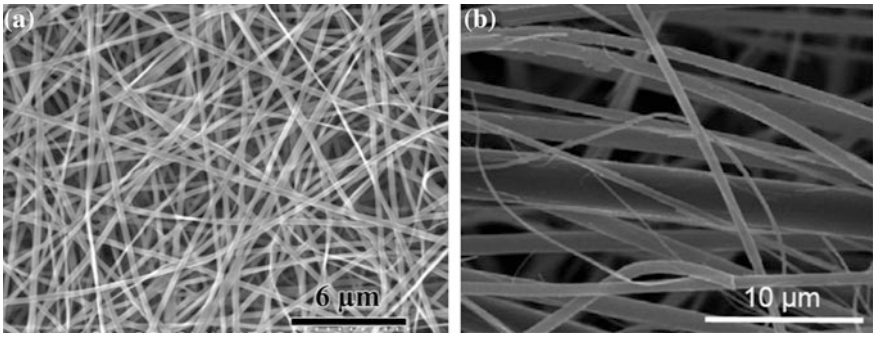

Fig. 5.10 **a** Borosilicate 13-93B1 glass with diameters in the range 150–450 nm prepared by electrospinning of a precursor solution (courtesy of C. Gao; Shinshu University, Japan); **b** bioactive glass with diameters in the range 100–800 nm, prepared from a melt-derived glass (courtesy of Mo-Sci Corp., Rolla, MO, USA) (Rahaman et al. 2011)

5.6 Categories of Bioactive Glasses

One of the major challenges of tissue engineering has been concerned with the design and development of materials and their bioresorbability after performing their function so that the tissue can be remodeled to its natural form again. Hence, it is important to get insight into the glass and its structural design. The various glass compositions are listed in Table 5.2 with three modes of preparation. From the compositional aspect of glasses, i.e., the main oxide in the glass and various other oxides as dopants, some of the reported bioactive glasses and their structural components are described as follows.

5.6.1 Silicate Glasses

The basic building block for silicate glasses is silicon–oxygen tetrahedral. These tetrahedral blocks are linked to each other to form a 3-D network (Fig. 5.11).

The Si–O bond angles are distributed over 120°–180°, centered at about 145°. The randomness in SiO_2 structure is due to variation in Si–O bond angles and bond lengths. The shortest Si–O and O–O distances observed in SiO_4 tetrahedron are 0.162 and 0.265 nm, respectively. Sometimes, stressed bonds and defects of oxygen vacancies are present in SiO_4 tetrahedron. Typical oxygen defects include oxygen vacancies, pero-oxy defects, and imperfections at impurity site. When alkali/alkaline earth oxides are added to SiO_2, the oxygen-to-silicon ratio increases than 2. This leads to the formation of single-bonded oxygens, which do not participate in the network. For univalent cations, one oxygen is required, whereas for divalent two such oxygens are mandatory. Alkali oxide (<10 %) containing glasses usually is difficult to melt due to their high viscosities. If the alkali oxide content increases, the coefficient of thermal

Table 5.2 Bioactive glasses with their composition and synthesis techniques

Glass label	SiO_2	B_2O_3	P_2O_5	MgO	Na_2O	CaO	CaF_2/Al_2O_3	TiO_2/ K_2O/SrO/BaO/CuO	ZnO	Technique used	Wt%/mol %
Silicate glasses											
Undoped	74.7					25.3			0	Sol-gel	wt%
Zn1	73.7					25.3			1.0	Sol-gel	wt%
Zn2	74.0					21.2			4.8	Sol-gel	wt%
ICSW 1	51.06				26.10	22.84				Sol-gel	mol%
A	42					5			53	Melt-quench	mol%
B	57					14			29	Melt-quench	mol%
BT110	40				10	10		20 SrO	20	Melt-quench	mol%
BT111	40				20	10		20 SrO	10	Melt-quench	mol%
BT112	40				30	10		20 SrO	0	Melt-quench	mol%
BT113	40				10	0		30 SrO	20	Melt-quench	mol%
BT114	40				20	0		30 SrO	10	Melt-quench	mol%
BT115	40				30	0		30 SrO	0	Melt-quench	mol%
70S30C	70					30				Sol-gel	
Phosphate/phosphoborate glasses											
10C50P			45.4		36.4	18.2				Melt-quench	mol%
20C50P			41.7		25	33.3				Melt-quench	mol%
30C50P			38.4		15.4	46.2				Melt-quench	mol%
40C50P			35.7		7.1	57.2				Melt-quench	mol%
50C50P			33.3		0	66.7				Melt-quench	mol%
CNP			50		20	30		0 SrO		Melt-quench	mol%
CNP Sr1			50		19	30		1 SrO		Melt-quench	mol%
CNP Sr3			50		17	30		3 SrO		Melt-quench	mol%

(continued)

Table 5.2 (continued)

Glass label	SiO_2	B_2O_3	P_2O_5	MgO	Na_2O	CaO	CaF_2/Al_2O_3	TiO_2/ K_2O/SrO/BaO/CuO	ZnO	Technique used	Wt%/mol %
CNP Sr5			50		15	30		5 SrO		Melt-quench	mol%
13-93B3		53	4	5	6	20		12 K_2O		Melt quench	wt%
13-93B3Cu		52.79	3.98	4.98	5.98	19.92		11.95 K_2O + 0.4 CuO		Melt quench	wt%
Phosphosilicate glasses											
13-93	53		4	5	6	20		12 K_2O		Melt-quench	wt%
1	64		5			26			5	Sol-gel	mol%
ICSW 2	47.84		2.16		26.67	23.33				Sol-gel	mol%
ICSW 3	44.47		4.42		27.26	23.85				Sol-gel	mol%
ICSW 4	37.28		9.25		28.52	24.95				Sol-gel	mol%
ICSW 5	40.96		6.78		27.87	24.39				Sol-gel	mol%
ICSW6	48.98		1.02		26.67	23.33				Sol-gel	mol%
ICSW7	47.07		1.95		27.19	23.78				Sol-gel	mol%
ICSW 8	43.66		3.62		28.12	24.60				Sol-gel	mol%
ICSW 9	38.14		6.33		29.62	25.91				Sol-gel	mol%
ICSW 10	40.71		5.07		28.91	25.31				Sol-gel	mol%
45S5	46.1		2.6		24.4	26.9				Sol-gel	mol%
45S5F	46.1		2.6		24.4	20.9	6	6		Sol-gel	mol%
63 S	63		9			28				Sol-gel	mol%
BGNP	80.7		2.5			16.8				Sol-gel	mol%
BGMP	55.5		8.7			35.8				Sol-gel	mol%
58S	58		9			33			0	Sol-gel	mol%
58S0.5Z	58		9			32.5			0.5	Sol-gel	mol%
58S4Z	58		9			29			4	Sol-gel	mol%

(continued)

Table 5.2 (continued)

Glass label	SiO_2	B_2O_3	P_2O_5	MgO	Na_2O	CaO	CaF_2/Al_2O_3	TiO_2/ K_2O/SrO/BaO/CuO	ZnO	Technique used	Wt%/mol %
A-3	54.5		6.0	8.5	12	15.0		4 K_2O		Melt-quench	wt%
A-5	56.5		6.0	8.5	11	15.0		3 K_2O		Melt-quench	wt%
A-6	54.8		5.8	8.2	10.7	14.6		3 TiO_2 + 2.9 K_2O		Melt-quench	wt%
6P57	56.5		6.0	8.5	11.0	15.0		3 K_2O		Melt-quench	wt%
6P61	61.1		6.0	7.2	10.3	12.6		2.8 K_2O		Melt-quench	wt%
6P68	67.7		6.0	5.7	8.3	10.1		2.2 K_2O		Melt-quench	wt%
46S6 [39]	46		6		24	24			0.00	Melt-quench	wt%
46S6Zn10	46		6		23.94	23.94			0.12 + 0.1 Zn	Melt-quench	wt%
HZ5	42.54		5.64		23.27	23.4			4.94	Melt-quench	wt%
HZ10	40.44		5.39		22.08	22.02			10.05	Melt-quench	wt%
HZ 20	37.14		4.64		18.75	18.86			20.13	Melt-quench	wt%
TCP-10	44.39		8.80	14.89		31.14	0.77			Melt-quench	wt%
TCP-20	38.84		13.37	13.03		33.98	0.77			Melt-quench	wt%
TCP-30	33.3		17.95	11.17		36.81	0.77			Melt-quench	wt%
TCP-40	27.75		22.53	9.31		39.65	0.77			Melt-quench	wt%
Zn-0	38.49		5.61	19.24		36.07	0.59		0	Melt-quench	mol%
Zn-2	38.49		5.61	17.24		36.07	0.59		2	Melt-quench	mol%
Zn-4	38.49		5.61	15.24		36.07	0.59		4	Melt-quench	mol%
Zn-6	38.49		5.61	13.24		36.07	0.59		6	Melt-quench	mol%
Zn-8	38.49		5.61	11.24		36.07	0.59		8	Melt-quench	mol%
Zn-10	38.49		5.61	9.24		36.07	0.59		10	Melt-quench	mol%
ICIE1	49.46		1.07		26.38	23.08		0 SrO		Melt-quench	mol%

(continued)

Table 5.2 (continued)

Glass label	SiO_2	B_2O_3	P_2O_5	MgO	Na_2O	CaO	CaF_2/Al_2O_3	TiO_2/ K_2O/SrO/BaO/CuO	ZnO	Technique used	Wt%/mol %
ICIE1 Sr2.5	49.46		1.07		1.07	22.5		0.58 SrO		Melt-quench	mol%
ICIE1 Sr10	49.46		1.07		1.07	20.77		2.31 SrO		Melt-quench	mol%
ICIE1 Sr50	49.46		1.07		1.07	11.54		11.54 SrO		Melt-quench	mol%
ICIE1 Sr100	49.46		1.07		1.07	0		23.08 SrO		Melt-quench	mol%
Phospho borosilicate glasses											
BG-B_0	60.68	0	3.49			35.83				Sol-gel	mol%
BG-B_{10}	49.02	9.98	1.54			39.46				Sol-gel	mol%
BG-B_{20}	29.87	20.00	1.70			48.43				Sol-gel	mol%
1b	39.82	4.43	2.65	13.27	4.43	30.97	4.43			Melt-quench	mol%
2	41.15	4.12	1.23	12.34	4.12	32.92	4.12			Melt-quench	mol%
3	41.82	3.80	1.15	11.41	3.80	34.22	3.80			Melt-quench	mol%
1	40.36	4.48	1.35	13.45	4.48	31.4	4.48			Melt-quench	mol%
1a	40.10	4.45	2.00	13.37	4.45	31.18	4.45			Melt-quench	mol%
D-Alk-B (13-93B2)	18	36	2	8	6	22		8 K_2O		Melt-quench	mol%
CP5	60	5	5			20			10	Sol-gel	mol%
CP10	60	5	10			15			10	Sol-gel	mol%
CP10	60	5	15			10			10	Sol-gel	mol%
CP20	60	5	20			5			10	Sol-gel	mol%
GCu2.5	60	5	10			22.5		2.5 CuO		Sol-gel	mol%
GCu5	60	5	10			20		5 CuO		Sol-gel	mol%
GCu7.5	60	5	10			17.5		7.5 CuO		Sol-gel	mol%
GCu10	60	5	10			15		10 CuO		Sol-gel	mol%

(continued)

Table 5.2 (continued)

Glass label	SiO_2	B_2O_3	P_2O_5	MgO	Na_2O	CaO	CaF_2/Al_2O_3	TiO_2/ K_2O/SrO/BaO/CuO	ZnO	Technique used	Wt%/mol %
Borosilicate glasses											
BZA (I)	40	10					0 Al_2O_3	30 BaO	20	Melt-quench	mol%
BZA (II)	40	7.5					2.5 Al_2O_3	30 BaO	20	Melt-quench	mol%
BZA (III)	40	5					5 Al_2O_3	30 BaO	20	Melt-quench	mol%
BZA (IV)	40	2.5					7.5 Al_2O_3	30 BaO	20	Melt-quench	mol%
BZA (V)	40	0					10 Al_2O_3	30 BaO	20	Melt-quench	mol%
CaAl	40	20				30	10 Al_2O_3			Melt-quench	mol%

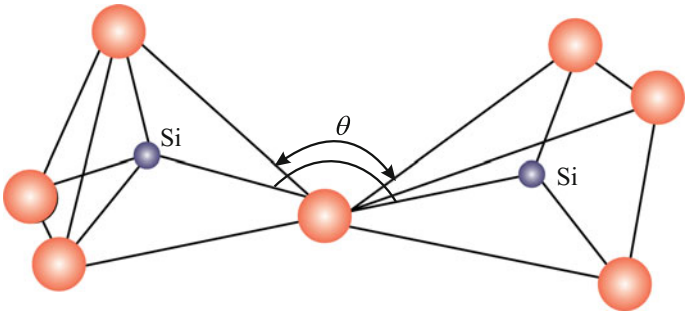

Fig. 5.11 SiO_4 tetrahedron and angle variation

expansion (CTE) of glasses increases due to the formation of more non-bridging oxygens. The alkali ions usually occupy interstices of the network and non-bridging oxygens (NBO) are associated with them. To express the concentration of bridging oxygen/tetrahedron, we use θ_n nomenclature. The tetrahedron with 4, 3, 2, 1, 0 linked oxygens is denoted by θ_4, θ_3, θ_2, θ_1 and θ_0; hence, n would represent the bridging oxygens. The θ_n model also makes an assumption that only two types of unit will exist in the composition. We will obtain expression for the content of alkali oxide (A_2O), for which all the oxygens are non-bridging as follows.

Let us take general composition to be $xA_2O + (100 - x)\ SiO_2$. Total oxygen content would be $[x + (100 - x)2]$. Every oxygen is shared by two tetrahedrons as shown in Fig. 5.10. For different oxygen sharing, we define θ_n as follow:

- $\theta_0 \rightarrow 0$ shared + 4 non-shared oxygens = 4 oxygen/tetrahedron
- $\theta_1 \rightarrow 1$ shared + 3 non-shared oxygens = 3.5 oxygen/tetrahedron
- $\theta_2 \rightarrow 2$ shared + 2 non-shared oxygens = 3 oxygen/tetrahedron
- $\theta_3 \rightarrow 3$ shared + 1 non-shared oxygens = 2.5 oxygen/tetrahedron
- $\theta_4 \rightarrow 4$ shared + 0 non-shared oxygens = 2 oxygen/tetrahedron

Usually, alkali oxide contributes in non-bridging oxygens. For the total oxygen to be shared between θ_4 and θ_3, we write the following equation:

$$\begin{aligned} \theta_4 + \theta_3 &= 100 - x \\ \Rightarrow \theta_4 &= (100 - x) - \theta_3 \end{aligned} \tag{5.12}$$

θ_4 shares 2 oxygens/tetrahedron and θ_3 shares 2.5 oxygen/tetrahedron; hence, we can write the following:

$$\text{Total oxygen} = \theta_4 \times 2 + \theta \times 2.5 = [(100 - x) - \theta_3] \times 2 + \theta_3 \times 2.5 \tag{5.13}$$

As already stated, total oxygen is $x(1) + (100 - x)2$; hence using Eq. (5.13), we write the following equation:

$$x + (100-x)2 = (100-x)2 - 2\theta_3 + 2.5\theta_3$$

$$\Rightarrow \theta_3 = 2x \tag{5.14}$$

And

$$\theta_4 = 100 - 3x \tag{5.15}$$

For $\theta_4 = 0$, i.e., all the oxygens will be non-bridging

$$\Rightarrow 100 - 3x = 0$$

$$\Rightarrow x = 33.3\ \%$$

This implies that for concentration of 33.3 %, the glass will contain no θ_4 unit. When alkaline atoms are also added to the glass composition, every A^{2+} alkaline earth metal shall have 2 neighboring NBO and every A^{+} alkali metal shall have one neighboring oxide. When A^{+} alkali metal ions are replaced by A^{2+} alkaline atoms, the net mobility of modifiers is reduced. For the alkali/alkaline aluminosilicate glasses, the alumina AlO_4 tetrahedra may also act as network former by replacing SiO_4 tetrahedra. Aluminum oxide is intermediate and does not form glass on its own but form glass when it replaces with SiO_4. That can be demonstrated as follows.

According to Pauling Packing rule

$$\frac{r(Al^{3+})}{r(O^{2-})} = \frac{0.53}{1.40} = 0.38 \quad [6 < CN < 4] \tag{5.16}$$

Al_2O_3 prefers octahedral coordination; hence,

$$\frac{\text{Charge of } Al^{3+}}{\text{CN of } Al^{3+}} = \frac{3}{6} = \frac{1}{2}$$

$$\frac{\text{Charge of } O^{2-}}{\text{CN of } O^{2-}} = \frac{2}{4} = \frac{1}{2}$$

This violates the Zachariasen's rule that oxygen atom cannot be linked to more than two cations. For A^{2+}, two AlO_4^{-} units are required because Al_2O_3 unit provides 1.5 oxygen/tetrahedron. Additional oxygen must be provided by A^{2+} or A^{+} to make the oxygen to be 2 oxygen/tetrahedron.

Although the basic tetrahedra $(SiO_4)^{4-}$ are present in most silica structures, the connectivity varies widely into 1-, 2-, and 3-dimensional arrangements. Both ionic and covalent natures of the Si–O bond contribute to the preference for $(SiO_4)^{4-}$ tetrahedron formation in both crystalline and glassy silica. In addition, each O anion is coordinated by two Si cations, corresponding to corner sharing of the oxide

tetrahedra, preventing the close-packing of anion layers and resulting in relatively open structures. Silicon plays a significant role in bone mineralization along with gene activation. Consequently, substitution of silicon for calcium into synthetic hydroxyapatites is the current area of investigation for many research groups. The intracellular and extracellular response of bioactive glass depends upon the release of soluble ionic forms of Si, Ca, P, and Na, from glass surface. 45S5BioglassW is a silica-based composition, which has shown increased secretion of vascular endothelial growth factor in vitro. SCK is Na_2O-free silica-based bioactive glass used for making scaffolds in which the bioactivity phenomena involve H^+/K^+ exchange process. 13-93 glass proposed by Fu and coworkers remained amorphous even after heat treatment confirmed by X-ray analysis. 13-93 glass has more facile viscous flow behavior than bioglass, and fewer tendencies to crystallize. The 13-93 scaffolds prepared by polymer replication method (Fig. 5.12a) consisted of a dense glass network and interconnected cellular pores with porosity, within the range 78–82 % and pores of size 100–500 μm. The SEM images of the 13-93 scaffolds immersed in the SBF for 14 days showed that the surfaces of the scaffolds consisted of a porous needle-like structure of nanometer-sized particles (Fig. 5.12b).

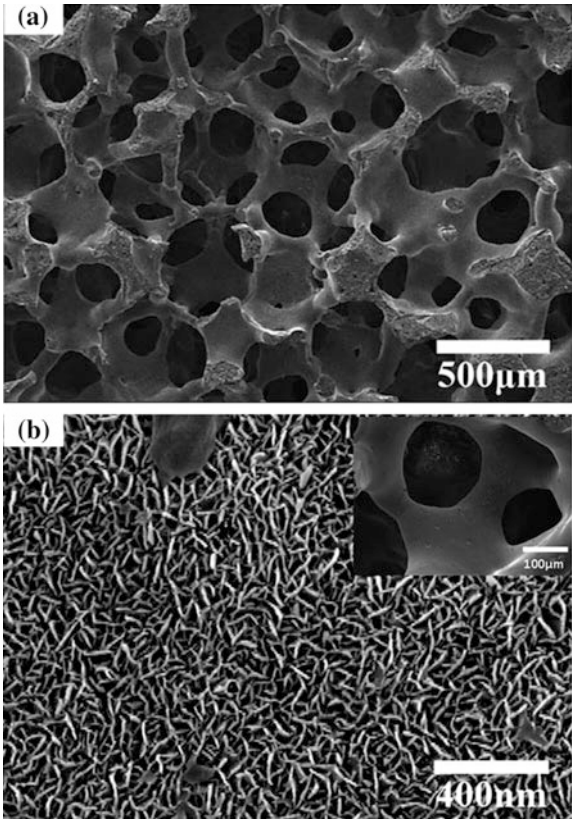

Fig. 5.12 **a** 13-93 scaffold prepared by polymer replication method and **b** HAp-like layer formation on 13-93 scaffold after 14 days dipping in SBF solution (Fu et al. 2010)

Silicate bioactive glasses (45S5 or 13-93) are well known to support the proliferation and differentiated function of osteoblastic cells such as murine MC3T3-E1 cells and MLO-A5 cells, during conventional in vitro cell culture. Goel and coworkers synthesized alkali-free system diopside 99. The system showed considerably smaller weight loss in comparison with 45S5 composition. In addition, during the 12 h of immersion in SBF, highest level of bioactivity was also observed. The sintered glass was found to be amorphous. Silica spheres along with organic ligands find suitable applications in immunoarrays and detection of biological molecules. Silica is also attracting attention of researchers in the field of nanomedicine and drug delivery. Kokubo found these materials to produce good prosthetic devices. Silica-based star-gels were developed by Du-Pont Corp. in 1995. These are organic–inorganic hybrids with unique structure of organic core surrounded by flexible arms. These arms terminate into alkylosilane groups.

5.6.2 Borate/Borosilicate Glasses

Boron occurs in tetrahedral (BO_4) and triangular (BO_3) coordination. To form a continuous structure for the vitreous boric oxide, the BO units shall be connected at the corner. For pure B_2O_3, $T_g \approx 260$ °C; hence, borate glasses have low T_g as compared to the silicate glasses ($T_g \approx 1100$ °C). The B–O–B angles are variable and may twist to give the out of plane boroxyl group. Alkali atoms in addition to the B_2O_3-based glasses cause increase of T_g and decrease in CTE. The alkali atom causes the change of boron coordination from triangular to tetrahedral (no NBO). Hence, no formation of NBO may lead to decrease in CTE and increase in $T_g(BO_3 \leftrightarrow BO_4)$. When the addition of alkali oxide is done above the required concentration, the reversal of properties is observed; i.e., the CTE increases and T_g decreases. This particular behaviour of borate containing melts is known as 'boron anomaly.' The boron anomaly can be explained as follows:

- The conversion of $BO_3 \leftrightarrow BO_4$ takes place only up to a certain critical concentration of alkali oxide.
- Above this critical concentration, the addition of alkali oxide causes formation of NBO, which reverses the trend of properties.

The boron anomaly does not occur for the glasses containing Al_2O_3:A_2O = 1:1, i.e., for the alkali aluminoborate glasses where alkali and Al_2O_3 share same ratio. If the alumina content is increased, then the boron anomaly should occur for higher alkali oxide content. Anyhow, the experimental studies indicate that the boron anomaly occurs for same concentration. The most commonly used glasses are borosilicate glasses. The alkali containing borosilicate glasses is usually rich in silica phase and alkali/boric oxide phases. Alkali borosilicate glasses are easy to manufacture. Alkaline earth oxide borosilicate glass systems are exploited much for their use as sealants. Brink and coworkers proposed the first borosilicate glasses for

biomedical applications in 1990. In order to get the desirable bioactive properties, the relative proportion of B_2O_3 was tailored. Borate glasses are very reactive and have lower chemical durability; hence, they convert more completely and rapidly to HAp than their silica counterparts. Huang and coworkers replaced SiO_2 with B_2O_3 in steps and found substantial increase in the conversion of the glass to HAp in aqueous phosphate solutions. The conversion mechanism of bioactive glass to apatite is similar to that of silicate 45S5 glass, with the formation of a borate-rich layer, similar to the silicate-rich layer of the former. The complete degradation rate of the glasses can be controlled within a wide range of time periods by replacing silica with boron. In addition to this, the sintering behavior of borate/borosilicate glass is more controlled than silicate glasses.

45S5 silicate compositions have been widely investigated over the course of many years but borate- and borosilicate-based compositions have recently been explored. Boron is a trace element, which is required for bone health. Borate glass leads to higher pH value of the culture medium. In vitro, borate glasses support cell proliferation along with differentiation, whereas in vivo they are reported to enhance tissue infiltration. However, $(BO_3)^{3-}$ ions are associated with the toxicity. Some of the reports indicate that certain compositions of borate glasses exhibited cytotoxicity under static conditions during in vitro culture testing, whereas no considerable toxicity was detected under more dynamic culture conditions. Prior to tissue culture, borate-based glass can be partially converted to hydroxyapatite so as to reduce the toxic effects. Other alternatives include dynamic cell culture or dilution of the phosphate solution for reducing toxicity of the medium. Borate glasses rapidly release high concentrations of boron resulting in high level of local concentrations of boron near the vicinity of the glass. However, the boron concentrations detected in the blood around borate glass pellets implantation in rabbit tibiae were found to be at an acceptable level. Hence, borate-based glasses offer opportunities to regulate and tailor the degradation rate of synthetic biomaterials. For the first time in 2005, scaffolds were derived from borate glasses using soft pressing and sintering treatment. 13-93B2 glass is of prime interest these days as it is one of the most promising materials for making foam-like scaffolds. Polymer foam replication was used to successfully produce 13-93B2 glass scaffolds. These scaffolds possessed microstructure nearly identical to human trabecular bone. The peculiar bioactive properties of sponge-derived borate glass scaffolds, as well as their mechanical behavior and structural similarity to trabecular bone, make them very promising candidates for clinical applications as bone grafts. Below a threshold concentration ($\sim$0.65 mM), borate ions released into the culture media due to conversion of the glass to HAp did not hinder the proliferation of bone marrow stromal cells. Moreover, extracts of the scaffold dissolution products supported the proliferation and function of murine MLO-A5 cells. The in vitro bioactivity of the glass was confirmed from the hydroxyapatite (HAp) layer on the glass surface after immersion of the scaffolds in a dilute phosphate solution (0.02 M K_2HPO_4) for 7 days. Though conversion of the scaffolds in the aqueous phosphate solution resulted in a weight loss of 13.0 %, an increase in the pH of the solution from 7.0 to 8.7 after 30 days was observed. The as-prepared scaffolds had a

compressive strength of 6.4 ± 1.0 MPa, which decreased to 1.5–2.0 MPa after 15–30 days immersion in the phosphate solution. The mechanism of conversion of 13-93B2 scaffolds in HAp after soaking in dilute phosphate solutions has been recently investigated in detail by Liu and coworkers. However, as demonstrated by Liu and coworkers, the progressive material degradation carries a significant drop in the 13-93B2 scaffold strength (from 6.2 to 2.8 MPa after soaking for 15 days in phosphate solution). Silica-free 13-93B3 borate glass scaffolds were reported to be toxic for murine MLO-A5 osteogenetic cells in vitro but the same scaffolds were harmless to cells in vivo and supported new tissue infiltration upon subcutaneous implantation in rats. Chronic osteomyelitis is a bone infection and its treatment remains a clinical challenge. The implantation of borate glasses loaded with the antibiotic teicoplanin into rabbit tibia [osteomyelitis was induced by methicillin-resistant Staphylococcus aureus (MRSA)] showed promising results for the treatment of osteomyelitis and its confirmation was done via microbiological, histological, and scanning electron microscopy techniques. Twelve-week postimplantation, the formation of HAp-like layer could be seen, which supported new bone ingrowth into the tibia defects (Fig. 5.13a–c). Anyhow, the animals treated with intravenous injection of teicoplanin for 4 weeks showed serious infection and a large amount of fibrosis after 12 weeks (Fig. 5.13d, e), indicating that intravenous teicoplanin was not effective for curing the infection.

The localized soft tissue angiogenic responses to silicate/borate bioactive glass microfiber (45S5, 13-93B3, and 13-93B3Cu) subcutaneous implants in rats have

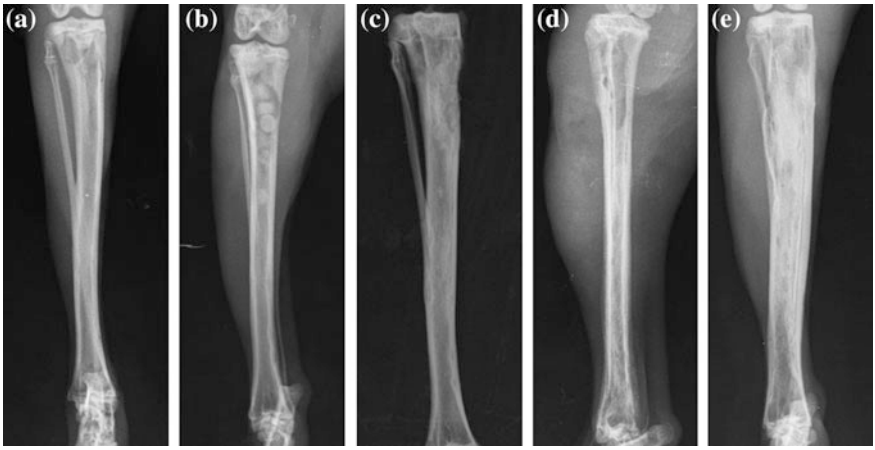

Fig. 5.13 Radiographic images showing **a** rabbit tibia with MRSA-induced osteomyelities; **b** implantation of teicoplanin-loaded borate bioactive glass (TBDC) pellets into rabbit tibia osteomyelitis model, **c** degradation of TBDC pellets in rabbit tibia 12 weeks of postimplantation, **d** tibia treated with intravenous injection of teicoplanin for 4 weeks, **e** deteriorated infection in tibia treated with intravenous teicoplanin (Zhang et al. 2010)

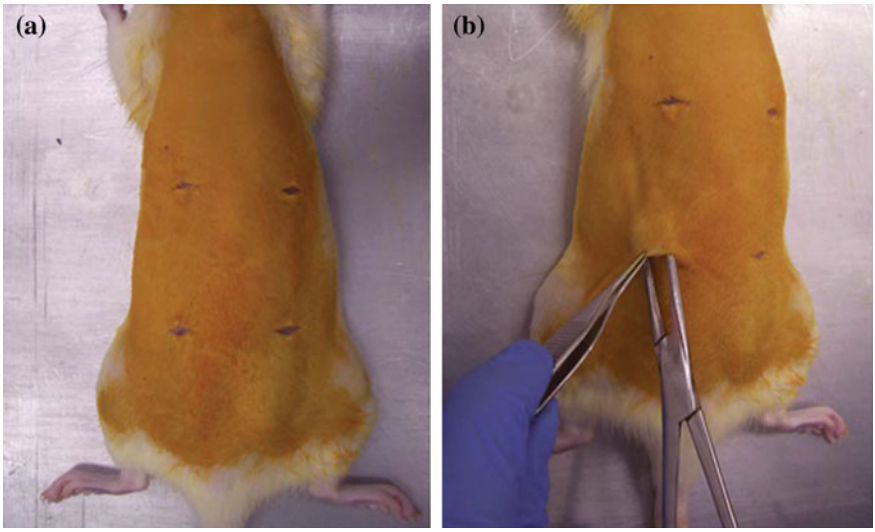

Fig. 5.14 **a** 1 cm incision on skin; **b** formation of subcutaneous pockets by blunt dissection for subcutaneous implantation (Lin et al. 2014)

also been studied by Lin and coworkers, followed by quantitative histomorphometric measurement and comparison of microvascular density control tissues and glass microfiber-implanted tissues. Male 12- to 15-week-old Sprague Dawley rats were chosen for the study. Intraperitoneal injection of ketamine (90 mg/kg) and xylazine (7 mg/kg) was given as anaesthesis followed by shaving and disinfecting the dorsal skin. Four transverse 7 mm incisions were made in the dorsum and then expanded into subcutaneous pockets by blunt dissection (Fig. 5.14a, b). Three different microfibrous samples were placed in three subcutaneous pockets and one pocket left empty to serve as a sham control.

Figure 5.15a–d shows four representative sections of tissues recovered after 4 weeks of postimplantation. The sham implant sites consisted mostly of adipose tissue with a low density of microvasculature. The sites implanted with 45S5 microfibrous glass (Fig. 5.15b) contained extensive fibrous tissue surrounding glass fibers but with a relatively low density of microvessels. The implantation sites of 13-93B3 glass microfibers (Fig. 5.15c) include moderate fibrous tissue, with almost little or no remaining glass, along with higher microvessel density than that of the sham tissue. The 13-93B3Cu glass microfibers implanted sites (Fig. 5.15d) contained heavy fibrous tissue with almost all the glass fibers dissolutions plus a moderate density of microvessels.

Hence, the borate-based 13-93B3 and 13-93B3Cu glass microfibers significantly increased the microvascular density in soft tissue.

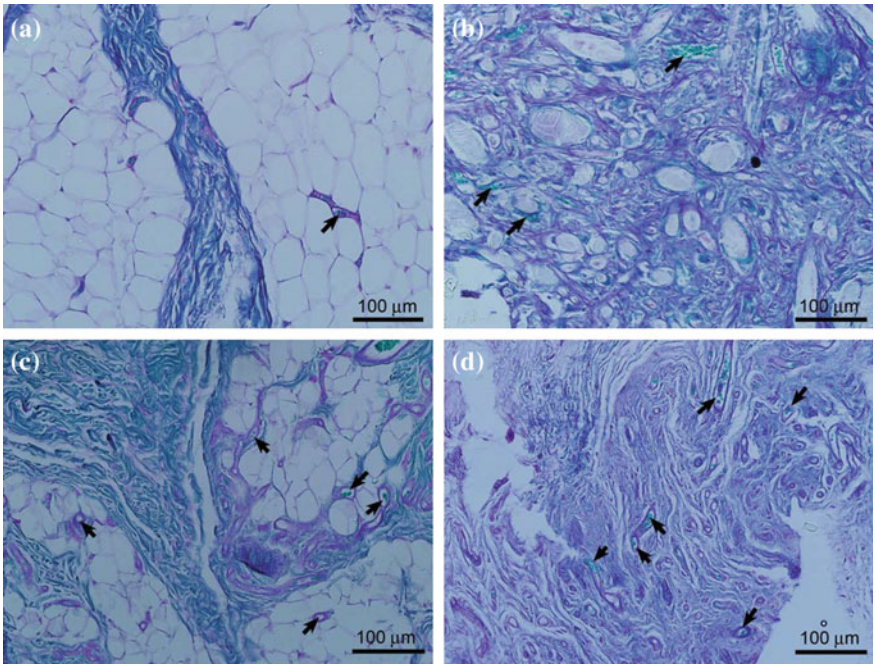

Fig. 5.15 PAS-stained sections of soft tissue recovered after 3 weeks from subcutaneous sites of implantation of **a** sham control; **b** 45S5 glass; **c** 13-93B3 glass; and **d** 13-93B3Cu glass bioactive glass microfibers. *Arrows* represent microvessels seen in the tissues (Lin et al. 2014)

5.6.3 Phosphate Glasses

Phosphate-based glasses were proposed in 1980 in which P_2O_5 acts as network former oxide. These glasses contain a phosphate [PO_4] tetrahedron structural unit, which is highly asymmetric in nature. This asymmetry is the origin of their low durability, along with the ease of P–O–P bonds hydration. Phosphate glasses have great potential as regenerative medicine because their solubility is strongly composition dependent. Hence, their dissolution rate is tailored by adding appropriate metal oxides, such as TiO_2, CuO, NiO, MnO, and Fe_2O_3 to the glass composition. Phosphate glasses have been widely investigated as controlled release vehicles of antibacterial ions such as silver, copper, zinc, and gallium along with 3-D construction of muscular tissues. Phosphate glasses can also be spun to fabricate glass fibers. This special feature of phosphate-based glasses provides the ability to be used in soft tissue engineering as guides for muscle or nerve repair. Therefore, some developments and in vivo tests have been performed on phosphate glass nerve guides, such as tubes or meshes. These tests yielded positive results and these glasses have been regarded by some as 'smart materials' for soft tissue engineering. For hard tissue engineering, the phosphate glasses are regarded as bone tissue

Table 5.3 Scaffolds prepared by mixing amorphous and crystallized contents of glasses

Scaffold code	Amorphous glass content	Crystallized glass content
A75C25	75	25
A25C75	25	75

regenerative materials in the form of bulk or powders in conjunction with polymers in composite materials. Vitale-Brovarone and coworkers manufactured phosphate glass-ceramic scaffolds using ICEL2 powders as glassy inorganic phase. GC-ICEL2 scaffolds were found to be resorbable as they underwent a process of continuous dissolution after soaking in water, Tris-HCl, and SBF. Moreover, GC-ICEL2 scaffolds were found to be bioactive because HAp layer was observed to form on their trabeculae after soaking in SBF. In addition to this, bone marrow stromal cells which were cultured on the scaffold materials exhibited regulated metabolic activity and proliferation as well as differentiation. Kim and coworkers fabricated calcium phosphate glass (CPG) scaffolds in the form of sponges, consisting of amorphous and crystallized CPG to enhance the scaffold mechanical properties as shown in Table 5.3.

Figure 5.16 shows the morphology of MG-63 cells adhered to the A25C75 disks; after 10, 60 min, and 24 h, more cell attaching has been observed for the D-AB than D-non within 10 min. After 10 min, cells adhered to D-non remained rounded in shape, whereas some cells adhered to D-AB had already spread. After 60 min, cells in D-non had spread, and surprisingly after 24 h, cell spreading for both D-non and D-AB was comparable. Hence, it can be concluded that silica- and boron-free phosphate glass scaffolds have desirable properties for the bone tissue engineering applications.

Abou Neel and coworkers studied Na_2O–CaO–SrO–P_2O_5 system and presented its physical and structural characterization as a bone regenerative material. Substitution of Na_2O with SrO from 0 to 5 mol% produced a significant increase in density, glass transition temperature, and degradation rate of these glasses. This increase in degradation rate was further supported by the levels of cations and anions released from these glasses, which in turn changes the pH of the surrounding medium. Sr^{2+} was found to be directly related to the amount of SrO in the glass and not to the degradation rate. Successful fabrication of 3-D trabecular scaffolds from phosphate glass using H_2O_2 foaming is also reported. Changing thermal treatment conditions and H_2O_2 concentration could vary the percentage of crystallinity, pore content, and size. The phosphate glass as reinforcing phase in b-TCP-based scaffolds (b-TCP/PG1) composite scaffolds exhibited superior mechanical properties (up to 6 MPa) with respect to pure b-TCP scaffolds (up to 2.3 MPa). This may be attributed to the fact that glass must have acted as a viscous binder during the sintering process, hence strengthening the final scaffold structure.

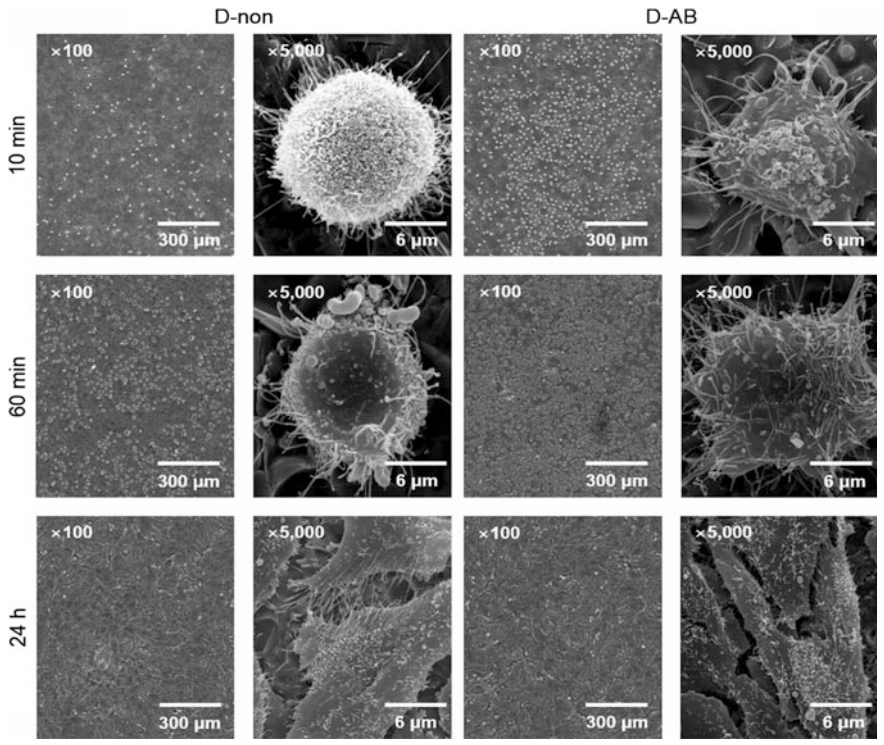

Fig. 5.16 Microstructures of MG-63 cells adhered to A25C75 disks after 10, 60 min, and 24 h (*D*-non: untreated and non-adsorbed, *D*-AB: Biotinylated and Avidin adsorbed) (Kim et al. 2015)

5.6.4 Doped Glasses

The composition of glass is modified using 'dopants' or additional additives in the glass composition to make it bioactive, bioresorbable, and/or biodegradable. The properties of bioactive glasses have been modified by doping with elements such as Cu, Zn, In, Ba, La, Y, Fe, Cr, and Sr. In addition, bioactive glass compositions doped with silver have been shown to elicit antibacterial properties while maintaining their bioactive function. In addition to SiO_2, B_2O_3, and P_2O_5, various amounts of other oxides may be incorporated into the glass composition to endow particular properties to the glass; e.g., CaO, K_2O, Na_2O, and MgO are useful to adjust the pH of surroundings, and ZnO, CuO, AgO, and TiO_2 allow the release of proper ions that can impart antibacterial properties to the material. Alumina has high bioinertness, high abrasion resistance, and high hardness, which makes it suitable material for dental and bone implants. Al_2O_3 is helpful to strengthen the mechanical properties of glasses. Zinc and magnesium are known to exert a stimulatory effect on the osteoblast proliferation, differentiation, and bone mineralization ability. Strontium incorporation of the bioactive glasses can stimulate

osteogenesis, accelerate bone-healing processes, and reduce bone resorption. The drug strontium ranelate has been reported to increase the fracture-healing ability of rat bones in terms of callus resistance. The group treated with only strontium ranelate showed a significant increase in callus resistance compared to the untreated control group. On adding dopants, the X-ray imaging contrast increases. Iron is considered useful for the cancer treatment because of its magnetic properties. Singh and coworkers doped a borosilicate glass composition with iron and found that only the samples having 10–15 % Fe_2O_3 showed the formation of an apatite layer on glass. Compositions having less than 5 % Fe_2O_3 did not yield any apatite. For treatment of cancer, Luderer also incorporated Fe_2O_3 in aluminoborosilicate glasses. Singh and coworkers also studied the effect on Al, Y, La, and Cr on the bioactive behavior of calcium borosilicate glasses. Yttria- and chromium-based glasses showed apatite formation after soaking in SBF solution. Though chromium is known to increase load resistance, at the same time yttria increases the devitrification resistance of glass. Recently, the study on barium zinc aluminoborosilicate glasses yielded that for $Al_2O_3 > 5$ %, the formation of brushite and whitlockite was apparent, though no hydroxyapatite formation could be observed on the glass surface.

Vitale-Brovarone and coworker developed the SiO_2–Na_2O–CaO–MgO (SNCM) glass system using three different organic starches (corn, potatoes, and rice) to make the scaffolds by their starch consolidation. The glass-ceramic possessed residual amorphous phase enriched with Mg^{2+} ions and $Na_2Ca_2(SiO_3)_3$ as the major crystalline phase. Excellent in vitro bioactivity was observed due to Mg^{2+}-enriched amorphous phase and good bioactivity index of $Na_2Ca_2(SiO_3)_3$. In addition to this, the scaffolds showed interesting mechanical properties as well as a certain degree of resorption. 13-93/13-93B1/13-93B2 and 6P53B compositions are doped with MgO. The sintered 6P53B glass scaffolds show a porosity (60 %) in the range of trabecular bone, whereas compressive strength of (136 $\pm$ 22 MPa) is obtained, which is comparable with human cortical bone. Titania-doped glass compositions based on the P_2O_5–CaO–Na_2O–TiO_2 system have shown controlled solubility. In addition to this, the chemical composition is close to the bone mineral phase. It further demonstrates that this glass has an advantage over polymeric scaffolds due to the fact that the glass can positively affect the material–cell interaction. According to reports by Branda and coworkers, the dopants such as La, In, and Ga decreased the bioactive behavior of glasses though indium-doped glasses exhibit higher HAp formation on their surface as compared to other glasses.

5.6.5 Metallic Glasses

The bulk metallic glasses [BMG] possess unique properties of superior strength, high elastic strain limit, high fracture toughness, and low Young's modulus. These glasses are biodegradable in vivo without hydrogen evolution. Zirconium-based metallic glasses have found applications in biomedical engineering as zirconium

has high mechanical strength and fracture toughness. Hiromoto has repassivated $Zr_{65}Cu_{17.5}Ni_{10}A_{l7.5}$ amorphous alloy in Hank's solution and found lower metal dissolution during the repassivation process. Morrison conducted cyclic polarization studies of $Zr_{41.2}Ti_{13.8}Ni_{10}Cu_{12.5}Be_{22.5}$ in phosphate-buffered saline solution and compared the corrosion resistance with conventional biomaterials such as 316L steel and Ti-6Al-4 V alloy. It was observed that BMG possesses superior properties than conventional biomaterials. Horton confirmed the biocompatibility of Zr–10Al–5Ti–17.9Cu–14.6Ni by viability of cells on the cell surface. The main drawback of BMG is the inclusion of nickel. Nickel causes an allergic response and is possibly carcinogenic. Hence, many researchers have been trying to develop Ni-free metallic glasses. Jin developed $(Zr_xCu_{100-x})_{80}(Fe_{40}Al_{60})_{20}(x = 62–81)$ glasses, which have shown remarkably good biocompatibility with the cell. Zirconium oxide formed on the surface of the bioglass presumably helps in controlling the dissolution of toxic ions. A series of MgZnCa glasses have been developed by Loffler SWISS group. These glasses exhibit high tensile strength. Huazhong group of China is also focusing on the studies of nickel free BMG glasses. Sometimes zirconium contains traces of radioelements. These effects of radioelements and its cytotoxicity were investigated using gamma rays on zirconium head, and no cytotoxicity was reported.

5.7 Hydroxyapatite Formation

Hydroxyapatite is a calcium-deficient, carbonated phosphate surface layer developed on the surface of bioactive glass when in contact with SBF through interfacial and cell-mediated reactions. This layer mimics the chemical and crystallographic characteristics of bone, which allows it to chemically bond to host bone. In fact, almost two-thirds of a bone are hydroxyapatite ($Ca_{10}(PO_4)_6(OH)_2$). Hydroxyapatite formation is highly bioactive glass composition dependent. The proposed structure for HAp is shown in Fig. 5.17 indicating its hexagonal symmetry with lattice parameters a = 9.5 and c = 6.8 Å.

For a material to be regarded as bioactive, biologically active carbonated hydroxyapatite (HCA) must form on its surface. Hydroxyapatite is the most stable phase among various calcium phosphates. It is stable in body fluid and when fired up to 1200 °C, it does not show decomposition. HAp is osteoconductive as it supports bone regeneration along the implant at the bone–implant interface. However, 45S5 bioglass is considered to be osteoconductive as well as osteoinductive as it supports the regeneration not only at the interface, but also away from the interface. In addition to bioactive glasses, hydroxyapatite and some other calcium phosphates also show an excellent ability to bond with bone, although the compositional properties of biological apatite, i.e., material to be substituted, should be evaluated. Biological apatites such as enamel, bone, and dentine exhibit a wide compositional range in their sublattices as compared to stoichiometric hydroxyapatite. First of all, the size of biological apatite crystals is smaller than 500 Å.

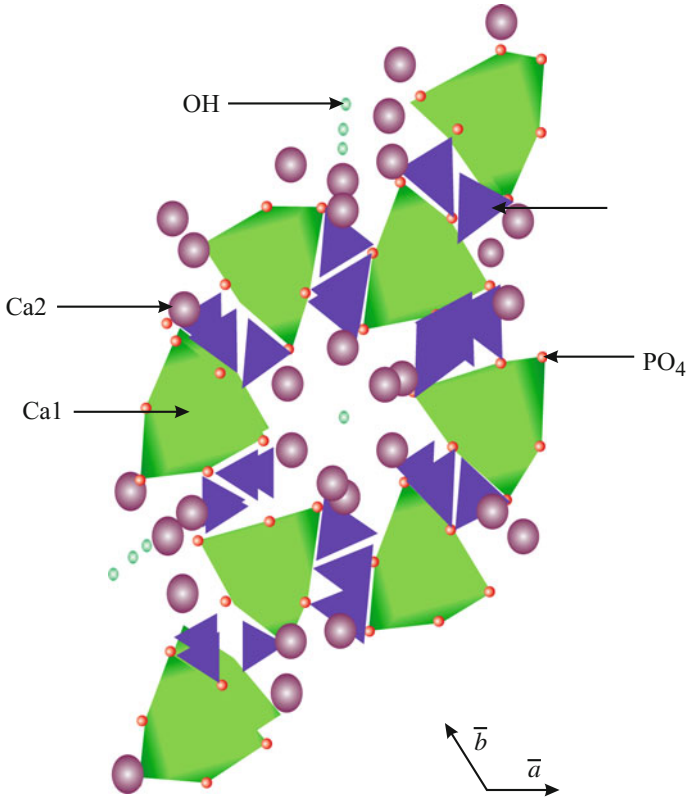

Fig. 5.17 Structure of hydroxyapatite

Biological apatites are endowed with carbonate in their structure and calcium deficiency leading to the non-stoichiometric phases. They also possess low crystallinity and large amounts of lattice defects. The presence of carbon in apatite is the cause of lattice distortion leading to crystalline defects and micro-stresses in the network. These stresses and defects play a vital role in the solubility of apatite. Hence, the synthetic apatites should exhibit small particle sizes along with the presence of CO^{3-} ions. At high temperatures, the carbonate ion occupies OH^{-} (mainly in synthetic aqueous systems) and they are known as A-type apatites, whereas in biological apatites the carbonates occupy PO_4^{3-} as a result of dissolved CO_2 in the aqueous phosphate solution and are known as B-type apatites. There is one more fundamental criterion, which is very helpful in determining the stoichiometry, acidity, and solubility of apatites, i.e., Ca/P ratio. Higher Ca/P ratio yields lower acidity and solubility and vice versa. The Ca/P ratio of the converted material generally varies from the surface of the reacted glass to the interior. Clinical investigations indicated that implanted hydroxyapatites and calcium phosphates are virtually inert and remain within the body for 6–7 years of

postimplantation. Though the degradation rates of amorphous HAp are high, it does not possess enough mechanical strength to build a 3-D porous network. Biomaterials to be implanted were previously chosen to be as inert as possible so as not to interact with the biological environment. Recently, for bone replacement, the attention has been inclined toward materials exhibiting chemical and crystallographic similarity to natural bone mineral hydroxyapatite (HAp), fluoroapatite, and other calcium phosphates in addition to their biodegradability. Calcium phosphate-based bioceramics, such as HAp, $Ca_{10}(PO_4)_6(OH)_2$, β-tricalcium phosphate (β-TCP), $Ca_3(PO_4)_2$, and biphasic calcium phosphate (BCP), and a mixture of HAp and β-TCP are inorganic materials composed of the same ions as bone and have received most attention for bone repair applications. HAp resorbs slowly and undergoes little conversion to a bone-like material after implantation, but possess a higher mechanical strength in comparison with other calcium phosphates. The use of BCP with different HAp to β-TCP ratios allows control over the degradation rate, in addition to other properties.

Bibliography

Hench LL (2006) The story of Bioglass VR. J Mater Sci Mater Med 17:967–978
Kaur G (2016) Solid oxide fuel cell components: interfacial compatibility among SOFC components, Springer
Chen Q, Liu L, Zhang SM (2010) The potential of Zr-based bulk metallic glasses as biomaterials. Front Mater Sci China 4:34–44
Qiang Fu, Rahaman MN, Fu H, Liu X (2010) Silicate, borosilicate, and borate bioactive glass scaffolds with controllable degradation rate for bone tissue engineering applications. I. Preparation and in vitro degradation. J Biomed Mater Res Part A 95:164–171
Zhang X, Jia W, Gu Y, Liu X, Wang D, Zhang C et al (2010) Teicoplanin-loaded borate bioactive glass implants for treating chronic bone infection in a rabbit tibia osteomyelitis model. Biomaterials 31:5865–5874
Lin Y, Brown RF, Jung SB, Day DE (2014) Angiogenic effects of borate glass microfibers in a rodent model. J Biomed Mater Res Part A 102:4491–4499
Brown RF, Jung SB, Day DE (2014) Angiogenic effects of borate glass microfibers in a rodent model. J Biomed Mater Res Part A 102:4491–4499
Kim M-C, Hong M-H, Lee B-H, Choi H-J, Ko Y-M Lee Y-K (2015) Ann Biomed Eng 43 (12):3004–3014
Rahaman et al (2011) Bioactive glass in tissue engineering. Acta Biomater 7:2355–2373
Kaur G et al (2014) Synthesis, cytotoxicity, and hydroxypatite formation in 27-Tris-SBF for sol–gel based CaO-P_2O_5-SiO_2-B_2O_3-ZnO bioactive glasses. Sci Rep. doi:10.1038/srep04392
Kaur G et al (2013) A review of bioactive glasses: their structure, properties, fabrication, and apatite formation. J Biomed Mater Res A 102:254–274
Davis JT (1963) Rideal EK in interfacial phenomena. Academic Press, New York
Flory PJ (1953) Principles of polymer chemistry, Cornel1 University Press. Ithaca, New York, Chapter IX
Hench LL, West JK (1990) The sol–gel process. Chem Rev 90:33–72
Hench LL, Wilson J (1993) Introduction to bioceramics. World Scientific, Singapore
West JK, Nikles R, LaTorre G In better ceramics through chemistry III, Brinker CJ, Clark DE (eds)
Ulrich DR (1998) Materials research society, vol 121. Pittsburgh, PA, p 219
Hulsenberg D, Harnisch A, Bismarck A (2008) Microstructuring of Glasses, Springer

Kaur G, Sharma P, Kumar V, Singh K (2012) Assesment of *in-vitro* bioactivity of SiO_2-BaO-ZnO-B_2O_3-Al_2O_3 glasses: an optico-analytical approach. Mater Sci Eng C 32(7): 1941–1947

Singh K, Bala I, Kumar V (2009) Structural optical and bioactive properties of calcium borosilicate glasses. Ceram Int 35:3401–3406

Regi MV (2001) Ceramics for medical applications. J Chem Soc, Dalton Trans 2:97–108

Zarzycki J Special methods of obtaining glasses and amorphous materials laboratory of science of vitreous materials. University of Montpellier, Montpellier, France

Pietrokowsky P (1963) Rev Sci Instr 34:445

Zarzycki I Naudin F (1967) Phys Chem Glasses 8:11–18

Chen HS, Miller CE (1976) Mat Res Bull 11:49–54

Topol LE, Hengsteinberg DH, Blander M, Happe RA, Richardson NL, Nelson LS (1973) J Non-Cryst Solids 12:377–390

Yao A, Wang D, Huang W, Fu Q, Rahaman MN, Day DE (2007) In vitro bioactive characteristics of borate-based glasses with controllable degradation behavior. J Am Ceram Soc 90:303–306

Huang WH, Day DE, Kittiratanapiboon K, Rahaman MN Kinetics and mechanisms of the conversion of silicate (45 S5), borate, and borosilicate glasses to hydroxyapatite in dilute phosphate solutions. J Mater Sci Mater Med 17:583–596

Liang W, Rahaman MN, Day DE, Marion NW, Riley GC, Mao JJ (2008) Bioactive borate glass scaffold for bone tissue engineering. J Non-Cryst Solids 354:1690–1696

Uysal T, Ustdal A, Sonmez MF, Ozturk F (2009) Stimulation of bone formation by dietary boron in an orthopedically expanded suture in rabbits. Angle Orthod 79:984–990

Lahl N, Singh K, Singheiser L, Hilpert K, Bahadur D (2000) Crystallisation kinetics AO- Al_2O_3-SiO_2-B_2O_3 glasses (A = Ba, Ca, Mg). J Mat Sci 35:3089–3096

Yang X, Zhang L, Chen X, Sun X, Yang G, Guo X, Yang H, Gao C, Gou Z (2012) Incorporation of B_2O_3 in CaO-SiO_2-P_2O_5 bioactive glass system for improving strength of low-temperature co-fired porous glass ceramics. J Non-Cryst Solids 358:1171–1179

Zhang X, Jia W, Gua Y, Wei X, Liu X, Wang D, Zhang C, Huang W, Rahaman MN, Day DE, Zhou N (2010) Teicoplanin-loaded borate bioactive glass implants for treating chronic bone infection in a rabbit tibia osteomyelitis model. Biomaterials 31:5865–5874

Wang XP, Li X, Ito A, Sogo Y (2011) Synthesis and characterization of hierarchically macroporous and mesoporous CaO-MO-$SiO_{(2)}$-$P_{(2)}O_{(5)}$ (M = Mg, Zn, Sr) bioactive glass scaffolds. Acta Biomater 7:3638–3644

Bellantone M, Williams HD, Hench LL (2002) Broad-spectrum bactericidal activity of Ag_2O-doped bioactive glass. Antimicrob Agents Chemother 46:1940–1945

Thamaraiselvi TV, Rajeswari S (2004) Biological evaluation of bioceramic materials—a review. Trends Biomater Artif Organs 18:9–17

Liu X, Huang W, Fu H, Yao A, Wang D, Pan H, Lu WW (2009) Bioactive borosilicate glass scaffolds: improvement on the strength of glass-based scaffolds for tissue engineering. J Mater Sci Mater Med 20:375–362

Liu X, Pan H, Fu H, Fu Q, Rahaman MN, Huang W (2010) Conversion of borate-based glass scaffold to hydroxyapatite in a dilute phosphate solution. Biomed Mater 5:15005

Liu X, Huang W, Fu H, Yao A, Wang D, Pan H, Lu WW, Jiang X, Zhang X (2009) Bioactive borosilicate glass scaffolds: In vitro degradation and bioactivity behaviours. J Mater Sci Mater Med 20:1237–1243

Vitale-Brovarone C, Miola M, Balagna C, Verne E (2008) 3D-glass-ceramic scaffolds with antibacterial properties for bone grafting. Chem Eng J 137:129–136

Marion NW, Liang W, Reilly GC, Day DE, Rahaman MN, Mao JJ (2005) Borate glass supports the in vitro osteogen differentiation of human mesenchymal stem cells. Mech Adv Mater Struct 12:239–246

Ning J, Yao A, Wang D, Huang W, Fu H, Liu X, Jiang X, Zhang X (2007) Synthesis and in vitro bioactivity of a borate-based bioglass. Mater Lett 61:5223–5226

Rahaman MN, Liang W, Day DE, Marion NW, Reilly GC, Mao JJ (2005) Preparation and bioactive characteristics of porous borate glass substrates. Ceram Eng Sci Proc 26:3–10

Marion NW, Liang W, Liang W, Reilly GC, Day DE, Rahaman MN, Mao JJ (2005) Borate glass supports the in vitro osteogenic differentiation of human mesenchymal stem cells. Mech Adv Mater Struct 12:239–246

Fu Q, Rahaman MN, Bal BS, Bonewald LF, Kuroki K, Brown RF (2010) Silicate borosilicate, and borate bioactive glass scaffolds with controllable degradation rate for bone tissue engineering applications. II. In vitro and in vivo biological evaluation. J Biomed Mater Res A 95:172–179

Abou Neel EA, Ahmed I, Blaker JJ, Bismarck A, Boccaccini AR, Lewis MP, Nazhat SN, Knowles JC (2005) Effect of iron on the surface, degradation and ion release properties of phosphate-based glass fibres. Acta Biomater 1:553–563

Bunker BC, Arnold GW, Wilder JA (1984) Phosphate glass dissolution in aqueous solutions. J Non-Cryst Solids 64:291–316

Gao H, Tan T, Wang D (2004) Dissolution mechanism and release kinetics of phosphate controlled release glasses in aqueous medium. J Control Rel 96:29–36

Abou Neel EA, Ahmed I, Pratten J, Nazhat SN, Knowles JC (2005) Characterisation of antibacterial copper releasing degradable phosphate glass fibres. Biomaterials 26:2247–2254

Ahmed I, Collins CA, Lewis MP, Olsen I, Knowles JC (2004) Processing, characterisation and biocompatibility of iron-phosphate glass fibres for tissue engineering. Biomaterials 25:3223–3232

Cai S, Xu GH, Yu XZ, Zhang WJ, Xiao ZY, Yao KD (2009) Fabrication and biological characteristics of b-tricalcium phosphate porous ceramic scaffolds reinforced with calcium phosphate glass. J Mater Sci Mater Med 20:351–358

Branda F, Arcobello-Varlese F, Costantini A, Luciani G (2002) Effect of the substitution of M_2O_3 (M = La, Y, In, Ga, Al) for CaO on the bioactivity of $2.5CaO.{}_2SiO_2$ glass. 23:711–716

Abou Neel EA, Mizoguchi T, Ito M, Bitar M, Salih V, Knowles JC (2007) In vitro bioactivity and gene expression by cells cultured on titanium dioxide doped phosphate-based glasses. Biomaterials 28:2967–2977

Vitale-Brovarone C, Verne E, Baino F, Ciapetti G, Leonardi E, Baldini N (2008) Bioresorbable phosphate scaffolds for bone regeneration. Key Eng Mater 361/363:241–244

Abou Neel EA, Knowles JC (2008) Physical and biocompatibility studiesof novel titanium dioxide doped phosphate-based glasses forbone tissue engineering applications. J Mater Sci Mater Med 19:377–386

Vitale-Brovarone C, Baino F, Bretcanu O, Verne E (2009) Foam-like scaffolds for bone tissue engineering based on a novel couple of silicate-phosphate specular glasses: synthesis and properties. J Mater Sci Mater Med 20:2197–2205

Valappil SP, Pickup DM, Carroll DL, Hope CK, Pratten J, Newport RJ, Smith ME, Wilson M, Knowles JC (2007) Effect of silver content on the structure and antibacterial activity of silver-doped phosphatebased glasses. Antimicrob Agents Chemother 51:4453–4461

Shah R, Sinanan ACM, Knowles JC, Hunt NP, Lewis MP (2005) Craniofacial muscle engineering using a 3-dimensional phosphate glass fibre construct. Biomaterials 26:1497–1505

Abou Neel EA, Chrzanowski W, Pickup DM, O'Dell LA, Mordan NJ, Newport RJ, Smith ME, Knowles JC (2009) Structure and properties of strontium-doped phosphate-based glasses. J R Soc Interf 6:435–446

Navarro M, Del Valle S, Martı´nez S, Zeppetelli S, Ambrosio L, Planell JA, Ginebra MP (2004) New macroporous calcium phosphate glass ceramic for guided bone regeneration. Biomaterials 25:4233–4241

Singh K, Bahadur D, Characterization of $SiO_2 \pm Na_2O \pm Fe_2O_3 \pm CaO \pm P2O5 \pm B2O3$ glass ceramics J Mat Sci Mat Med 10:481–484

Saboori A, Sheikhi M, Moztarzadeh F, Rabiee M, Hesaraki S, Tahriri M (2009) Sol–gel preparation, characterisation and in vitro bioactivity of Mg containing bioactive glass. Adv Appl Ceram 108:155–161

Luderer AA, Borrelli NF, Panzarina JN, Mansfield GR, Hess DM, Brown JL, Barnett EH, Hawn EW (1983) Glass-ceramic-mediated, magnetic-field-induced localized hyperthermia: response of a murine mammary carcinoma. Radiation Res 94(1):190–198

Vitale–Brovarone C, Verne E, Bosetti M, Appendino P, Cannas M (2005) Microstructural and in vitro characterization of SiO_2-Na_2O-CaO-MgO glass-ceramic bioactive scaffolds for bone substitutes. J Mat Sci Mat Med 16:909– 917

Fu Q, Saiz E, Tomsia AP (2011) Direct ink writing of highly porous and strong glass scaffolds for load-bearing bone defects repair and regeneration. Acta Biomater 7:3547–3554

Navarro M, Ginebra MP, Clement J, Martinez S, Avila G, Planell JA (2003) Physico-chemical degradation of soluble phosphate glasses stabilized with TiO_2 for medical applications. J Am Ceram Soc 86:1345–1352

Navarro M, Clement J, Ginebra MP, Martinez S, Avila G, Planell JA (2002) Improvement of the stability and mechanical properties of resorbable phosphate glasses by the addition of TiO_2. Proceedings of the 14th international symposium on ceramics in medicine. Bioceramics 14, 14–17 Palms Springs, USA, 2002, pp. 275–278

Johnson WL (1999) Bulk glass-forming metallic alloys: science and technology. MRS Bull 24 (10):42–56

Wang WH, Dong C, Shek CH (2004) Bulk metallic glasses. Mater Sci Eng R Rep 44(2–3):45–89

Kawamura Y, Shibata T, Inoue A et al (1997) Workability of the supercooled liquid in the Zr65Al10Ni10Cu15 bulk metallic glass. Acta Mater 46(1):253–263

Hiromoto S, Tsai AP, Sumita M (2000) Effect of chloride ion on the anodic polarization behavior of the Zr65Al7.5Ni10Cu7.5 amorphous alloy in phosphate buffered solution. Corros Sci 42 (9):1651–1660

Hiromoto S, Tsai AP, Sumita M (2000) Effect of pH on the polarization behavior of Zr65Al7.5Ni10Cu17.5 amorphous alloy in a phosphate-buffered solution. Corros Sci 42 (9):2193–2200

Hiromoto S, Tsai AP, Sumita M (2000) Effects of surface finishing and dissolved oxygen on the polarization behavior of Zr65Al7.5Ni10Cu17.5 amorphous alloy in phosphate buffered solution. Corros Sci 42(12):2167–2185

Hiromoto S, Hanawa T (2002) Re-passivation current of amorphous Zr65Al7.5Ni10Cu17.5 alloy in a Hanks' balanced solution. Electrochimica Acta 47(9):1343–1349

Morrison ML, Buchanan RA, Peker A (2004) Cyclic-anodicpolarization studies of a Zr41.2Ti13.8Ni10Cu12.5Be22.5 bulk metallic glass. Intermetallics 12(10–11):1177–1181

Morrison M L, Buchanan R A, Leon RV (2005) The electrochemical evaluation of a Zr-based bulk metallic glass in a phosphate-buffered saline electrolyte. J Biomed Mater Res Part A 74 (3):430–438

Horton JA, Parsell DE (2003) Biomedical potential of a zirconium-based bulk metallic glass. Mater Res Soc Symp Proc 754:CC1.5.1

Jin KF, Löffler JF (2005) Bulk metallic glass formation in Zr-Cu-Fe-Al alloys. Appl Phys Lett 86 (24):241909

Zberg B, Arata ER, Uggowiter PJ (2009) Tensile properties of glassy MgZnCa wires and reliability analysis using Weibull statistics. Acta Mater 57(11):3223–3231

Zberg B, Uggowiter PJ, Löffler JF (2009) MgZnCa glasses without clinically observable hydrogen evolution for biodegradable implants. Nat Mater 8(11):887–891

Maruyama N, Hiromoto S, Ohnuma M (2005) Fretting fatigue properties of Zr-based bulk amorphous alloy in phosphate buffered saline solution. J Japan Inst Metals 69(6):481–487

Liu L, Yu Y, Chan KC (2009) Bio-activation of Ni-free Zr-based bulk metallic glass by surface modification. Intermetallics 18:1978–1982

Day RM, Maquet V, Boccaccini AR, Jerome R, Forbes A (2005) In vitro and in vivo analysis of macroporous biodegradable poly(D, L-lactide-co-glycolide) scaffolds containing bioactive glass. J Biomed Mater Res A 75:778–787

Seeley Z, Bandyopadhay A, Bose S (2007) Influence of TiO_2 and Ag_2O addition on tricalcium phosphate ceramics. J Biomed Mater Res A 82:113–121

Novak S, Druce J, Chen QZ, Boccaccini AR (2009) TiO_2 foams with poly-(D,L-lactic acid) (PDLLA) and PDLLA/Bioglass® coatings for bone tissue engineering scaffolds. J Mater Sci 44:1442–1448

Jones JR, Ehrenfried LM, Hench LL (2007) Optimising bioactive glass scaffolds for bone tissue engineering. Biomaterials 27:964–973

Hollinger JO, Brekke J, Groskin E, Lee D (1999) Role of bone substitutes. Clin Ortho Rel Res 324:55–65

Fukasawa T, Ando M, Ohji T, Kanzaki S (2001) Synthesis of porous ceramics with complex pore structure by freeze drying processing. J Am Cer Soc 84:230–232

Deville S, Saiz E, Tomsia A (2006) Freeze coating of hydroxyapatite scaffolds for bone tissue engineering. Biomaterials 27:5480–5489

Kaur G, Pickrell G, Sriranganathan N, Kumar V, Homa D (2016) Review and the state of the art: sol–gel or melt quenched bioactive glasses fosr tissue engineering. J Biomed Mater Res Part B Appl Biomater 104(6):1248–1275. doi:10.1002/jbm.b.33443

Kaur G, Pickrell G, Pandey OP, Singh K, Chudasama BN, Kumar V (2016) Combined and individual Doxorubicin/Vancomycin drug loading, release kinetics and apatite formation for the CaO-CuO-P_2O_5- SiO_2- B_2O_3 mesoporous glasses. RSC Adv 6:51046–51056

Kaur G, Pickrell G, Kimsawatde G, Allbee H, Sriranganathan N (2014) Synthesis, cytotoxicity, and hydroxypatite formation in 27-Tris-SBF for sol–gel based CaO-P_2O_5-SiO_2-B_2O_3-ZnO bioactive glasses. Sci Rep. doi:10.1038/srep04392

Chapter 6
Apatites: A Mark of Bioactivity

Gurbinder Kaur

Bioceramics are employed to perform biologically inert roles since 1970, and especially hydroxyapatite has been the most extensively investigated bioceramics due to its excellent interaction with the host tissues. The lattice structure of apatites is quite similar to the bones and therefore regarded as a tool for improving bone regeneration and tissue biocompatibility. This chapter would review the apatites, their nature, composition, and deposition mechanism.

6.1 What Are Apatites?

In 1788, Werren described 'apatite' as the group of minerals with various color tints such as green, pink, and yellow, and the apatites were mistaken for the precious gemstones and colored minerals (amethyst, topa2, aquamarine, etc.). The chemical formula of these apatite mineral is $M_{10}(PO_4)_6X_2$, where M is usually metal like calcium and X is halogen, hydroxide, etc. The apatites have family of compounds with hexagonal system and space group P63/m. More precisely, the apatites constitute a group or family in super group with formula $M1_2M2_3(XO_4)_3Z$, where PO_4 predominantly occupies XO_4 sites, larger divalent or trivalent cations that occupy M1 and M2 positions. Calcium apatites have hydroxyl groups as Z and are widely investigated due to their resemblance with the bone mineral. CO_3^{2-}/HCO_3^{-} can occupy for the XO_4 and Z-sites, whereas hydrogen phosphate ion HPO_4^{3-} can occupy b site or replace XO_4 (Z-sites are a-sites and XO_4 sites are b-sites). Apatites can be natural or synthetic depending upon their mode of occurrence. Biologic apatites are usually inorganic phases of calcified tissues such as teeth and bones. As carbonate is associated with biological apatites, they are speculated to be similar like mineral dahllite (carbonate-containing apatite) or staffellite (carbonate- and fluoride-containing apatite). X-ray diffracting infrared spectroscopy and chemical

G. Kaur, *Bioactive Glasses*, Series in BioEngineering,
DOI 10.1007/978-3-319-45716-1_6

analysis techniques yielded carbonate apatites by the chemical formula (Ca, Mg, Na)$_{10}$ (PO_4, CO_3, HPO_4)$_6$ (CO_3, OH)$_2$. Bone, dentin and enamel apatite contain organic phase is primarily collagen for the bone, dentin, with small quantity of non-collagenous proteins. In contrast to this, the enamel consists of amelogenin, the main inorganic non-collagenous protein carbonate hydroxyapatite (CHA) or fluoride-containing apatite (CFA) are principal inorganic phases for normal calcified tissue (bones and teeth). The chemical composition of inorganic part of dental enamel is proposed to be $Ca_{8.856}Mg_{0.088}Na_{0.292}K_{0.010}(PO_4)_{5.312}(HPO_4)_{0.280}(CO_3)_{0.407}Cl_{0.078}(CO_3)_{0.050}$.

The biological apatites may occur as the mineral phases in pathologic calcifications, such as urinary stones, vascular calcification, and dental calculus. Some common examples include octacalcium phosphate (OCP, $Ca_8H_2(PO_4)_6{\cdot}5H_2O$), dicalcium phosphate dehydrate (DCPD, $CaHPO_4{\cdot}2H_2O$), amorphous calcium phosphate (ACP, $Ca_x(PO_4)_y$), calcium pyrophosphate dehydrate (CPPD, $Ca_2P_2O_7{\cdot}2H_2O$), and magnesium substituted tricalcium phosphate (β-TCP, (Ca, Mg)$_3$ (PO_4)$_2$).

6.2 Bone, Enamel, and Dentin Apatites

Dental hard tissue consists of enamel, dentin, and cementum. Dentin is the bulk dental hard tissue covering soft tissue (dental pulp) within the core of the tooth. Enamel and cementum are the outer layers that cover the dentin area in the crown area and root area, respectively. Enamel is a naturally beautiful masterpiece, which has inspired the development of tooth-colored restorative material due to its strength durability and aesthetic sense. Dentin materials are excellent biocomposite materials with excellent durability and mechanical properties.

Calcium phosphate tissues are the main building blocks for alveolar bone, dental hard tissues and exist in gingival crevicular fluid precipitations and saliva for the entire lifetime. The difference between enamel, bone and dentin apatite is due to the difference in crystallinity, concentrations of minor constituents and crystal size as shown in Table 6.1.

Dentine and bone apatites have shown minimum crystallinity as compared to the enamel. In addition to this, the solubility of these apatites differs as enamel ≪ dentin ≪ bone, and this difference in solubility is attributed to the concentration of minor constituents such as Mg, CO_3, and HPO_4. Hydroxyapatites, known as bone mineral, have Ca/P = 1.67 stoichiometric value and the biological apatites are usually calcium deficient, i.e., Ca/P < 1.67. With course of the time, the dissolution of tooth mineral occurs due to acids produced by oral bacteria and hence the precipitation of biological apatites occurs in human enamel and dental caries. For the oral and dental therapeutics, calcium phosphate-based restorative dental materials, periodontal regeneration biomaterials, enamel remineralization systems, and dental implant coatings have gained considerable popularity over recent decades.

Table 6.1 Composition (%) of human enamel, bone and dentin apatites

Ions	Bone	Enamel	Dentin
Calcium Ca^{2+}	34.8	36.5	35.1
Phosphorous P	15.6	17.7	16.2
Ca/P (molar)	1.71	1.63	1.63
Mg^{2+}	0.72	0.34	1.23
Na+	0.9	0.5	0.6
Chlorine, Cl^-	0.13	0.30	0.01
Fluorine, F^-	0.03	0.01	0.06
Carbonate, CO_3^2	7.4	3.5	5.6
Potassium, K^+	0.03	0.06	0.05
Pyrophosphate	0.07	0.02	0.10
Inorganic	65	97	70
Organic	25	1.5	20
Absorbed H_2O	10	1.5	10

6.2.1 Structure of Dental Hard Tissues

Dental hard tissues form a highly complex but organized structure, which can withstand mastication-induced mechanical loading, thus avoiding any mechanical failure. Cementum covers dentin in root area and anchors periodontal ligament fibers, which provide support for the dental movements. Dentin biocomposite is a highly rigid and durable biological structure comprising of complex protein assemblies and organized mineral components. The osteoblasts differentiate from ectomesenchymal cells of dental papilla and lead to the formation of dentin. This process is known as dentinogenesis. During dentinogenesis, the cytodifferentiation of the odontoblasts followed by mantle dentin formation and control of mineralization of primary dentin organic matrix occurs. The final step of dentinogenesis includes secretion of secondary and tertiary dentin. Primary dentin includes the mental and circumpulpal components, whereas secondary dentin is a layer, which gets secreted after the root formation. Once the tooth is fully formed, tertiary dentin is secreted in response to stimulus of caries or wear. Figure 6.1a, b gives the structure of the dentin. Dentin composes of packed dentinal tubules (1–2 μm diameter) surrounded by hypermineralized peritubular dentin layer.

Cytoplasmic extensions of odontoblasts lie in the dentinal tubules and these extensions are involved in secretion of dentin matrix. Dentinal tubules also carry protein and proteoglycans-rich dentinal fluid. Intertubular dentin composes of supramolecular aggregates of collagen molecules, which are assembled into type I fibrils interconnected via water and non-collagenous component. Hence, a hydrated organic network is formed, which acts as an excellent matrix for apatite crystal formation. However, the peritubular dentin contains phosphorylated proteins, proteoglycans, and glycosaminoglycans lacking collagen fibrils. Dentin has permeable structure as compared to the enamel. The composition of dentin is 50 vol% carbonated hydroxyapatite, 30 vol% of collagenous/non-collagenous proteins, and rest

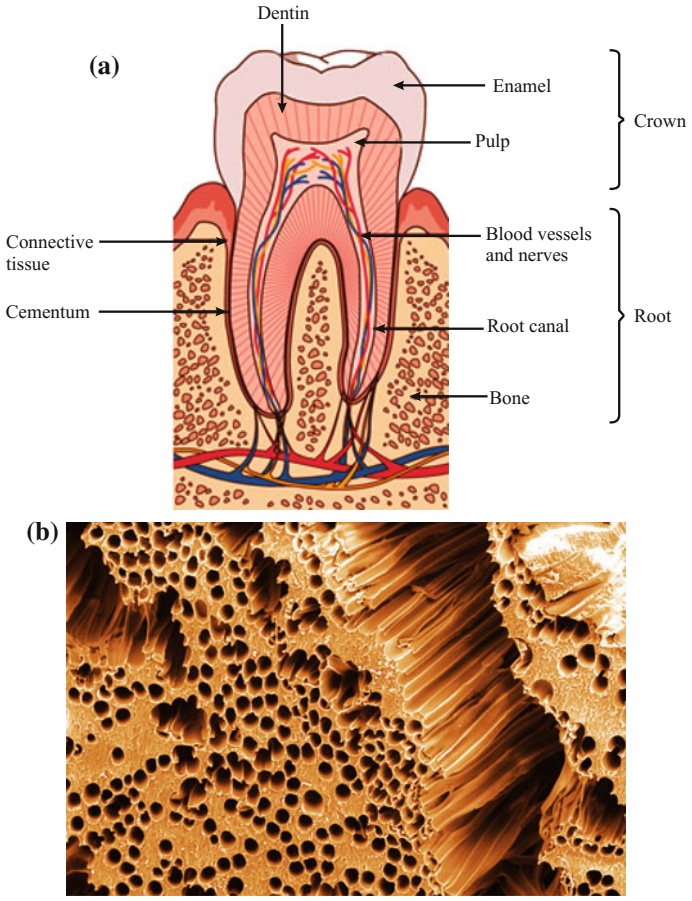

Fig. 6.1 **a** Human tooth anatomy and **b** microstructure of dentin structure (Haeri et al. 2014)

is fluids. Collagen type I constitutes almost 90 wt% of the organic dentin phase. Other proteins involved in mineral-matrix binding events contain γ-carboxyglutamate and phosphoproteins. Among the proteoglycans (PG), biglycan and decorin are the leucine-rich members, which are predominantly expressed in dentin.

Cementum is a vascular connective tissue comprising of 23 wt% organic matrix, 12 wt% water, and 65 wt% hydroxyapatite minerals, and hence cementum possesses similarity with bone. 90 % of the organic matrix of cementum comprises of collagen type I fibrils. The process of formation of cementum is secreted by cementoblasts and once the tooth development completes, the roots of the tooth are highly covered by cementum. Usually, cementum belongs to two categories, i.e., acellular and cellular cementum. The acellular cementum is unorganized and covers

cervical protein of the root, whereas cellular cementum consists of organized lacunar structure as that of bone and covers the 1/3rd of the root.

Dental enamel consists of ~96 wt% inorganic materials (especially carbonated hydroxyapatite) and is the highly mineralized tissue of the human body. Enamel lacks the ability to regenerate itself and possesses acellular/avascular structure. The process of enamel formation is amelogenesis which includes three stages, i.e., cytodifferentiation, matrix secretion, and maturation. Ameloblasts (enamel-forming cells) secrete organic matrix into the extracellular space adjacent to dentinoenamel junction (DEJ). Enamel matrix proteins are non-collagenous in nature consisting of tuftelin, enamelin, and ameloblastin. Proteases break down the protein-rich enamel matrix, which gets replaced by mineral deposition on the preexisting apatite crystals. Once the maturation occurs, the ameloblasts disappear completely, thereby prohibiting the enamel deposition or repair. After the maturation, a highly mineralized hard tissue is formed, known as hydroxyapatite [$Ca_{10}(PO_4)(OH)_2$], containing CO_3^{2-}, Cl^-, Na^+, Mg^{2+}, K^+, and F^- as trace constituents. When bundles of dozens of enamel rods are combined, then Hunter-Schreger bands are formed, which are approximately 50 μm wide and also visible due to different directions reflected or transmitted by light.

6.2.2 Mechanical Properties of Enamel, Dentin, and Cementum

The mechanical properties are very well obtained from the nanoindentation techniques as it is a nondestructive method at the submicroscopic level. In the nanoindentation experiments, the elastic modulus/Young's modulus (E) is given by:

$$E = \left(\frac{1 - \mu_s^2}{E_s} + \frac{1 - \mu_i^2}{E_i} \right)^{-1} \tag{6.1}$$

where E_s and E_i are the elastic modulus of sample and indentor, respectively, μ_s and μ_i are Poisson's ratio of sample and indentor, respectively. The hardness of enamel/dentin can be estimated as:

$$H = \frac{P_{\max}}{A} \tag{6.2}$$

Hardness is the resistance of the material to permanent deformation under the indentation. The nanoindentation hardness is the ratio of contact presence of the indenter and the contact area (A) of the sample. The hardness for the enamel is reported in the range of 3.4 ± 0.15–5.2 ± 0.5 GPa and elastic modulus is given in the range of 83.4 ± 7.1–105.2 ± 1.3 GPa. The hardness and elastic modulus of enamel are highly dependent on the site of indentation. The enamel is less

mineralized at the dental enamel function and more mineralized at the surface. The indenter tip and applied load are deciding factors for the determination of elastic moduli.

The hardness and elastic modulus values are higher at the top surface of enamel as compared with the non-sectional lateral surface. When the force is applied perpendicular to the enamel rods, then lower values of E and μ are obtained due to presence of less stiff organic sheath. The hardness of dentin is obtained in between 0.15 ± 0.03 GPa for the intertubular area of inner dentin, whereas for the peritubular dentin, it is 2.45 ± 0.14 GPa. The elastic modulus for dentin lies in the range of 11.59 ± 3.95–29.8 ± 9 GPa. Primary dentin has lower mechanical strength as compared to the permanent dentin attributed to the higher mineral content in permanent tooth dentin. The dentin close to dentinoenamel junction has higher hardness and elastic modulus as compared to the inner dentin due to higher thickness of peritubular dentin in outer dentin as compared to lower density of dentinal tubules. Similarly like enamel, the mechanical response of dentin is lower, when the applied load is perpendicular to tubules compared to when load is parallel with dentinal tubules. The mechanical properties of dentin are highly dependent on hydration and dehydration of dentin tissues because dentin contains almost 20 % water. Figure 6.2 indicates the hardness and elastic modulus for the dry and wet dentin. Dry dentin has higher hardness value than the wet dentin samples. Moreover, when the samples are held for a holding time, then the hardness and elastic modulus values are enhanced both for dry and wet dentin.

Cementum is a living tissue present in the root of tooth. Cementum may undergo remodeling, which is similar to the basic tissue and is distinctive feature among

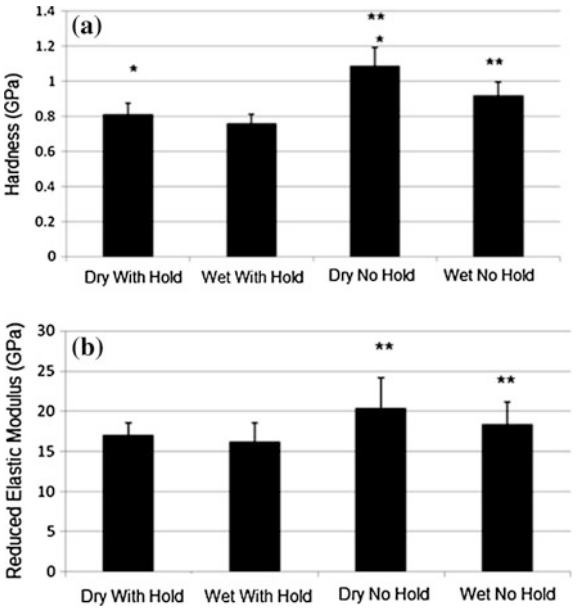

Fig. 6.2 **a** Hardness and **b** elastic modulus of dry and wet dentin (Nissan 2014)

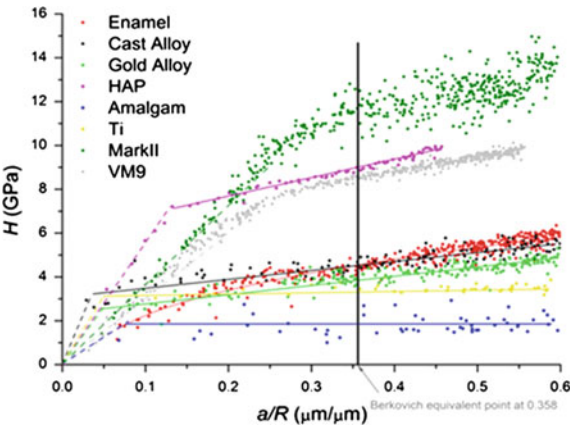

Fig. 6.3 Stress–strain for various materials (He 2008)

dental hard tissues. The enamel and dentin undergo compressive forces, whereas cementum has majority of tensile forces. To quantify the mechanical properties of cementum, nanoindentation techniques are used. The elastic modulus of cementum is reported from 2.4 to 20.8 GPa for the apical portion to polished transversal sections. The hardness value lies between 0.25 ± 0.1 and 0.65 ± 0.06 GPa. Due to the higher content of collagenous proteins at the cementum–dentin junction, the cementum has lower elastic modulus and hardness values. The stress–strain relationship for dental material is shown in Fig. 6.3.

For the pure hydroxyapatite, the prominent elastic–plastic transition point is observed, whereas the enamel yields smooth curve. The response of enamel is different from hydroxyapatite indicating the presence of organic components in enamel making it a viscoelastic material. Enamel strain relationship is more resembling to the metals than the apatites/ceramics. Hence, the presence and role of organic components in the dentin and enamel provide excellent clue for the design of biomaterials with improved structure and mechanical properties. For the biological applications, especially orthodontic therapy and periodontal diseases, the mechanical aspect shall be carefully chosen.

6.3 Calcium Orthophosphates/Bone Cements in Bone Regeneration

Apatites can be prepared via sol-gel techniques, electrodeposition, biometric precipitation, solid-state reaction, precipitation, or hydrolysis method. During preparation of apatites, if the pH is kept between 5 and 9, then calcium deficient apatites are formed. Above 1200 °C sintering temperature of HAp, thermal decomposition occurs resulting in β-tricalcium phosphate (β-TCP), α-TCP and amorphous calcium

Table 6.2 Composition and properties of CaP

Name and abbreviations	Chemical formula	Ca/P ratio	Solubility at 25 °C	pH stability range
Tetracalcium phosphate (TTCP/hilgenstockite)	$Ca_4(PO_4)_2O$	2	~0.0007	
Hydroxyapatite (HAp)	$Ca_{10}(PO_4)_6(CH)_2$	1.67	~0.0003	9.5–12
Oxyapatite (OXA/OAp)	$Ca_{10}(PO_4)_6O$	1.67	~0.087	
Fluorapatite (FAp)	$Ca_{10}(PO_4)_6F_2$	1.67	~0.0002	7–12
Calcium deficient hydroxyapatite (CDHAp)	$Ca_{10-x}(HPO_4)_x(PO_4)_{6-x}(OH)_{2-x}$ $(0 < x < 1)$	1.5–1.67	~0.0094	6.5–9.5
Amorphous calcium phosphate (ACP)	$Ca_xH_y(PO_4)_2{\cdot}nH_2O$ $n = 3–4.5$	1.2–2.2		5.12
α-Tricalcium phosphate (α-TCP)	$\alpha–Ca_3(PO_4)_2$	1.5	~0.0025	
β-Tricalcium phosphate (β-TCP) (Brushite)	$\beta–Ca_3(PO_4)_2$	1.5	~0.0005	
Octacalcium phosphate (OCP)	$Ca_8(HPO_4)_2(PO_4)_4{\cdot}5H_2O$	1.33	~0.0081	5.5–7.0
Dicalcium phosphate anhydrous (DCPA)	$CaHPO_4$	1	~0.048	
Dicalcium phosphate dihydrate (DCPD)	$CaHPO_4{\cdot}2H_2O$	1	~0.088	2–6
Monocalcium phosphate anhydrous (MCPA)	$Ca(H_2PO_4)_2$	0.5	~17	
Monocalcium phosphate monohydrate (MCPM)	$Ca(H_2PO_4)_2{\cdot}H_2O$	0.5	~18	0–0.2

phosphate (ACP). In 1920, Albee used apatites as scaffolds for bone and tooth regeneration.

Bone has the ability to regenerate itself, but in certain cases, such as tumor and aging effects, the ability of the bone to regenerate gets diminished. Three types of bone grafts are used for replacing bones, i.e., autogenous bone grafts are used for bone replacement and bone is harvested from the iliac crest or other sites, allogenic bone grafts are obtained from tissue banks, and alloplastic bone substitutes are used to fill bone cavities, hence sewing as scaffold material for the bone regeneration. Synthetic bone graft materials such as bioactive glasses, calcium phosphate [tricalcium phosphate (TCP), biphasic calcium phosphate (BCP), and hydroxyapatite (HAp)] have been extensively used for the autogenous bone repair. Many research groups are actively engaged in studying CaP, especially their different compositions, processing manufacturing biological properties along with their applications. Table 6.2 lists the various CaP and their compositions.

Several injectable CaP hydraulic cements have been developed, which strengthen the bone defects. The composites of bioceramics and fibrin sealants are interesting

candidates for the bone repairs [TricOs® + fibrin gel]. By adding bioactive factors, such as fibrin glasses, the performance of bioceramics can be increased because the fibrin glue enhances the stability of granules at implantation site and hence endows bioceramics with excellent osteogenic property. Macroporous biphasic calcium phosphate (MBCP) TricOs® contains HAp/β-TCP in 60:40 ratio. MBCP gel is a non-self-hardening injectable bioceramics composed of BCP granules associated with a hydrosoluble polymer. MBCP gel (In'Oss™) exhibits plasticity and hence can be molded into desired shape with high biocompatibility and solubility. Calcium phosphate cements (CPS) are self-setting injectable cements used due to minimal invasive surgery (MIS). In 1982, LeGeros and coworkers introduced the concept of CaP bone cements. CaP cements exhibit good mechanical properties but these materials lack macroporosity and hence do not provide rapid bone substitution. The calcium cements are apatite cement (AC), apatite-forming cement, brushite cement, and brushite-forming cement. It is reported that α-TCP sets to form calcium deficient hydroxyapatite (Ca: HAp: $Ca_9(HPO_4)(PO_4)_5)OH$) with Ca/P ≈ 1.5 upon hydration of α-TCP in water at 60–100 °C and pH ≈ 8.1–11.4. In 1986, Brown and coworkers worked on composite of TTCP ($Ca_4(PO_4)$) and DCPA ($CaHPO_4$)/DCPD ($CaHPO_4{\cdot}2H_2O$), which gets set in 30–60 min upon mixing with aqueous solution. In 1987, Lemaitre and coworkers invented brushite cement, which is also known as DCPD cement. The setting reaction of apatite cement includes dissolution precipitation and entanglement of precipitated apatite crystals. α-TCP have higher solubility in water and when it is mixed with water, it dissolves and supplies Ca^{2+} and PO_4^{3-} into water as given below:

$$3Ca_3(PO_4)_2 \rightarrow 9Ca^2 + 6PO_4^{3-} \tag{6.3}$$

The solution is also in state of equilibrium with other calcium deficient hydroxyapatite with lower solubility as compared to α-TCP. Hence, the solution is supersaturated with respect to the calcium deficient hydroxyapatite, which causes the precipitation of calcium deficient hydroxyl apatite crystals as:

$$9Ca^{2+} + 6PO_4^{3-} + H_2O \rightarrow Ca_9(HPO_4)(PO_4)_5(OH) \tag{6.4}$$

Due to the precipitation of calcium deficient hydroxyapatite, the solution gets undersaturated causing dissolution of α-TCP in solution. The chain of these reactions would continue, causing the entanglement of calcium deficient hydroxyapatite crystals, and the overall reaction is given by:

$$3Ca_3(PO_4)_2 + H_2O \rightarrow Ca_9(HPO_4)(PO_4)_5(OH) \tag{6.5}$$

The setting of brushite also follows similar set of reactions, but with a difference of final products. Brushite is stable at pH of 2–4.2; hence, the brushite cement shall

contain calcium and phosphate and form cement paste at pH 2.0–4.2. The best example of brushite cement is the mixture of β-TCP and monocalcium phosphate monohydrate. The solubility of monocalcium phosphate monohydrate is higher and its dissolution causes formation of acidic solution as given below:

$$Ca(H_2PO_4)_2 \cdot H_2O \rightarrow Ca^{2+} + 2HPO_4^{2-} + 2H^+ + H_2O \tag{6.6}$$

The acidic solution tends to cause dissolution of β-TCP and the solution gets supersaturated with respect to brushite. This causes the precipitation of brushite crystals:

$$Ca_3(PO_4)_2 \rightarrow \underset{\text{(Supersaturated solution)}}{3Ca^{2+} + 2PO_4^{3-}} \tag{6.7}$$

$$4Ca^{2+} + 2PO_4^{3-} + 2HPO_4^{2-} + 2H^+ + 8H_2O \rightarrow 4CaHPO_4 \cdot 2H_2O \tag{6.8}$$

Overall Reaction:

$$Ca(H_2PO_4)_2 \cdot H_2O + Ca_3(PO_4)_2 + 7H_2O \rightarrow 4CaHPO_4 \cdot 2H_2O \tag{6.9}$$

The brushite cements are resorbed at a much faster rate as compared to the apatite cements because apatite is thermodynamically stable phase at physiological condition, whereas the body fluid is supersaturated w.r.t. apatite. The apatite cement gets replaced with bone where resorption of apatite crystals occurs by osteoclasts. Osteoclasts induces Howship's lacuna with acidic conditions and then apatite gets dissolved. If the apatite contains carbonate, then the fast replacement of bone occurs as compared to the carbonate free apatite. Brushite is metastable phase at physiological pH and gets dissolved when exposed to body fluid, i.e.,

$$CaHPO_4 \cdot 2H_2O \rightarrow Ca^{2+} + HPO_4^{2-} + 2H_2O \tag{6.10}$$

If the body fluid circulation is limited, then Ca^{2+} and HPO_4^{2-} dissolved from brushite gets precipitated as apatite/carbonate apatite:

$$10Ca^{2+} + 6HPO_4^{2-} + 2H_2O \rightarrow Ca_{10}(PO_4)_6(OH)_2 + 8H^+ \tag{6.11}$$

$$10Ca^{2+} + 4HPO_4^{2-} + 3CO_3^{2-} + 2H_2O \rightarrow Ca_{10}(PO_4)_4(CO_3)_3(OH)_2 + 6H^+ \tag{6.12}$$

The precipitated hydroxyapatite/carbonate apatites are excellent for the osteoconductivity. Table 6.3 lists some of the commercially available apatite and brushite cements.

Table 6.3 Commercially available brushite and apatite cements

Name	Composition	Type of cements
Calcios	MCPM (0.78 g) + $CaSO_4 \cdot H_2O$	Brushite
	Liquid: 0.05 mol/L H_3PO_4	
Vitalos	B-TCP (1.34 g) + $Na_2H_2P_2O_7$(0.025 g)	Brushite
	Liquid: 0.05 H_3PO_4mol/L	
	pH ≈ 7.4 PBS	
Calcibon®	Powder: α-TCP (61 %) + DCPA (26 %) + $CaCO_3$ (10 %) + HAp(3 %)	Apatite
	Liquid: disodium phosphate solution	
Biopex®	α-TCP + TTCP + DCPD + HAp + $Mg_3(PO_4)_2$	Apatite
	Liquid: succinic acid, chondroitin sulfate	
Eurobone®	98 % β-TCP + 2 % $Na_4P_2O_7$	Brushite
	Liquid: 3 mol/L H_3PO_4 + 0.1 mol/L H_2SO_4	
Rebone	TTCP + DCPA	Apatite
	Liquid: water	
Pimafix®	TTCP + DCPD	Apatite
	Liquid: sodium dextran sulfate sulfur 5	
Norian SRS®	85 % α-TCP + 12 % $CaCO_3$ + 3 % MCPM	Apatite
	Liquid: disodium phosphate solution	
Cerapaste®	TTCP + DCPA	Apatite
	Liquid: sodium dextran sulfate sulfur 5	
Nimix™	TTCP + α-TCP + $C_6H_5O_7Na_3 \cdot 2H_2O$	Apatite
	Liquid: citric acid	
Bioben®	50 % ACP + 50 %DCPD	Apatite
	Liquid: saline	
Cementek®	TTCP + α-TCP + $Ca(OH)_2$ + sodium glycerophosphate	Apatite
	Liquid: acidic calcium phosphate	
Chron OS™ inject	73 % β-TCP + 21 % MCPM + 5 % $MgHPO_4 \cdot 3H_2O$ + <1 % $MgSO_4$ + <1 % $Na_2H_2P_2O_7$	Brushite
	Liquid: 0.5 % sodium hyaluronate	

6.4 Fundamental Properties of CaP Apatites

There are many criteria, where CaP materials shall fulfill in order to be considered for their biological and medical application. Figure 6.4 lists the fundamental physiochemical and biologic properties of the apatites. CaP bioceramics are associated with the resorption, dissolution, and absorption process. When the pore size is increased, the increase in surface area enhances the dissolution rate and the lattice defects also contribute to the dissolution. Unlike other biomaterials, Ca and PO_4 ions are absorbed during the process of bone regeneration instead of their degradation and elimination out of the body.

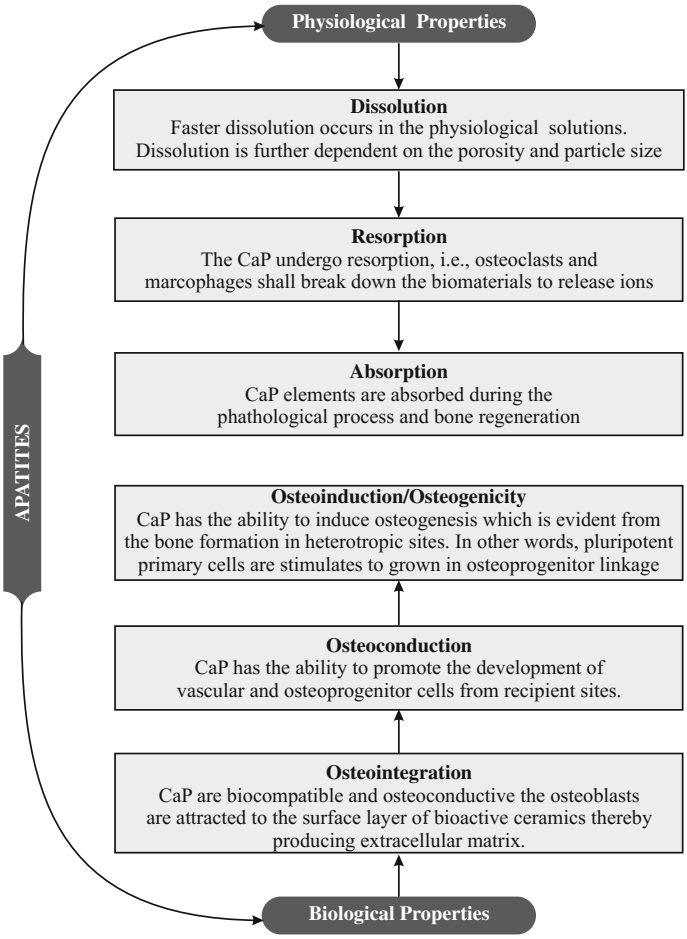

Fig. 6.4 The physiochemical and biological properties of apatites

CaP exhibits bone-bonding capability known as osseocoalescence (bonding between CaP bioceramics and bony crystals). CaP promotes osteoconduction, i.e., the surface allows bone ingrowth into the pore channels and on its surface. CaP also exhibits osteoinduction, which is the induction of undifferentiated inducible osteoprogenitor cells that are not yet committed to the osteogenic lineage to form osteoprogeniter cells.

6.5 Hydroxyapatite as an Intelligent Ceramic

In the clinical histories and scientific discoveries, hydroxyapatite is the most successful apatite due to its excellent responses toward the physiochemical environment and biocompatibility. The biomaterial industry has been growing day by day

and alone in the USA, and the organ replacement technology exceeds 1 % of the gross national product. Metallic biomaterial has been one of the most reliable products due to their excellent mechanical properties and load-bearing applications. Anyhow, due to the corrosion and release of ions may pore problem and the lower biological response may be obtained. Hence, for providing excellent biocompatibility and enhanced healing process, the surface of material is coated with the biocompatible hydroxyapatite as it forms a strong interfacial bond between implant bone, thereby promoting prosthesis fixation.

In 1788, Proust and coworkers reported the similarity between the bone composition and calcium phosphate bioceramics. The production of ceramic material for dental and medical applications started during 1960–1970, and Levitt and coworkers introduced it for the first time. By mid-1970s, the researchers across the globe were actively engaged for the development and commercialization of hydroxyapatite as such a powerful tool.

The greek word 'hydroxyapatite' was coined in 1786 by Werner and its meaning is 'to deceive.' Hydroxyapatite is a hydrated calcium phosphate mineral with formula $Ca_{10}(PO_4)_6$ $(OH)_2$ with Ca/P ratio ≈ 1.67. The composition and chemical formula of hydroxyapatite is similar to the bone, and the density of HAp is 3.22 g cm^{-3}. Biological apatites are non-stoichiometric attributed to the vacancies or substitutions within the structural lattice, whereas synthetic HAp is stoichiometric material. Figure 6.5 gives the unit cell and simplified arrangement of HAp (Fig. 1.1—Bioceramic Book).

The unit cell of HAp consists of $6(PO_4)$, 10 calcium, and two OH groups as depicted in Fig. 6.5. The OH groups are located at the corners of the unit cell and are surrounded by two sets of Ca (II) atoms arranged in triangular pattern at $\left(z = \frac{1}{2}, 0\right)$, PO_4 tetrahedron is also arranged in triangular patterns, and Ca (I) atoms form a hexagonal array. PO_4 groups are tightly packed and any substitution in them affects the lattice parameters, dissolution, thermal properties, and morphology.

HAp is monoclinic structure with lattice parameters of $a = 9.4214$ Å, $b = 2a$, $c = 6.8814$ Å, and $\gamma = 120°$, with lattice volume of 528.8 $Å^3$. Table 6.4 gives the lattice parameters obtained after substitution in synthetic and biologic apatites.

Figure 6.6 gives the phase diagram of HAp without water and in the presence of water.Without water in the surrounding atmosphere, the HAp can decompose to tricalcium phosphate (TCP), monetite (C_2P), tetracalcium phosphate (TTCP), and CaO + C_4P mixtures. With water, HAp is stable up to 1550 °C and the phase equilibrium is largely affected by the partial pressure of water, which is present in the vicinity.

When HAp is heated, then three processes take place, i.e., water evaporation, dehydration, and decomposition. Following reaction mechanisms may follow for the dehydration:

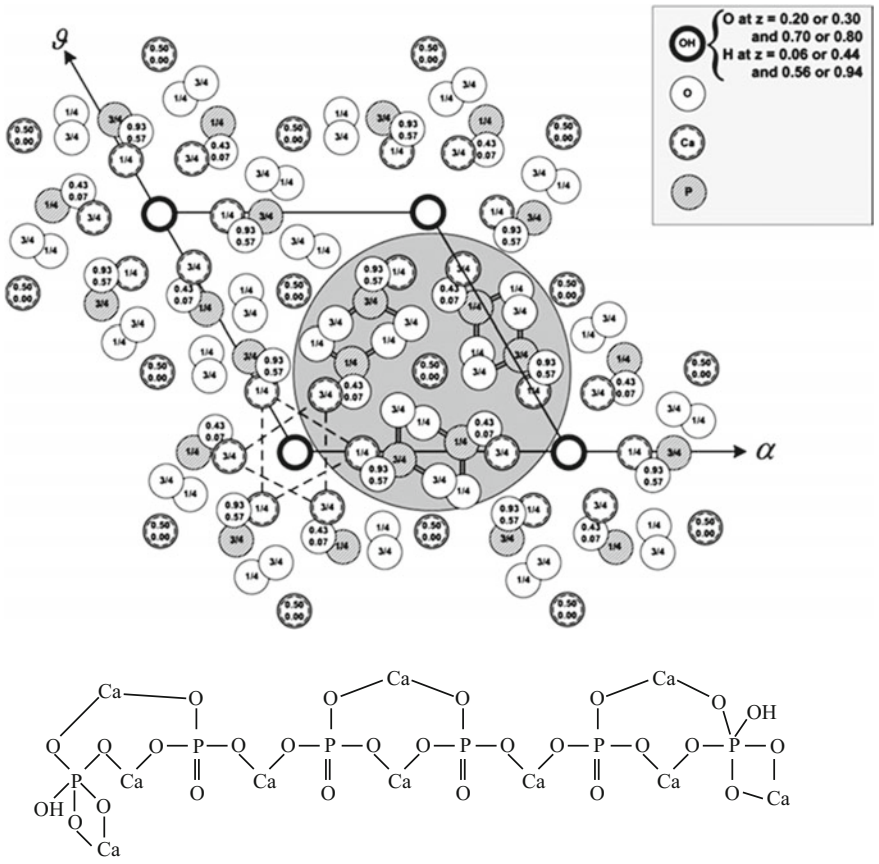

Fig. 6.5 Unit cell and arrangement of hydroxyapatite (HAp) (Nissan 2014)

$$\underset{\text{(Hydroxyapatite)}}{Ca_{10}(PO_4)_6(OH)_2} \longrightarrow \underset{\text{(Oxyhydroxyapatite)}}{Ca_{10}(PO_4)_6(OH)_{2-2x}O_xV_x} + xH_2O \downarrow \underset{\text{(Oxyapatite)}}{Ca_{10}(PO_4)_6O_xV_x} + (1-x)H_2O \tag{6.13}$$

The water may get trapped within the pores of HAp, which starts to evaporate upon heating. Oxyhydroxyapatite (OHA) is a hydroxyl ion-deficient product consisting of bivalent oxygen ion and vacancy substitute for two monovalent OH^- ions of HAp. The formation of OHA is followed by the oxyapatite (OA) formation, but if water is present, then both oxyapatite and oxyhydroxyapatite convert back to hydroxyapatite, i.e., OA + OHA ↔ HAp. Figure 6.7 depicts the decomposition and thermal behavior of HAp but the prediction of exact temperatures is difficult.

Table 6.4 Lattice parameters after substitution in synthetic apatites

Apatite/mineral	Substitution	Lattice parameters (+0.0003 nm)	
		a-axis	*c*-axis
OH apatite	–	0.94214	0.6881
F-apatite	$F \leftrightarrow OH$	0.9375	0.6880
Cl-Apatite	$Cl \leftrightarrow OH$	0.9646	0.6771
CO_3 Apatite	$CO_3 \leftrightarrow OH$	0.9544	0.6859
Dahllite mineral	$CO_3 \leftrightarrow PO_4$	0.9380	0.6885
Marine phosphorite mineral	$CO_3 \leftrightarrow PO_4$	0.9322	0.6882
	$F \leftrightarrow OH$		
Staffelite mineral	$CO_3 \leftrightarrow PO_4$	0.9345	0.6880
	$F \leftrightarrow OH$		
OH apatite (synthetic aqueous)	$HPO_4 \leftrightarrow PO_4$	0.9462	0.6879
F-apatite (synthetic aqueous)	$F \leftrightarrow OH$	0.9382	0.6880
CO_3–OH apatite	$CO_3 \leftrightarrow PO_4$	0.9298	0.6924
CO_3–F apatite	$CO_3 \leftrightarrow PO_4$	0.9268	0.6924
	$F \leftrightarrow OH$		
(Cl–OH) apatite	$Cl \leftrightarrow OH$	0.9515	0.6858
Ba-apatite	$Ba \leftrightarrow Ca$	1.0161	0.7722
Sr-apatite	$Sr \leftrightarrow Ca$	0.9739	0.6913
Pb-apatite	$Pb \leftrightarrow Ca$	0.9894	0.7422
Human enamel (natural)	$(CO_3, HPO_4) \leftrightarrow PO_4$	0.9441	0.6882
	$(Na, Mg) \leftrightarrow Ca$		
	$Cl \leftrightarrow OH$		

In physiological media, the HAp is very stable and the dissolution rates of different CaPs follow the order:

$$CaO > TCP > ACP > TTCP > OHA/OA > HAp$$

Usually, during the preparation of bioactive glasses, CaO is introduced due to its high biocompatibility. However, due to the higher dissolution rates of CaO, it is considered detrimental if used beyond maximum concentration. If the dissolution persists, then the mechanical strength of apatite is compromised, although the dissolved phase promotes bone and tissue regeneration.

6.6 Similartiy of Bone and Hydroxyapatite

HAp implant coatings support growth of human tissue on the bone. Hence, the idea about the different bones and their microstructure shall be clear for getting insight of the phenomena of apatite formation. The bones tissue can be broadly classified into

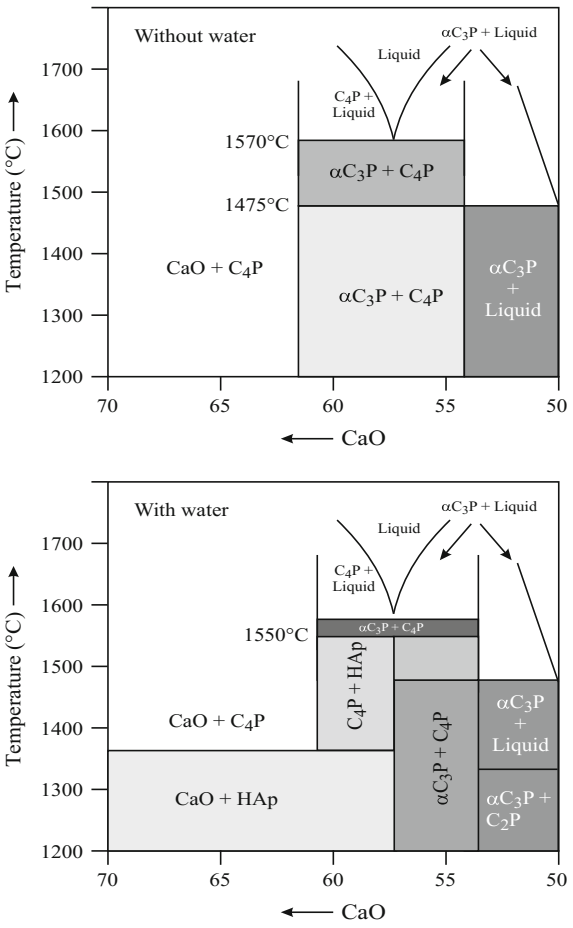

Fig. 6.6 Phase diagram of HAp with and without water at high temperature

two categories, i.e., high-density bone and low-density bone. High-density bone are found in the diaphysis (middle part of bone) and in the outer part of bone known as cortical bone. The bone has porosity from 5–10 and 80–85 % skeletal bone mass for providing strength and protection to the entire bone. Low-density bones are endowed with 75–95 % porosity trabecular bone (Cancellous/spongy bone). Low-density bones have almost 200-μm-thick matrix and are found in the epiphysis (log end of the bone). Almost 80 % of the bone surface is formed of the trabeculae of the cancellous bone. The bone matrix keeps on changing and the primary structure is replaced by the secondary structure. Figure 6.8a gives the schematic of bone structure. The composition of bone is water, HAp mineral, collagen, proteoglycans, and non-collagenous particles.

Collagen protein is found in many tissues and organs of human body and constitutes almost 30 % of organic substance of bone matrix, whereas HAp and water constitute rest 70 % organic substance of the bone (25 % H_2O + 45 % HAp).

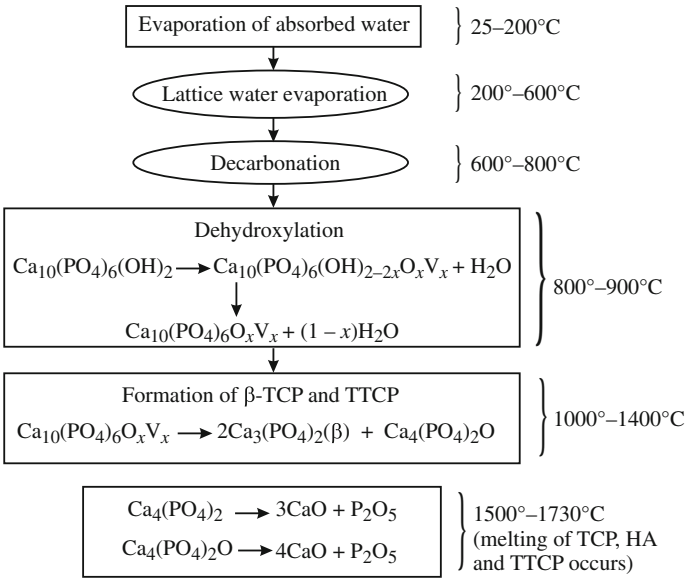

Fig. 6.7 The thermal dependence of hydroxyapatite (HAp)

For the bone modeling and remodeling, i.e., formation and resorption of bone material, type of bone cells are involved as follows (Fig. 6.8b).

- **Osteoclasts**: These cells cover ~1 % of the bone surface. These cells are multinuclear, amoebic cells responsible for the resorption of the bone matrix. Osteoclasts produce acids, which demineralize the bone surface, thereby dissolving the bone collagen with enzymes.
- **Osteoblasts**: These cells are over the surface of bone-forming areas and produce collagen as well as other components of the organic bone matrix. These cells are mononuclear and cuboidal with ~20 μm diameter. Osteoblasts also control the osteoclasts and hence are indirectly involved in the bone resorption processes.
- **Osteocytes**: During the bone resorption modeling process, certain osteoblasts enclose themselves into the matrix. Some encased osteoblasts are converted (~10 %) into osteocytes, which are responsible for the prolonged bone matrix functioning. Osteocytes are well connected to each other via canaliculi (net of channels). Canaliculi are responsible for internal mineralization and hence promote transfer of minerals.

The bone formation process can occur via endochondral and the intramembranous modeling process. The bone matrix is mineralized and cartilage provides a base for the bone-mineralizing cells. Two bone growing zones are situated near the bone because bones grow along their axis. Then, the secondary bone matrix gets mineralized and osteoclasts/osteoblasts remodel the bone. This entire process of mineralization and bone modeling is known as secondary ossification. Once the

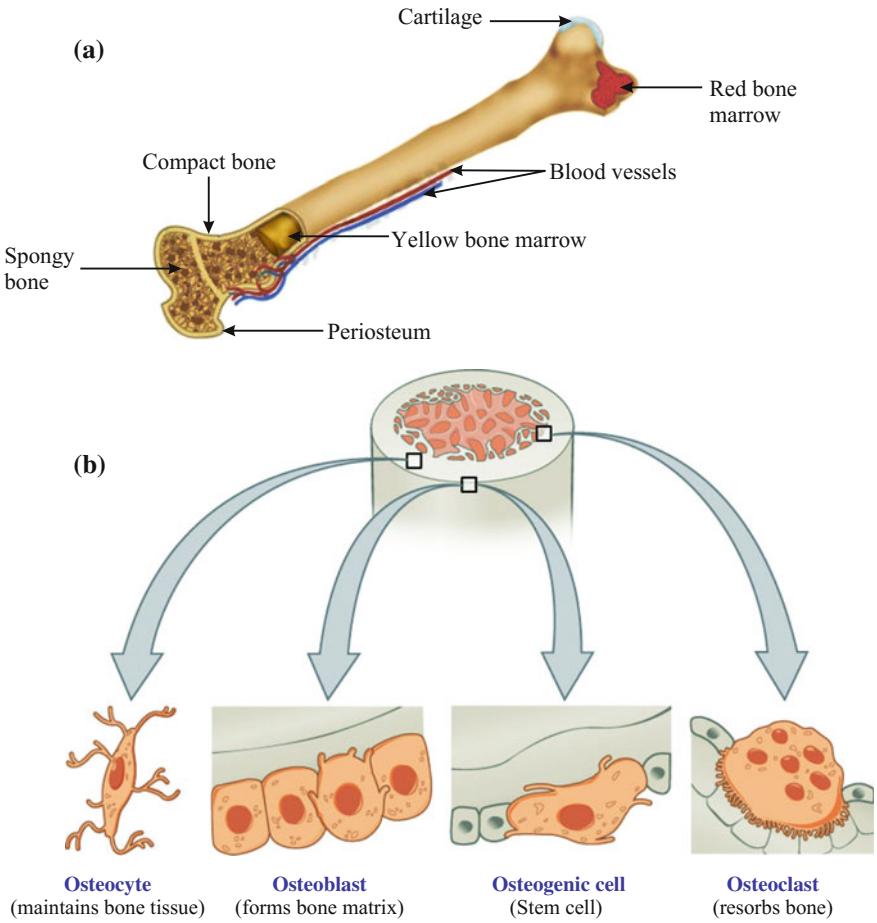

Fig. 6.8 **a** Human bone structure and **b** different types of bone cells

Table 6.5 Bone and HAp composition

Elements	Ca	P	Ca/P	Mg	CO_3^{2-}	Na	K
Bone	24.5	11.5	1.65	0.55	5.8	0.7	0.03
HAp	39.6	18.5	1.67	Trace	Trace	Trace	–

modeling is complete, the permanent remodeling occurs and the body is able to repair small damage of the bone matrix. During the bone remodeling process, osteoblasts and osteoclasts crack together as basic multicellular units (BMUs), i.e., the old tissues are resorbed and new tissues are formed. Table 6.5 compares the bone and HAp composition.

HAp contains structural units, which have substitution sites. Mostly, phosphate (HPO_4), chloride, fluoride, carbonate, potassium, sodium, and magnesium are the

substituents, whereas the trace elements are lead, barium, and strontium. The compressive strength of HAp, cortical bone, and cancellous bone are 350–450, 130–180 and 4–12 MPa, respectively. Cortical bone has tensile strength of 50–151 HPa, whereas for HAp, it lies in between 38 and 48 MPa, respectively.

6.7 Properties of Hydroxyapatite

HAp coating or powder can be developed according to the application and hence structural aspects such as porosity, microstructure, and mechanical strength shall be taken care of. The mechanical and thermal properties of HAp are listed in Table 6.6.

HAp have higher coefficient of thermal expansion than the Ti6Al4V orthopedic alloy, i.e., CTE of HAp $\approx 13.3 \times 10^{-6}$ K^{-1} and CTE of Ti6Al4V is 9×10^{-6} K^{-1}. The difference between Young's modulus of HAp and surrounding bone is ≈20 GPa and hence the strain may develop at the bone HAp coating interface leading to degradation of the bone matrix. The hardness of HAp decreases when the amorphous content increases or the content of CaO is increased. The larger CTE of HAp causes higher expansion than the metal and compressive stress arises at the implant coating interface.

When HAp coating is done on implant surface, then the coating thickness determines the shear strength. Usually for minimizing the fatigue failure, thinner coatings ≈100 μm shall be used. Anyhow, the coating shall be sufficient to sustain the bone cell adhesion, growth, and proliferation.

Table 6.6 Mechanical and thermal properties of HAp

Properties	Value
Mechanical	
Young's modulus (GPa)	41.5–60.1
Elastic limit (MPa)	50
Tension	0.50–3.42
Poisson's ratio	0.3
Density (g/cm^3)	2.8–2.9
Compression	3.17–5.20
Flexural strength	3.72–4.31
Shear strength (MPa)	11.7–20
Fracture toughness (MPa $m^{1/2}$)	0.6–1.41
Thermal	
Melting point (°C)	1600–1700
Coefficient of thermal expansion (K^{-1})	13.3×10^{-6} (820 °C)
Specific heat (J kg^{-1} K^{-1})	700 (100 °C)
Thermal conductivity (W m^{-1} K^{-1})	2.16 (1079)
Thermal diffusivity (cm^2 s^{-1})	5.7×10^{-3}

6.8 Hydroxyapatite in Orthopedics

Hydroxyapatite has been used in hip and knee arthroplasty since 1982. Non-resorbable polycrystalline HAp is used for the prolonged stability in order to protect prosthesis loosening and maintenance of stable interface between bone and implant. In orthopedic surgery, total hip arthroplasty (THA) has been the most successful methods and it involves polymethyl methacrylate (PMMA) for fixing the components. Anyhow, the long-term stability cannot be promised by the cement fixation techniques because bone cement is not osteoconductive. Oonishi and coworkers implied interface bioactive bone cement (IBBC) techniques, which can be described as flow chart shown in Fig. 6.9.

In the first generation (1982–1988), the granule size of 0.3–0.5 mm for HAp was used, whereas for the second generation (1989–1997) HAp granule size was 0.1–0.3 mm. For the third generation (1998–2001), the HAp granule size was 0.3–0.5 mm

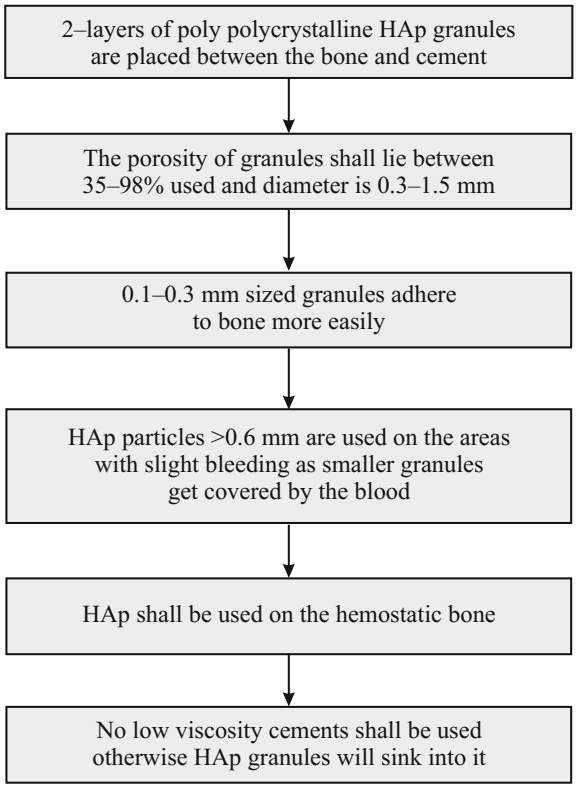

Fig. 6.9 Conditions of interface bioactive bone cement (IBBC) techniques

Table 6.7 Clinical outcomes of IBBC technique on patients

	Span	Patients	Outcomes
Group I	1982–1985	IBBC in 12 joints as trials	No loosening between bone and bone cements up to 27 years for IBBC technique
		A conventional bone cement in 79 joints	For non-IBBC hip replacements, loosening occurred for 80 % of the cases
Group II	1985–1986	16 patients with survival in both hips	For IBBC hips, osteolysis and radiolucent lines appeared in limited areas
			In non-IBBC hips, the prostheses loosened in five hips in the acetabulum and in two hips in the femur
Group III	1986–1989	IBBC in 212 patients (285 joints)	For IBBC, osteolysis and radiolucent line appeared in limited areas. Extensive bone formation could be seen

and since 2001 (for the fourth generation), HAp granule size is 0.3–0.5 mm with anchoring holes more than 6 mm in diameter. Long-term clinical results were performed using IBBC techniques and the trials were divided into three groups (Table 6.7).

Figure 6.10 shows the Group 3 results with the non-IBBC and IBBC techniques. For the non-IBBC hips, the prostheses loosened in five hips in the acetabulum and also in two hips in the femur (within 20 years). Within 15–20 years, seven hips were revised at the radiolucent line and osteolysis increased gradually. For the IBBC hips, excellent bone formation could be seen at the interface of bone and bone cement due to interposing HAp granules. Even in the survival cases of hips with both IBBC/non-IBBC, osteolysis, wide radiolucent lines, and loosening could be seen more in non-IBBC cases, whereas only small fraction of these could be seen in the IBBC hip replacements.

The HAp coating increases the bone ingrowth as well as attachment leading to the enhanced bone fixation as compared to the cemented bones. If HAp granules are polycrystalline in nature, then they are scarcely absorbed. Dense bone ingrowth could be seen for the specimens retrieved from the superior wall of the acetabulum, and cancellous bone ingrowth could be seen for the specimens retrieved from inferomedial wall of the acetabulum. Generally, bone formation around HAp could be affected by the mechanical factors as well. For example, if superior wall is considered to be the principal weight-bearing site and inferomedial wall is regarded as the auxiliary weight-bearing site, then the bone formation is highly affected. If HAp is used with THA, then potential drawbacks like foreign body reaction or interdigitation of cement with bone may occur.

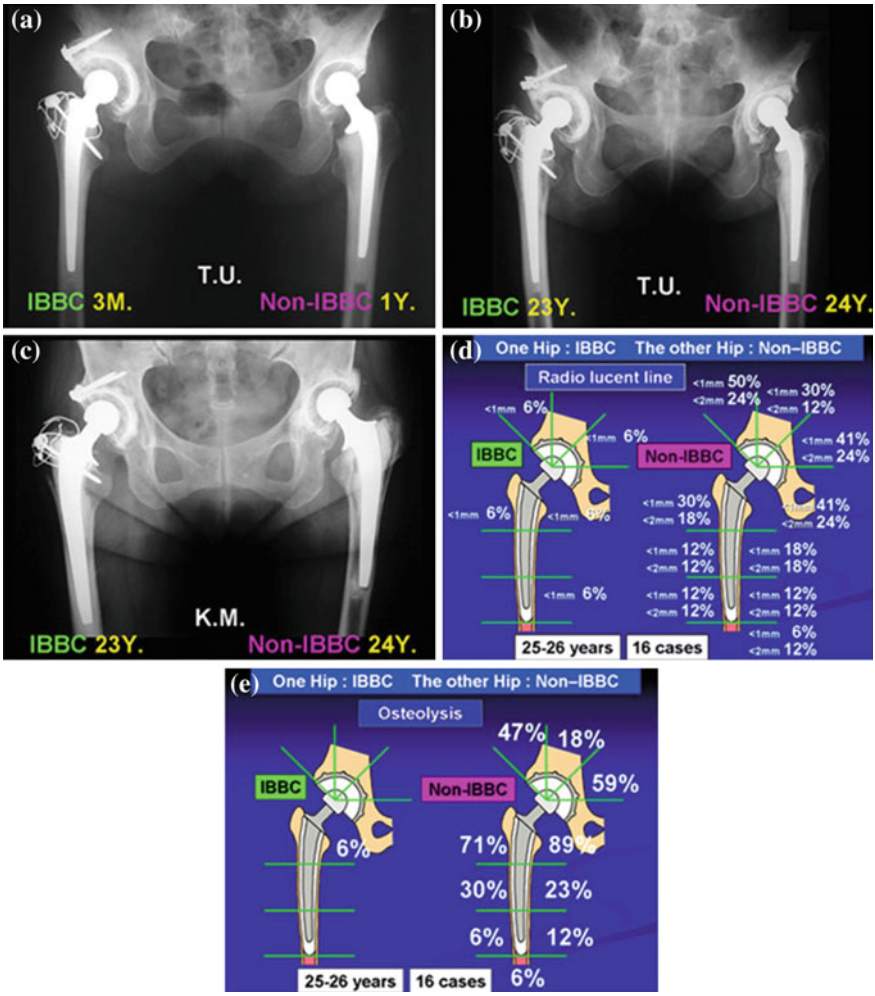

Fig. 6.10 **a** NonIBBC in the *left* hip after 1 year and IBBC in the *right* hip after 3 months, **b** *right* hip with IBBC after 23 years (neither radiolucent line nor osteolysis) and *left* hip with non-IBBC after 24 years (both radiolucent line and osteolysis in both acetabulum and femur), **c** *right* hip with IBBC after 23 years and *left* hip with non-IBBC after 24 years (osteolysis and stem loosening were seen in the femur). **d** comparative appearance rate of radiolucent line 25–26 years after THA with IBBC and non-IBBC for the same patient. **e** comparative appearance rate of osteolysis 25–26 years after THA with IBBC and non-IBBC performed in the same patient (Nissan 2014)

6.9 Simulated Body Fluid (SBF) as Physiological Media

SBF/Kokubo's solution contains the same inorganic ions as that of blood plasma in similar compositions (Table 6.8).

For testing the bioactivity of ceramics/glass, SBF is prepared and then samples are dipped in it at 37 °C for different durations to observe the formation of apatite

Table 6.8 Ion concentration in standard SBF, human blood plasma (HBP), and modified plasma

Ions	Standard SBF	Ca-SBF	P-SBF	pH-SBF	HBP
Ca^{2+}	2.5	3.7	2.5	2.5	2.5
HCO^{3-}	4.2	4.2	4.2	4.2	27.0
HPO_4	1.0	1.0	1.9	1.0	1.0
pH	7.25	7.25	7.25	7.42	7.4
Ion activity product (IAP)	−96.35	−95.01	−95.04	−95.02	−117.2
Induction period	>14 days	5.4 h	16.1 h	18.6 h	–

crystals on the ceramic samples. The mechanism of apatite formation involves series of reactions. The dissociation of C(IV) and P(V) depends on the pH of physiological media.

The activity of H_3PO_4 ions under different pH can be given as

$$\log \frac{\left(HPO_4^-\right)}{\left(H_2PO_4^-\right)} = -7.19 + \text{pH} \tag{6.14a}$$

$$\log \frac{\left(PO_4^-\right)}{\left(HPO_4^{3-}\right)} = -12.03 + \text{pH} \tag{6.14b}$$

Equation (6.14a, 6.14b) indicates that at pH of 12.03, PO_4^- and HPO_4^{3-} yield same activity and at pH 7.19, HPO_4^- and $H_2PO_4^-$ have the same activity. The formation of HAp in physiological media occurs via precipitation phenomena as summed up in Eq. (6.15)

$$10Ca^{2+} + 6H_nPO_4^{3-n} + 2OH^- \rightarrow Ca_{10}(PO_4)_6(OH)_2 + nH^+ \quad (n = 0{-}2) \tag{6.15}$$

Ca/P ratio measures the non-stoichiometry of the apatite and for HAp this ratio is ≈1.67. According to charge compensation principle, one vacant site at Ca site is created upon replacing two PO_4^{3-} ions at b-sites with two HPO_4^{2-} ions. Reverse of Eq. (6.15) may take place if the imperfections lattice energy and surface energy are not balanced properly. In other words, higher degree of imperfection causes strains in the lattice, thereby destabilizing it and decreasing the crystallite size, so that excess energy might be stored as the surface energy.

The dissolution of calcium phosphates is favored due to small size and higher surface area which cause the reverse reaction Eq. (6.15) to follow. The energy of hydration of the constituent ions primarily depends on pH of the medium, whereas dissolution process is affected by the lattice energy. For the biological material–cell interactions, under the body environment, apatite deposition, biodegradation, and in vivo resorption/protein adsorption are the vital mechanisms. When a bioactive material shows apatite layer formation, then it assures the bonding with the bone of the host. Figure 6.11 lists the living tissue interaction with the ceramics

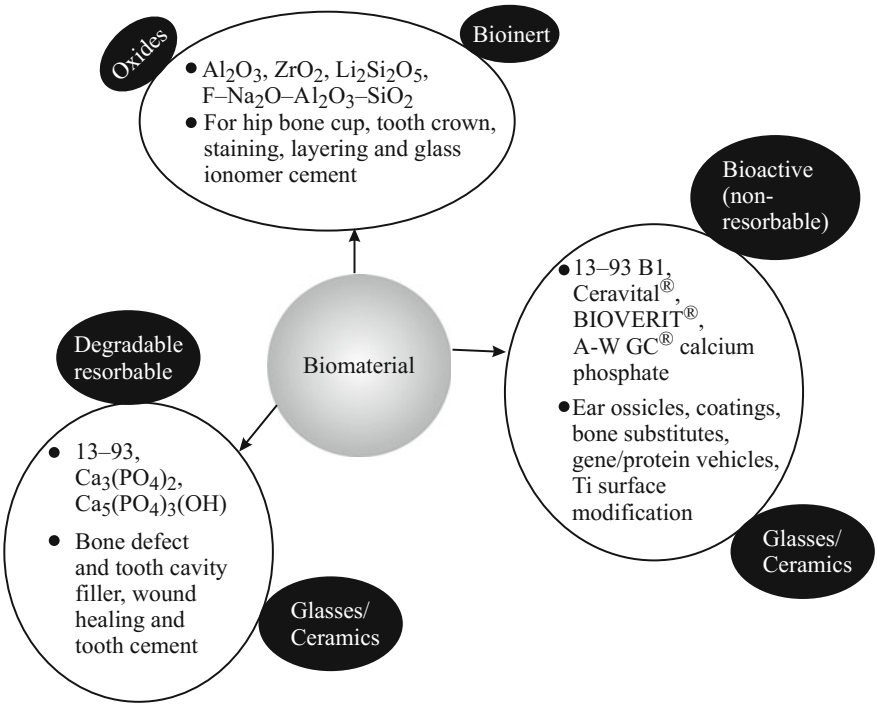

Fig. 6.11 Interaction of biomaterial list tissue interaction

6.10 Apatite Layer Formation on Glasses

The formation of apatite on the glass surface takes a sequential mechanism. The Si–O–Na^+ silica-rich layers act as heterogenous nucleation sites. Hayakawa and coworker proposed that the orthophosphate ions in SBF convert to pyrophosphate and reside on the surface of inert glass. The discovery of 45S5 silicate glass by Hench has revolutionized the biomaterial world as these materials were first man-made glasses to show the bone-bonding and apatite formation. 45S5 glass (bioglass) releases calcium ions and hydroxyl ions, which suprasaturate the solution and hence trigger the nucleation mechanism of apatite formation. In 1973, Ceravital® was introduced by Bromer, though its composition was refined by Gross and coworkers to improve the mechanical properties. The composition of Ceravital contains 38 % SiO_2–13.5$Ca_3(PO_4)_2$–31 % CaO–4 % Na_2O–1 % TiO_2, and traces of Al_2O_3/Ta_2O_5. TiO_2 are added to the glass composition to inhibit the crystallization. Ceravital® has shown apatite formation on its surface and depicted stable properties at bone–HAp interface. Kyoto and Jena commercialized Cerabone (A–W GC®) and BIOVERIT®, respectively. BIOVERIT® II glass has a composition of 45 % SiO_2–30Al_2O_3–12MgO–9 % ($Na + K)_2O$ + 4 % F and this glass undergoes phase separation and phase formation upon heating. One phase is cordierite and other one is spherically arranged

lamellar fluorophlogopite. Though alumina is present in the glass composition and is known to exhibit apatite suppression, but due to its involvement in the glass cordierite phase, apatite formation could be seen on the glass surface.

The glasses with wider working temperature range and involving magnetic phases are used to treat hypothermia. Ebisawa and coworkers developed magnetic bioactive glass ceramics with ferrites, and the wollastonite phase precipitated out, which endowed the glasses with the bioactivity. Xynos and coworkers reported that the dissolution products of 4555 Bioglass® can stimulate the gene expressions relevant to human osteoblasts. But certain glasses like 58S has not provided satisfactory results for the osteoblasts marker gene expression. Process of apatite formation is shown in Fig. 6.12 on a HAp-coated surface.

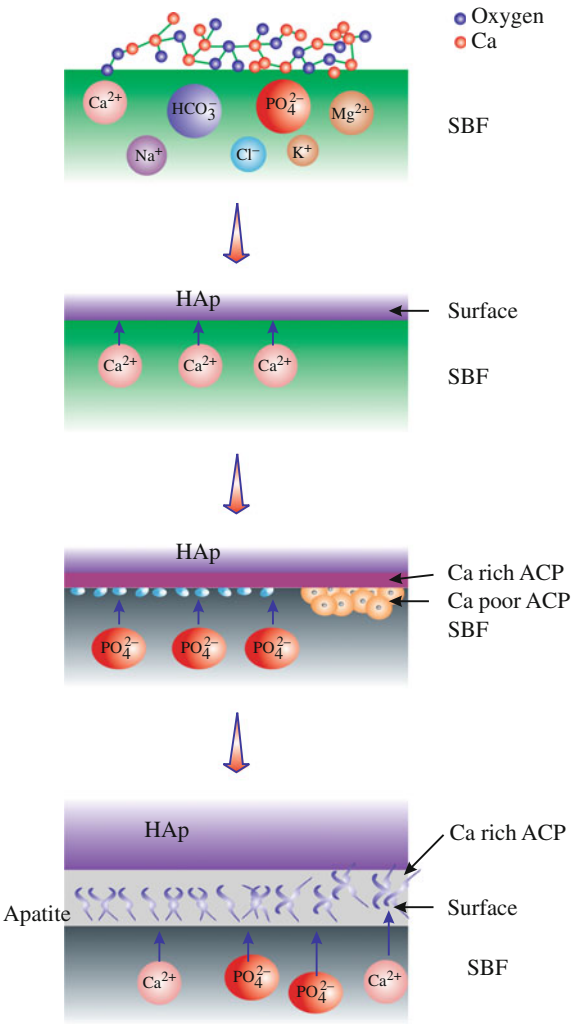

Fig. 6.12 Process of formation of natural bone apatite on HAp coating

Cerabone A–W® contains fluoride and they were subjected to crystallization and sintering. Ionic F are free ions and are coordinated with corresponding modifier atoms, whereas covalent F is covalently bonded as Si–F/P–F bonds are present, then the susceptibility of hydrolysis increases upon contact with the physiological fluid SBF.

Bibliography

Haeri M, Goldberg AJ (2014) Mimicking dentin structure Bio-inspired scaffolds for dental tissue engineering. Mater Today 17:10

Nissan BB (2014) Advances in calcium phosphate biomaterials, Springer series in biomaterials science an dengineering

He LH (2008) Mechanical behaviour of human enamel and the relationship to its structural and compositional characteristics. University of Sydney, Sydney

Hayakawa S, Tsuru K, Iida H, Ohtsuki C, Osaka A (1996) MAS-NMR studies of apatite formation on $50CaO{\cdot}50SiO_2$ glass in a simulated body fluid. Phys Chem Glasses 37(5):188–192

Gross U, Stunz V (1985) The interface of various glasses and glass ceramic with a bony implantation bed. J Biomed Mater Res 19(3):251–271

Vogel W, Hoalnd W (1987) The development of glass ceramics for medical applications. Angew Chem 26:527–544

Ebisawa Y, Miyaji F, Kokubo T, Ohura K, Nakamura T (1997) Bioactivity of ferrimagnetic glass-ceramics in the system FeO–Fe2O3–CaO–SiO2. Biomaterials 18(19):1277–1284

Xynos ID, Edgar AJ, Buttery LDK, Hench LL, Polak JM (2001) Gene-expression profiling of human osteoblasts following treatment with the ionic products of Bioglass W45 S5 dissolution. J Biomed Mater Res 55:151–157

Spătaru M, Ţârdei C, Nemţanu MR, Bogdan F (2008) Rheology of tricalcium phosphate (β-tcp) suspensions. Rev Roum Chim 53(10):955–959

Mandel S, Tas AC (2010) Brushite ($CaHPO_4{\cdot}2H_2O$) to octacalcium phosphate ($Ca8(HPO_4)2(PO_4)4{\cdot}5H_2O$) transformation in DMEM solutions at 36.5 °C, Mater Sci Eng C 30(2):245–254

Tardei C, Grigore F, Pasuk I, Stoleriua S (2006) The study of Mg2 + /Ca2 + substitution of β -tricalciumphosphate. J Optoelectron Adv Mater 8(2):568–571

Ryu H-S, Youn H-J, Hong KS, Chang B-S, Lee C-K, Chung S-S (2002) An improvement in sintering property of b-tricalcium phosphate by addition of calcium pyrophosphate. Biomaterials 23:909–914

Porter AE, Patel N, Skepper JN, Best SM, Bonfield W (2003) Comparison of in vivo dissolution processes in hydroxyapatite and silicon-substituted hydroxyapatite bioceramics. Biomaterials 24:4609–4620

Wang YJ, Lai C, Wei K, Chen X, Ding Y Zhong, Wang L (2006) Investigations on the formation mechanism of hydroxyapatite synthesized by the solvothermal method. Nanotechnology 17:4405–4412

Gross KA, Berndt CC, Herman H (1998) Amorphous phase formation in plasma-sprayed hydroxyapatite coatings. J Biomed Mater Res 39

Oudadesse H, Dietrich E, Gal YL, Pellen P, Bureau B, Mostafa AA, Cathelineau G (2011) Apatite forming ability and cytocompatibility of pure and Zn-doped bioactive glasses. Biomed Mater 6:035006

Ragel CV, Vallet-Regi M, Rodriguez-Lorenzo LM (2002) Preparation and in vitro bioactivity of hydroxyapatite/solgel glass biphasic material. Biomaterials 23:1865–1872

Kasuga T (2005) Bioactive calcium pyrophosphate glasses and glass-ceramics. Acta Biomater 1:55–64

Bohner M, Lemaitre J (2009) Can bioactivity be tested in vitro with SBF solution? Biomaterials 30:2175–2179

Sandeep G, Varma HK, Kumary TV, Suresh Babu S, John A (2006) Characterization of novel bioactive glass coated hydroxyapatite granules in correlation with in vitro and in vivo studies. Biomater Artif Organs 19(2):99–107

Ramila A Padilla S, Munoz B, Vallet-Reg M (2002) A new hydroxyapatite/glass biphasic material: in vitro bioactivity. Chem Mater 14:2439–2443

Stanic V, Dimitrijevi S, Stankovi JA, Mitric M, Jokic B, Plecas IB, Raicevic S (2010) Synthesis, characterization and antimicrobial activity of copper and zinc-doped hydroxyapatite nanopowders. Appl Surf Sci 256:6083–6089

Lo S-S, Huang D, Tu CH, Hou C-H, Chen C-C (2009) Raman scattering and band-gap variations of Al-doped ZnO nanoparticles synthesized by a chemical colloid process. J Phys D: Appl Phys 42:095420

Doostmohammadi A, Monshi A, Fathi MH, Karbasi S, Braissant O, Daniels AU (2011) Direct cytotoxicity evaluation of 63S bioactive glass and bone-derived hydroxyapatite particles using yeast model and human chondrocyte cells by microcalorimetry. J Mater Sci Mater Med 22:2293–2300

Ramay HR, Zhang M (2003) Preparation of porous hydroxyapatite scaffolds by combination of the gel-casting and polymer sponge methods. Biomaterials 24:3293–3302

Stanciu GA, Sandulescu I, Savu B, Stanciu SG, Paraskevopoulos KM, Chatzistavrou X, Kontonasaki E, Koidis P (2007) Investigation of the hydroxyapatite growth on bioactive glass surface. J Biomed Pharm Eng 1:34–39

Agathopoulos S, Tulyaganov DU, Ventura JMG, Kannan S, Karakassides MA, Ferreira JMF (2006) Formation of hydroxyapatite onto glasses of the CaO–MgO–SiO_2 system with B_2O_3, Na_2O, CaF_2 and P_2O_5 additives. Biomaterials 27:1832–1840

Sivakumar M, Panduranga Rao K (2002) Preparation, characterization and in vitro release of gentamicin from coralline hydroxyapatite–gelatin composite microspheres. Biomaterials 23:3175–3181

Kaur G, Pickrell G, Kimsawatde G, Homa D, Allbee HA, Sriranganathan N (2014) Synthesis, cytotoxicity, and hydroxyapatite formation in 27-Tris-SBF for sol-gel based CaO-P_2O_5-SiO_2-B_2O_3-ZnO bioactive glasses. Sci Rep

Vallet-Regí M, Romero AM, Ragel CV, LeGeros RZ (1999) XRD, SEM-EDS, and FTIR studies of in vitro growth of an apatite-like layer on sol-gel glasses. J Biomed Mater Res 44:416–421

Erol M, Ozyuguran A, Celebican O (2010) Synthesis, characterization, and in vitro bioactivity of sol-gel-derived Zn, Mg, and Zn-Mg co-doped bioactive glasses. Chem Eng Technol 33:1066–1074

Sing KSW, Everett DH, Haul RAW, Moscou L, Pierotti RA, Rouquerol J et al (1985) Reporting physisorption data for gas/solid systems. Pure Appl Chem 57:603–619

Bretcanu O, Chen Q, Misra SK, Boccaccini AR, Verne´ E, Vitale- Brovarone C (2007) Biodegradable polymer coated 45S5 Bioglassderived glass-ceramic scaffolds for bone tissue engineering. Glass Tech Eur J Glass Sci Tech A 48:227–234

Chen QZ, Thompson ID, Boccaccini AR (2006) 45S5 BioglassVR –derived glass-ceramic scaffolds for bone tissue engineering. Biomaterials 27:2414–2425

Wu SC, Hsu HC, Hsiao SH, Ho WF (2009) Preparation of porous 45S5 BioglassVR-derived glass-ceramic scaffolds by using rice husk as a porogen additive. J Mater Sci Mater Med 20:1229–1236

Vitale-Brovarone C, Verne´ E, Robiglio L, Appendino P, Bassi F, Martinasso G, Muzio G, Canuto R (2007) Development of glass-ceramic scaffolds for bone tissue engineering: characterisation, proliferation of human osteoblasts and nodule formation. Acta Biomater 3:199–208

Vitale-Brovarone C, Baino F, Verne´ E (2009) High strength bioactive glass-ceramic scaffolds for bone regeneration. J Mater Sci Mater Med 20:643–653

Liu X, Huang W, Fu H, Yao A, Wang D, Pan H, Lu WW, Jiang X, Zhang X (2009) Bioactive borosilicate glass scaffolds: in vitro degradation and bioactivity behaviours. J Mater Sci Mater Med 20:1237–1243

Cannillo V, Sola A (2009) Potassium-based compositions for a bioactive glass. Ceram Int 35:3389–3393

Bellucci D, Cannillo V, Ciardelli G, Gentile P, Sola A (2010) Potassium based bioactive glass for bone tissue engineering. Ceram Int 36:2449–2453

Bang HG, Kim SJ, Park SY (2008) Biocompatibility and the physical properties of bio-glass ceramics in the Na2O-CaO-SiO2-P2O5 system with CaF2 and MgF2 additives. J Ceram Process Res 9(6):588–590

Implants for surgery–hydroxyapatite–Part 1: ceramic hydroxyapatite. BS ISO 13779-1:2000

Carter DR, Hayes WC (1976) Bone compressive strength: the influence of density and strain rate. Science 194:1174–1176

Webster TJ, Siegel RW, Bizios R (1999) Osteoblast adhesion on nanophase ceramics. Biomaterials 20:1221–1227

Schneider OD et al (2008) Cotton wool like nanocomposite biomaterials: in vitro bioactivity and osteogenic differentiation of human mesenchymal stem cells J Biomed Mater Res B: Appl Biomater 84:350–362

Gao T, Aro H T, YlaKnen H, Vuorio E (2001) Silica-based bioactive glasses modulate expression of bone morphogenetic protein-2 mRNA in Saos-2 osteoblasts in vitro. Biomaterials 22:1475–1483

Vern´e E, Ferraris S, Vitale-Brovarone C, Spriano S, Bianchi C L, Naldoni A, Morra M, Cassinelli C (2010) Alkaline phosphatase grafting on bioactive glasses and glass ceramics. Acta Biomater 6:229–240

Reilly GC, Radin S, Chen AT, Ducheyne P (2007) Differential alkaline phosphatase responses of rat and human bone marrow derived mesenchymal stem cells to 45S5 bioactive glass. Biomaterials 28:4091–4097

Varanasi VG, Saiz E, Loomer PM, Ancheta B, Uritani N, Hoa SP, Tomsia AP, Marshall SJ, Marshall GW (2009) Enhanced osteocalcin expression by osteoblast-like cells (MC3T3-E1) exposed to bioactive coating glass (SiO2–CaO–P2O5–MgO–K2O–Na2O system) ions. Acta Biomater 5:3536–3547

Valerio P, Pereira MM, Goes AM, Leite MF (2004) The effect of ionic products from bioactive glass dissolution on osteoblast proliferation and collagen production. Biomaterials 25:2941–2948

Kaur G, Pandey OP, Singh K, Homa D, Scott B, Pickrell G (2013) A review of bioactive glasses: their structure, properties, fabrication, and apatite formation. J Biomed Mater Res A 102:254–274

Kaur G, Sharma P, Kumar V, Singh K (2012) Assesment of *in-vitro* bioactivity of SiO_2-BaO-ZnO-B_2O_3-Al_2O_3 glasses: an optico-analytical approach. Mater Sci Eng C 32(7): 1941–1947

Kaur G, Pickrell G, Sriranganathan N, Kumar V, Homa D (2016) Review and the state of the art: sol-gel or melt quenched bioactive glasses for tissue engineering. J Biomed Mater Res Part B Appl Biomater 104(6):1248–1275. doi:10.1002/jbm.b.33443

Kaur G, Pickrell G, Pandey OP, Singh K, Chudasama BN, Kumar V (2016) Combined and individual Doxorubicin/Vancomycin drug loading, release kinetics and apatite formation for the CaO-CuO-P_2O_5- SiO_2- B_2O_3 mesoporous glasses. RSC Adv 6:51046–51056

Kaur G, Pickrell G, Kimsawatde G, Allbee H, Sriranganathan N (2014) Synthesis, cytotoxicity, and hydroxypatite formation in 27-Tris-SBF for sol-gel based CaO-P_2O_5-SiO_2-B_2O_3-ZnO bioactive glasses. Sci Rep. doi:10.1038/srep04392

Chapter 7
Mechanical Behavior of Bioactive Glasses/Ceramics

Gurbinder Kaur

The properties of glasses and ceramics shall be guided according to the application so as to improve their in vivo performances. Bioactive glasses have attained wide attention as implant materials, especially for the orthopedic applications. For the implant materials, the mechanical behavior of materials should be well understood for predicting the failure and hence crack propagation. Any stress zones shall be avoided, while fabricating the implants, so as to increase their lifetime for load-bearing application. This chapter lists the outline of mechanical properties and use of statistical analysis for improving the strength of the glasses/ceramics.

7.1 Glass Viscosity

Viscosity (η) usually increases with pressure, but for certain glass-forming silicate liquids such as dacite, basalt, and albite, one order of decrease in velocity has been observed upon 2–5 times increase in pressure. Hence, there are exceptions to the positive pressure dependence of viscosity, specifying negative pressure dependence. This has been explained with the help of free volume theory. According to Gibbs' phase rule, temperature and pressure can be chosen as independent variables, which determine other parameters for a system, i.e.,

$$\eta = \eta(p, T) \tag{7.1}$$

Skripov and coworkers determined following conclusions for a set of experiments, i.e.,

$$\left.\begin{array}{l} \left(\frac{\partial \eta}{\partial T}\right)_P < 0 \\ \left(\frac{\partial \eta}{\partial p}\right)_T > 0 \end{array}\right\} \tag{7.2}$$

G. Kaur, *Bioactive Glasses*, Series in BioEngineering,
DOI 10.1007/978-3-319-45716-1_7

Equation (7.2) indicates that the viscosity must increase with increasing pressure at isothermal conditions, whereas it must increase with decreasing temperature at isobaric conditions. Hence following identity is derived on the basis of purely mathematical consideration, i.e.,

$$\left(\frac{\partial \eta}{\partial T}\right)_P \left(\frac{\partial T}{\partial p}\right)_\eta \left(\frac{\partial p}{\partial \eta}\right)_T = -1 \tag{7.3}$$

The behavior of partial derivatives could be explained by taking the concept of 'free volume' into account. Frenkel demonstrated free volume as follows:

- Pressure and temperature cannot separately determine free volume, but total volume V (p, T) can help in determining the free volume.
- The value of viscosity η can be determined from the free volume.

For the constancy of viscosity, the total volume of the system must be constant, even if slight variation in temperature and pressure (dT and dp) is observed, respectively:

$$\begin{aligned} \mathrm{d}V(p,T) &= \left(\frac{\partial V}{\partial p}\right)_T \mathrm{d}p + \left(\frac{\partial V}{\partial T}\right)_p \mathrm{d}T = 0 \\ \Rightarrow \left(\frac{\partial T}{\partial p}\right)_V &\cong \left(\frac{\partial T}{\partial p}\right)_\eta = \frac{-\left(\frac{\partial V}{\partial p}\right)_T}{\left(\frac{\partial V}{\partial T}\right)_p} \end{aligned} \tag{7.4}$$

From Eq. (7.3), we obtain

$$\left(\frac{\partial \eta}{\partial p}\right)_T = \left(\frac{\partial \eta}{\partial T}\right)_p \frac{-\left(\frac{\partial V}{\partial p}\right)_T}{\left(\frac{\partial V}{\partial T}\right)_p} = -\frac{k(p,T)}{\alpha(p,T)} \left(\frac{\partial \eta}{\partial T}\right)_p \tag{7.5}$$

In Eq. (7.5), α and k are isobaric thermal expansion coefficient and isothermal compressibility, respectively, i.e.,

$$\alpha = \frac{1}{V}\left(\frac{\partial V}{\partial T}\right)_p, \quad k = -\frac{1}{V}\left(\frac{\partial V}{\partial p}\right)_T \tag{7.6}$$

The derivatives in Eq. (7.3) are dependent on the sign of α, which generally is positive quantity, i.e., thermal expansion increases with increasing temperature.

Frenkel described the motion of building units of particles in liquid or oscillations around temporary average positions, and after average stay time τ_R, the temporary centers of the oscillations are changed. Furthermore, the mean distance between the two subsequently occupied centers of oscillation is comparable to the molecule size. The shear viscosity η is the quantitative measure for the ability of the system to flow, and its relationship with average stay time, τ_R, is given by:

$$\left.\begin{aligned}\tau_R &= \tau_{RO}\exp\left(\frac{E_o}{k_B T}\right)\\ \Rightarrow \eta &= \eta_o \exp\left(\frac{E_o}{k_B T}\right)\end{aligned}\right] \tag{7.7}$$

T is the absolute temperature, k_B the Boltzmann constant, and E_o the activation energy of viscous flow. In the field of glass science, the viscosity temperature relations are of utmost importance and given by the most well-known empirical relations regarded as Vogel–Fulcher–Tammann (VFT) equation

$$\eta = \eta_o \exp\left[\frac{A}{k_B(T - T_\infty)}\right] \tag{7.8}$$

where η_o, A, and T_∞ are substance-dependent empirical constants. Vogel developed this relation on the basis of viscosity–temperature variation for the technical greases, whereas Fulcher analyzed viscosity for the silicate glasses; Tammann investigated it for the glass-forming organic substances. According to VFT equation, the viscosity tends to infinity for $T \rightarrow T_\infty$. To a good approximation, for the glass-forming substances:

$$\left.\begin{aligned}\frac{T_\infty}{T_m} &\approx 0.5\\ \frac{T_\infty}{T_g} &\approx \frac{3}{4}\end{aligned}\right] \tag{7.9}$$

where T_m and T_g are the glass melting and glass transition temperatures, respectively. Viscosity of a melt can be attained in simple ways, and other viscosity-dependent kinetic coefficients of glass-forming liquids can also be estimated. These kinetic coefficients are important from the vitrification and crystallization point of view. For example, kinetic parameters Z, , impingement rate and D_o, self-diffusion coefficient of building units of melt. The impingement rate usually gives the number of collision of molecules of the melt with unit hypothetical surface area. The Stoke's law yields force acting on the sphere of diameter d, moving with velocity v in a continuum of viscosity η as:

$$F = 3r\,\eta dv \tag{7.10}$$

Using Einstein's approach for the description of Brownian motion, the D_o can be written as:

$$D_o = \frac{k_B T}{3r\eta dv} \tag{7.11}$$

Equation (7.11) can be written more precisely in terms of Eyring's absolute rate theory:

$$D_o = \frac{k_B T}{\eta d} \tag{7.12}$$

(Equation (7.12) differs from Eq. (7.11) in terms of numerical factors only)

The relationship between D_o and τ_R can be approximated as:

$$D_o \approx \frac{d_o^2}{\tau_R} \tag{7.13}$$

where d_o is the average displacement associated with a jump to new position. Usually, $d \approx d_o$, as d is almost of order of one of mean building units of melts, which gives:

$$D_o \approx \frac{d^2}{\tau_R} \tag{7.14}$$

From Eqs. (7.10)–(7.14), it can be obtained:

$$\tau_R \approx \frac{d^3 \eta}{k_B T} \tag{7.15}$$

Equation indicates that η and T share direct dependence on each other, instead of exponential dependence of viscosity on temperature. Maxwell, Kelvin, and Voigt described the relation between macroscopic relaxation time of melt, τ_R, with viscosity.

$$\tau_R \approx \frac{\eta}{G^*} \tag{7.16}$$

where G^* is the factor of proportionality with significance and dimensions of modulus of elasticity, and its order can be given by:

$$G^* \approx \frac{k_B T}{d^3} \tag{7.17}$$

The relation between impringement factor Z and viscosity η can be derived as follows:

$$Z = \frac{1}{4} n \bar{v} \tag{7.18}$$

where n is average number of molecule/volume, and $\bar{v}$ is the average of absolute velocity of translation of liquid molecule. $\bar{v}$ average velocity can be approximated as $\approx \frac{d}{\tau_R}$ as per Frenkel's model, whereas $n \approx \frac{1}{d^3}$ for condensed systems. Using these two approximations in Eq. (7.18), we obtain:

$$Z \approx \frac{1}{d^2 \tau_R} \tag{7.19}$$

Combining Eq. (7.19) with (7.15), we obtain:

$$Z \approx \frac{k_B T}{d^5 \eta} \tag{7.20}$$

Anyhow, the equations derived are from the spherical shape of view, whereas for complex structures, additional steric factors shall also be considered. Viscosity is also related to the constant shear stress σ_{xy} and engineering shear strain rate $\dot{\gamma}_{xy}$ as follows:

$$\sigma_{xy} = \eta \dot{\gamma}_{xy} \tag{7.21}$$

Basically expression (7.21) holds good for glass in liquid condition responding to constant shear stress after deformation with constant engineering shear strain $\dot{\gamma}_{xy}$. The deformation is said to be Newtonian, when viscosity is independent of the strain rate. Viscosity is given by poise (CGS) or Pascal second (SI). The viscosities for glasses differ at different temperatures. Figure 7.1 gives the typical variation of viscosity with temperature.

When the glass is formed, annealing is performed to reduce the internal thermal stresses. The viscosity can be 13.5 Pa s at strain point, whereas it reduces to 12 Pa s at the annealing point temperature. The stress can be relieved gradually over several hours via straining, whereas annealing causes stress reduction within minutes. At the glass transition temperature (T_g), the viscosity is $\approx 10^{11.3}$ Pa s

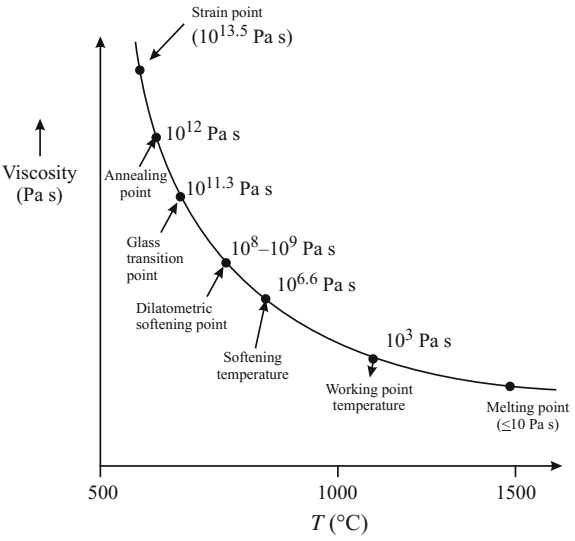

Fig. 7.1 Different viscosities for different temperatures of glass melt

followed by the viscosity value of 10^8–10^9 Pa s at dilatometric softening temperature (T_d). At viscosity of $10^{6.6}$ Pa s, the melt achieves viscosity, which can prevent the deformation under its own weight. The melt is migrated to processing chamber at a viscosity of 10^3 Pa s. For the melting temperature, the viscosity of $\leq$10 Pa s is obtained for most of the glasses. The melt shall be viscous enough to flow under acceptable stresses but maintaining the fluid shape as well.

7.2 Elastic Properties of Glass/Ceramics

Under applied stress, the ceramics/glasses may undergo elastic deformation, and these parameters shall be controlled or optimized for obtaining desired mechanical parameters. According to Hooke's law, stress (σ) is directory proportional to strain (ε), up to a proportional limit.

$$\sigma = \varepsilon E \tag{7.22}$$

where σ is normal stress (F/A), ε is normal strain ($\Delta L/L_o$), and E is Young's modulus/elastic modulus, obtained from the slope of stress–strain curve. The relation between shear stress (τ) and shear strain (γ) is given by:

$$\tau = G\gamma \tag{7.23}$$

where G is modulus of rigidity and relates to Poisson's ration (μ) as follows:

$$\mu = \frac{E}{2G} - 1 \tag{7.24}$$

$$\left[\text{where } \mu = \frac{\left(\frac{\Delta d}{d}\right)}{\left(\frac{\Delta l}{l}\right)} = \frac{\text{thickness decrease upon extending a sample}}{\text{length increase upon extending a sample}}\right]$$

The Poisson's ratio lies between 0.2 and 0.25 for most of the materials, and Eq. (7.24) is valid for isotropic body, i.e., the elastic constant is independent of direction and hence yields single value in all the directions.

The relative strain for isotropic pressure conditions yields applied pressure p equivalent to the stress—p in every direction and the following relation is obtained.

$$\begin{aligned} \varepsilon &= -\frac{p}{E} + \frac{\mu p}{E} + \frac{\mu p}{E} \\ \Rightarrow \varepsilon &= \frac{p}{E}[2\mu - 1] \end{aligned} \tag{7.25}$$

The bulk modulus K can be defined as isotropic pressure divided by the relative volume change and is given by:

$$K = -\frac{p}{\Delta V/V} = -\frac{p}{3\varepsilon} = \frac{E}{3(1-2\mu)} \tag{7.26}$$

$$[\because \text{The relative volume charge} = 3 \times \text{relative strain}(\varepsilon)]$$

The Young's modulus, bulk modulus, and shear modulus are related as:

$$E = \frac{4KG}{3K+G} \tag{7.27}$$

For glass-forming melts, the elastic moduli cannot be regarded as constant as it is dependent on time. More precisely, glass-like liquids are regarded as viscoelastic/anelastic. The elastic modulus can be measured via two limits, i.e., the relaxed modulus or unrelaxed modulus. The relaxed modulus is determined when the load is applied and strain is measured for long times, whereas for the time-dependent deformation provided for small time of measurements, the initial ratio of stress and strain are taken, which is referred to as unrelaxed modulus. Relaxed modulus is smaller than the unrelaxed modulus, because the long-time strain is larger than the instantaneous strain.

Time-dependent modulus is given in the form:

$$E(t) = E_o + \int_{-\infty}^{\infty} H(t'_R) \exp\left(-\frac{t}{t'_R}\right) d \ln t'_R \tag{7.28}$$

where E_o is the relaxed modulus at equilibrium, t_R is the relaxation time, and H (t'_R) describes the distribution of relaxation times, characterizing the relaxation process. The anelastic behavior of materials can be well understood with the help of periodic stress on strain. Upon applying periodic stress, the delayed extension causes strain to lag behind stress by some angle δ. Hence, for an applied stress of

$$\sigma = \sigma_0 \sin \omega t \tag{7.29}$$

the strain can be given as:

$$\varepsilon = \frac{\sigma_0}{E} \sin(\omega t - \delta) \tag{7.30}$$

$$\left[E = \underbrace{\frac{\sigma_0}{E}\left(\sin \omega t \cos \delta\right)}_{\text{In phase withs stress}} - \underbrace{\frac{\sigma_0}{E}\left(\cos \omega t \sin \delta\right)}_{90^\circ \text{ out of phase with stress}} \right]$$

$$\Rightarrow \qquad \frac{\varepsilon}{\sigma_0} = D^* = \text{complex compliance}$$

The imaginary part of the complex compliance corresponds to the energy loss as given below:

$$\Delta U = \int \sigma d\varepsilon = \frac{\pi \sigma_0^2}{E} \sin \delta \tag{7.31}$$

The relation between complex elastic modulus and compliance is given as:

$$E^* = \frac{1}{D^*} \tag{7.32}$$

Figure 7.2 gives the behavior of real and imaginary parts of elastic modulus with frequency.

To determine the energy dissipation/cycle, tan δ is used, i.e.,

$$2\pi \tan \delta = \frac{\Delta U}{U} \tag{7.33}$$

Similarly, for the mechanical loss, logarithmic decrement is given, which is defined as:

$$\Delta = \ln \frac{A_n}{A_{n+1}} \tag{7.34}$$

A_n and A_{n+1} are the amplitudes of successive oscillations. The relation between tan δ and logarithmic decrement is given by Eq. (7.35).

$$\Delta \approx \pi \tan \delta \tag{7.35}$$

For alkali glasses, usually two loss peaks are observed at temperatures below glass transformation range, i.e., one peak corresponds to stress-induced motion of

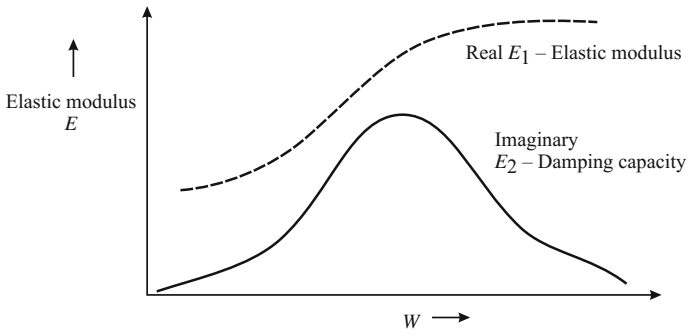

Fig. 7.2 Complex elastic modulus behavior with frequency

alkali ion (usually occurs at low temperature) and the other peak corresponds to the loss corresponding to non-bridging oxygens (NBO) (usually occurs at high temperatures).

7.3 Fracture and Crack Initiatations

Ceramics and glasses are brittle materials, whereas the crystalline materials show fracture via cleavage over certain crystallographic planes. Usually, fracture represents the separation of material into two or more parts under stress. The stress may be compressive, tensile, shear, or torsional in nature. Fracture usually consists of two stages, i.e., crack initiation and crack propagation. On the basis of a material to undergo plastic deformation, the fractures can be ductile fracture and brittle fracture. Brittle fractures are seen in glasses and in some of the cast iron and are very unstable fractures. Brittle fractures propagate at a faster rate with very less micro-deformation.

Once brittle crack nucleates, it keeps on propagating without even any other applied stress. During ductile fracture, substantial plastic deformation occurs prior to and during the crack propagation. Ductile cracks are often stable, and fractured surface exhibits plastic deformation. Ductile fracture is still safer than the brittle fracture because latter occurs suddenly/catastrophically and propagates rapidly.

Figure 7.3 lists the categories of fractures dependence on material, stress state, and loading rate.

Shear fracture usually occurs due to shear stresses and due to extensive, slip on active slip planes. In contrast to this, cleavage fracture is initiated by the tensile stresses acting normal to the crystallographic cleavage planes. For the intercrystalline fracture, the crack propagation occurs along the grain boundaries and is

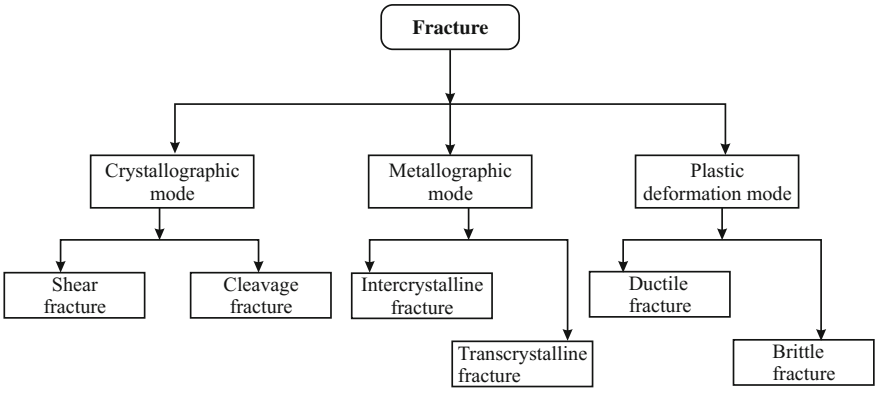

Fig. 7.3 Categorization of fracture on the basis of various factors

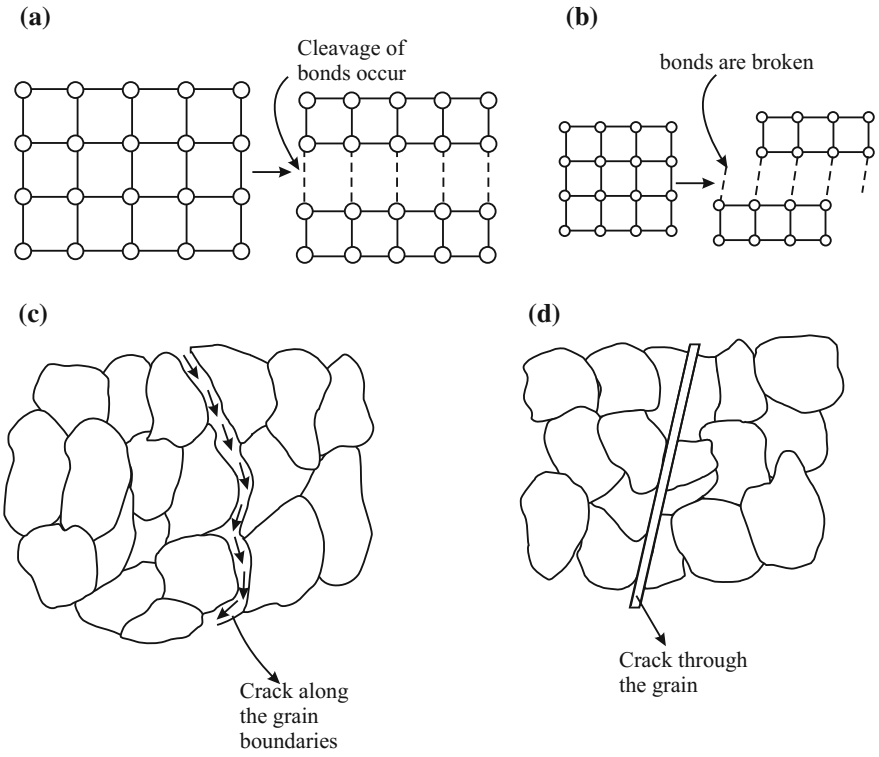

Fig. 7.4 The mechanism of fracture occurrence in **a** cleavage fracture, **b** shear fracture, **c** intercrystalline fracture, and **d** transcrystalline fracture

observed when the low melting phase or brittle phase is present along the grains boundaries. In the transgranular fractures, the crack propagates through the grains. Figure 7.4 demonstrates different mechanisms of fracture.

7.4 Griffith's Theory of Fracture and Stress Concentration

In 1920, Griffith proposed that small microscopic flaws or cracks are always present in the interior of material or at its surface under normal conditions. Furthermore, these sites act as the stress concentrations.

An applied stress is amplified or concentrated at the crack tip, and the amplification depends directly on the geometry and orientation of the crack. As demonstrated in Fig. 7.5, the crack tip exhibits maximum stress σ_m and decreases with distance away from tip till it becomes equal to the nominal stress. For an elliptical crack, the maximum stress σ_m is given by:

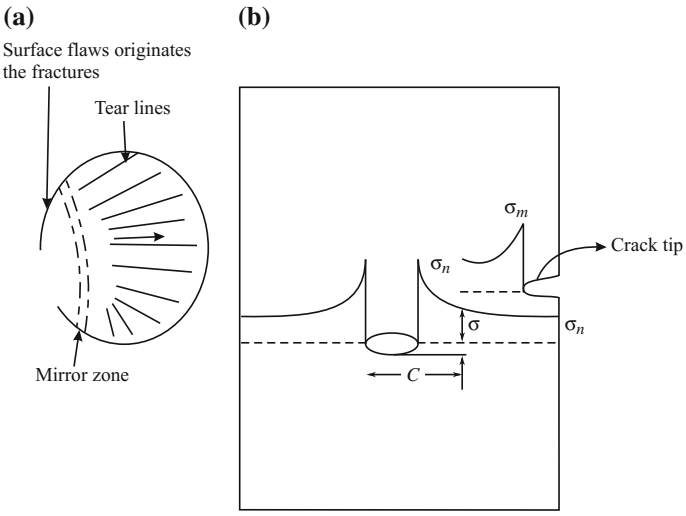

Fig. 7.5 **a** Fracture in glass, **b** schematic of stress distribution at the crack tip

$$\sigma_{\mathrm{m}} = \sigma_{\mathrm{n}}\left[1 + 2\left(\frac{C}{\rho}\right)^{1/2}\right] \tag{7.35}$$

where C is surface crack length (equivalent to half length of crack) and ρ is radius of curvature of tip of the crack. Equation (7.35) reduces to Eq. (7.36) for relatively larger micro-cracks with small tip radius, i.e.,

$$\sigma_{\mathrm{m}} = 2\,\sigma_{\mathrm{n}}\left(\frac{C}{\rho}\right)^{1/2} \tag{7.36}$$

The most probable positions of stress occurrence are sharp corners, internal defects, and matches. Usually, the relation between σ_{m} and Young's modulus is given by (discussed later):

$$\sigma_{\mathrm{m}} = \left(\frac{E\gamma'}{a_{\mathrm{o}}}\right)^{1/2} \tag{7.37}$$

where γ' is the surface energy of material and a_{o} is the interatomic separation. Upon combining Eqs. (7.36) and (7.37), we get:

$$\sigma_{\mathrm{n}} = \sigma_{\mathrm{f}} = \left[\frac{\gamma' E}{4C}\left(\frac{\rho}{a_{\mathrm{o}}}\right)\right]^{1/2} \tag{7.38}$$

where σ_n becomes the fracture strength (σ_f) of the material with crack. For the sharpest crack, $\rho = a_o$, then Eq. (7.38) becomes:

$$\sigma_f = \left(\frac{\gamma' E}{4C}\right)^{1/2} \tag{7.39}$$

According to the Griffith, the discrepancy between the observed and calculated fracture strength lies in the presence of flaws in brittle materials. He postulated that the brittle materials contain large number of cracks and during crack propagation, elastic strain is released. In addition to this, the free surfaces are created as faces of crack during crack propagation. For the formation of new free surfaces, additional energy is required to overcome cohesive forces, which increases the surface energy. Hence, Griffith's theory for crack theory postulates:

> The crack propagation occurs when the energy required for formation of new crack surface is equal to decrease in the elastic strain energy. The magnitude of crack is governed by the thermodynamic relationship between these two energies.

The critical fracture stress (σ_c) given by Griffith is known as Griffith's equation and is given by:

$$\sigma_c = \left(\frac{2E\gamma'}{\pi c}\right)^{1/2} \tag{7.40}$$

σ_c is the critical value of stress required for the propagation of crack of length $2c$. Equation (7.40) certifies that crack in brittle materials cannot propagate until critical stress value is attained.

7.5 Model for Fracture Strength of Glasses/Ceramics

Upon breaking the bonds between atoms facing each other initiate crack. When the interatomic separation between atoms is increased under the effect of tensile force, the repulsive forces decreases rapidly than the attractive forces. At a particular interatomic separation, the repulsive forces are negligible, and this point corresponds to maximum in the curve. For an applied stress/cohesive force (σ), the interatomic distance can be given by a sine curve, i.e.,

$$\sigma = \sigma_m \sin\frac{2\pi r}{\lambda} \tag{7.41}$$

($r = a - a_o$, corresponding to displacement in atomic spacing in crystal lattice).

For very small displacements, $\sin \pi \approx \pi$, hence,

$$\sigma = \sigma_{\mathrm{m}} \frac{2\pi r}{\lambda} \tag{7.42}$$

Brittle solids follow Hooke's law

$$\sigma = \varepsilon E = \frac{Er}{a_{\mathrm{o}}} \tag{7.43}$$

Combining Eqs. (7.42) and (7.43), we get:

$$\sigma_{\mathrm{m}} = \frac{E\lambda}{2\pi a_{\mathrm{o}}} = \frac{E}{\pi} \quad \left[a_{\mathrm{o}} \approx \frac{\lambda}{2}\right] \tag{7.44}$$

For ideal brittle elastic fractions, the entire energy is absorbed in creating two new surfaces, during the fracture. The total energy of these two surfaces is $2\gamma'$ J/m^2 [γ' J/m^2 corresponding to each surface]. The total work done/area (W) of fracture surface used in initiating fracture in the glass material is given as:

$$W = \int_0^{\frac{\lambda}{2}} \sigma_{\mathrm{m}} \sin \frac{2\pi r}{\lambda} = \frac{\lambda \sigma_{\mathrm{m}}}{r} \tag{7.45}$$

As this work done is impended in creating two new surfaces with total energy $2\gamma'$, then:

$$\begin{aligned} \frac{\lambda \sigma_{\mathrm{m}}}{r} &= 2\gamma' \\ \Rightarrow \quad \lambda &= \frac{2\pi\gamma'}{\sigma_{\mathrm{m}}} \end{aligned} \tag{7.46}$$

Using Eq. (7.44) in Eq. (7.46), we get:

$$\text{Fracture strength } \sigma_{\mathrm{m}} = \left(\frac{E\gamma'}{a_{\mathrm{o}}}\right)^{1/2} \tag{7.47}$$

Anyhow, it must be noted that the real fracture strength of material is lower than the theoretical strength. Griffiths also elucidated fracture toughness, which is defined as the fracture resistance of material in the presence of cracks/flaws. Orowan introduced a term γ_ρ which gives the plastic work necessary for extension of the crack walls during fracture, and hence the fracture toughness was given by:

$$K' = 2\left(\gamma + \gamma_p\right) \tag{7.48}$$

where K' defines the fracture toughness and gives the strain energy/area of the crack surface. The critical value of stress for crack propagation is related to γ_p as follows:

$$\sigma_c = \left(\frac{2E\gamma_p}{\pi c}\right)^{1/2} \tag{7.49}$$

Usually, the γ_p values are quite larger than the γ values, i.e., 10^2–10^3 J/m^2 for γ_p and 1–2 J/m^2 for γ. In addition to this, γ_p can be increased by changing the microstructure of the material. After modifications and assumptions, the Griffith's cracking criterion is given by:

$$K' = \frac{\pi\sigma^2 c}{E} \tag{7.50}$$

For the crack extension, $\frac{\pi\sigma^2 c}{E} > K'$.

The most common parameter for the expression of fracture toughness is K_{1c} and is given by:

$$K_{1c} = \sigma_f\sqrt{\pi c} \tag{7.51}$$

Expression (7.51) is valid for sharp cracks in wide plane under normal tensile stress to the crack faces. K_{1c} increases upon increasing σ_f and c. A geometrical factor α is also added to a material of finite width, and hence Eq. (7.51) changes to:

$$K_{1c} = \alpha\sigma_f\sqrt{\pi c} \tag{7.52}$$

For a glass with tensile strength 1.2 GPa, crack length of 8 mm in interior, and fractures at 0.3 GPa, the fracture toughness K_{1c} is given by:

$$\begin{aligned} K_{1c} &= 0.3 \times 10^9\left(3.14 \times 4 \times 10^{-3}\right)^{1/2} \quad 2c = 8 \\ &= 33.62\,\text{MPa}\sqrt{m} \end{aligned}$$

Another important mechanical parameter is hardness, which indicates the resistance of material to the change in shape upon the application of compressive force. Hardness measurement can be a done via scratch testing, rebound, and indentation. Scratch hardness is a measured of how resistant a sample is to fracture/plastic deformation due to friction produced by any sharp object. Usually, Mohs scale is used to obtain scratch hardness especially in mineralogy applications. Rebound hardness/dynamics hardness gives the height of 'bounce' of a diamond tipped hammer, when dropped from a fixed height onto a material. The indentation hardness gives the resistance of sample to material deformation upon constant

compression load from a sharp object. Rockwell, Vickers, and Brinell are common indentation hardness scales. Vicker's hardness (in SI) is given by:

$$\mathrm{HV} = \frac{F}{A} \approx \frac{0.01819F}{d^2} \tag{7.53}$$

where F is in Newton and d is in mm (d is the average length of the diagonal made by the indenter in mm).

7.6 Statistical Analysis of Strength

For glasses/ceramics, the measurement of strength in identical samples may still cause considerable scatter of the data (due to size position and orientation of the cracks causing failure). Usually, a large specimen produces higher degree of flaws than a small specimen under same applied stress due to higher probability of higher stress. Weibull statistics is one such qualitative analysis, which provides insight of the strength mechanisms.

Let us take large number of specimens, such that the probability of measuring strength in the range of σ to $\sigma + d\sigma$ is given by $P(\sigma)\, d\sigma$. According to normalization condition, unit probability of failure at any stress is given by:

$$\int_0^\infty P(\sigma) d\sigma = 1 \tag{7.54}$$

The mean strength can be given by:

$$\bar{\sigma} = \int_0^\infty \sigma P(\sigma) d\sigma \tag{7.55}$$

The deviation of strength is given by:

$$\Delta = \sigma - \bar{\sigma} \tag{7.56}$$

The standard deviation s is root-mean-square deviation and is given by:

$$\text{Variance,} \quad s^2 = \int_0^\infty \Delta^2 \mathrm{d}\,\sigma = \int_0^\infty (\sigma - \bar{\sigma})^2 \mathrm{d}\,\sigma \tag{7.57}$$

Another factor, cumulative probability of failure $P_f(\sigma)$, is defined as the failure occurrence due to stress σ. The relation between $P_f(\sigma)$ and $P(\sigma)$ is given by:

$$P_f(\sigma) = \int_0^{\sigma} P(x)(dx)$$

Furthermore, the cumulative probability of survival is $P_s(\sigma)$ and is given by:

$$P_s(\sigma) = 1 - P_f(\sigma) \tag{7.58}$$

In addition to this, the probability distributions are obtained for large systems. If n values of σ are measured, i.e., $\sigma_1, \sigma_2, \sigma_3, \ldots \sigma_n$, then the mean strength is given by:

$$\bar{\sigma} = \frac{1}{n}\sum_{i=1}^{n} \sigma_i$$

And the variance s^2 can be given by:

$$s^2 = \left(\frac{1}{n-1}\right)\sum_{i=1}^{n} \Delta_i^2 \tag{7.59}$$

(The purpose of using $(n - 1)$ is that one degree of freedom is used for calculating the mean). Usually, strength distribution functions can be categorized as:

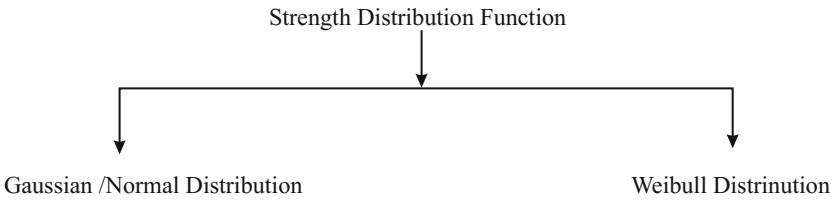

The Gaussian/Normal distribution is given as:

$$P(\sigma) = \frac{1}{s(2\pi)^{1/2}} \exp\left(-\frac{(\Delta)^2}{2s^2}\right) \tag{7.60}$$

Equation (7.60) gives the symmetrical distribution of probability about the mean $\bar{\sigma}$. Anyhow, it must be noted that the Gaussian distribution cannot be corrected for strengths deviating highly from the mean. The values of strength, which deviate much from the mean value, give finite value of occurrence of negative strength. However, the log normal distribution (where log σ is taken instead of σ) provides better fit for better analysis.

For analyzing strength of data, Weibull parameter is better choice and the two-parameter distribution is given by:

$$P_{\mathrm{f}}(\sigma) = 1 - \exp\left[-\left(\frac{\sigma}{\sigma_{\mathrm{o}}}\right)^{m}\right] \tag{7.61}$$

where m is Weibull modulus/Weibull shape parameter and corresponds to the inverse measure of distribution width, and low value of m gives broader distribution. σ_{o} is the Weibull scale parameter, which measures centrality (in fact 68 %, i.e., the probability of failure occurring at or below a stress σ_{o} is 0.63). The mean $\bar{\sigma}$ and standard deviation are given by:

$$\bar{\sigma} = \sigma_{\mathrm{o}}\Gamma\left(1 + \frac{1}{m}\right)$$

where Γ is gamma function and is defined by:

$$\Gamma(x) = \int_0^{\infty} y^{x-1}e^{-y}\mathrm{d}y \tag{7.62}$$

and

$$s^2 = \sigma_{\mathrm{o}}^2\left[\Gamma\left(1 + \frac{2}{m}\right) - \Gamma^2\left(1 + \frac{1}{m}\right)\right]$$

Coefficient of variation C_{v} is given by:

$$C_{\mathrm{v}} = \frac{s}{\bar{\sigma}} \approx \frac{1.28}{m} \tag{7.63}$$

[Equation (7.63) remains valid only up to $m \geq 15$]

The three-parameter Weibull distribution is given by:

$$P_{\mathrm{f}}(\sigma) = \begin{cases} 1 - \exp\left(-\left(\frac{\sigma-\sigma_{\mathrm{u}}}{\sigma_{\mathrm{o}}}\right)^{m}\right) & \sigma > \sigma_{\mathrm{u}} \\ 0 & \sigma \leq \sigma_{\mathrm{u}} \end{cases} \tag{7.64}$$

σ_{u} is the stress level below, which the probability of failure is zero. Usually for brittle ceramics/glasses, $\sigma_{\mathrm{u}} = 0$ because the probability of existence of very large flow is almost zero. The Weibull parameters for lanthanum borosilicate glass are shown in Fig. 7.6. The characteristic Weibull strength $\mathrm{K_o}$ is highest for magnesium lanthanum borosilicate glass, which can be due to its high bond strength. Weibull modulus is highest for barium lanthanum borosilicate glass sample and low for calcium lanthanum borosilicate glass sample, indicating high data dispersion in barium-based glass sample.

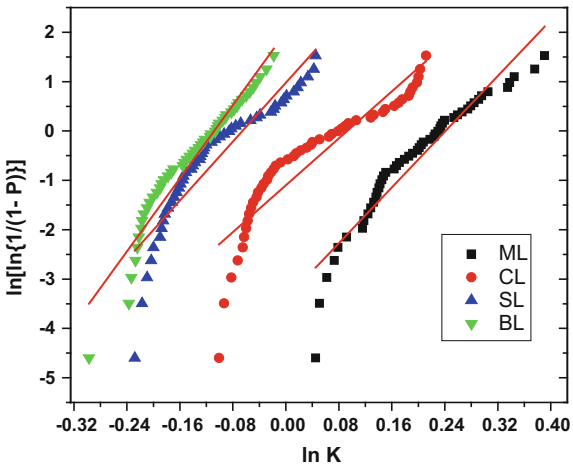

Fig. 7.6 Weibull plots for the indentation toughness of magnesium (ML)-, calcium (CL)-, strontium-, and barium (BL)-based lanthanum borosilicate glasses (Kaur et al. 2012)

For brittle ceramics such as bismuth vanadate, the hardness/flexural strength and TEM of various grain sizes are shown is Figs. 7.7 and 7.8, respectively. The samples have hardness in the range 5.66–7.35 GPa and fracture toughness variation in between 2.8 and 4.3 MPa $m^{1/2}$. An increasing trend of hardness as well as fracture toughness has been observed with increasing dopant concentration, i.e., $x = 0.05$ to 0.2. The toughness value depends upon many parameters such as microstructure variables, starting powder, sintering parameter, and testing techniques. Fracture strength of a brittle material is not a characteristic material property as it depends upon size of flaws and their distribution in the specimen. Fracture strength is generally lowered by defects such as flaws, cracks, or inclusions existing in the sintered sample. However, grain size strongly influences the toughness of ceramics. The finer microstructure may substantially yield higher hardness and fracture toughness. From Fig. 7.8, the highly symmetrical aligned bright spots are observed, indicating crystalline structure. Some superlattice peaks are also observed along both sides of the basal planes. The diffuse streaking between Bragg's spots also indicates superlattice peaks. Patterns with a sharp superlattice are of two types: The first type includes bright superlattice reflections at n/3 along a* and b*. The second pattern has superlattice reflections at n/2 positions along a* and b*. Sometimes the pattern does not have very sharp superlattice diffraction but possesses some area of diffused intensity between the main Bragg spots. This indicates oxygen ordering of any other structural element of short-range type. Other patterns usually indicate long-range order.

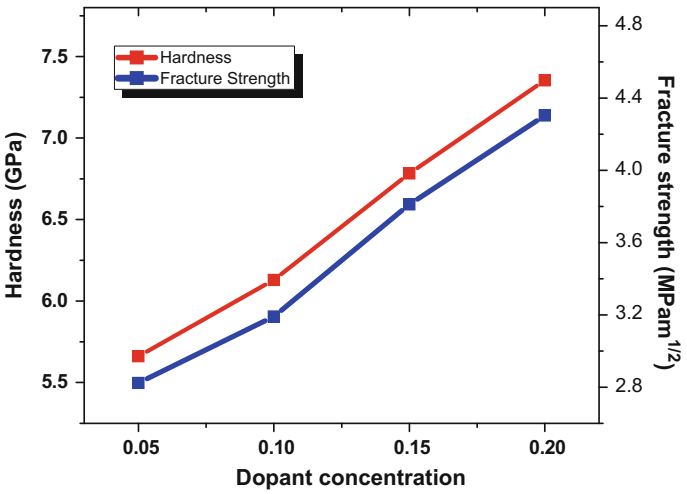

Fig. 7.7 Variation in hardness (H) and fracture strength (K) with concentration of dopants [$Bi_2V_{1-x}Ti_xO_{11-\delta}$ ($0.05 \le x \le 0.2$ in the steps of 0.05)] (Kaur et al. 2014)

Weibull parameters can be defined by least-square fitting or the method of maximum likelihood. The probability of failure of the whole specimen is given by:

$$P_f = 1 - \exp\left[-V\left(\frac{\sigma}{\Sigma_o}\right)^m\right] \tag{7.65}$$

where V is the specimen volume and Σ_o has dimensions of $\left[\text{stress} \times (\text{volume})^{1/m}\right]$ or probability per unit volume $\left(\sigma_o = \Sigma_o V^{-1/m}\right)$.

Taking natural log of Eq. (7.65), we get:

$$\begin{aligned} \ln\left(\frac{1}{1-P_f}\right) &= \ln V + m\ln\sigma - m\ln\Sigma_o \\ &= m\ln\sigma - m\ln\sigma_o \end{aligned} \tag{7.66}$$

By fitting, $\ln\left[\frac{1}{1-P_f}\right]$ as a function of $\ln\sigma$, m, and σ_o can be calculated from the slope as shown in Fig. 7.9. Though σ and m calculations are straightforward but for calculating P_f, a rank is assigned to each strength after sorting into ascending order such that n corresponds to higher strength and one corresponds to lowest strength.

For the ith value, the failure probability is given by:

$$P_f = \frac{i - 0.5}{n} \tag{7.67}$$

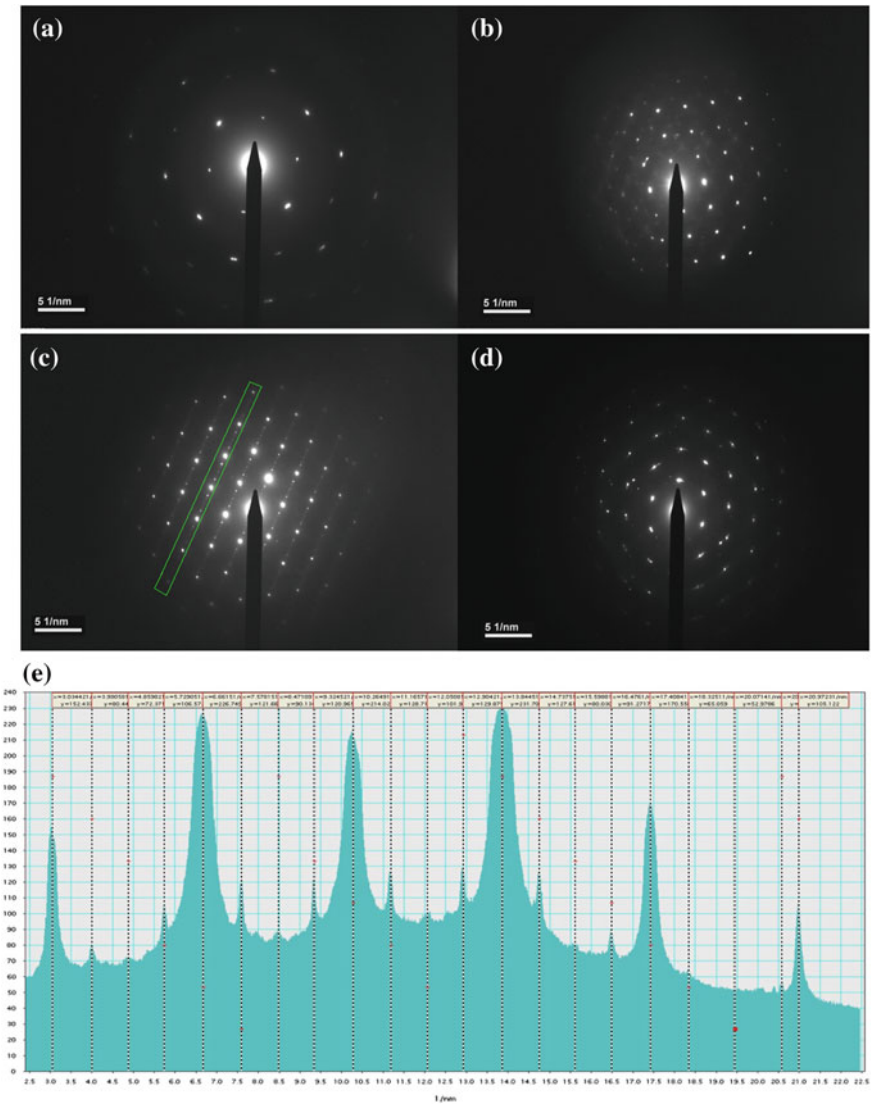

Fig. 7.8 **a–d** SAED patterns for $Bi_2V_{0.95}Ti_{0.05}O_{11-\delta}$ sample for different grains and **e** line profile of atoms along the plane shown in Fig. 7.8c (Kaur et al. 2014)

The specimen size also affects the probability of failure. Let P_f be the probability of failure for volume V_1 with strength σ_1: Volume V_2 with strengths σ_2, then:

$$\ln\left(\frac{1}{1-P_f}\right) = \begin{cases} \ln V_1 + m\ln\sigma_1 - m\ln\Sigma_o & (7.68a) \\ \ln V_2 + m\ln\sigma_2 - m\ln\Sigma_o & (7.68b) \end{cases}$$

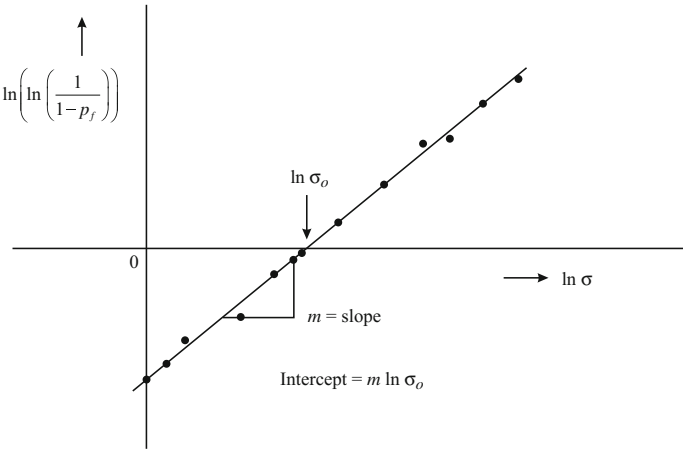

Fig. 7.9 Weibull plot demonstrating the evaluation of Weibull parameters

Subtracting Eq. (7.68a) and (7.68b), we get:

$$\frac{\sigma_1}{\sigma_2} = \left(\frac{V_2}{V_1}\right)^{\frac{1}{m}} = \frac{\overline{\sigma_1}}{\overline{\sigma_2}} \tag{7.69}$$

Hence, the mean strength is higher for smaller specimens and vice versa.

7.7 Relationship Between Glass Transition Temperature (T_g) and Mechanical Properties

Glass transformation range is the temperature region between the equilibrium liquid and frozen solid, such that the enthalpies at both points are known. Usually, the glass transformation occurs over a range of temperature, and hence one particular temperature cannot be regarded as accurate T_g. T_g indicates the approximate temperature at which the supercooled liquid converts to a solid upon cooling. In other words, we can say that the glass solid behaves as viscoelastic solid on heating. T_g is a material property of non-crystalline materials, whereas crystalline material has melting temperature (T_m).

Let us consider a material with 50 % crystalline and 50 % amorphous phases. As it is clear from Fig. 7.10, below T_g, both phases are brittle, whereas above T_g, the amorphous phase is ductile and the crystalline phase is still brittle. The melting occurs at $T > T_m$, for both the phases and the material is regarded as ductile. More precisely, the effect of glass transition and melting temperature can be described via Fig. 7.11.

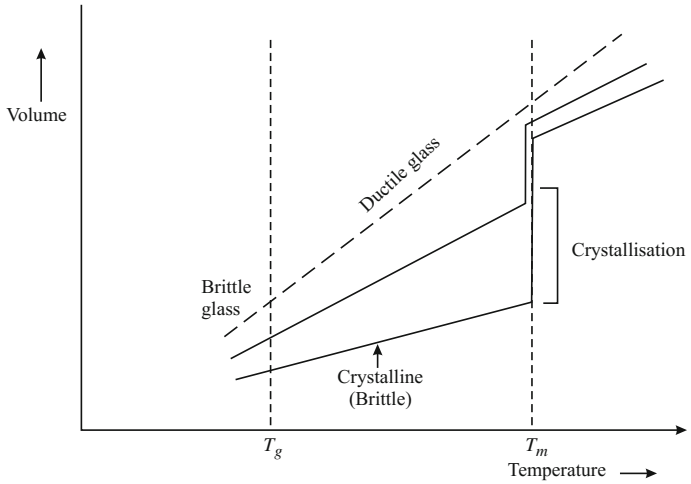

Fig. 7.10 Glass transition and mechanical properties

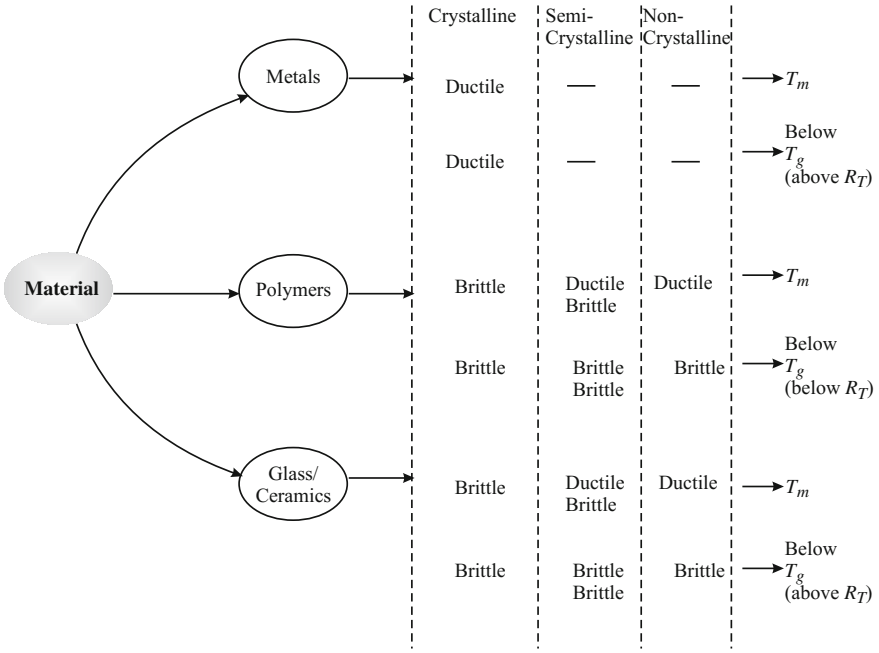

Fig. 7.11 Effect of glass melting and glass transition on the ductile and brittle nature of materials

Any non-crystalline material may possess T_g such as glasses, whereas materials such as ceramics/polymers have semi-crystalline nature. Metals only possess non-crystalline phases, if they are quenched relatively fast. The non-crystalline

materials are brittle below T_g and ductile above T_g. In contrast to this, pure crystalline materials are brittle above and below T_g. The semi-crystalline materials have crystalline and amorphous/non-crystalline phases. Hence, below T_g, the crystalline and non-crystalline phases are brittle, whereas above T_g the non-crystallization phases are ductile.

7.8 Tough and Soft Bioactive Materials

When bioactive inorganic components such as silica and titania are combined with flexible organic components, then bioactive materials with low elastic moduli can be obtained. Figure 7.12 demonstrates the bioactive organic–inorganic hybrid prepared via sol-gel technique.

The inorganic component of these hybrids is derived from tetraethyl orthosilane (TEOS, $Si(OC_2H_5)_4$) and polycondensation of these precursors. The organic component is derived from polydimethyl silane (PDMS) or polytetramethylene ($((C_2H_5O)_3Si(CH_2)_3$ $NHCOO–((CH_2)_4O)_n–CONH(CH_2)_3$ Si $(OC_2H_5)_3)$ terminated with 3-isocyanatopropyltriethoxysilyl. These hybrids have large apatite-forming ability and exhibit elastic modulus almost similar to human cancellous bone. One major drawback of these hybrids is the absence of apatite formation when CaO is not present in the inorganic precursors. However, when calcium salts such as $CaCl_2/Ca(NO_3)_2$ are incorporated into the inorganic precursors, then the mechanical strength is compromised. The PDMS–TiO_2 binary hybrids obtained via sol-gel route with no ability along with Young's modulus/bending strengths equal to human cancellous bone.

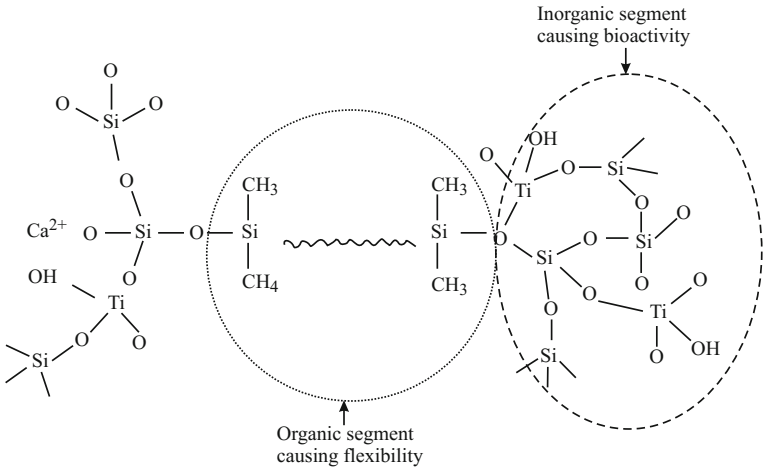

Fig. 7.12 Structure for organic–inorganic hybrid depicting the organic segment and inorganic segment for flexibility and bioactivity, respectively

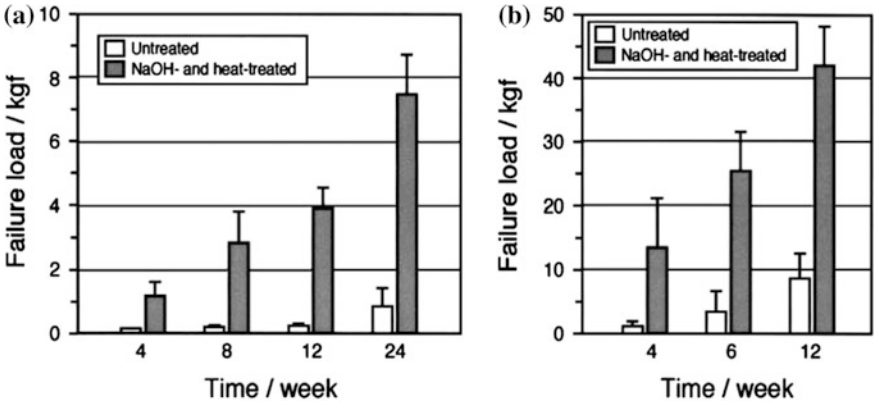

Fig. 7.13 **a** Detaching fracture loads of the untreated and the NaOH- and heat-treated titanium metals implanted in a rabbit tibia (**b**) and the pull-out fracture loads of implantations in a rabbit femur (Kokubo et al. 2003)

On the surfaces of non-bioactive materials, the bioactivity can be induced by either coating their surface by ceramic phases or by forming functional groups, which are able to form apatite-like layer. Among the strong bioactive materials, titanium metals and its alloys have proven to be strong materials, especially for the dental and orthopedic applications. To enhance the bioactivity of titanium-based alloys, their surface is coated with hydroxyapatite layer (HAp), but usually the layer might get delaminated from the substrate after short span of implantation. By preparing titanium and its alloys using NaOH and heat treatments, knee joints, spinal cages, and dental roots are prepared, when tantalum metal is also treated with NaOH and heating, then the fracture toughness and malleability gets increased. Figure 7.13a, b indicates the bone-bonding strength of NaOH/heat-treated Ti metal implanted in rat tibia. Figure 7.14 gives the titanium artificial hip joint, whereas macroporous titanium surface layer is formed by plasma spraying technique.

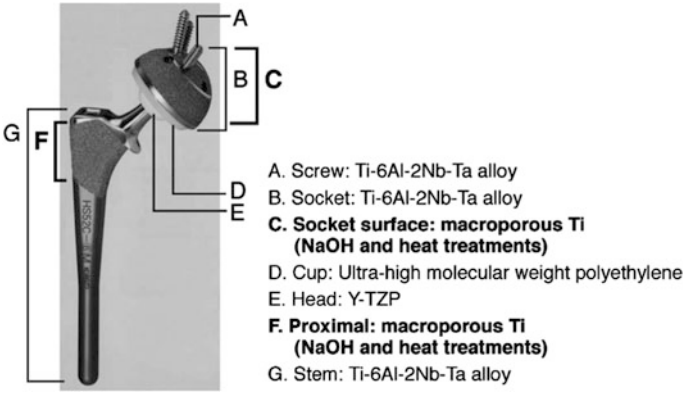

Fig. 7.14 Clinical hip joint system fabricated from titanium metal (photograph courtesy of Kobe Steel Ltd., Japan)

7.9 Mechanical Properties of Bioactive Glass/Ceramics

Bioactive implant shall exhibit strong interfacial bond with hard and soft tissues for clinical uses. Bioactive glasses usually have high brittleness and poor mechanical strength. Mechanical properties of bioactive ceramics and human bones are given in Table 7.1.

Table 7.1 indicates that the bioactive ceramic and A-W Cerabone® (34.4 SiO_2–16.3P_2O_5–44.9CaO–0.5CaF_2–4.6MgO) have higher mechanical properties than Bioglass and hydroxyapatite. Therefore, A-W glass is excellent for vertebral replacements because large compressive strength is required. Bioglass® falls at lowest interfacial load 0.75 ± 1.80 kg as compared to Ceravital with a failure load of 352 ± 1.48 kg, both within the material. As the glass-ceramics exhibit lower toughness than the natural load-bearing bones, the bioactive glass composition shall be modified to yield better mechanical properties. Moreover, emphasis shall be paid to develop alternate materials with superior mechanical and bioactive properties. The bioactive glass/composite should have matching elastic modulus as that of the bone, with increased toughness, strength, fatigue resistance, and bioactivity. Glass-ceramics and composites are better candidates than the glasses in terms of mechanical strength. Usually, the glass-ceramics possess embedded crystalline phases in amorphous glassy matrix. The crystalline phases increase the strength of glass-ceramics and hence endow them with high fracture toughness. The major concern of crystallized glasses is decrease in bioactivity. Kokubo and coworkers reported that A/W glass-ceramics did not form HAp layer when immersed in Tris-buffer solution. But, when the A-W glass-ceramic is exposed to SBF, then polycrystalline HCA layer formation could be seen on its surface. Hench and coworkers found that 40 % crystallinity did not affect the bioactivity. In fact, for 100 % crystallinity, the HCA formation is slowed down [Class A bioactive material still revealed enhanced layer formation]. Figure 7.15 gives the strength and fracture

Table 7.1 Mechanical properties of bioactive glasses and human bones

	Strength (MPa)	Young's modulus (GPa)	K_{1c} ($MPam^{1/2}$)
Glass Bioglass® 45S5	42 (bending)	35	0.6
Glass-Ceramics Cerabone A-W	680 (bending)	118	2
Ceravital		1000	
HAp	115–200 (bending)	80–110	1
Human bones			
Carvillous bone	10–20 (bending)	7–30	2–12
Cortical bone	50–150 (bending)	0.05–0.5	0.1

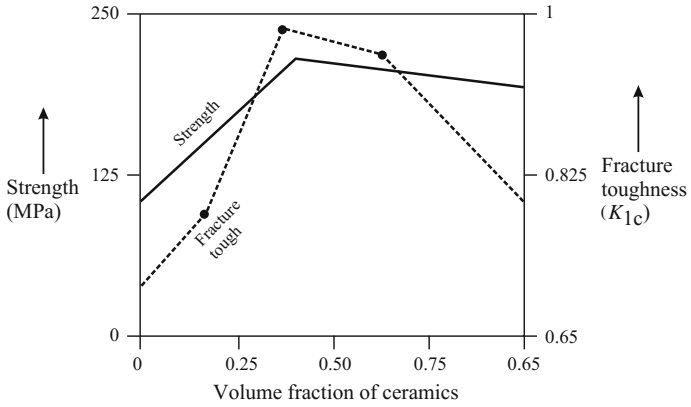

Fig. 7.15 Strength and fracture toughness for SSP6 glass-ceramic

toughness (K_{lc}) for SSP6 glass-ceramic (47.58 SiO_2–24.1Na_2O–22.77Ca–5.53P_2O_5) with varying volume fraction of ceramic.

7.10 Mechanical Strength of Bioactive Composites

When bioactive glasses/ceramics are reinforced with toughened ceramic particles or tough phase such as metal fibers, then the fracture toughness of bioactive ceramics can be improved. Figure 7.16 gives the range of mechanical properties for various biomaterials.

When zirconia is added to the A-W glass-ceramics, then the strength increases from 680 MPa to 703 MPa and the toughness improves to 4 MPa $m^{1/2}$, and hence these composites can be used for the higher load-bearing applications. Polyethylene and polysulphone have been excellent polymer matrices for the bioactive glass composite fabrication. The Bioglass®/Polysulphone composite have higher modulus than the Bioglass®/polyethylene, hydroxyapatite/polyethylene, and A-W glass ceramics/polyethylene composite system. The Bioglass®/polysulphone composite has matching modulus as that of cortical bone. Anyhow, the synthetic composites lag behind somewhat to match the natural bone modulus and it may be due to the fact that the polymer/bioceramic interface is weak. This indicates that the interfacial strength between bioceramic and the polymer shall be taken into consideration as well. Table 7.2 gives the mechanical parameters for polysulfone and polyethylene Bioglass® composites.

A quality index I_q is elucidated on the basis of material properties, so that a criterion can be set for the material performance as that of natural bone I_q is given by:

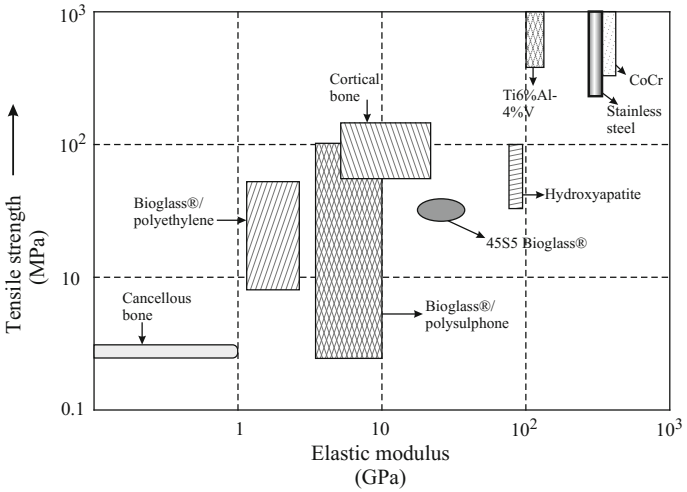

Fig. 7.16 Different biomaterials with range of mechanical properties

Table 7.2 Mechanical properties of Bioglass®/polymer composite

Material	Volume	Tensile strength (MPa)	Young's modulus (GPa)	Fracture strain (%)
Bioglass®/ polyethylene	0	17.89	0.65	>360
	10	14.34	1.05	105.1
	20	12.69	1.12	64
	40	10.75	254	8.5
Bioglass®/polysulfone	0	107	2.5	5
	20	2.5	4.65	2.5
	40	1.5	6.7	1.5
A-W glass ceramic/polyethylene	0	17.89	0.65	>360
	10	17.32	0.96	>180
	20	16.67	1.34	130
	30	14.68	1.83	28.7
	40	14.87	2.84	5.3

$$I_q = \frac{\text{Fracture toughness} \times \text{Index of bioactivity} \times \text{Tensile strength}}{\text{Young's Modulus}} \tag{7.70}$$

The I_q value for a material to be equivalent to cortical bone shall be ≈500, whereas for the cancellous bone, I_q is ≈7.5.

7.11 Effect of Bioactive Glass Composition on the Mechanical Parameters

The processing conditions, composition, precursors, and particle size affect the mechanical properties and bioactivity to a huge extent. The apatite-mullite (A-M) and apatite-wollastonite (A-W) were heat treated (A-M and A-W) [bioceramic salts were processed using indirect SLS route] to obtain 50–60 % dense structure with open porous structures required for bone ingrowth and vascularisation by Dalgarno and coworkers. Figure 7.17 gives the flexural strength of samples with different particle sizes and porosity along with standard cancellous and cortical bone characteristics.

It is evident that upon mixing 45–90 μm A-M with phosphate glass, almost double strength is obtained such that it becomes equivalent to the strength of cancellous bone. A-W materials are still stronger than the A-M and cancellous bone. The A-M and A-W are implants into the metaphysic of a tibia of six mature male rabbits using aseptic surgical techniques. After 4-week implantation, the bone has grown into porous implant structure (Fig. 7.18).

Hence, both materials have shown ability to bond rapidly to bone, indicating that the processing route did not alter bioactive response of commerce available A-W glass. In addition to this, the SLS-synthesized A-W has excellent mechanical properties in line with those depicted by the cortical bone. Hsu and coworkers studied the mechanical properties of three different compositions of calcium phosphate bioceramic following immersion in Ringer's solution/distilled water. Table 7.3 lists the samples with three different ratios of α-TCP/β-TCP/HAp.

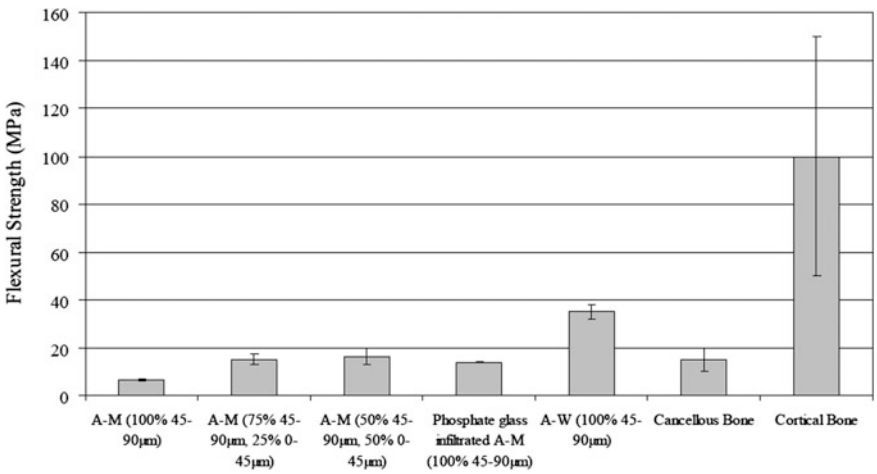

Fig. 7.17 Flexural strength of various glass composites (Dalgarno et al. 2005)

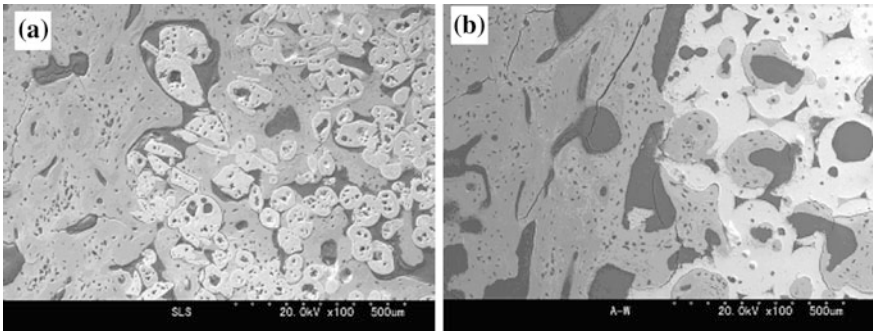

Fig. 7.18 SEM of **a** implanted A-M material and **b** implanted A-W material (Dalgarno et al. 2005)

Table 7.3 Calcium phosphate bioceramic composition (%)

Sample name	α-TCP	β-TCP	HA
COMP1	2.31	21.73	75.96
COMP2	20.81	41.98	37.21
COMP3	0	96.72	3.28

The four-point bend testing was calculated using the formula:

$$\sigma = \frac{3F(l - l_1)}{2bd^2} \tag{7.71}$$

where F is applied force (N), b is sample width, d is sample thickness, l and l_1 represent span of the support loaders and separation of the loading span (in mm). Figure 7.19 depicts the four-point bend strength after immersion in Ringer's solution at pH 7.2 and distilled water at pH 4.0 for almost 26 weeks.

COMP1 (with highest HAp content have greatest strength, whereas COMP3 with minimum HAp of 3.28 % have lowest strength irrespective of their time of immersion). COMP3 show reduction in strength in distilled water, but remain almost same in Ringer's solution. The compressive strength also followed the same trend, i.e., COMP1 > COMP2 > COMP3. With the increase in immersion time, the bending strength also increases for COMP1, but no obvious trends for COMP2 have been observed. No observable decrease in compressive strength was obtained for samples aged in Ringer's solution/distilled water for up to 26 weeks.

Though hydroxyapatite is the most common osteoconductive material used for the bone tissue engineering, dense HAp has lower fracture toughness and higher Young's modulus than the human cortical bone. Recently, forsterite (Mg_2SiO_4) is being investigated as a new bioceramic due to its superior mechanical properties than the calcium phosphate ceramics. Anyhow, the mechanical strength of forsterite is not enough as per load-bearing applications, and hence research is focused on

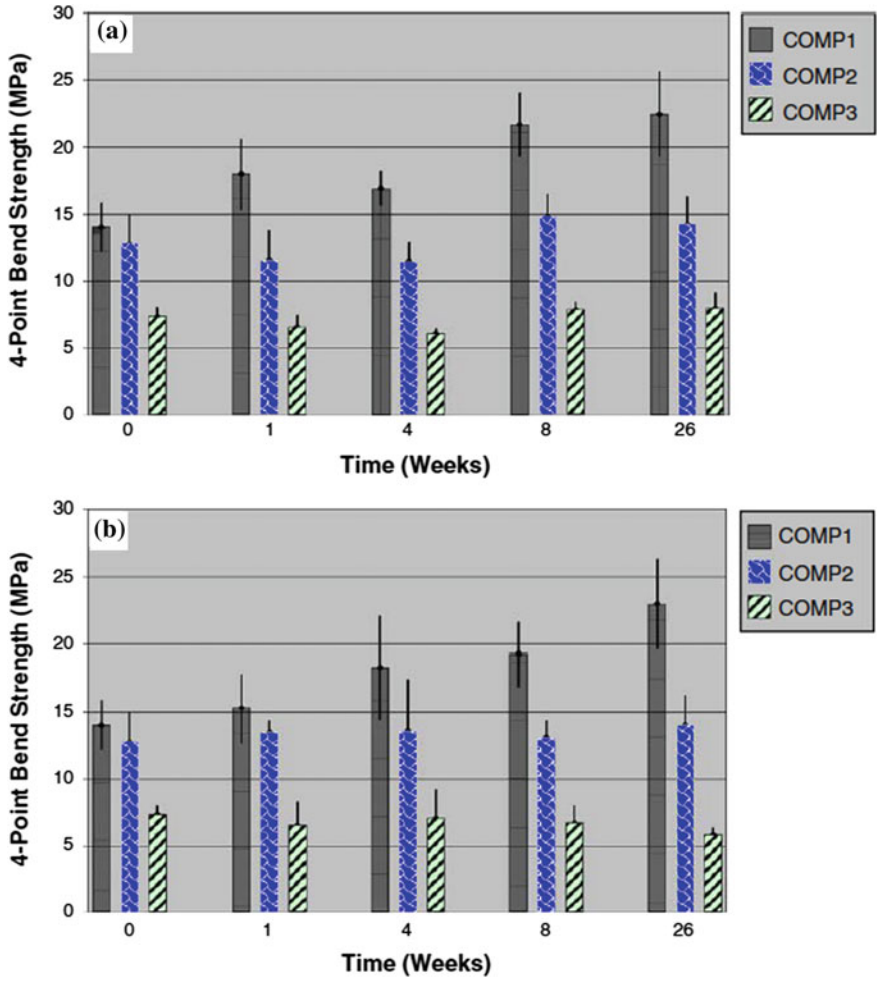

Fig. 7.19 Change in four-point bend strength **a** after immersion in Ringer's solution at pH 7.2 and **b** distilled water at pH 4.0, for 26 weeks

developing nanostructured materials. Webster and coworker designed first nanophase ceramics with improved osteointegrative properties. Kim and coworkers obtained improved biocompatibility, osteoblast adhesion, and proliferation for the nanostructured materials due to high fraction of grain boundaries. Nanosized forsterite exhibits better apatite formation ability as compared to the forsterite microparticles. Kharaziha and coworkers prepared forsterite nanopowder via sol-gel methodology and mechanical alloying method. The fracture toughness was determined using the Nilihara's formula:

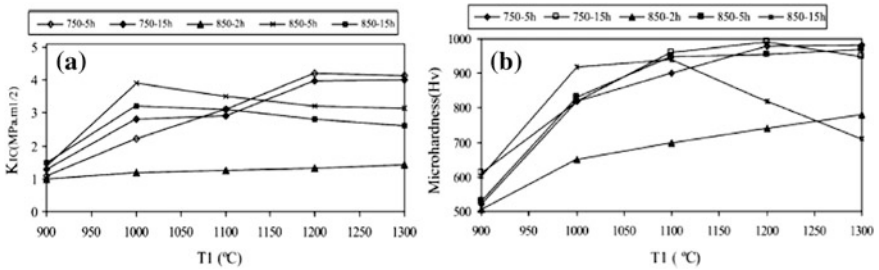

Fig. 7.20 Fracture toughness and Vicker's hardness for the forsterite as function of sintering temperature (Kharaziha et al. 2010)

$$K_{1c} = 0.203\left(\frac{c}{a}\right)^{-3/2} H_{\gamma} a^{1/2} \tag{7.72}$$

where H_{γ} is the hardness and c is the crack length measured from indentation centre to half of the average length of both indent diagonals. Figure 7.20a, b gives the fracture toughness and Vicker's hardness of forsterite bulk samples as a function sintering temperature. The hardness and fracture toughness are 0.55 ± 15 H_{γ} and 3.2 ± 0.25 MPa $m^{1/2}$, respectively. Kharaziha and coworker's work is based on the preparation of forsterite nanopowder using two-step sintering method, i.e., heating the samples up to 600 °C and holding for 60 min at this temperature, followed by heating and holding the samples at 0–900 °C for 6 min. The concluding treatment is cooling down to 750–850 °C and holding for at least 2–15 h at this temperature. The forsterite prepared via the sol-gel induces lattice cytocompatibility and sinterability.

In normal sintering method, the green compacts are heated at a pre-determined rate and held at this temperature until required densification is attained. This causes reduction in the fracture toughness due o continuously increasing grain size. The two-step sintering (TSS) method yields the optimization of mechanical strength and grain size as green compacts are heated to high temperatures and then held at this temperature to reduce pore size up to subcritical scale followed by cooling for completing the sintering process. Through this method, the fully dense forsterite ceramic with small grain size (120–150 nm) and very high fracture toughness of 4.3 MPa $m^{1/2}$ have been obtained [HAp have $K_{1c} \approx 0.75$–1.2 MPa $m^{1/2}$]. The forsterite synthesized by TSS also promoted G292 osteoblast cell adhesion spread and growth on the forsterite ceramic. For low concentrations of 6.25–50 mg/ml (for MTT assay), the cells proliferated more actively after 7-day culture. Ni and coworkers synthesised fully dense forsterite from coarse grain forsterite powder with relative density of 92.9 % by uniaxially pressing at 10 MPa and then cold isostatic pressing at 200 MPa. The samples were sintered at 1450 °C for 8 h and maximum K_{1c} value was 2.4 MPa $m^{1/2}$.

Bioactive glass scaffold have been unreactive nucleus for the bone repair due to their ability to observed bond formation with the surrounding tissue. Bioactive glass

45S5 have the tendency to density and cannot be pulled to the fibers. 45S5 BG have inherent brittleness, and hence the porous structure can collapse affecting the bone tissue ingrowth negatively. Xu and coworkers modified 45S5 composition by adding it to new novel composition CBS (19.5 B_2O_3–48.2CaO–30.2SiO_2–2.1P_2O_5 wt%) prepared by sol-gel methodology, i.e., 45S5/xCBS powder was prepared with x = 0, 5, 10 and 20 wt%. The compressive strength of 45S5 BGC was significantly improved for $x \leq 10$ % of CBS. The maximum compressive strength was observed in the temperature range of 850–900 °C, and above 950 °C the strength reduced significantly. The compressive strength of 45S5/CBS10 porous scaffolds sintered at 850–900 °C, showing a slight decrease in strength after immersion in TRIS. As the sintering temperature is increased to 1000 °C, the highest compressive strength is observed for $(45S5/CBS10)_{TRIS} < (45S5/CBS10)_{SBF}$. A boron-rich composition (> 10 %) possesses a melting temperature at ∼960 °C as demonstrated by Yang and coworkers. Hence, the intergranular liquid-phase CBS nanoparticles are full-phase formation of CBS (at 850–900 °C). Above sintering temperature of 800 °C, 45S5 crystallizes to $Na_2Ca_2Si_3O_9$ crystalline phase. At higher sintering temperatures, the thermal expansions mismatch may influence the mechanical integrity of 45S5/CBS integrity. Hence, the CBS-assisted sintering is favorable at low temperatures before the full densification occurs. As shown in Fig. 7.21a, b, the densification is reduced of the biphasic composite due to the presence of liquid phase and viscous flow.

The silicate-based bioactive glass 13–93 exhibits modified 45S5 composition, low tendency to crystallize, and more facile viscous flow than the 45S5 glass composition 13–93 can be pulled into fibers and can be sintered without denitrification to obtains porous scaffolds. Fu and coworkers synthesized 13–93 scaffolds using polymers form replication method, and Fig. 7.22 gives the stress–strain behavior of the as-fabricated 13–93 scaffolds.

The valleys and peaks in the curve correspond to the progressive breaking of the solid particulate network. During the initial compression, the glass shows elastic

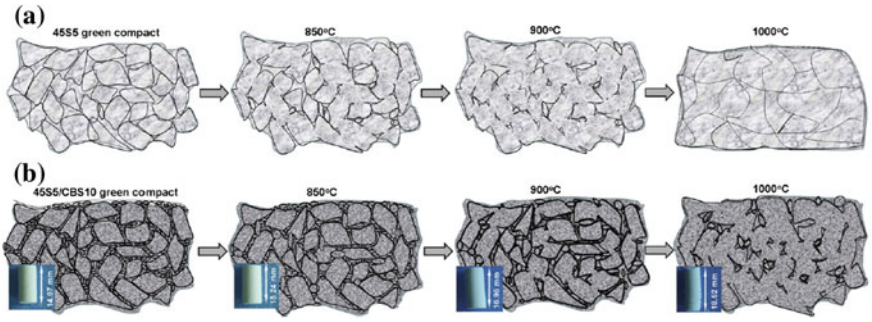

Fig. 7.21 Proposed microstucture of **a** 45S5 and **b** 45S5/CBS10 green compact at different temperatures (Xu et al. 2014)

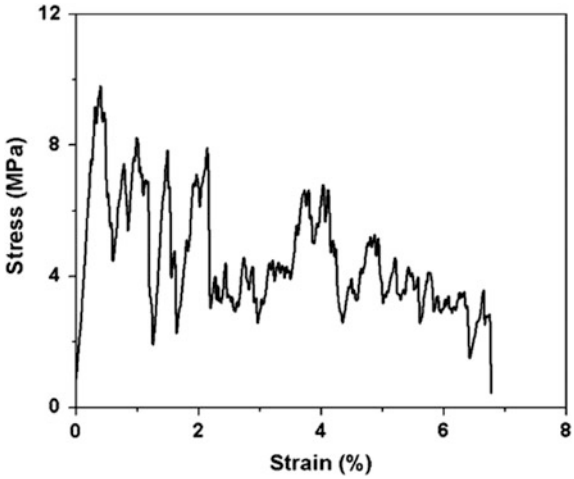

Fig. 7.22 Stress–strain curve for 13-93 BG under compression (Fu et al. 2008)

behavior, followed by a decrease in stress attributed to the fracture of some struts in solid network. Struts were fractured upon increasing the strain and hence micro-cracks propagated through the scaffold, causing the stress to drop down to zero. The modulus is 3.0 ± 0.5 GPa, and the average compressive strength is 11 ± 1 MPa (≈compressive strength of trabecular bone, i.e., 2–12 MPa). The mechanical behavior is assumed using Gibson and Ashby model, which gives the compressive strength of ceramic/glass as:

$$\frac{\sigma}{\sigma_s} = C\left(\frac{\rho}{\rho_0}\right)^{3/2} \frac{1+\left(\frac{t_i}{t}\right)^2}{\sqrt{1-\left(\frac{t_i}{t}\right)^2}} \tag{7.73}$$

$$\Rightarrow \frac{\sigma}{\sigma_s} = C(1-P)^{3/2} \frac{1+\left(\frac{t_i}{t}\right)^2}{\sqrt{1-\left(\frac{t_i}{t}\right)^2}} \tag{7.74}$$

where P is the porosity of foam, ρ and ρ_0 are densities of foam and fully dense solid, σ_s is the modulus of rupture of struts of foam, and t_i/t gives the ratio of central void size of struts to the strut size. For brittle foams, $C \approx 0.2$ and the compressive strength is predicted to be 2–15 MPa as $t_i/t = 0$, for fully dense struts and $P = 0.83$ –0.84. 13–93 scaffolds yield mechanical strength higher than the HAp constructs of similar porosity and polymer ceramic composites (prepared by TIPS method). 45S5 bioactive glass constructs yield a compressive strength of 0.3–0.4 MPa for porosity 70–77 %, 0.2 MPa for porosity 86 %, respectively, and is 1 MPa for 93 % porosity in HAp constructs coated with apatite-wollastonite glass-ceramic. HAp constructs prepared from rapid prototyping and gas foaming techniques yield compressive

strength of 17 MPa (73 % porosity) and 30 MPa, respectively. The elastic modulus of 13–93 glass scaffold is 3 ± 0.5 GPa and is obtained by:

$$\frac{E}{E_o} = A\left(\frac{\rho}{\rho_0}\right)^n = A(1-P)^n \tag{7.75}$$

where A and n are constants dependent upon the microstructure, and E and E_o correspond to elastic modulus of porous material and fully dense solid. For dense solid $A = 1$, whereas for open network, $A = 0.3$, n lies in between 1–4 and have value 2 for open cell structure.

Liu and coworkers prepared grid-like porous scaffolds of 13–93 glass using robocasting technique (Fig. 7.23a). The as-fabricated scaffold possesses grid-like microstructure with pore width of 150 ± 10 μm in the z-direction of deposition. The Weibull plots of flexural and compressive strength data (Fig. 7.23b, c) indicate the linearity of data except at low and high stress values. The compression strength and elastic modulus are 86 ± 9 MPa and 13 ± 2 GPa, respectively, whereas the flexural strength and flexural modulus values are 11 ± 3 MPa and 13 ± 2 GPa, respectively. The 13–93 scaffolds were tested under a cyclic stress of 1–10 MPa, indicating their fatigue like $> 10^6$ cycles in air, but when tested in phosphate-buffered saline, the mean fatigue like is not significantly affected. The compressive strength and modulus decreased rapidly after two-week implantation

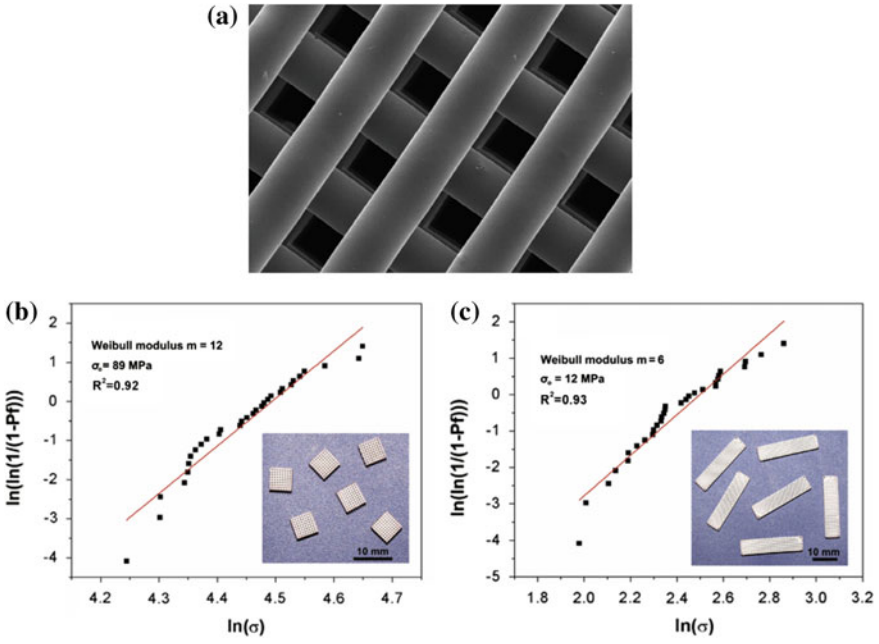

Fig. 7.23 **a** SEM of 13-93 glass scaffolds prepared by robocasting method, **b** Weibull plot of compressive strength and **c** Weibull plot of flexural strength for 13-93 BG scaffolds (Liu et al. 2013)

of the scaffolds in rat subcutaneous sites. The in vitro and in vivo strength decreased to 8.5 ± 5 MPa and 35 ± 4 MPa after two-week implantation.

After 12-week implantation, in vivo, the strength scaffolds decreased to 16 ± 4 MPa, whereas in SBF, it was 52 ± 10 MPa. Interestingly, the scaffolds implanted in vivo exhibit elastoplastic response after 2–4 weeks, and instead of fracturing, they still maintained the integrity and became more deformable. The fracture toughness of 13–93 prepared by robocasting is 0.48 ± 0.04 MPa $m^{1/2}$, which is much lower as compared to that of the human cortical bone (2–12 MPa $m^{1/2}$). The compressive strength decreased in vivo, which can be explained using following assumption, i.e., power low relation

$$\sigma_t = \sigma_o \left(1 - \frac{x}{a}\right)^n \tag{7.75}$$

where σ_t is the scaffold compressing strength at time t (σ_o = 86 MPa for the as-fabricated 13–93 scaffold), a and x are radii of glass filaments and thickness of converted layer, respectively. n = 6.1 gives the best fit to Eq. (7.75), and hence the degradation of compressive strength can be predicted in vivo if the conversion rate of bioactive glass to HAp is known.

Bibliography

Webster JJ, Siegel LW, Bizies R (1998) An in vitro evaluation of nanophase alumina for orthopeadic/dental applications In: Lolesss RZ, Lelyernc JP (eds) Bioceramis/Proceedings of the 11th International symposium on ceramics in Medicine, World Scientific, New York, pp 273

Kim TN, Balakrishnan A, Lee BC et al (2008) In vitro fibroblast response to ultra fine grained titanium produced by a sever plastic deformation process. J Mater Sci Mater Med 19:553

Ni S, Chou L, Chang J (2007) Preparation and characterization of forsterite (Mg_2SiO_4) bioceramics. 33:83–88

Ni S, Chang J, Chou L (2008) In vitro studies of novel CaO-SiO_2-MgO system composite bioceramics. J Mater Sci Mater Med 19(1):359–367

Kharaziha M, Fathi MH (2010) Improvement of mechanical properties and biocompatibility of forsterite bioceramic addressed to bone tissue engineering materials. J Mech Behav Biomed Mater 3:530–537

Kaur G, Pandey OP, Singh K (2012) Effect of modifier field strength on optical, structural and mechanical properties of lanthanum borosilicate glasses. J Non-Cryst Solids 358:2589–2596

Kaur G, Kumar M, Arora A, Pandey OP, Singh K (2011) Influence of Y_2O_3 on structural and optical properties of SiO_2 –BaO – ZnO – xB_2O_3 - (10-x) Y_2O_3 glasses and glass ceramics. J Non-Cryst Solids 357:858–863

Kaur G, Singh K, Pandey OP, Homa D, Scott B, Pickrell G. Mechanical, UV-Vis and TEM assessment of titania doped bismuth vanadate oxides. Bull Mater Sci

Hsu YH, Turner IG, Miles AW (2009) Mechanical properties of three different compositions of calciumphosphate bioceramic following immersion in Ringer's solution and distilled water. J Mater Sci Mater Med 20:2367–2374

Yang X, Zhang L, Chen X, Sun X, Yang G, Guo X, Yang H, Gao C, Gou Z (2012) Incorporation of B_2O_3 in CaO-SiO_2-P_2O_5 bioactive glass system for improving strength of low-temperature co-fired porous glass ceramics. J Non-Cryst Solids 358:1171–1179

Fu Q, Rahaman MN, Sonny Bal B, Brown RF, Day DE (2008) Mechanical and in vitro performance of 13–93 bioactive glass scaffolds prepared by a polymer foam replication technique. Acta Biomater 4:1854–1864

Kokubo T, Kim H-M Kawashita M (2003) Novel bioactive materials with different mechanical-properties. Biomaterials 24:2161–2175

Liu X, Rahaman MN, Hilmas GE, Sonny Bal B (2013) Mechanical properties of bioactive glass (13-93) scaffolds fabricated by robotic deposition for structural bone repair. Acta Biomater 9:7025–7034

Dalgarno KW, Wood DJ, Goodridge RD, Xiao K, Ohtsuki C, Genever P, Dyson J (2005) Mechanical properties and biological responses of bioactive glass ceramics processed using indirect SLS

Chen ZQ, Thompson ID, Boccaccini AR (2006) 45S5 Bioglass_-derived glass–ceramic scaffold for bone tissue engineering. Biomaterials 27:2414–2425

Callcut S, Knowles JC (2002) Correlation between structure and compressive strength in a reticulate glass-reinforced hydroxyapatite foam. J Mater Sci Mater Med 13:485–489

Kim HW, Knowles JC, Kim HE (2005) Hydroxyapatite porous scaffold engineered with biological polymer hybrid coating for antibiotic vancomycin release. J Mater Sci Mater Med 16:189–195

Jun I-K, Song J-H, Choi W-Y, Koh Y-H, Kim H-E (2007) Porous hydroxyapatite scaffolds coated with bioactive apatite–wollastonite glass–ceramics. J Am Ceram Soc 90:2703–2708

Dong J, Kojima H, Uemura T, Kikuchi M, Tateishi T, Tanaka J (2001) In vivo evaluation of a novel porous hydroxyapatite to sustain osteogenesis of transplanted bone marrow-derived osteoblastic cells. J Biomed Mater Res 57:208–216

Jones JR, Ehrenfried LM, Hench LL (2006) Optimising bioactive glass scaffolds for bone tissue engineering. Biomaterials 27:964–973

Zheng X, Wen G, Song L, Huang XX (2008) Effects of P_2O_5 and heat treatment on crystallization and microstructure in lithium disilicate glass ceramics. Acta Mater 56:549–558

O'Donnell MD (2011) Predicting bioactive glass properties from the molecular chemical composition: glass transition temperature. Acta Biomater 7:2264–2269

Watts SJ, Hil RG, O'Donnell MD, Law RV (2010) Influence of magnesia on the structure and properties of bioactive glasses. J Non-Cryst Solids 356:517–524

Wachtman JB, Rogercannon W, Matthewson MJ (2009) Mechanical properties of ceramics, 2nd edn

Boyd D, Towler MR (2005) The processing, mechanical properties and bioactivity of zinc based glass ionomer cements. J Mater Sci Mater Med 16:843–850

Larrañaga A, Diamanti E, Rubio E, Palomares T, Alonso-Varona A, Aldazabal P, Martin FJ, Sarasua JR (2014) A study of the mechanical properties and cytocompatibility of lactide and caprolactone based scaffolds filled with inorganic bioactive particles. Mater Sci Eng C 42:451–460

Kübler J, Gauckler LJ (2010) Mechanical properties of ceramics or mechanical behavior of brittle materials of brittle materials. Materials Science II, Ceramic Materials, Chapter 6, Part 5

Xu S, Yan X, Chen X, Shao H, He Y, Zhang L, Yang G, Gou Z (2014) Effect of borosilicate glass on the mechanical and biodegradation properties of 45S5-derived bioactive glass-ceramics. J Non-Cryst Solids 405:91–99

Thompson ID, Hench LL (1998) Mechanical properties of bioactive glasses, glass-ceramics and composites. J Eng Med 1998 212:127

Li HC, Wang DG, Hu JH, Chen CZ. Crystallization, mechanical properties and in vitro bioactivity of sol–gel derived Na_2O–CaO–SiO_2–P_2O_5 glass–ceramics by partial substitution of CaF_2 for CaO

Rahaman MN, Day DE, Sonny Bal B, Fu Q, Jung SB, Bonewald LF, Tomsia AP (2011) Bioactive glass in tissue engineering. Acta Biomater 7:2355–2373

Ponsonnet L, Reybier K, Jaffrezic N, Comte V, Lagneau C, Lissac M, Martelet C (2003) Relationship between surface properties (roughness, wettability) of titanium and titanium alloys and cell behaviour. Mater Sci Eng C 23:551–560. (doi:10.1016/S0928-4931(03)00033-X)

Wirth C, Comte V, Lagneau C, Exbrayat P, Lissac M, Jaffrezic-Renault N, Ponsonnet L (2005) Nitinol surface roughness modulates in vitro cell response: a comparison between fibroblasts and osteoblasts. Mater Sci Eng C 25:51–60. (doi:10.1016/j.msec.2004.06.001)

Schakenraad JM, Busscher HJ, Wildevuur CR, Arends J (1988) Thermodynamic aspects of cell spreading on solid substrata. J Cell Biophys 13:75–91

Hallab N, Bundy K, O'Connor K, Clark R, Moses R (1995) Cell adhesion to biomaterials: correlations between surface charge, surface roughness, adsorbed protein and cell morphology. J Long-Term Effects Med Implants 53:209–231

Sepulveda P, Jones JR, Hench LL (2002) Bioactive sol-gel foams for tissue repair. J Biomed Mater Res A 49:340–348

Mukherjee DP, Das SK (2013) SiO_2–Al_2O_3–CaO glass–ceramics: effects of CaF_2 on crystallization, microstructure and properties. Ceram Int 39:571–578

Delben JRJ et al (2009) Synthesis and thermal properties of nanoparticles of bioactive glasses containing silver. J Therm Anal Calorim 97:433–436

Liu H, Webster TJ (2007) Nanomedicine for implants: a review of studies and necessary experimental tools. Biomaterials 28 354–369

Andersson OH, Karlsson KH, Kangasniemi K, Yli- Urpo A (1988) Models for physical properties and bioactivity of phosphate opal glasses. Glastech Ber 61:300–305

Gross U, Kinne R, Schmitz HJ, Strunz V (1988) The response of bone to surface active glass/glass–ceramics. In: Williams DF (ed) CRC critical reviews in biocompatibility. Boca Raton, CRC Press p 2

Kaur G, Pandey OP, Singh K, Homa D, Scott B, Pickrell G (2013) A review of bioactive glasses: their structure, properties, fabrication, and apatite formation. J Biomed Mater Res A 102:254–274

Kaur G, Sharma P, Kumar V, Singh K (2012) Assesment of *in-vitro* bioactivity of SiO_2-BaO-ZnO-B_2O_3-Al_2O_3 glasses: an optico-analytical approach. Mater Sci Eng C 32(7): 1941–1947

Kaur G, Pickrell G, Sriranganathan N, Kumar V, Homa D (2016) Review and the state of the art: sol-gel or melt quenched bioactive glasses for tissue engineering. J Biomed Mater Res B Appl Biomater 104(6):1248–1275. doi:10.1002/jbm.b.33443

Kaur G, Pickrell G, Pandey OP, Singh K, Chudasama BN, Kumar V (2016) Combined and individual Doxorubicin/Vancomycin drug loading, release kinetics and apatite formation for the CaO-CuO-P_2O_5- SiO_2- B_2O_3 mesoporous glasses. RSC Adv 6:51046–51056

Kaur G, Pickrell G, Kimsawatde G, Allbee H, Sriranganathan N (2014) Synthesis, cytotoxicity, and hydroxypatite formation in 27-Tris-SBF for sol-gel based CaO-P_2O_5-SiO_2-B_2O_3-ZnO bioactive glasses. Sci Rep. doi:10.1038/srep04392

Chapter 8
Influence of Preparation Techniques on the Properties of Bioactive Glasses

Gurbinder Kaur

Usually two techniques are followed for the glass fabrication, i.e., sol-gel and melt-quenching. Melt-quenching provides glasses with high mechanical properties such as enhanced hardness, flexural strength, and fracture toughness. In contrast to this, the sol-gel method endows the glass with uniform pore size, homogeneity, high surface area, and enhanced bioactive formation. When the sol-gel glasses are prepared using CTAB, P123, or F127 structure-directing agents, the mesopores are formed in the glass network, which are used for the drug loading for targeted drug delivery. Hence, the effect of preparation techniques deeply influences the properties of bioactive glasses such as cytotoxicity, density, pore volume, surface area, zeta potential, porosity, mechanical properties, and apatite formation. This chapter is intended to provide a brief overview of the properties, which are affected by the preparation techniques.

8.1 Density, Porosity, and Surface Area

For the tissue engineering applications, the diameter of the interconnecting pore apertures is the deciding parameter of the pore network. For the tissue growth and vascularization process, the modal interconnected pore diameter should be greater than 100 μm. Li and coworkers observed that substitution of CaF_2 for CaO exhibits remarkable influence on the sol-gel glass apparent porosity and volume density. The considerable change in density and porosity of CaF_2-substituted glass should be attributed to the higher relative molecular mass of CaF_2. CaO-based 45S5 glass exhibits porosity of 51.16 %, whereas CaF_2-doped 45S5-F glass possesses higher density of 3.88 g/cm^3 and porosity of 29.53 %. In addition to this, CaF_2 enhances crystallization, thereby increasing the crystallized phase content of the glass, which ultimately leads to the increase in the glass density. The sol-gel 63S composition yields the size of particles between 126 and 470 nm in physiological saline. Major 40 % of the particles possess an average size of 216.1 nm, 30 % particles have

G. Kaur, *Bioactive Glasses*, Series in BioEngineering,
DOI 10.1007/978-3-319-45716-1_8

particle size of the order 471.8 nm, and other 30 % have an average diameter of 126.5 nm. The bioactive glass particles obtained were relatively agglomerated physiological saline with an average specific surface area of 224 m^2/g. In contrast to this, the theoretical density and particle size of the 63S glass particles is 1.08 g/cm^3 and 25 nm (particle size obtained from the adsorption measurements), respectively.

sol-gel-synthesized BGMP (60 % SiO_2–36 % CaO–4 % P_2O_5) has lower silica content with skeletal density of 2.46 g/cm^3. The specific surface area of BGNP (bioactive glass nanoparticles synthesized by the sol-gel route) is 533.5 m^2/g, which is almost seven times higher than the specific surface area of BGMP. BGMP has the pore volume of 0.38 cm^3/g, whereas BGNP exhibits pore volume of 1.11 cm^3/g. In contrast to this, the modal pore diameter for BGMP and BGNP was more or less same and no significant difference could be seen. Therefore, BGNP can be regarded to exhibit potential for the hard tissue engineering applications especially 3-D macroporous scaffolds. When the bioactive particles are immersed in SBF, the zeta potential of the BG particle surfaces varies with the immersion times (Fig. 8.1) and can be explained as follows:

(a) First, the silanols (Si–OH) are formed on BG (bioactive glass) surface upon soaking in the SBF. The calcium ions are released from the surface by means of an exchange with H_3O^+, Na^+, and K^+ ions in SBF, which ultimately causes the formation of –OH groups. Si–O–Si bonds break down and silanol formation occurs due to the loss of soluble silica to solution in $Si(OH)_4$, form.

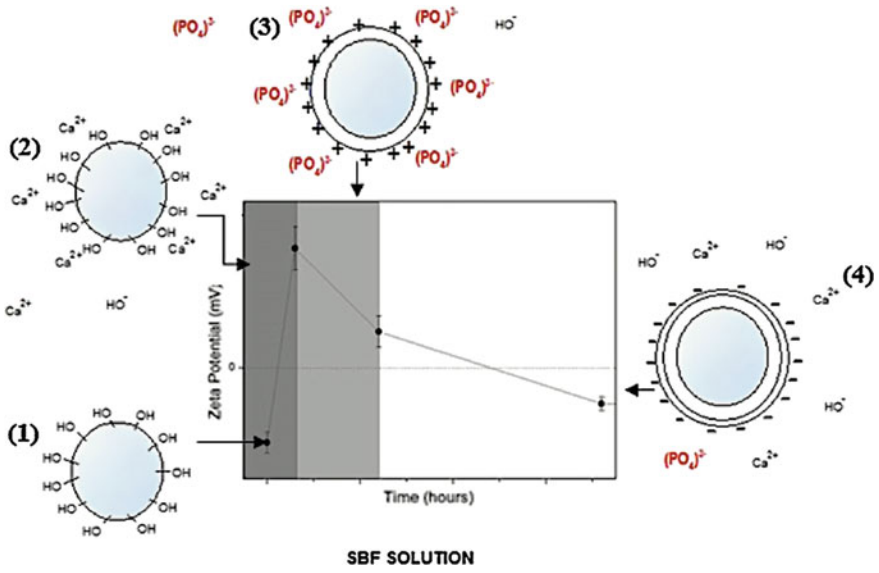

Fig. 8.1 Relationship between the surface structure change and the zeta potential of BG particles during the HAp formation process in SBF (Oliviera et al. 2013)

(b) Local supersaturation of Ca^{2+} ions is established and Si–OH groups are formed on the glass surface. These silanol groups have a tendency to endow the surface with negative charges.
(c) With the increase in soaking duration time, a selective combination of OH^- charged surface and the Ca^{2+} ions from the SBF solution occurs. This combination results in the accumulation of calcium ion accumulate on the surface. Gradually, the surface would gain an overall positive charge.
(d) The concentration of HPO_4^{2-} is much higher than that of PO_4^{3-}, which favors the migration of PO_4^{3-} ions from the bulk to the surface of the glass along with the incorporation of HPO_4^{2-} ions in the BG surface. Furthermore, the incorporation of ions results in calcium deficiency, causing the surface to become negatively charged.
(e) The phosphate ions (PO_4^{3-} and HPO_4^{2-}) and the calcium ions combine to form amorphous calcium phosphates ($Ca_3(PO_4)_2$ and $CaHPO_4$, which spontaneously convert to the apatite via incorporation of CO_3^{2-} and OH^- species from the solution to form hydroxyl carbonate apatite (HCA) layers.
(f) Once apatite formation initiates, more and more layers of crystals grow by consuming calcium and phosphate ions from the SBF

Courtheoux and coworkers obtained homogenous porosity in the range of 50–100 nm for sol-gel glasses with low Zn content. The low Zn-doped glasses exhibit an increase in the specific surface area, considered to be beneficial as it provides more nucleation sites for the formation of phosphocalcic precipitates. For the high dopant concentration, larger pore size between 50 and 400 nm was obtained attributed to the glass network modification due to the incorporation of Zn atoms in the SiO_2–CaO structure.

It has been reported that the surface areas of Zn- and Mg-containing sol-gel bioactive glasses lie in the range of 55–206 and 126–274 m^2/g, respectively. For CaO–SiO_2–P_2O_5–ZnO, CaO–SiO_2–P_2O_5–MgO, and CaO–SiO_2–P_2O_5–ZnO–MgO sol-gel glass compositions, the density values of 1.32, 1.39, and 1.68 g/cm^3, respectively, were obtained by Erol and coworkers. The highest porosity of 14.5 % was reported for Zn-doped glasses, whereas for magnesium-based glass it was 7.1 % only. The porosity and density values of Mg-containing glass samples increased to 7.8 % and 2.16 g/cm^3, respectively, upon immersing in SBF solution, which further increased the HAp layer formation on the glass surface. Due to the higher density values for Mg-doped glasses and their high bioactivity, it was depicted that the thickness of the HAp layer of Mg-containing glass was higher than that of Zn-containing glass. In addition to this, among all the sol-gel-derived bioactive glass samples, the highest surface area of 221 m^2/g was possessed by Mg-containing glass sample, which is due to the incorporation of MgO into the glass composition.

Melt-quenched D-Alk-B glass with density 2.6 g/cm^3 was obtained by Liu and coworkers, which was further used for the scaffold formation. S1, S2, S3, and S4

scaffold compositions were prepared with relative porosity of 86.7, 80.4, 73.3, and 67.7 %, respectively. With the increase in D-Alk-B glass content, the decrease in porosity was observed, whereas an increasing trend was shown by the relative density ratio of green body. The condition of suitable pore size for osteoconduction was satisfied by interconnected 3-D porous structure whose pore size lies in the range of 200–300 μm.

Jones and coworkers used sol-gel-derived 70S30C bioactive glasses to fabricate bioactive glass scaffolds having a bulk density of 0.25 g cm^{-3} and modal interconnected pore diameter of approximately 100 μm by foaming method. BJH analysis from the desorption branch of the nitrogen sorption isotherms and its variation with respect to the sintering temperature (T_s) was used to obtain the textural porosity pore size distributions. The modal textural pore diameter of 17.1 nm lying in the mesoporous range (2–50 nm) was yielded by the foams sintered at 600 °C. As the sintering temperature was increased up to 700 °C, the modal textural pore diameter was increased to 17.5 nm. Surprisingly, it was detected that pore diameter was reduced such that it does not lie within the detection limits of BJH analysis when the temperature T_s was increased up to 1000 °C. The macropores with a maximum diameter of 400 μm appear when T_s is increased to 800 °C, which still appear to be well connected. As the T_s increases from 700 to 1000 °C, a decrease from 122.7 to 12.8 m^2/g in the specific surface area of the foams was reported. The porosity for 58S and 58S4Z and 58S0.5Z sol-gel glasses as well as glass-ceramics is obtained by Du and coworkers. As comparing to glasses, glass-ceramics possessed lower porosities. The porosity for 58S and 58S4Z was reported higher than that of 58S0.5Z and porosity higher than 40 % was exhibited by all the glass samples. The porosity 12.6 % is reported for 58S glass-ceramic as compared to the 58S0.5Z glass-ceramic (17.7 %) and 58S4Z glass-ceramic (32.9 %). Fredholm and coworkers observed that as the calcium content is replaced by the strontium for the SiO_2–P_2O_5–CaO–Na_2O–SrO glass composition, density of the glasses increased from 2.71 to 3.10 g cm^{-3}. Kaur and coworkers obtained that the lowest particle size is given by CP20 sol-gel glass, whereas highest size is possessed by CP10. An increase of density was resulted when glass to glass ceramics was changed due to devitrification upon heat treatment. High cross-linking density in the network of CP5 glass/glass-ceramics was indicated due to its high density. Furthermore, mitigation of glass subsequently filling gaps or pores is lead by the crystallization process and which further increases the density. Conclusively, for sol-gel-prepared glasses, the particle size and textural porosity as well as specific surface area are higher. Murphy and coworkers deduced that for the Ca–Sr–Na–Zn–Si melt-quenched glass composition, and the surface area is between 4 and 16 m^2/g. BT114 glass has the highest surface area of 15.94 m^2/g, whereas for lowest surface area of 4.39 m^2/g is deduced for BT115 glass.

After incubation in MEM medium used for osteoblasts cultures, Aina and coworkers estimated the change in specific surface area of H, HZ5, and HZ20 melt-quenched bioactive glasses as function of time. The initial specific surface areas obtained for H, HZ5, and HZ20 glass were 2, 0.8, and 2.6 m^2/g, respectively. The high surface area for zinc-free glasses was clearly represented by an increase in

specific surface area of H, HZ5, and HZ20 by 133, 35, and 18 m^2/g, respectively. The same group observed that the reference glass without zinc (H glass) undergoes a very high increase in surface area during the initial hours of reaction. After 1 h of contact with Tris solution, the surface area reaches the value of 160 m^2/g, which becomes 200 m^2/g after 6 h. Along with this, it was observed that a much smaller surface area is developed by zinc-containing glass compared to zinc-free composition. After 1 week of contact with the Tris solution, the area becomes 52 m^2/g for HZ5 and 25 m^2/g for HZ20. The surface area of HZ5 and HZ20 becomes 43 and 24 m^2/g, respectively, after 1 week of contact with the Dulbecco's modified Eagle's medium (DMEM). This surface area evolution indicates that glasses dissolute faster in Tris medium than in DMEM solution. The slow rate of glass dissolution is due to the high ion concentration and amino acids in the DMEM solution.

8.2 Mechanical Properties

Bretcanu and coworkers used porous inorganic matrix of GC-Bioglass and coated it with the polymer P3HB, which strengthened the GC-Bioglass scaffold structure to fabricate porous composites. These prepared composite scaffolds exhibited the compressive strength up to 1.5 MPa, that is, almost twice of pristine GC-Bioglass scaffolds (up to 0.4 MPa). Vitale-Brovarone and coworkers fabricated foam-like GC-CEL2 scaffolds, which exhibits marvelous biocompatibility with osteoblasts and compressive strength up to 1 MPa. Furthermore, by successfully optimizing the processing conditions, the same research group obtained scaffolds with even higher strength of 5–6 MPa. Similarly, by altering the processing conditions and parameters, the strength of 13-93B2 glass scaffolds got enhanced up to 10 MPa (pore content of 70 vol%). Liu and coworkers observed the significant material degradation of 13-93B2 in phosphate solution, which resulted in decrease of scaffold strength from 6.2 to 2.8 MPa after soaking for 15 days. During the fabrication of GC-Bioglass scaffolds, Wu and coworkers used rice husk as a pore former. The porosity content was an issue for the scaffold integrity during implantation, in spite of comparable mechanical strength of the GC-Bioglass scaffolds to that of spongy bone. Porous bone grafts require >50 vol% of porosity content, whereas the GC-scaffolds could yield the porosity of 45 vol% only.

Cannillo and coworkers fabricated a new glass BioK from the traditional bioglass which involves the full substitution of Na_2O with K_2O. Bellucci and coworkers used PE burning method with BioK powder to produce scaffolds with porosity 70–78 vol%. Their mechanical strength was between 0.14 and 0.18 MPa, despite their porosity comparable to that of spongy bone, which is totally unsuitable for the implantation.

Recently, for the sol-gel glass-ceramics, our results have shown better mechanical properties than their contemporary glasses. As compared to other glasses whose hardness lies between 4.42 and 4.83 GPa, the hardness of glass-ceramics lies between 59 and 87 GPa. The glass-ceramics exhibited highest

flexural strength up to 113.28 MPa, whereas the flexural strength of glasses was between 6.44 and 7.33 MPa. Boyd and coworkers reacted polyalkenoic acid (PAA) with the melt-quenched calcium–zinc–silicate glasses (glasses A and B) to obtain the glass ionomer cement (GIC). The compressive and flexural strengths of these cements are influenced by the concentration and molecular weight of PAA as well as by the maturation time. In previous studies, similar trends have been observed for the aluminum-based GICs, though their strength was more than the GIC obtained by reacting polyalkenoic acid (PAA) with glasses A and B. Mean compressive strength of 57 MPa is possessed by AE9/50 wt% cement after 30 days, which is almost comparable to the compressive strength of acrylic orthopedic cement Simplex P (67 MPa). The high flexural strengths of these cements are due to the presence of labile ionic bonds between the carboxylate groups on the PAA and Zn^{2+} ions.

Li and coworkers studied the influence of geometrical parameter t (strut thickness)/l (strut length) on the strength of scaffold. Usually, the decrease in l of the sintered scaffold is due to the greater shrinkage of heavily coated green bodies, whereas the strut length of green bodies can be the same as employed templates which consequently increases the geometrical parameter leading to the enhancement of compressive strength. The compressive strength of human cancellous bone has been almost 4–12 MPa and the scaffold S4 (with highest glass concentration of 68.4 % melt-quenched glass D-Alk-B) yielded a compressive strength of about 10 MPa. The maximum compressive load of 768 N is obtained due to the compact microstructures of S4 scaffolds.

Sol-gel method was used to fabricate and characterize the boron-rich, phosphorus-low $CaO–SiO_2–P_2O_5–B_2O_3$ at considerably lower temperatures than required for conventional melting method. The BG-Bx-derived BGC materials can be sintered up to 950 °C, and at above 800 °C sintering temperature crystallization occurred and glass-ceramics with wollastonite and calcium borate were formed. By doping B, the melting temperatures of the BG-Bx were lowered to ∼950 °C, and the size range of the BG-Bx particles can be of 200–900 nm. Even in fully crystallized BG-Bx, crystallization decreased the kinetics but did not inhibit the development of HCA layer, and the biodegradation rate of the BG-Bx was based on the boron content. The sintering temperature of BGC porous constructs can be lowered by improved thermal and biological properties of boron-rich, phosphorus-low quaternary system, for improving bone regeneration and defect repair in situ. BGB20-reinforced 45S5 BGC having compressive strengths of 5 and 10 % was nearly 1.43-fold and 4.15-fold as compared to that of unreinforced porous 45S5 BGC sintered at 850 °C are shown in Fig. 8.2a. The primary reason for this is that further densification is obtained by the high temperature, which also softens the BG-B20 particles. The fracture face of the porous samples sintered at 700 °C shows that the nanoscale BG-B20 particles (∼250 nm in size) were embedded by the 45S5 particles (2–8 μm in size), but those which were sintered at 850 °C were confusingly large 45S5 particles (Fig. 8.2a, inset). To damp and

coalesce the 45S5 particles, the BG-B20 nanoparticles turn into a viscous liquid, while to increase rigidity, there is progressive microstructure coarsening and bonding. Similarly, without doping BG-B20, the flexural strength of the BGCs composed of 45S5 and BG-B20 showed an increase compared with 45S5 (Fig. 8.2b). The considerable bending strength ($\sim$3.21 MPa) is exhibited for long, rod-like 10 % BG-B20-reinforced 45S5 BGC which was more than fourfold that of single 45S5 BGC (0.67 MPa). It could be deduced that a significant improvement in the mechanical properties of 45S5 BGC is caused by the addition of a small amount of low melting point BG.

The biocompatibility of melt-quenched bioglass compositions ($46.1SiO_2$–$26.9CaO$–$24.4Na_2O$–$2.6P_2O_5$) is obtained by Bang and coworkers, where CaF_2 and MgF_2 would substitute for the Na_2O. Ca^{2+}- and Mg^{2+}-doped glasses increase the mechanical properties but decrease the thermal expansion coefficient. The higher values for flexural strength (141 MPa) and Vickers hardness (5.6 GPa) is shown by glass with 10 % MgF_2 as compared to the conventional bioglass composition with flexural strength of 57 MPa and Vickers hardness 4.6 GPa, respectively. As diopside crystalline phase provides higher mechanical strength compared to the wollastonite or anorthite phase for 10 MF glass-ceramic, this glass shows higher values for flexural strength and Vickers hardness.

Jones and coworkers showed that the compressive strength of 70S30C sol-gel glasses is also increased with the increase in the sintering temperature (T_s), i.e., at softening temperature of 600, 700, 800, and 1000 °C, the compressive strength of 0.36, 0.51, 2.26, and 2.25 MPa, respectively, is obtained for 70S30C glasses. Compressive strength between 2 and 12 and 2.4 MPa is recorded for human trabecular bone and the porous ceramic bone implant, respectively. The compressive strength of 2.26 MPa was achieved for the scaffolds due to the reduction in the textural porosity and hence an increase in the density of the macropore walls at T_s of 800 °C.

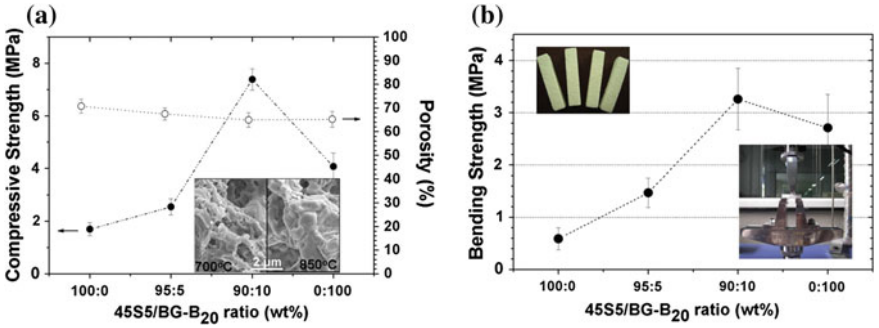

Fig. 8.2 **a** Compressive strength, porosity (*insets* represent SEM images of the porous materials sintered at 700 and 850 °C), **b** flexural strength of the BG-B20-reinforced 45S5 BG porous materials heat treated at 850 °C (*insets* represent the cuboid samples and three-point bending test images) (Yang et al. 2012)

8.3 Cytotoxicity Assays

By inducing hydroxyapatite (HAp) precipitation in physiological fluids such as simulated body fluid (SBF), bioactive glasses show the biological response. By studying their cellular responses in the tissue reaction or the functional replacement, the tissue regeneration can be improved chemically and biologically around implants. For the regulation of phosphate metabolism, bone formation, osteoblast differentiation and mineralization, involves an enzyme named alkaline phosphatase (ALP). When animal-derived cells, human osteoblasts, and rat mesenchymal stem cells are grown on the bioactive glass, the ALP activity gets enhanced. The presence of silicon in glasses is the most important stimulating factor in osteoblast ALP production. The cytotoxicity is due to surface modifications and depends on the composition of glasses.

To check the viability and cytotoxicity of the glass samples, techniques such as MTT and MTS are used, because these methods usually evaluate cytotoxicity for bulk structures indirectly using the extraction of materials. The continuous monitoring of the metabolic activity of living cells is allowed by isothermal micro-nanocalorimetry (IMNC) technique by measuring the heat production or consumption rate in the l W range with a constant temperature calorimeter. Doostmohammadi and coworkers had shown the growth and proliferation of chondrocytes by isothermal micro-nanocalorimetry (IMNC) technique in contact with 63S bioactive glass particles as well as bone-derived hydroxyapatite by rather than using conventional methods such as MTT and MTS for checking the viability and cytotoxicity. IMNC with yeast and cultured human chondrocyte cells was used to evaluate direct cytotoxicity of these well-known bioceramics. To evaluate different biological effects (inhibition of cellular growth and cytotoxicity) induced by the materials, the yeast Saccharomyces cerevisiae as an experimental model was used, which can be manipulated easily. Although a single cell processes with metazoan systems, it is true eukaryote that share fundamental cell. This provides complementary approaches and insights into functions of larger eukaryotes by offering a unique tool to the cell biologist. Cytotoxicity screening has been demonstrated for the usefulness of eukaryotic organisms such as yeast in materials. To determine the amount of bioceramic particles needed for the experiments with human cells, yeast model assay can be used as a predeterminer tool.

Uo and coworkers studied the dissolution of glasses due to which change in pH and ion concentration was studied, which further was the cause of the cytotoxicity of the glasses. A decrease in pH was reported due to high dissolution rates, which increases the concentration of the ions in the media, resulting in high cytotoxicity. In the $NaO_{0.5}$–CaO–$PO_{2.5}$ system, the dissolution rate and cytotoxicity were directly dependent for all the glass samples. Due to ion dissolution of the glasses containing more than half of $PO_{2.5}$, the pH of the media became acidic. The pH of the media was unaffected, even though the glasses containing 50 mol% of $PO_{2.5}$ changed the ion concentration of the media.

The cytotoxicities of the samples were low for these compositions except for 0C50P. Due to the extremely high dissolution rate of the sample, high cytotoxicity of 0C50P sample could be related to the change in ion concentration. High dissolution rates cause a decrease of pH or an increase of the ion concentration of the media; that is why the cytotoxicity was nearly related to the dissolution rate of the glasses. It was difficult to determine the initial dissolution rate exactly and in both distilled water and SBF, the CaO-free samples (0C80P, 0C70P, 0C50P) showed extremely high dissolution rates. After cytotoxicity tests, it shows the optical microscope image of the pulp cells (Fig. 8.3a–d). The morphology of cells that extend over the dish surface was not changed in the samples 10C50P (Fig. 8.3b) and 20C50P (Fig. 8.3c), which showed low cytotoxicity as compared to the control (Fig. 8.3a). The morphology of pulp cells was changed to a shrunk form for 20C50P, which contained no CaO and showed high cytotoxicity as shown in Fig. 8.3d.

Oliviera and coworkers worked in the presence of sol-gel bioactive glass nanoparticles [BGNP] and found that the mitochondrial osteoblast viability was higher by 27 and 16 % after a period of 6 and 24 h, respectively, rather than bioactive glass microparticles (BGMP). The bioactivity of NP is enhanced by fast release of Ca and P (due to higher surface-to-volume ratio) and hence at the early stage of incubation, their higher cell viability is resulted. The ALP activity in

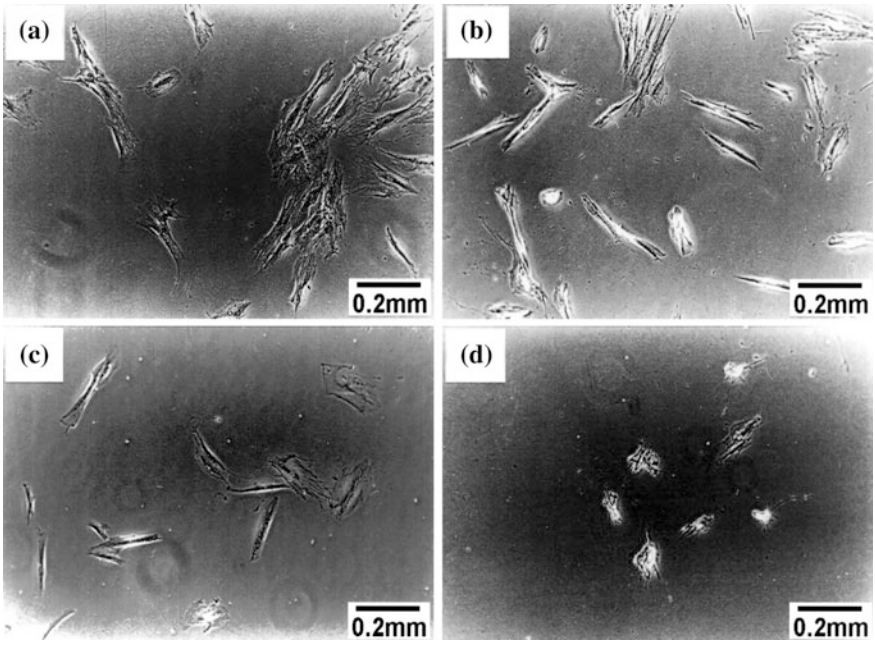

Fig. 8.3 Optical microscope observation of pulp cells after cytotoxicity tests: **a** control, **b** 10C50P, **c** 20C50P, **d** 0C50P (Uo et al. 1998)

osteoblast cells yielded higher values as compared to the controls indicating the tendency of BG particles to induce bone regeneration and upregulation of gene expression in osteoprogenitor cells due to fast dissolution of ions. During the initial stages of incubation, the higher ALP activity and stimulating effect on osteoblast proliferation is attributed to the increased HAp nucleation on the nanoparticle surface. Luz and coworkers seeded L929 cells with their leachables and assessed the effect of sol-gel bioactive glass nanoparticles on the cell metabolic activity. For all the glass samples, an increase in viability from day three to day seven with a slight decline in the cellular metabolic activity is shown by MTT assays. For all of the studied conditions, high biocompatibility is ensured by non-toxicity of the materials at different pH and heat treatments.

Du and coworkers applied MTT assay to obtain the concentration-dependent proliferation profile of osteoblasts and at the dilution ratio of 1:320, the osteoblast differentiation value was 65.3 % higher than that of negative control. After 3 days of incubation, the cell densities showed little increase, whereas after only 1 day of culture the osteoblasts exhibited good attachment on all samples. Furthermore, the cell osteoblast density on glass ceramic increased with increase in ZnO content as compared to that on glass samples; i.e., highest osteoblast proliferation had been shown by 58S4Z sol-gel glass ceramic. Oh and coworkers assessed that higher cell growth on day 3 is exhibited by the zinc-containing sol-gel glasses at low and medium granule concentration of 3 and 10, respectively. The cell viability of the glass compositions granules became similar as that of the blank control when affected by the glass due to increased culture period. In the presence of various glasses, alkaline phosphatase (ALP) activity of the mesenchymal stem cells (MSCs) cultured showed an increased level at day 14 and at granule concentration of 10, which further enhances with the increase in the zinc concentration. The obtained expression of the osteogenic marker bone sialoprotein (BSP) by using immunofluorescence staining is produced by the cells in the presence of bioactive glass granules. As the addition of glass granules concentration enhances the expression of BSP, more prominent immunofluorescence stain is exhibited by samples containing glass granules than in control. The red-colored spots were observed near the bioactive glass granules, which represented the expressed BSP, when compared to the blank control.

Kaur and coworkers found through MTS assays the toxicity reduces with crystallinity (Fig. 8.4). At low concentrations, above control level, the pristine glasses also give cytotoxicity. At concentration 7.81 μg/mL, the almost non-toxic glass samples are the sol-gel glass sample CP5 (5 mol% P_2O_5) and CP15 (15 mol% P_2O_5). At concentration 1.95 μg/mL, all the glasses show non-toxic behavior except CP20 (20 mol% P_2O_5). Furthermore, at higher concentrations, the glass ceramics are non-toxic indicating the non-toxicity of phases formed in them. At concentration of 1.95 μg/mL, the maximum viability of 72.3, 94.2, and 81.4 % by CP, CP10, and CP20, respectively. In contrast to this, even at higher concentrations, the glass-ceramics tend to exhibit higher cell viabilities; i.e., live cell viability given by CP10 and CP20 glass-ceramics is 95 % at 125 μg/mL and 90 % at 500 μg/mL, respectively.

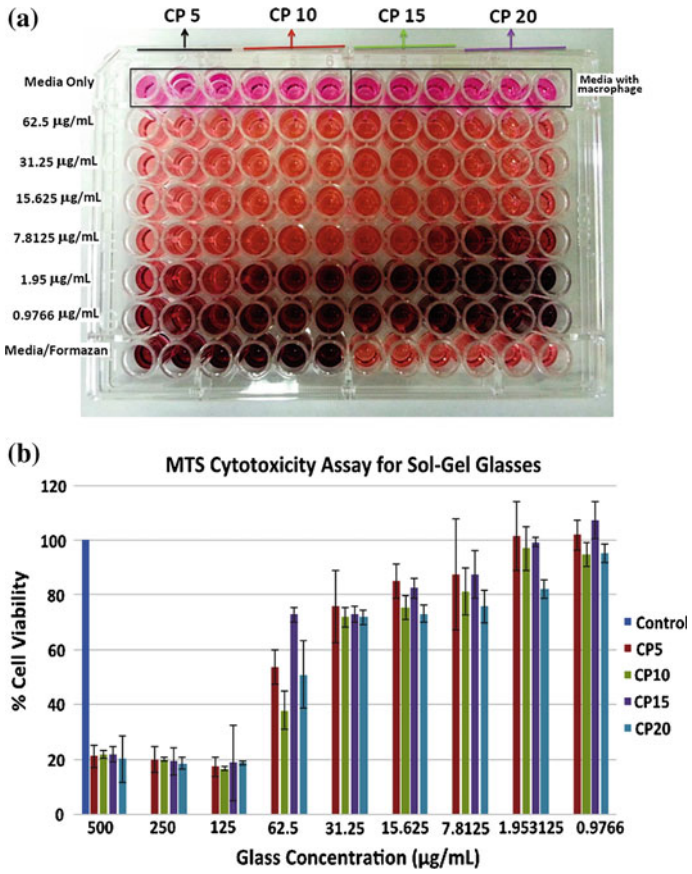

Fig. 8.4 **a** Plates for cytotoxicity assays of sol-gel glasses and **b** MTS cytotoxicity assay results for glasses at different concentrations for murine cells culture (Kaur et al. 2014)

The results of Oudadesse and coworkers showed that after soaking in different medium concentrations (L-929 fibroblast cells), 46S6 and 46S6Zn10 melt-quenched glass samples with particle size between 500 and 600 µm were non-toxic (Fig. 8.5). After soaking in different concentrations of the medium (10, 50, and 100 %), both bioactive glass samples with particle size between 500 and 600 µm show no sign of toxicity. After 72 h of soaking, the cell viability of all samples diluted or not is of about 89 and 100 % as compared to the control.

Furthermore, non-toxic behavior is exhibited by both the glasses with particle size between 40 and 63 µm, and at 10 % dilution and dilution of 50–100 %, the cell viability decreases to 10–15 % compared to the control sample. This infers that due to the higher ionic exchanges between the glass particles and the extracted environment, the reactivity of the particles with 40–63 µm size is more. Cytotoxicity is due to the higher release of ions consecutive to the surface area increase, not

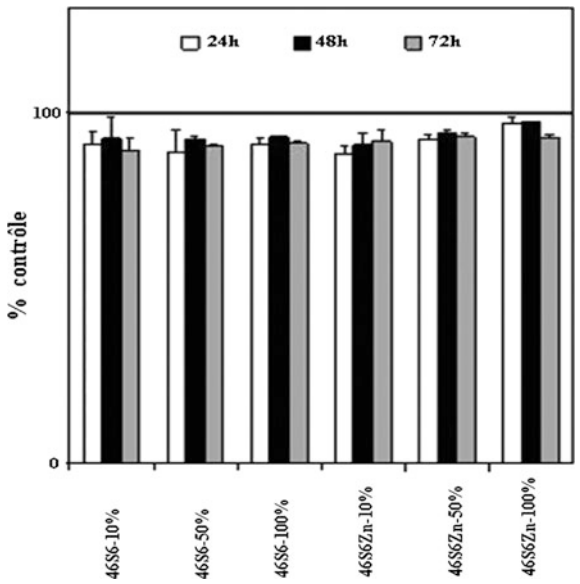

Fig. 8.5 MTT test of glass powders with grain sizes of 500–600 μm (Oudadesse et al. 2011)

because of Zn addition in the glass matrix. The composition and higher reactivity of compounds is related to cytotoxicity. Surface modifications resulted in this phenomenon, and the reactivity of the particles with 40–63 μm size is justified by this explanation. The ionic exchanges between particles and the extracted environment are more important. The higher cytotoxicity is resulted due to higher exchange of ionic concentrations.

Aina and coworkers studied that after 24-h incubation of MG-63 human osteoblast cells with melt-quenched HZ glasses, there was a significant decrease in the intracellular thiols. Glutathione (GSH), which scavenges reactive oxygen species and free radicals, is the major thiol redox buffer in the cell. Due to the oxidation of glutathione to intracellular glutathione disulfide (GSSG), glutathione reductase–Ellman reagent recycling assay indicates decrease in intracellular GSH for HZ glasses. HZ20 activated pentose phosphate pathway (PPP), which did not occur during coincubation of bioglass with ascorbate or EDTA. On the other hand, zinc-free H glass does not affect GSH/GSSG ratio, PPP metabolism, and thiols level. With increasing zinc content of the glass, Western blot experiments indicated the amplified expression of heme oxygenase-1 (HO-1) in MG-63 cells.

Upon the incorporation of strontium, Abou Neel and coworkers studied the cellular response of the melt-quenched glasses and obtained increased number of cells attached to the surface in strontium-containing glasses. For the glass containing 1 mol% of strontium, highest degradation rate and decrease in the pH of the surrounding medium were observed, whereas strontium-free glasses possessed lowest degradation rate. Abou Neel and group have demonstrated the surface-free energy (SFE) to understand the cell adhesion and proliferation for all the samples. The wettability of the surface influences the biological properties of biomaterials as

well as their cellular response. Lower fractional polarity (FP) as an indication of better fibroblast proliferation is demonstrated in the previous studies, whereas low SFE materials exhibit poor cell spreading. The highest total SFE and the lowest FP is possessed by strontium-free glass CNP and glass with 5 % strontium CNPSr5. Furthermore, the cell viability studies revealed that no cells after 24 h of culture for CNP and CNPSr5 glasses attributed to their high degradation rate.

The viability of cells exposed to phosphate-free melt-quenched BT110, BT111, BT112, and phosphate-based Novabone glass was obtained by Murphy and coworkers. Between day 1, day 7, and day 30 extracts, Novabone shows no significant statistical difference in cell viability. After day 1, BT112 and Novabone possess higher viabilities than BT111. After day 7 and 30, BT112 exhibits higher cell viabilities of 120 ± 10.1 % and 137.2 ± 4.9 %, respectively, than all other glass extracts. As the incubation time period is increased from day 1 to day 30, all glass compositions show increased cell viability by day 30.

The antioxidant behavior of the glasses as well as the initial attachment of MG-63 osteoblasts to zinc and strontium codoped alkali-free phosphosilicate melt-quenched glasses was studied by Kapoor and coworkers. The proliferation of MG63 cells for the ZS-2, ZS-4, ZS-6, and ZS-8 glasses was 89.0 ± 4.2, 86.7 ± 3.9, 80.25 ± 3.6, and 72.8 ± 3.1 %, respectively. For the Sr- and Zn-doped bioactive glasses, the cell viability obtained is higher which decreased with SrO and ZnO concentration in glasses beyond ZS-4 (Fig. 8.6). The cell viability under oxidative stress at the LD50 dose of H_2O_2 was observed for glass ZS-2 (163 %), followed by ZS-4 (151 %),

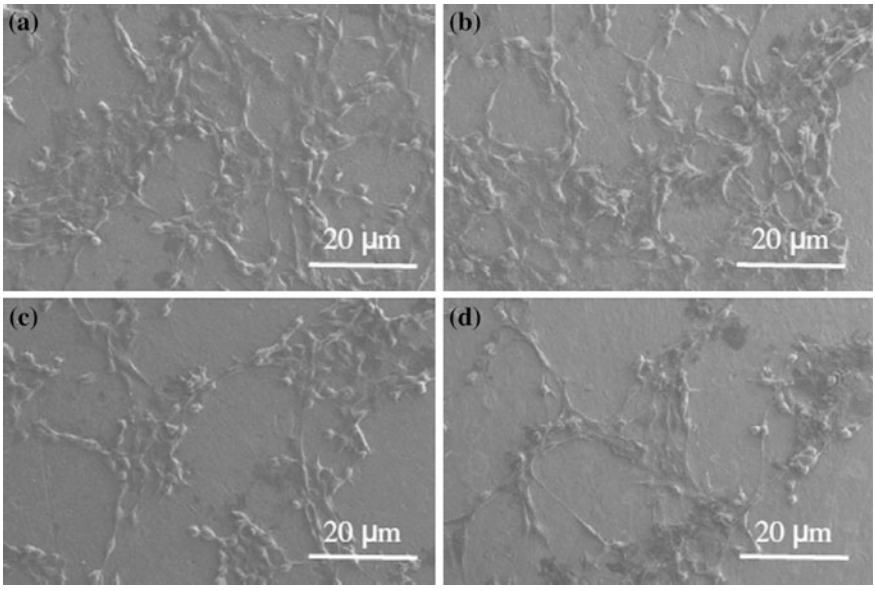

Fig. 8.6 SEM morphologies of cells (MG63 cell line) at the semiconfluent stage on the surface of glass samples during culture for 3 days: **a** ZS-2, **b** ZS-4, **c** ZS-6 and **d** ZS-8 (Kapoor et al. 2014)

ZS-6 (138 %), and ZS-8 (135 %), compared to control. H_2O_2 contributes to the oxidative damage when leaked from mitochondria in the cells. Cell proliferation in MG63 cells is hindered when H_2O_2 reduces the level of cycline B1 and induces G2 cell cycle arrest.

It was revealed that the antioxidant potential of bioglasses was Zn- and Sr-dose dependent. The released concentrations of zinc and strontium were confined to 62 and 610 ppm, respectively. Accordingly, the cell viability was enhanced and the effect of oxidative stress induced by the addition of H_2O_2 to the cell culture medium was negated when glasses ZS-2 and ZS-4 exhibited good antioxidant behavior.

Liang and coworkers utilized unconverted sodium calcium borate melt-quenched glass to fabricate scaffolds, which were then cultured in vitro with bone marrow-derived human mesenchymal stem cells (hbMSCs) and hbMSCs-derived osteoblasts (MSC-Obs). Metabolic activity during live cell assay showed cell viability as an evidence for both hBMSCs and MSC-Obs on the partially converted borate glass and the fully converted borate glass scaffolds. As compared to partially converted borate glass, when hBMSCs were seeded on the fully converted borate glass scaffolds, it showed less cell viability. For alkaline phosphatase (ALP) activity, hBMSCs on all borate glass substrates showed faint staining. Early stages of osteogenic differentiation was indicated by positive alkaline phosphatase synthesis, which was given by MSC-Obs. Good cell growth on the borate glass was suggested by scaffolds adhered by hBMSCs and MSC-Obs.

Buzzi and coworkers melted the constituents (of purity between 99.99 and 99.999 %) and the MTT was performed on 3T3 cells (embryonic mouse fibroblast cell line) to prepare metallic glasses with composition $(Zr_x\ Cu_{100-x})_{80}\ (Fe_{40}\ Al_{60})_{20}$ with $x = 62 - 81$. Remarkable cell growth is already shown in the as-cast state by the Zr-based metallic glasses. By passivating with nitric acid, improvement was seen in both cell viability and metabolic activity. Indeed, the values for both alloys were comparable to those of the negative control after this surface treatment. Zr-based metallic glasses usually show good corrosion resistance, because they possess a natural passive oxide layer. Amorphous alloys are generally more corrosion resistant than their crystalline counterparts, which is an additional benefit presented by their amorphous and homogeneous structure. In addition, local segregation of elements in the alloy or small surface defects in the micro- or nanorange provide this passive layer locally less stable and therefore, in the presence of chloride ions, is subjected to pitting corrosion.

8.4 Apatite Formation Ability

Composition, structure, surface charge, particle size, and morphology of the material are the parameters which define their ability to stimulate cellular proliferation and differentiation; bioactivity, which is an interface-driven phenomenon, is also dependent on these parameters. Bioactivity of glasses is defined as their ability to induce hydroxyapatite (HAp) formation upon their contact with a physiological

environment such as simulated body fluid (SBF). In other words, to determine whether the glass is bioactive or not, the formation of HAp layer on surface of bioglasses in vitro is a preliminary test. Hydroxyapatite (Ca_{10} $(PO_4)_{6-x}$ $(HPO_4)_x$ $(OH)_{2-x}$), which possess needle-like structure, is the predominant bone mineral (with smaller quantities of intermediate calcium phosphates and calcium carbonate) which on the surface of the glasses transforms to cauliflower-like clusters. The SBF possesses same pH and ionic concentration as that of human blood plasma, and the formation of silanol groups on their surface subsequently nucleating a hydroxyapatite layer is lead by an exchange of ions of bioactive glasses with SBF. There are two main steps for the formation of HAp layer: firstly, formation of dicalcium phosphate ($CaHPO_4$) via combination of calcium and phosphorus ions in the body fluid and then conversion of dicalcium phosphate into HAp or tricalcium phosphate ($Ca_3(PO_4)_2$) through sequential reactions. After interacting with the biological fluid, the spontaneous formation of HAp layer on the surface of glasses in the $CaO–SiO_2–P_2O_5$ ternary system is shown by so many reports in literature. A preferentially layer formation exhibited on the surface of glass with composition CaO, P_2O_5, and SiO_2 involving the Si–OH group induces a heterogeneous nucleation of apatite. Calcium and phosphate ions from the body fluid are consumed by these apatite crystals and subsequently agglomerate on the surface of the glass.

Due to their high surface area for ion exchange with biological fluids such as SBF, sol-gel glasses possess fast reaction kinetics and due to which these tend to form the hydroxyapatite (HAp) surface layer more rapidly as compared to melt-derived glasses. Good bone bonding and HAp layer formation on the surface is shown by sol-gel glasses having 90 mol% silica. Sepulveda and coworkers prepared scaffolds using sol-gel foaming process because this process produces scaffolds possessing a bimodal porous structure and mesoporous texture. Luz and coworkers showed that the desired characteristics of bone bonding and biodegradability upon immersion in SBF were possessed by the sol-gel BG-NPs prepared in the ternary system ($SiO_2–CaO–P_2O_5$) and hence proved to be potential biomaterials for bone tissue engineering. When the nanoparticles are prepared at pH 11.5 and they are subjected to the thermal treatment at 700 °C, the bioactivity of BG-NPs is further improved.

O'Donnell and coworkers found that after immersing all the sol-gel ICSW glasses in SBF for 21 days, apatite formation was faster, as the phosphate content is increased in the parent glass indicating increased network connectivity with P_2O_5 addition. Hence, rather than the silicate phase, Q^0 phosphate species can be regarded as an important factor for bioactivity. Fast apatite formation kinetics in the glasses with high phosphate content is due to the interconnected orthophosphate morphology and high surface area exposed to the SBF may cause continuous phosphate leaching.

By measuring DMEM composition as a function of interaction time, physico-chemical reactions between the sol-gel bioactive glass powders and the biological fluids were studied by Courtheoux and coworkers. The amount of Zn released increases when zinc concentration increases from 1 to 4.8 wt% in the glass. The extent of Ca precipitation was almost none even when content of CaO was small,

after initial 4 days of soaking. Ca–P layer is formed on the glass surface due to the decrease in P concentration, which was maximum for Zn5 sample in biological medium. Cell differentiation and alkaline phosphatase production in the CaO–P_2O_5–SiO_2 samples is shown by Zn-doped bioactive glasses. The glass dissolution is delayed by the doping of glasses with zinc, and early precipitation of phosphate ions is felicitated from the biological fluids at the glass surface resulting in gradual crystallization of stable HAp in vivo providing a better bone-bonding interface. Yang and coworkers found that the Ca/P ratio (1.66) of the surface layer was almost same as that of stoichiometric HAp and flake-shaped particles covered the entire Zn-containing bioactive glass surface, after 28 days of immersion in SBF. The content of the Ca^{2+} and P^{5+} ions increased on the sample surface with the Ca/P ratio of 1.7, for the Mg–Zn-containing bioactive glass sample immersed in SBF for 28 days, which is close to the value of HAp.

Li and coworkers found that the bioactivity and apatite layer formation is not inhibited by the crystallization. Peitl and coworkers found that the apatite layer can result even in fully crystallized glass-ceramic, whereas certain research groups have found the reduced bioactivity of glasses after crystallization [145–146]. After 2 days soaking, the characteristic peaks of matrix phase $Na_2CaSi_3O_8$, carbonated hydroxyapatite (Ca_{10} $(PO_4)_3$ $(CO_3)_3$ $(OH)_2$), and small diffraction peaks of Ca_{10} $(PO_4)_6$ $(OH)_2$ appeared on the surface of 45S5 sample. Carbonated hydroxyapatite ($Ca_{10}(PO_4)_3(CO_3)_3(OH)_2$) showed an increasing trend for the characteristic peaks, whereas after 7 days of soaking the extent of matrix phase $Na_2CaSi_3O_8$ was reduced. When CaO is partially substituted by CaF_2, very sharp (Ca_{10} $(PO_4)_3$ $(CO_3)_3$ $(OH)_2$) peaks were obtained. After soaking of sample 45S5-F in SBF for 14 days, HAp peaks appeared and $Na_2CaSi_3O_8$ almost disappeared. The bioactivity results indicated that the sample doped with CaF_2 has better bioactivity than the sample 45S5. Delben and coworkers concluded that because of the formation of Si–O–NBO groups, higher modifier concentration in the glasses causes depolymerization. Due to their open network resulting in faster precipitation of apatite crystals on the glass surface, ion exchange with the solution is faster for low silica compositions. For the 3 and 5 % silver doping in the $60SiO_{2-3}6CaO–4P_2O_5$ glass system, the intensity of bands attributed to phosphate and bridging oxygen (BO) increased. Its solubility is reduced in SBF due to the hygroscopic decrease of bioactive glass with higher silver content.

Doostmohammadi and coworkers explained that the apatite layer formation is enhanced due to small particle size and hence high surface area of 63S glass than exact the same mass of larger bioactive glass particles. Around pH 7.4, the particles form 100–500 nm aggregates, which are regarded as the musculoskeletal extracellular environment attributed to their low negative zeta potential in physiological saline solution. The cell attachment and proliferation of osteoblasts is enhanced by the negative zeta potential.

Oliveira and coworkers obtained better bioactive properties for the BGNP causes rapid release of Ca- and P-promoting cellular adhesion, biomineralization process as well as enhanced osteoblast proliferation and differentiation due to their small grain size. HAp nucleation on the surfaces of BGNP particles lead to higher cell

viability and also increase ALP activity is suggested by fast zeta potential variations, in the osteoblast cultures at the early stages of incubation. As the particles of higher zeta potential have more repulsion between them, particles with low zeta potential have tendency to come together, leading to no flocculation or segregation of the particles. Kaur and coworkers discussed that all the sol-gel glasses possess positive zeta potential initially; as the soaking duration is increased, it becomes negative. The zeta potential becomes negative after 588 h of soaking duration for the CP5 and CP10, whereas after almost 288 h of immersion in the SBF, CP15, and CP20 glasses give negative zeta potential. Du and coworkers showed that during early stage of SBF immersion, the HAp nucleation and growth are hindered by the Zn content in the bioactive glasses. After 1 day of soaking in SBF solution, as compared to zinc-free 58S glass, the Zn-containing glass exhibited large size of HAp nuclei on their surface. As Zn ions get absorbed on the growth sites of HAp, zinc is known as an inhibitor of the apatite crystal growth, which inhibits apatite layer on the (0001) face. For the apatite layer formation, less nuclei is possessed by Zn-containing 58S4Z and 58S0.4Z glasses, as compared to the 58S glass. As compared to Ca–O (110 kJ/mol), Zn–O posses higher bond energy of 180 kJ/mol, which makes diffusion of Zn ion inside the glass network into SBF difficult. At the same time, as the soaking time is increased, more and more Ca^{2+} from the solution accumulated on the glass surface, gradually covering it by the HAp layer. An increased deposition rate of HAp on the glass-ceramic surface is shown by the crystallization effect of Zn.

Kaur and coworkers concluded that with the increase in the phosphorous content as well as the soaking duration, apatite layer formation on the surface of both glass and glass-ceramic increases (Fig. 8.7a–f). CP5 glass-ceramic shows almost no layer formation on its surface attributed to its high crystallinity even after 5 days of soaking in SBF, whereas some flake formation is exhibited on the surface of CP5 glass. The formation of acicular lath-shaped particles partially covering the surface is shown by CP10 glass ceramics. After soaking for 5 days, some noduses were observed on the surface of CP15 glass-ceramic and glass. Moreover, after 30 days of soaking, the surface of CP15 glass is almost covered with apatite layer revealing its good bioactive response. After 30 days of immersion for CP20 glass in SBF, the maximum pH of 9.02 is obtained implying its better apatite-forming ability as compared to other samples, which correlates with the microstructural analysis.

Oh and coworkers by using three different concentrations of 3, 10, and 30 sol-gel glass granules containing 0, 2, and 5 % Zn each studied the cellular responses of growth and osteoblastic differentiation for mesenchymal stem cells (MSCs) extracted from rat bone marrow. After second- and third-week soaking, on the surface of glass granules, the flattened cell bodies with cytoskeletal extensions grew actively. After 21 days of soaking, the mineral-like products could be observed. When grown in the presence of zinc-containing glass granules, the ALP activity was significantly enhanced. Due to the ions released from the bioactive glasses, ARS staining and calcium quantification of samples confirmed the cellular mineralization. Salinas et al. demonstrated different in vitro behavior in SBF for the melt-quench glass G13, glass-ceramic GC13 (obtained by thermal treatment of G13),

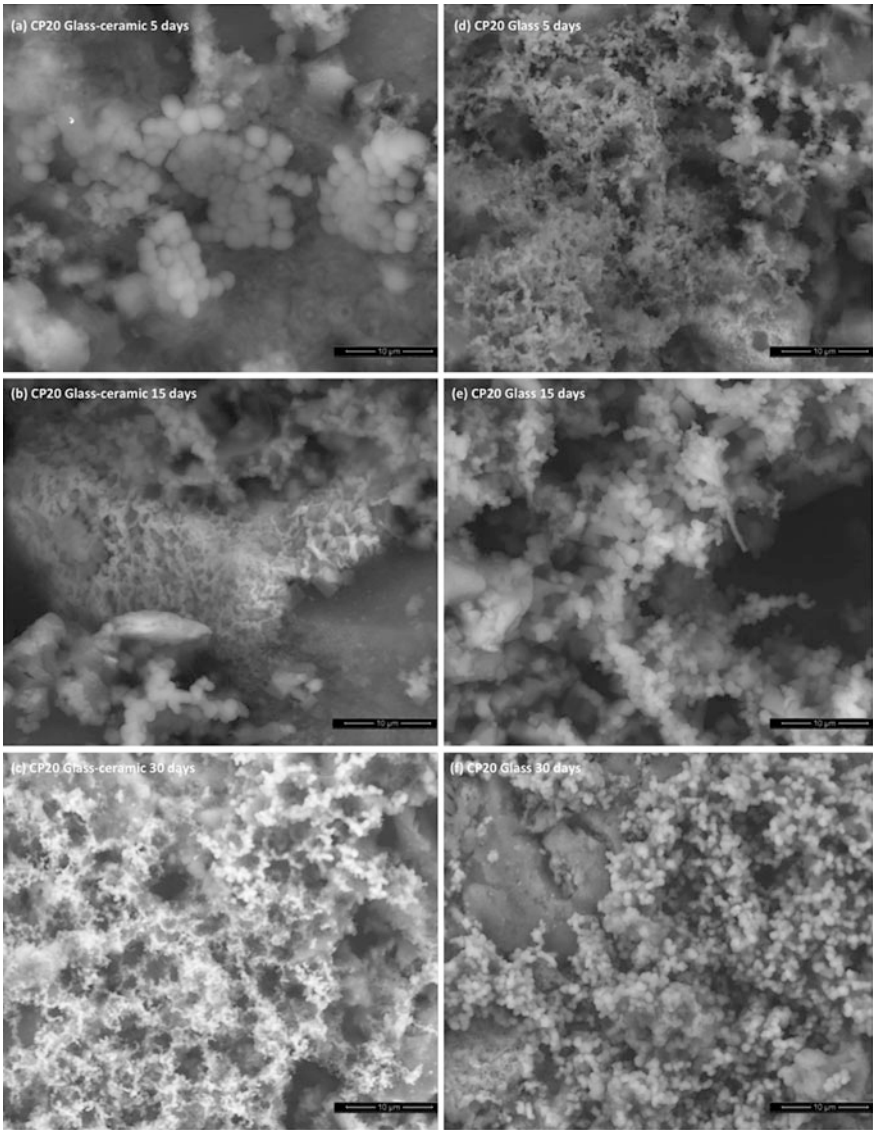

Fig. 8.7 Apatite layer formation for **a** 5, **b** 15, and **c** 30 days SBF-soaked CP20 glass-ceramics: Apatite layer formation for **d** 5, **e** 15, and **f** 30 days SBF-soaked CP20 glass (Kaur et al. 2014)

and GC13-HCl (obtained by chemical etching GC13 with HCl). In less than 7 days of soaking in SBF, XRD, SEM, and EDS confirmed high apatite-forming ability for G13 glass, whereas even after 6 weeks of immersion in SBF, GC13 could not form Ca–P rich layer. In contrast to this, after 4 day of soaking in SBF, some calcium phosphate-rich regions were observed for the GC13-HCl.

Many research groups reported that for the apatite formation on the surface of glasses, minimum 1-week incubation time is required. Agathopoulos and coworkers reported that on the bioactivity of the glasses with minimum incubation time of about 7 days for the formation of the first calcium phosphate flakes on the surface of glass, additives such as B_2O_3, Na_2O, CaF_2, and P_2O_5 exhibit considerable effect. HAp layer almost completely covered the glass surfaces, after immersing in SBF for 14–21 days. In contrast to increasing CaO and SiO_2 contents, increasing phosphates favors deposition of A-type carbonated HAp. Pazo and coworkers reported that the range of firing temperatures is limited by the glass softening and viscosity as well as glass/metal reactivity. During heating, doping of glass with small amounts of titania reduces the dissolution rate of the oxide formed. This further makes the reactivity more controllable and broadens the time–temperature range to achieve good bond.

The composition-dependent response of the coatings for glasses in the SiO_2–Na_2O–CaO–P_2O_5 system including bioglasses is widely reported. Carbonated apatite layer grew in vitro on the surface of the coatings with lower silica content (6P57), whereas coatings with higher silica content hindered apatite formation as reported by Saiz and coworkers. After 2 weeks of immersion SBF, almost 10-μm-thick silica-rich layer is observed for the coatings made from 6P57 glasses. Ohure and coworkers and Andersson and coworkers observed that even though some Al_2O_3 could be detected as an impurity in the coatings, but it did not interfere with the bone bonding and apatite formation. Usually, the bone-bonding ability of bioactive glasses is reduced by higher alumina content. Hopeite ($Zn_3(PO_4)_2{\cdot}4H_2O$) formation at the surface of cement AE9/50 wt% is reported by Boyd and coworkers. Due to the low calcium content in the glass, the HAp was not optimum to induce the nucleation of apatite at the cement surface. Contrastingly, after 24 h of immersion in SBF, the SBF–cement interface supersaturated by high concentrations of zinc is released by adding to the precipitation of hopeite.

The behavior of zinc-containing bioactive glass is demonstrated by Oudadesse and coworkers. For pure glass 46S6 and Zn-doped glass 46S6Zn10, marked difference is exhibited by the HCA layer formed. At 470, 795, and 1220 cm^{-1}, shoulders appear for Si–O–Si bend, Si–O–Si symmetric stretch, and the P=O stretch, respectively, which decrease in intensity until they eventually disappear after 15 days of soaking in SBF. The Si–O–Si asymmetric stretch band also shifts to 1040 from 1080 cm^{-1}. For reduction in the overall leaching activity of HZ glasses compared with the zinc-free parent 45S5 bioactive glass, Aina and coworkers reported Zn to be responsible. For the glass with maximum zinc content, i.e., HZ20, excessive reduction in the dissolution activity is observed; hence, tendency of the glass to form HAp layer on its surface is completely suppressed. In addition to this, when zinc content increases, the incubation time increases from 6 h to 1 week for HAp formation. As compared to that of HZ5 glass where the incubation times lie between 1 day and 1 week, the HAp is formed between initial 3 and 6 h of soaking for H glass. After 14 days of soaking in SBF, the fluorinated apatite (mixture of fluoroapatite and HAp) and strontium pyrophosphate (SrP_2O_7) for the ZS-4 and ZS-8 glasses are obtained by Kapoor and coworkers. For the ZS-4 glass, the phase concentration is observed to be on higher side.

Uo and coworkers obtained extremely fast dissolution rates in SBF for CaO-free glasses which decreased with increasing CaO content and decreasing P_2O_5 content. This could be attributed to the soluble species of glass such as Na^+, Ca^{2+}, and HPO_4^{2-}. Branda and coworkers observed that the substitution of Al_2O_3/Y_2O_3 for CaO in the binary CaO–SiO_2 glass composition suppresses the calcium phosphate layer formation after exposure to the simulated body fluid (SBF). The difference in the ionic field strength of the substituting cation and Ca^{2+} is the reason behind reduction in layer formation.

Bibliography

Oudadesse H et al (2011) Apatite forming ability and cytocompatibility of pure and Zn-doped bioactive glasses. Biomed Mater 6:035006–035015

Yang X et al (2012) Incorporation of B_2O_3 in CaO-SiO_2-P_2O_5 bioactive glass system for improving strength of low-temperature co-fired porous glass ceramics. J Non-Cryst Solids 358:1171–1179

Uo M et al (1998) Properties and cytotoxicity of water soluble Na_2O-CaO-P_2O_5 glasses. Biomaterials 19:2277–2284

Kaur G et al (2014) Synthesis, cytotoxicity, and hydroxypatite formation in 27-Tris-SBF for sol-gel based CaO-P_2O_5-SiO_2-B_2O_3-ZnO bioactive glasses. Sci Rep. doi:10.1038/srep04392

Kaur G et al (2013) A review of bioactive glasses: their structure, properties, fabrication, and apatite formation. J Biomed Mater Res A 102:254–274

Chevalier J, Gremillard L (2009) Ceramics for medical applications: a picture for the next 20 years. J Eur Ceram Soc 29:1245–1255

Rahaman et al (2011) Bioactive glass in tissue engineering. Acta Biomater 7:2355–2373

Oki A, Parveen B, Hossain S, Adeniji S, Donahue H (2004) Preparation and in vitro bioactivity of zinc containing sol-gel–derived bioglass materials. J Biomed Mater Res A 69A(2):216–221. doi:10.1002/jbm.a.20070

O'Donnell MD, Watts SJ, Hill RG, Law RV (2009) The effect of phosphate content on the bioactivity of soda-lime-phosphosilicate glasses. J Mater Sci Mater Med 20:1611–1618

Courtheoux L, Lao J, Nedelec JM, Jallot E (2008) Controlled bioactivity in zinc-doped sol-gel-derived binary bioactive glasses. J Phys Chem C 112:13663–13667

Li HC, Wang DG, Hu JH, Chen CZ (2013) Crystallization, mechanical properties and in vitro bioactivity of sol–gel derived Na_2O–CaO–SiO_2–P_2O_5 glass–ceramics by partial substitution of CaF_2 for CaO. J Sol-Gel Sci Technol. 67(1):56–65. doi:10.1007/s10971-013-3050-5.

Du RL, Chang J, Ni SY, Zhai WY (2006) Characterization and in vitro bioactivity of zinc-containing bioactive glass and glass-ceramics. Biomater Appl 20:341

Doostmohammadi A et al (2011) Bioactive glass nanoparticles with negative zeta potential. Ceram Int 37:2311–2316

De Oliveira AAR et al (2011) Synthesis, characterization and cytocompatibility of spherical bioactive glass nanoparticles for potential hard tissue engineering applications. Biomed Mater 8:025011–025025

Agathopoulos S et al (2006) Formation of hydroxyapatite onto glasses of the CaO–MgO–SiO_2 system with B_2O_3, Na_2O, CaF_2 and P_2O_5 additives. Biomaterials 27:1832–1840

Jones JR, Ehrenfried LM, Hench LL (2006) Optimising bioactive glass scaffolds for bone tissue engineering. Biomaterials 27:964–973

Pazo A, Saiz E, Tomsia AP (1998) Silicate glass coatings on Ti-based implants. Acta Mater 46:2551–2558

Saiz E, Goldman M, Gomez-Vega JM, Tomsia AP, Marshall GW, Marshall SJ (2002) In vitro behavior of silicate glass coatings on Ti_6Al_4 V. Biomaterials 23:3749–3756

Boyd D, Towler MR (2005) The processing, mechanical properties and bioactivity of zinc based glass ionomer cements. J Mater Sci Mater Med 16:843– 850

Liu X et al (2009) Bioactive borosilicate glass scaffolds: improvement on the strength of glass-based scaffolds for tissue engineering. J Mater Sci Mater Med 20:365–372

Aina V et al (2007) Cytotoxicity of zinc containing bioactive glasses in contact with human osteoblasts. Chemico-Bio Int 167:207–218

Aina V, Malavasi G, Pla AF, Munaron L, Morterra C (2009) Zinc-containing bioactive glasses: surface reactivity and behaviour towards endothelial cells. Acta Biomater 5:1211–1222

Goel A et al Alkali-free bioactive glasses for bone tissue engineering: a preliminary investigation

Kaur G, Sharma P, Kumar V, Singh K (2012) Assesment of *in-vitro* bioactivity of SiO_2-BaO-ZnO-B_2O_3-Al_2O_3 glasses: an optico-analytical approach. Mater Sci Eng C 32(7): 1941–1947

Singh K, Bala I, Kumar V (2009) Structural optical and bioactive properties of calcium borosilicate glasses. Ceram Int 35:3401–3406

Goel A et al Structural role of zinc in biodegradation of alkali-free bioactive glasses. J Mater Chem B 1:3073

Kapoor S et al (2014) Role of glass structure in defining the chemical dissolution behavior, bioactivity and antioxidant properties of zinc and strontium co-doped alkali-free phosphosilicate glasses. Acta Biomater 10:3264–3278

Abou Neel EA et al (2009) Structure and properties of strontium-doped phosphate-based glasses. J R Soc Interf 6:435–446

Murphy S, Wren AW, Towler MR, Boyd D (2010) The effect of ionic dissolution products of Ca-Sr-Na-Zn-Si bioactive glass on in vitro cytocompatibilty. J Mater Sci Mater Med 21: 2827–2834

Murphy S, Boyd D, Moane S, Bennett M (2009) The effect of composition on ion release from Ca–Sr–Na–Zn–Si glass bone grafts. J Mater Sci Mater Med 20:2028–2035

Fredholm YC, Karpukhina N, Law RV, Hill RG (2010) Strontium containing bioactive glasses: glass structure and physical properties. J Non-Cryst Solids 356:2546–2551

Regi MV (2001) Ceramics for medical applications. J Chem Soc, Dalton Trans 2:97–108

Tilocca A, Cormack AN (2010) Surface signatures of bioactivity: MD simulations of 45S and 65S silicate glasses. Langmuir 26(1):545–551

Erol M, Ozyuguran A, Celebican O (2010) Synthesis, characterization, and in vitro bioactivity of sol-gel-derived Zn, Mg, and Zn-Mg co-doped bioactive glasses. Chem Eng Technol 33: 1066–1074

Sing KSW, Everett DH, Haul RAW, Moscou L, Pierotti RA, Rouquerol J et al (1985) Reporting physisorption data for gas/solid systems. Pure Appl Chem 57:603–619

Bretcanu O, Chen Q, Misra SK, Boccaccini AR, Verne E, Vitale- Brovarone C (2007) Biodegradable polymer coated 45S5 Bioglassderived glass-ceramic scaffolds for bone tissue engineering. Glass Tech Eur J Glass Sci Tech A 48:227–234

Chen QZ, Thompson ID, Boccaccini AR (2006) 45S5 BioglassVR –derived glass-ceramic scaffolds for bone tissue engineering. Biomaterials 27:2414–2425

Wu SC, Hsu HC, Hsiao SH, Ho WF (2009) Preparation of porous 45S5 BioglassVR -derived glass-ceramic scaffolds by using rice husk as a porogen additive. J Mater Sci Mater Med 20:1229–1236

Vitale-Brovarone C, Verne E, Robiglio L, Appendino P, Bassi F, Martinasso G, Muzio G, Canuto R (2007) Development of glass-ceramic scaffolds for bone tissue engineering: characterisation, proliferation of human osteoblasts and nodule formation. Acta Biomater 3:199–208

Vitale-Brovarone C, Baino F, Verne E (2009) High strength bioactive glass-ceramic scaffolds for bone regeneration. J Mater Sci Mater Med 20:643–653

Liu X, Huang W, Fu H, Yao A, Wang D, Pan H, Lu WW, Jiang X, Zhang X (2009) Bioactive borosilicate glass scaffolds: in vitro degradation and bioactivity behaviours. J Mater Sci Mater Med 20:1237–1243

Cannillo V, Sola A (2009) Potassium-based compositions for a bioactive glass. Ceram Int 35:3389–3393

Bellucci D, Cannillo V, Ciardelli G, Gentile P, Sola A (2010) Potassium based bioactive glass for bone tissue engineering Ceram Int 36:2449–2453

Sullivan A, Hill RG (2000) J Mat Sci 35:1125

Towler MR, France RR, Billington RW (19980 J Dent Res 77/B:Abs#3117

International standard 9917:1991 (E). Dental water based cements. International organization for standardization. Case postale 56, CH-1211, Geneve, Switzerland

Nicholson JW, Brookman PJ, Lacy OM, Sayers GS, Wilson AD (1988) J Biomed Mat Res 22:623

Giesen EBW, Ding M, Dalstra M, van Eijden TMGJ (2001) J Biomech 34:799. doi:10.1016/S0021-9290(01)00030-6.

Yeni YN, Fyhrie DP (2001) J Biomech 34:1649. doi:10.1016/S0021-9290(01)00155-5.

Bang HG, Kim SJ, Park SY (2008) Biocompatibility and the physical properties of bio-glass ceramics in the Na_2O-CaO-SiO_2-P_2O_5 system with CaF_2 and MgF_2 additives. J Ceram Proc Res 9(6):588–590

Implants for surgery–hydroxyapatite–Part 1: Ceramic hydroxyapatite. BS ISO 13779-1:2000

Carter DR, Hayes WC (1976) Bone compressive strength: the influence of density and strain rate. Science 194:1174–1176

Webster TJ, Siegel RW Bizios R (1999) Osteoblast adhesion on nanophase ceramics. Biomaterials 20:1221–1227

Schneider O D et al (2008) Cotton wool like nanocomposite biomaterials: in vitro bioactivity and osteogenic differentiation of human mesenchymal stem cells. J Biomed Mater Res B Appl Biometer 84 350–362

Gao T, Aro H T, YlaKnen H and Vuorio E (2001) Silica-based bioactive glasses modulate expression of bone morphogenetic protein-2 mRNA in Saos-2 osteoblasts in vitro. Biomaterials 22:1475–1483

Verne E, Ferraris S, Vitale-Brovarone C, Spriano S, Bianchi CL, Naldoni A, Morra M Cassinelli C (2010) Alkaline phosphatase grafting on bioactive glasses and glass ceramics. Acta Biomater 6:229–240

Reilly GC, Radin S, Chen AT Ducheyne P (2007) Differential alkaline phosphatase responses of rat and human bone marrow derived mesenchymal stem cells to 45S5 bioactive glass. Biomaterials 28:4091–4097

Varanasi VG, Saiz E, Loomer PM, Ancheta B, Uritani N, Hoa SP, Tomsia AP, Marshall SJ Marshall GW (2009) Enhanced osteocalcin expression by osteoblast-like cells (MC3T3-E1) exposed to bioactive coating glass (SiO_2–CaO–P_2O_5–MgO–K_2O–Na_2O system) ions. Acta Biomater 5:3536–3547

Valerio P, Pereira MM, Goes AM, Leite MF (2004) The effect of ionic products from bioactive glass dissolution on osteoblast proliferation and collagen production. Biomaterials 25:2941–2948

Doostmohammadi A et al (2011) Direct cytotoxicity evaluation of 63S bioactive glass and bone-derived hydroxyapatite particles using yeast model and human chondrocyte cells by microcalorimetry. J Mater Sci Mater Med 22:2293–2300

Zhang K, Washburn NR, Simon CG (2004) Cytotoxicity of threedimensionall ordered macroporous sol–gel bioactive glass (3DOM-BG). Biomaterials 26:4532–4539

Li P, Kai Z, Clifford W (2005) Indirect cytotoxicity evaluation of silver doped bioglass Ag-S70C30 on human primary keratinocytes. Key Eng Mater 284:431–434

Cervinka M, Puza V, Hroch M, Cervinkova Z (1994) In vitro cytotoxicity testing of metal alloys used in medicine: comparison of different approaches. Toxicol Vitro 8:783–785

Fontana AJ, Hansen LD, Breidenbach RW, Criddle RS (1990) Microcalorimetric measurement of aerobic cell metabolism in unstirred cell cultures. Thermochim Acta 172:105–113

James AM (1987) Thermal and energetic studies of cellular biological systems. Bristol, Wright, pp 147–166

Beezer AE (1980) Biological microcalorimetry. Academic press, London

Luz GM, Manoosteoblast JF (2011) Preparation and characterization of bioactive glass nanoparticles prepared by sol–gel for biomedical applications. Nanotechnology 22:494014

Oh SA et al Effects on growth and osteogenic differentiation of mesenchymal stem cells by the zinc-added sol-gel bioactive glass granules. J Tissue Eng 2010:475260

Ponsonnet L, Reybier K, Jaffrezic N, Comte V, Lagneau C, Lissac M, Martelet C (2003) Relationship between surface properties (roughness, wettability) of titanium and titanium alloys and cell behaviour. Mater Sci Eng C 23:551–560. doi:10.1016/S0928-4931(03)00033-X

Wirth C, Comte V, Lagneau C, Exbrayat P, Lissac M, Jaffrezic-Renault N, Ponsonnet L (2005) Nitinol surface roughness modulates in vitro cell response: a comparison between fibroblasts and osteoblasts. Mater Sci Eng C 25:51–60. doi:10.1016/j.msec.2004.06.001

Schakenraad JM, Busscher HJ, Wildevuur RH, Arends J (1988) Thermodynamic aspects of cell spreading on solid substrata. J Cell Biophys 13:75–91

Hallab N, Bundy K, O'Connor K, Clark R, Moses R (1995) Cell adhesion to biomaterials: correlations between surface charge, surface roughness, adsorbed protein and cell morphology. J Long-Term Effects Med Implants 53:209–231

Li M, Zhao L, Liu J, Liu A-L, Zeng W-S, Luo S-Q, et al (2009) Hydrogen peroxide induces G2 cell cycle arrest and inhibits cell proliferation in osteoblasts. Anat Rec (Hoboken) 292: 1107–1113

Liang W et al (2008) Bioactive borate glass scaffold for bone tissue engineering. J Non-Cryst Solids 354:1690–1696

Lu HH, Pollack SR, Ducheyne P (2000) J Biomed Mater Res 51:80–87

Benhayoune H, Charlier D, Jallot E, Laquerriere P, Balossier G and Bonhomme P (2001) J Phys D Appl Phys 34:141–147

Hench LL (1998) J Am Ceram Soc 81:1705–1728

Li P, Ohtsuki C, Kokubo T, Nakanishi K, Soga N, de Groot K (1994) The role of hydrated silica, titania, and alumina in inducing apatite on implants. J Biomed Mater Res 28:7–15

Kokubo T, Kushitani H, Ohtsuki C and Sakka S (1992) Chemical reaction of bioactive glass and glass–ceramics with a simulated body fluid. J Mater Sci Mater Med 3:79–83

Kokubo T, Kim H-M, Kawashita M (2003) Novel bioactive materials with different mechanical properties Biomaterials 24:2161–2175

Kokubo T (2005) Design of bioactive bone substitutes based on biomineralization process Mater Sci Eng C 25:97–104

Vitale-Brovarone C, Baino F, Tallia F, Gervasio C and Verne E (2012) Bioactive glass-derived trabecular coating: a smart solution for enhancing osteointegration of prosthetic elements. J Mater Sci Mater Med 23:2369–2380

Li L, Clark AE, Hench LL (1991) An investigation of bioactive glass powders by sol-gel processing. J Appl Biomater 2:231–239

Sepulveda P, Jones JR, Hench LL (2002) Bioactive sol-gel foams for tissue repair. J Biomed Mater Res A 49:340–348

O'Donnell MD, Watts SJ, Law RV, Hill RG (2008) Effect of P_2O_5 content in two series of soda lime phosphosilicate glasses on structure and properties—part I: NMR. J Non-Cryst Solids 354:3554–3560. doi:10.1016/j.jnoncrysol.2008.03.034

O'Donnell MD, Watts SJ, Law RV, Hill RG (2008) Effect of P_2O_5 content in two series of soda lime phosphosilicate glasses on structure and properties—part II: physical properties. J Non-Cryst Solids 354:3561–3566. doi:10.1016/j.jnoncrysol.2008.03.035

Balamurugan A, Balossier G, Kannan S, Michel J, Rebelo AHS, Ferreira JMF (2007) Acta Biomater 3:255

Peitl O, Zanotto ED, Hench LL (2001) Highly bioactive P_2O_5– Na_2O–CaO–SiO_2 glass–ceramics. J Non Cryst Solids 292:115–126

Mukherjee DP, Das SK (2013) SiO_2–$Al2O_3$–CaO glass–ceramics: effects of CaF_2 on crystallization, microstructure and properties. Ceram Int 39:571–578

Delben JRJ et al (2009) Synthesis and thermal properties of nanoparticles of bioactive glasses containing silver. J Therm Anal Calorim 97:433–436

Liu H, Webster TJ (2007) Nanomedicine for implants: a review of studies and necessary experimental tools. Biomaterials 28:354–369

Kanzaki, N, Onuma K, Treboux G, Tsutsumi S, Ito A (2001) Effect of Impurity on two-dimensional nucleation kinetics: case studies of magnesium and zinc on hydroxyapatite (0001) face. J Phys Chem B 105(10):1991–1994

Noriko K, Onuma K, Treboux G, Tsutsumi S, Ito A (2000) Inhibitory effect of magnesium and zinc on crystallization kinetics of hydroxyapatite (0001) face. J Phys Chem B 104(17): 4189–4194

Filho OP, LaTorre GP Hench LL (1996) Effect of crystallization on apatite-layer formation of bioactive glass 45S5. J Biomed Mater Res 30(4):509–514

Ito A, Kawamura H, Otsuka M, Ikeuchi M, Ohgushi H, Ishikawa K, Onuma K, Kanzaki N, Sogo Y, Ichinose N (2002) Zinc-releasing calcium phosphate for stimulating bone formation. Mater Sci Eng C 22(1):21–25

Fuierer TA, Lore M, Puckett SA Nancollas GH (1994) A mineralization adsorption and mobility study of hydroxyapatite surfaces in presence of zinc and magnesium ions. Langmuir 10 (12):4721–4725

Salinas AJ et al (2000) In vitro bioactivity of glass and glass-ceramics of the 3CaO- P_2O_5. CaO-SiO_2. CaO-MgO-2SiO_2 system. Biomaterials 21:251–257

van Kemenade MJJM, de Bruyn PL (1987) A kinetic study of precipitation from supersaturated calcium phosphate solutions. J Colloid Interface Sci 118:564–585

Kokubo T, Kim HM, Kawashita M, Nakamura T (2003) Novel ceramics for biomedical applications. J Aust Ceram Soc 36:37–46

Ohtsuki C, Kokubo T, Yamamuro T (1992) Mechanism of apatite formation on CaO–SiO_2–P_2O_5 glasses in a simulated body fluid. J Non-Cryst Solids 143:84–92

Pazo A, Santos C, Guitian F, Tomsia AP, Moya JS Scripta Metall (1996) 34:1729

Ogino M, Hench LL (1980) Formation of calcium phosphate films on silicate glasses. J Non-Cryst Solids 38&39:673–678

Ogino M, Ohuchi F, Hench LL (1980) Compositional dependence of the formation of calcium phosphate films on bioglass. J Biomed Mater Res 15:55–64

Hill R (1996) An alternative view of the degradation of bioglass. J Mater Sci Lett 15:1122–1125

Brink M, Turunen T, Happonen RP, Yli-Urpo A (1997) Compositional dependence of bioactivity of glasses in the system Na_2O–K_2O– MgO–CaO–B_2O_3–P_2O_5–SiO_2. J Biomed Mater Res 37:114–121

Kim CY, Clark AE, Hench LL (1989) Early stages of calcium phosphate layer formation in bioglasses. J Non-Cryst Solids 113:195–202

Kim CY, Clark AE, Hench LL (1992) Compositional dependence of calcium phosphate layer formation in fluoride bioglasses. J Biomed Mater Res 26:1147–1161

Ohura K, Nakamura T, Yamamuro T, Ebisawa Y, Kokubo T, Kotoura Y, Oka M (1992) Bioactivity of CaO SiO_2 glasses added with various ions. J Mater Sci 3:95–100

Andersson OH, Karlsson KH, Kangasniemi K (1988) Yli- Urpo A. Models for physical properties and bioactivity of phosphate opal glasses. Glastech Ber 61:300–315

Gross U, Kinne R, Schmitz HJ, Strunz V (1988) The response of bone to surface active glass/glass–ceramics. In: Williams DF (ed) CRC critical reviews in biocompatibility. CRC press, Boca Raton, p 2

Branda F, Arcobello-Varlese F, Costantini A, Luciani G (2002) Effect of the substitution of M_2O_3 (M = La,Y,In, Ga,Al) for CaO on the bioactivity of 2.5CaO-2SiO_2 glass. Biomaterials 23: 711–716

Hum J, Boccaccini AR (2012) Bioactive glasses as carriers for bioactive molecules and therapeutic drugs: a review. J Mater Sci Mater Med 23:2317–2333

Wu C, Chang J (2012) Mesoporous bioactive glasses: structure characteristics, drug/growth factor delivery and bone regeneration application. Interface Focus 2:292–306

Garcia A, Cicuendez M, Izquierdo-Barba I, Arcos D, Vallet-Regi M (2009) Essential role of calcium phosphate heterogeneities in 2D-hexagonal and 3D-cubic SiO_2– CaO–P_2O_5 mesoporous bioactive glasses. Chem Mater 21:5474–5484. doi:10.1021/cm9022776

Yan X et al (2006) The in-vitro bioactivity of mesoporous bioactive glasses. Biomaterials 27:3396–3403. doi:10.1016/j.biomaterials.2006.01.043

Leonova E et al (2008) Multinuclear solid-state NMR studies of ordered mesoporous bioactive glasses. J Phys Chem C 112:5552–5562. doi:10.1021/jp7107973

Zhu M, Zhang L, He Q, Zhao J, Limin G, Shi J (2011) Mesoporous bioactive glass-coated poly (L-lactic acid) scaffolds: a sustained antibiotic drug release system for bone repairing. J Mater Chem 21:1064–1072

Ostomel TA, Shi Q, Tsung CK, Liang H, Stucky GD (2006) Spherical bioactive glass with enhanced rates of hydroxyapatite deposition and hemostatic activity. Small 2:1261–1265

Vallet-Regi M, Izquierdo-Barba I, Colilla M (2012) Review: structure and functionalization of mesoporous bioceramics for bone tissue regeneration and local drug delivery. Phil Trans R Soc Lond A 370:1400–1421

Kaur G, Sharma P, Kumar V, Singh K (2012) Assesment of *in-vitro* bioactivity of SiO_2-BaO-ZnO-B_2O_3-Al_2O_3 glasses: an optico-analytical approach. Mater Sci Eng C 32(7):1941–1947

Kaur G, Pickrell G, Sriranganathan N, Kumar V, Homa D (2016) Review and the state of the art: sol-gel or melt quenched bioactive glasses for tissue engineering. J Biomed Mater Res B Appl Biomater 104(6):1248–1275. doi:10.1002/jbm.b.33443

Kaur G, Pickrell G, Pandey OP, Singh K, Chudasama BN, Kumar V (2016) Combined and individual Doxorubicin/Vancomycin drug loading, release kinetics and apatite formation for the CaO-CuO-P_2O_5- SiO_2- B_2O_3 mesoporous glasses. RSC Adv 6:51046–51056

Chapter 9
Bioactive Glasses in Angiogenesis and Wound Healing: Soft Tissue Repair

Gurbinder Kaur

Bioactive glasses have shown immense potential in the field of orthopedics and dental applications. Many research articles have been published over years based on the tissue engineering and orthopedic/bone regeneration capabilities of bioactive glasses. Due to high osteoconductive and osteostimulative properties of bioactive materials, they are the most preferred biomaterials. Bioactive glasses have the ability to bond directly to the bone, thereby extending its interaction with soft tissues as well. After the discovery of 45S5 Bioglass®, the biomaterial world was revolutionized [45S5 Bioglass® composition is known as the grandfather composition]. After bioglass, other two compositions, which received wide attention, are 13-93 and S53P4 compositions due to their excellent clinical outcomes. Apart from the bone and tissue regeneration, glasses have been studied for the soft tissue repair, angiogenesis, and wound repair capabilities as well.

9.1 Bioactive Glass and Soft Tissue Interaction

When bioactive glass (BG) comes in contact with the physiological fluids, then a series of ion dissolution and precipitation reactions occur on the surface of BG. These set of reactions cause change in pH and HAp layer formation. Upon implantation of bioactive glasses in body, two types of interactions occur, i.e., intracellular and intracellular (Fig. 9.1).

It must be noted that the functional material and structural properties of components of cell adhesion and physicochemical parameters are determined by the surface topography. Moreover, the composition of BG plays a crucial role in determining the interaction mechanism. The pH of ions and progenitor cell populations determine the rate of regeneration and degree of bonding mechanism. For the interaction of soft tissues and BG, long-time interfacial bonding without inflammatory response and rapid interfacial layer formation governed by

G. Kaur, *Bioactive Glasses*, Series in BioEngineering,
DOI 10.1007/978-3-319-45716-1_9

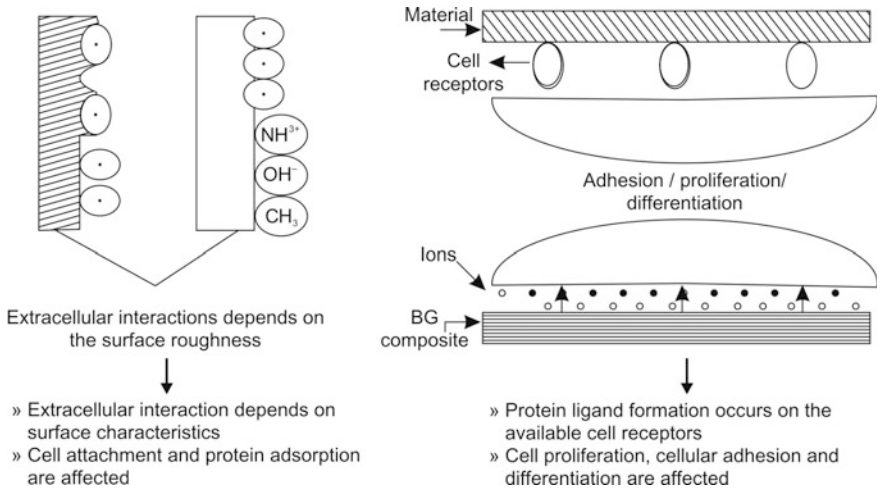

Fig. 9.1 Effect of the cell interactions on the tissues

extracellular cell matrix shall take place. Additionally, stress transfer gradient is required across the interface in order to avoid cell signaling for either tissue or implant resorption.

9.2 Applications of Soft Tissue Repair

Hard–soft tissue interfaces, particularly in BG/polymer composite, are investigated widely and furthermore, the surface modification of BGs is carried out to enhance their bioactivity/biocompatibility. Due to the 'hard' physical characteristics of BG, hard tissue interaction has been studied and less attention has been paid to the soft tissue interaction. Wilson and coworkers have performed wide in vivo and in vitro experiments to study the Bioglass® cytocompatibility and toxicity, when in contact with various soft tissues.

Bioactive glasses such as 45S5, 45S5F, and 52S4.6 have been used for in vitro investigations on hamsters, chickens, mice and rats, whereas dish-shaped BG were implanted subcutaneously and intramuscularly in the peritoneal cavity of mammals (like dogs). The results indicated tissue growth and adhesion around the implants, and the autopsy result indicated no inflammatory response of the host tissue. Gatti and coworkers implanted glass granules of size ~ 300 μm, in the dorsal muscle and under dorsal skin of rabbits. In addition to this, the defects were created surgically in the sheep jaw, and glass granules were implanted into them to understand the hard/soft tissues interaction with glass. After 2-month and 3-month excision in rabbits and sheep, respectively, it could be seen that the BG granules and their surroundings exhibited almost similar morphology, indicating that the nature of

reactions is independent of the implantation site and tissue type. Though the literature reports extensive study on bioactive glasses and other biomaterials (metallic implants, polymers, polymer/bioactive glass composites), sporadic studies are available on the bioglass in soft tissue applications, such as angiogenesis and wound healing. The prime focus of this chapter would be to list all these applications one by one.

9.3 Bioactive Glass in Angiogenesis

Angiogenesis is the mechanism of formation of new blood levels from the preexisting one. Angiogenesis is vital for granulation tissue formation and the wound healing mechanism. Various growth factors such as vascular endothelial growth factor (VEGF), TGF-β, and fibroblast growth faction (FGF) regulate angiogenesis. VEGF increases the capillary numbers in given site and hence acts as a major contributor to the angiogenesis. Due to increased blood flow at the affected area, VEGF is unregulated with muscle contraction causing increased mRNA production of VEGF receptors. Matrix metallic proteinase (MMP) inhibition prevents the formation of new capillaries because they degrade the protein, which keeps the vessels walls strong, thereby allowing the endothelial cells to escape into interstitial matrix, resulting in sprouting angiogenesis.

For the regeneration process to occur, neurovascularization is an essential criterion so that the growing cells are with provided oxygen and nutrients. Hence, the angiogenic potential of bioactive materials is receiving attention for the tissue engineering application. Angiogenesis is a process that can take place during normal tissue regeneration as well as during the pathogenic conditions such as malignant tumors/cancer. Angiogenesis form the basis of tissue engineering, and hence the mass transport and oxygenation mechanics are to be regulated.

Gorustovich and coworkers provided a broad review of the in vitro/in vivo effects of glasses on the angiogenesis listing experimental evidences. Keshaw and coworkers studied angiogenic growth factor release from the cells encapsulated in alginate beads with bioactive glass. Alginic acid was derived from the *macrocystis pyrifera,* and 45S5 Bioglass® was used for the CCD-18Co normal colon fibroblast human cells. The alginate beads containing 0.01 and 0.1 % 45S5 Bioglass® released higher VEGF after 3, 6, 9, and 17 days postencapsulation. VEGF is endothelial cell-specific mitogen and is involved in pathological and physiological angiogenesis. For the same concentrations, fibroblasts culture revealed an increase in the bioactive glass-coated surfaces. For the alginate beads containing 0.1 % 45S5 Bioglass®, significant increase in the endothelial cells is observed attributed to the presence of VEGF and other angiogenic factors in optimum concentration.

It must be noted that the concentration of 45S5 Bioglass® shall be optimized, i.e., if 45S5 Bioglass® content is quite high, then VEGF secretion reduces, most likely due to the cytotoxic effects. The alginate beads containing 0.01–0.1 % 45S5

Bioglass® lysed with EDTA, yielded high VEGF as compared to the beads with 0–1 % 45S5 Bioglass® glass. Day found the stimulation of angiogenesis and angiogenic growth facture using bioactive glass 45S5. For the 45S5 Bioglass® coating of 0.03125–0.625 mg/cm^2 in tissue culture wells with human intestinal fibroblasts, enhanced amount of VEGF could be observed. To assess the effect of growth factors secreted from fibroblasts in response to 45S5 Bioglass® on angiogenesis, an in vitro model of human angiogenesis was used. It was observed that 45S5 Bioglass® stimulates fibroblasts to secrete growth factors thereby causing a significant increase in angiogenesis. Significant increase in the endothelial tubules number and number of tubule junctions could be observed within the conditioned media obtained from fibroblasts cultured on the 45S5 Bioglass®. The number of endothelial tubules, tubule length, and tubule junctions were reduced as compared to controlled endothelial cells due to the presence of 20 μM suramin, an angiogenesis inhibitor (Fig. 9.2).

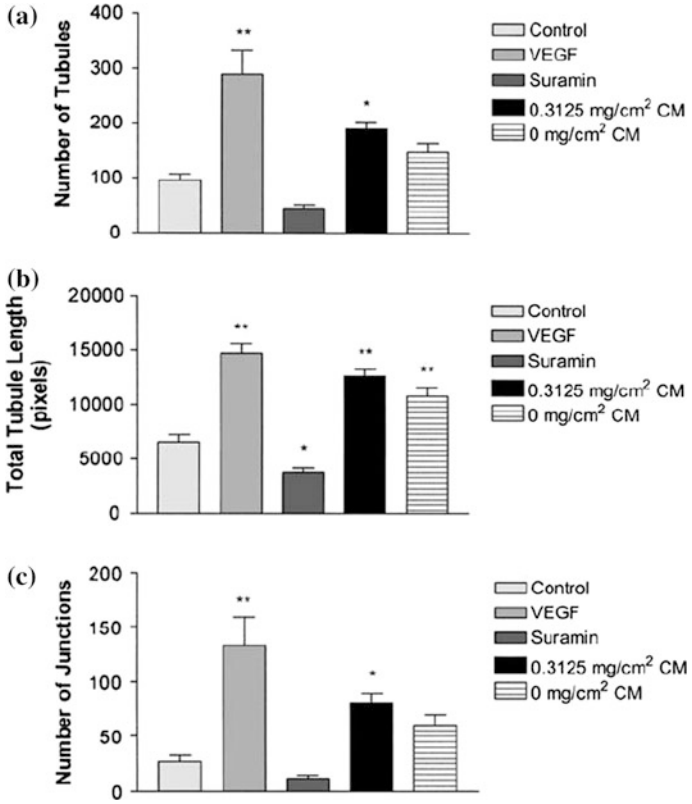

Fig. 9.2 **a** Number of tubules; **b** total tubule length; **c** number of junctions formed in the conditioned medium, produced by CCD-18Co fibroblasts grown on Bioglass® at 0.3125 mg/cm^2, or in medium without Bioglass®, on angiogenesis in vitro (Day 2005)

The studies carried out by Day also demonstrated that small quantities of bioglass could stimulate the expression of VEGF and hence enhance in vitro angiogenesis, though it is not clear whether other angiostatic factor is also released. Complex network of interconnected tubules and tubule branching could be seen in addition to fibroblast-conditioned medium produced in 45S5 Bioglass® presence (in vitro). These tubules mimic the essential stages for the angiogenesis, involving cell migration, proliferation, anastomosis, and vessel branching.

Leach and coworkers coated VEGF-secreting polymeric scaffolds with the 45S5 Bioglass® (45 % SiO_2, 24.4 % $N9_2O$, 24.6 % CaO, 6 % P_2O_5). VEGF enhances osteoconductivity via biomineralization, and localized VEGF delivery has been beneficial for bone regeneration as the neurovascularization osteoblast migration and bone turnover are promoted. The porous scaffolds were poly (lactide-co-glycolide) for the localized protein delivery, and then the surface was coated with 45S5 Bioglass® (up to 0.5 ± 0.2 mg of BG could be deposited). Mitogenic effect could be observed on the human micro-vascular endothelial cells (HMVEC) by the VEGF released from BG-coated and non-coated scaffolds. Though after day 6, the BG-coated blank scaffolds could support enhanced HMVEC proliferation, but not detectable by day 9, probably due to complete dissolution of the material. After 10 days, the proliferation values decreased for VEGF-releasing scaffolds along with mitogenicity comparable to VEGF-secreting uncoated scaffold. It suggests that with the material degradation, the BG coating contribution is degrading upon seeding the scaffolds with HMSCs and differences in alkaline phosphatase activity could not be observed between scaffolds at different time points. The BG-coated scaffolds were implanted in cranial defects of Lewis rats. VEGF-releasing BG (BGV) depicted higher neurovascularization in the defect (117 ± 20 vessel/cm^2) as compared to BG-coated scaffolds (66 ± 8 vessel/cm^2).

Figure 9.3 reveals higher vascularization and angiogenic capacity in BG-coated scaffolds. Robust angiogenic response could be seen by the coated scaffolds lacking VEGF, in the studies conducted on similar model by Murphy and coworkers. Bone mineral density results indicated that the prolonged VEGF delivery from polymeric substrates improved the maturation of newly formed bone. With BGV scaffolds, a slight increase in the newly formed bone within the defect could be seen as compared to BG-coated scaffolds.

Day and coworkers assessed the effect of 45S5 Bioglass® on VEGF secretion using a rat fibroblast cell line (208F). Enzyme-linked immunosorbent assay (ELISA) of media collected from the fibroblasts grown for 24 h on 45S5 Bioglass® particles-coated surface [via a suspension of 45S5 Bioglass® in distilled and deionized water) yielded increased VEGF concentration. The same group conducted similar studies on PLGA disks containing different concentrations of Bioglass® with particle size <5 μm. Increased VEGF secretion is observed upon culturing fibroblasts L929 on PLGA disks with 0.01–1 % 45S5 Bioglass® particles. The results of Day and Keshaw revealed that endothelial cell proliferation was increased by conditioned medium collected capable of inducing proliferation. However, for the bovine aortic endothelial cells (BAEC), plated on zinc-doped 45S5 bioactive glasses, significantly higher bovine aortic endothelial cells could be

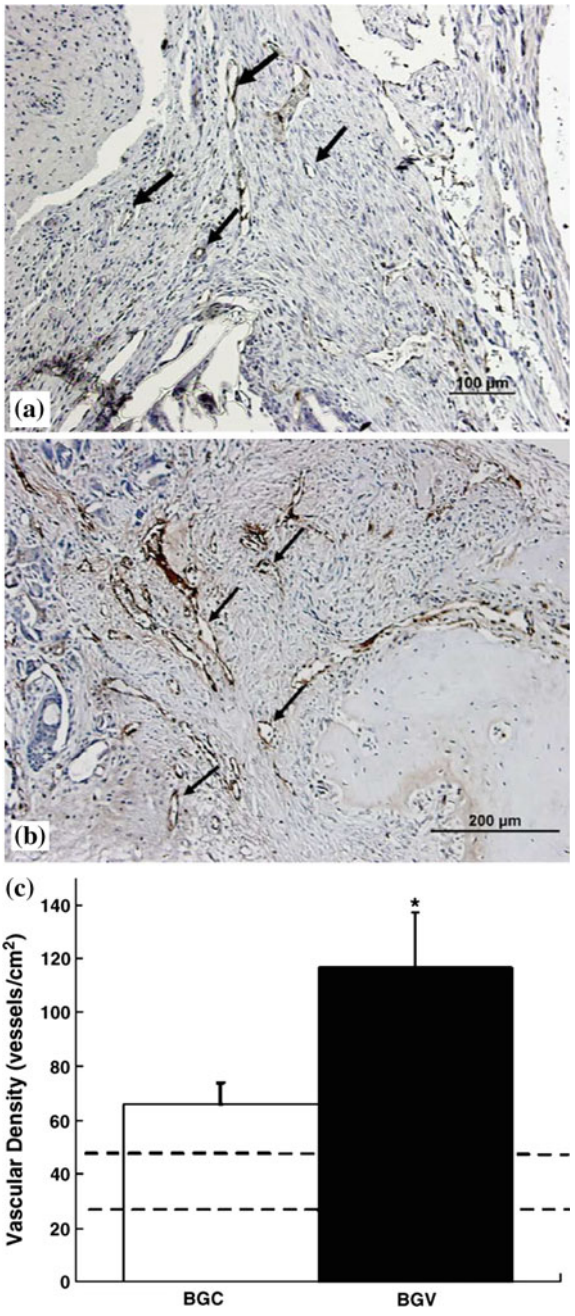

Fig. 9.3 Staining for vWF of decalcified tissues treated with **a** BGC scaffolds and **b** BGV scaffolds, at 2 weeks. *Arrows* denote circular vessels are visible in both samples. **c** Quantitative analysis of vessels in each study group (Leach et al. 2006)

seen on 5 % ZnO-containing glasses as compared to 20 % ZnO-containing glasses and control 45S5 glass. The high rate of dissolution for the 20 % ZnO-containing glasses causes pH changes and hence affects the cell proliferation.

Leu and coworkers found a dose-related proliferative response of endothelial cells cultured with Bioglass®-loaded collagen toward the soluble products of the constructs. The collagen sponges loaded with 1.2 mg Bioglass® particles yielded highest proliferative response, whereas considerable inhibition of endothelial cell proliferation could be observed with the sponges with highest bioglass content of 12 mg. In addition to this, the endothelial cells exposed to 1.2 and 0.12 mg Bioglass® demonstrated higher VEGF mRNA secretion after 72 h of exposure.

Leu and coworkers also explored the proangiogenic potential of 45S5 Bioglass® by exploring its tubule-generating ability within coculture of endothelial cells and fibroblasts. The stimulation of cocultures was performed with conditioned medium from 45S5 Bioglass®-treated rat aortic rings, and like endothelial proliferation assays and dose-related tubule formation response of Bioglass® could be seen. For the 1.2 mg 45S5 Bioglass®, highest number of tubules could be seen, whereas for 6, 0.12, and 0.6 mg Bioglass®-loaded sponges, no tubule formation over the collagen sponges could be seen.

Durand and coworkers studied the angiogenic effects of ionic dissolution products released from boron-doped 45S5 bioactive glass [45S5.2B: 45 % SiO_2, 24.5 % Na_2O, 24.5 % CaO, 6 % P_2O_5 and 2 % B_2O_3]. 45S5.2B composition is also reported to enhance the bone formation upon implantation into the intramedullary canal of the rat tibiae. In addition to this, the human umbilical vein endothelial cells (HUVECs) possess greater migratory and proliferative response, enhanced secretion of proangiogenic cytokines (IL-6 and bfGF), and higher tubule formation capacity, upon stimulation from the ionic dissolution products. The ELISA test carried out to determine the endogenous levels of integrin α_v β_3 in chorioallantoic membrane (CAM) of quail embryos revealed that upon treatment (2 days) with ionic dissolution products from bioactive glass 45S5.2B, the levels of expression are 2.5- to 3-fold higher than those treated with Hank's balanced salt solution (HBSS). Moreover, greater expression of β_3 subunit of integrin α_v β_3 was seen in the Western blot test.

As for as the vascular density results are concerned, no significant differences of CAM treated with HBSS + 45S5.2B/bFGF or HBSS + 45S5.2B for the vascular density could be observed when compared to negative control (HBSS) even after five days of treatment (Fig. 9.4).

Anyhow, for the CAM treated with 4BSS + 45S5.2B and 4BSS + 45S5.2B/bFGF, higher vascular density of 30 and 73 % is observed, respectively, which is comparable to the response observed with HBSS + bFGF. The authors further investigated the effect of boron concentration on the angiogenic activity in the CAM treated with HBSS enriched with the 45S5.2B dissolution product. For the boron concentrations of 5, 50, and 150 μM, the corresponding CAM yielded greater vascular density as compared to the control HBSS after 5 days of treatment (Fig. 9.5).

For the HBSS containing 50 or 150 μM borate, no significant differences in the angiogenic response could be seen after 2 or 5 days of treatment. The studies of Durand and coworkers confirmed that the ionic dissolution products did not induce any angiogenic response and hence did not affect the normal development of the

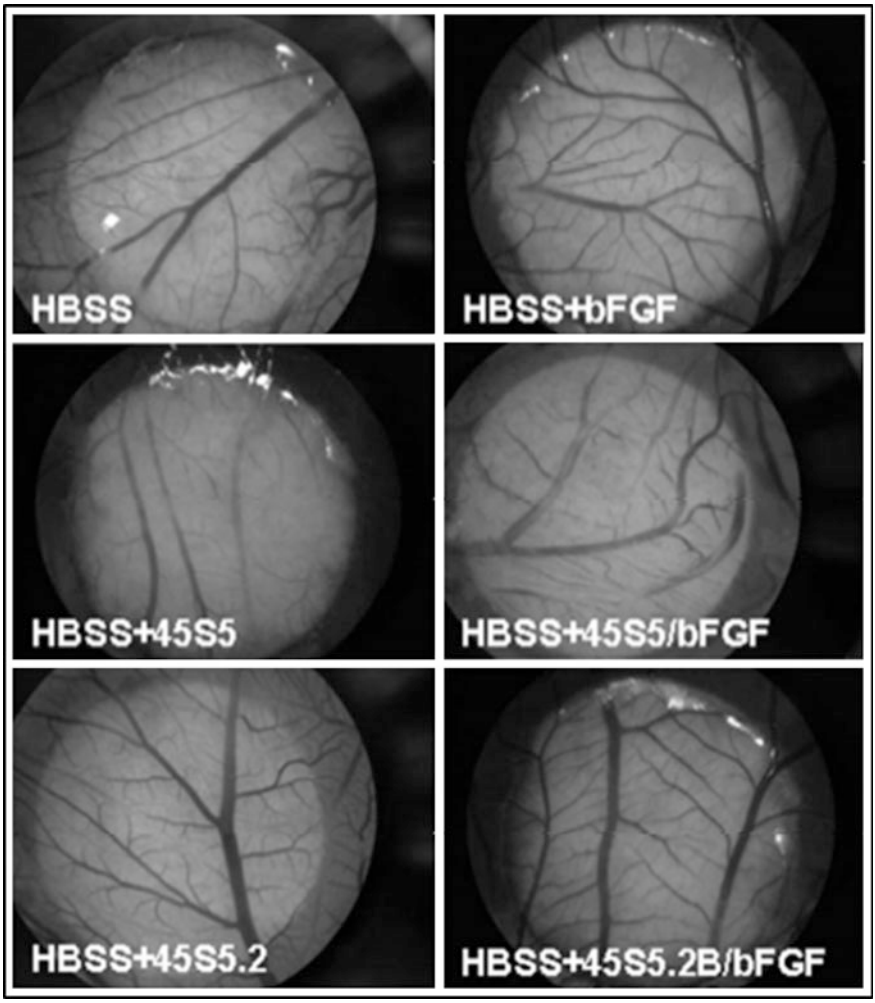

Fig. 9.4 The angiogenic response of CAM, five days posttreatment (Durand et al. 2014)

embryonic quail CAMs' vasculature. This could be due to the smaller contact area of CAM with the scaffolds causing insufficient ion release. Boron in the form of H_3BO_3 activates the mitogen-activated protein kinase (MAPK) signaling pathway to enhance cell proliferation and growth at low concentrations and inhibiting them at higher concentrations. Angiogenesis involves vascular growth factors and extracellular matrix interacting molecules like integrins. α_v β_3, a heterodimer integrin, is expressed at low levels on quiescent endothelial cells in vivo but is upregulated during vascular remodeling and angiogenesis. Lin and coworkers

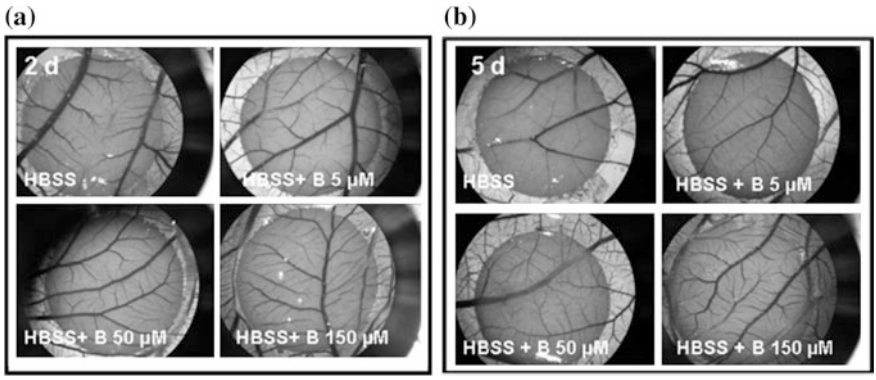

Fig. 9.5 **a** 2-day and **b** 5-day angiogenic response after treatment with HBSS and different borate concentrations (Durand et al. 2014)

demonstrated that no systemic cytotoxicity could be observed upon subcutaneous implantation of 13-93B3 glass (53 wt% B_2O_3) microfibers in rats, even when high amount of glass up to 1120 mg/animal was used. The controlled release of borate ions could represent promising alternative for the neurovascularization in regenerative medicine.

Mahmood and coworkers demonstrated the relation between glass porous matrix and in vivo vascularization. A fiber-based bioactive glass was used with composition of 32.24 % CaO, 9.26 % P_2O_5, 41 % SiO_2, and 17.5 % Al_2O_3 with recombinant human bone morphogenetic protein–2 (rhBMP–2). Vascularization was evaluated by mRNA expression of KDR and Flt-1, two VEGF receptors.

The scaffolds were designed in two shapes, i.e., bundle shape and porous ball constructs. The receptors KDR and Flt-1 did not express for the subcutaneously implanted bundle-shaped scaffolds in rats, 2–4 weeks postimplantation, but the same receptors expressed in porous ball scaffolds under same conditions. The histology results also revealed that after 2–4 weeks of subcutaneous implantation of scaffolds, higher bone formation could be seen for porous ball constructs compared to the bundle-shaped scaffolds. rhBMP promotes vascularization and also induces bone formation.

Ghosh and coworkers evaluated the biological response of BG block with the composition of 43.7 SiO_2, 19.2 % CaO, 5.46 % P_2O_5, 9.4 % B_2O_3, and 22.24 % Na_2O upon implantation in the radius bone of Bengal goats. After 3-month implantation, a well-formed vascularization and bone tissue ingrowth, directly integrating with the neighboring bone, could be seen. The same group worked on the same experimental model with glass composition of 58.6 SiO_2, 23.66 % CaO, 3.38 % P_2O_5, 3.78 % B_2O_3, 1.26 % TiO_2, and 9.32 % Na_2O, and found the establishment of vascular supply and well-organized transimplant angiogenesis across the bone defects.

Andrade and coworkers evaluated the angiogenic and inflammatory response of BG-coated collagen scaffolds upon subcutaneous implantation in mice. It was observed that the hemoglobin (Hb) content extracted from implants is higher in glass-coated collagen implants compared to glass-free group, after 14 days of implantation. No inflammatory response associated with the glass-coated collagen samples could be observed for in the presence of Hb, as revealed by the control group. Gerhardt and coworkers investigated the angiogenic effect of BG by comparing composite PDLLA/BG scaffolds with plain poly (D, L Lactide) (PDLLA) and obtained marked increase in the VEGF release by fibroblasts cultured on PDLLA/BG composites compared to plain PDLLA films. The in vivo experiments on a rat model confirmed enhanced vascularization and higher percentage of blood vessel formation, as shown by the stereological examination.

9.4 Phases in Wound Healing

Whenever the skin breaks, muscle tear or the burns occur; then, the tissue integrity is compromised, resulting in wounds. The phases of wound healing involve the following:

(a) Barrier protection: The wound shall be protected from the external environments by applying dressing and hydrogen. Hydrogels provide soothing barrier, which help in insulating the wounds against hot and cold stimuli along with acting as cushion against external physical conditions such as temperature and pressure of touch.
(b) Inflammatory Phase: The body responses naturally during this phase. After the occurrence of wounding, the clot formation would occur due to contraction of blood vessels in the wound bed. Upon stoppage of bleeding or hemostasis, the dilation of blood vessel occurs to allow growth factors, enzymes, antibodies, white blood cells, and nutrients to reach the wound site. Changes in vascular phase may cause inflammation, which is normal and prerequisite of healing. Injured tissue can cause histamine release causing blood vessels to dilate (vasodilation), resulting in blood exudation creating hot, swollen, reddened, and painful area around the wound. Near to the wound, the white blood cells adhere to the dilated endothelial walls. The phagocytosis also occurs, which is a cellular process of engulfing solid particles by the cell membrane to yield a phagosome known as food vacuole. Phagocytosis is very crucial step for the pathogen and cell debris removal. After few days, another phagocyte known as macrophage will predominate and stay in the wound until the inflammation ceases. The macrophages play dual role, i.e., to stimulate lymphocytes/immune cells to respond to the pathogen and to phagocytose cellular debris and pathogens. Usually, wound healing occurs without infection due to the

microbicidal capacity of macrophages. Another cell known as fibroblast start responding to the chemical signals released by the macrophages. Fibroblasts are well known for providing structural framework to many tissues and secrete the precursors for the extracellular matrix components.

(c) Proliferation/fibroblastic phase: Rebuilding follows, once the inflammatory phase is completed; fibroblasts are the building blocks of this phase. During this phase, the wound gets resurfaced and strength is imparted to it. Around blood vessel, loose tissues are present, containing mesenchymal cells that release fibroblasts. Another granulation tissue involved in this phase is comprised of collagen and extra cellular matrix (into which the blood network develops or angiogenesis occurs). During this phase, three processes, i.e., epithelialization, wound contraction, and collagen production, occur to achieve coalescence and closure of wounds. In addition to this, healthy granulation tissue depends on the fibroblast receiving healthy environment via adequate nutrient and oxygen supply. Healthy granular tissue possesses uneven texture and is red/pink in color. The undamaged epithelial cells at the wound margin start producing through mitosis, coursing a periphery formation around the wound. But in case the wound is extensive or it is a necrotic tissue, then the epithelial migration cannot proceed due to poor oxygen availability and dehiscence may occur. Dehiscence is the splitting or premature bursting of the wound. To facilitate epithelialization, moist dressings shall be done such as hydrogel dressings, which protect the wound from traumas.

The wound surface is closed by epithelialization, and then the contraction pulls the entire wound together causing defect shrinkage. A specialized cell known as myofibroblast is involved in the contraction process. Myofibroblast represents a cell that occurs in between smooth muscle cell and fibroblast during differentiation. Myofibroblasts attach to the skin margins and then pull entire epidermal layer inwards. The conclusive step during wound heating is collagen production by fibroblasts. To enhance fibrous tissue production, the adequate oxygen, (Zn, Fe, Cu) cofactors, nutrients, and ascorbic acid are required.

(d) Maturation/remodeling phase: During this phase, the wound has closed and collagen remodeling from type III to type I is involved. During this phase, reduction in cellular activity and blood vessels near the wounded area could be observed. The collagen synthesis occurs at a high rate, but no further increase in scar mass occurs. With the help of enzyme collagenase, the old collagen is broken down and new one is created to maintain the equilibrium, and this process continues until the remodeling ends depending upon the state and depth of injury. In case the process of healing does not take properly, then the keloid or hypertrophic scar could be formed due to the collagen overproduction. Keloids are rubbery firm lesions, which are shiny and benign in nature, whereas hypertrophic scar is raised as red lump over the injury. Figure 9.6 depicts all the stages of wound healing.

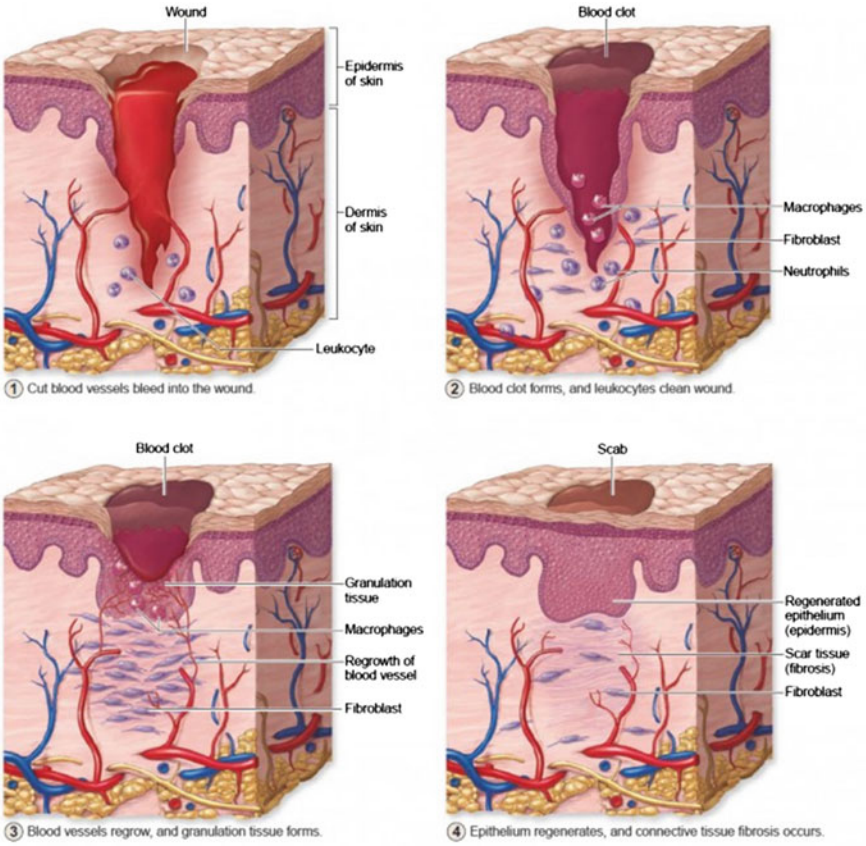

Fig. 9.6 Stages in wound healing (Photocourtesy by: Biology Forms)

9.5 Bioactive Glasses in Wound Healing

Ma and coworkers synthesized BG glass ceramics-based man fibrous membranes for the wound dressing [30 % SiO_2, 27 % CaO, 20 % B_2O_3, 4 % P_2O_5, 1.5 CuO, 1 % ZnO, 3 % K_2O, 9 % Na_2O, wt%] using electrospinning technique with varying chitosan: gelatin ratios (C/G ratio) (Fig. 9.7).

It is clear from the SEM observations that the G/C nanofibers are composed of open pores with several micron dimensions. As the C/G ratio increases from 1/19 to 5/15 in the solution, the presence of beads could be observed in the fiber body prone to aggregation. The sol-gel-derived glass is highly dispersible with nanoscale-dimensional size. The fiber morphology is changed with an increasing BG/(chitosan + gelatin) ratio, i.e., from 6 to 15 %, where the BG is introduced via electrospinning technique for C/G ratio of 3/17. As shown in Fig. 9.8, upon increasing the BG/(G+C) ratio to 15 %, the mats grow blade like continuous fibrous

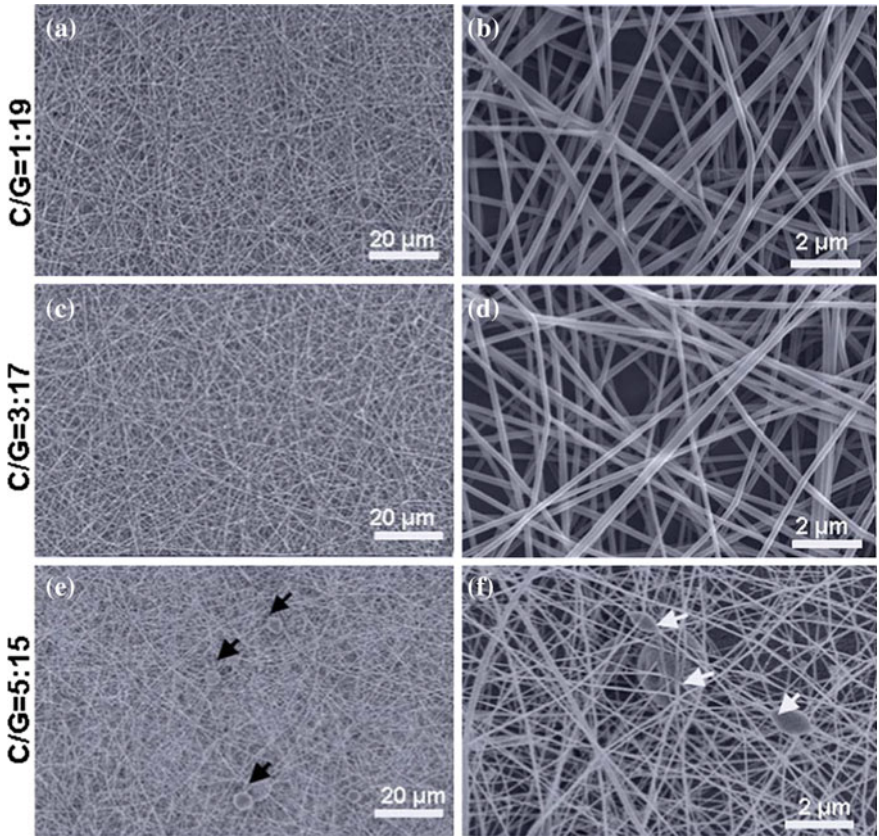

Fig. 9.7 SEM images of the G/C nanofibrous mats with different C/G mass ratios (Ma et al. 2014)

networks. The bioactive glass particles could be seen anchoring in the fiber matrix with scarce expose in porous network upon increasing BG content. BG-introduced mats exhibited high tensile strength, almost 2–4 folds higher than the pure organic mats. Upon addition of 15 % BG, the average elongation ratio of mats increased by 150 %, favoring it for the biomedical application. Collagen is one of the most abundant insoluble structural fibers inside the human body and is controlled hydrolysis yields gelatin. The gelatin temperature of human physiological fluid and gelatin is close to each other, which makes it necessary to cross-link the gelatin-based dressings carefully for improving the structural and thermal stabilities. The G/C–15 BG and G/C–0BG mats were subcutaneously implanted in rats, and it was observed that after 2 weeks of implantation, no inflammation or adverse response of the host tissue could be seen, indicating their high biocompatibility as depicted in Fig. 9.9. After 4 weeks of implantation, the degradation of the G/C-15 BG and G/C–0BG mats was observable. The bioactive potential of G/C–BG mats

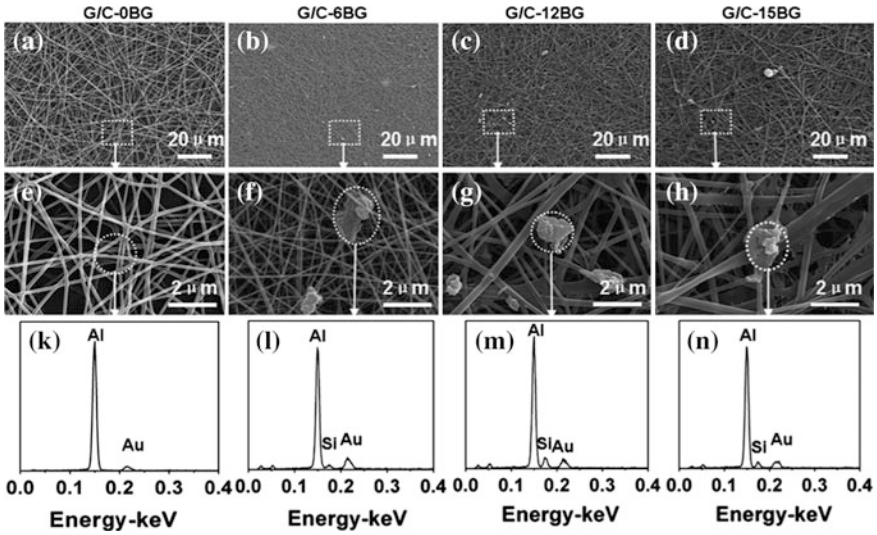

Fig. 9.8 (A-H) SEM observation and (K–N) EDX analysis of the G/C–xBG membranes with different amount of BG at C/G ratio 3/17 via the electrospinning technique (Ma et al. 2014)

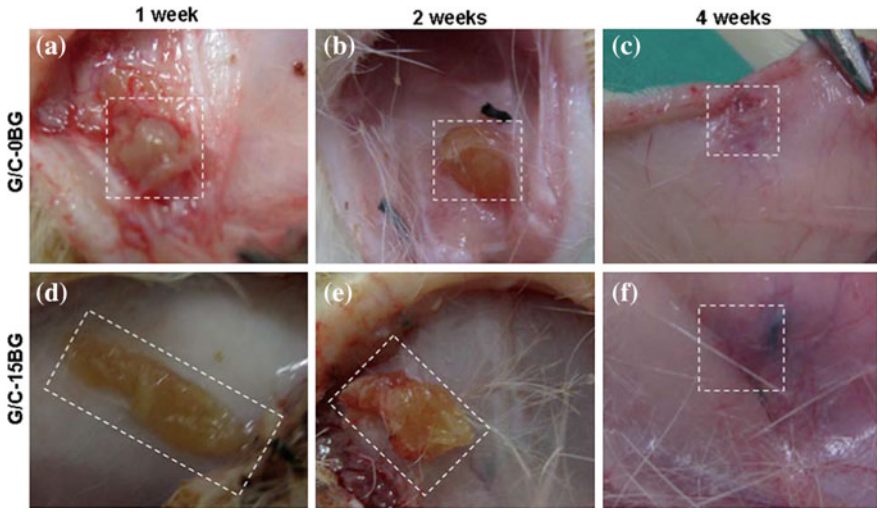

Fig. 9.9 Wound healing upon implanting G/C-xBG in subcutaneous tissue of rats (Ma et al. 2014)

can be due to two aspects: the release of inorganic ion products via BG dissolution and beneficial G/C functions on the wound site. Due to these two factors, the cellular signaling gets improved and at the same time nanofibrous network

containing BG provides modified surface properties and anti-bacterial activities, which prove beneficial for the anti-adhesion on wet wounds.

Cong and coworkers used Yunnan Baiyao (YB), a well-known Chinese herbal medicine as hemostatic agent, and 45S5 Bioglass® on the diabetic wound healing in diabetic rats. Yunnan Baiyao can cause release of platelet constituents along with enhancing surface glycoprotein's expression on platelets under stimulated conditions which cause shortening clotting/bleeding times in rabbits and rats. The rats were separated into eight groups as shown in Table 9.1.

Figure 9.10 gives the observation after 7, 14, and 21 days for the wounds treated with different methods. After 7 days of treatment, except for the groups 5 and 7, the red granulation tissue has filled up all the wounds. For all the groups, wounds were regularly shaped with rough surface in all groups. Slight enlargement of skin tissue could be seen in all the diabetic groups. After 14 days, all groups showed considerable reduction in wound size, particularly for group I and group VI. Compared with day 7, the edge of wounds was much normal and the inflammatory reaction disappeared. After 21 days, the wounds could be seen covered by new epidermis and showed healing in the groups 1 and 6. For the groups 2 and 3, still open wounds could be seen. The bioactive glass and Yunnan Baiyao ointments have healing

Table 9.1 Coding of experimental animal rats with wounds

	CODES	Ointment	Method of treatment
Each group with 15	1		Non-diabetic saline-treated rat
	2		Saline treated
	3		Vaseline treated
	4	84 % Vaseline + YB	Ointment V treated
	5	84 %Vaseline + 45S5 ointment	Ointment I treated
Rates	6	5 % YB	Ointment II treated
	7	10 % YB	Ointment III treated
	8	20 % YB	Ointment IV treated

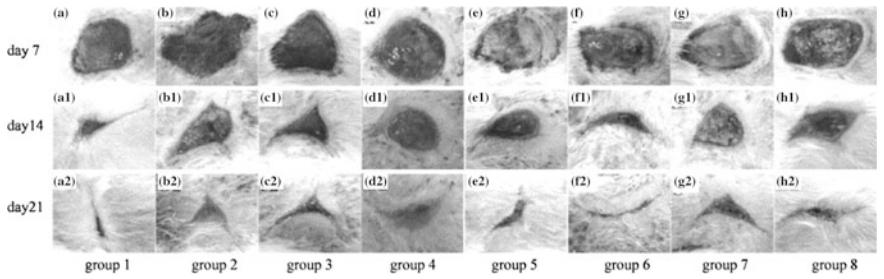

Fig. 9.10 Wound healing in the rat groups using different ointments (Cong et al. 2014)

effects on wounds in diabetic rats. Group 6 containing 5 % Yunnan Baiyao had better results than any other ointment. Diabetic wounds are much more complicated due to neuropathic, vascular, biochemical, and immune function abnormalities. Patients with diabetes have impaired wound healing due to high blood glucose levels. The bioactive glass containing ointments can be better alternatives for curing such diabetic wounds.

Lin and coworkers also worked on producing Vaseline-based ointments with 18 wt% of 58S glass (SGBG-58S), nanoscale BG 58S (NBG-BS), and melt-derived 45S5 glass powders for the treatment of superficial injuries in diabetic rats. The bioactive glass with the ointment and Vaseline were applied directly on the full thickness wounds. Figure 9.11 demonstrates that the wound healing was accelerated in the presence of bioglass, especially SGBG-585, after day 16. In contrast to this, the wounds were still open for the control group, and it took little longer for the healing. Increased proliferation of fibroblast could be seen along with new capillary formation and granulation tissues for the BG-treated ointments, and immunohistochemical assays showed the VEGF presence in all tissues at day 7.

No adverse reaction or inflammatory response could be seen in the animals treated with bioactive glass ointments. Moreover, the wound healing results demonstrated quick healing of wounds with the sol-gel-derived glasses than the melt-quenched 45S5 glass, attributed to the larger surface area of the sol-gel glasses.

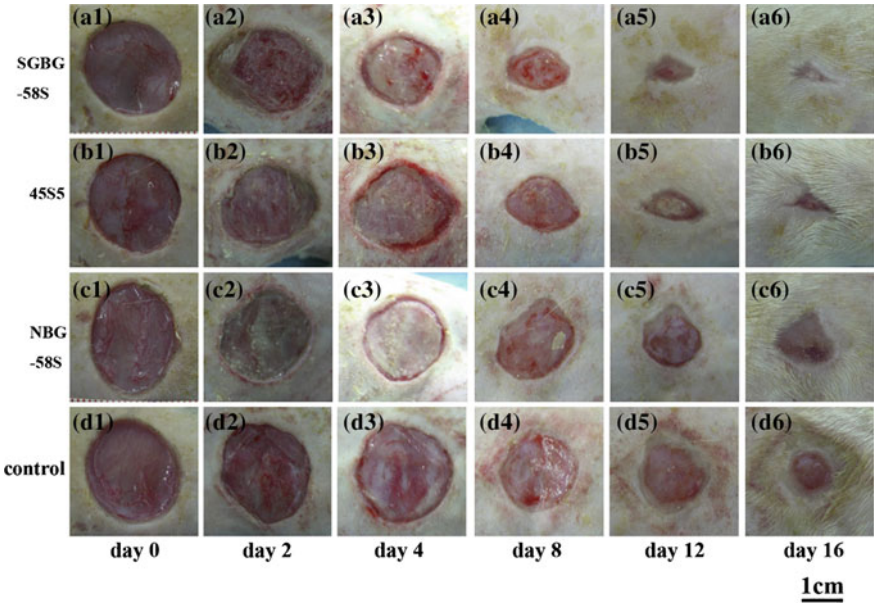

Fig. 9.11 Healing in BG-treated and untreated wounds from days 0–16 (Lin et al. 2012)

Yang and coworkers conducted comprehensive evaluation of HAp conversion and cell–glass interactions under both dynamic and static modes. The nano/microfibers used are of 45S5, 13-93B3, and 1605 [6 % Na_2O, 12 % K_2O, 5 % MgO, 20 % CaO, 4 % P_2O_5, 51.6 % B_2O_3, 0.4 % CuO, 1 % ZnO, wt%) for their effect on wound healing as well on the human fibroblast skin line (CCL-10). The morphology of fibers under a dynamic flow condition with continuous fresh media supply is shown in Fig. 9.12. The fibers possessed smooth surface with fewer fine structures such as flakes and whiskers. The 45S5 fibers had eroded/porous inner structures. For the 13-93B3 fibers, a polished surface morphology with porous granule network underlying the surface layers could be seen. Highly roughened surface and protruded spherical structures could be seen for the borate-based 1605 fibers.

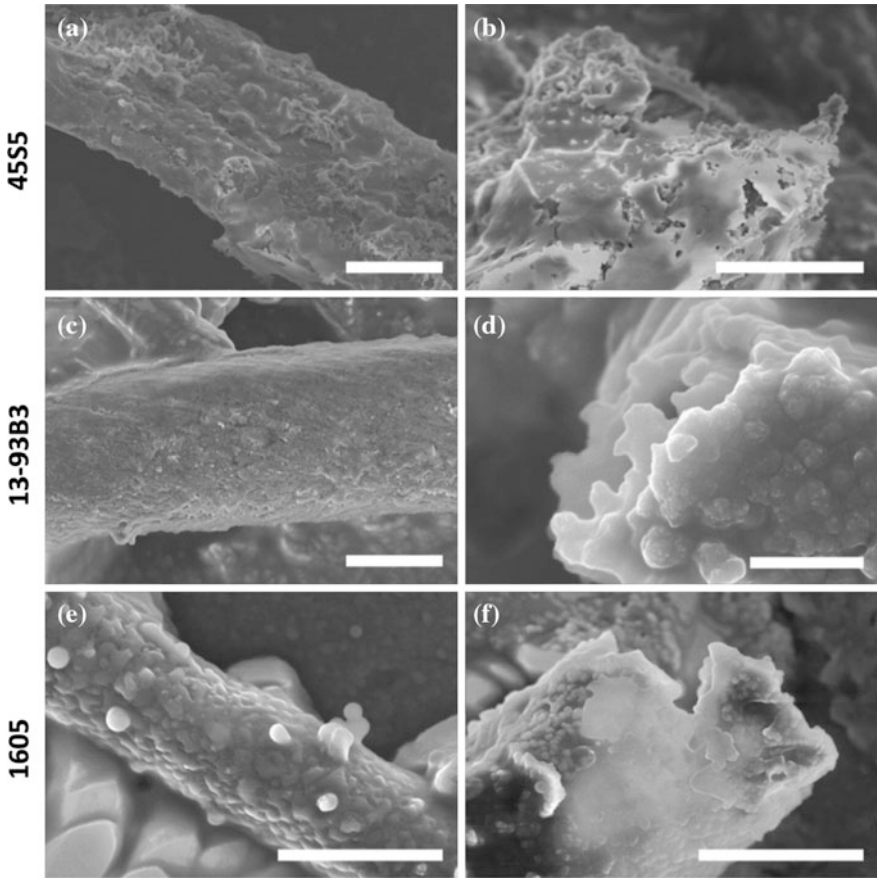

Fig. 9.12 SEM images of **a**, **b** 45S5 **c**, **d** 13-93B and **e**, **f** 1605 bioactive fiber surface and end-face after dynamic-mode soaking in cell culture medium for 5 days (Yang et al. 2015)

Eroded fiber surfaces and hollowed cross section could be seen upon viewing the fibers under high magnification. The fibers had a negative effect on cell viability at high dosages. For 45S5 and 1605 glass, high cell proliferation could be observed for the dosages of ≤ 750 μg/ml and ≤ 250 μg/ml, respectively. The cell viability has been function of both the treatment time and fiber dosage. The fiber dosage <200 μg/ml provided better viability than the control. If the fiber is presoaked with serum-free cell culture medium, then cell proliferation got stimulated by 35–40 % by 45S5 and 13-93B3, even after 1-h soaking. The cytotoxicity could be reduced by the partial conversion of fibers, attributed to the rapid refreshing rate of dissolved calcium and boron, along with improved surface elemental deposition. Higher cell viabilities could be seen for the fiber groups with dynamic control group as compared to the static control. Though silicate 45S5 fibers have wider dosage range for positive cell proliferation, but borate-based fiber can stimulate higher cell viabilities than the silicate glass fibers. Under static mode, negative impact on the cell migration was observed in all fiber-treated groups, with higher impairment effects caused by the borate glasses. The formation of new tissue around the wound is characterized by cell migration and keratinocyte/fibroblasts proliferation. The tissue repairing mechanism could be seen by 45S5, 13-93B3 and 1605, along with the fiber-stimulating effect on cell proliferation and migration abilities.

Gillette and coworkers applied BG with particulate <20 μm into surgically made open wounds in nine dogs. The wounds made were bilateral, so that the BG-treated wound and control could be studied together. Small slurry of BG and blood was produced, which was then applied to the wounds. A small amount of this paste lied between the wounds edges, whereas most of the mixture stayed in the subcutaneous area of the wound. After 5 days of application, no significant difference could be observed in the breaking strength of healed skin in all the samples, but increase in breaking strength of healed cutaneous/subcutaneous trunci in treated wounds could be seen as compared to control wounds. In addition to this, no inflammatory response of the host tissue could be seen.

Wray worked on repairing the wounds on small scale for worst-case diabetic patients using 13-93B3 glass nanofibers ranging from 5 μm to 300 nm. Accelerated healing of the wounds could be observed along with marked decrease in scar tissue formation as compared to congenitally treated wounds. Silver-containing nanoporous bioactive glass (n-BGS) has been investigated for its anti-bacterial dressings and hemostatic properties compared to the bioactive glass without nanopores (BGS). n-BGS possesses higher surface area compared to the BGS, resulting in its higher water absorption efficacy. n-BGS released Ag^+ ions rapidly, though the concentration of silver in solution was same after 24 h of incubation in phosphate-buffered solution (PBS). For n-BGS at 0.02 wt% silver concentration, highest anti-bacterial rate of 99 % could be obtained for the Escherichia coli, after 12-h incubation time. n-BGS and BGS particles were applied to the damaged femoral arteries and veins of male New Zealand white rabbits. n-BGS has significantly lower clotting times in both prothrombine time (PT) and activated partial

thromboplastin time (APTT) in vitro. Hence, silver-doped n-BGS accelerates clotting, provides bactericidal effect, and promotes hemorrhage control.

Zhao and coworkers fabricated wound dressings comprising of copper doping (0–3 wt% CuO) in the 13-93B3 microfibers. Copper is considered to be an essential component of angiogenic response as they stabilize the expression of hypoxia-inducible factor (HIF-1α), mimicking hypoxia and hence playing a crucial role in the recruitment and differentiation of the cells as well as blood vessel formation. Cu^{2+} release also stimulates the expression of proangiogenic factors such as transforming growth factor-β (TGF-β). Cu^{2+} ions enhance implant vascularization when used in combination with the VEGF and bFGF. It was observed that after 7 days of cell culture, Cu-doped microfibers proliferated HUVEC better than the cell cultured on the ionic dissolution product of undoped microfibers. HUVEC incubated with the ionic dissolution product of Cu-doped microfibers yielded elongated and tube-like structures (after incubating on the matrigel substratum for 12 h). Anyhow, incomplete or sparse tubular network formation could be seen, when HUVECs are treated with the ionic dissolution product of undoped microfibers. VEGF, bFGF, and PDGF gene expressions for fibroblasts incubated in the ionic dissolution products of microfibers enhanced as the content of CuO increased in fibers, indicating the proangiogenic potential of the bioactive glass microfibers. The wound images with the application of Cu-doped 13-93B3 are shown in Fig. 9.13 at 0, 6, 10, and 14 days.

The smallest wound size was observed in the 3Cu-BG group though the wound size decreased with the healing time for all the groups. The wound closed by day 14, upon its treatment with 3Cu-BG. For the quantification of wound, following equation is used.

$$\% \text{ Wound size reduction} = [(A_o - A_t)/A_o] \times 100 \tag{9.1}$$

where A_o and A_t are wound areas initially and at each time point. The micro-CT showed a high number density of blood vessels in the defects treated with 3Cu–BG microfibers than the untreated or BG microfiber-treated wounds. Histological analysis of Masson's trichrome-stained section of the three treatment groups is shown as in Fig. 9.14.

Extensive collagen deposition and thick wavy collagen fibers could be observed in wound areas treated with BG microfibers as compared to the untreated defects. The 3Cu-BG microfibers treated wound showed highest collagen fibers arranged in an orderly fashion similar to the normal skin. For both 3Cu-BG and BG, the accelerated formation of hair follicles and sebaceous glands, 14 days postsurgery, could be obtained. Together, all these results indicated that the Cu-doped borate bioactive glass microfibers are promising candidates for wound dressing.

Li and coworkers studied the wound healing treatment using Bioglass® by affecting gap function connexin 43 mediated endothelial cell behavior. All the endothelial cell behaviors are related to gap junctional cell-to-cell communications

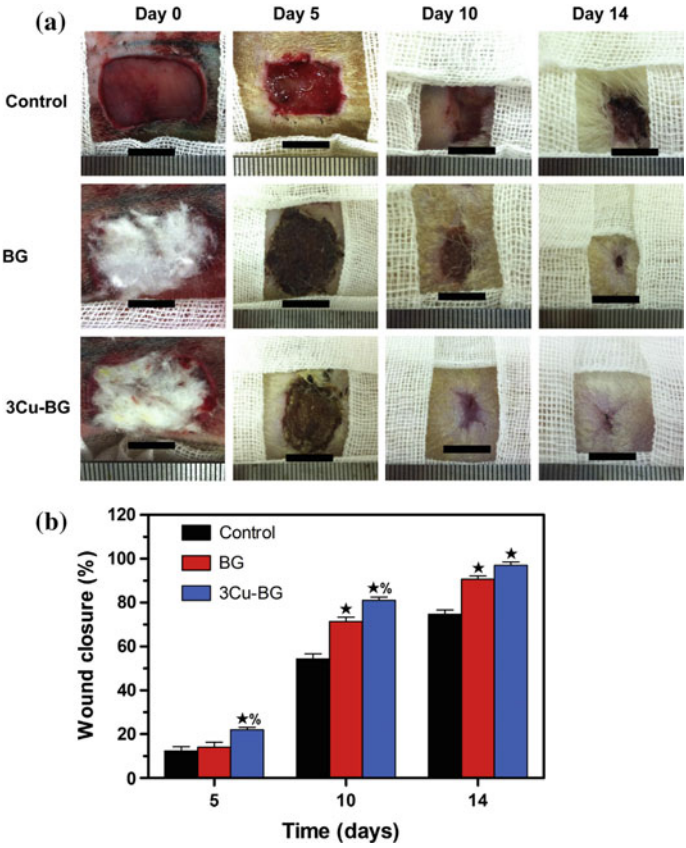

Fig. 9.13 **a** Skin defects in rodents, left untreated (control) or treated with the BG or 3Cu-BG microfibers, at 0, 5, 10, and 14 days postsurgery. **b** Percent wound closure for the untreated defects (control) and the defects treated with the BG or 3Cu-BG microfibers at 5, 10, and 14 days postsurgery (Zhao et al. 2015)

as connexin 43 (C × 43) plays imperative role in determining the fate of endothelial cell along with cell-to-cell communication mercenary for angiogenesis and wound heating. C × 43 is the most ubiquitous connexins in skin located in dermal appendages, fibroblasts as well as cutaneous vasculature. C × 43 anti-sense C × 43 mimetic peptides and C × 43 hemichannels play an important role in the wound healing. The 45S5 BG extracts were diluted in endothelial cell medium at ratios of 1/8, 1/16, 1/32, 1/64, 1/128, 1/256, and 1/512. For BG 1/8 and BG 1/16, the proliferation of HUVEC is suppressed as compared to the medium alone. Under hypoxia conditions, almost 80 % of HUVEC cultured in BG 1/128 ion extracts remained viable and the survival was same as that of the non-hypoxic conditions. For BG 1/152, only 65 % cells remain alive, indicating that BG at appropriate

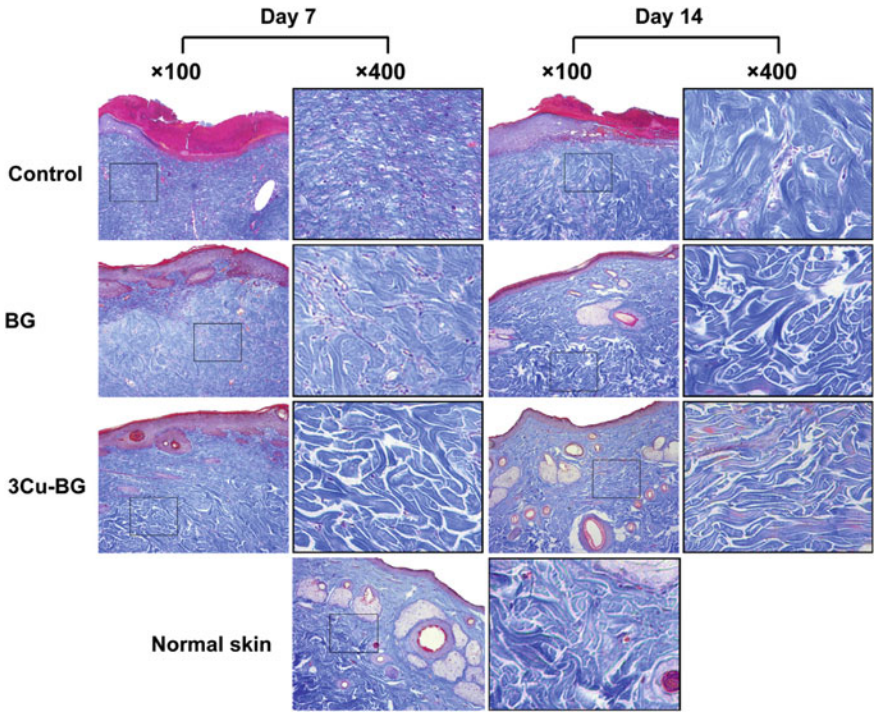

Fig. 9.14 Masson's trichrome-stained sections of the untreated defects (control) and the defects treated with the BG or 3Cu-BG microfibers at 7 and 14 days postsurgery, indicating collagen deposition (Zhao et al. 2015)

concentration could protect HUVECs exposed to hypoxic conditions. After 1-day culture in HUVEC, the culture media containing BG 1/64, BG 1/128, and BG 1/256 upregulated the bFGF, VEGF, and KDR gene expression. After 7 days, the VEGF and KDR expressions in HUVECs are shown as in Fig. 9.15.

Immunofluorescence staining yielded more positive results for in KDR HUVECs cultured in BG 1/64, BG 1/128, and BG 1/256 than the cell cultures in BG 1/32 and BG/512. The KDR expression in HUVECs cultured with BG 1/64, BG 1/128, and BG 1/256 is higher than the control results. C × 43 expression in HUVECs cultured in BG 1/64 and BG 1/128 for 7 days is much higher than the cells cultured in endothelial medium alone BG 1/32, BG 1/512. For the wound treated with BG, the granulation tissue formation could be seen in the form of vascularized endodermis (beginning day 6). After 12 days, the granulation tissue is much more organized, but no neoepidermis formation could be seen for the untreated wound though eschar and noticeable granulation tissue formation could be seen. Figure 9.15 gives the immunolabeling of C × 43 in wound sites at days 2 and 12. C × 43 expression could be seen after 2 days of operation in control and BG-treated wounds. After 12 days of operation, highest C × 43 expression could

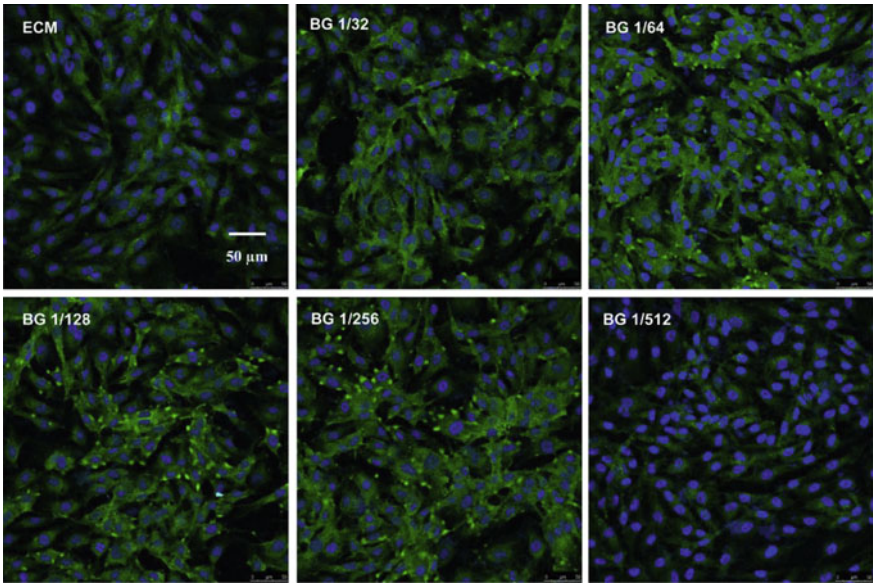

Fig. 9.15 KDR protein expression and localization in HUVECs cultured with different media for 3 days (Li et al. 2016)

be seen for the BG-treated wounds than the untreated ones. Hence, the results can be summed up as:

- BG protects endothelial cells by reducing open probability of hemichannels during the early stages of wound healing during which hypoxia can occur.
- During the cell migration and proliferation, BG stimulates endothelial cells to migrate into wound bed and upregulate VEGF from the existing endothelial cells.
- Gap junctional communication between endothelial cells is increased, once the endothelial cells reach at the wound bed, thereby stimulating vascularization.

Rai and coworkers fabricated poly (3-hydrony-octanoate) composite forms with nanosized bioactive glass (nBG) for the wound dressings. With increasing proportion of glass nanoparticles, the toughness is increased with enhanced polymer wettability along with decreased clothing time of citrated whole blood. Increased cell proliferation could be seen when human keratinocytes were cultured on the composite films attributed to the increased surface area of the nBG.

Bibliography

Li H, He J, Yu H, Green CR, Chang J (2016) Bioglass promotes wound healing by affecting gap junction connexin 43 mediated endothelial cell behavior. Biomaterials 84:64–75. doi:10.1016/j.biomaterials.2016.01.033

Ma W, Yang X, Ma L, Wang X, Zhang L, Yang G, Gou Z (2014). Fabrication of bioactive glass-introduced nanofibrous membranes with multifunctions for potential wound dressing. RSC Adv 4(104):60114–60122. doi:10.1039/C4RA10232K

Day RM (2005) Bioactive glass stimulates the secretion of angiogenic growth factors and angiogenesis in vitro. Tissue Engineering 11(5):768–777. doi:10.1089/ten.2005.11.768

Yang Q, Chen S, Shi H, Xiao H, Ma Y (2015) In vitro study of improved wound-healing effect of bioactive borate-based glass nano-/micro-fibers. Materials Science and Engineering C 55:105–117. doi:10.1016/j.msec.2015.05.049

Zhao S, Li L, Wang H, Zhang Y, Cheng X, Zhou N, Zhang C (2015) Wound dressings composed of copper-doped borate bioactive glass microfibers stimulate angiogenesis and heal full-thickness skin defects in a rodent model. Biomaterials 53:379–391. doi:10.1016/j.biomaterials.2015.02.112

Kent Leach J, Kaigler D, Wang Z, Krebsbach PH, Mooney DJ (2006) Coating of VEGF-releasing scaffolds with bioactive glass for angiogenesis and bone regeneration. Biomaterials 27 (17):3249–3255. doi:10.1016/j.biomaterials.2006.01.033

Lin C, MaO C, Jhang J, Li Y, Chen X (2012) Healing effect of bioactive glass moment on full thickness skin wounds. Biomed Mater 7(4):045017

Haro Durand LA, Vargas GE, Romero NM Vera-Mesones R, Porto-López JM, Boccaccini AR, Gorustovich A (2015) Angiogenic effects of ionic dissolution products released from a boron-doped 45S5 bioactive glass. J Mater Chem B 3(6):1142–1148. doi:10.1039/C4TB01840K

Cong M, Lin C, Chen X (2014) Enhanced healing of full-thickness diabetic wounds using bioactive glass and Yunnan baiyao ointments. J Wuhan Univ Tech, Mater Sci Ed 29(5):1063–1070. doi:10.1007/s11595-014-1044-y

Fujibayashi S, Neo M, Kim HM, Kokubo T, Nakamura T (2003) Biomaterials 24:1349–1356

Wilson J, GH Pigott, FJ Schoen, LL Hench (1981) J Biomed Mater Res 15(6):805–817

Gatti aM, Valdrè G, Andersson OH (1994) Analysis of the in vivo reactions of a bioactive glass in soft and hard tissue. Biomaterials 15(3):208–212

Murphy WL, Simmons CA, Kaigler D, Moona DJ (2004) J Den Res 83:204–210

Aina V, Malavasi G, Pla AF, Munaron L, Morterra C (2009) Zinc-containing bioactive glasses: surface reactivity and behaviour towards endothelial cells. Acta Biomater 5:1211–1222

Leu A Leach JK (2008) Pharn Res 25:1222

Lin Y, Brown RF, Jung SB, Day DE (2014) J Biomed Mater Res A 102:4491–4499

Mahmood J, Takita H, Ojima Y, kobayshi M, Kohgo T, Kubole Y (2001) J Biochem 129:163

Ghosh SK, Nandi SR, Rumdu B, Datta S, De DK, Roy SR, Baseu D (2008) J Biomed Mater Res Part B 86:217

Nandi SK, Kundu B, Datta S, De DK, Basu D (2009) Res Vet Sci 86:162

Andrade AL, Andrade SP, Domingues RZ (2006) J Biomed Mater Res B 79:122

Gerhardt L-C, Widdows KL, Erol MM, Burch CW, Sanz-Herrera JA, Ochoa I et al (2011) The pro-angiogenic properties of multi-functional bioactive glass composite scaffolds. Biomaterials 32(17):4096–4108

Gillette RL, Swaim SF, Sartin EA, Bradley DM, Coolman SL (2001) Am J Vet Res 62(7):1149–1153

Wray P (2011) Am Ceram Sec Bull pp 25–29

Hu G, Xiao L, Tong P, Bi D, Wang H, Ma H (2012) Int J Nauomedicine 7:2613–2620

Rai R, Boccaccini AR (2010) ATP Conf Proc 1255:126–128

Baino F, Novajra G, Miguez-Pacheco V, Boccaccini AR, Vitale-Brovarone C (2016) Bioactive glasses: special applications outside the skeletal system. J Non-Cryst Solids 432:15–30. doi:10.1016/j.jnoncrysol.2015.02.015

Krishnan V, Lakshmi T (2013) Bioglass: a novel biocompatible innovation. J Adv Pharm Tech Res 4(2):78–83. doi:10.4103/2231-4040.111523

Nganga S (2013) Glass-Fiber reinforced cpmposite for bone implants. Evaluation of antimicrobial effect and implant fixation

Tobergte DR, Curtis S (2013) No title no title, vol 53. J Chem Inf Model. doi:10.1017/CBO9781107415324.004

Fujibayashi S, Neo M, Kim H-M, Kokubo T, Nakamura T (2003) A comparative study between in vivo bone ingrowth and in vitro apatite formation on Na_2O-CaO-SiO_2 glasses. Biomaterials 24(8):1349–1356. doi:10.1016/S0142-9612(02)00511-2

Khader B, Curran D, Peel S, Towler M (2016) Glass polyalkenoate cements designed for cranioplasty applications: an evaluation of their physical and mechanical properties. J Funct Biomater 7(2):8. doi:10.3390/jfb7020008

Gorustovich, AA Roether JA, Boccaccini AR (2010) Effect of bioactive glasses on angiogenesis: a review of in vitro and in vivo evidences. Tissue Eng Part B Rev 16(2):199–207. doi:10.1089/ten.TEB.2009.0416

Keshaw H, Forbes A, Day RM (2005) Release of angiogenic growth factors from cells encapsulated in alginate beads with bioactive glass. Biomaterials 26(19):4171–4179. doi:10.1016/j.biomaterials.2004.10.021

Kiefer K, Amlung M, Aktas OC, De Oliveira PW, Abdul-Khaliq H (2016) Novel glass-like coatings for cardiovascular implant application: preparation, characterization and cellular interaction. Mater Sci Eng C 58:812–816. doi:10.1016/j.msec.2015.09.063

Kokubo T (1991) Bioactive glass ceramics: properties and applications. Biomaterials 12(2):155–163. doi:10.1016/0142-9612(91)90194-F.

Miguez-pacheco V, Greenspan D (2015) Bioactive glasses in soft tissue repair. American Ceram Soc Bull 94(6):27–31. Accessed from http://ceramics.org/wp-content/uploads/2009/06/Aug_Feature.pdf

Miguez-Pacheco V, Hench LL, Boccaccini AR (2015) Bioactive glasses beyond bone and teeth: emerging applications in contact with soft tissues. Acta Biomater 13:1–15. doi:10.1016/j.actbio.2014.11.004

Chapter 10
Bulk Metallic Glasses for Healthcare: State of the Art and Prospects for the Future

Gurbinder Kaur and J.C. Mauro

The implantation of material inside the human body is based on the material selection and hence can be designed as per the specific requirement. Metallic alloys have found widespread applications in the biomedical engineering and the biocompatibility can be enhanced due to sophistication of metallurgical aspects of fabrication. However, the corrosion-related problems and wear and tear of metals along with the elasticity issues have been a potential cause of concern. The glass-ceramics have shown excellent potential, but their low mechanical strength poses a serious issue on the long-term applications. Though metals and steels such as titanium-based alloys, Ni–Ti alloy, and cobalt bases alloys have been successfully used as biomaterials. A new class of biomaterials i.e., bulk metallic glasses (BMG) have been of interest since past three decades. A wide spectrum of BMG such as Mg, Pd, Au, Zr, Cr, Cu, Ni, Ti and Pt based materials have been studied. The current chapter deals with the applications, progress, and future perspectives of bulk metallic glasses.

10.1 Introduction to Bulk Metallic Glasses

Bulk metallic glasses vitrify at low cooling rates and exhibit ease to avoid crystallization during the solidification process. Bulk metallic glasses do not exhibit long-range atomic order and lack of atomic order yields BMG with significant chemical, physical, mechanical, and biological properties. The glass-forming ability (GFA) of BMG is high, depicting their relative ease of glass formation at low cooling rates yielding high critical diameter upon casting into the copper mold. BMG can be plastically shaped under low applied forces (hot embossing, injection, and extrusion) within the supercooled region i.e., region between glass transition temperature (T_g) and glass crystallization temperature (T_c). As compared to the metallic glass (MG), the BMG can be obtained at lower cooling rates (<100 K/s) and the required specimen size can be obtained. In addition to this, BMG exhibits

G. Kaur, *Bioactive Glasses*, Series in BioEngineering,
DOI 10.1007/978-3-319-45716-1_10

strong resistance to the crystallization particularly for the supercooled liquid state. The superior properties of BMG can be attributed to the fact that it combines the properties of elemental metal compositions and the conventional amorphous bioactive glasses together.

Bulk metallic glasses posses unique properties attributed to the random atomic arrangements and lack of dislocations slip planes. More scientifically, bulk metallic glasses are defined as the amorphous alloys exhibiting glass transition, from which it derives the properties of high flexibility, extreme strength, and tailorable physical properties. Figure 10.1 indicates the relationship between bioactive glasses, bimetallic alloys, and bulk metallic glasses. A number of empirical rules have been suggested for the formation of BMG based on interatomic bonding, atomic size, and election density. Inoue and coworkers suggested that for the BMG fabrication, the alloy must be multicomponent system (more than three elements), with the difference in size ratios >12 %. In addition to this, the elements shall have negative heat of mixing.

The BMGs possess extremely high elastic limit of 2 % as compared with the elastic limit of 1 % of the bone. BMG are used for the biomedical implants, artificial prostheses, and absorbable sutures. BMG are homogenous and isotropic on small length scales and also provide better corrosion properties in physiological solutions compared to commonly used biomaterials.

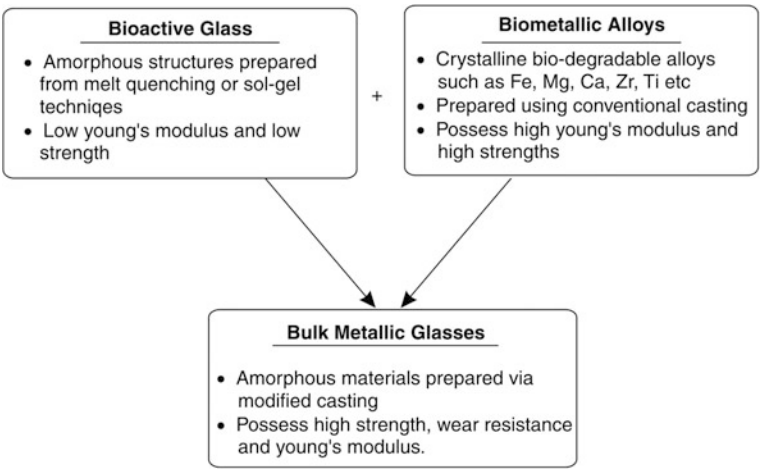

Fig. 10.1 Relationship between bioactive glass, alloys, and BMG

10.2 Inoue's Criteria for BMG Classification

To understand the characteristics of BMGs, the classification shall be done in precise manner. Inoue classified the BMGs into five categories based on the atomic size differences and characteristics of constituent elements. Anyhow, the classification system given by Inoue revealed the alloys system but not the range of glass-forming region for that particular composition. For instance, Zr–Al–Ni system is regarded as single BMG unit, but the BMGs consisting of Ni, Al and Zr are neither Zr nor Al bases BMGs. In addition to this, Zr–Al–Ni system exhibits wide composition range such that the formation of amorphous phase is more toward the aluminum rich region as compared to the formation of metallic glasses over the Ni-rich region. In the previous classification, the inclusion of Pd and Pt alloys is not made, in spite of the fact that these alloys are potentially accepted for the BMG formation. Figure 10.2a gives the previous BMG classification system proposed by Inoue.

It is evident that the previous classification system has five groups of the BMGs. The first four groups, G(I)–G(IV), have three in five groups of elements i.e., late transition metal (LTM), lanthanide metal (Ln) and early transition metal (ETM), metalloid, metal, and group of elements such as Al, Ga, and Sn. The third group is a multicomponent system consisting of (Al, Ga, Fe—metalloid).

The G(V) group consists of elements from the group late transition metals and metalloid. Figure 10.2b gives the recent classification of BMG proposed by Takeuchi and coworkers. On comparison of Fig. 10.2a, b, it could be seen that the LTM is extended as LTM/BM and Al–Ga–Sr Al–Ga–Sn is modified as Al–Ga. According to current criteria, the BMGs can be classified into seven groups discussed as follows:

- G-I : ETM/Ln–LTM/BM—Al/Ga
- G-II : ETM/Ln–LTM/BM—metalloid
- G-III: Al/Ga–LTM/BM—metalloid
- G-IV: IIA–ETM/Ln—LTM/BM
- G-V: LTM/BM—metalloid
- G-VI: ETM/Ln—LTM/BM
- G-VII: II A—LTM/BM.

The Inoue classification can be depicted diagrammatically as shown in Fig. 10.3.

Sn is previously classified in the group of elements of Al, Ga, Sn on the basis of Ti–Ni–Cu–Sn system. Many Sn-based BMG systems have been investigated such as $Ni_{59}Zr_{20}Ti_{16}Si_2Sn_3$, Ni–Ti–Zr (Si, Sn), Ti–Cu–Ni–Sn, Ti–Cu–Ni–B–Si–Sn, and Ni–Nb–Sn. In recent classification, Sn is shifted from (Al, Ga, Sn) to LTM/BM group because the major constituents decide the BMG characteristics, which leads to the conclusion of classifying similar BMG into similar group. When Sn is placed in LTM group of elements, then Sn-containing BMGs are classified as Ti–Cu–Ni–B–Si–Sn in G-II, Ni–Ti–Zr–Sn in G-IV, Ti–Cu–Ni–Sn in G-VI, and $Ni_{59}Zr_{20}Ti_{16}Si_2Sn_3$ in G-II. $Ni_{59.5}Nb_{33.6}Sn_{6.9}$ and $Ni_{60}Nb_{30}Ta_{10}$ BMGs exhibit

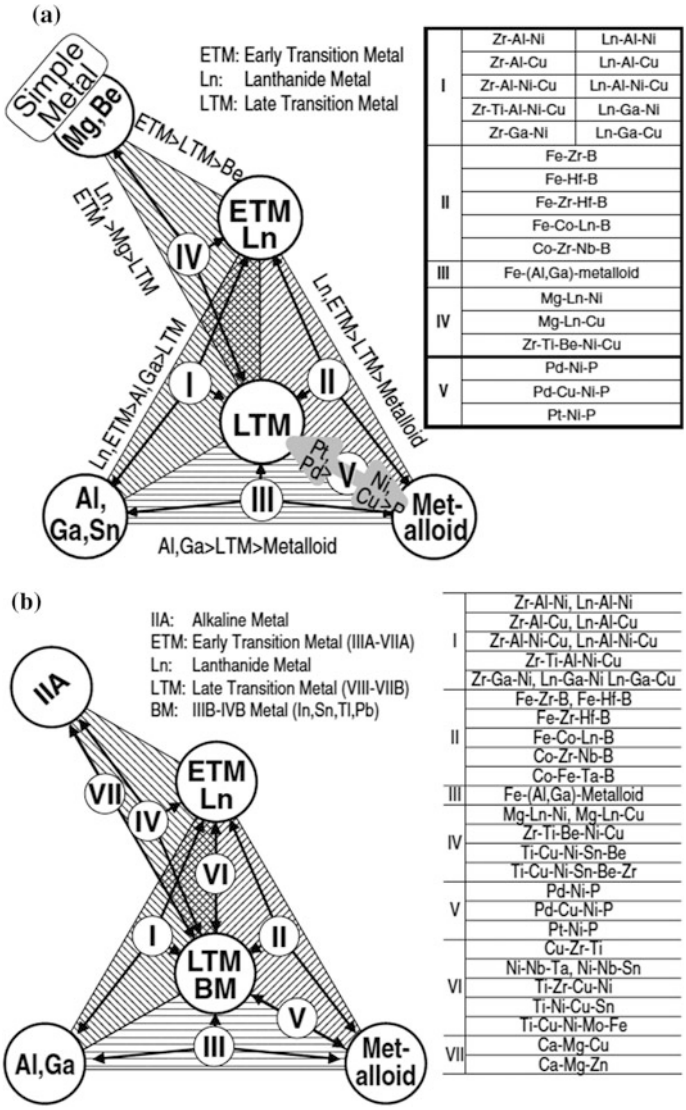

Fig. 10.2 Classification of BMG **a** old according to Inoue and **b** Recent up to date (Takeuchi and Inoue 2005)

similarity with each other in terms of enthalpy of mixing (ΔH^{mix}), atomic raiders and composition. ΔH^{mix} (Nb–Sn) and ΔH^{mix} (Nb–Ta) are −1 and 0 kJ/mol, respectively, whereas ΔH^{mix} (Ni–Sn)/ΔH^{mix} (Ni–Ta) exhibit negative values. The atomic radii of Ni, Nb, Sn, and Ta are 0.125, 0.143, 0.137, and 0.145, nm, respectively, and hence due to their similarity, the criteria of listing similar BMG into same category become strong. The simple metal (Be, Mg) is extended to IIA

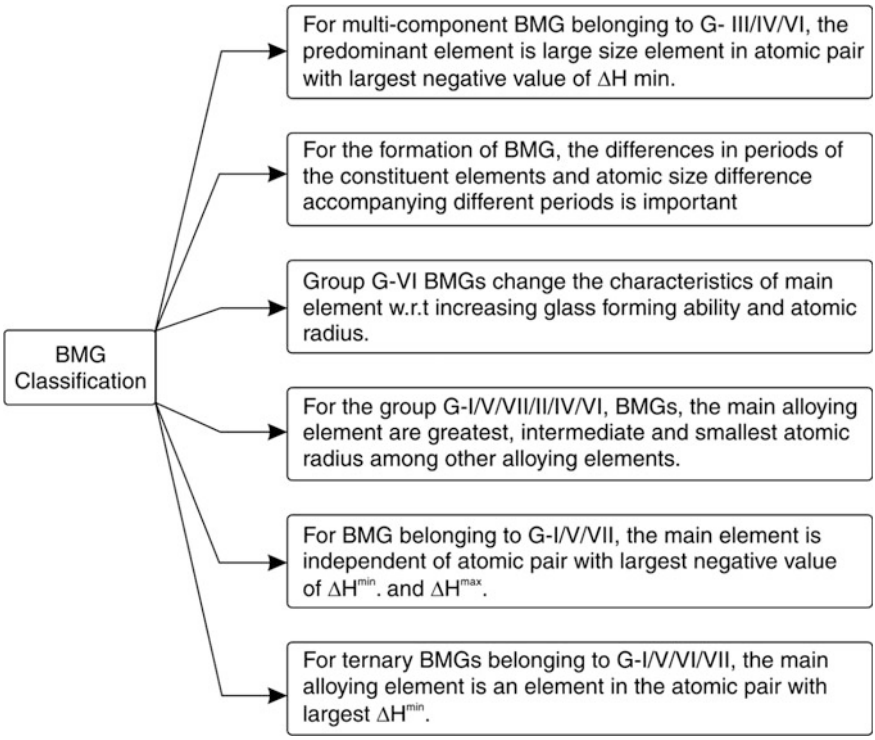

Fig. 10.3 Criteria for classification of BMG

and the grouping is based on the atomic radii, atomic size differences, and enthalpy of mixing. The atomic radii of Be, Mg and Ca are 0.113, 0.160 and 0.197 nm, respectively. Mg is the predominant element for group Mg–Cu–Y system (Mg, Cu and Y have radii 0.160, 0.128 and 0.182, nm, respectively) and Ca remains the main element for Ca–Mg–Zn (G-VII system).

Ni and Pd are also considered a part of LTM group and the classification is based on the tendency of atomic radii of transition metals to increase considerably between fourth and fifth period of periodic table. G-V and G-VII BMG are categorized by the same constituent elements falling into same group in the periodic table. For instance, Nb–Ta, Ni–Ti, and Ti–Zr atomic pairs have relatively small atomic radii difference i.e., the atomic radii of Ni, Nb, and Ta are 0.123, 0.143, and 0.145 nm, respectively. For the BMGs, with their constituent elements in the same group the enthalpy of mixing are almost 0 kJ/mol G-II group exhibits different characteristics as compared to other groups. G-VI group have a probability of having two or more main elements e.g., $Ti_{34}Zr_{11}Cu_{47}Ni_8$ BMG, have the BMG forming composition range on both Zr and Ti rich systems attributed to the exchange ability of Ni and Cu, conclusively.

10.3 Cooling Rates for BMG

The metallic liquid solidifies to a crystalline structure with the periodic atomic configurations over a long scale, when the metallic liquid temperature is greater than melting temperatures, it is cooled at a slow cooling rate = 1 K/s. In 1960, Duwez group synthesized the $Au_{75}Si_{25}$ amorphous alloys, which was found after discovering that very high cooling rate of $\approx 10^6$ K/s for the metallic liquids, leads to the formation of disordered atomic configuration similar to the liquid structure. Many studies were conducted afterward and it was concluded from the experimental results that very high cooling rates of 10^6 K/s are required for the formation of amorphous phase (as conventional metallic alloys exhibit high atomic mobility). The metallic metals and alloys possess disordered atomic configurations and for the retention of non-crystalline structures, liquids shall be quenched at remarkably high cooling rates in order to suppress the equilibrium crystalline place formation. For obtaining frozen liquid structure, the critical cooling rate is 10^5–10^6 K/s for the alloys. $Au_{75}Si_{25}$, melt (produced at CalTech), was quenched using cold metal plate instead of oil/H_2O used conventionally. For the rapid thermal diffusion, the droplets spread into thin layers upon coming in contact with the cold metal plate. Furthermore, the formation of gaseous layers is prohibited due to the good contact between the cold metal and liquid droplets.

Another method to produce BMG was to use the melt spinning technique, where the cooling rates of 10^3–10^6 K/s produce 10–50 μm thick ribbon. The small size dimensions of the glasses were a drawback and the increase in their size caused the amorphous alloy to lose material properties due to crystalline phase precipitation/structural relaxation leading to catastrophic embrittlement. If the amorphous alloys were heated, then crystalline phases were formed without any supercooled region or glass transition temperature. Hence, the need of formation of bulk metallic glasses persisted till the 1990s, because for the practical applications, bulk size was required. But noble metal-based alloys, such as Pd–Cu–Si and Pd–Ni–P could yield a bulk size $\approx$10 mm with very low critical cooling rate of 10 K/s. However, due to the cost of platinum and palladium, these BMG could not make a big impact on the material science community. The discovery of BMG by Inoue and coworkers revolutionized the field of metallic glasses, as no expensive glass formers like Pd/Pt was required, and the BMG consisted primarily of the transition elements. The properties of BMG change significantly upon annealing due to structural relaxation.

The supercooled liquid is an internal equilibrium state, when is fully relaxed reference state for the quantitative evaluation of configuration enthalpy change due to annealing. The schematic of continuous cooling transformation curves for the amorphous alloys, crystalline, and glassy alloys is given in Fig. 10.4. As compared to the amorphous alloys, the lowest critical cooling rate of 0.067 K/s for glass formation can be obtained, which is almost 10^8 times smaller than the amorphous alloys. Attributed to such high thermal stability, the BMG with different shapes could be obtained (Fig. 10.5).

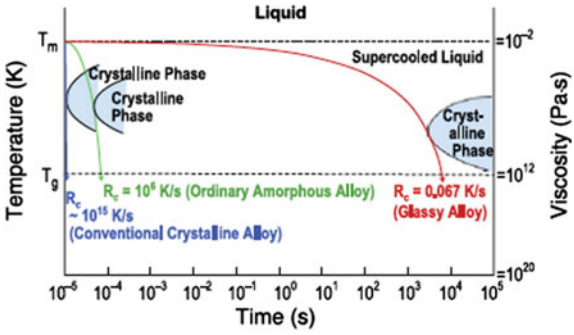

Fig. 10.4 High stability of the supercooled liquids for prolonged durations (Inoue and Takeuchi 2011)

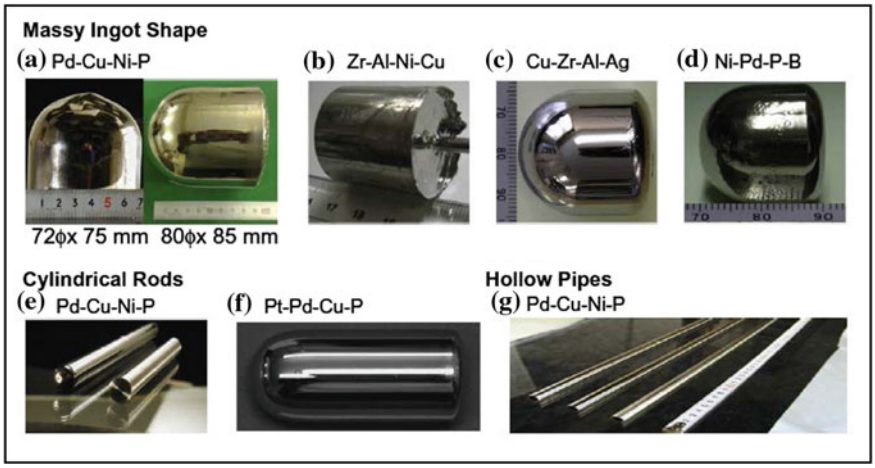

Fig. 10.5 Different geometries of the Pd-, Cu-, Zr-, Ni-, and P-based BMG (Inoue and Takeuchi 2011)

As demonstrated below:

- ≈1 mm thick hollow pipes with 10 mm outer diameter e g. Zr–Al–Ni–Cu, La–Al–Ni–Cu and Pd–Cu–Ni–P systems.
- 100 mm long cylindrical rods with 40 mm diameter for Pd–Cu–Ni–P system.
- 300 mm long cylindrical rods with 25 mm in diameter for Pd–Cu–Ni–P system.
- 40–50 mm high massy ingot shape with ≈25–30 mm diameter for Cu–Zr–Al–Ag, Ni–Pd–P–B and Zr–Al–Ni–Cu system.
- 75 mm high and 72 mm diameter massy ingot for the Pd–Cu–Ni–P system.

Hence, it is observed that the glassy alloys ranging from micrometer to centimeter dimensions can be obtained leading to significant development of BMG.

10.4 Structural Aspect of BMG

For the BMG synthesis, good glass formers of the composition usually belong to the eutectic points corresponding to the equilibrium binary phase diagram, which confers the resemblance of BMG with frozen metallic liquids (eutectic are stable liquid phase with low melting temperature). The eutectic system in quaternary and higher system are rarely investigated because more than three components are difficult to represent on the phase diagram. For the glass formation, the occurrence of the crystals below T_g during cooling shall be avoided. The high viscous liquids exhibit better glass-forming ability and belong to more stable liquid state because the crystal nucleation depends upon diffusivity of alloy melts (diffusivity depends upon viscosity from Stokes–Einstein equation). Face-centered cubic (fcc) and hexagonal close packed (hcp) are regarded as the most dense structures, but icosahedral are considered to be the most ideal atomic motif for the BMG and stable supercooled liquid due to their lack of translational periodicity and highly close-packed structure. The BMG glass formers exhibit very narrow compositional range, which causes loss of glass-forming ability even if the composition is slightly changed. For the formation of BMG, Bernal's model is the most acceptable model, which treats metallic glasses as frozen liquids with atomic arrangements assessed by the geometrical sphere packing.

The Bernal's idea:

- successfully define systems of monatomic metals and alloys with the compositional species with almost comparable atomic sizes.
- Do not provide the explanation for the medium and short-range order obtained in multi component glassy systems with very low critical cooling rates.
- Do not explain metal–metalloid alloys with significant chemical short-range order.

After these shortcomings, Gaskell proposed that for a metal–metalloid alloy system, the local unit of nearest neighbors shall have the singular structure corresponding to the crystalline compounds. Gaskell could not explain the stability of supercooled liquid state and hence could not support metal–metal-based metallic glasses. Miracle proposed another theory as follow:

- Local structural units contain densely packed solute-centered atomic clusters.
- These clusters can be idealized as spheres
- The 3-D structure is produced by the fcc and hcp arrangement of these spherical clusters as shown in Fig. 10.6.
- Hence, a glassy structure can be constructed on the basis of sequence of clusters/glue atoms, followed by random rotations of clusters followed by annealing induced structural relaxation.

The above mentioned postulates agree well with the experimental results obtained for the Zr–Al–Cu glassy system, indicating that the packing on larger scale plays determining role for the supercooled liquid stabilization especially for the multi component alloy systems satisfying following empirical criteria.

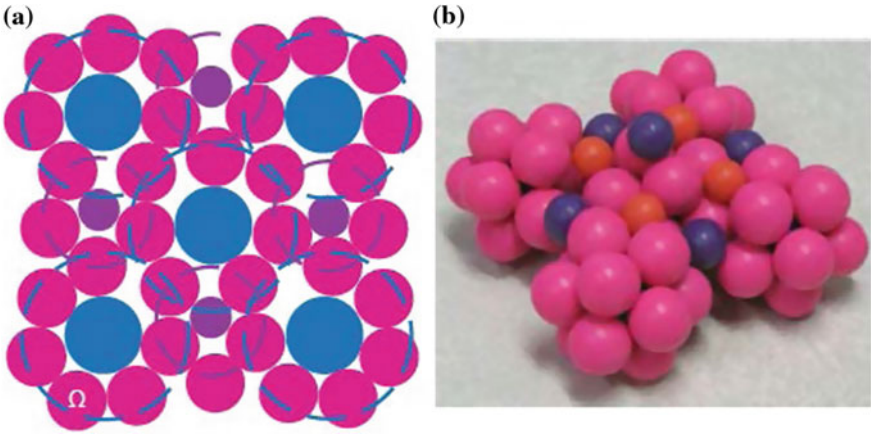

Fig. 10.6 **a** Dense cluster packing structure in the (100) plane **b** Zr–(Al,Ti)–(Cu,Ni)–Be alloystructure, zirconium solvent spheres (*pink*) form relaxed icosahedra around each solute atom (Miracle 2004)

- High degree of closely/densely packed atomic units.
- Long-range homogeneity (with attractive interaction)
- New atomic configurations different from the corresponding crystalline phase.

Shang and co-workers tried to resolve the atomic-level structure of amorphous alloys using an alternative cluster packing scheme. Shang elucidated that the icosahedral fivefold packing is more desirable for the short-range order cluster–cluster connection in metallic glasses compared to the hcp or fcc configuration. Though ab initio molecular dynamics and Monte Carlo methods have been investigated to judge the metallic glass structure, but these methods cannot provide unique atomic configurations for the supercooled liquid state, structural relaxation corresponds to increase in the shear modulus, and viscosity upon cooling resulting in glass formers change from liquid to viscoelastic. Above T_g, the superior glass former exhibits larger relaxation time and slower dynamics. For the glass formation, development of icosahedra short-range order in supercooled liquid regions is indispensable because densely packed structure initiates slow dynamics near T_g leading to dynamic arrest.

10.5 BMG for Biomedical Applications

Interaction of materials with cells and host tissue in vitro and in vivo yield the results for the biocompatibility. The biocompatibility is imperative criterion to avoid any host response, hypersensitivity, toxicity or inflammatory effects. Depending on the host requirement and bioinertness, the BMGs can be divided into

Table 10.1 Common BMGs for biomedical application along with their mechanical parameters

Chemical compositional (%)	Young's modulus	Compressive fracture strength (MPa)	Hardness (kg/mm^2)
Fe_{41} Ca_7 Cr_{15} Mo_{14} C_{15} B_6 Y_2	–	3500	1253
Fe_{70} B_{20} Si_{10}	–	2500	714
Fe_{49} Cr_{15} Mo_{14} $C_{(13+x)}$ $B_{(8-x)}$ Er1 (x = 2, 4, 5, 6)	210–220	4000–4150	–
Fe_{48} Cr_{15} Mo_4 C_{15} B_6 Er_2	213	4200	1122
Fe_{55} Cr_8 Mo_{14} C_{15} B_6 Er_2	209	–	1122
Zr_{61} $Cu_{17.5}$ Ni_{10} $Al_{7.5}$ Si_4	–	~1800	510
Zr_{60} Nb_5 Cu_{20} Fe_5 Al_{10}	72	1795	–
Zr_{60} Ti_6 Cu_{19} Fe_5 Al_{10}	70	1652	–
Zr_{65} $Pd_{17.5}$ Fe_{10} $Al_{7.5}$	–	~1500	422
Zr_{65} $Pd_{12.5}$ Ag_5 Fe_{10} $Al_{7.5}$	–	~1500	410
$Zr_{60.14}$ $Cu_{22.31}$ $Fe_{4.84}$ $Al_{9.7}$ Ag_3	~82	1720	–
Zr_{46} $Cu_{37.6}$ $Ag_{8.4}$ Al_8	~90–92	2158	~550
$Zr_{51}Ti_5$ Ni_{10} Cu_{25} Al_9	100	1962	~540
$Zr_{52.5}$ Al_{10} Ti_5 $Cu_{17.9}$ $Ni_{14.6}$	90	~1700	590
$Zr_{62.5}$ Al_{10} Fe_5 $Cu_{22.5}$	80	~1700	459
Zr_{56} Al_{16} Co_{28}	83	~1830	–
Zr_{60} Nb_5 $Cu_{22.5}$ Pd_5 $Al_{7.5}$	70–85	~1724	–
Zr $_{(60+x)}$ $Ti_{2.5}$ Al_{10} Fe $_{(12.5-x)}$ Cu_{10} Ag_5	70–80	1450–1600	440–460
Ti_{40} Zr_{10} Cu_{38} Pd_{12}	~100		~765
Ti_{40} Zr_{10} Cu_{36} Pd_{14}	~82	1950	–
Ti_{45} Zr_{10} Cu_{31} Pd_{10} Sn_4(arc melting)	95	1970	650
Ti_{45} Zr_{10} Cu_{31} Pd_{10} Sn_4(spark plasma sintering)	–	~2060	–
Ti_{40} Zr_{10} Cu_{34} Pd_{14} Sn_2	–	~2000–2150	–
$Ti_{41.5}$ $Zr_{2.5}$ Hf_5 $Cu_{37.5}$ $N_{7.5}$ Si_1 Sn_5	~80	~2000	600
$Ti_{41.9}$ $Zr_{2.5}$ Hf_5 $Cu_{42.5}$ $Ni_{7.5}$ Si_1	103	~2080	–
$Ti_{41.3}$ $Cu_{43.7}$ $Hf_{13.9}$ $Si_{1.1}$	95	~1685	–
Ti_{47} Cu_{38} $Zr_{7.5}$ $Fe_{2.5}$ Sn_2 Si_1 Ag_2	~100	~2080	588
$Ti_{43.3}$ $Zr_{21.7}$ $Ni_{7.5}$ $Be_{27.5}$	95	~1790	–
(Ti_{40} Zr_{10} Cu_{38} Pd_{12}) (100 – x)Nbx (x = 0, 2, 3, 4)	100–105	1200–2000	610–820
Zn_{38} Ca_{32} Mg_{12} Yb_{18}	36.6	640	–
Zn_{40} Mg_{11} Ca_{31} Yb_{18}	–	663	–
Mg_{60} Cu_{29} Y_{10} Si_1	66	–	400
Mg_{67} Zn_{28} Ca_5	–	817	216
Mg_{67} Cu_{25} Y_8/Mg_{65} Cu_{25} Gd_{10}	–	~800	250
Mg_{66} Zn_{30} Ca_{4-x} Sr $_{x(x=0,\ 0.5,\ 1,\ 1.5)}$	48–49	787–848	245–251

(continued)

Table 10.1 (continued)

Chemical compositional (%)	Young's modulus	Compressive fracture strength (MPa)	Hardness (kg/mm^2)
Mg_{66} Zn_{30-x} Ca_4 $Ag_{x(x=0,1,3)}$	–	~780	235
Sr_{40} Mg_{20} Zn_{15} Yb_{20} Cu_5	20.6	408	–
Sr_{60} Li_5 Mg_{15} Zn_{20}	18.4	–	–
Ca_{65} $Li_{9.96}$ $Mg_{8.54}$ $Zn_{16.5}$	23.4	530	135
Ca_{65} Mg_{15} Zn_{20}	20	~364	142
Ca_{50} Mg_{20} Zn_{30}	46	–	70
$Ca_{52.5}$ Mg_{20} $Zn_{27.5}$	39	–	140
$Ca_{52.5}$ $Mg_{17.5}$ Zn_{30}	44	–	140
Ca_{55} $Mg_{17.5}$ $Zn_{27.5}$	36	–	90
Ca_{48} Zn_{30} Mg_{14} Yb_8	31.9	~600	–
Ca_{20} Mg_{20} Zn_{20} Sr_{20} Yb_{20}	19.4	~370	–
Zr_{50} Cu_{40} Al_{10}	88	~1860	–
Zr_{60} Cu_{20} Al_{10} Ni_{10}	80	~1750	–
$Zr_{62.5}$ $Cu_{22.5}$ Al_{10} Fe_5	88	~1584	–
Zr_{48} Cu_{36} Al_8 Ag_8	102	~1850	–
Sr_{60} Li_{11} Mg_9 Zn_{20}	18.4	–	–
Sr_{60} Mg_{20} Zn_{15} Cu_5	19.9	–	–

Ti-/Co-based systems, iron-based systems, magnesium-based systems, and zirconium-based systems. Table 10.1 lists the most common BMG along with their mechanical parameters used for biomedical applications.

10.6 Zr-Based BMG

Zr-based BMG usually exhibit potential as non-absorbable medical devices, Zr-based BMG possess hardness twice as that of the conventional steels, such as 316LSS and CoCrMn alloys. Zr-based BMG have been recognized as potential engineering materials hence Zr–Be–Ti–Ni–Cu, Zr–Al–Co, Zr–Cu–Al–Ag, Zr–Al–Ni, Zr–Al–(Ni, Cu) systems have been investigated widely. The critical diameter of few zirconia-based alloys is given in Table 10.2.

The hypoeutectic Zr-based BMG containing higher Zr content tends to exhibit improved mechanical properties as compared to the eutectic compositions. Even for the as-cast and annealed samples, the Poisson's ratio is higher for the hypoeutectic compositions than the eutectic compositions. The hypoeutectic alloy containing

Table 10.2 Critical diameter of Zr-based BMG

Composition	Critical diameter (mm)	Composition	Critical diameter (mm)
Zr_{61} Ti_2 Cu_{25} Al_{12}	6	Zr_{50} Cu_{40} Al_{10}	22
$Zr_{52.5}$ Al_{10} Ti_5 $Cu_{17.9}$ $Ni_{14.9}$	7	Zr_{65} $Cu_{17.5}$ $Al_{7.5}$ N_{10}	16
Zr_{56} Al_{16} Co_{28}	18	$Zr_{62.5}$ $Cu_{22.5}$ Al_{10} Fe_5	20
$Zr_{60.14}$ $Cu_{22.31}$ $Fe_{4.85}$ $Al_{9.7}$ Ag_3	10	Zr_{65} $Pd_{17.5}$ Fe_{10} $Al_{7.5}$	6
Zr_{65} $Pd_{12.5}$ Ag_5 Fe_{10} $Al_{7.5}$	6	Zr_{55} Cu_{30} Al_{10} Ni_5	30
$(ZrxCu_{100-x})$ $80(Fe_{40}$ $Al_{60})$ 20 (x = 68 − 77)	x = 72.5 yields 13	Zr_{42} Cu_{42} Al_8 Ag_8	14
		Zr_{48} Cu_{36} Al_8 Ag_8	25

∼70 % Zr content, yield Poisson's ratio of 0.387 and Young's modulus of 78 Gpa. This infers that the increasing Zr content increases Poisson's ratio, but reduces the Young's modulus. For the hypoeutectic 70 % Zr alloy, strain rate of 1.6×10^{-1} s^{-1} and distinct plastic elongation of 1.7 % is observed and the strain rate shows an increase up to 5×10^{-1} s^{-1} upon increase is plastic elongation to 2.8 % (Fig. 10.7a).

Poisson's ratio and shear transformation zone (STZ) exhibit strong dependence on each other, where STZ represents nanoscale volume of material that could undergo plastic flow. Furthermore, STZ are prone to poor ductility and mechanical failure because STZ causes localized shear band formation. To measure STZ, nanoindentation techniques are used, and it is observed that for the Pd- and Zr-based BMG, the STZ shown an increase from 1.3 to 1.9 mm upon increasing Poisson's ratio from 0.31 to 0.45. Figure 10.7b gives the compressive stress strain curve for Ni-free Zr BMGs and the tensile stress elongation for $Zr_{70}Al_8Ni_{16}Cu_6$ BMG is shown in Fig. 10.7b.

Figure 10.7b indicates that for all BMGs, fracture strength and yield strength over 1600 and 1300 MPa, respectively, could be obtained. These BMG also exhibit considerably large plastic strain and low elastic strain ≈70–80 GPa. The modulus for Ti–6Al–4V and 316L SS steel are 125 and 200 GPa, respectively. $Zr_{70}A_8Ni_{16}Cu_6$ BMG exhibits high resistance against corrosion failure under tensile deformation mode in 3 % NaCl solution. $Zr_{70}Al_8Ni_{16}Cu_6$ are promising materials as corrosion resistant structural materials with high Poisson's ratio of 0.393, Young's modulus of 70 GPa and large STZ of 2.5 nm. The sliding speed and shear stress of the shear band of $Zr_{70}Al_8Ni_{16}Cu_6$ is obtained to be, 2–4 m/s and 640–690 MPa, respectively (shear band thickness ∼15 nm). Using the following relation, the viscosity could be estimated.

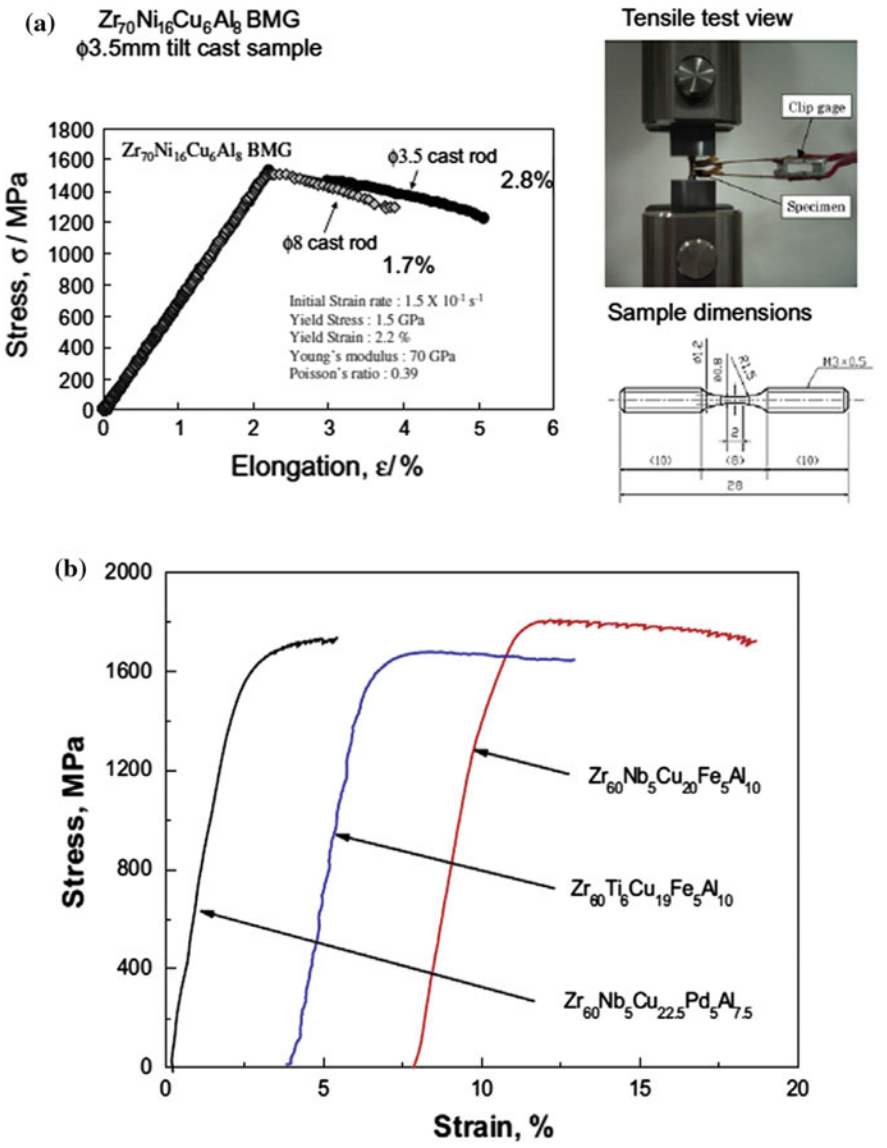

Fig. 10.7 **a** Tensile stress elongation of Zr-based BMG rod (Yokoyama et al. 2009) and **b** compressive stress strain curves for Ni-free Zr-based BMGs (Li and Zheng 2016)

$$\text{Viscosity} = \text{Shear stress} \times \frac{\text{shear band thickness}}{\text{sliding speed}} \tag{10.1}$$

The temperature dependence of viscosity for $Zr_{70}Al_8Ni_{16}Cu_6$ alloy indicated that the temperature in the shear band may reach 840 K, which indicates that the tensile shear sliding takes place via viscous flow mode for instantaneous time.

Due to the high strength of Zr-based BMG, rate of restenosis can be reduced, making it potentially applicable for the cardiovascular stents. In addition to this, the bone screws prepared from Zr BMG have deeper threads and thinner shank, empowering then with larger holding power for the fracture bones. Liu and coworkers did cytotoxicity and in vitro corrosion testing for Zr–Cu–Al–Ag alloy system. It was observed that the silver containing BMG show antibiotic effects, which may lead to reduction in surgical infections. In Hank's solution, silver containing BMG exhibit better performance than the Ti6Al4V alloy, attributed to the Al_2O_3 passivation caused by increased Ag content. Improved cell viability of Ag-containing BMG could be seen with the L929 cells as compared to Ti6Al4V. No immune response, inflammation, or gas response could be seen upon in vivo implantation of Ag-containing BMG.

Buzzi and coworkers studied the biocompatibility of $Zr_{58}Cu_{22}Fe_8Al_{12}$ BMG for 3T3 embryonic mouse fibroblast cell line and the studies were compared with nickel containing $Zr_{58.5}Cu_{15.6}Ni_{12.8}Al_{10.3}Nb_{2.8}$. Nickel may show anti-proliferative results along with allergic reactions in some area. Upon surface passivation, both alloys yield viability comparable to the control line. After analysis of growth media following cell cultures, it could be seen that Cu and Zr diffused into the media with concentrations <1 mg/l. Drastic reduction of Cu and Ni ion diffusion by a fraction of 6–9 and 24, respectively, could be seen after surface passivation of BMG in nitric acid. The increased viability of passivated samples indicates the improved cell growth and stabilization of the oxide layer on the passivated sample. Change in chemical composition and anodic passivation leads to improved corrosion resistance. Zr-based metallic glasses exhibit the formation of natural oxide layer, exhibiting good corrosion resistance. The pitting corrosion may take place due to the rendering of passive layer caused by small surface defects in micro/nano range or local segregation of elements in the alloy.

Liu and coworkers applied micro-arc oxidation (MAO)/technique for the surface modification of Zr-based BMG, which resulted in enhanced biocompatibility. The surface modification of $Zr_{60.5}Cu_{19.5}Fe_5Al_{9.5}Ti_{5.5}$ was done by MAO, and the layer consisted primarily of Zr, Si, and O atoms and Ca as a trace element. Anyhow, negligible amount of Cu could be seen in MAO layers indicating that Cu out of diffusion is suppressed upon MAO layer formation. Figure 10.8a–d gives the XRD pattern and micro-structure change of the MAO-treated samples after immersion in SBF solution for 3, 5 and 10 days, respectively. As indicated from the SEM micrographs, immediate formation of apatite layer could be seen on the BMG surface after immersing it in SBF solution. Furthermore, the apatite layer continues to grow with increase in soaking time duration. For all cases, apatite layer formed

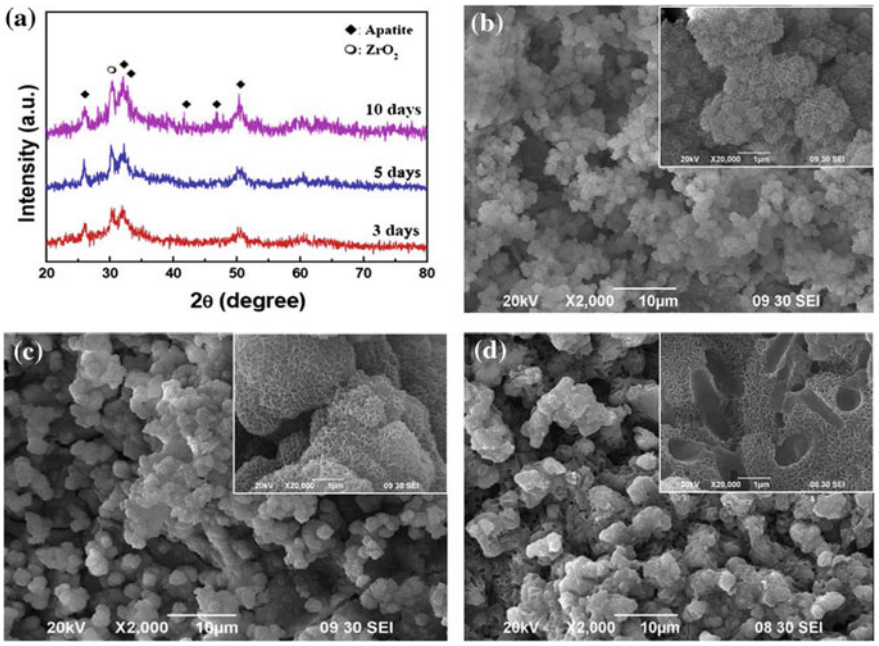

Fig. 10.8 **a** XRD patterns of the MAO-treated $Zr_{60.5}Cu_{19.5}Fe_5Al_{9.5}Ti_{5.5}$ BMG; microstructure of MAO-treated $Zr_{60.5}Cu_{19.5}Fe_5Al_{9.5}Ti_{5.5}$ BMG after immersion in SBF for **b** 3 days, **c** 5 days and **c** 10 days, respectively (Liu et al. 2010)

have ball-like structure covering entire surface uniformly. The size of ball increased from 1 to 5 μm upon increase in soaking duration from 3 to 5 days.

After 5 days, the apatite phase became porous along with increase in the density. Interestingly, the apatite morphology and growth style are desirable for the medical implants as it can strengthen the bonding between biotissues and metal implant. The instantaneous formation of apatite layer on the MAO modified BMG indicates that MAO is an effective approach for the surface modification. The bioactivation of BMG upon MAO can be attributed to

- Formation of rough and porous ZrO_2 outer layer.
- Porous and rough ZrO_2 layer attract calcium and phosphorous ions from SBF due to high specific surface area.
- The apatite formation gets accelerated due to porous structure.

In addition to this, the porous microstructure is advantageous for the cell migration, adhesion, and new bone tissue ingrowths.

Horton and coworker conducted a series of experiments on the zirconia-based metallic glasses especially on BAM-11 system I e. $Zr_{10}Al_5Ti_{17.9}Cu_{14.6}Ni$. BAM-11 displayed good cytocompatibility, but the inclusion of Ni is detrimental due to its carcinogenic effects.

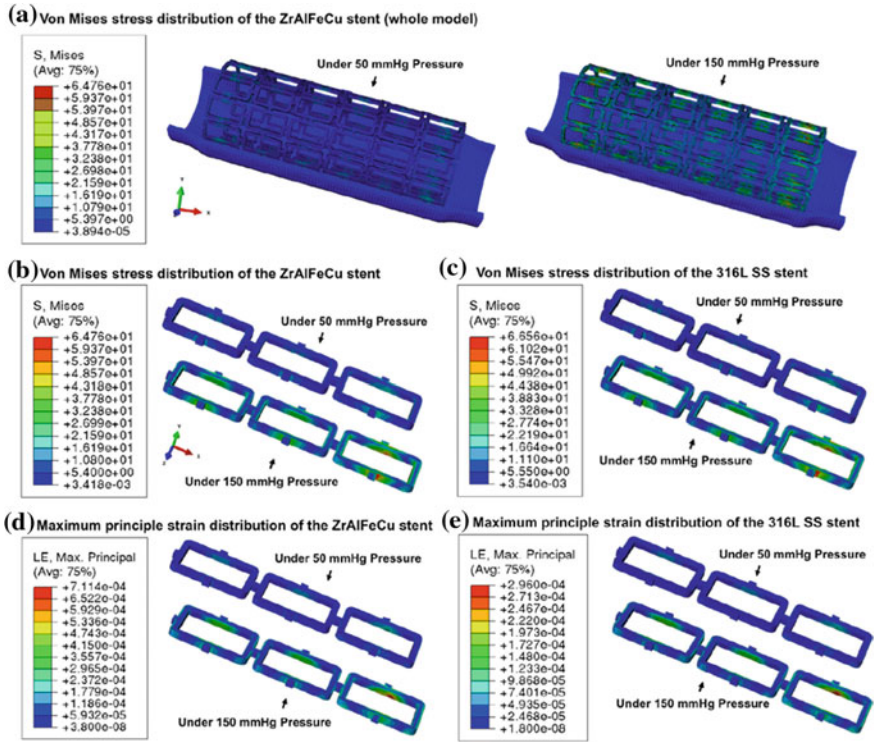

Fig. 10.9 **a**–**c** Finite element analyses on the Von-Mises stress and **d**, **e** maximum principle strain distributions of ZrAlFeCu BMG and 316L SS stent under 50 or 150 mmHg pressure load (Huang et al. 2015)

Huang and coworkers investigated the corrosion resistance, cytocompatibility, and mechanical properties of $Zr_{62.5}Al_{10}Fe_5Cu_{22.5}$ BMG (6 mm dia). The mechanical property revealed high strengths under both cyclic loadings and quasi-static loadings, which facilitated the thinner strut design of stents reducing restenosis risk. The micro-hardness of $Zr_{62.5}Al_{10}Fe_5Cu_{22.5}$ was obtained to be 4.5 GPa, and under quasi-static compression, the yield strength of 1.7 GPa and Young's modulus of 80 GPa could be obtained. The BMG could survive 10^7 cycles of loading below maximum applied stress of 1.054 GPa. The finite element analysis of truss like stent vessel system is shown in Fig. 10.9a–e.

The strain energy density functions for hyperplasic model are given as follows:

$$W = a_{10}(I_3-3) + a_{01}(I_2-2) + a_{20}(I_1-3)^2 + a_{11}(I_1-3)(I_2-3) + a_{30}(I_1-3)^3 \tag{10.2}$$

where a_{ij} are constitutive model parameters, W is the strain energy density function, and $I_1/I_2/I_3$ are strain invariants. Von-Mises stress and maximum principle strain

were modeled over fully expanded stent under applied pressure loads from 50 to 150 mm Hg (the simulation was done in accordance with the systolic and diastolic pressures from the vessel). Under 150 mm Hg pressure loading, maximum Von-Mises stress of 65 MPa and maximum strain of 7.1×10^{-4} could be obtained. The strain value is obtained to be twice as larger for $Zr_{62.5}Al_{10}Fe_5Cu_{22.5}$ than the 316L SS indicating that the BMG is more flexible and can be deformed more easily during the beats of blood vessel.

Lower Young's modulus of the BMG made it a more compliant material for the stent applications. The compliance mismatch between stent and the native artery is associated with intimate hyperplasia particularly at the distal end of the stent. The BMG also revealed higher corrosion resistance as compared to the 316L SS steel indicating its high stability and inertness in aggressive physiological environment such as PBS solution. Zr–Al–Fe–Cu BMG has demonstrated higher pitting resistance than the Zr–Al–Ni–Cu BMG attributed to the formation of ZrO_2 on the surface of the alloy. Surface modification of BMG also affects thrombosis and neointimal hyperplasia in addition of affecting corrosion-related properties. Activation of leukocytes and platelets is by the release of metal ions from the BMG. $Zr_{62.5}Al_{10}Fe_5Cu_{22.5}$ demonstrated good cell viability with the human aortic endothelial cells (HAECs) and human aortic smooth muscle cells (HASMCs) (Fig. 10.10). Fast coverage of endothelial cells and lower growth of smooth muscle cells was observed on the Zr BMG than on the stainless steel. HAECs showed stronger adhesion on the BMG compared to 316L SS as evident from the flow test.

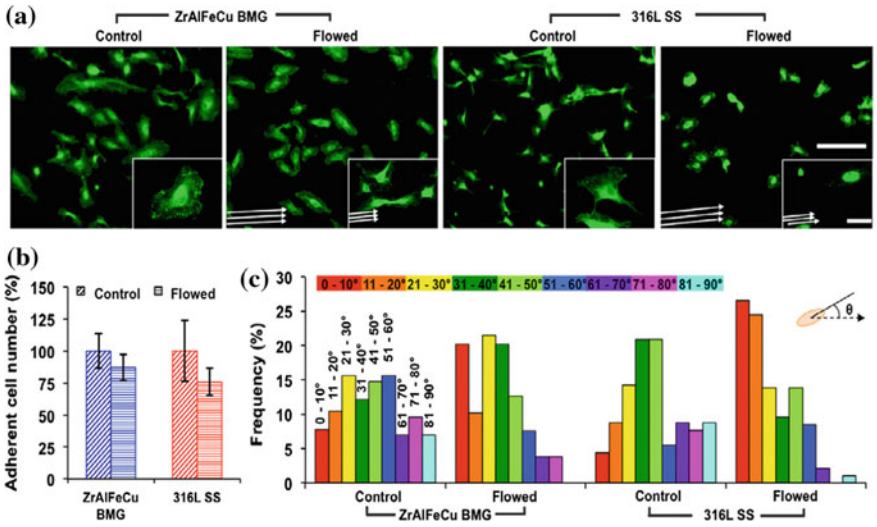

Fig. 10.10 HAEC adhesion after 2 h flow test: **a** immunostained focal adhesions of HAECs on BMG and 316L SS (*white arrows* indicate flow directions); **b** number of adherent cells before and after flow test, **c** cell orientation angle relative to the long axis of the specimen obtained from analysis of over 80 cells per group (Huang et al. 2015)

Cell realignment was quite strong under the flow for 316L SS substrate, which indicates that 316L SS were more susceptible to the flow. On 316L SS, more polarized HAEC were formed during static incubation, though the HAEC are smaller but circular in morphology.

The in vivo–in vitro biocompatibility of $Zr_{60}Ti_6Cu_{19}Fe_5Al_{10}$ BMG is evaluated by implanting BMG samples into the central regions of back of white rabbits for a period of 4–12 weeks by Liu and coworkers. For the comparison, the Ti6Al4V alloy with same dimensions was also implanted in the rabbit. Four weeks after implantation, the growth of fibrous encapsulation with local infiltration could be seen around the BMG and Ti6Al4V, without any edema. Initially, the inflammatory response could be seen inside and outside of the fibrous capsule surrounding BMG, whereas it was observed only inside the fibrous capsule around Ti6Al4V. With the increase in implantation time, the inflammatory response weaken, and after 12 weeks implantation, both Ti6Al4V and BMG implants were completely encapsulated by mature fibrous connective tissue without expressing any active proliferation (Fig. 10.11a, b). Slight inflammation could be seen in both the cases though it persisted only inside the fibrous capsule (the circles in Fig. 10.11a, b indicate multinucleated giant cells and lymphocytes). Additionally, no corrosion pits could be seen on the BMG surface after 12 weeks of implantation.

Lin and coworkers tested the Zr- and Ti-based metallic glasses in human serum and Hank's solution. It was found that the electrochemical activity and corrosion were accelerated for Cu content >17.5 at.%. The ionic products of high Cu alloy exhibited acute cytotoxicity to the D1 bone marrow cells, though the bulk samples did not reveal any cytotoxicity. Hua and coworkers compared the biocompatibility of Ti6Al4V biomedical alloy and low Cu containing $Zr_{65}Ti_{12.5}Fe_{7.5}Cu_{10}Ag_5$ BMG for MC3TC-E1 mouse osteoblast cell. The BMG composition was further optimized to enhance the toughness and bulk compressive plasticity up to 12 % by keeping the compressive strength to be the same.

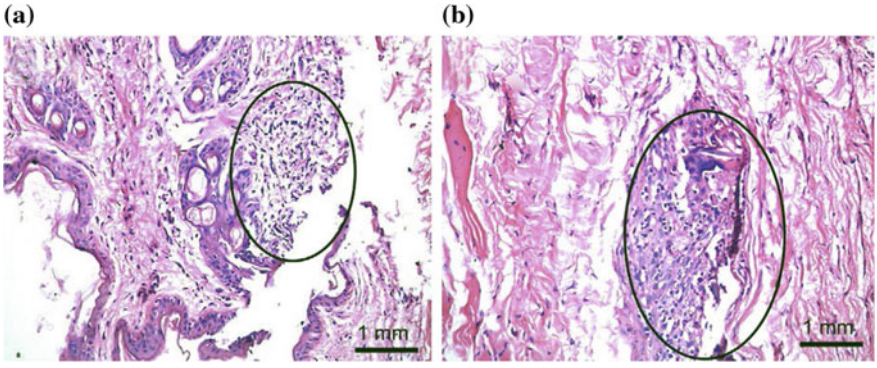

Fig. 10.11 HE strained results of **a** $Zr_{60}Ti_6Cu_{19}Fe_5Al_{10}$ BMG and **b** Ti–6Al–4V after implantation for 12 weeks (Liu et al. 2009)

The morphologies of MG63 cultured on $Zr_{60.14}Cu_{22.31}Fe_{4.85}Al_{9.7}Ag_3$, crystalline Zr, and crystalline Ti6Al4V alloy for 3 days could be seen in Fig. 10.12. Large number of cells were attached and spread on the surface. As compared to the free growing control cells (Fig. 10.12f), the cells cultured with three different samples i.e., $Zr_{60.14}Cu_{22.31}Fe_{4.85}Al_{9.7}Ag_3$, crystalline Zr and crystalline Ti6Al4V alloy,

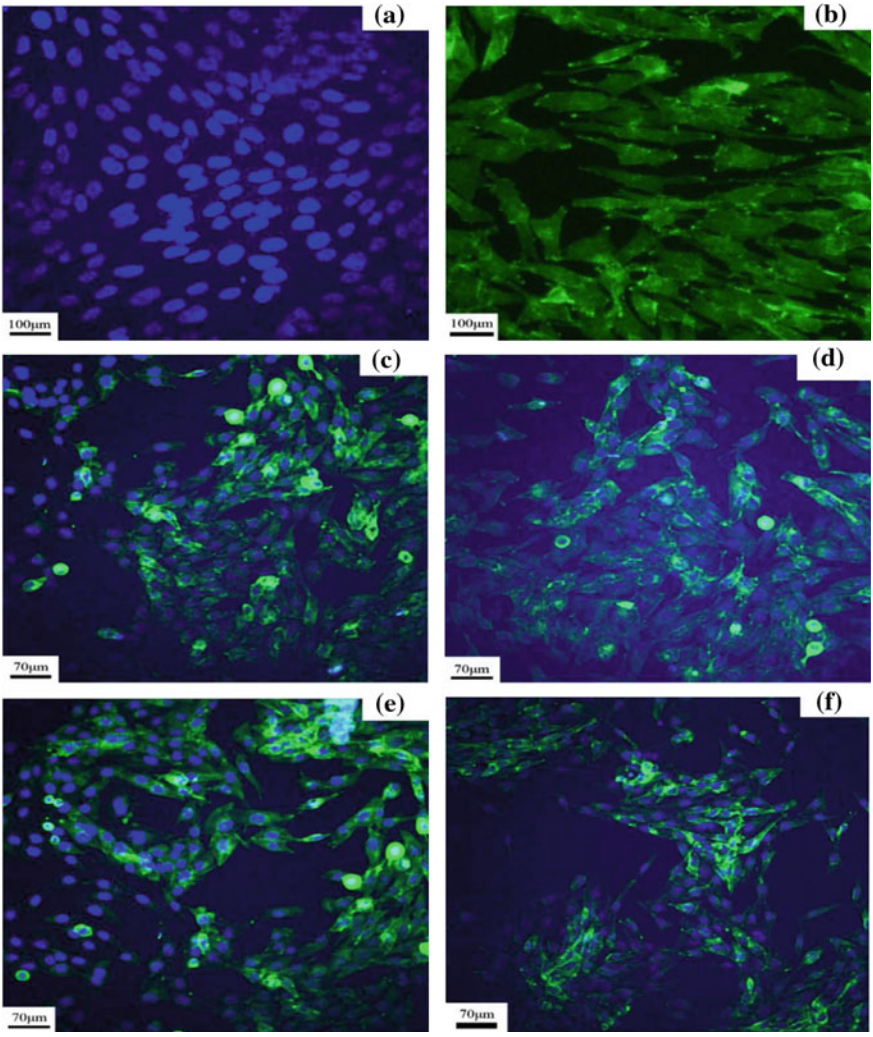

Fig. 10.12 MG63 cell morphologies cultured on **a** $Zr_{60.14}Cu_{22.31}Fe_{4.85}Al_{9.7}Ag_3$ BMG stained with Hochest-33258; **b** $Zr_{60.14}Cu_{22.31}Fe_{4.85}Al_{9.7}Ag_3$ BMG stained with FITC–phalloidin; **c** $Zr_{60.14}Cu_{22.31}Fe_{4.85}Al_{9.7}Ag_3$ BMG stained with both Hochest-33258 and FITC–phalloidin; **d** pure Zr stained with both Hochest-33258 and FITC–phalloidin; **e** Ti6Al4V alloy stained with both FITC–phalloidin and Hochest-33258; and **f** positive control for 3 days (Li and Zheng 2016)

exhibit large footprint area (Fig. 10.12c–e). The actin filaments are aligned in parallel directions and the focal adhesion plaques (represented in green) could be seen at the cell periphery. Apart from this, no observable differences could be seen in the adhesion morphology for these substrates. From the above discussion about the work of various research groups, it is evident that the Zr-based BMG have depicted acceptable biocompatibility with HASMCs, HAECS, MG63 esteoblast cell, mouse preosteoblast MC3T3E1, murine fibroblast cell (L929 cell/NIH3T3 cell), macrophage cells, and human vein umbilical endothelial cells as compared to the conventionally used steels and alloys such as Ti6Al4V and 316L SS. This indicates the excellent potential of Zr-based metallic glasses for the biomedical implantations.

10.7 Ti-Based BMG

Many Ti-based systems including Ti–Ni–Cu–Sn–Fe–Zr, Ti–Zr–Cu–Ni–Sn, Ti–Zr–Ni–Be, Ti–Zr–Si, Ti–Zr–Cu–Pd, and Ti–Zr–Cu–Pd–Sn have been investigated for the biomedical applications. Pure Ti and Ti6Al4V are most commonly used forms of titanium alloy, though there are few drawbacks of the material also. One is the release of toxic ions through the wear and corrosion process, which lead to the reduced biocompatibility and provoked inflammations. Another one is the tissue loss and implant failure due to the Young's modulus mismatch between the implant and bone i.e., bone have Young's modulus of $\sim$10–30 GPa as compared to the 110–120 GPa for pure Ti6Al4V alloy. Due to good bioactive behavior of titanium, Ti-based metallic glasses are investigated extensively. In 1977, the first Ti-based metallic glass was reported with only two elements i.e., Ti and Be. In 1994, Peker and coworker discovered BMG for the Ti–Zr–Ni–Be system and till date many compositions have been proposed and investigated. The Young's modulus and strength of Ti-based BMG is 100 GPa and $\sim$2000 MPa, respectively. Though, titanium-based BMG exhibit lower compressive plasticity at room temperature as compared to Zr-based and Pt-based BMGs, but $Ti_{45}Cu_{40}Ni_{7.5}Zr_5Sn_{2.5}$ BMG exhibits plastic strain up to 14.8 % attributed to the chemical heterogeneity upon solidification. Titanium exhibits poor GFA, hence the other alloying elements shall be carefully chosen. Table 10.3 lists the elements with their characteristic parameters and alloying effects with Ti.

For some Ni-free Ti–Zr–Cu–Pd-based metallic glasses, the mechanical property, corrosion behavior, microstructure, and bioactivity have been studied. To improve the ductility of $Ti_{40}Zr_{10}Cu_{36}Pd_{14}$ BMG, two approaches, namely changing the composition and heat-treatment of BMG, have been implied. The as-cast BMG has typical glassy structure and have no crystallinity or ordered phase could be seen. But upon annealing the BMG, a mixture of nanocrystalline phases embedded in glassy structure could be seen. If $Ti_{40}Zr_{10}Cu_{36}Pd_{14}$ is annealed at 723 K, then Ti_3Cu_4 nanoparticle growth could be seen and at 823 K, orthorhombic Ti_2Pd_3 and tetragonal Ti_2Pd could be seen in addition to the Ti_3Cu_4 phase. For the alloys

Table 10.3 Atomic radius, atomic ratio (r_A/r_{Ti}) atomic ratio mismatch, heat of mixing ($\Delta H^{mix}{}_{(Ti-\Delta)}$), and biological safety for the different alloying elements

Element	Atomic number/atomic radius (nm)	$[(r_A/r_{Ti})]/[(r_A-r_{Ti})/r_{Ti}]$	$\Delta H^{mix}{}_{(Ti-\Delta)}$	Effect of alloying with titanium	Nature
Be	4/0.1128	0.77/0.228	–30	β-eutectoid	Toxic
B	5/0.0820	0.561/0.439	–58	Insoluble in Ti	Biocompatible
Mg	12/0.1601	1.096/0.095	16	β-eutectoid	Biocompatible
Al	13/0.1432	0.980/0.021	–30	α-stabilizer	Toxic
Si	14/0.1153	0.789/0.211	–66	β-eutectoid	Biocompatible
P	15/0.1060	0.726/0.275	100.5	Insoluble in Ti	Biocompatible
Ca	20/0.1980	1.355/0.353	43	Insoluble in Ti	Biocompatible
V	23/0.1316	0.901/0.099	–2	β-isomorphus	Toxic
Cr	24/0.1249	0.855/0.145	–7	β-eutectoid	Toxic
Mn	25/0.1350	0.924/0.076	–8	β-eutectoid	Toxic
Fe	26/0.1241	0.849/0.151	–17	β-eutectoid	Toxic
Co	27/0.1251	0.856/0.144	–28	β-eutectoid	Toxic
Ni	28/0.1245	0.852/0.148	–36	β-eutectoid	Toxic
Cu	29/0.1278	0.875/0.126	–9	β-eutectoid	Toxic
Zn	30/0.1395	0.955/0.045	–15	β-eutectoid	Toxic
Ti	22/0.1461	1/0	–	–	Biocompatible
Sr	38/0.2150	1.472/0.474	53	Insoluble	Biocompatible
Zr	40/0.1602	1.097/0.096	0	Neutral	Biocompatible
Nb	41/0.1429	0.978/0.022	+2	β-isomorphus	Biocompatible
Mo	42/0.1362	0.932/0.067	–4	β-isomorphus	Biocompatible
Pd	46/0.1375	0.941/0.059	–65	β-eutectoid	Biocompatible
Ag	47/0.1445`	0.989/0.011	–2	β-eutectoid	Toxic
In	49/0.1659	1.136/0.135	–5	β-eutectoid	Biocompatible
Sn	50/0.1620	1.109/0.081	–21	Neutral	Biocompatible
Ta	73	0.979/0.021	+1	β-isomorphism	Biocompatible
Pt	78	0.949/0.051	−74	β-eutectoid	Biocompatible
Au	79	0.987/0.013	−47	β-eutectoid	Biocompatible

annealed at 693 K, distinct plastic deformation of 0.8 % and high strength of 2100 MPa are observed. When Nb is added to the Ti–Zr–Cu–Pd BMG, plastic strain up to 6.5 %, Young's modulus of ∼80 GPa, and high-yield strength of 2050 MPa could be observed. $Ti_{40}Zr_{10}Cu_{36}Pd_{14}$ exhibited higher corrosion resistance as compared to Ti6Al4V alloy in Hank's solution. Figure 10.13 gives the potentiodynamic polarization curve of Ti6Al4V pure Ti and BMG in Hank's Solution at 310 K. The BMG and its crystalline counterparts are passivated, which breaks down with further increase in anodic potential. The pitting potentials and passive current densities have strong dependence on the annealing temperatures. For instance, fully crystalline alloy annealed at 823 K possess lower pitting

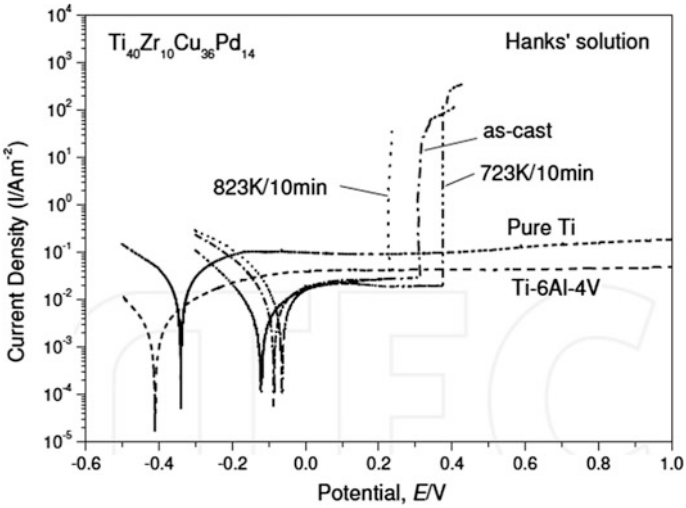

Fig. 10.13 Potentiodynamic polarization curve of Ti6Al4V pure Ti and BMG in Hank's Solution at 310 K (Qin et al. 2011)

potential and higher passive current density. The higher corrosion of Ti-based BMGs can be attributed to the partial nanocrystallisation of the glassy alloys. Due to annealing, the stress release and structural relaxation occurs, which decreases free energy of the alloy (and hence elemental reactivity) and thereby increasing corrosion resistance. The application of hydrothermal, electrochemical, and pre-calcification treatment on $Ti_{40}Zr_{10}Cu_{36}Pd_{14}$ metallic glasses accelerates the apatite nucleation and growth rates in Hank's solution. Due to the hydrothermal–electrochemical treatment, the surface area and thickness of titanium oxide on the $Ti_{40}Zr_{10}Cu_{36}Pd_{14}$ increases. In addition to this, the HPO_4^{2-}/Ca^{2+} ions adsorption increases due to the formation of microporous network on the BMG surface. The porous surface layer increases the apatite layer formation and hence apatite layer formation kinetics are fastened.

Sugiyama and coworkers worked on the direct formation of a bioactive titanate nanomesh layer on a $Ti_{39.6}Zr_{9.9}Cu_{35.6}Pd_{13.9}Ca_1$ BMG, using the hydrothermal–electrochemical technique. The hydrothermal–electrochemical treatment induced nanomesh titanate layer, which causes hydroxyapatite formation upon immersion, in SBF. As shown in Fig. 10.14, no observable difference in surface morphology could be seen after 2 days, whereas after 7 days of immersion in SBF is $\sim$2.5 μm spherical hydroxyapatite deposition could be seen. The surface of BMG was covered with these spherical hydroxyapatite after 12 days SBF immersion. On bare BMG, the hydroxyapatite formation could not be seen indicating the inertness of BMG to SBF, but the deposited titanium nanomesh layer have great potential for exhibiting in vivo bioactivity.

It has been reported that $Ti_{40}Zr_{10}Cu_{34}Pd_{14}Sn_2/Ti_{40}Zr_{10}Cu_{34}Pd_{12}Sn_4$ alloys exhibit full glassy structure and can be casted into 10 mm rods. These two alloys

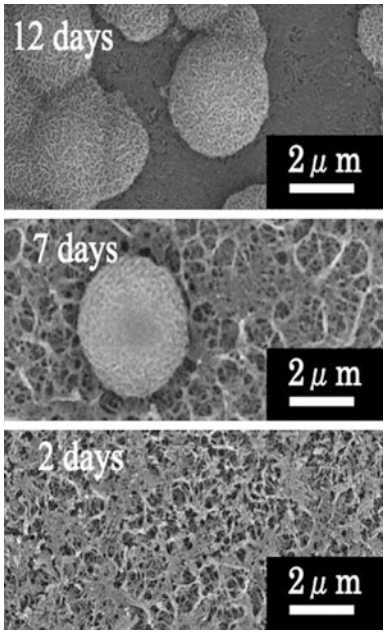

Fig. 10.14 Hydroxyapatite formation on the titanate nanomesh layer after immersion in the SBF for different durations (Sugiyama et al. 2009)

possess largest glass-forming ability for the Ni-free titanium-based BMGs. In contrast to this, $(Ti_{40}Zr_{10}Cu_{36}Pd_{14})_{97}Nb_3$ BMG is the most ductile, Ni-free titanium-based BMG, and it displays distinct plastic strain of 8.5 %.

Blanquer and coworker studied the effect of surface modifications of $Ti_{40}Zr_{10}Cu_{38}Pd_{12}$ BMG and Ti6Al4V alloy on human osteoblasts (HTB-85) cells. The surface modification is done via two routes i.e., electrochemical surface modification after which the nanomesh surface is obtained, and the physical surface modification after which the surface becomes micro-scratched. After the electrochemical treatment in NaOH, an amorphous sodium titanate gel is obtained as shown below:

$$NaOH + TiO_2 \rightarrow NaHTiO_3 \tag{10.3}$$

$$NaHTiO_3 + H_2O \rightarrow TiO_2 \cdot OH^- + NaOH + H^+ \tag{10.4}$$

Equation (10.4) depicts that when the samples are completely washed by distilled water, then sodium ions are released from the surface via NaOH dissolution in H_2O. The surface modification enhances the implant tissue osteointegration. Clear focal adhesion plaques were obtained on the nanomesh surfaces, though they were not detected in the micro-scratched surface. The cells growing on the micro-scratched surface displayed more elongated morphology and showed well-defined stress fibers as compared to the cell morphology obtained on the nanomesh surface. Thin and long filopodia of the cells grown on the nanomesh surface could be seen. The confocal laser scanning microscope (CLSM) images of

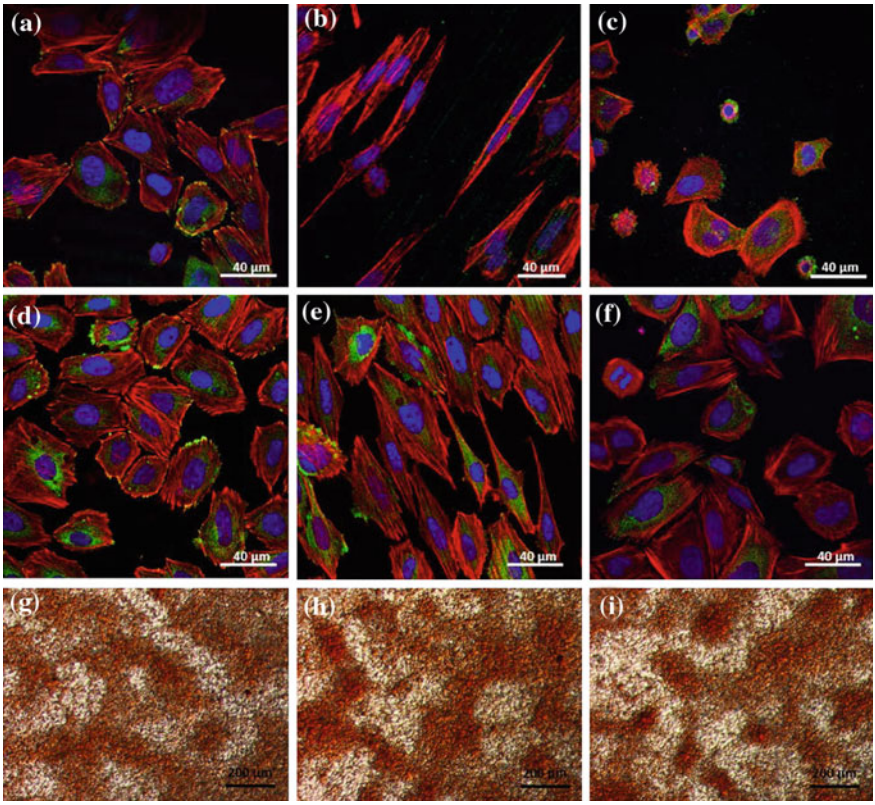

Fig. 10.15 Adherence of Saos-2 onto the surface of TiZrCuPd (**a**–**c**) and Ti–6Al–4V (**d**–**f**) alloys: mirror-like (**a**, **d**), micro-scratched (**b**, **e**) and nanomesh (**c**, **f**). Stress fibers (*red*), focal contacts (*green*) and nuclei (*blue*) can be observed. (Blanquer et al. 2016)

the samples were done to obtain the cell orientation and cytoskeleton distribution and are shown in Fig. (10.15).

No well-defined orientation could be seen for the cell grown on the nanomesh surface, whereas stress fibers were oriented along the longitudinal axis of scratched surface. Cell grown on the nanomesh surface had random orientation with angles 38° and 47°, respectively. For $Ti_{40}Zr_{10}Cu_{38}Pd_{12}$ and Ti6Al4V alloy, strong orientation of cell grown on scratched surface is observed, with mean angles 15.9° and 10.2°, respectively. Hence, the contact angles for all the surfaces below 90° revealed hydrophobicity.

Oak and coworkers prepared copper-free Ti–Pd–Zr–Si BMG with high hardness, strength, ductility, and corrosion resistance but with poor GFA. Lin and coworkers fabricated Ti–Zr–Ta–Si-based BMG, which was free of any toxic element and at the same time yielded high mechanical strength and corrosion resistance as compared to the conventional 316L SS and Ti6Al4V alloys.

Table 10.4 Critical diameter (d) for Ti-based BMGs

Chemical composition	*d* (mm)	Chemical composition	*d* (mm)
$Ti_{41.3}$ $Cu_{43.7}$ $Hf_{13.9}$ $Si_{1.1}$	3	Ti_{40} Zr_{10} Cu_{36} Pd_{14}	6
$Ti_{41.5}$ $Zr_{2.5}$ Hf_5 $Cu_{42.5}$ $Ni_{7.5}$ Si_1	~5	Ti_{40} Zr_{10} Cu_{38} Pd_{12}	3
Ti_{40} Zr_{10} Cu_{32} Pd_{14} Sn_4	10	Ti_{45} Zr_{10} Cu_{31} Pd_{10} Sn_4	15
Ti_{40} Za_{10} Cu_{34} Pd_{14} Sn_2	10	Ti_{45} Ni_{15} Cu_{25} Sn_3 Be_7 Zr_5	5
Ti_{47} Cu_{38} $Zr_{7.5}$ $Fe_{2.5}$ Sn_2 Si_1 Ag_2	7	Ti_{40} Zr_{10} Hf_{20} Fe_{20}	2
Ti_{40} Zr_{10} Cu_{38} Pd_{12}	2.5	Ti_{40} Zr_{10} Cu_{36} Pd_{14}) 100–*x* Nb*x* (*x* = 1, 3, 5)	2

$Ti_{41.5}$ $Zr_{2.5}$ Hf_5 $Cu_{37.5}$ $Ni_{7.5}$ Si_1 Sn_5 (TZHCNSS) BMG showed better biocompatibility in vitro for the human osteoblast SaOS2 cells than the Ti45Ni and Ti6Al4V alloy. Even murine fibroblast cells (L929 cell and NIH3T3) could attach well on all surface with filopodia and numerous cytoplasmic extensions. TZHCNSS were implanted into the mandibles of beagle dog along with pure titanium, and no inflammation could be seen around the operation site. Both implants yielded new bone formation and the distance between metallic sample and bone tissue was not more than 5 μm. Table 10.4 gives the critical diameter obtained for various Ti-based BMG.

Hynowska and coworkers prepared $Ti_{40}Zr_{20}Hf_{20}Fe_{20}$ rods and the cytotoxic results for the mouse MC3T3-E1 mouse preosteoblasts (ATCC) revealed no toxic effect as more than 97 % of preosteoblasts were alive. Cell adhesion studies revealed that cells are completely attached to the alloy surface by focal contacts at cell periphery along with the colocalisation with the actin filaments. The differentiation studies for the $Ti_{40}Zr_{20}Fe_{20}Hf_{20}$ BMG indicated formation of calcium nodules among the preosteoblasts after culture in the differentiation medium. Pang and coworkers synthesized novel $Ti_{47}Cu_{38}Zr_{7.5}Fe_{2.5}Sn_2Si_1Ag_2$ BMG, and it is reported to be the largest Ni- and Be-free Ti-based MBG with low noble metal content. As compared to Ti6Al4V, Ti-based glassy alloy possess relatively lower Young's modulus, higher specific strength, higher biocompatibility, and corrosion resistance. The in vitro biocompatibility of $Ti_{47}Cu_{38}Zr_{7.5}Fe_{2.5}Sn_2Si_1Ag_2$ was evaluated through cell culture using MC3T3-E1 cell line. The osteoblasts adhere and spread out on the alloy surface with cytoplasmic extension and filopodia. It is reported that Ag/Ag^+ ions exhibit anti-viral, anti-fungi, and anti-algae activities. Oak and coworkers prepared Ni-free Ti-based $Ti_{45}Zr_{10}Pd_{10}Cu_{31}Sn_4$ BMG, which excludes any harmful elements. The $Ti_{45}Zr_{10}Pd_{10}Cu_{31}Sn_4$ alloy revealed high GFA with wide supercooled region of 56 K. The Vickers hardness and elastic modulus of the BMG are 650 HV and 95 GPa, respectively, which are superior as compared to the Ti6Al4V alloy and pure Ti. $Ti_{45}Zr_{10}Pd_{10}Cu_{31}Sn_4$ BMG also depicts high corrosion resistance, better passivity, and lower passive current density of $\sim 10^{-2}$ A/m^2 in PBS aqueous solution and 1 mass% lactic acid.

Fornell and coworkers investigated the in vitro corrosion of $Ti_{40}Zr_{10}Cu_{38}Pd_{12}$BMG and revealed good wear and corrosion resistance. With the increase in annealing temperature, decrease in corrosion current density and increase in polarization resistance is observed. Wang and coworkers developed Ni-/Al-/Be-free $Ti_{41.3}Cu_{43.7}Hf_{13.9}Si_{1.1}$ BMG with high glass-forming ability. Quaternary Ti–Cu–Hf–Si alloy system is chosen for the biomedical application as $Ti_{57}Cu_{43}$, $Cu_{56.4}Hf_{43.6}$, and $Ti_{86.5}Si_{13.5}$ melt at low temperature and are line compound products for the eutectic reactions. The composition can be written as follows:

$$C = \alpha(Ti_{57}Cu_{43}) + \beta(Cu_{56.4}Hf_{43.6}) + \gamma(Ti_{86.5}Si_{13.5}) \tag{10.5}$$

where α, β, and γ represent the coefficients for three basic units. Using the heat of mixing of clusters, the values of α, β, and γ can be obtained as.

$$\begin{aligned} &\alpha = 0.6 \\ &\beta = 0.318 \quad \begin{cases} (\Delta H)_{Ti_{57}Cu_{43}} = -9\ \text{kJ/mol} \\ (\Delta H)_{Eu_{56.4}Hf_{43.6}} = -17\ \text{kJ/mol} \\ (\Delta H)_{Ti_{86.5}Si_{13.5}} = -66\ \text{kJ/mol} \end{cases} \\ &\gamma = 0.082 \end{aligned} \tag{10.6}$$

Using, the values given in Eq. (10.6), the ΔH of composition can be calculated. The strength and Young's modulus of BMG are 1685 MPa and 95 GPa, respectively. The polarization curves of $Ti_{41.3}Cu_{43.7}Hf_{13.9}Si_{1.1}$ BMG in NaCl and Hank's solution are given in Fig. 10.16.

For comparison purpose, the results are tested for pure Ti metal and Ti6Al4V alloy. Higher value of corrosion potential (F_{corr})for BMG i.e., −0.165 V in NaCl and 0.624 V in Hank's solution is obtained than for the Ti/Ti6Al4V alloy. In addition to this, the BMG exhibited lower polarization resistance (R_p) than the Ti-counterparts indicating the formation of more protective passive films on the BMG demonstrating its excellent corrosion resistance. The higher anti-corrosion properties of BMG can be discussed in two ways i.e., lack of structural defects and chemical homogeneity, whereas for the crystalline Ti/Ti6Al4V, structural defects such as dislocations, grain boundaries, and dispersed second phases can act as localized corrosion initiation sits. Hf is the most influential alloying element for depicting corrosion resistance, due to the enrichment of Hf ion in the protective films formed on the Ti–Cu–Hf–Si BMG.

Xie and coworkers also produced Ni-free $Ti_{45}Zr_{10}Cu_{31}Pd_{10}Sn_4$ BMG with almost 15 mm critical diameter. The samples sintered at 643 K by spark plasma system (SPS). A loading pressure of 600 MPa yielded high densification and fully dense structure with high strength. The potentiodynamic polarization revealed flat passive region after active dissolution at open circuit potential.

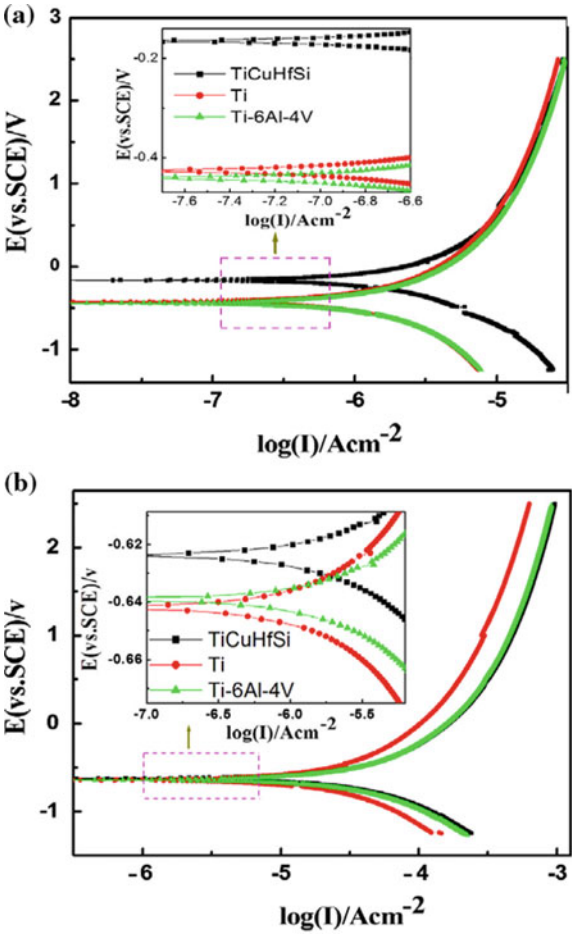

Fig. 10.16 Potentiodynamic polarization curves of pure Ti metal, Ti–6Al–4V alloy, and TiCuHfSi BMG in **a** NaCl solution and **b** Hank's solution in air at 37 °C (Wang et al. 2014)

10.8 Fe-Based BMG

As compared to Titanium-based and Zr-based BMG, Fe-BMG has low costs and attractive biomedical applications. The Fe-based BMGs have good glass-forming ability (GFA), and the first Fe-based BMG was developed in Fe–Al–Ga–P–C–B system in 1995. The other Fe-based systems include Fe–Ga–(P/C/B/Si), Fe–Co–Ln [Ln = Tm/Er], and Fe–(Zr/Hf/Nb)–B. Anyhow Fe-based BMG materials are functional and structural materials with magnetic properties. Therefore, during MRI diagnosis, the magnetic implants present inside the body get magnetized and interrupt with the diagnosis. Hence, magnetic devices with low magnetic susceptibility are required to decrease the artifacts. In 2003, non-magnetic Fe-based BMG were fabricated by Ponnambalam and coworkers with a composition similar to the stainless steel i.e., with Fe, Cr, and Mo elements. Fe-based BMGs have shown

Table 10.5 Critical diameter of Fe-based BMG

Composition	*d* (mm)	Composition	*d* (mm)
Fe_{63} Mo_{14} C_{15} B_6 Er_2	3	Fe_{44} Cr_{10} $Mo_{12.5}$ Mn_{11} C_{15} B_6 $Y_{1.5}$	2–5
Fe*x* (*x* = 63 − 71) Cr *y* (*y* = 0 − 3) Mo *z* (*z* = 5 − 12) P_{12} C_{10} B_2	2.5–3	Fe_{60} Cr_{10} Mo_{10} P_{13} C_7	6
Fe_{55} Cr_8 Mo_{14} C_{15} B_6 Er_2	>4	Fe_{50} Cr_{20} Mo_{10} P_{13} C_7	6
($Fe_{71.2}$ B_{24} $Y_{4.8}$) 96 Nb_4	3	Fe_{55} Cr_{20} Mo_5 P_{13} C_7	6
($Fe_{71.2}$ B_{24} $Y_{4.8}$)96 Ti_4	<2	Fe_{49} Cr_{15} Mo_{14} $C_{(13-x)}$ $B_{(8-x)}$ Er_1 (*x* = 2, 4, 5, 6)	3–6
($Fe_{71.2}$ B_{24} $Y_{4.8}$)96 Nb_1 Ti_3	3	Fe_{80} P_{13} C_7	2
($Fe_{71.2}$ B_{24} $Y_{4.8}$)96 Nb_3 Ti_1	3	Fe_{56} Co_7 Ni_7 Zr_{10} B_{20}	2
Fe_{41} Co_7 Cr_{15} Mo_{14} C_{15} B_6 Y	16	Fe_{48} Cr_{15} Mo_{14} C_{15} B_6 Er_2	12

fracture strengths up to 300 MPa and hardness in the range of 1200–1800 MPa, with comparable bioactivity as that of state of art materials (though the mechanical properties of Fe-based BMGs are much better). Fe-BMG glassy rods can be prepared with dimensions ranging from 2 to 16 mm as shown in Table 10.5. Fe–Cr–Mo–P–B system has been investigated widely and Co, Nb, and Mn are added as the rare earth elements to BMG to enhance glass-forming ability.

Li and coworkers fabricated a novel series $Fe_{80-x-y}Cr_xMo_yP_{13}C_7$($x$ = 10/y = 10, x = 20/y = 5, x = 20/y = 10) i.e., $Fe_{55}Cr_{20}Mo_5P_{13}C_7$, $Fe_{50}Cr_{20}M_{10}P_{13}C_7$, and $Fe_{60}Cr_{10}Mo_{10}P_{13}C_7$ with maximum of 6 mm diameter have been prepared by combination of J-quenching and fluxing technique. The BMGs have shown higher corrosion resistance in artificial saliva solution than in the Hank' solution indicating its more potential perspective in dental applications. The BMG with high Cr content reveal high corrosion resistance as compared to the BMG with high Mo content because Cr leads to more stable passivation film. The Fe-based BMG revealed corrosion resistance similar to the TC4 alloy. 316L SS have depicted higher concentration of ions especially Ni, Mn, Cr, Fe, and Mo ions, than those released from TC4 and Fe-based BMGs attributing to higher corrosion resistance of Fe-based BMGs and TC4. The cell viability of samples with NIH3T3 mouse embryonic fibroblast revealed lowest viability for 316L SS steel. In contrast to this, TC4 and Fe-based BMG yielded similar viability results. This is attributed to the high release of Ni and Cr ions released from 316L SS alloy. After 2 days culture of NIH3T3 cells on the specimen, Fe-based BMG are completely covered with the NIH3T3 cells. Among all the samples, $Fe_{55}Cr_{20}Mo_5P_{13}C_7$ exhibits high corrosion resistance and best biocompatibility, indicating its potential as a biomedical implant. Wang and coworkers studied the corrosion behavior of Ni-free Fe-based $Fe_{41}Co_7Cr_{15}Mo_{14}C_{15}B_6Y_2$ (BMG1) in simulated body fluid. Fe-BMG has better corrosion resistance in artificial saliva than in the Hank's solution. However, higher impedance values have been obtained for the BMG indicating that oxide film or

BMG is more corrosion resistant. The same group worked on $Fe_{44}Cr_5Co_5Mo_{13}Mn_{11}C_{16}B6)_{98}Y_2$ (BMG2) and $Fe_{48}Cr_{15}Mo_{14}C_{15}B_6Er_2$ (BMG3) for the corrosion behavior and cytotoxicity evaluation. Both BMGs displayed higher pitting potential values and lower corrosion current density in Hank's solution and saliva solution as compared so the 316L SS. The cytotoxicity test for murine fibroblast L929 cells cultured on 316L SS and Fe-based BMG is shown in Fig. 10.17, which indicates no adverse effect on the cell viability, morphology, and proliferation. After 4 days of culture, the cell number grows quickly with no obvious difference between experimental groups and negative controls. The cells appear spindle shaped with longitudinal alignment at high densities. Zohdi and coworkers also obtained larger polarization values for $Fe_{51}Cr_{18}Mo_7B_{16}C_4Nb_4$ than that of Ti6Al4V and 316L SS.

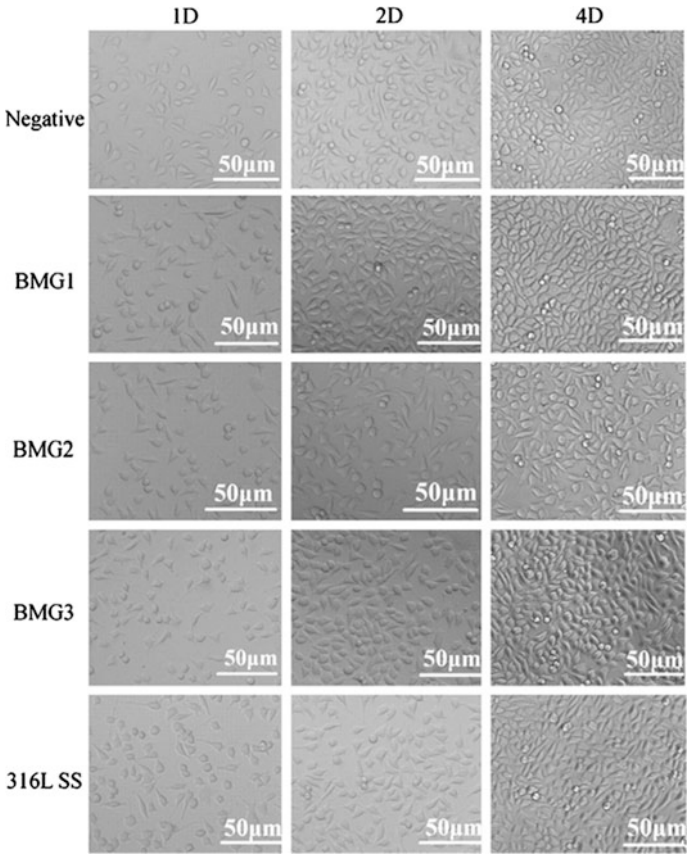

Fig. 10.17 L929 cell morphology upon culturing with Fe-based BMGs and 316L SS sample extraction media after 1, 2, 4 days (Wang et al. 2012)

10.9 Other Ca-/Mg-/Sr-Based Biodegradable BMG

Magnesium, calcium, and strontium have been regarded as biodegradable metal. Magnesium-based BMG minimize the galvanic corrosion, thereby enhancing the bioactive properties as well. Zberg and coworkers developed Mg–Ca–Zn glass with tissue compatibility comparable to the crystalline counterparts. For the Zn content of 21–35 wt%, the formation of passive layer takes place on surface. Gu and coworkers obtained that the L929 and MG63 cells are well adherent and show proliferation on the $Mg_{66}Zn_{30}Ca_4$ alloy surface.

The development of magnesium-based alloy faces some challenges like pitting corrosion, fast corrosion rates, and lack of mechanical strength. Mg-based BMG exhibits higher strength and lower elastic moduli than the pure Mg and conventional alloys. The fracture strength of $Mg_{70}Zn_{25}Ca_5$ is 565 MPa and for $Mg_{66}Zn_{30}Ca_4$, is 531 MPa, which is much higher than the pure Mg sample fracture strength of 198 MPa. For $Mg_{66}Zn_{30}Ca_4$ and $Mg_{70}Zn_{25}Ca_5$ BMG, healthy elongated and spindle shaped cells could be seen adhered on the surface as compared to the unhealthy round cells seen on the pure Mg sample surface. Gu and coworkers studied the Mg–Sr alloy system intramedullary implantation in animal model. The optimal Sr content is 2 wt%, excessive Sr cause poor mechanical property and below 2 wt%, the strength and corrosion resistance of Mg are obtained. The Mg–2Sr alloy exhibits grade I ctyotoxicity along with the increased ALP activity. Mg–2Sr alloy also promoted bone mineralization and bone formation without any inflammatory or adverse reaction.

Yu and coworkers doped 0.5–4 % Yb into the Mg–Zn–Ca glasses and the improved ductility and bending strength of the Mg-based BMGs was found. The Yb addition enhanced the in vitro bicompatability of cell adhesion and proliferation. Cao and coworkers obtained slower corrosion rate of $Mg_{65}Zn_{30}Ca_5$ BMG as the release rate of Mg ions into the media was approximately half as that of pure Mg. After 72 h culture period, the cell viabilities of L929 cells were relatively high. $Mg_{60}Zn_{35}Ca_5$ BMG implantation in porcine abdominal tissue revealed the typical fibrous capsule foreign body reaction as shown in Fig. 10.18. No inflammatory reaction or tissue imprinted hydrogen gas cavities has been formed.

The first Ca-based BMG was reported in 2002, and Ca is two most studied nutrient of human body. CaO and coworkers also studied the Ca–Mg–Zn system extensively and synthesized Ca-rich BMG in the Ca–Mg–Zn ternary alloy system (Fig. 10.19).

The main aim of choosing the composition was to improve thermal stability, thermoplastic processing, and corrosion resistance. The composition with highest and lowest calcium content is $Ca_{57.5}Mg_{15}Zn_{27.5}$ and $Ca_{50}Mg_{20}Zn_{30}$, respectively. The Ca–BMG displayed higher corrosion rates as compared to their crystalline counterparts and some hydrogen evolution still occurred during dissolution in spite of more noble corrosion potentials of Ca-based BMG. Calcium possess inherent reactive nature than magnesium and by increasing the Zn content in the alloy, the

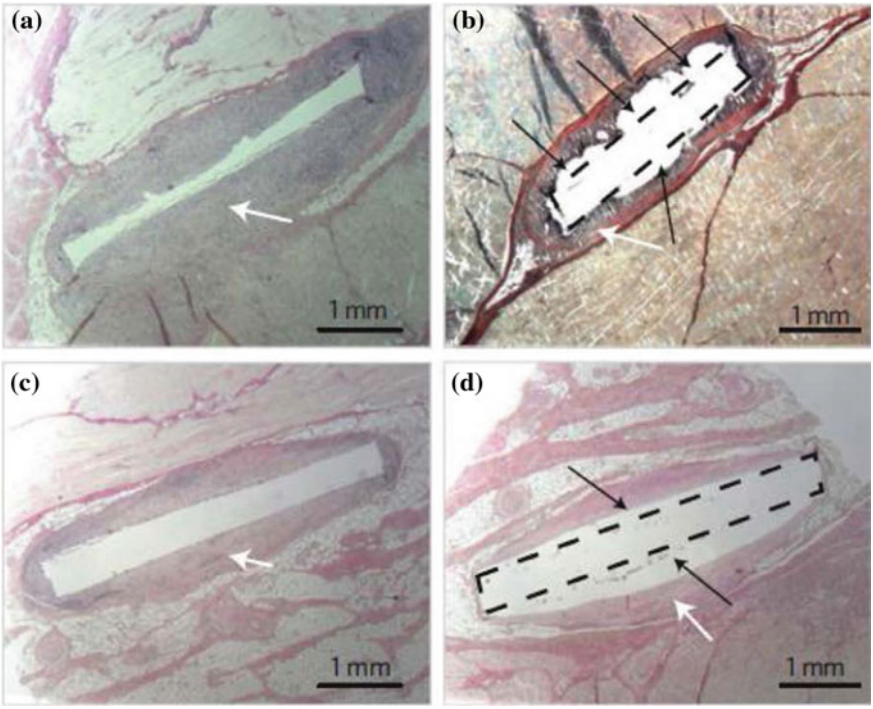

Fig. 10.18 Glassy $Mg_{60}Zn_{35}Ca_5$ (**a**, **c**) and crystalline Mg alloy reference (WZ21) (**b**, **d**) in porcine abdominal tissue (subcutis after 91 days (**c**, **d**) and muscle after 27 days (**a**, **b**) of implantation) (Li and Zheng 2016)

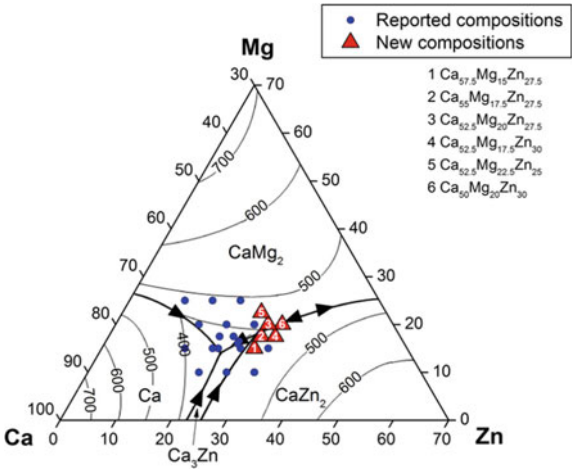

Fig. 10.19 Scheme of the Ca–Mg–Zn phase diagram (Villars et al. 1994)

dissolution of Ca-based BMG can be improved. The corrosion morphology in Ca-based BMG was more of incongruent dissolution similar to dealloying.

Wang and coworkers developed $Ca_{65}Mg_{15}Zn_{20}$ metallic glasses with Young's modulus, compressive fracture strength, and compression fracture strain of 19 GPa, 354 Mpa, and 1.92 ± 0.15 %, respectively. The Ca–Mg–Zn rods were implanted in the distal femur and no translucent areas could be seen. In addition to this, no inflammation could be seen around the operation site and no mice died after surgery. The Ca–Mg–Zn rods degraded and dispersed in the medullary cavity with the increase in implantation time.

One week after implantation, reactive hyperplasia of bone could be soon around the cortical zone of distal femur. The histological observations after 4-week implantation revealed higher bone thickness around the implanted Ca–Mg–Zn rod as compared to the normal bone as depicted in Fig. 10.20a–c.

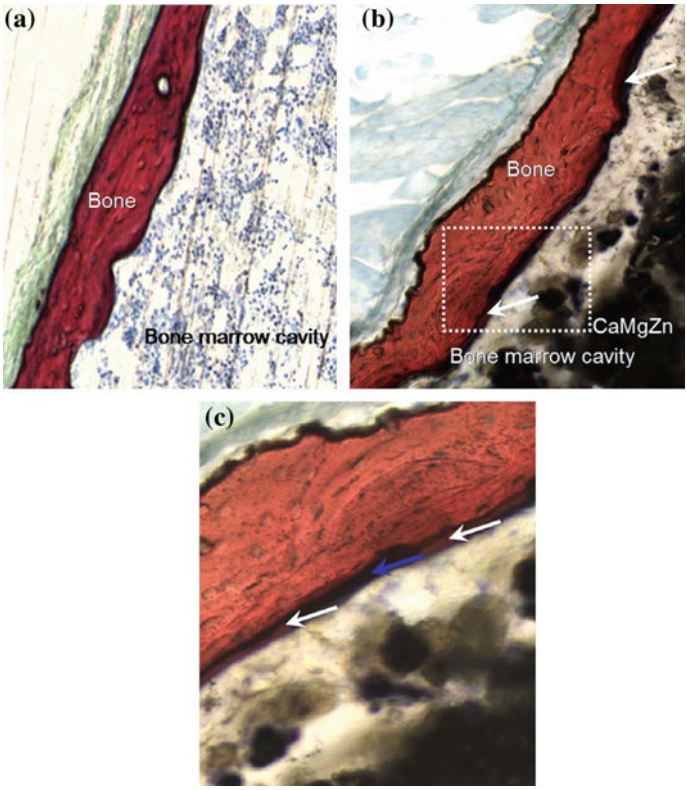

Fig. 10.20 Histology of cortical bone using Van Gieson staining. **a** Normal bone and the bone marrow cavity, **b** CaMgZn BMG rod in the femur of a mouse 4 weeks after implantation, *arrows* indicate new bone formation, **c** magnification of the white rectangular frame (Wang et al. 2011)

After 4 weeks of implantation, the Ca–Mg–Zn rod degraded and debris diffused into the bone marrow cavity, stimulating new bone formation from the inner edge of residual cortical bone. Some particulate deposition of Ca–Mg–Zn could also be seen along with the new bone at inner edge of the cortical bone. Anyhow, due to rapid degradation and pH value increase, cartilage formation could be seen in distal femur along with osteolysis. Usually Ca–Mg–Zn alloys are oxidation resistant but they degraded quickly when placed in SBF. Following degradation mechanism may have taken place.

$$M + 2H_2O \rightarrow M(OH)_2\downarrow + H_2 \uparrow (M = Mg, Ca, Zn) \tag{10.7}$$

$$Zn + 2OH^- \rightarrow ZnO \downarrow + H_2O \tag{10.8}$$

$$2ZnO + Ca(OH)_2 + 3H_2O \rightarrow Ca(Zn(OH)_3)_2 \cdot H_2O \tag{10.9}$$

$$3M^{2+} + 2PO_4^{3-} \rightarrow M_3(PO_4)_2 \tag{10.10}$$

$$M^{2+} + CO_3^{2-} \rightarrow M(CO_3)$$

The biocorrosion model proposed by Wang and coworkers is shown in Fig. 10.21. The figure can be illustrated as follows.

- Firstly, hydroxides are generated on the Ca–Mg–Zn BMG surface. Upon hydrogen evolution from the surface, the porosity of corrosion layer increases. Through the pores, surrounding solution penetrates and reacts with the inner metal layer.
- Dissolution—precipitation occurs near surface zone, though under normal conditions, $ZnO/Mg(OH)_2/Ca(OH)_2$ are indissoluble. In the presence of chloride ions, the corrosion of Ca–Mg–Zn proceeds and homeostasis could be disrupted.
- The apatite and carbonate formation takes place during the biocorrosion process.

Though $ZnO/ZnCO_3$ could form a protective layer on Ca–Mg–Zn, but the formation of Zn rich products did not stop the corrosion process. Ca–Mg–Zn BMG extracts show good biocompatibility over wide concentration range and did not cause the death of L929, VSMC, and ECVO 4 cell lines. For a concentration range of 10–30 %, the viability of MG63 cells as well as the ALP production is promoted. At higher concentrations, the MG63 undergo apoptosis and change in cell morphology.

Li and coworkers fabricated high entropy $Ca_{20}Mg_{20}Zn_{20}Sr_{20}Yb_{20}$ (CMZSY) bulk metallic glasses, for orthopedic applications. Ytterbium possesses unlimited solubility in calcium and also improves corrosion resistance along with enhancing glass-forming ability. The Young's modulus and fracture strength of CMZSY BMG is 19.4 GPa and 370 MPa, respectively. The fracture strength of CMZSY is found to be higher than the human cortical bone (130–180 MPa) and $Ca_{65}Mg_{15}Zn_{20}$ (300 MPa). CMZSY has depicted low degradation rate of 0.17 mg/cm^2/h and with the addition of Sr and Yb, H_2 evolution decreased significantly. The MG63 cells

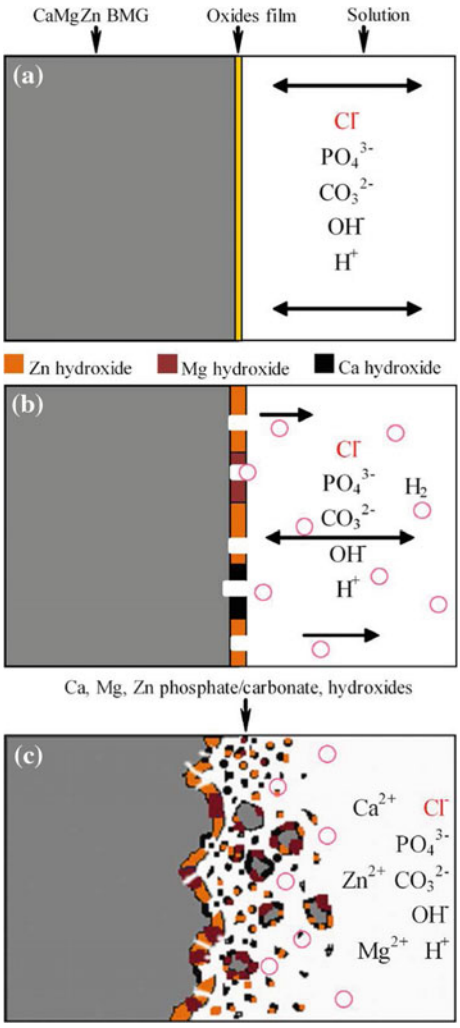

Fig. 10.21 Corrosion mechanism of Ca–Mg–Zn BMG in simulated body fluid (Wang et al. 2011)

cultured in CMZSY showed higher cell viability and ALP activity than the control group, indicating that the BMG promoted proliferation and differentiation of osteoblasts. CMZSY is implanted in the distal femora and the radio graphs are shown in Fig. 10.22. It is evident that the CMZSY high entropy BMG does not degrade faster during the entire experiment. No translucency could be seen around the metal alloys and BMG rods are well positioned. No gas shadows due to hydrogen gas evolution could be seen. No inflammation could be seen around the BMG rods and no mice died after implantation. After 3–4 weeks of implantation, circumferential osteogenesis could be seen, which indicates the thickness of the cortical bone around the rods, indicating new bone formation. CaLi-based BMG

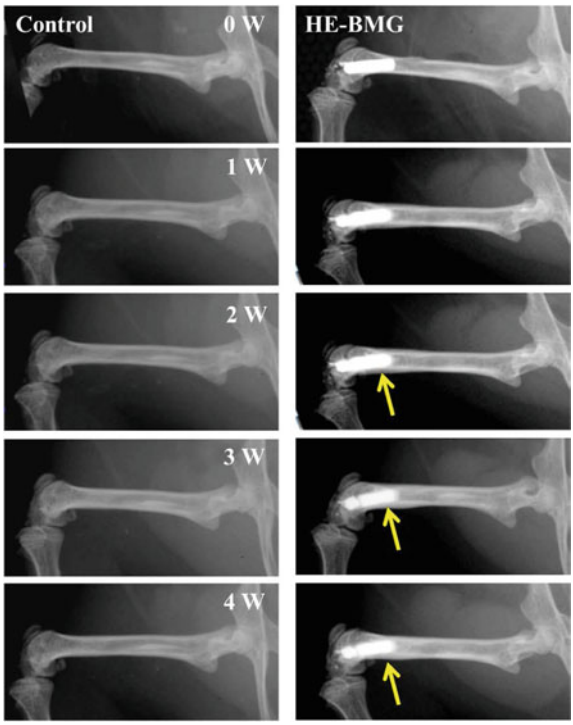

Fig. 10.22 Radiographs of mice distal femora with CMZSY HE-BMG rod implants and control group for 0, 1, 2, 3, and 4 weeks of implantation (Li et al. 2013)

with ultralow density (<2 g/cm^3) have also been developed, and these glass show polymer-like thermoplastic formability with excellent plastic-like deformability.

Jiao and coworkers obtained Young's modulus and high fracture strength of 31.9 GPa and 600 MPa, respectively, for $Ca_{48}Zn_{30}Mg_{14}Yb_8$ BMG. Strontium is found to have bone affinity and inhibit bone resumption in vitro and in vivo. The drug strontium ranelate has shown to reduce the fractures in osteoporotic patients. Magnesium, strontium, and calcium belong to the same group of periodic table and Ca/Sr physiological distribution is same i.e., 99 % of elements are being stored in the bone. In 2009, the Sr-based BMG were first reported by Li and coworkers and Sr-based BMG possess low Young's modulus and low density. Strontium can replace calcium in HAp structure for wide range of compositions and also increase osteoblast number and reduce osteoclasts. $Sr_{60}Mg_{18}Zn_{22}Sr_{60}Li_5Mg_{15}Zn_{20}$ BMG have very fast degradation rate and get degraded within 1 min in deionized water. Li and coworker studied the orthopedic potential of $Sr_{40}Mg_2$ $Zn_{15}Yb_{20}Cu_5$ BMG and obtained the compression strength and Young's modulus to be 408 MPa and 20.6 GPa, respectively, which is higher than conventional BMG (Ca_{65} Mg_{15} Zn_{20}) and cortical bone. The corrosion behavior of Sr-/Ca-/Mg-based BMG and Mg alloys is given in Table 10.6.

From Table 10.6, it is evident that Sr-based BMG depict high corrosion resistance. The Sr-based $Sr_{40}Mg_{20}Zn_{15}Yb_{20}Cu_5$ exhibits satisfactory cell viability for

Table 10.6 Corrosion behavior of Sr/Ca BMG and Mg alloys

Material	Corrosion current density (a/cm^2/h)	H2 generation rate (ml/cm^2/h)
Mg—1.22 Ca	63	
Mg—1 Ca	546.09	0.136 in SBF
Pure Mg	0.108 in SBF	86.06 in SBF
$Ca_{60}Mg_{15}Zn_{25}$	–	7.509 (deionized water)
$Sr_{40}Mg_{20}Zn_{15}Yb_{20}Cu_5$	22.780	0.04175

the MG63 cells. Though BMG have great biomaterial potential, but still the studies are focused to improve BMG sizes, developing BMG coatings/foams, and BMG composites. The research is also focused on eliminating toxic beryllium, nickel, and palladium elements from the BMG composition.

Bibliography

Inoue A, Takeuchi A (2011) Recent development and application products of bulk glassy alloys. Acta Mater 59(6):2243–2267. doi:10.1016/j.actamat.2010.11.027

Takeuchi A, Inoue A (2005) Metallic glasses by atomic size difference, heat of mixing and period of constituent elements and its application to characterization of the main alloying element. Mater Trans 46(12):2817–2829. doi:10.2320/matertrans.46.2817

Miracle DB (2004) Nature Mater 3:697

Li HF, Zheng YF (2016) Recent advances in bulk metallic glasses for biomedical applications. Acta Biomater 6(7):2740–2750. doi:10.1016/j.actbio.2016.03.047

Liu L, Chan KC, Yu Y, Chen Q (2010) Bio-activation of Ni-free Zr-based bulk metallic glass by surface modification. Intermetallics 18(10):1978–1982. doi:10.1016/j.intermet.2010.02.039

Huang L, Pu C, Fisher RK, Mountain DJH, Gao Y, Liaw PK, He W (2015) A Zr-based bulk metallic glass for future stent applications: materials properties, finite element modeling, and in vitro human vascular cell response. Acta Biomater 25:356–368. doi:10.1016/j.actbio.2015.07.012

Liu L, Qiu CL, Huang CY, Yu Y, Huang H, Zhang SM (2009) Biocompatibility of Ni-free Zr-based bulk metallic glasses. Intermetallics 17(4):235–240. doi:10.1016/j.intermet.2008.07.022

Qin F, Dan Z, Wang X (2011) Ti-based bulk metallic glasses for biomedical applications, pp 249–268

Sugiyama N, Xu H, Onoki T, Hoshikawa Y, Watanabe T, Matsushita N, Yoshimura M (2009) Bioactive titanate nanomesh layer on the Ti-based bulk metallic glass by hydrothermal-electrochemical technique. Acta Biomater 5(4):1367–1373. doi:10.1016/j.actbio.2008.10.014

Blanquer A, Hynowska A, Nogués C, Ibáñez E, Sort J, Dolors Baró M, Barrios L (2016) Effect of surface modifications of Ti 40 Zr 10 Cu 38 Pd 12 bulk metallic glass and Ti 6Al4V alloy on human osteoblasts in vitro biocompatibility, pp 1–15. doi:10.1371/journal.pone.0156644

Wang YB, Xie XH, Li HF, Wang XL, Zhao MZ, Zhang EW, Qin L (2011) Biodegradable CaMgZn bulk metallic glass for potential skeletal application. Acta Biomater 7(8):3196–3208. doi:10.1016/j.actbio.2011.04.027

Wang G, Fan HB, Huang YJ, Shen J, Chen ZH (2014) A new TiCuHfSi bulk metallic glass with potential for biomedical applications. Mater Des 54:251–255. doi:10.1016/j.matdes.2013.08.075

Wang YB, Li HF, Zheng YF, Li, M (2012) Corrosion performances in simulated body fluids and cytotoxicity evaluation of Fe-based bulk metallic glasses. Mater Sci Eng C 32(3):599–606. doi:10.1016/j.msec.2011.12.018

Villars P, Prince A, Okamoto H (1994) Handbook of ternary alloy phase diagrams. Materials park, OH, ASM international

Zberg B, Arata ER, Uggowiter PJ (2009) Tensile properties of glassy MgZnCa wires and reliability analysis using Weibull statistics. Acta Mater 57(11):3223–3231

Zberg B, Uggowiter PJ, Löffler JF (2009) MgZnCa glasses without clinically observable hydrogen evolution for biodegradable implants. Nat Mater 8(11):887–891

Yokoyama Y, Fujita K, Yavari AR et al (2009) Malleable hypoeutectic Zr-Ni-Cu-Al bulk glassy alloys with tensile plastic elongation at room temperature. Philos Mag Lett 89(5):322–334

McGregor DB, Baan RA, Partensky C (2000) Evaluation of the carcinogenic risks to humans associated with surgical implants andother foreign bodies—a report of an IARC Monographs Programme Meeting. Eur J Cancer 36(3):307–313

Jin KF, Löffler JF (2005) Bulk metallic glass formation in Zr-Cu-Fe-Al alloys. Appl Phys Lett 86 (24):241909

Liu Y, Wang YM, Pang HF, Zhao Q, Liu L (2013) Acta Biomater 9:7043

Lin CH, Huangn CH, Chuang JF, Uuang JC, Jang JSC, Chen CH (2013) Mat Sci Eng 33:4520

Hua N, Sluang L, Chen W, He W, Zhang T (2014) Mat-Su Eng C 44:4000

Oak JJ, Inoue A (2008) J Non Cryst Solids 354:1828

Lin HC, Tasi PH, Ke JH, Li JB, Jang JSC, Huang CH, Haung JC (2014) Intermetallices 55:22

Ponnambalam V, Poon SJ, Shiflet GJ, Keppens VM, Tayler R, Petculiscu G (2003) Appl Phy Lett 83:1131–1133

Zohdi H, Shativerdi HR, Hadavi SMM (2012) Electrochem Commun 13:840–843

Gu XN, Zheng YF, Zhong SP (2010) Biomaterials 1093–1103

Yu HJ, Wang JQ, Shi XT, Luzgin L, Wu HK, Perepezko JH (2013) Adv Funct Mater 23:4793–4800

Cao JD, Martens P, Laws KJ, Boughton P, Ferry M (2013) J Biomed mater Res B Appl Biomater 101:43–49

Jiao W, Li HF, Zhao K, Bai HY, Wang YB, Zheng YF et al (2011) J Non Cryst Solids 357:3830–3840

Meagher P, O'Cearbhaill ED, Byrne JH, Browne DJ (2016) Bulk metallic glasses for implantable medical devices and surgical tools. Adv Mater. doi:10.1002/adma.201505347

Schroers J, Kumar G, Hodges TM, Chan S, Kyriakides TR (2009) Bulk metallic glasses for biomedical applications. Jom 61(9):21–29. doi:10.1007/s11837-009-0128-1

Buzzi S, Jin K, Uggowitzer PJ, Tosatti S, Gerber I, Löffler JF (2006) Cytotoxicity of Zr-based bulk metallic glasses. Intermetallics 14(7):729–734. doi:10.1016/j.intermet.2005.11.003

Nowosielski R, Cesarz K, Babilas R (2013) Structure and corrosion properties of Mg70-xZn30Cax (x = 0,4) alloys for biomedical applications. J Achievements Mater Manuf Eng 58(1):7–15

Zhu SJ, Liu Q, Qian YF, Sun B, Wang LG, Wu JM, Guan SK (2014) Effect of different processings on mechanical property and corrosion behavior in simulated body fluid of Mg-Zn-Y-Nd alloy for cardiovascular stent application. Front Mater Sci 8(3):256–263. doi:10.1007/s11706-014-0259-3

Ali E, Neel A, Mark D, Padinhara S, John R (1990) Phosphate based glasses: a perspective journal

Fakult D, Universit T, Doktoringenieur G (1982) Ni-free Ti-based bulk metallic glasses: glass forming ability and mechanical behavior

Zeng RC, Qi WC, Song YW, He QK, Cui HZ, Han EH (2014) In vitro degradation of MAO/PLA coating on Mg-1.21Li-1.12Ca-1.0Y alloy. Fronti Mater Sci 8(4):343–353. doi:10.1007/s11706-014-0264-6

Horton JA, Parsell DE (2002) Biomedical potential of a zirconium-based bulk metallic glass. MRS Proc 754:6–11. doi:10.1557/PROC-754-CC1.5

Chen MW (2011) A brief overview of bulk metallic glasses. Npg Asia Mater 3:82–90. doi:10.1038/asiamat.2011.30

Li HF, Xie XH, Zhao K, Wang YB, Zheng YF, Wang WH, Qin L (2013) In vitro and in vivo studies on biodegradable CaMgZnSrYb high-entropy bulk metallic glass. Acta Biomater 9 (10):8561–8573. doi:10.1016/j.actbio.2013.01.029.

Song R, Liu D-B, Liu Y-C, Zheng W-B, Zhao Y, Chen M-F (2014) Effect of corrosion on mechanical behaviors of Mg-Zn-Zr alloy in simulated body fluid. Front Mater Sci 8(3):264–270. doi:10.1007/s11706-014-0258-4

Gu XN, Xie XH, Li N, Zheng YF, Qin L (2012) In vitro and in vivo studies on a Mg-Sr binary alloy system developed as a new kind of biodegradable metal. Acta Biomater 8(6):2360–2374. doi:10.1016/j.actbio.2012.02.018

Hynowska A, Blanquer A, Pellicer E, Fornell J, Suriñach S, Baró MD, Sort J (2013) Novel Ti-Zr-Hf-Fe nanostructured alloy for biomedical applications. Materials 6(11):4930–4945. doi:10.3390/ma6114930

Xie G, Qin F, Zhu S, Inoue A (2012) Ni-free Ti-based bulk metallic glass with potential for biomedical applications produced by spark plasma sintering. Intermetallics 29:99–103. doi:10.1016/j.intermet.2012.05.006

Wang HB, Ma LX, Li L, Zhang B (2015) Fabrication of Fe-based bulk metallic glasses from low-purity industrial raw materials. J Alloy Compd 629(1–4). doi:10.1016/j.jallcom.2014.11.228

Cao JD, Kirkland NT, Laws KJ, Birbilis N, Ferry M (2012) Ca-Mg-Zn bulk metallic glasses as bioresorbable metals. Acta Biomater 8(6):2375–2383. doi:10.1016/j.actbio.2012.03.009

Fornell J, Van Steenberge N, Varea A, Rossinyol E, Pellicer E, Suriñach S, Sort J (2011) Enhanced mechanical properties and in vitro corrosion behavior of amorphous and devitrified Ti40Zr10Cu38Pd12 metallic glass. J Mech Behav Biomed Mater Mater 4(8):1709–1717. doi:10.1016/j.jmbbm.2011.05.028

Oak J-J, Louzguine-Luzgin DV, Inoue A (2007) Fabrication of Ni-free Ti-based bulk-metallic glassy alloy having potential for application as biomaterial, and investigation of its mechanical properties, corrosion, and crystallization behavior. J Mater Res 22(5):1346–1353. doi:10.1557/jmr.2007.0154

Pang S, Liu Y, Li H, Sun L, Li Y, Zhang T (2015) New Ti-based Ti-Cu-Zr-Fe-Sn-Si-Ag bulk metallic glass for biomedical applications. J Alloy Compd 625:323–327. doi:10.1016/j.jallcom.2014.07.021

Zhao K, Li JF, Zhao DQ, Pan MX, Wang WH (2009) Degradable Sr-based bulk metallic glasses. Scripta Mater 61(11):1091–1094. doi:10.1016/j.scriptamat.2009.08.042

Li S, Wei Q, Li Q, Jiang B, Chen Y, Sun Y (2015) Development of Fe-based bulk metallic glasses as potential biomaterials. Mater Sci Eng C 52:235–241. doi:10.1016/j.msec.2015.03.041

Wang YB, Li HF, Cheng Y, Wei SC, Zheng YF (2009) Corrosion performances of a Nickel-free Fe-based bulk metallic glass in simulated body fluids. Electrochem Commun 11(11):2187–2190. doi:10.1016/j.elecom.2009.09.027

Gu XN, Li SS, Li XM, Fan YB (2014) Magnesium based degradable biomaterials: a review. Front Mater Sci 8(3):200–218. doi:10.1007/s11706-014-0253-9

Li HF, Zhao K, Wang YB, Zheng YF, Wang WH (2012) Study on bio-corrosion and cytotoxicity of a Sr-based bulk metallic glass as potential biodegradable metal. J Biomed Mater Res Part B Appl Biomater 100(2):368–377. doi:10.1002/jbm.b.31958

Chen Q, Liu L, Zhang S-M (2010) The potential of Zr-based bulk metallic glasses as biomaterials. Front Mater Sci China 4(1):34–44. doi:10.1007/s11706-010-0004-5

Johnson WL (1999) Bulk glass-forming metallic alloys: science and technology. MRS Bull 24(10):42–56

Wang WH, Dong C, Shek CH (2004) Bulk metallic glasses. Mater Sci Eng R Rep 44(2–3):45–89

Hiromoto S, Tsai AP, Sumita M (2000) Effect of chloride ion on the anodic polarization behavior of the Zr65Al7.5Ni10Cu7.5 amorphous alloy in phosphate buffered solution. Corros Sci 42(9):1651–1660

Kawamura Y, Shibata T, Inoue A (1997) Workability of the supercooled liquid in the Zr65Al10Ni10Cu15 bulk metallic glass. Acta Mater 46(1):253–263

Hiromoto S, Tsai AP, Sumita M (2000) Effect of pH on the polarization behavior of Zr65Al7.5Ni10Cu17.5 amorphous alloy in a phosphate-buffered solution. Corros Sci 42(9):2193–2200

Hiromoto S, Tsai AP, Sumita M (2000) Effects of surface finishing and dissolved oxygen on the polarization behavior of Zr65Al7.5Ni10Cu17.5 amorphous alloy in phosphate buffered solution. Corros Sci 42(12):2167–2185

Hiromoto S, Hanawa T (2002) Re-passivation current of amorphous Zr65Al7.5Ni10Cu17.5 alloy in a Hanks' balanced solution. Electrochimica Acta 47(9):1343–1349

Morrison ML, Buchanan RA, Peker A (2004) Cyclic-anodicpolarization studies of a Zr41.2Ti13.8Ni10Cu12.5Be22.5 bulk metallic glass. Intermetallics 12(10–11):1177–1181

Morrison ML, Buchanan RA, Leon RV (2005) The electrochemical evaluation of a Zr-based bulk metallic glass in a phosphate-buffered saline electrolyte. J Biomed Mater Res Part A 74 (3):430–438

Maruyama N, Hiromoto S, Ohnuma M (2005) Fretting fatigue properties of Zr-based bulk amorphous alloy in phosphate buffered saline solution. J Japan Inst Metals 69(6):481–487

Chapter 11
Future Perspectives of Bioactive Glasses for the Clinical Applications

V. Kumar, G. Pickrell, S.G. Waldrop and N. Sriranganathan

11.1 Introduction

Tissue engineering is continuously evolving as an exciting and multidisciplinary field aiming to develop biological substitutes to restore, replace, or regenerate defective tissues. Scaffolds, cells, and growth-stimulating signals are the basic components of tissue engineering. However, researchers often encounter an enormous variety of choices when selecting scaffolds for tissue engineering. Typically, glass, ceramics, or polymeric biomaterials are used for making scaffolds, which provide the structural support for cell attachment and subsequent tissue development.

A three-dimensional scaffold plays a pivotal role by providing a substrate for attachment of cells to proliferate and form an extracellular matrix. These scaffolds should be able to facilitate the diffusion of nutrients and metabolic waste removal in addition to adequate mechanical properties for providing required biomechanical support during the process of tissue regeneration. Hence, a balance between total pore volume and mechanical strength is required. The biggest challenge in the selection of materials for scaffold fabrication is attaining biocompatibility and maintaining controlled degradation so that the space occupied by the initial scaffold is replaced by regenerated host tissue.

Among the numerous available materials, synthetic bioresorbable polyesters, such as polylactides and polylactones, have attracted a great deal of attention for scaffold fabrication because of their biocompatibility, biodegradability, and easily controlled (tunable) properties. However, these polymers lack the necessary specific bioactive abilities to induce adequate proliferation and differentiation of cells which make addition of phosphate or silicate-based bioactive fillers a suitable option to

G. Kaur, *Bioactive Glasses*, Series in BioEngineering,
DOI 10.1007/978-3-319-45716-1_11

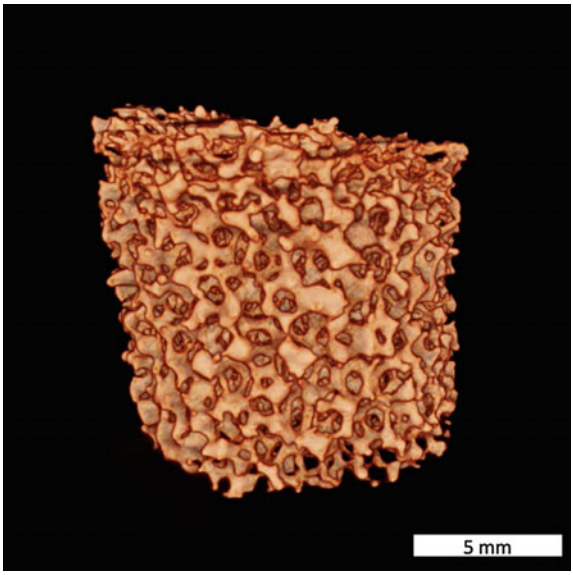

Fig. 11.1 Fluorapatite glass-ceramic scaffold reconstructed image (Isabelle et al. 2016)

impart bioactivity to bioresorbable synthetic polymers in the regeneration of hard and soft tissues.

Although many research groups have reported application of bioactive ceramics for bone repair, little attention has been paid to their application in the regeneration of soft tissues. Some recent studies have demonstrated the ability of bioactive glasses to promote angiogenesis and enhance neocartilage formation during in vitro culture and these properties are critical for numerous applications such as healing of soft tissue wounds. Soft biomaterials with elastomeric behavior are desirable for the regeneration of soft tissues, and this explains the reason why there is a need to study the combinations of bioactive ceramics with thermoplastic materials which show behavior ranging from glassy to elastomeric state, covering a wide range of mechanical properties found in real body tissues.

Several researchers have proposed incorporation of a biocompatible and bioresorbable polymer to bioactive glass shown in Fig. 11.1 or hydroxyapatite scaffolds for improving the toughness of the ceramic scaffolds. Many studies have shown improved mechanical properties for polymer scaffolds loaded with hydroxyapatite or bioglass particles due to the presence of stiff particles in a soft polymer matrix. This also promotes osteointegration of the scaffold with the surrounding bone, and according to the literature, cells seeded on bioglass or hydroxyapatite-filled polymer scaffolds show improved in vitro growth and osteogenic differentiation compared to the unfilled counterparts.

11.2 3-D Scaffolds

Indeed, the past two decades have been associated with sustained interdisciplinary efforts to design and develop synthetic scaffolds encompassing a wide range of materials from ceramics to polymers, including composite, cell-bearing, protein-loaded, or growth factor-carrying scaffolds mixing both inorganic and organic phases. As mentioned earlier, an ideal scaffold material for synthetic bone grafts should be osteoinductive, osteoconductive, promote osteointegration, with an ability to deliver osteogenic agents, anti-infectives, stem cells, and degrade at the same rate as new bone forms. Calcium phosphate ceramic scaffolds are therefore excellent candidates, offering a large palette of design options as detailed below.

11.2.1 Scaffold and Its Functions

11.2.1.1 Osteoinduction and Biodegradation

Osteoinduction can be defined as the chemical stimulation of human mesenchymal stem cells into bone-forming osteoblasts, thereby inducing osteogenesis. It is the ability of a material to form bone in an ectopic site, and certain calcium phosphate ceramics (CPC) have demonstrated to be osteoinductive. It is postulated that osteoinductivity arises from the combination of micro- and macroporosity which is capable of entrapping and concentrating growth factors that are directly involved in mesenchymal stem cell differentiation into an osteoblastic lineage. A major role is played by surface and bulk chemistry of the crystalline phases involved, and the HAp crystalline structure consists of highly exchangeable sites, where both anionic and cationic substitutions can take place. Mg^{2+}, Si^{4+}, and Sr^{2+} are the dopants widely studied, Mg^{2+} promotes angiogenesis, Sr^{2+} enhances osteogenesis, and Si^{4+} induces angiogenesis and has been shown to play a key role in mineralization processes. The clinical confirmation that silicon-doped calcium phosphates play an important role in the formation of bone and cartilage systems has also generated a lot of interest. The osteoinductive properties of ceramics can be synergistically enhanced by the combination of dopants. The crystalline structures of HAp have highly exchangeable nature which can serve as a powerful design tool in bone tissue engineering.

11.2.1.2 Osteoconduction by Scaffold Structure

Osteoconduction means that new 'bone can grow onto a surface,' and this is a highly desirable property for a synthetic bone graft substitute as shown in Fig. 11.2. For an ideal scaffold, the diameter of macrospores should be in the range of 150–500 μm and it should exhibit 60–80 % interconnected porosity. This structure is similar to that of open cell or cellular ceramics.

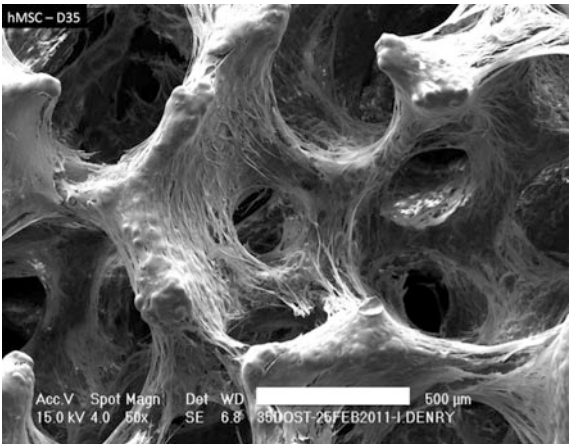

Fig. 11.2 Colonization of glass-ceramic scaffold by mesenchymal stem cells (Isabelle et al. 2016)

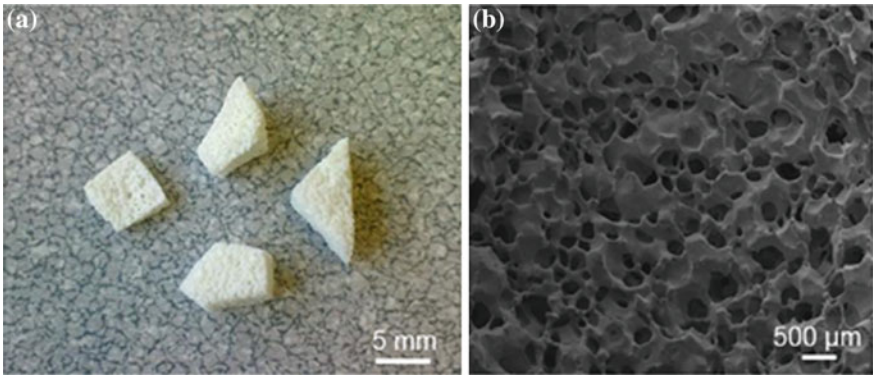

Fig. 11.3 **a** Scaffolds of different shapes and sizes produced by shaping the starting polymeric template (Vitale-Brovarone et al. 2009). **b** 3-D microstructure of highly interconnected porous network of foam-like scaffolds (Renghini et al. 2013)

Porous ceramics compared to cellular have interconnected porous network. Scaffold with open cell structure is most widely prepared by replication technique, in which polymer foam is coated with well-dispersed ceramic slurry. The coated foam is then slowly dried and burned out, leading to an open cell ceramic construct. The polymer is selected based on its modulus of elasticity, which dictates its reproducibility, and it must also burn out with minimal residue. This technique has been successfully used in the processing of bioglasses as well as hydroxyapatite and combinations of hydroxyapatite and bioglass scaffolds Fig. 11.3. Gel casting, foaming, and addition of porogens are some other green fabrication techniques available for producing open cell ceramics. HAp inks have been successfully

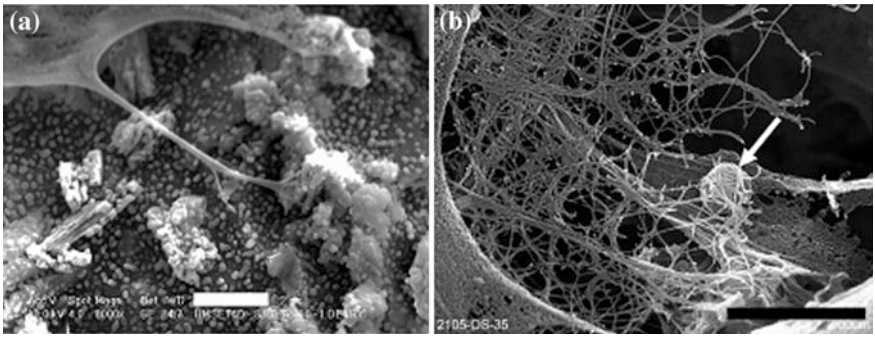

Fig. 11.4 **a** Interaction between fluorapatite glass-ceramic and a human mesenchymal stem cell (hMSC) after 4 days and **b** differentiation of hMSCs into an osteoblastic lineage after 35 days (Isabelle et al. 2016)

developed for the production of 3-D scaffolds by direct ink writing. Ceramic scaffold production techniques require firing or sintering in final step, which may result in shrinkage phase transformation, and crystallization. Bioactive glasses can play an effective role over here as their chemical composition can be tailored to widen the sintering window which allows full sintering to occur before the onset of crystallization.

11.2.1.3 Osseointegration

The formation of a chemical bond between bone and the surface of an implanted material without fibrous tissue formation is known as osseointegration. Although scaffolds are designed to biodegrade over time and promote osseointegration by microporosity, wettability, nanotopography, surface charge, and haemocompatibility studies have shown that each surface parameter plays an important role in implant/blood interactions.

Since wettability and surface charge are not easy to tailor in case of ceramic materials, microporosity and nanotopography can be maneuvered through thermal treatment by adjusting heating rate, temperature, or time duration. Figure 11.4 a, b clearly depict the interaction of submicrometer spherical crystals in fluorapatite glass-ceramic scaffold microstructure with human mesenchymal stem cell (hMSC) and further differentiation of hMSCs into osteoblast cells.

11.2.1.4 Role in Delivery of Osteogenic Factors

For successful bone regeneration, addition of cytokines, stem cells, growth factors, and anti-infectives is required. Ceramic scaffolds have the tendency to adsorb and concentrate angiogenic and osteoinductive molecules naturally present in the body

which enhance bone healing, and many of these molecules are therefore preloaded on ceramic scaffolds before implantation so as to improve the bone formation. Some of the osteogenic factors delivered by ceramic scaffolds for dental and orthopedic application include platelet-derived growth factor (PDGF-BB), bone morphogenetic proteins (e.g., BMP-2 and BMP-7), human growth hormone (hGH), platelet-rich plasma (PRP), transforming growth factor beta-3 (TGF-3), and fibroblast growth factor-2 (FGF-2). The role of an efficient delivery system is important as it controls the release of growth factor at a low dose locally in a controlled manner within the wound site. Osteogenic molecules are added to ceramic scaffolds after the final thermal treatment or sintering, so as to avoid any damage to biological activity by the heat. The technique of coating growth factor over scaffold surface is now preferred over simple adsorption for combining growth factors with scaffold as in later phenomenon there is a burst release. The biological effects of growth factors strongly depend upon the release kinetics, and consistent release is much required. Some workers have encapsulated the growth factor inside a polymer, which is then applied as a coating over the ceramic scaffold so as to optimize the delivery of growth factor. The application of a polymer as an outer layer, which does not damage the biological activity of the growth factors, can improve the ability of ceramic scaffold to act as an osteogenic drug delivery vehicle as well as a scaffold.

11.3 Different Scaffold Materials for Drug Delivery

11.3.1 Composite Scaffolds

Gentile and coworkers synthesized composite shell scaffolds, using bioactive glass and commercial hydroxyapatite coated with bioresorbable gelatin, incorporated with drug-loaded polymer nanoparticles so as to mimic the natural bone structure and to obtain a controlled in vitro release of indomethacin (IDMC). The composite scaffold fabricated from HAp BGCaM (70 wt% BGCa/Mix and 30 wt% HAp powders) based on protocols specified by Bellucci and coworkers was obtained by mixing glass powders with grain size below 45 μm, with proper amounts of commercial HA powders. For drug delivery, the sintered porous scaffolds were impregnated with 5 wt% drug (IDMC) loaded in polymer nanoparticles followed by surface coating of scaffold with gelatin. The presence of a polymeric coating slowed the drug release (up to 7 days), by entrapping IDMC delivered by nanoparticles in the gelatin swollen network. Results of MTT test to evaluate cell viability and ALP (alkaline phosphatase) activity on all prepared scaffolds showed an increase of cell viability along the cell incubation period. Cell adhesion, in particular, did not show any significant differences among samples after 24-h incubation. The in vitro drug release tests showed a 65–70 % release of IDMC during the first week of incubation, which is effective in preventing postoperative

infections and inflammation after scaffold implantation in vivo. The bone-forming osteoblast-like cells on the functionalized composite scaffolds assessed by ALP tests indicated that drug-loaded polymeric nanoparticles did not affect the ALP activity of the osteoblasts. However, according to Idowu and coworkers, there is an increase in stiffness due to the scaffold mineral content, which modulates cell interaction with the substrate, and this is an important feature for osteoblast differentiation. This work indicates that biomimetic coated composite scaffolds having desired porosity, pore size, and mechanical properties can be promising candidates for bone tissue regeneration and having therapeutic potential.

11.3.2 Polymer-Based Scaffold

Polymers like polylactides and polylactones are biodegradable and biocompatible and can be tuned easily which makes them suitable for tissue engineering. The materials like poly(L-lactide) (PLLA), poly(ε-caprolactone) (PCL), and poly (L-lactide/ε-caprolactone) (PLCL) with 90 % porosity have been investigated as scaffold materials. Researchers are working on these bioresorbable polymers incorporated with inorganic bioactive particles (hydroxyapatite or bioglass) for in vitro study of the cytocompatibility and adhesion of adipose-derived stem cells (ADSCs) and their effect on the mechanical properties. Incorporation of hydroxyapatite or bioglass particles (Fig. 11.5a, b) imparts stiffness to a soft polymer matrix, thus improving their mechanical properties. In the case of bioactive ceramics, major focus has been on bone repair, and more work needs to be done regarding their application in the regeneration of soft tissues. Regeneration of soft tissues requires soft biomaterials having elastomeric behavior; for this reason, we need to study the combinations of thermoplastic materials with bioactive ceramics, with a typical behavior which ranges from glassy to elastomeric state, and matching with most of the mechanical properties found in real body tissues.

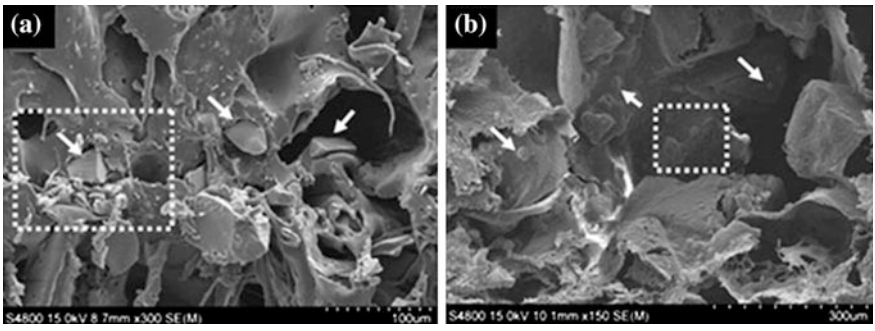

Fig. 11.5 **a** Microstructure of highly porous PLCL scaffold filled with bioglass particles (**b**) highly porous PLLA scaffold filled with hydroxyapatite particles (Larrañaga et al. 2014)

Polymer scaffolds with highly porous structure and well-interconnected pores are suitable for tissue engineering application, and the only drawback is reduction in the mechanical properties due to the presence of pores. Gibson–Ashby approach was best fit for predicting a relation between the porosity and the Young's modulus, and based on the literature reports, results for PLLA and PCL samples are similar to those for trabecular bone, indicating that both PLLA and PCL could be suitable for bone tissue engineering applications.

Whereas PLCL scaffolds incorporated with bioglass or hydroxyapatite reveal high elastic recovery capacity along with ability to withstand high deformation at break, which makes them suitable for soft tissue engineering applications, where the main requirement is elastomeric behavior of materials. The incorporated bioglass can promote angiogenesis and neocartilage formation, thus promoting bioactive behavior in PLCL scaffolds for regeneration of soft tissues.

Primary cultures of human adipose-derived stem cells (ADSCs) seeded on porous scaffolds and non-porous films have been studied for their adhesion and morphology. As shown in Fig. 11.6, both porous and non-porous samples show

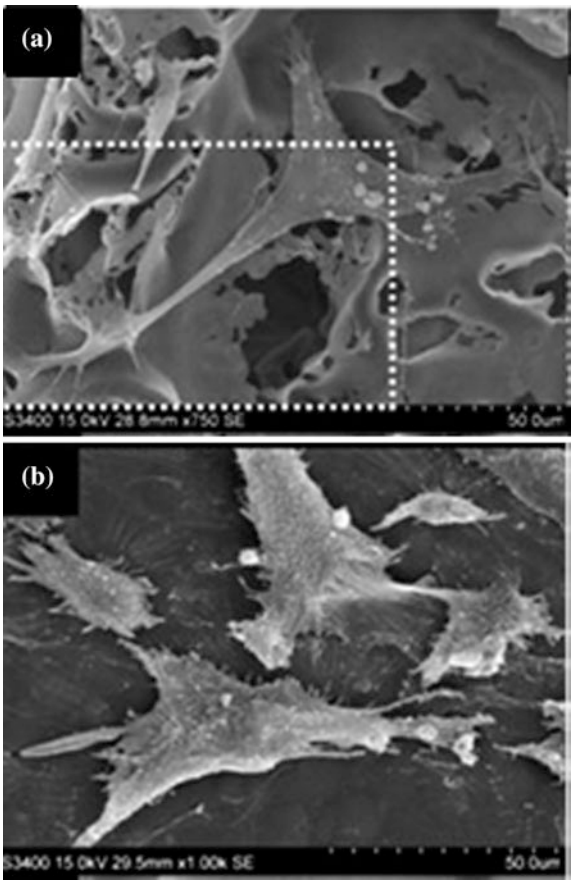

Fig. 11.6 ADSCs seeded on **a** porous PCL scaffold and **b** non-porous PLLA (Larrañaga et al. 2014)

excellent adhesion of the ADSCs. Results from MTT assays indicate no cytotoxicity of the studied materials for ADSCs. These results demonstrate that the polymeric materials can be used in scaffold fabrication, which makes them suitable candidates for their application in tissue engineering.

11.3.3 Bioactive Glass Scaffold

Silicate glass-ceramics and bioactive glasses are a special subgroup of bioceramics, as they are highly bioactive and have the ability to stimulate new bone formation by activating genes in osteoblast cells. Application of bioactive glass material as a drug delivery system is being studied more in detail now, as previous studies by Yagmurlu and coworkers and Zhang and coworkers mainly focused on biopolymers and reported the inability of polymer material in chemical bonding with bone, making them unsuitable for bone repair. Many researchers are working on mesoporous glass materials as a drug delivery system, new formulations of bioactive glass as porous scaffolds for drug delivery and their ability to treat infections in vitro are being assessed.

11.3.3.1 In Vitro Drug Release Studies

The drug release mechanism and kinetics, for glass scaffolds in different dissolution mediums has been studied by fitting the release data in Higuchi (Eq. 11.1), Hixson–Crowell (Eq. 11.2), and Korsmeyer–Peppas (Eq. 11.3) models shown below:

$$A_t = k_{\mathrm{H}} t^{0.5} \tag{11.1}$$

$$(AR_t)^{1/3} = k_{\mathrm{HC}} t \tag{11.2}$$

$$(A_t / A\infty) = k_{\mathrm{KP}} t^n \tag{11.3}$$

where A_t represents the amount of drug released at time t; the amount of unreleased drug at time t is denoted by AR_t; at time ∞, the amount of drug released is denoted by $A\infty$; and the release constants for the Higuchi, Hixson–Crowell, and Korsmeyer–Peppas models are k_{H}, k_{HC}, and k_{KP}, respectively. In Eq. 11.3, 'n' represents the exponent indicative of the release mechanism.

A high silica content up to 60 mol% in addition to high sodium and calcium contents and also high CaO/P_2O_5 ratio promote bioactivity in glass. Considering, the biological point of view, magnesium content in glass works to bind calcium and fluorine for bone building. Some researchers have also used zinc in glass compositions, as it can enhance protein synthesis in the bone tissues, promote bone formation, and has the ability to modify bioactivity.

11.3.3.2 Drug Delivery System

A bioceramic scaffold can accommodate drug molecules in four different states and act more like a reservoir. A large number of drug molecules are attached to the exterior surface of the bioactive glass scaffold, and still, a greater chunk of drug molecules exist in three different states trapped in the pore channels. Some drug molecules occupy the pore channel openings, and rest of them exist in the pore channels where they may or may not be bonded to the pore wall surface. When scaffolds are loaded by immersing them in drug solution and applying negative pressure, drug molecules get attached to the pore channels and the surface. There is also a possibility that drug molecules containing highly electronegative atoms/groups, such as OH^-, F^-, and N^{3-}, could form hydrogen bonds with the P–OH and Si–OH groups at pore wall surface or inside the scaffold. This facilitates the quick release of the drug molecules adhered to the surface compared to those inside the pore channels which will be released in a controlled manner, as the drug has to diffuse through the channel. It has already been mentioned that coating the scaffolds could significantly subdue burst release, and chitosan being antibacterial and antifungal with wound-healing ability is a natural polymer and it is biocompatible, biodegradable, non-toxic, and bioresorbable, which makes it desirable coating material.

11.4 Dental Materials

Bioactive glasses (BGs) are widely used for the treatment of various bone diseases, and now, they are also finding application as dental materials. Alveolar bone loss can occur in a way similar to normal bone, which motivates various research groups to study bioactive glass for use in local dentistry. Suitable BGs along with anti-osteoporotic drug, which would favor apatite (HAp, hydroxyapatite) formation and enhance the bioactivity of BG, are being studied.

There are reports which have investigated the application of bioactive glass in combination with bisphosphonates during surgery as a filling material of bone defect. Rosenqvist et al. (2013) proposed that bisphosphonates promote the beneficial effect of bioactive glass on bone. Studies suggest that when bioactive glass is used in combination with clodronate for dental application to treat periodontitis, there is an apparently strong interaction between the two resulting in an enhanced ion exchange and formation of apatite layer, HAp on the surface of the bioactive glass. The level of bioactivity of BG and amount of HAp formation depend on the particle size of the BAG and the amount of clodronate used.

11.4.1 Treatment of Incipient Enamel Eroded Lesions

Worldwide, large numbers of people are affected by dental caries, caused by acid released from fermentation of dietary sugars by plaque bacteria. This causes demineralization of enamel due to undersaturation of plaque fluids and saliva with regard to hydroxyapatite constituents. Such enamel lesions can be remineralized naturally at a slow rate or by using remineralizing agents, such as calcium phosphate, Na_2F, and phosphorus subject to condition that there is no further sugar challenge. Highly organized hierarchical microstructure consisting of carbonated hydroxyapatite nanocrystals, having thickness of 20–25 nm and width of 50–70 nm, imparts high strength and extreme hardness to dental enamel. Bakry and coworkers used a paste composed of 45S5 bioglass and phosphoric acid for treating early human dental enamel caries and lesions. The most popular bioglass 45S5 synthesized by Hench has weight composition as follows: 45 % SiO_2, 24.5 % Na_2O, 24.5 % CaO, and 6 % P_2O_5; it has the potential to act as bioactive implant material that can stimulate bone repair. When immersed in body fluids, it has the ability to deposit a layer of hydroxyl carbonate apatite on the surface of the glass. It has unique ability to bond with bone as well soft connective tissues and has many similarities to hard tissues found in oral and body environment. Mixing of 45S5 bioglass powder with the aqueous solution of 50 % phosphoric acid leaches out sodium, phosphate, and calcium crystals out of the bioglass into the aqueous acidic media. On the other hand, when enamel comes in contact with acidic gel, it releases calcium and phosphate ions. Finally, phosphate ions released from enamel and 45S5 bioglass react with calcium ions to form acidic calcium phosphate salts (i.e., brushite, $CaHPO_4 \cdot 2H_2O$) which precipitates on top of the enamel surface as shown in Fig. 11.7. Recent studies have reported that a paste consisting of Bioglass 45S5 and 50 % phosphoric acid has the potential to block dentinal tubule orifices by forming an 'interaction layer'; thus, it can be a potential candidate for treating dentin hypersensitivity lesions.

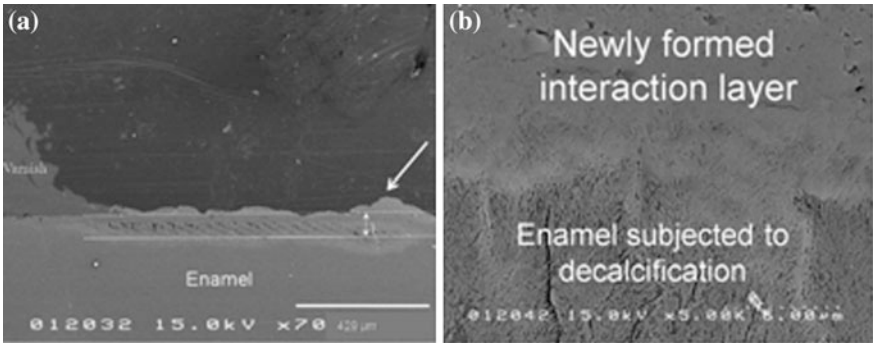

Fig. 11.7 **a** Interaction layer formation above the decalcified enamel (marked with *white arrow*) and **b** interface of the newly formed interaction layer at high magnification (Bakry et al. 2014)

11.5 Bioactive Glasses in Ophthalmology

Since 1970 when Hench demonstrated bioglasses can bond to bone and stimulate new bone growth, various glass materials have been extensively investigated, worldwide by several researchers for orthopedic and dental applications. The other attractive features of glasses and glass-ceramics such as transparency to visible light, biocompatibility, and relative ease of processing, along with the ability to stimulate tissue regeneration and cell activity, have made them suitable for use in ocular surgery Table 11.1. S53P4 glass with weight composition 53 % SiO_2, 23 % Na_2O, 20 % CaO, and 4 % P_2O_5 has recently been reported for the repair of orbital bone fractures [110–112]. Kinnunen and coworkers used melt-derived S53P4 glass for the repair of orbital floor defects after trauma and none of the patients showed evidence of implant-related postoperative complications and their clinical outcomes were better than those who received conventional cartilage grafts.

Aitasalo and coworkers studied S53P4 glass implants in 36 patients, there was no foreign body reaction in the bone or soft tissue, and no implant displacement/extrusion, infection or hemorrhage of implant after 1 year; tomographic scans revealed new bone growth around the implanted bioactive glass.

Table 11.1 Role of bioactive glasses in ophthalmology (Baino et al. 2014)

Type of device and glass	Type of host	Application	Outcome
Porous skirt, bioactive glass	In vitro tests with cells	Keratoprosthesis	Positive results with keratocytes
Disk, bioactive glass-ceramic	Animal	Keratoprosthesis	Material found unsuitable after testing in rabbits
Titanium coated with bioactive A/W glass-ceramic	Animal	Keratoprosthesis	Tested in rabbits, titanium coated with glass ceramic, used to fix prosthesis to the host corneal tissue
Bioverit I and II, bioactive glass	Animal	Keratoprosthesis	Tested as materials for the porous skirt in rabbits
Ceravital, bioactive glass	Human	Keratoprosthesis	Poor resorption, unsuitable for use
Porous sphere, glass-ceramic	Animal	Orbital implant	Tested in rabbits
Aesthetic shells, glass	Human	Ocular prosthesis	Unsuitable and replaced by PMMA for making artificial eyes
Transparent lens (optical core)	Human	Keratoprosthesis	Used in ‘champagne cork’ prosthesis
Glass plates, S53P4 glass	Human	Orbital floor repair	Slow resorption
Hollow sphere glass	Human	Orbital implant	Used in nineteenth century now declared unsuitable

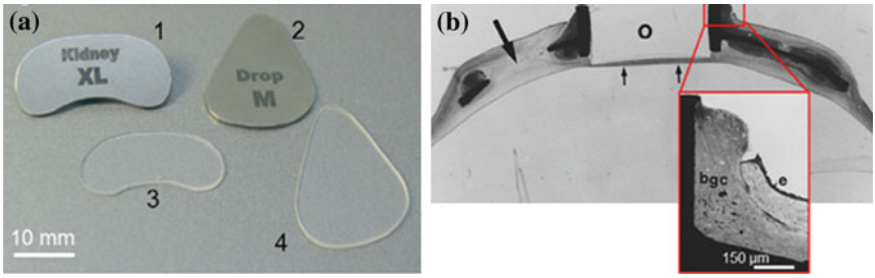

Fig. 11.8 **a** Bioactive glass plates (objects *3* and *4*) and stainless steel templates (Peltola et al. 2008) and **b** eye with a keratoprosthesis supported by bioactive glass-ceramic-coated titanium flange (Linnola et al. 1996)

Peltola and coworkers showed the results for S53P4 glass used for orbital floor reconstruction using stainless steel templates for choosing the correct glass plate which can fit in the surrounding orbital bone anatomy and defect margins with maximum accuracy (Fig. 11.8a, b). In Fig. 11.8b, the intact aspect of the cornea below the optic 'O' is marked by a small arrow and the hole in the left half of the supporting flange is shown by the larger arrow. The inset picture shows tight contact between the corneal matrix tissue and the glass-ceramic coating, and the area marked 'e' is corneal epithelium, which shows no ingrowth but has attached to the bioactive glass-ceramic (BGC) coating on the part supporting the optic.

At the end of 2 years, there was new bone formation on glass surfaces with no signs of implant-related infection, extrusion, or displacement, and no foreign body reaction was observed. It highlights that bioglass S53P4 plates can be promising and reliable solution for orbital floor reconstruction as it is bioactive, biocompatible, and slowly biodegradable. High-quality aesthetic and functional results can be achieved if glass implant shape and size are carefully selected.

Bioglass and bioglass ceramics also find application in the fabrication of artificial corneas. Till date, glass has been used to fabricate the optical part of the keratoprosthesis (the transparent core); however, in recent times, some bioglass compositions have been tested for the fabrication of the prosthetic skirt so as to improve the incorporation of the device in the host tissue. Initiation of the biocolonization of the porous skirt requires it to allow the penetration of biological fluids from the host tissue, and for this reason, the skirt materials should preferably be hydrophilic in nature Chirila. Bioglasses and bioglass ceramics can successfully fulfill this criterion, as they can expose hydroxyl groups after contact with aqueous solutions and have good water wettability.

Keratoprostheses can suffer from infections, extrusion of the prosthesis, or growth of retroprosthetic membrane and secondary glaucoma if there is an ingrowth of corneal or conjunctival epithelium into the anterior chamber. Linnola and coworkers suggested an apatite/wollastonite (A/W) glass-ceramic coating to solve this issue. The challenge was to find a material that could fasten the prosthesis to the corneal tissue before the epithelium grows inward and thus prevent many of these

complications. Prostheses having an optic part made up of transparent PMMA supported by a flange consisting of bare or A/W glass-ceramic-coated titanium was tested in vivo. When implanted in rabbit corneas, these prevented any significant ingrowth of epithelium in areas of the A/W glass-ceramic-coated and bare titanium prostheses; hence, glass-ceramic coatings were proposed as an effective strategy to hinder the corneal epithelium ingrowth.

11.6 Bioactive Glasses for Bone Tissue Repair

Currently, there is a steady increase in clinical need of biomaterials, which promote the bone growth and regeneration. A biomaterial should exhibit bioactive nature along with an optimum degradation rate without causing any inflammation during the replacement of normal tissue. Many efforts have been made to recreate normal functions of the skeletal system with a variety of bone substitute materials. However, still there are some limitations, and it is very important for a biomaterial to elicit favorable response from cells or tissues in a particular situation. Before any implantable device is put into application, it must be proven safe through in vitro and in vivo experiments followed by clinical trials. Considering the need for bone replacement materials, bioactive and biocompatible glasses have been developed, and they can control gene transcription through glass dissolution products and also get resorbed by a combination of cellular mechanism and chemical dissolution which leads to bone generation. Although in recent years research in the field of bioactive glasses is on the rise, still only a few bioactive glasses are available as implant materials for clinical use. At present, silica-based melt-quenched glass compositions are being studied in orthopedics and dentistry for hard tissue repair as substitutes for bone graft. Considering the scaffold formation for tissue engineering application, high Na_2O content in bioglass is a drawback, and for excellent bioactive properties, controlled chemical dissolution, high mechanical strength, and good sintering ability, there is a need to design low-alkali-content silicate glasses. For applications in human biomedicine, bioactive glasses in the $CaO–MgO–SiO_2$ system have been doped with P_2O_5, Na_2O, CaF_2, and B_2O_3 so as to obtain Q_2 (Si)-dominated silicate glass network. Investigations of these glasses reported stimulation of osteoblast proliferation in cell culture medium, remarkable biomineralization upon immersion in simulated body fluid, and devoid of toxicity or any other negative effects in the functionality of cells. Treatment of jawbone defects of adult humans in the age-group 19–60 years was carried out over a period of 8 months using these bioactive glass (BG) particulates Fig. 11.9. The clinical trials showed interesting results, and the glass demonstrated homeostatic effect as it formed a cohesive mass with patient's blood. However, there is a need to improve grafting procedure by using bioactive glass or biodegradable organic composites so as to avoid undesired loss of glass particulates.

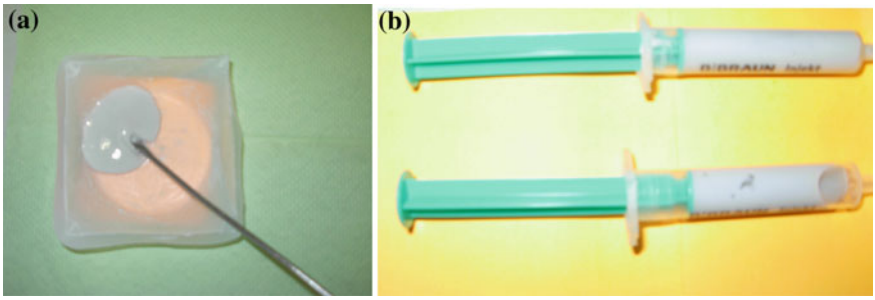

Fig. 11.9 **a** A paste based on BG glass particulates and organic carrier; **b** experimental paste-filled standard syringes (Tulyaganova et al. 2015)

11.7 Bone Tissue Regeneration

Solgel-prepared bioactive glasses emerged in early 1990s; contrary to melt-derived bioglasses, these did not require high processing temperatures, and in addition, they have high surface area and porosity aiding higher bone-bonding rates along with very good resorption/degradation properties. Recent investigations on quaternary bioglass system SiO_2–CaO–P_2O_5–MgO have revealed their ability to support the growth of human fetal osteoblastic cells (hFOB). Also for the in vivo goat model, this material proved to be compatible in segmental defects as well non-toxic in nature. It is important for a solgel system to have antimicrobial properties, and it was observed that the SiO_2–CaO–P_2O_5 solgel systems yielded antimicrobial activity against Escherichia coli on addition of Ag_2O (up to 3 wt%), without causing any damage to its bioactivity. These results motivated researchers to extend this work to Streptococcus mutants in the system Na_2O–CaO–SiO_2 and also to solgel glass scaffolds for bone tissue engineering applications.

Another important application of bioactive solgel glasses is providing bioactivity to other functional biomaterials through the preparation of composites and intimate mixtures. For example, it provides in vitro bioactivity to acrylic polymers, which act as drug delivery systems. Some researchers have also tried to osteointegrate magnetic seeds with the help of SiO_2–CaO–P_2O_5-based solgel. Bioceramics with magnetic iron oxides having low bioactivity are used to synthesize these materials. Magnetic glass ceramics provide magnetic hyperthermia treatment against potential metastasis and strengthen the bone site after surgery extirpation. Osteointegration of permanent and biocompatible implants is facilitated by the inclusion of solgel glasses, and they also improve the bioactive behavior of biocompatible bioceramics such as hydroxyapatite.

The solgel processing occurs around room temperature, thus facilitating the incorporation of biological and organic molecules in the network and even cells within silica matrices. This technique has helped in the generation of highly ordered mesoporous materials, which have tremendous potential as drug delivery systems. Mesoporous bioactive glass (MBG) preparation involves gelling, drying, and

surfactant calcinations. These glasses have higher surface area and porosity compared to conventional solgel glass; therefore, they show fast and intense bioactivity. MBG-58 is a mesoporous glass having composition $58SiO_2$–$36CaO$–$6P_2O_6$, and it exhibits intense Ca^{2+} release when soaked in SBF, resulting in a growth of amorphous calcium phosphate (ACP) onto the MBG surface. This material exhibits a CaP–OCP–HCA maturation, and it has mineral maturation almost equal to that in vertebrates.

Mesoporous glass with high silica content, MBG-85 (3-D cubic one) $85SiO_2$–$9CaO$–$6P_2O_6$, develops a nanocrystalline CHA within 1 h after being soaked in SBF, and it adsorbs large amount of serum proteins when it comes in contact with vitronectine- and fibronectine-containing medium. MBGs during biodegradation release products, which are biocompatible and in vitro test have indicated favorable behavior of fibroblasts, osteoblast, and lymphocytes in the presence of these materials. The most interesting application for these mesoporous bioglasses is preparation of scaffolds for bone tissue engineering or in situ implantation.

11.8 Bioactive Glasses in Prosthetic Joints

Each year, worldwide, more than a million prosthetic knee and hip replacement surgeries are performed and bacterial infection is a serious complication of these articular prosthetic implants *Staphylococcus aureus* (*S. aureus*) or coagulase-negative Staphylococci bacterium is generally responsible for these infections in implants. They get firmly attached to implant surface and produce biofilms containing complex communities of bacteria, which can resist antimicrobial agents and host defenses. Poly (methyl methacrylate) (PMMA) cement has been widely used for treating these bacterial infections in orthopedic surgery. The cement acts as a carrier material for the antibiotics. However, it is non-biodegradable, and a secondary bacterial infection can occur over its surface. During the last three decades, lots of efforts have been made to replace PMMA bone cement with an alternate antibiotic delivery vehicle. Currently, some of the materials being used or under development for treating bacterial infection in orthopedic surgery are given in Table 11.2. Biodegradable materials considerably reduce the risk of secondary infection. Considering the recent advances, bioactive glass-based materials are showing promising results as drug delivery agents for inhibiting the bacterial growth in vitro and in extermination of osteomyelitis in animals and humans. Studies on bioactive glass S53P4 have shown it is antibacterial and very effective in the treatment of bone infection in humans without any toxic reactions. It can act as bone substitute in the treatment of osteomyelitis because of its osteoconductive and bone-bonding properties. Other bioactive glasses being developed have yet to show antibacterial properties comparable to those of S53P4. In a rabbit tibial model, in vivo titanium implants coated with the Ag-doped borate bioactive glass was successful in fracture fixation and removal of infection.

Table 11.2 Different categories of biomaterials for treating bacterial infections in orthopedic surgery (Rahaman et al. 2014)

Type of delivery material	Method of antibiotic release	Degradation/resorption of deliver material
Delivery materials under research and development		
Polyesters: (PGA, PLA, PLGA)	Properties of polymers can be used to tailor the antibiotic release, which occurs by either diffusion through bulk-eroding delivery material or erosion of delivery material or both	Biodegradable
Bioactive glass: Particles or porous scaffolds	Ions release by dissolution of the glass or diffuse through the glass	Glass degrades resulting in the formation of hydroxyapatite
Composites: Composed of polymer matrix or calcium phosphate cement incorporated with bioactive glass particles	Dissolution of the matrix releases the antibiotics, or they diffuse through the biodegradable matrix	Matrix degrades, whereas glass converts to hydroxyapatite after degradation
Calcium phosphates: (a) Calcium phosphate cement	The degradation of cement is slow, and antibiotic diffuses out through it	Slow resorption
(b) Porous hydroxyapatite or β-tricalcium phosphate granules and scaffolds	Desorption from the surface of scaffolds and impregnated granules	Rapid resorption of β-TCP and slow resorption of HA
Carrier materials in clinical use		
Poly(methyl methacrylate) (PMMA) cement beads	Antibiotic incorporated within the beads diffuses out; the entire antibiotic is not released	Due to their non-biodegradable nature, they shall be removed upon completion of treatment
Calcium sulfate beads or pellets	Degradation of calcium sulfate is faster; less antibiotic release and loss of strength; dissolution of beads/pellets impregnated with antibiotic	Biodegradable/resorbable
Collagen sponge	Combination of mechanisms decides the release of impregnated antibiotic; rapid release kinetics of antibiotic; effective while using adjunct to the systemic antibiotic treatment	Biodegradable

A composite consisting of calcium phosphate cement-bonded bioactive glass particles was loaded with vancomycin for the treatment of Methicillin resistant Staphylococcus aureus (MRSA)-induced osteomyelitis in rabbit tibiae. After

completion of 8 weeks, borate bioactive glass composites loaded with vancomycin-cured infection in most of the rabbits; however, postimplantation eradication of the osteomyelitis was significantly lower. An important finding of the study was that pellets of the vancomycin-loaded borate bioactive glass composites showed a compressive strength of 21 ± 4 MPa after immersion for 30 min in SBF compared to 5 ± 2 MPa for $CaSO_4$ beads loaded with vancomycin. This proved borate bioactive glass composites are better than $CaSO_4$ in the treatment of infections in load-bearing defects in trabecular bone.

Although borate bioactive glass composites loaded with antibiotic are proving effective in treating osteomyelitis and bone regeneration in animal models, they still can be toxic for cells in the event of high boron concentration. In small animal models, borate bioactive glasses have shown biocompatibility which indicates that glass is non-toxic in vivo. Composites made up of chitosan-bonded borate glass have shown tendency better than $CaSO_4$ in reconstituting the defect and promoting new bone formation. For the treatment of MRSA-induced osteomyelitis in rabbit tibiae, pellets of the chitosan-bonded borate bioactive glass composites and $CaSO_4$ were loaded with teicoplanin and implanted for 12 weeks. During the evaluation of the specimen, it was observed that borate bioactive glass composite converted to HAp and integrated with the host bone after the 12-week implantation, which promoted new bone formation. However, there was a complete degradation of $CaSO_4$ beads with little new bone formation in the defects. Borate bioactive glass composites were successful in regenerating the bone at the infected sites; in the future, they could eliminate the need for bone reconstruction.

11.9 Future Scope

Over the last 40 years, a lot of investigations have been done on silicate bioactive glasses based on the 45S5. In recent studies, borate- and borosilicate-based bioactive glasses have been explored for application in tissue engineering. Studies have shown that borate glasses are non-toxic in small animals; this has sufficiently addressed the concerns about the toxicity of borate glasses for cells and tissues. In vivo studies for small animals have been successful so far to eradicate bone infection and to stimulate new bone formation, and still, considerable research and development are required before they can be clinically used to reconstruct large bone defects resulting from infected prosthetic implants. Bioactive glasses support osteogenesis, there are reports which show their proangiogenic potential, and it implies future bioactive glass application for soft tissue repair. Although brittle in nature, bioactive glass has the ability to undergo controlled degradation and convert to hydroxyapatite-like material, which helps it in bonding firmly to hard and soft tissues. During degradation, it releases ions, which have beneficial effect on angiogenesis and osteogenesis, and recent studies predict they might have beneficial effect on chondrogenesis. Future research is now focused over finding new mechanisms to limit the brittleness of bioactive glasses by improving their design

and processing parameters so as to have maximum gains from their favorable properties especially in case of their application as load-bearing bones. Limitations concerning mechanical properties have always been an issue with melt-derived and sol-gel glasses, for this reason organic–inorganic hybrid materials that exhibit bioactive behavior are being explored as an attempt to overcome this drawback. The future hybrid implants must be primarily developed for bone tissue regeneration instead of bone substitution, and more sophisticated systems can be developed controlling the implant–tissue interface. Finally, development of osteoregenerative bioglasses through the control of their chemical composition, mesoporosity, and macroporosity or by means of osteogenic agent incorporation should play a main role in biomaterial science.

Bibliography

Denrya I, Liisa T (2016) Kuhn design and characterization of calcium phosphate ceramic scaffolds for bone tissue engineering. Dent Mater 32:43–53

Bakry AS, Takahashid H, Otsukie M, Tagamie J (2014) Evaluation of new treatment for incipient enamel demineralization using 45S5 bioglass. Oper Dent Mater 30:314–320

Tulyaganova DU, Reddy AA, Siegelc R, Ionescud E, Riedeld R, Ferreira JMF (2015) Synthesis and in vitro bioactivity assessment of injectable bioglass_organic pastes for bone tissue repair. Ceram Int 41:9373–9382

Renghini C, Giuliani A, Mazzoni S, Brun F, Larsson E, Baino F et al (2013) Microstructural characterization and in vitro bioactivity of porous glass ceramic scaffolds for bone regeneration by synchrotron radiation X-ray microtomography. J Eur Ceram Soc 33:1553–1565

Rahaman MN et al (2014) Mater Sci Eng C 41:224–231

Larrañaga A, Diamanti E, Rubio E, Palomares T, Alonso-Varona A, Aldazabal P, Martin FJ, Sarasua JR (2014) A study of themechanical properties and cytocompatibility of lactide and caprolactone based scaffolds filled with inorganic bioactive particles. Mater Sci Eng C 42: 451–460

Gentile P, Bellucci D, Sola A, Matt C, Cannillo V, Ciardelli G (2015) Composite scaffolds for controlled drug release: role of the polyurethane nanoparticles on the physical properties andcell behavior. J Mech Behav Biomater 44:53–60

Chan BP, Leong KW (2008) Scaffolding in tissue engineering: general approaches and tissue-specific considerations. Eur Spine J 17(4):467–479

Bellucci D, Cannillo V, Sola A (2011a) Calcium and potassium addition to facilitate the sintering of bioactive glasses. Mater Lett 65:1825–1827

Bellucci D, Sola A, Cannillo V, (2012b) Low temperature sintering of innovative bioactive glasses. J Am Ceram Soc 95:1313–1319

Bellucci D, Sola A, Cannillo V (2013a) Bioactive glass-based composites for the production of dense sintered bodies and porous scaffolds. Mater Sci Eng C Mater Biol Appl 33:2138–2151

Idowu B, Cama G, Deb S, DiSilvio L (2014) In vitro osteoinductive potential of porous monetite for bone tissue engineering. J Tissue Eng 5:1–14 (2041731414536572)

Blaker J, Maquet V, Jérome R, Boccaccini AR, Nazhat SN (2005) Mechanical properties of highly porous PDLLA/bioglass composite foams as scaffolds for bone tissue engineering. Acta Biomater 1:643–652

Soundrapandiana C, Mahatob A, Kundu B, Datta S, Sac B, Basu D (2014) Development and effect of different bioactive silicate glass scaffolds: invitro evaluation for use as a bone drug delivery system. J Mech Behav Biomater 40:1–1 2

Rosenqvist K, Airaksinen S, Vehkamäki M, Juppo AM (2014) Evaluating optimal combination of clodronate and bioactive glass for dental application. Int J Pharm 468:112–120

Bakry AS, Takahashi H, Otsuki M, Sadr A, Yamashita K, Tagami J (2011) CO_2 laser improves 45S5 bioglass interaction withdentin. J Dent Res 90(2):246–250

Baino F, Brovarone CV (2014) Bioceramics in ophthalmology. Acta Biomater 10:3372–3397

Kinnunen I, Aitasalo K, Pollonen M, Varpula M (2000) Reconstruction of orbital fractures using bioactive glass. J Craniomaxollofac Surg 28:229–234

Peltola M, Kinnunen I, Aitasalo K (2008) Reconstruction of orbital wall defects with bioactive glass plates. J Oral Maxillofac Surg 66:639–646

Chirila TV (2001) An overview of the development of artificial corneas with porous skirts and the use of PHEMA for such an application. Biomaterials 22:3311–3317

Linnola RJ, Happonen RP, Andersson OH, Vedel EA, Yli-Urpo U, Krause U et al (1996) Titanium and bioactive glass-ceramic coated titanium as materials for keratoprosthesis. Exp Eye Res 63:471–478

Tulyaganov DU, Agathopoulos S, Valerio P, Balamurugan A, Saranti A, Karakassides MA, Ferreira JM (2011) Synthesis, bioactivity and preliminary biocompatibility studies of glasses in the system $CaO–MgO–SiO_2–Na_2O–P_2O_5–CaF_2$. J Mater Sci Mater Med 22:217–227

Tulyaganov DU, Makhkamov ME, Urazbaev A, Goel A, Ferreira JMF (2013) Synthesis, processing and characterization of a bioactive glass composition for bone regeneration. Ceram Int 39:2519–2526

Arcos D, Regí MV (2010) Sol–gel silica-based biomaterials and bone tissue regeneration. Acta Biomater 6:2874–2888

Bellantone M, Coleman NJ, Hench LL (2000) Bacteriostatic action of a novel four component bioactive glass. J Biomed Mater Res 51:484–490

Rezwan K, Chen QZ, Blaker J, Boccaccini AR (2006) Biodegradable and bioactive porous polymer/inorganic composite scaffolds for bone tissue engineering. Biomaterials 27:3413–3431

Fu Q, Saiz E, Rahaman MN, Tomsia AP (2011) Bioactive glass scaffolds for bone tissue engineering: state of the art and future perspectives. Mater Sci Eng C 31:1245–1256

Blaker J, Maquet V, Jérome R, Boccaccini AR, Nazhat SN (2005) Mechanical properties of highly porous PDLLA/bioglass composite foams as scaffolds for bone tissue engineering. Acta Biomater 1:643–652

Thomson RC, Yaszemski MJ, Power JM, Mikos AG (1998) Hydroxyapatite fiber reinforced poly (α-hydroxy ester) foams for bone regeneration. Biomaterials 19:1935–1943

Roether JA, Boccaccini AR, Hench LL, Maquet V, Gautier S, Jérome R (2002) Development and in vitro characterization of novel bioresorbable and bioactive composite materials based on polylactide foams and bioglassfor tissue engineering applications. Biomaterials 23:3871–3878

Maquet V, Boccaccini AR, Pravata L, Notingher I, Jérome R (2004) Porous poly (α-hydroxyacid)/bioglass composite scaffolds for bone tissue engineering I: preparation and in vitro characterization. Biomaterials 25:4185–4194

Chen JP, Chang YS (2011) Preparation and characterization of composite nanofibers of polycaprolactone and nanohydroxyapatite for osteogenic differentiationof mesenchymal stem cells. Colloids Surf B: Biointerfaces 86:169–175

Kim SS, Park MS, Jeon O, Choi CY, Kim BS (2006) Poly(lactide-co-glycolide)/hydroxyapatite composite scaffolds for bone tissue engineering. Biomaterials 27:1399–1409

Kim HW, Lee HH, Chun GS (2008) Bioactivity and osteoblast responses of novel biomedical nanocomposites of bioactive glass nanofiber filled poly(lactic acid) J Biomed Mater Res Part A 85:651–663

Gerhardt LC, Boccaccini AR (2010) Bioactive glass and glass-ceramic scaffolds for bone tissue engineering. Materials 3:3867–3910

Rahaman MN, Day DE, Bal BS, Fu Q, Jung SB, Bonewald LF, Tomsia AP (2011) Bioactive glass in tissue engineering. Acta Biomater 7:2355–2373

Lee J, Guarino V, Gloria A, Ambrosio L, Tae G, Kim et al YH (2010) Regeneration of Achilles' tendon: the role of dynamic stimulation for enhanced cell proliferation and mechanical properties. J Biomater Sci 21:1173–1190

Jeong SI, Kim SH, Kim YH, Jung Y, Kwon JH, Kim et al BS (2004) Manufacture of elastic biodegradable PLCL scaffolds for mechano-active vascular tissue engineering. J Biomater Sci Polym Ed 15:645–660

Calori GM, Mazza E, Colombo M, Ripamonti C (2011) The use of bone-graft substitutes in large bone defects: any specific needs? Injury—Int J Care Inj 42:56–63

Albrektsson T, Johansson C. Osteoinduction (2001) Osteoconduction and osseointegration. Eur Spine J 10:96–101

Minardi S, Corradetti B, Taraballi F et al (2015) Evaluation of the osteoinductive potential of a bio-inspired scaffold mimicking the osteogenic niche for bone augmentation. Biomaterials 62:128–137

Wang L, Zhang B, Bao C et al (2014) Ectopic osteoid and bone formation by three calcium-phosphate ceramics in rats, rabbits and dogs. PLoS One 9(9):e107044

Daculsi G, Fellah BH, Miramond T (2014) The essential role of calcium phosphate bioceramics in bone regeneration. In: BenNissan B (ed), Advances in calcium phosphate biomaterials, Springer-Verlag, Berlin, pp 71–96

Landi E, Logroscino G, Proietti L et al (2008) Biomimetic Mg-substituted hydroxyapatite: from synthesis to in vivo behaviour. J Mater Sci Mater Med 19(1):239–247

Maier JAM, Bernardini D, Rayssiguier Y, Mazur A (2004) High concentrations of magnesium modulate vascular endothelial cell behaviour in vitro. Biochim Biophys Acta—Mol Basis Dis 1689(1):6–12

Marie PJ, Ammann P, Boivin G, Rey C (2001) Mechanisms of action and therapeutic potential of strontium in bone. Calcif Tissue Int 69(3):121–129

Marquis P, Roux C, Diaz-Curiel M et al (2007) Long-term beneficial effects of strontium ranelate on the quality of life in patients with vertebral osteoporosis (Soti study). Calcif Tissue Int 80:137–138

Ortolani S, Vai S (2006) Strontium ranelate: an increased bone quality leading to vertebral antifracture efficacy at all stages. Bone 38(2):19–22

Pors Nielsen S (2004) The biological role of strontium. Bone 35(3):583–588

Li H, Chang J (2013) Bioactive silicate materials stimulate angiogenesis in fibroblast and endothelial cell co-culture system through paracrine effect. Acta Biomater 9(6):6981–6991

Pietak AM, Reid JW, Stott MJ, Sayer M (2007) Silicon substitution in the calcium phosphate bioceramics. Biomaterials 28(28):4023–4032

Schwartzwalder K, Somers AV (1963) Inventors. General motors corporation, assignee. Method of making porous ceramic articles. US patent 3,090,094

Chang BS, Lee CK, Hong KS et al (2000) Osteoconduction at porous hydroxyapatite with various pore configurations. Biomaterials 21(12):1291–1298

Saiz E, Gremillard L, Menendez G et al (2007) Preparation of porous hydroxyapatite scaffolds. Mater Sci Eng C-Biomim Supramol Syst 27(3):546–550

Tian JT, Tian JM (2001) Preparation of porous hydroxyapatite. J Mater Sci 36(12):3061–3066

Padilla S, Sanchez-Salcedo S, Vallet-Regi M (2007) Bioactive glass as precursor of designed-architecture scaffolds for tissue engineering. J Biomed Mater Res Part A 81(1): 224–232

Santos JD, Knowles JC, Reis RL, Monteiro FJ, Hastings GW (1994) Microstructural characterization of glass-reinforced hydroxyapatite composites. Biomaterials 15(1):5–10

Colombo P, Hellmann JR (2002) Ceramic foams from preceramic polymers. Mater Res Innov 6(5–6):260–272

Shepherd JH, Best SM (2011) Calcium phosphate scaffolds for bone repair. JOM 63(4):83–92

Lewis JA, Smay JE (2005) Three-dimensional periodic structures. Cell Ceram Struct Manuf Properties Appl pp 87–100

Lewis JA, Smay JE, Stuecker J, Cesarano III J (2006) Direct ink writing of three-dimensional ceramic structures. J Am Ceram Soc 89(12):3599–3609

Simon JL, Michna S, Lewis JA et al (2007) In vivo bone response to 3D periodic hydroxyapatite scaffolds assembled by direct ink writing. J Biomed Mater Res Part A 83(3):747–758

Hutmacher DW (2000) Scaffolds in tissue engineering bone and cartilage. Biomaterials 21 (24):2529–2543

Descamps M, Duhoo T, Monchau F et al (2008) Manufacture of macroporous beta-tricalcium phosphate bioceramics. J Eur Ceram Soc 28(1):149–157

Descamps M, Richart O, Hardouin P, Hornez JC, Leriche A (2008) Synthesis of macroporous beta-tricalcium phosphate with controlled porous architectural. Ceram Int 34(5):1131–1137

Michna S, Wu W, Lewis JA (2005) Concentrated hydroxyapatite inks for direct-write assembly of 3-D periodic scaffolds. Biomaterials 26(28):5632–5639

Denry I, Holloway JA (2014) Low temperature sintering of fluorapatite glass-ceramics. Dental Mater 30(2):112–121

Fu Q, Saiz E, Rahaman MN, Tomsia AP (2011) Bioactive glass scaffolds for bone tissue engineering: state of the art and future perspectives. Mater Sci Eng C—Mater Biol Appl 31(7): 1245–1256

Barrere F, Mahmood TA, de Groot K, van Blitterswijk CA (2008) Advanced biomaterials for skeletal tissue regeneration: Instructive and smart functions. Mater Sci Eng R Rep 59(1–6):38–71

Barrere F, van Blitterswijk CA, de Groot K (2006) Bone regeneration: molecular and cellular interactions with calcium phosphate ceramics. Int J Nanomed 1(3):317–332

Davies JE (2007) Bone bonding at natural and biomaterial surfaces. Biomaterials 28(34):5058–5067

Woodard JR, Hilldore AJ, Lan SK et al (2007) The mechanical properties and osteoconductivity of hydroxyapatite bone scaffolds with multi-scale porosity. Biomaterials 28(1):45–54

Diaz-Rodriguez P, Gonzalez P, Serra J, Landin M (2014) Key parameters in blood-surface interactions of 3D bioinspired ceramic materials. Mater Sci Eng C-Mater Biol Appl 41: 232–239

Seyfert UT, Biehl V, Schenk J (2002) In vitro hemocompatibility testing of biomaterials according to the ISO 10993–4. Biomol Eng 19(2–6):91–96

ISO (2002) Standard 10993-4 Biological evaluation of medical devices—part 4: selection of tests for interactions with blood

LeGeros RZ (2002) Properties of osteoconductive biomaterials: calcium phosphates. Clin Orthop Relat Res 395:81–98

Autefage H, Briand-Mesange F, Cazalbou S et al (2009) Adsorption and release of BMP-2 on nanocrystalline apatite-coated and uncoated hydroxyapatite/beta-tricalcium phosphate porous ceramics. J Biomed Mater Res B Appl Biomater 91(2):706–715

Liu Y, de Groot K, Hunziker EB (2005) BMP-2 liberated from biomimetic implant coatings induces and sustains direct ossification in an ectopic rat model. Bone 36(5):745–757

Roldan JC, Detsch R, Schaefer S et al (2010) Bone formation and degradation of a highly porous biphasic calcium phosphate ceramic in presence of BMP-7, VEGF and mesenchymal stem cells in an ectopic mouse model. J Craniomaxillofac Surg 38(6):423–430

Guicheux J, Gauthier O, Aguado E et al (1998) Human growth hormone locally released in bone sites by calcium-phosphate biomaterial stimulates ceramic bone substitution without systemic effects: a rabbit study. J Bone Miner Res 13(4):739–748

Thomson RC, Yaszemski MJ, Power JM, Mikos AG (1998) Hydroxyapatite fiber reinforced poly (α-hydroxy ester) foams for bone regeneration. Biomaterials 19:1935–1943.

Lee J, Guarino V, Gloria A, Ambrosio L, Tae G, Kim YH (2010) Regeneration of Achilles' tendon: the role of dynamic stimulation for enhanced cell proliferation and mechanical properties. J Biomater Sci 21:1173–1190

Jeong SI, Kim SH, Kim YH, Jung Y, Kwon JH, Kim BS et al (2004) Manufacture of elastic biodegradable PLCL scaffolds for mechano-active vascular tissue engineering. J Biomater Sci Polym Ed 15:645–660

Yunos DM, Bretcanu O, Boccaccini A (2008) Polymer–bioceramic composites for tissue engineering scaffolds. J Mater Sci Mater Med 43:4433–4442

Yagmurlu MF, Korkusuz F, Guersel I, Korkusuz P, Ors U, Hasirci V (1999) Sulbactam-cefoperazone polyhydroxybutyrate-co-hydroxyvalerate (PHBV) local antibiotic delivery

system: in vivo effectiveness and biocompatibility in the treatment of implant-related experimental osteomyelitis. J Biomed Mater Res 46:494–503

Zhang X, Wyss UP, Pichora D, GoosenMF (1994a) Biodegradable controlled antibiotic release devices for osteomyelitis: optimization of release properties.J Pharm Pharmacol 46:718–724

Zhang X, Wyss UP, Pichora D, Goosen MFA (1994b) Amechanistic study of antibiotic release from biodegradable poly (d, 1-lactide)cylinders. J Control Release 31:129–144

Domingues ZR, Cortés, ME, Gomes TA, Diniz HF, Freitas CS, Gomes JB, Faria AMC, Sinisterra RD (2004) Bioactive glass as a drug delivery system of tetracycline and tetracycline associated with β-cyclodextrin. Biomaterials 25:327–333

Czarnobaj K (2008) Preparation and characterization of silica xerogels as carriers for drugs. Drug Deliv 15:485–492

Merchant HA, Shoaib HM, Tazeen J, Yousuf RI (2006) Once- daily tablet formulation and in vitro release evaluation of cefpodoxime using hydroxypropyl methylcellulose: a technical note. AAPS PharmSciTech 7:78

Bang H-G, Kim S-J, Park S-Y (2008) Biocompatibilityandthe physicalpropertiesofbio-glassceramicsinthe Na_2O–CaO–SiO_2–P_2O_5 system withCaF_2 and MgF_2 additives. J Ceram Proc Res 9:588–590

Aina V, Malavasi G, Fiorio Pla A, Munaron L, Morterra C (2009) Zinc-containing bioactive glasses: surface reactivity and behaviour towards endothelial cells. Acta Biomater 5:1211–1222

Ma ZJ, Yamaguchi M (2001) Role of endogenous zinc in the enhancement of bone protein synthesis associated with bone growth of newborn rats. J Bone Miner Metab 19:38–44

Xia W, Chang J (2006) Well-ordered mesoporous bioactive glasses (MBG): a promising bioactive drug delivery system. J Control Release 110:522–530

Kundu B, Soundrapandian C, Nandi SK, Mukherjee P, Dandapat N, Roy S, Datta BK, Mandal TK, Basu D, Bhattacharya RN (2010b) Development of new localized drug delivery system based on ceftriaxone-sulbactam composite drug impregnated porous hydroxyapatite: a systematic approach for in vitro and in vivo animal trial. Pharm Res 27:1659–1676.

Noble L, Gray AI, Sadiq L, Uchegbu IF (1999) A non-covalently cross-linked chitosan based hydrogel. Int J Pharm 192:173–182

Rossi S, Marciello M, Sandri G, Bonferoni MC, Ferrari F, Caramella C (2008) Chitosan ascorbate: a chitosan salt with improved penetration enhancement properties. Pharm Dev Technol 13:513–521

Ubaidulla U, Khar RK, Ahmad FJ, Tripathi P (2009) Optimization of chitosan succinate and chitosan phthalate microspheres for oral delivery of insulin using response surface methodology. Pharm Dev Technol 14:96–105

Baldrick P (2010) The safety of chitosan as a pharmaceutical excipient. Regul Toxicol Pharmacol 56:290–299

Kong M, Chen XG, Liu CS, Liu CG, Meng XH, Yu le J (2008) Antibacterial mechanism of chitosan microspheres in a solid dispersing system against E. coli. Colloids Surf 65:197–202

Park Y, Kim MH, Park SC, Cheong H, Jang MK, Nah JW, Hahm KS (2008) Investigation of the anti fungal activity and mechanism of action of LMWS-chitosan. J Microbiol Biotechnol 18:1729–1734

Rosenqvist K, Airaksinen S, Fraser SJ, Gordon KC, Juppo AM (2013) Interaction of bioactive glass with clodronate. Int J Pharm 452:102–107

Cross KJ, Huq NL, Stanton DP, Sum M, Reynolds EC (2004) NMR studies of a novel calcium, phosphate and fluoride delivery vehicle-alpha(S1)-casein(59-79) by stabilized amorphous calcium fluoride phosphate nanocomplexes. Biomaterials 25(20):5061–5069

Borges BC, de Souza Borges J, de Araujo LS, Machado CT, DosSantos AJ, de Assuncao Pinheiro IV (2011) Update on nonsurgical, ultraconservative approaches to treat effectivelynon-cavitated caries lesions in permanent teeth. Eur J Dent 5(2):229–236

Fan Y, Sun Z, Moradian-Oldak J (2009) Controlled remineralizationof enamel in the presence of amelogenin and fluoride. Biomaterials 30(4):478–483

Nganga S, Zhang D, Moritz N, Vallittu PK, Hupa L (2012) Multi-layerporous fiber-reinforced composites for implants: in vitrocalcium phosphate formation in the presence of bioactiveglass. Dent Mater 28(11):1134–1145

Hench LL (1991) Bioceramics—from concept to clinic. J Am Ceram Soc 74(7):1487–1510

Bunker BC, Tallant DR, Headley TJ, Turner GL, Kirkpatrick RJ (1988) The structure of leached sodium borosilicate glass. Phys Chem Glasses 29(3):106–120

Hench LL, Splinter RJ, Allen WC, Greenlee TK (1972) Bonding mechanisms at the interface of ceramic prosthetic materials. J Biomed Mater Res 2:117–141

Aitasalo K, Kinnunen I, Palmgren J, Varpula M (2001) Repair of orbital floor fractures with bioactive glass implants. J Oral Maxillofac Surg 59:1390–1396

Tesavibul P, Felzmann R, Gruber S, Liska R, Thompson I, Boccaccini AR et al (2012) Processing of 45S5 Bioglass—by lithography-based additive manufacturing. Mater Lett 74:81–84

Vitale-Brovarone C, Baino F, Verné E (2009) High strength bioactive glass-ceramic scaffolds for bone regeneration. J Mater Sci Mater Med 20:643–653

Izquierdo-Barba I, Salinas AJ, Vallet-Regí M (2013) Bioactive glasses: from macro tonano. Int J Appl Glass Sci 4:149–161

Merceron C, Vinatier C, Clouet J, Colliec-Jouault S, Weiss P, Guicheux J (2008) Adipose-derived mesenchymal stem cells and biomaterials for cartilage tissue engineering. Joint Bone Spine. Rev Rhum 75:672–674

Schneider OD, Weber F, Brunner TJ, Loher S, Ehrbar M, Schmidlin PR, Stark WJ (2009) Invivo and in vitro evaluation of flexible, cottonwool-like nano composites as bone substitute material for complex defects. Acta Biomater 5:1775–1784

Weiss P, Layrolle P, Clergeau LP, Enckel B, Pilet P, Amouriq Y, Daculsi G, Giumelli B (2007) The safety and efficacy of an injectable bone substitute in dental sockets demonstrated in a human clinical trial. Biomaterials 28:3295–3305

Williams DF (2008) On the mechanisms of biocompatibility. Biomaterials 29:2941–2953

Ducheyne P (2011) Biomaterials. In: Ducheyne P (ed), Comprehensive biomaterials, Elsevier, Oxford, pp 1–4

Hench LL, Day DE, Höland W, Rheinberger VM (2010) Glassand medicine. Int J Appl Glass Sci 1:104–117

Hoppe A, Guldal NS, Boccaccini AR (2011) A review of the biological response toionic dissolution products from bioactive glasses and glass–ceramics. Biomaterials 32:2757–2774

Xynos ID, Edgar AJ, Lee DK, Larry B, Hench L, Polak JM (2001) Gene-expression profiling of human osteoblasts following treatment with the ionic productsof Bioglass 45S5 dissolution. J Biomed Mater Res 55:151–157

Hench LL (1994) Bioactive ceramics: theory and clinical applications, Oxford

Agathopoulos S, Tulyaganov DU, Valerio P, Ferreira JM (200) A new model formulation of the SiO_2–$Al2O_3$–$B2O_3$–MgO–CaO–Na_2O–F glass–ceramics. Biomaterials 26:2255–2264

Kansal I, Tulyaganov DU, Goel A, Pascual MJ, Ferreira JMF(2010) Structural analysis and thermal behavior of diopside–fluorapatite–wollas-tonite-based glasses and glass–ceramics. Acta Biomater 6:4380–4388

Tulyaganov DU, Agathopoulos S, Ventura JM, Karakassides MA, Fabrichnaya O, Ferreira JMF (2006) Synthesis of glass–ceramics in the CaO–MgO–SiO_2 system with B_2O_3, P_2O_5, Na_2O and CaF_2 additives. J Eur Ceram Soc 26:1463–1471

Agathopoulos S, Tulyaganov DU, Ventura JMG, Kannan S, Saranti A, Karakassides MA, Ferreira JMF (2006) Structural analysis and devitrification of glasses based on the CaO–MgO–SiO_2 system with B_2O_3, Na_2O, CaF_2 and P2O5 additives. J Non Cryst Solids 352:322–328

Rezwan K, Chen QZ, Blaker JJ, Boccaccini AR (2006) Biodegradable and bioactive porous polymer/inorganic composite scaffolds for bone tissue engineering. Biomaterials 27:3413–3431

Saboori A, Rabiee M, Mutarzadeh F, Sheikhi M, Tahriri M, Karimi M (2009) Synthesis, characterizations and in vitro bioactivity of sol–gel-derived SiO_2–CaO–P_2O_5–MgO bioglass. Mater Sci Eng C 29:335–340

Catauro M, Raucci MG, De Gaetano F, Marotta A (2004) Antibacterial and bioactive silver-containing Na_2O–CaO–$2SiO_2$ glass prepared by sol–gel method. J Mater Sci Mater Med 15:831–837

Ragel CV, Vallet-Regí M (2000) In vitro bioactivity and gentamicin release from glass–polymer-antibiotic composites. J Biomed Mater Res 51:424–429

Arcos D, Ragel CV, Vallet-Regi M (2001) Bioactivity in glass/PMMA composites used as drug delivery system. Biomaterials 22:701–708

Ladrón de Guevara S, Ragel CV, Vallet-Regí M (2003) Bioactive glass–polymer materials for controlled release of ibuprofen. Biomaterials 24:4037–4043

Arcos D, Peña J, Vallet-Regí M (2003) Influence of a SiO_2–CaO–P_2O_5 sol–gel on the bioactivity and controlled release of a ceramic/polymer/antibiotic mixed materials. Chem Mater 15:4132–4138

Arcos D, del Real RP, Vallet-Regí M (2002) A novel bioactive and magnetic biphasic material. Biomaterials 23:2151–2158

Ruiz E, Serrano MC, Arcos D, Vallet-Regí M (2006) Glass–glass ceramic thermoseeds for hyperthermic treatment of bone tumours. J Biomed Mater Res 79:533–543

Serrano MC, Portoles MT, Pagani R, Sáez de Guinoa J, Ruíz-Fernández E, Arcos D et al (2008) In vitro positive biocompatibility evaluation of glass–glass ceramic thermoseeds for hyperthermic treatment of bone tumours. Tissue Eng 14:617–627

Ragel CV, Vallet-Regí M, Rodríguez-Lorenzo LM (2002) Preparation and in vitro bioactivity of hydroxyapatite/solgel-glass biphasic material. Biomaterials 23:1865–1872

Vallet-Regí M, Rámila A, Padilla S, Muñoz B (2003) Bioactive glasses as accelerators of the apatites bioactivity. J Biomed Mater Res 66:580–585

Campostrini R, Carturam G (1996) Immobilisation of plant cells in hybrid sol–gel material. J Sol-Gel Sci Technol 7:87–97

Pope Edgard JA (1997) Bioartificial organs I: silica gel encapsulated pancreatic islets for the treatment of diabetes mellitus. J Sol-Gel Sci Technol 8:635–639

Vallet-Regí M (2006) Revisiting ceramics for medical applications. Dalton Trans 44:5211–5220

Vallet-Regí M, Balas F, Arcos D (2007) Mesoporous materials for drug delivery. Angew Chem Int Ed 46:7548–7558

López-Noriega A, Arcos D, Izquierdo-Barba I, Sakamoto Y, Terasaki O, Vallet- Regí M (2006) Ordered mesoporous bioactive glasses for bone tissue regeneration. Chem Mater 18:3137–3144

Izquierdo-Barba I, Arcos D, Sakamoto Y, Terasaki O, López-Noriega A, Vallet- Regí M (2008) High-performance mesoporous bioceramics mimicking bone mineralization. Chem Mater 20:3191–3198

Leonova E, Izquierdo-Barba I, Arcos D, López-Noriega A, Hedi N, Vallet-Regí M et al (2008) Multinuclear solid-state NMR studies of ordered mesoporous bioactive glasses. J Phys Chem C 112:5552–5562

Garcia A, Cicuendez M, Izquierdo-Barba I, Arcos D, Vallet-Regí M (2009) Essential role of calcium phosphate heterogeneities in 2D-hexagonal and 3D-cubic SiO_2–CaO–P_2O_5 mesoporous bioactive glasses. Chem Mater 21:5474–5484

Donlan RM, Costerton JW (2002) Clin Microbiol Rev 15:167

Hanssen AD (2005) Clin Orthop Relat Res P 437

Brown RF, Rahaman MN, Dwilewicz AB, Huang W, Day DE, Li Y, Bal BS (2009) J Biomed Mater Res A 88:392

Zhang D, Munukka E, Hupa L, Ylänen HO, Viljanen MK, Hupa M (2007) Key Eng Mater 173:330–332

Fu Q, Huang W, Jia W, Rahaman MN, Liu X, Tomsia AP (2011) Tissue Eng A 17:3077

Kaur G, Pandey OP, Singh K, Homa D, Scott B, Pickrell G (2013) A review of bioactive glasses: their structure, properties, fabrication, and apatite formation. J Biomed Mater Res A 102: 254–274

Kaur G, Sharma P, Kumar V, Singh K (2012) Assesment of *in-vitro* bioactivity of SiO_2-BaO-ZnO-B_2O_3-Al_2O_3 glasses: an optico-analytical approach. Mater Sci Engg C 32(7):1941–1947

Kaur G, Pickrell G, Sriranganathan N, Kumar V, Homa D (2016) Review and the state of the art: Sol-gel or melt quenched bioactive glasses for tissue engineering. J Biomed Mater Res: B Appl Biomater 104(6):1248–1275. doi:10.1002/jbm.b.33443

Kaur G, Pickrell G, Pandey OP, Singh K, Chudasama BN, Kumar V (2016) Combined and individual Doxorubicin/Vancomycin drug loading, release kinetics and apatite formation for the CaO-CuO-P_2O_5- SiO_2- B_2O_3 mesoporous glasses. RSC Adv 6:51046–51056

Kaur G, Pickrell G, Kimsawatde G, Allbee H, Sriranganathan N (2014) Synthesis, cytotoxicity, and hydroxypatite formation in 27-Tris-SBF for sol-gel based CaO-P_2O_5-SiO_2-B_2O_3-ZnO bioactive glasses. Sci Rep. doi:10.1038/srep04392

Index

G. Kaur, *Bioactive Glasses*, Series in BioEngineering,
DOI 10.1007/978-3-319-45716-1